JAERI-M
88-069

ANNUAL REPORT OF THE NAKA FUSION RESEARCH ESTABLISHMENT FOR THE PERIOD OF APRIL 1, 1986 TO MARCH 31, 1987

March 1988

Naka Fusion Research Establishment

日本原子力研究所
Japan Atomic Energy Research Institute

JAERI-Mレポートは，日本原子力研究所が不定期に公刊している研究報告書です。
入手の問合わせは，日本原子力研究所技術情報部情報資料課（〒319-11茨城県那珂郡東海村）あて，お申しこしください。なお，このほかに財団法人原子力弘済会資料センター（〒319-11 茨城県那珂郡東海村日本原子力研究所内）で複写による実費頒布をおこなっております。

JAERI-M reports are issued irregularly.
Inquiries about availability of the reports should be addressed to Information Division Department of Technical Information, Japan Atomic Energy Research Institute, Tokai-mura, Naka-gun, Ibaraki-ken 319-11, Japan.

編集兼発行　日本原子力研究所
印　　刷　いばらき印刷㈱

JAERI-M 88-069

Annual Report of the Naka Fusion Research Establishment for the period of April 1, 1986 to March 31, 1987

Naka Fusion Research Establishment
Japan Atomic Energy Research Institute
Naka-machi, Naka-gun, Ibaraki-ken

(Received February 19, 1988)

Research and development activities of the Naka Fusion Research Establishment for the period of April 1986 to March 1987 are described.

In JT-60 experiments, second phase experiments with Joule-heated plasma were performed in June and July 1986 and plasma discharge of $\bar{n}\tau_E = 3.1\times10^{-19}$ $m^{-3}\cdot sec$ with very low impurities was achieved in divertor configuration.

Initial heating experiments in JT-60 were performed for August-November 1986 and January-March 1987. The highest central ion temperature in hydrogen discharge of 130 Million degrees, and plasma current drive by RF of 2 MA were achieved.

The integrated performance tests of the NBI and RF heating systems of JT-60 were completed in July 1986, and the initial heating experiments were followed and finished in March 1987. By these tests and experiments, performance of the heating systems were confirmed. Especially, the excellent completeness of the NBI system was demonstrated by achieving the full rating injection of 75keV-20MW within three months in the initial heating experiments.

The diagnostic system of JT-60 was successfully operated and produced large amount of valuable data. In JT-60 operation during this fiscal year, plasma discharges of 1,854 shots were made in total. Among them, 389 shots with NBI, 341 shots with RF, and 241 shots with NBI plus RF were included. The JT-60 operation was carried out by two shifts.

In Doublet III experiments, H-mode discharges with good confinement characteristics were achieved in divertor configurations.

Discussions on the next step device program were completed by Nuclear Fusion Council and Atomic Energy Commission of Japan, and the fundamental plane was determined. Based on this plan, design studies

of the next step device were proceeded. Examinations of the next machine concept with negative ion NBI and fundamental concept on safety were progressed.

In JFT-2M non-circular plasma experiments remarkable results on H-mode discharge were achieved. That is, not only in divertor configuration but also even in limiter configuration and not only by NBI heating but also by ICRF heating, the H-mode discharges were obtained. Moreover, by combined with pellet injection, almost twice confinement time of Joule-heated plasma was achieved.

In theoretical and computational plasma studies, analyses of high-β by second stability region, non-linear behavior of plasma configuration due to resistive instability, transport by ballooning mode, repple diffusion of α-particle, current drive by fast wave, were advanced.

As to studies on plasma-surface interaction, production of C_2 and C_3 compounds by chemical sputtering was confiremed and compared with the case of diamond-like surface. Data were accumurated for carbonization coating.

A ceramic rotor driven by gas turbine was tested and successfully demonstrated continuous operation at 30,000 rpm in magnetic field. This is noteworthy. Based on the results, a proto-type ceramic rotor turbomolecular pump of pumping speed 0.1 m^3/s was manufactured and completed at the end of this fiscal year.

Excellent achievement was the success of negative ion beam extraction of 21keV-1.26A from an volume production type negative ion source. The modification and movement of the test stand ITS-2 from Tokai to Naka site were completed.

Development of 120GHz Gyrotron was started focusing its objective to high power output.

Experiments of IEA Large Coil Task were successfully carried out at ORNL. That is, in six coil test the rating magnetic field was produced on Japanese coil successfully in Aug. 1986, and by the end of this fiscal year simulations rating operation of six coils and pulsed field experiments were carried out. In next fiscal year, extended test is planned and then the ten years plan of LCT will be closed.

The demonstration poloidal coil program was progressed: Fablications of the coil and cryogenic system, and extention works of power supply from JT-60 proceeded.

Cold tests of Tritium Process Laboratory (TPL) were continued.

Design and fabrication of the first phase experimental apparatus of TPL proceeded.

Keywords: Annual Report, Fusion Research, JT-60, Plasma, Divertor, Current Drive, Confinement, Heating Experiment, Diagnostics, NBI, RF, Doublet III, H-mode, JFT-2M, Theory, Vacuum, Gyrotron, LCT, FER, TPL, JAERI

那珂研究所年報（昭和61年度）

日本原子力研究所那珂研究所

（1988年2月19日受理）

昭和61年度における那珂研究所の研究開発の現状と成果について述べる。

ＪＴ－60の実験は本格的な段階に入った。第Ⅱ期ジュール実験（61年6月～7月）においては，ダイバータ配位により不純物の少ないターゲット・プラズマを生成し，平均密度×閉じ込め時間（$\bar{n}\tau_E$）では，$3.1\times10^{19}m^{-3}\cdot s$というＪＥＴの最高値と並ぶ値を実現した。

加熱装置結合試験と並行して実施した初期加熱実験（NBI／RF）及び電流駆動実験（61年8月～11月，62年1月～3月）においては，中心イオン温度約1億3千万度以上という水素プラズマとしての最高値を記録するとともに，低域混成波により2ＭＡのプラズマ電流駆動に成功するなどの特記すべき成果を挙げた。

粒子入射（NBI）加熱装置及び高周波（ＲＦ）加熱装置については，総合調整試験を61年7月に終了，引続きプラズマとの結合試験（加熱装置結合試験）を実施し，本年度末に予定通りこれを完了して来年度早々の装置完成を迎えるばかりとなった

NBI装置では，試験開始後3ケ月にして75keV，20ＭＷの中性ビーム入射に成功するなど装置の完成度の高さが実証された。

計測システムが不断の調整・整備のもとに順調に稼動され，プラズマ諸量の詳細な計測・診断が可能となり，上記したような多くの顕著な成果をもたらした。とくに不純物の挙動についてＪＴ－60の優れたダイバータ特性が明らかにされた。

本年度においては，総計1,854ショットの実験運転を行ったが，うちNBI入射ショットは389ショット，ＲＦ入射ショットは341ショット，NBI×ＲＦ複合入射ショットは241ショトであった。

絶縁不良や真空リーク等修復に時間を要するトラブルの発生は担当者の努力により年度後半には激減し，稼動率は上昇してきた。ＪＴ－60実験運転は本年度からは2交替制により行われた。

ダブレットⅢ実験では，ダイバータ配位でのＨモードの実現に成功するなど閉じ込め特性の優れた高温高密度のプラズマが得られた。

原子力委員会・核融合会議における核融合次期計画に関する広汎な検討が終了し，次期大型装置計画の基本方針が策定された（61年10月）。この方針に基づいて，複数の設計オプションの

那珂研究所：〒311－01　茨城県那珂郡那珂町大字向山801－1

比較検討など，次期大型装置の基本設計開始に向けてその基本概念を固めるための設計・検討が進捗した。さらに，負イオン源による中性ビーム入射方式を用いた炉概念の検討，安全性に関する基本的な考え方の検討などが進展した。

61年7月開始したＪFT－2Mの非円形断面プラズマの実験で，今年度高効率閉込め放電（いわゆるHモード）に関する注目すべき成果を得た。すなわちダイバータ配位のみならずリミタ配位においても，NBI 加熱に限らずICRF 加熱によっても，質の差はあるもののHモードを実現した。さらにペレット入射と組合わせて，ジュール加熱時の2倍近い閉込め時間を達成した。

プラズマに関する理論的研究では，第2安定化領域による高ベータ化，抵抗性不安定によるプラズマ配位の非線形的振舞い，バルーニングモード乱流による輸送，α粒子のリップル拡散，速波による電流駆動等の解析に成果を得た。

黒鉛の化学スパッタリングによるC_2，C_3化合物の生成を確認した他，ダイヤモンド構造についても実験をして，黒鉛との比較を行った。炭素のその場コーティングに関しては，放電ガスの種類，基盤温度等を変えて実験データを蓄積した。

前年度試作したセラミックス回転体（ガスタービン駆動，ガスベアリング使用）について所定の高磁場中30,000rpm連続運転試験に成功したことは特筆すべき成果である。また，その成果に基づく排気速度0.1m^3／sのセラミックス製ターボ分子ポンプの試作品も年度末に完成した。

加熱技術については，まず体積生成型負イオン源を用いた1.26Ａ，21keVの負水素イオンビームの引出し実験の成功が特記される。なお，テストスタンドＩＴＳ－2の改造・那珂地区への移設も完了した。

目標を大電力化にしぼって120GH_Z帯ジャイロトロン開発を開始した。

ＩＥＡによる大型電導コイルの国際協力LCTの実験が順調に進められた。すなわち前年度開始された全数6個のコイルによる実験で61年8月末日本のコイル上で定格磁界（8Ｔ）の発生に成功，本年度末までに6個のコイルの同時定格運転，パルス磁界印加実験を終了した。次年度から拡張試験（extended test ）を行い協定調印以来10年に及ぶ計画を終了の予定である。実証ポロイダルコイルの計画も，コイル及び冷凍系の製作，電源（ＪＴ－60電源を利用）の整備を鋭意進めた。また極低温構造材料の開発・試験，液体ヘリウム用大容量循環ポンプ，減圧ポンプの試作に成果を得た。

トリチウムプロセス研究棟に関しては，内装設備のコールド試験を継続した。また，関連する許認可手続きを終えてトリチウムガスの購入手続きを行った。また，実験装置（第1期）の設計・製作も順調に進められた。

Contents

目　　次

I. PLASMA THEORY AND COMPUTATION

1. Introduction

During the period from April 1, 1986 to March 31, 1987, emphases of the theoretical works were put on the studies of (1) stability analyses in relation with anomalous transport in a tokamak, and analyses of RF current drive and heating, (2) MHD stability analyses concerning the limiting beta optimization and the disruptions, and (3) analyses of the burning plasma physics, such as the fusion reactivity enhancement and alpha particle behavior.

Transport analyses were carried out on the dissipative trapped ion mode and it was concluded that there were a variety of equilibria corresponding to the values of the plasma viscosity. The study of the RF current drive was carried out extensively on the dependence of the antenna phase on the global efficiency and gave a direction for the design of an experiment. The aim of the linear MHD stability analyses was to search for a high beta equilibrium, especially, in relation to the next generation tokamak such as INTOR. It was shown that the high beta equilibrium which partially entered into the second stability region of the ballooning mode instability was obtained by current profile optimization and conducting shell stabilization. Disruption study was continued and new disruption scenario based on the nonlinear free-boundary mode evolution was extensively analyzed. As for the analyses of the burning plasma physics the fusion reactivity enhancement by the deformation of the velocity space distribution due to the additional heating was calculated. Ripple loss process of the fusion alpha particles in the burning plasma was also studied on the basis of different models and the previous results were reconfirmed by the new analytical calculation. Some physics codes in the TRITON-II system were developed. Development and improvement of the supporting codes in the TRITON-II system were also continued.

2. Transport and Heating Studies

2.1 Introduction

Considering the importance of the dissipative trapped ion modes (DTIM) in a high-ion-temperature tokamak plasma realized by the recent high power NBI and/or RF heating experiments, we studied the nonlinear saturation of the DTIM on the basis of the model proposed by LaQuey et al.[1] By steady state operation of tokamak reactor with RF current drive the current profile is apt to become skin-like, which is, usually, believed unstable against tearing modes. An optimizing procedure for stability of tearing modes with skin current profile was devised and existence of a stable equilibrium with such a current profile was shown.

As for the analyses of RF heating and current drive, the effects of ion-tail formation on absorbed RF power and wave propagation were studied and antenna phase dependence of current drive efficiency by ICRF wave was investigated.

2.2 Transport

2.2.1 Non-linear saturation of dissipative trapped ion modes[2]

The dissipative trapped ion mode is a low-frequency electrostatic drift-wave-like mode propagating in the electron diamagnetic direction. This mode is destabilized by electron collision and stabilized by ion collision, as was first shown by Kadomtsev and Pogutse[3]. The Landau damping due to the circulating and trapped ions is effective for stabilization of the modes with short wavelength. Taking into account the E×B coupling energy transfer from unstable long wavelength modes to short wavelength modes stabilized by the ion Landau damping, LaQuey, Mahajan, Rutherford, and Tang(LMRT) found coherent satutated state composed of many Fourier modes by using a one dimensional nonlinear model and multi-scale length expansion.[1] Later, Cohen et al. concluded that the LMRT solution was unstable and a different solution with a stable two-mode state could be realized[4]. To reexamine the results of LaQuey et al. and Cohen et al. we studied the time dependent behavior of the LMRT model equation numerically and obtained the following results.

Though for some values of the viscosity parameter steady two-mode equilibria are realized as was shown by Cohen et al., there exists many kinds of different solutions for different values of the viscosity. For example, turbulent behavior was observed at low viscosity region but there exist multi-mode equilibria at middle viscosity region. In the two-mode equilirium case the fluctuating energy was larger by factor 3 than that in other cases, i.e., multi-mode equilibria, traveling, oscillating and turbulent states.

2.2.2 Stabilization of tokamak with skin current profile[5)]

Steady state operation of tokamak by RF current drive is believed to have many benefits for a commercial reactor. For the current drive scenarios of a normal current distribution peaked at the center, however, very low density operation of tokamaks is needed, which makes the fusion reactor unattractive as a power source because of the low power density and short energy confinement time. If we apply the RF current drive for a plasma with a higher density the current profile becomes skin-like (tubular) one. Usually such a current profile is believed unstable against the double tearing mode.

We analyzed the stability of the plasma with such a tubular current profile and by the following tailoring procedure of the current profile we showed that stable equilibria with the tubular profile could exist for a given q-profile. By paying attention to the fact that the resonant surface of the unstable mode with the poloidal mode number m and toroidal mode number n is just inside of the position of the jump of the current density[j], we move the position of the current jump outwards and get rid of the instability driving term [j]/(m-nq) outside the resonant surface. Repeating this procedure with keeping a total plasma current constant until all the m/n modes become stable, we can get a stable current profile for given q-surface.

2.3 Heating and current drive

2.3.1 Second cyclotron ICRF heating in a tokamak plasma

The ion-tail formation by the ICRF second cyclotron resonance heating was investigated by employing the realistic wave field in the tokamak plasma which was obtained from the wave-propagation analysis.[6)]

The quasi-linear diffusion coefficient was determined from the spatial structure of the electric field. Due to the Doppler-shift of the resonance condition, the diffusion coefficient has the structure in the velocity space depending on the antenna k_z spectrum and the perpendicular wave number. The ion distribution function and the resultant wave absorption are determined by solving the 2-D Fokker-Planck equation with an above diffusion coefficient. The spatial profile of the power absorption was obtained in the medium-size tokamak and an increase of the total antenna loading was observed. It is found that the power absorption strongly depends on the structure of the diffusion coefficient and is affected by the finite Larmor radius effect especially in the case of rather lower toroidal magnetic field machine such as JFT-2M.

2.3.2 Antenna phase dependence of global current-drive efficiency by ICRF wave[7)]

The analysis of the ICRF current-drive by using the mode-converted Ion-Bernstein wave is carried out in the medium size tokamak such as JFT-2M machine by combining the wave propagation analysis and the Fokker-Planck calculation. The phase dependence of the global current-drive efficiency η_G is investigated by changing the launching condition such as the total antenna number N and the antenna spacing Δz. With an increase of the phase difference between two adjacent antennas $\Delta\phi$, the total induced current rises up according to $I \sim k_z N^2/\Delta z \Delta\phi$ around $\Delta\phi=0$, where k_z is the dominantly excited toroidal wave number. It is found that when the wave propagation is dominated by the cavity resonance, η_G has a weak dependence on the antenna phase $\Delta\phi$. The maximum global efficiency does not strongly depend on the total antenna number if the antenna phase is well optimized. However, the driving efficiency is sensitive to the antenna spacing Δz. With increasing Δz away from the optimum spacing, η_G reduces significantly, because of counter current generation associated with the higher modes of the antenna spectrum.

References

1) LaQuey, R.E., Mahajan, S.M., Rutherford, P.H., Tang, W.M., Phys. Rev. Letters 34 (1975) 391.
2) Tuda, T., "Non-linear saturation of dissipative trapped ion modes", Proc. 1987 International Conf. on Plasma Physics, Kiev, Vol.1, p.246.
3) Kadomtsev, B.B., Pogutse, O.P., Sov. Phys. JETP 24 (1964) 1172.
4) Cohen, B.I., Krommes, J.A., Tang, W.M., Rosenbluth, M.N., Nucl. Fusion 16 (1976) 971.
5) Tuda, T., "Tubular operation of tokamak reactor", Proc. 14th European Conf. on Controlled Fusion and Plasma Phys.
6) Morishita, T., Fukuyama, A., Hamamatsu, K., Itoh, S-I., Itoh, K., "Analysis of the minority velocity distribution and the power deposition profile in the ICRF heating in tokamak", Institute for Fusion Theory (Hiroshima Univ.) Report, HIFT-124 (August 1986).
7) Kishimoto, Y., Hamamatsu, H., Fukuyama, A., Itoh, S-I., Itoh, K., Nucl. Fusion 27 (1987) 549.

3. MHD Stability Analyses

3.1 Introduction

The limiting beta value and disruption phenomena were extensively studied as in the previous fiscal year. Especially, high beta equilibria which partially entered into the second stability region were persued by optimizing the current profile against the ballooning mode and making use of the stabilization effect of the conducting wall against the external kink mode. As for the disruption phenomena new scenario of the major disruption was investigated in which the plasma column subject to the free-boundary kink mode with m/n=2/1 shrank to an equilibrium state with smaller cross section stable against the m/n=2/1 mode but unstable against the m/n=1/1 mode.

References

1) LaQuey, R.E., Mahajan, S.M., Rutherford, P.H., Tang, W.M., Phys. Rev. Letters 34 (1975) 391.
2) Tuda, T., "Non-linear saturation of dissipative trapped ion modes", Proc. 1987 International Conf. on Plasma Physics, Kiev, Vol.1, p.246.
3) Kadomtsev, B.B., Pogutse, O.P., Sov. Phys. JETP 24 (1964) 1172.
4) Cohen, B.I., Krommes, J.A., Tang, W.M., Rosenbluth, M.N., Nucl. Fusion 16 (1976) 971.
5) Tuda, T., "Tubular operation of tokamak reactor", Proc. 14th European Conf. on Controlled Fusion and Plasma Phys.
6) Morishita, T., Fukuyama, A., Hamamatsu, K., Itoh, S-I., Itoh, K., "Analysis of the minority velocity distribution and the power deposition profile in the ICRF heating in tokamak", Institute for Fusion Theory (Hiroshima Univ.) Report, HIFT-124 (August 1986).
7) Kishimoto, Y., Hamamatsu, H., Fukuyama, A., Itoh, S-I., Itoh, K., Nucl. Fusion 27 (1987) 549.

3. MHD Stability Analyses

3.1 Introduction

The limiting beta value and disruption phenomena were extensively studied as in the previous fiscal year. Especially, high beta equilibria which partially entered into the second stability region were persued by optimizing the current profile against the ballooning mode and making use of the stabilization effect of the conducting wall against the external kink mode. As for the disruption phenomena new scenario of the major disruption was investigated in which the plasma column subject to the free-boundary kink mode with m/n=2/1 shrank to an equilibrium state with smaller cross section stable against the m/n=2/1 mode but unstable against the m/n=1/1 mode.

3.2 Ideal MHD beta limit

3.2.1 Second stability access in a tokamak with conventional cross section[1,2)]

The scaling law of the beta limit of a tokamak with conventional (circular or dee shaped) cross section is approximately given by $\beta(\%)=gI_p(MA)/a(m)B_t(T)$ with g=3~4 and this scaling law predicts a fairly low value of beta limit for present design of fusion reactors such as the INTOR tokamak. One possibility of beta enhancement of such a tokamak is optimization of plasma current profiles against ballooning modes aiming at realization of the second stability equilibrium. The direct access to second stability without passing unstable region was demonstrated by using the stabilizing effect in the low shear region with $q_o>1$ (q_o: safety factor at the magnetic axis). Consequently, it is possible to obtain equilibria such that its beta value is unlimited by the $n=\infty$ ballooning mode stability. However the optimization yields a hollow current profile unfavourable to external kink modes. A conducting wall close to the plasma surface is necessary to render such high beta equilibria stable against kink modes. The conducting wall located at $a_w=1.2a$ (a_w and a are the horizontal radii of the conducting wall and the plasma) gives the beta limit of $\beta\geq 8\%$ with g=6-8.

3.2.2 Database assessment of confinement and beta limit for INTOR plasma[3)]

Evaluation of the beta limit in an INTOR-like tokamak plasma was carried out as a contribution to the INTOR workshop (phase IIA part 3). Theoretical prediction has been presented by using ideal beta limit in a wide range of geometrical parameters and profiles of plasma parameters. From the prediction, we proposed the "Troyon factor" of g~3.5 ($g=\beta/(I_p/aB_T)$) as the guide line. We pointed out the possibility of the degradation in g for $q_s<3$ (q_s: the safety factor at the plasma surface). We also proposed to use the second stability region of the ballooning modes in a dee-shaped cross section as an innovative concept of a tokamak reactor. Taking account of the instabilities for both high and low toroidal mode numbers, we have shown that the Troyon factor g can be g=6-8. The other issue is the prediction of the energy confinement time. The contribution to this

issue owed to the collaboration with the plasma experimental laboratory.

3.3 Nonlinear MHD analyses and disruption

3.3.1 Nonlinear evolution of free-boundary modes in a tokamak[4)]

Nonlinear calculations of free-boundary modes in a cylindrical tokamak plasma were carried out by taking account of the parallel diffusion of plasma resistivity. The final states of saturation are classified into three cases according to the initial values of the safety factor at the plasma surface, q_a. For $q_0/q_a=0.5$, where q_0 is the safety factor at the magnetic axis, the plasma shrinks for low q_a values, $1.75 \lesssim q_a \lesssim 1.9$, due to free-boundary kink mode and expands for middle q_a, $1.90 \lesssim q_a \lesssim 2.3$, due to free-boundary kink mode and surface tearing mode, and for higher q_a values, usual tearing mode saturations are observed. In expansion cases, the plasma forms the "vacuum bubbles" or "magnetic islands" for small and large values of q_a, respectively, and the boundary between these two cases are mainly determined by the value of the parallel diffusion coefficient of resistivity.

3.3.2 Plasma shrinkage due to interaction with limiter[4)]

The effect of limiter is included to the nonlinear MHD calculations mentioned in section 3.3.1. When the limiter is placed sufficiently close to the plasma surface, the expansion or deformation of plasma column is completely inhibited, and the plasma always shrinks into the stable state against m/n=2/1 free-boundary kink mode. By this shrinkage process, the value of q_a becomes smaller than the initial one because of plasma area contraction with constant plasma total current. Especially, when $q_a \cong 2$ and $q_0 \gtrsim 1$, the final value of q_a becomes nearly equal to one or even less than one, and the plasma becomes unstable against m/n=1/1 free-boundary kink mode, which causes the current disruption easily[5)].

References

1) Seki, S., Tsunematsu, T., Azumi, M., Nemoto, T., Nucl. Fusion 27 (1987) 330.

2) Yamazaki, K., et al., "Second stability access in tokamak plasmas", in Proc. of Eleventh International Conf. on Plasma Phys. and Controlled Nucl. Fusion Research, 1986 Kyoto IAEA-CN-47/E-I-1.
3) Tsunematsu, T., Tokuda, S., Nemoto, T., Azumi, M., Takeda, T., "Data set for benchmark calculation on ideal MHD beta limit of INTOR plasma", JAERI-M 86-172 (November 1986).
4) Kurita, G., Takizuka, T., Azumi, M., Takeda, T., "Nonlinear evolution of free-boundary kink mode in a tokamak", JAERI-M 86-156 (October 1986).
5) Alexander, K.F., et al., Nucl. Fusion 24 (1984) 631.

4. Analyses of burning plasma in a tokamak

4.1 Introduction

The reactivity for a DT plasma in a tokamak was investigated. The enhancement of the reactivity by beam and ICRF heating was analyzed on the basis of local Fokker-Planck calculation. The enhanced reactivity in a beam-heated plasma was given by a simple equation, and the fusion power multiplication was studied by using this simple equation.

The transport of high-energy alpha particles in a tokamak with toroidal field ripple was investigated. By using a mapping-method Monte-Carlo code with very short computation time, the same results on the ripple-enhanced transport was obtained as those by the three-dimensional orbit-following Monte-Carlo code. The collisional diffusion in the rippled field was analyzed on the basis of the transport equation in a single-resonance system, and the diffusion coefficient was obtained analytically.

4.2 Fusion reactivity

4.2.1 Fusion reactivity enhancement by beam and ICRF heating[1)]

Fusion reactivity enhancement due to ion tail formation by neutral-beam (D^0) injection and second harmonic ion (D^+) cyclotron heating in a 50:50 D-T plasma was investigated on the basis of local Fokker-Planck calculation. Deformation of the deuteron velocity distribution function was examined analytically and comparison was

2) Yamazaki, K., et al., "Second stability access in tokamak plasmas", in Proc. of Eleventh International Conf. on Plasma Phys. and Controlled Nucl. Fusion Research, 1986 Kyoto IAEA-CN-47/E-I-1.
3) Tsunematsu, T., Tokuda, S., Nemoto, T., Azumi, M., Takeda, T., "Data set for benchmark calculation on ideal MHD beta limit of INTOR plasma", JAERI-M 86-172 (November 1986).
4) Kurita, G., Takizuka, T., Azumi, M., Takeda, T., "Nonlinear evolution of free-boundary kink mode in a tokamak", JAERI-M 86-156 (October 1986).
5) Alexander, K.F., et al., Nucl. Fusion 24 (1984) 631.

4. Analyses of burning plasma in a tokamak

4.1 Introduction

The reactivity for a DT plasma in a tokamak was investigated. The enhancement of the reactivity by beam and ICRF heating was analyzed on the basis of local Fokker-Planck calculation. The enhanced reactivity in a beam-heated plasma was given by a simple equation, and the fusion power multiplication was studied by using this simple equation.

The transport of high-energy alpha particles in a tokamak with toroidal field ripple was investigated. By using a mapping-method Monte-Carlo code with very short computation time, the same results on the ripple-enhanced transport was obtained as those by the three-dimensional orbit-following Monte-Carlo code. The collisional diffusion in the rippled field was analyzed on the basis of the transport equation in a single-resonance system, and the diffusion coefficient was obtained analytically.

4.2 Fusion reactivity

4.2.1 Fusion reactivity enhancement by beam and ICRF heating[1)]

Fusion reactivity enhancement due to ion tail formation by neutral-beam (D^0) injection and second harmonic ion (D^+) cyclotron heating in a 50:50 D-T plasma was investigated on the basis of local Fokker-Planck calculation. Deformation of the deuteron velocity distribution function was examined analytically and comparison was

made with numerical results by using a Fokker-Planck code. The reactivity is given by $\langle\sigma v\rangle=\int d\vec{v}\, f(\vec{v})\, G(v)$, where f is the deuteron distribution and G is called 'σv-function' averaged by the isotropic triton distribution. The profile of the integrand typically presents two humps in velocity space for the beam-induced tail. This results in large reactivity enhancement for high energy beam injection. For the case of the RF-induced tail, a 'wing' rather than a hump is formed. ICRF waves well couple with the beam-induced tail ions and enhance the reactivity, especially when the beam is injected perpendicularly to the magnetic field. The possibility that the combined effects of NBI and second harmonic ICH can exceed the each effect on the reactivity enhancement in the efficiency is indicated.

4.2.2 Reactivity for DT plasma with beam-induced tail[2)]

The reactivity for a DT plasma in the magnetic confinement system is presented by useful and simple equations. The reactivity for a DT Maxwellian plasma is given as a function of the ion temperature, and that enhanced by the beam-induced tail is shown as a function of the ion and electron temperatures, the injection energy, and the beam power density. By using these simple expressions, the fusion power multiplication in a beam-heated plasma is studied on the basis of a local analysis. The value of $n_e\tau_E$ to achieve Q=1 (n_e: electron density, τ_E: gross energy confinement time, Q: fusion multiplication factor) becomes smaller by $2.7/T^{1.1}$(keV) than that in a Maxwellian plasma without tail component for the plasma temperature of 5keV<T<8 keV.

4.3 Alpha particle transport

4.3.1 Ripple enhanced transport of suprathermal alpha particles[3)]

We have developed two types of Monte-Carlo codes to study the ripple transport of suprathermal alpha particles. These codes much reduce the computational time compared with that of a three-dimensional orbit-following Monte-Carlo code (OEMC code). In a mapping-method Monte-Carlo code (MMMC code), the motion of a banana alpha particle in a toroidal field ripple is described by a mapping method. In a diffusion-model Monte-Carlo code (DMMC code), the

radial displacement of banana orbit is given by the diffusion coefficient obtained from the MMMC code or the OFMC code.

The ripple loss of alpha particles during slowing down has been estimated by the MMMC code as well as the DMMC code. We find the existence of ripple resonance diffusion from the numerical calculations by OFMC code and MMMC code. Both results are in good agreement with each other. The resonance diffusion becomes unimportant in the high energy region, and the diffusion coefficient approximates to D^{CB}, the confinement-banana diffusion coefficient. As for the ripple loss of alpha particles during slowing down, both calculation results from MMMC code and DMMC code agree well with the result from OFMC code.

4.3.2 Collisional diffusion of alpha particles in a rippled toroidal field

In a tokamak with the toroidal field ripple, the position of the banana tip of a trapped particle is moved by nonaxisymmetric effect. The radial displacement of the banana tip, δr, depends on ∇B drift speed, ripple size, and toroidal angle at the banana tip, ϕ: $\delta r=\delta r_0 \sin N_\phi$ (N is the number of toroidal coils). When δr_0 is larger than a threshold, the trajectory of the banana tip becomes erogdic and the ergodic diffusion arises. When δr_0 is smaller, the trajectory is stable and closed without collisions, but the collisional diffusion results from the change of ϕ due to pitch-angle scattering by collisions. This collisional diffusion is considered to be the main loss mechanism of high-energy alpha particles in a typical tokamak test reactor with ripple size of 1% at the plasma surface.

The following transport equation in a single-resonance system was employed for the model equation of this collisional diffusion;

$$\frac{\partial f}{\partial t} + x\frac{\partial f}{\partial \theta} + \varepsilon \sin\theta \frac{\partial f}{\partial x} = D_\theta \frac{\partial^2 f}{\partial \theta^2} \quad ,$$

where x and θ correspond to r and ϕ, respectively. We analysed this equation by considering $f_+ \neq f_-$ in the resonant region, $C=x^2+2\varepsilon \cos\theta < 2\varepsilon$ ($f_\pm$ coresponds to $x = \pm\sqrt{C-2\varepsilon \cos\theta}$). The averaged diffusion coefficient in x direction, D, over both resonant and nonresonant regions ($-L < x < L$), was obtained as

$$D = \frac{3\varepsilon^2 D_\theta}{2L^2} \Big/ \left[1 - \frac{(2\varepsilon)^{3/2}}{L^3} \left(1 - \frac{3D_\theta^{1/2}}{\sqrt{2}\,\varepsilon^{1/4}} \right) \right] .$$

This result agrees well with the simulation result, and explains the empirical relation by Rechester et al., $D/\varepsilon^2 \sim D_\theta + a\varepsilon^2 D_\theta^{2/3}$.[4)]

References

1) Yamagiwa, M., Takizuka, T., Kishimoto, Y., "Fusion reactivity enhancement due to ion tail formation by beam and ion cyclotron heating", JAERI-M 87-065 (May 1987).
2) Takizuka, T., Yamagiwa, M., "Reactivity for DT plasma with beam-induced tail in magnetic confinement system", JAERI-M 87-066 (May 1987).
3) Tani, K., Takizuka, T., Azumi, M., "Ripple enhanced transport of suprathermal alpha particles", IPPJ-REV-2 (September 1986) p.176.
4) Rechester, A.B., Rosenbluth, M.N., White, R.B., Phys. Rev. A 23 (1981) 2664.

5. TRITON System

5.1 Introduction

Physics codes and supporting codes were developed as componets of the TRITON-II system. Many of them are extension or improvement of the previously developed codes. Inverse equilibrium solver was developed for linear MHD stability calculation with high accuracy and the nonlinear resistive MHD codes are being developed in accordance with the development of the numerical study of disruption phenomena.

In order to attain a high performance computation efforts to optimize the computer programs for the vector-type supercomputer system are also being continued. Supporting codes on the graphic output and database control program for the numerical results of simulations were also improved and refined.

$$D = \frac{3\varepsilon^2 D_\theta}{2L^2} \Big/ \left[1 - \frac{(2\varepsilon)^{3/2}}{L^3} \left(1 - \frac{3D_\theta^{1/2}}{\sqrt{2}\,\varepsilon^{1/4}} \right) \right] .$$

This result agrees well with the simulation result, and explains the empirical relation by Rechester et al., $D/\varepsilon^2 \sim D_\theta + a\varepsilon^2 D_\theta^{2/3}$.[4)]

References

1) Yamagiwa, M., Takizuka, T., Kishimoto, Y., "Fusion reactivity enhancement due to ion tail formation by beam and ion cyclotron heating", JAERI-M 87-065 (May 1987).
2) Takizuka, T., Yamagiwa, M., "Reactivity for DT plasma with beam-induced tail in magnetic confinement system", JAERI-M 87-066 (May 1987).
3) Tani, K., Takizuka, T., Azumi, M., "Ripple enhanced transport of suprathermal alpha particles", IPPJ-REV-2 (September 1986) p.176.
4) Rechester, A.B., Rosenbluth, M.N., White, R.B., Phys. Rev. A 23 (1981) 2664.

5. TRITON System

5.1 Introduction

Physics codes and supporting codes were developed as componets of the TRITON-II system. Many of them are extension or improvement of the previously developed codes. Inverse equilibrium solver was developed for linear MHD stability calculation with high accuracy and the nonlinear resistive MHD codes are being developed in accordance with the development of the numerical study of disruption phenomena.

In order to attain a high performance computation efforts to optimize the computer programs for the vector-type supercomputer system are also being continued. Supporting codes on the graphic output and database control program for the numerical results of simulations were also improved and refined.

5.2 Physics codes and numerical methods

5.2.1 Solution of the inverse equilibrium equation by using Newton's method[1)]

FCT (Flux Conserving Tokamak) equilibria in the inverse equilibrium form were obtained numerically. The high-beta tokamak ordering was used to get the explicit boundary conditions for the FCT equilibria. The partial differential equation was reduced to the simultaneous quasi-linear ordinary differential equations by using the moment method. The regularity conditions for solutions at the singular point of the equations can be expressed correctly by this reduction and the problem to be solved becomes a tractable boundary value problem on the quasi-linear ordinary differential equations. This boundary value problem was solved by Newton's method, which is equivalent to the method of quasi-linearization to solve nonlinear boundary value problems numerically. Equilibria with different boundary shapes can be obtained by this method together with the trace of solutions.

5.2.2 Nonlinear resistive MHD code based on "pseudo-vacuum" model

The nonlinear free-boundary reistive MHD code based on "pseudo-vacuum" model developed in the last fiscal year was single-helicity version and the evolution of plasma resistivity was pushed only by the convection equation[2)]. In this fiscal year, it was revised to contain parallel and perpendicular resistivity diffusion to magnetic field line, just the same as the equation of electron temperature. The mapping method, used in the old verson, was also employed in the new one. In this method, the radial plasma displacement, S, is solved instead of resistivity equation, that is,

$$\frac{\partial S}{\partial t} = [S,\phi] + \kappa_{/\!/}\left[[X,\Psi] + \frac{\eta''}{\eta'} X^2 \right] + \kappa_{\perp}\Delta^{*}S,$$

$$X = [S,\Psi],$$

where

$$[S,\Psi] \equiv \frac{1}{r}\left[\frac{\partial S}{\partial r}\frac{\partial \Psi}{\partial \theta} - \frac{\partial \Psi}{\partial r}\frac{\partial S}{\partial \theta} \right] .$$

The additional term, $(\eta''/\eta')X^2$, appeared as a result of the variable transformation of $\eta \rightarrow S$, and plays a very important role in the resistivity evolution of free-boundary case.

5.2.3 Vectorization of alpha particle pressure calculation code

In a tokamak reactor with high-temperature plasma, the pressure of high-energy alpha particles becomes important in the total plasma pressure. The anisotropy of the alpha particle pressure is not negligible, from the viewpoints of the equilibrium and MHD instabilities, especially, in the presence of toroidal field ripple. In order to evaluate this anisotropic pressure distribution, an orbit-following Monte-Carlo code has been used. The particle number for calculation is ~10^4, and the long computation time has been required. Therefore, we have vectorized this orbit-following Monte-Carlo code and we raise the computation speed by ~4.

5.2.4 Vectorization of MHD equilibrium and stability codes[3)]

An MHD equilibrium code SELENE and a stability code ERATO-J were vectorized. Vectorization reduces the computational time to about a third through a quater of the original version on the Fujitsu VP-100 computer system.

5.3 Supporting codes

5.3.1 Graphic system ARGUG-V5

Continuous presentation of a series of graphic output data as a movie is very effective to understand the physics implication of the results of numerical simulations. Considering the effectiveness we are developing the movie output system ARGUS-V5. In the fiscal year automatic input facility of graphic attributes such as color and line type to all the frames by specifying them only once at the output of the first frame was developed for the ARGUS-V5 system. Also the functions for editing the graphic data to be deleted or to be merged and for superimposing them were added to the system.

5.3.2 Interactive graphic display in the GAEA database system

Graphite display function was given to the GAEA database system by incorporating ARGUS-V4 in the GAEA system.[4)] User can draw

interactively one dimensional graph of data stored on the system as both KEY and MASS data.

5.3.3 Improvement of EOS77 preprocessor

New version of EOS77 (EOS77.V3) was developed. This version supports real type size variables, intrinsic functions and control statements (IF-THEN-ELSE statements) in the size block. Users can define sets of 'COMDECKs' in the text block and can refer the set instead of COMDECKs. The set algebra (intersection, union and complement of sets) is also supported.

References

1) Tokuda, S., Tsunematsu, T., Takeda, T., "Numerical computation of FCT equilibria by inverse equilibrium method", JAERI-M 86-171 (November 1986).
2) Kurita, G., et al., Nucl. Fusion 26 (1986) 449.
3) Nemoto, T., Tsunematsu, T., "Vectorization of MHD equilibrium and stability code", JAERI-M 87-062 (April 1987).
4) Tokuda, S., Tsunematsu, T., Takeda, T., Comput. Phys. Commun. 44 (1987) 21.

II. TOROIDAL CONFINEMENT EXPERIMENT JFT-2M

1. Introduction

The commissioning of a medium sized tokamak JFT-2M was completed in April 1983. Until December 1984, experiments on plasma heating with ICRF and NBI, and on current drive and electron heating with LH wave and ECH were done for circular-discharges. For three months from the end of December 1984, JFT-2M experiments were stopped by installation of the poloidal power supply for non-circular plasma discharges and divertor operation.

In non-circular plasma experiments which started from April 1985, a full rating D-shape operation of 500 kA plasma current was realized, vertical instability of elongated plasma with the growth rate up to 500 sec^{-1} was suppressed, and wide veriety of plasma shapes was obtained on ellipticity $\kappa \lesssim 1.7$ and triangularity $\delta \lesssim 0.7$. In the fall of 1985 both single-null and double-null open-divertor configurations were obtained, and since then confinement studies on additionally heated plasmas with divertor configurations have been in progress in JFT-2M. The 2nd-harmonic electron cyclotron heating experiments with two 60 GHz Varian gyrotrons were also done from January to March 1986. MHD fluctuations with the poloidal mode number of m=3 were suppressed through profile control by the application of ECH pulse.

In the present reporting period (April 1986 to March 1987) main subjects of JFT-2M experiments were confinement studies on additionally heated plasmas (especially H-mode and improved confinement with pellet injection), and radio-frequency current drive on improvement of LHCD using ECH and on 200 MHz fast wave.

In JFT-2M, H-mode discharges with single-null and double-null open-divertor configurations were realized in hydrogen, helium and deuterium plasmas for ICRF heating as well as NBI heating. Confinement improvement in these H-mode discharges was clearly shown, and the global energy confinement time of the H-mode discharges exceeded the ohmic one in hydrogen plasmas. Also in limiter configuration, the H-mode discharges was demonstrated. A very high confinement mode was achieved in pellet-fueled, NBI-heated plasmas where a pellet was

injected just before H-transition to reach the inner part of the heated plasma.

On radio-frequency current drive, the selective perpendicular heating of energetic electrons by ECH was observed in ECH experiments combined with LHCD. This result demonstrated possible improvement of LHCD by ECH. As the first step to explore the fast wave current drive in a high density regime, a preliminary test with a 100kW-class oscillator of 200 MHz, was performed. Acceleration of high energy electrons was observed experimentally.

The following subsection II.2 describes confinement studies, especially H-mode results in JFT-2M. Improved confinement in NBI-heated plasma with pellet injection is described in subsection II.3, and radio-frequency current drive experiment is summarized in subsection II.4. In subsection II.6 a multi-channel bolometer array is described, which was newly applied to JFT-2M for measurements of radiation profile.

2. Confinement Study in JFT-2M

2.1 Characteristics of the H-mode in divertor and limiter discharges

Several tokamaks with a divertor have shown a possibility of the high confinement mode (H-mode). JFT-2M[1] has capability of elongated limiter discharges and open divertor discharges, and in both configurations the H-mode has been observed[2,3,4]. Poloidal limiters and divertor plates are made of graphite, stand apart from inner wall surface by 65 mm and 80 mm respectively. Co- and counter injection of hydrogen neutral beam with each maximum power of 0.8 MW were used, net input power is estimated as 90% of torus input for co-injection and 70% for counter-injection. Good monitors for the H-transition are H_α/D_α signals from 3 directions, edge temperature T_{edge} by ECE, edge density n_{edge} by FIR interferometer and plasma stored energy w_s by magnetics (diamagnetics and magnetic fitting method).

As well known, there exist the threshold input power P_{th} and electron density n_{th} for the H-transition and they depend on various parameters such as magnetic configuration, safety factor, gas species, cleanliness, direction of ion grade B drift and so on. In divertor

injected just before H-transition to reach the inner part of the heated plasma.

On radio-frequency current drive, the selective perpendicular heating of energetic electrons by ECH was observed in ECH experiments combined with LHCD. This result demonstrated possible improvement of LHCD by ECH. As the first step to explore the fast wave current drive in a high density regime, a preliminary test with a 100kW-class oscillator of 200 MHz, was performed. Acceleration of high energy electrons was observed experimentally.

The following subsection II.2 describes confinement studies, especially H-mode results in JFT-2M. Improved confinement in NBI-heated plasma with pellet injection is described in subsection II.3, and radio-frequency current drive experiment is summarized in subsection II.4. In subsection II.6 a multi-channel bolometer array is described, which was newly applied to JFT-2M for measurements of radiation profile.

2. Confinement Study in JFT-2M

2.1 Characteristics of the H-mode in divertor and limiter discharges

Several tokamaks with a divertor have shown a possibility of the high confinement mode (H-mode). JFT-2M[1] has capability of elongated limiter discharges and open divertor discharges, and in both configurations the H-mode has been observed[2,3,4]. Poloidal limiters and divertor plates are made of graphite, stand apart from inner wall surface by 65 mm and 80 mm respectively. Co- and counter injection of hydrogen neutral beam with each maximum power of 0.8 MW were used, net input power is estimated as 90% of torus input for co-injection and 70% for counter-injection. Good monitors for the H-transition are H_α/D_α signals from 3 directions, edge temperature T_{edge} by ECE, edge density n_{edge} by FIR interferometer and plasma stored energy w_s by magnetics (diamagnetics and magnetic fitting method).

As well known, there exist the threshold input power P_{th} and electron density n_{th} for the H-transition and they depend on various parameters such as magnetic configuration, safety factor, gas species, cleanliness, direction of ion grade B drift and so on. In divertor

discharge, n_{th} has no clear dependence on safety factor and is nearly the same for H, D and He plasma, its range is $1.5\text{-}2.0\times10^{13}/cm^3$. In limiter discharges, however, n_{th} rises about twice of divertor case [5].

The threshold input power P_{th} was investigated with I_p-scan and B_t-scan. P_{th} increases with B_t and decreases with I_p. So its parameter dependence can be summarized as dependence on the surface safety factor q_s. In the H-mode two types of H_α/D_α signal (burst and burst-free) are recognized. For the burst case, increases of electron density and radiation power are pulled down at every burst. On the other hand, for the burst-free case density and radiation power increase up to some limit where H- to L-transition occurs, then during the L-phase reduction of radiation power seems to prepare again necessary conditions for the H-transition. These features of H-mode depend especially on input power level. For H plasma, power range of the burst type is comparatively wide up to about double of P_{th}. For D plasma, the burst-free type is dominant and the burst type is limited to be appear around P_{th}. The P_{th} dependences on the safety factor and gas species for divertor discharges are shown in Fig. II.2-1[6]. The P_{th} increases nearly with q_s in high q region (>3) and roughly constant in low q region (<3). It must be noted that P_{th} is well expressed only with q_s for different plasma current. In limiter discharges, P_{th} is about double of divertor case, but dependence on q_s is almost similar.

Gas species also affect P_{th}. At same q_s of 3, P_{th} for H plasma is about 0.5 MW and larger than P_{th} of 0.2 MW for D plasma. P_{th} for He plasma was checked at one case and just below that for H plasma. Other factors observed experimentally are Ti-gettering and direction of ion gradB drift, they affect P_{th} by a factor of 2. Finally, outer clearance between plasma surface and limiters is a severe factor, as we can suppress the H-transition by insertion of a outer movable limiter nearly to plasma surface. Necessary outer clearance for the H-mode is 3-4 cm at power level of 0.8 MW. Top and bottom clearance is not so severe as outer one, and inner one can be guessed to be not severe from the H-transition in inside-touched limiter discharges. These clearance conditions suggest a key importance of scrape-off layer for the H-mode.

Confinement improvement in the H-mode is clearly seen as additional increase of stored energy w_s by magnetics. This increase of w_s seems to come from formation of the so-called 'pedestal' in electron temperature and density profiles at the begining of the H-mode, then density increase contributes on w_s rise rather than increase of temperatures. Throughout the H-phase is there some process to maintain the predestal at the plasma edge. The edge electron temperature T_{edge} by ECE jumps up at the H-transition and keeps almost constant during the H-phase for H plasma, but decreases gradually down to the L-phase value for D plasma. And for high q case without sawtooth oscillations, T_{edge} rises slowly. So it is difficult to find out a threshold value for T_{edge}. Different time behaviour of T_{edge} between H and D plasma seems to come from impurity accumulation level measured as radiation loss power. On the other hand, electron density keeps to rise up till the H- to L-transition occurs. Though precise pressure profiles have not been obtained, formation of pressure pedestal may be a key feature and gradP at the edge may be limited by some pressure-driven instabilities and/or MHD instabilities.

Improved confinement can be expressed with the global energy confinement time τ_E^G and the incremental confinement time determined from power-scan experiments. But the latter involves large ambiguity within limited power-scan range, because of power dependent features of H-mode types especially in H plasma. So the τ_E^G of H-mode at same power level is compared for H, D and He plasma together with that of ohmic phase τ_{OH}. The τ_E^G for the H-mode is defined around peak of w_s, because there is no steady state for the burst-free case. The τ_{OH} is a peak value in the density-scan data. So the density region for each confinement times is spread widely. Dependence of confinement times on I_p is shown in Fig. II.2-2. The τ_{OH} is nearly constant against I_p and depends on gas species. However, the τ_E^G is linearly proportional to I_p up to the lowest q limit of 2 and no dependence on gas species can be seen. This feature of H-mode confinement is very simple and interesting. Especially for H plasma, that τ_E^G exceeds the τ_{OH} enough at the lowest q. Figure II.2-3 shows dependence of confinement times on B_t. The τ_{OH} is linearly proportional to B_t and there exists also dependence on gas species. But the τ_E^G has no dependence on B_t and gas

species. The reason for these features of the H-mode remains as an open question, but it is clearly shown that the global energy confinement time of the H-mode can exceed the ohmic one in H plasma. In limiter discharges, confinement improvement is rather small compared with divertor discharges. It may comes from strong interaction with limiters or low shear at plasma edge.

2.2 H-mode discharge during ICRF heating

Three sets of high field side antennas are used in JFT-2M to launch fast waves in a two-ion hybrid resonance heating mode. A mixture of deuterium and hydrogen gas is used, with a hydrogen to deuterium density ratio of approximately 40%. The plasma is heated via electron Landau damping of the ion Bernstein wave converted from the fast wave at the thick mode conversion layer in the center of the machine. The high energy ion tail created by the heating is very small. The frequency of the launched wave is 16.8 MHz, which is the cyclotron frequency at 1.1 T of the magnetic field. The toroidal magnetic field is 1.2-1.25 T at the plasma center during the heating. The maximum RF power available at the generator is 4.5 MW; however, because of the small loading impedance of the antenna, the maximum power coupled to the plasma is 2.2 MW in D-shaped limiter discharges and 1.4 MW in the single-null divertor configuration.

Figure II.2-4 shows an H-mode transition during ICRF heating with JFT-2M in a single-null open divertor configuration. The plasma dischrge parameters are as follows: plasma current, I_p = 255 kA, Toroidal magnetic field, B_T = 1.26 T, surface q-value = 3.73, ellipticity, κ = 1.43, and triangularity, δ = 0.19. The time evolution of an L-mode discharge with similar discharge conditions is also shown in the figure, denoted by thin lines. The sudden drop in the H_α/D_α emission is accompanied by increasing radiation loss, electron density and plasma stored energy. During the H-phase, the increase in stored energy, and thus the improvement in energy confinement time, is associated with an improvement in the particle confinement time. These parameters continue to increase until H_α/D_α emission increases suddenly, at which time they decrease despite the constant level of RF heating power. At the time of the transition, the plasma one-turn voltage initially drops, but then starts to

increase. The time evolution of the ratio of the two-line averaged electron densities measured vertically at R = 110 cm and R = 124 cm, in the second box from the bottom of the figure, indicates that the electron density profile broadens at the time of the transition.

Confinement times of single-null plasma with similar discharge conditions are plotted versus line averaged electron density in Fig. II.2-5. An improvement of the energy confinement after the transition can be seen. Here, the global energy confinement time is defined as

$$\tau_E^G = \frac{W}{(P_{OH}+P_{RF}-dW/dt)}$$

where W is the plasma stored energy, P_{OH} is the ohmic input power. P_{RF} is the RF heating power which is radiated from the antenna into the torus, and dW/dt is the time rate of change of the stored energy. In Fig. II.2-5, the squares represent Ohmic confinement time values; the triangles show the confinement times during ICRF heating without transitions. For these discharges, the total heating power $P_{TOT}=P_{OH}+P_{RF}$, is about 900 kW - close to the threshold power for the H-mode transition in this lower single null configuration. Solid circles represent confinement times during the H-mode phase. The total heating powers for these discharges are approximately 1 MW, which is just above the threshold for the transition. At the transition, confinement times improve with the simultaneous increase of the electron density. In addition, Kaye-Goldston L-mode confinement times are shown for comparison by crosses.

Figure II.2-6 is a plot of global energy confinement times versus total heating power, with total plasma stored energies. The L-mode values are represented by open circles and solid circles indicate the maximum H-mode confinement times. For reference, the Kaye-Goldston L-mode scaling confinement times are indicated by crosses. The energy confinement times of H-mode discharges almost stays constant or slowly decreases up to P_{TOT}=1.1 MW. Above this, the global energy confinement time drops, and comes close to those of L-mode states. However, the H-mode stage above 1.2 MW of the total heating power is rather close to L-mode. This phenomena seems to be one type of soft beta saturation. Troyon factor saturates at 1.7 in high power region,

and the same saturation value is also observed in NBI/H-model experiments with the same plasma configuration.

2.3 Improvement of the confinement characteristics of the H-mode

2.3.1 Introduction

The confinement characteristics of the H-mode discharges are shown to be affected by the plasma fueling or particle control [2,3,8,9]. In this subsection, several methods to improve the confinement of the H-mode discharges by fueling optimization of ungettered discharges are demonstrated. It is shown that how the fueling optimization affects the H-mode confinement.

2.3.2 Simulation experiment of toroidally uniform fueling [2]

In order to demonstrate how the strongly localized puff fueling affects the confinement and to simulate a toroidally uniform fueling, three gas-puff systems, A, B and C, are distributed toroidally about 120° apart. The amount of the gas flow rate is shown in Fig. II.2-7(b) for both single and distributed puff systems. The effects of the distribution can be clearly seen both on $\bar{n}_e^c$, from which the neutral builds up and the confinement time degrades, and τ_E^G as shown in Fig. II.2-7(a), i.e. the improvement in $\bar{n}_e^c$ is about 35% and that of τ_E^G is 20 to 30% at higher density of the H-mode discharge.

This method suppresses the neutral buildup [Fig. II.2-7(c)].

2.3.3 Effect of a pump limiter on confinement [8]

Used pump limiter PL has throats in both electron and ion drift side (3.5 cm wide) and an expansion chamber (V=78ℓ) followed by Zr/Al getter pump. The effective pumping speed at the expansion chamber is about 800 ℓ/s. The clearance Δ is measured from the pump limiter head to the magnetic surface contacts with inner limiter or divertor separatrix. The pump limiter is installed on the top of the torus because the enough clearance between the plasma and limiter at the outer midplane is required for the limiter H-mode transition [3,4].

In the ohmic heating (OH) phase of limiter discharges, the global energy confinement time τ_E^G is improved by the pump limiter at around the critical density above which the gas pressure begins to build up [2] [$\bar{n}_e=(3\text{-}4)\times10^{13}$ cm^{-3} in Fig. II.2-8(a)]. In the H-mode phase with

pump limiter, where the particle intake to the pump limiter is drastically decreased, τ_E^G is comparable to the value without pump limiter. However, the pump limiter allows continuous gas feed during NBI phase and exhibits the highest $n\tau$ value [a data set of open squares over closed squares in Fig. II.2-8(a)]. Without the pump limiter, the attainable $n\tau$ with the continuous gas feed is lower than that of the standard gas-puff case.

In the divertor H-mode discharges, we also observe the similar effect of the pump limiter with 0.8 MW co-injection while Δ is about 3 cm from the separatrix surface (mechanical limit) as shown in Fig. II.2-8(b).

2.3.4 Improvement of $n\tau$ value of the beam-heated H-mode by electron cyclotron wave (ECW) [9]

Expecting the effect of the enhanced wall fueling (fueling by desorbed hydrogen from the wall) on the confinement, the ECW with about 100 kW of the launched power is applied to the H-mode of beam-heated single-null divertor discharges.

The gas-puff valve is closed during the beam heating phase in order to prevent the confinement degradation[2] for relatively low density ($<4\times10^{13}$ cm^{-3}) discharges. Energy confinement time of the H-mode discharges for beam only case is degraded when the strong gas-puff fuel is introduced during the beam heating phase in order to raise $\bar{n}_e$ over 4×10^{13} cm^{-3} (in Fig. II.2-9). With the assist of off-resonanced, ECW, however, this raised fuel rate during the additional heating phase is allowable. It appears that the fueling efficiency is improved by the ECW. This results in higher attainable density without the degradation in τ_E^* (defined in the figure) as shown in Fig. II.2-9. The resultant $n\tau$ value is improved over 40%.

References

[1] T. Shoji, et al., in Proc. of 11th Europ. Conf., (Achen 1983) Vol. 1, p.55

[2] S. Sengoku, et al., "Confinement and Fueling Studies during Additional Heating Phase in JFT-2M Tokamak" in 7th Int. Conf. on

Plasma-Surface Interactions in Controlled Fusion Devices, (Princeton, May 1986), J. Nucl. Mater. 145-147 (1987) 556.

[3] S. Sengoku, et al., "Regime of Improved Confinement in Neutral-Beam-Heated Limiter Discharges of a Tokamak", Phys. Rev. Lett. 59 (1987) 450.

[4] K. Odajima, et al., "Confinement Studies of Additionally Heated Plasma in JFT-2M Tokamak" in Proc. of 11th Int. Conf. on Plasma Phys. and Cont. Nucl. Fusion Research (Kyoto, Nov. 1986), IAEA-CN-47/A-III-2.

[5] H. Matsumoto, et al., "Studies of H-mode in the Limiter Discharges on JFT-2M Tokamak", in Proc. of 14th Europ. Conf. (Madrid, June 1987), Vol. 11D, Part I, p.5.

[6] N. Suzuki, Y. Miura, et al., "Characteristics of the H-mode in Divertor Configuration on JFT-2M Tokamak", ibid. [5], p.217.

[7] H. Matsumoto, et al., "H-mode Phenomena Durng ICRF Heating on JFT-2M", Nucl. Fusion, 27 (1987) 1181.

[8] S. Sengoku, et al., "Effect of Particle Control by a Pump Limiter on Confinement in JFT-2M", ibid. [5], p.164.

[9] S. Sengoku, et al., "Enhancement of Wall Fueling and Improvement in $n\tau$ of a Beam-Heated H-mode Discharge by Electron Cyclotron Wave in the JFT-2M Tokamak", J. Jpn. Phys. Soc. Jpn., 57 (1988) 902.

3. Pellet Injection Experiment in JFT-2M

3.1 Introduction

Injection of a high-speed hydrogenic pellet is being considered as a means for fueling in future fusion reactors. A fresh fuel is deposited directly on the innermost flux surfaces by this method. Especially, in a reactor with D-T burn, tritium inventory on a wall is a very important problem, which must be solved. The high-speed pellet injection should be expected to decrease the tritium inventory.

In JFT-2M, the pellet injection study has been proposed in 1981[1]. Main objects of pellet injection experiments are as follows.

1) Improvement of plasma parameters (confinement time, density-limit, beta) in limiter and divertor configurations.

Plasma-Surface Interactions in Controlled Fusion Devices, (Princeton, May 1986), J. Nucl. Mater. 145-147 (1987) 556.

[3] S. Sengoku, et al., "Regime of Improved Confinement in Neutral-Beam-Heated Limiter Discharges of a Tokamak", Phys. Rev. Lett. 59 (1987) 450.

[4] K. Odajima, et al., "Confinement Studies of Additionally Heated Plasma in JFT-2M Tokamak" in Proc. of 11th Int. Conf. on Plasma Phys. and Cont. Nucl. Fusion Research (Kyoto, Nov. 1986), IAEA-CN-47/A-III-2.

[5] H. Matsumoto, et al., "Studies of H-mode in the Limiter Discharges on JFT-2M Tokamak", in Proc. of 14th Europ. Conf. (Madrid, June 1987), Vol. 11D, Part I, p.5.

[6] N. Suzuki, Y. Miura, et al., "Characteristics of the H-mode in Divertor Configuration on JFT-2M Tokamak", ibid. [5], p.217.

[7] H. Matsumoto, et al., "H-mode Phenomena Durng ICRF Heating on JFT-2M", Nucl. Fusion, 27 (1987) 1181.

[8] S. Sengoku, et al., "Effect of Particle Control by a Pump Limiter on Confinement in JFT-2M", ibid. [5], p.164.

[9] S. Sengoku, et al., "Enhancement of Wall Fueling and Improvement in $n\tau$ of a Beam-Heated H-mode Discharge by Electron Cyclotron Wave in the JFT-2M Tokamak", J. Jpn. Phys. Soc. Jpn., 57 (1988) 902.

3. Pellet Injection Experiment in JFT-2M

3.1 Introduction

Injection of a high-speed hydrogenic pellet is being considered as a means for fueling in future fusion reactors. A fresh fuel is deposited directly on the innermost flux surfaces by this method. Especially, in a reactor with D-T burn, tritium inventory on a wall is a very important problem, which must be solved. The high-speed pellet injection should be expected to decrease the tritium inventory.

In JFT-2M, the pellet injection study has been proposed in 1981[1]. Main objects of pellet injection experiments are as follows.

1) Improvement of plasma parameters (confinement time, density-limit, beta) in limiter and divertor configurations.

2) Improvement of heating efficiency on the auxiliary heating (NB, ICRF).

3) Identification of particles mainly contributed to the pellet ablation (ablation mechanism).

The single-pellet injector for JFT-2M[2] is basic type developed at Oak Ridge National Laboratory. The pneumatic injector with a design-size of 1.65 mmϕ×1.65mmL was used in a series of injection experiments till November 1986. Injected pellet velocity is 714-833 m/s in usual experiments (maximum velocity is 970 m/s), which corresponds to 80-95% of the calculated velocity from ideal gun model. The injected pellet size into a plasma is less than 50% of the design-size.

The 4 Pellet injector, which has 4 independent main-housing /barrel-housing (gun barrel) assemblies and common heat exchanger, has been built and operated since March 1987. This injector is newly developed for JFT-2M. Design-size of pellets is 1.28mmϕ×1.4mmL (3 pellets) and 1.48mmϕ×1.6mmL (1 pellet). Each pellet has a different injection-velocity. Observed maximum velocity is about 1.4 km/s for H_2 pellet (with H_2 propellant gas).

A single deuterium pellet has been injected into plasmas heated by NB or ICRF wave. Very high confinement has been acheived in both heatings[3].

3.2 Pellet injection into auxiliary heated single-null divertor plasmas

The single-null divertor plasmas transfer from the lower confinement mode (L-mode) to the high confinement mode (H-mode) during auxiliary heating. Pellets were injected into the L-mode or H-mode. Hydrogen NB power is about 0.77 MW (net heating power is about 0.67 MW). In the first case, the D_2 pellet with about 700 m/s was fueled before H-transition (in L-mode)[3]. The increment of $\bar{n}_e$ by the pellet is about 1.5×10^{19} m^{-3}, following linear increasing of $\bar{n}_e$ (Fig. II.3-1). The D_α line intensity near the limiter or the gas puffing decreases after the pellet injection. The time behaviors of $\bar{n}_e$ and D_α line indicate that the particle recycling reduced and the particle confinement was improved. The radiation loss power P_{rad} (including the charge exchanged loss power) is linearly increasing up to the time

of sudden increase of D_α line intensity. The global energy confinement time is determined from the magnetic fitting method ($\tau_E=W_s/(P_{total}-dW_s/dt)$, W_s: stored energy, P_{total}: total input energy). τ_E is nearly the same value as that in ohmically heated discharges in the same density region, but decreases as increasing the density and the radiation loss power. This degradation may be due to the increase of the radiation loss from the center region of the plasma. These properties are similar to the H-mode achieved in gas fueling.

The very high confinement mode was achieved in the large-pellet fueled discharges ($\Delta\bar{n}_e=4.5\times10^{19}$ m^{-3}) (Fig. II.3-2). the pellet is mainly ablated around r=0.1 m and passes through the center of the outer magnetic surface (Fig. II.3-3). The value W_s is linearly increasing up to 34 kJ. After that, $\tilde{B}_\theta$ singal (5 kHz) always grows, where the safety factor (q_ψ) is close to 2.5 and the plasma energy is bursted out. Then $<\beta_t>$ is about 1.6% and the factor of g ($<\beta_t>=gI_p/(aB_t)$) is about 2.2. This result agrees with the range of theoretical limits due to kink and ideal balloning modes with free boundary. The energy burst may be due to β-limit. The increment of W_s is mainly due to the increase of both electron and ion temperatures. The plasma is cooled down, following the pellet injection, but after 30-40 ms both temperatures are approximately the same and the plasma heats to about 0.8 keV (Fig. II.3-4). The values P_{rad} and D_α line intensity do not increase till W_s saturates. These facts indicate that impurity accumulation into a plasma core and particle recycling rate is very little compared with those in the H-mode discharges. The value τ_E increases to 60-75 ms and this level is sustained for about 20 ms, which exceeds τ_E in H-mode by a factor of 2. Some discharges with properties of very high confinement is not disrupted and the saturation level of W_s keeps. The characteristics of these discharges are concluded that the very high confinement mode terminates when $<\beta_t>$ touches close to the β-limit softly, and the discharges turn to the H-mode. The value τ_E in the small pellet fuelded discharges is 50-55 ms and degrades to the level of H-mode in gas-fueled discharges (Fig. II.3-5). The very high confinement (60-75 ms) was achieved around $\bar{n}_e$ of 6×10^{19} m^{-3} by the large pellet.

Pellet injection into the H-mode discharges during NB heating deteriorates the energy confinement. This is due to large ablation near the peripheral region, where the electron temperature goes up after H-transition.

References

[1] S. Kasai, Y. Miura, K. Hasegawa, S. Sengoku, H. Ogawa, et al.: JAERI-M 86-109 (1986).

[2] S. Kasai, K. Hasegawa, Y. Miura, I. Ishibori: JAERI-M 86-035 (1986) (in Japanese).

[3] Y. Miura, S. Kasai, S. Sengoku, K. Hasegawa, N. Suzuki, et al.: JAERI-M 86-148 (1986).

4. Radio-Frequency Current Drive Experiment

4.1 Introduction

Current drive by lower-hybrid (LH) waves has been successfully achieved in a number of tokamaks. These experiments have shown that the LH waves produce a current-carrying fast electron tail. Recently, electron cyclotron heating (ECH) in the presence of a mildly relativistic electron tail has received a lot of interest because of the need of supplemental heating and current profile control in the high-phase-velocity RF current driven plasmas and of possible improvements, using ECH, of the current drive by the LH waves (LHCD) and electron-cyclotron (EC) waves[1,2].

On the other hand, in a high-temperature and high-density fusion plasma the LH waves can only drive a skin current since for a plasma having large value of f_{pe}^2/f_{ce}^2 a lower bound of the allowed parallel refractive index $N_{//}$ is restricted to relatively high value and the wave power is then absorbed near the plasma surface. Fast waves (FW) in the frequency range of $f_{ci}<f_0<f_{LH}(0)$ ($f_{LH}(0)$ is the maximum LH resonance frequency in the plasma), however, can penetrate into the plasma core even for a hot and dense plasma. The current drive by the fast waves (FWCD) is based on the same mechanism as LHCD namely that

Pellet injection into the H-mode discharges during NB heating deteriorates the energy confinement. This is due to large ablation near the peripheral region, where the electron temperature goes up after H-transition.

References

[1] S. Kasai, Y. Miura, K. Hasegawa, S. Sengoku, H. Ogawa, et al.: JAERI-M 86-109 (1986).

[2] S. Kasai, K. Hasegawa, Y. Miura, I. Ishibori: JAERI-M 86-035 (1986) (in Japanese).

[3] Y. Miura, S. Kasai, S. Sengoku, K. Hasegawa, N. Suzuki, et al.: JAERI-M 86-148 (1986).

4. Radio-Frequency Current Drive Experiment

4.1 Introduction

Current drive by lower-hybrid (LH) waves has been successfully achieved in a number of tokamaks. These experiments have shown that the LH waves produce a current-carrying fast electron tail. Recently, electron cyclotron heating (ECH) in the presence of a mildly relativistic electron tail has received a lot of interest because of the need of supplemental heating and current profile control in the high-phase-velocity RF current driven plasmas and of possible improvements, using ECH, of the current drive by the LH waves (LHCD) and electron-cyclotron (EC) waves[1,2].

On the other hand, in a high-temperature and high-density fusion plasma the LH waves can only drive a skin current since for a plasma having large value of f_{pe}^2/f_{ce}^2 a lower bound of the allowed parallel refractive index $N_{//}$ is restricted to relatively high value and the wave power is then absorbed near the plasma surface. Fast waves (FW) in the frequency range of $f_{ci}<f_0<f_{LH}(0)$($f_{LH}(0)$ is the maximum LH resonance frequency in the plasma), however, can penetrate into the plasma core even for a hot and dense plasma. The current drive by the fast waves (FWCD) is based on the same mechanism as LHCD namely that

the current carrying electrons are accelerated through Landau damping, and is expected to be applicable to the fusing plasma.

4.2 Experimental Setup

The JFT-2M tokamak has a D-shaped vacuum vessel with major radius R_0=1.31 m and 0.415m×0.595 m minor cross-section[3]. The ECH system consists of two gyrotrons and two oversized waveguide transmission lines[4]. The RF power is generated by a Varian gyrotron capable of producing 200 kW at 60 GHz for up to 0.1 sec. The extraordinary mode is radiated at an injection angle of θ=80° to the direction of the toroidal magnetic field from a conical horn antenna propagating TE_{11} mode. The horn antennas are placed outside of torus in the midplane. The LH waves are launched by a four waveguides array which is fed by four 0.75 GHz klystrons. The phase difference between adjacent waveguides is set at 90°, and thus the Brambilla RF spectrum is concentrated between $N_{//}$=1 and 5. The fast wave system consists of a 200 MHz RF source capable of 100 kW for up to 0.1 sec feeding to a phased two-loop antennas array [5]. The RF power is divided into the two lines by a 3dB hybrid coupler. The phase difference between the antennas $\Delta\Phi_{FW}$ is adjusted by a line strecher. The impedance of each line is matched using $\lambda/8$ double stub tuners.

4.3 Experimental Results

4.3.1 Selective Electron Cyclotron Heating

ECH experiments combined with LHCD have been carried out to investigate the EC wave interaction with mildly relativistic electrons[6].

Figures II.4-1 (a)-(b) and (c) show the time evolution of the soft x-ray photon counts integrated over different energy ranges for three viewing angles, θ_{sx}=0°, 90° and 180°, respectively, at B_t=1.34 T. The x-ray radiation parallel (θ_{sx}=0°) and perpendicular (θ_{sx}=90°) to the magnetic field is measured simulataneously by two intrinsic germanium detectors with pulse-height analyzer systems. The parallel backward (θ_{sx}=180°) radiation is also measured by changing the direction of the plasma current. It is seen that the ECH produces remarkable enhancement of the perpendicular radiation, appreciable increase in the backward radiation and a little decrease in the

forward radiation. This result indicates the selective EC perpendicular heating of the energetic electrons but no enhanced absorption efficiency of the LH power, which is consistent with the magnetic measurement.

4.3.2 Current drive by the fast waves

In this section, initial experimental results using 200 MHz fast wave are presented. Figure II.4.2 shows the time behavior of the relevant plasma parameters for two typical discharge shots at $\bar{n}_e=1.5\times10^{19}$ m^{-3} and $B_t=1.32$ T. The solid line indicates the result of FW combined with ECH and the dashed line indicates the result of independent application of the ECH and FW pulses in a shot. The radiated ECH and FW powers are $P_{ECH}=100$ kW and $P_{FW}=40$ kW, respectively. The value of $\Delta\Phi_{FW}$ is set at 135° and RF spectrum of the fast waves is thus calculated to have a mild peak around $N_{//}=3$ in the direction of the current carrying electron drift. The working gas is deuterium and the plasma current is kept constant at $I_p=200$ kA. The present plasma parameters give us 1.1-5 for the accessible $N_{//}$ at the plasma center and r/a=0.9 for the radial position of the LH resonance layer at 200 MHz. The combination of the ECH and FW pulses is seen to make an appreciable increase in the EC emissions with the frequencies 50.4 GHz and 78.4 GHz which correspond to $f_T/(2f_{c0})=0.68$ and 1.06, respectively. Note that the emission at 50.4 GHz comes from nonthermal electrons since 50.4 GHz is not the electron cyclotron frequencies in the plasma. The emission in the extraordinary mode was measured in the horizontal direction with a calibrated heterodyne receiver. A little increase in the loop voltage is also seen during the FW pulse in both shots. At the same time, an increase in the line intensity of metal impurities was observed. We have also measured the soft x-ray radiation, which shows noticeable increase in the tail for electron in the range of 40-100 keV by the FW pulse.

The observed results indicate an appreciable interaction of the fast waves and the energetic electrons which leads to the current drive at the higher density. No indication of FWCD has been, however, obtained from the measurement of the loop voltage. The reason for this could be that the RF power and the shape of RF spectrum are not sufficient to overcome the increase of the loop voltage due to

enhanced impurity flux. From the calculation [7], a driven current less than 10 kA is predicted in the present experimental conditions assuming 1% of the fraction of the energetic electrons with the temperature of 40 keV. This would result by itself in a relative drop of the loop voltage of only a few percent.

References

[1] Fidone, I., et al., in Heating in Toroidal Plasma (Pro. 4th Int. Symp. Rome, 1984) Vol. 2 (1984) 872.
[2] Krivenski, V., et al., Nucl. Fusion 25 (1984) 2468.
[3] Shoji, T., et al., in Controlled Fusion and Plasma Physics (Pro. 11th Europ. Conf. Aachen 1983) Vol. 1 (1983) 55.
[4] Hoshino, K., et al., Japan Atomic Energy Research Institute Report, JAERI-M 85-169 (1985).
[5] Uesugi, Y., et al., Japan Atomic Energy Research Institute Report, JAERI-M 86-103 (1086).
[6] Yamamoto, T., et al., in Controlled Fusion and Plasma Heating (Pro. 13th Europ. Conf. Schliersee) Vol. 10C part II (1986) 437.
[7] Yamamoto, T., et al., Japan Atomic Energy Research Institute, Report, JAERI-M 86-115 (1986).

5. Development of a Multi-Channel Bolometer Array and its Application to the JFT-2M Tokamak Plasma

5.1 Introduction

Multi-channel bolometer array is installed to measure the radiation profile in the various plasmas of JFT-2M tokamak.

On the designing of a bolometer array, the following characteristics are required to the sensor head of bolometer:

(i) high sensitivity to gain the signal to noise ratio even in the profile measurement,
(ii) long colling time to remove the effect of heat loss during plasma pulse,
(iii) quick response to pick up the rapid raise at the onset of the heating pulse.

enhanced impurity flux. From the calculation [7], a driven current less than 10 kA is predicted in the present experimental conditions assuming 1% of the fraction of the energetic electrons with the temperature of 40 keV. This would result by itself in a relative drop of the loop voltage of only a few percent.

References

[1] Fidone, I., et al., in Heating in Toroidal Plasma (Pro. 4th Int. Symp. Rome, 1984) Vol. 2 (1984) 872.
[2] Krivenski, V., et al., Nucl. Fusion 25 (1984) 2468.
[3] Shoji, T., et al., in Controlled Fusion and Plasma Physics (Pro. 11th Europ. Conf. Aachen 1983) Vol. 1 (1983) 55.
[4] Hoshino, K., et al., Japan Atomic Energy Research Institute Report, JAERI-M 85-169 (1985).
[5] Uesugi, Y., et al., Japan Atomic Energy Research Institute Report, JAERI-M 86-103 (1086).
[6] Yamamoto, T., et al., in Controlled Fusion and Plasma Heating (Pro. 13th Europ. Conf. Schliersee) Vol. 10C part II (1986) 437.
[7] Yamamoto, T., et al., Japan Atomic Energy Research Institute, Report, JAERI-M 86-115 (1986).

5. Development of a Multi-Channel Bolometer Array and its Application to the JFT-2M Tokamak Plasma

5.1 Introduction

Multi-channel bolometer array is installed to measure the radiation profile in the various plasmas of JFT-2M tokamak.

On the designing of a bolometer array, the following characteristics are required to the sensor head of bolometer:

(i) high sensitivity to gain the signal to noise ratio even in the profile measurement,
(ii) long colling time to remove the effect of heat loss during plasma pulse,
(iii) quick response to pick up the rapid raise at the onset of the heating pulse.

Based on the above requirements, a semi-conductor type of bolometer head is adopted. It has high sensitivity of an order of magnitude than the conventional metal film bolometers, and also has long cooling time by using in "free standing" state. Pulse response is almost comparable as the metal type one.

5.2 Apparatus

Used sensor head is Thinister 51K1C237 (Victory Engineering Corporation). Characteristics of the thinister are as follows: the size of 2mm×2mm square, electric resistance of about 200kΩ and response time of about 0.2ms.

Used sensor head is suspended by fine metal leads in order to minimize the heat conduction which is called "free standing". Cooling time in the vacuum is about 10s which is enough long than the JFT-2M pulse duration of about 1s. Therefore, the bolometer can be applied without additional thermal correction.

In Fig. II.5-1 the installation of the bolometer array on JFT-2M tokamak is shown. The bolometer array is constructed by twenty nine sensor heads of thinistor. Before the installation, the relative sensitivity of each sensor is calibrated by the irradiation of standard illuminant (tungusten filament, wavelength from 2000Å to 10000Å) located in front of the entrance slit. Each relative sensitivity agrees well with the $\cos\theta$-dependence.

The block diagram of bolometer measurement system is shown in Fig. II.5-2. Thinister bolometer changes its resistance with negative temperature coefficient by the wide spectrum range of irradiation from soft X-ray to infrared. The change of the resistance is converted to the corresponding voltage change through the bridge-balanced circuit and the amplifiers. Final output from the isolation amplifier is fed to CAMAC data processing system, and stored in JFT-2M data acquisition system.

5.3 Application to the JFT-2M tokamak plasma

With using the bolometer array, vertical radiation profile of the several type of discharges, especially the H-mode phase, on JFT-2M tokamak plasma is obtained. Figure II.5-3 shows the radiation profile with the H-mode transition during NBI heating in upper single-null

divertor plasma. The profile is the line-integrated one. Figures II.5-3(a) and 3(b) show the time behavior and the slice cut of Fig. II.5-3(a) at a fixed time, respectively. In the ohmic phase there appears the intense radiation locality at the sight line including the separatrix, which conserves the remote radiative cooling. After the transition to the H-mode phase at 710ms, the radiation profile at the first stage is similar to that of the ohmic phase, but gradually peeks at the plasma center, which indicates the metal impurity accumulation due to the increased particle confinement.

Another array is being designed to observe in the vertical line of sight which can be corresponding to the strong locality of radiation profile in the inside/outside of the torus like as the "Marfe" phenomenon.

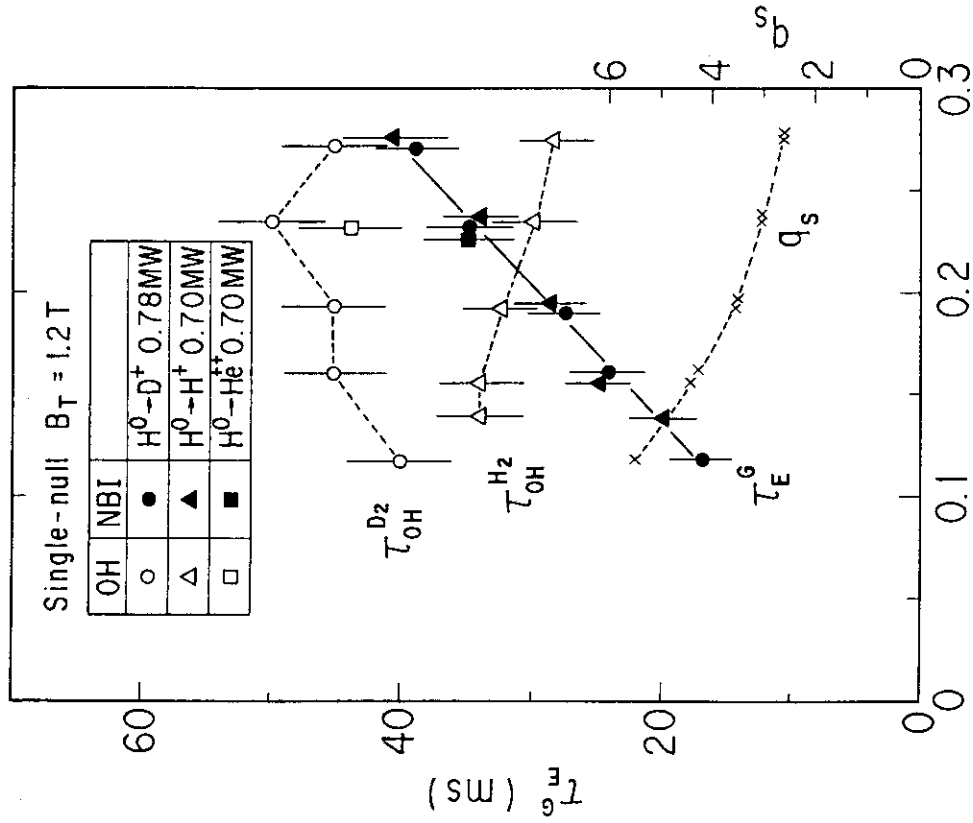

Fig. II.2-2 Dependence of global energy confinement times on I_p for H, D and He plasma. Confinement time of H-mode for H plasma exceeds enough that of ohmic phase at low q region.

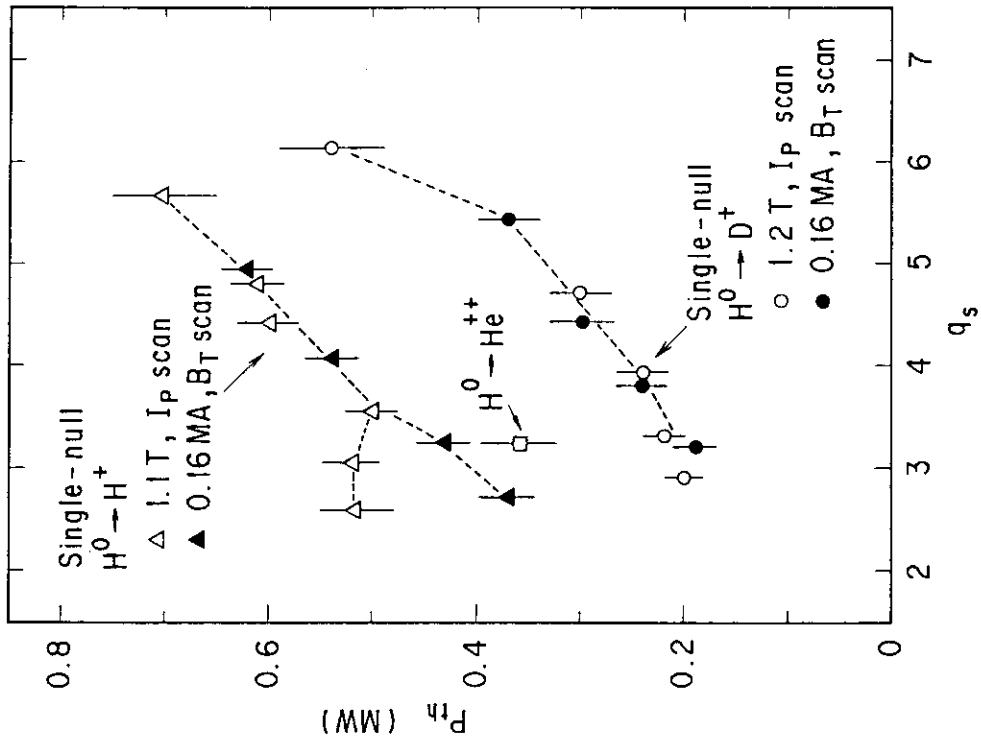

Fig. II.2-1 Threshold power P_{th} for the H-transition in divertor discharges. I_p-scan (0.11－0.28 MA), B_t-scan (0.65－1.4 T). q_s: surface safety factor.

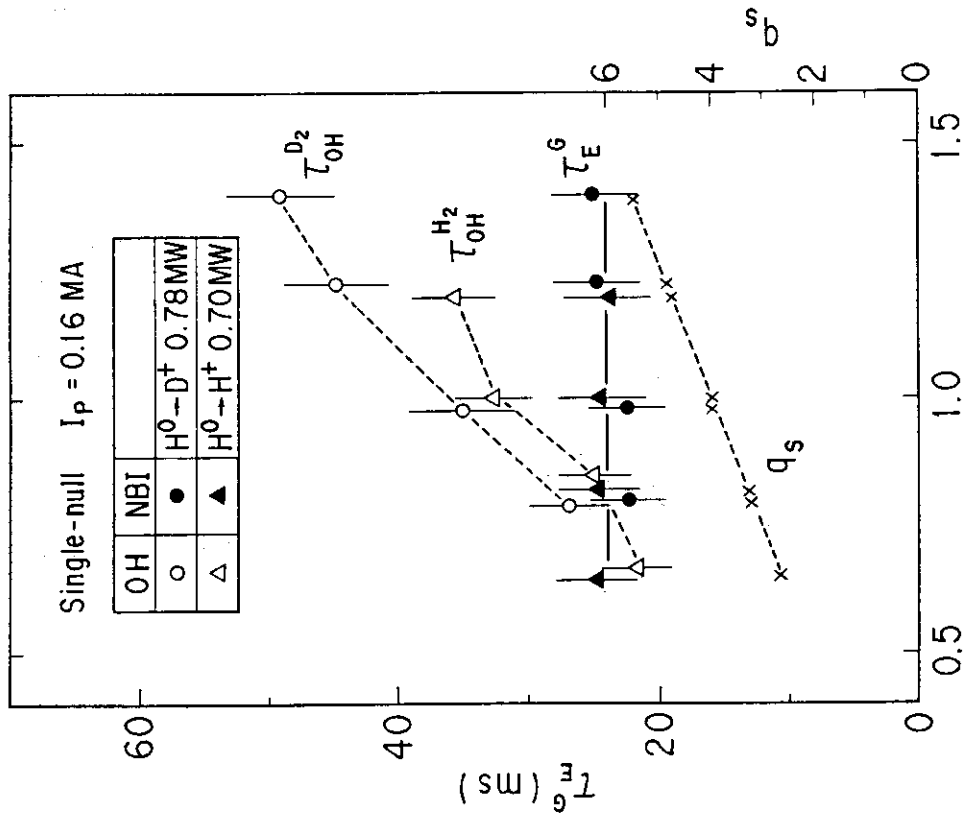

Fig. II.2-3 Dependence of global energy confinement times on B_t for H, D and He plasma. Confinement time of H-mode has no dependence on B_t, in contrast with that of ohmic case.

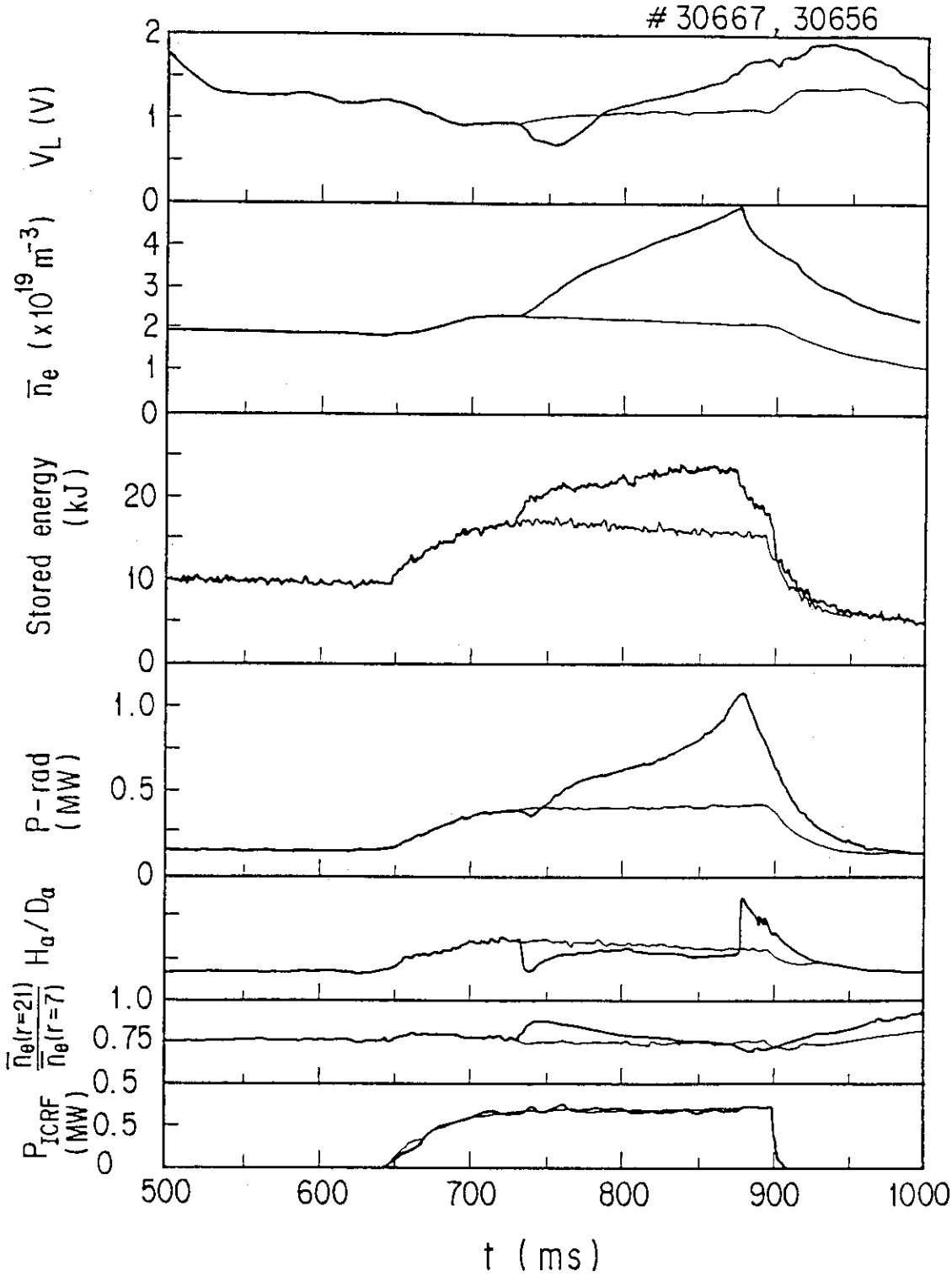

Fig. Ⅱ.2-4 Time evolution of H-mode transition during ICRF heating. Thin lines show L-mode discharge with similar discharge conditions.

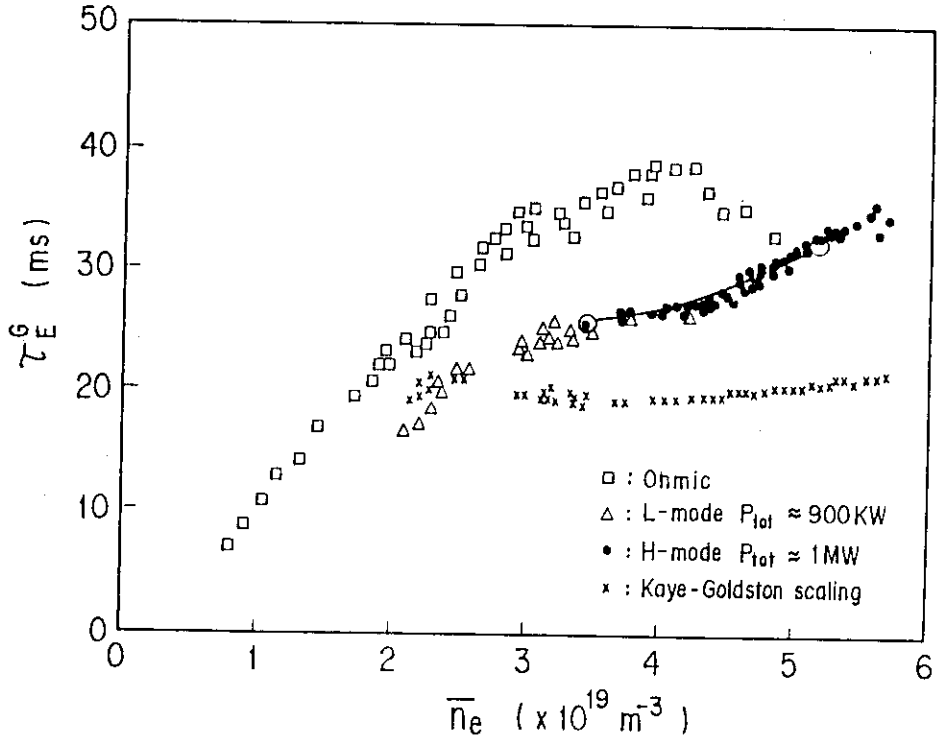

Fig. II.2-5 Electron density dependence of global energy confinement times for ohmic, L-mode and H-mode discharges.

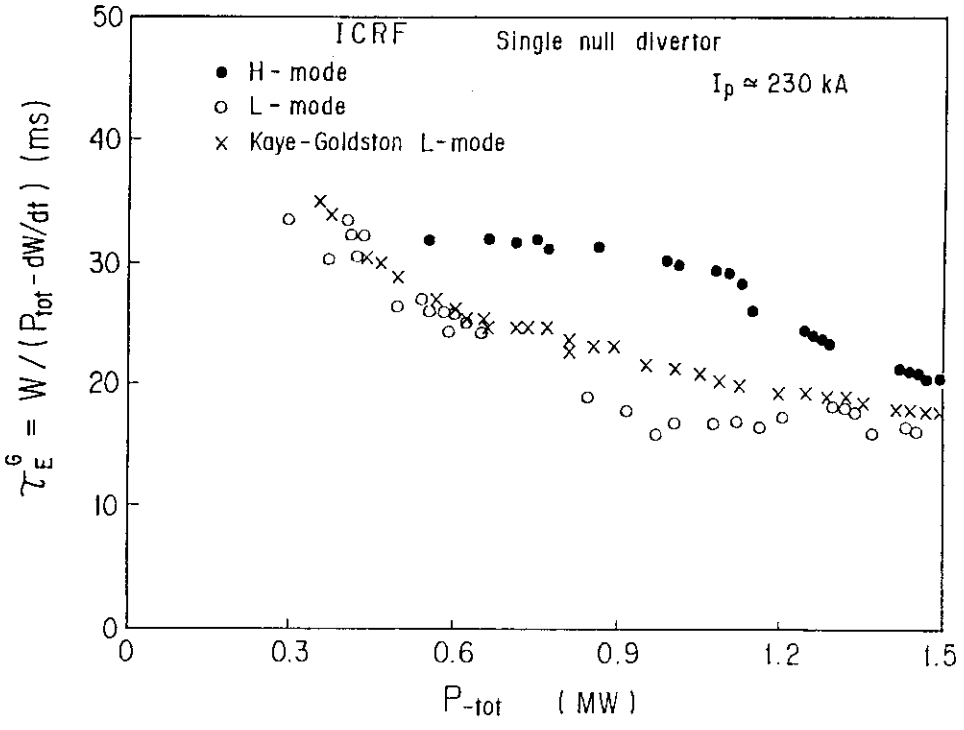

Fig. II.2-6 Power dependence of global energy confinement times for L-mode and H-mode discharges.

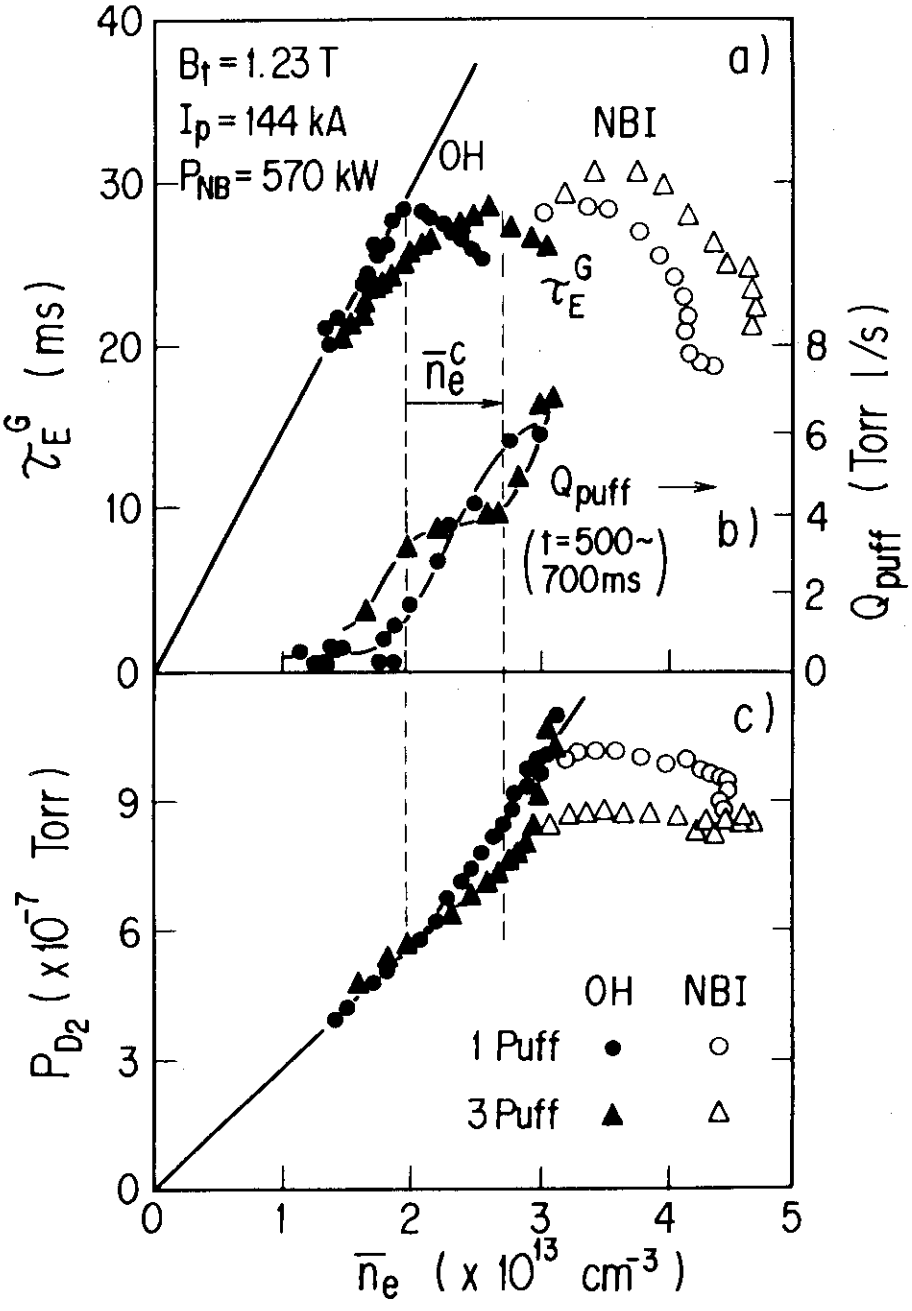

Fig. II.2-7 The plots of (a) energy confinement time τ_E^G, (b) required gas flow rates Q_{puff} and the resulting D_2 pressure P_{D_2} against $\bar{n}_e$. The gas-puff program was fixed up to t = 400 ms and then Q_{puff}^A (t = 400 - 700 ms) was scanned for the single-puff case; Q_{puff}^B and Q_{puff}^C (t = 500 - 700 ms) were added for the distributed-puff case.

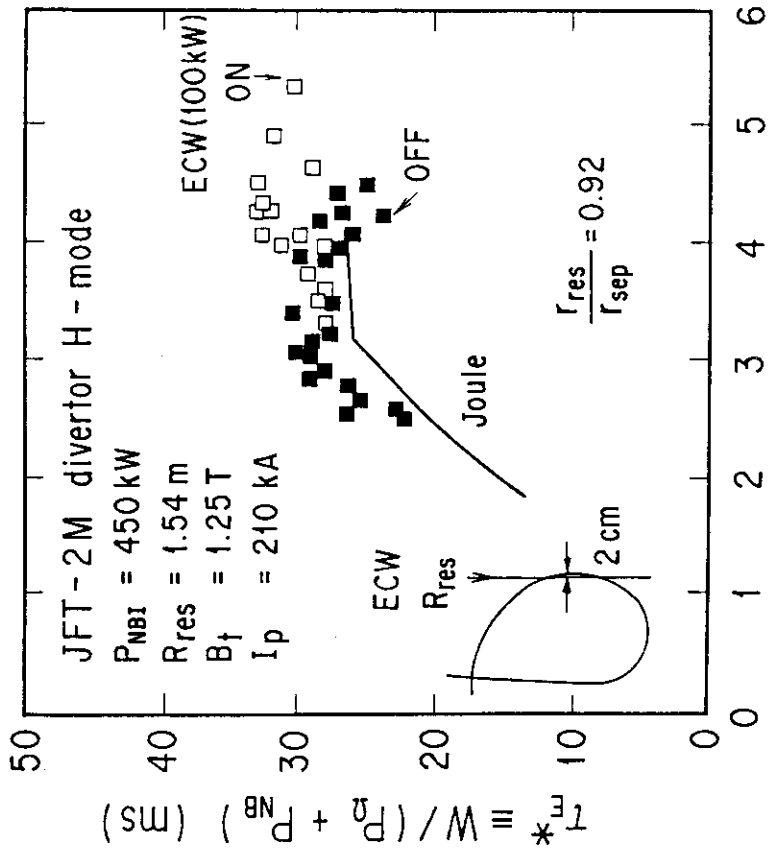

Fig. II.2-9 The density dependences of energy confinement time τ_E^* for Joule heating phase and H-mode phase with and without ECW. The ratio of minor radii of the ECW resonance r_{res} and the separatrix surface r_{sep} is 0.92.

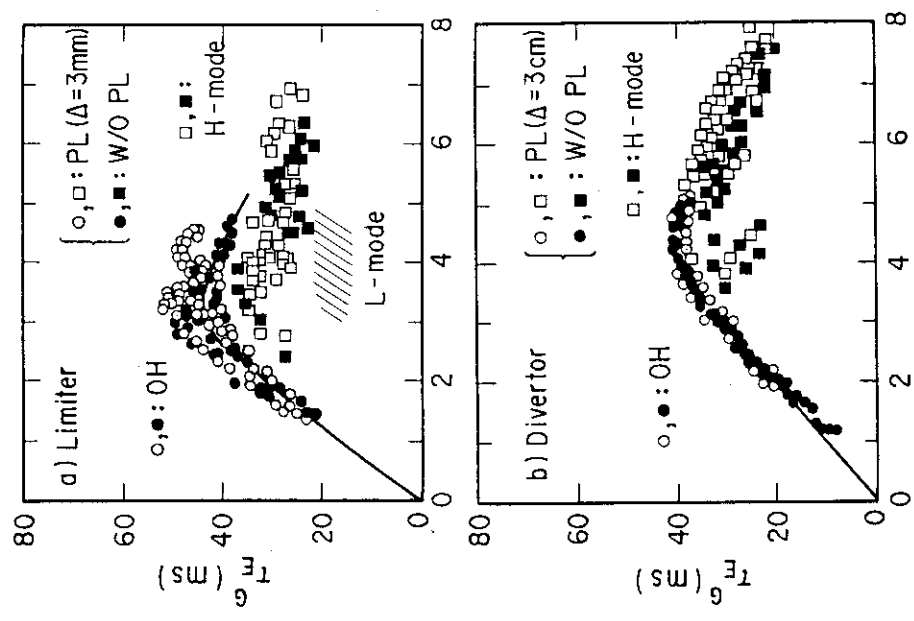

Fig. II.2-8 Comparison of τ_E^G for the OH, L- and H-mode phases of a) limiter and b) divertor discharges with and without pump limiter. (-0.1 MW $< dW_s/dt < 0.2$ MW)

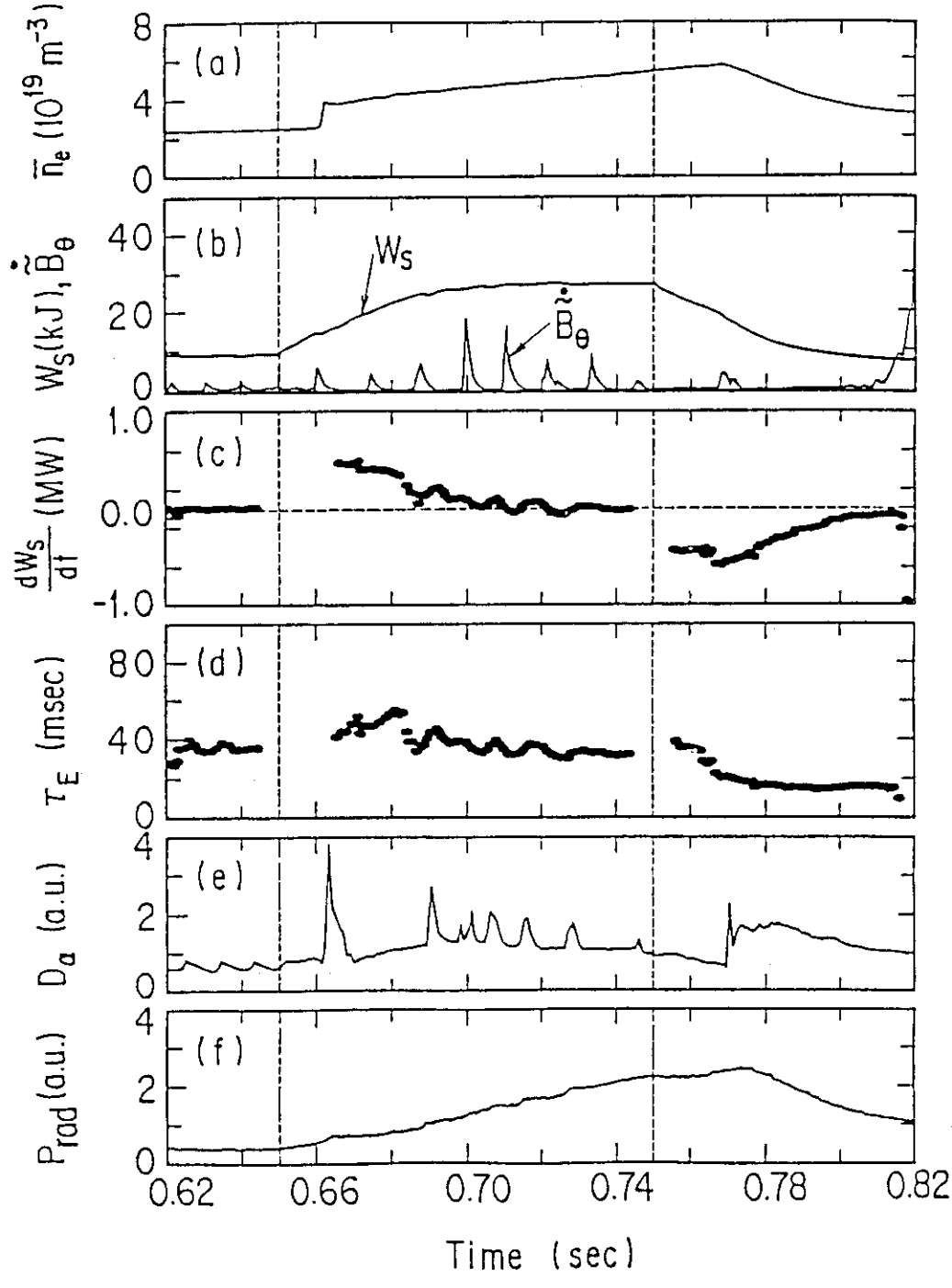

Fig. II.3-1 Time evolution of various plasma parameters in the small pellet injection: (a) line-averaged electron density ($\bar{n}_e$), (b) stored energy (W_s) and half envelope of $\tilde{B}_\theta$ signal, (c) differential of W_s determined by fitting 5 points (5 msec) of W_s to cubic function, (d) global energy confinement time (τ_E), (e) D_α-intensity apart from the singular point, (f) sum of radiation and charge exchange loss power from lower half of plasma measured by the bolometer.

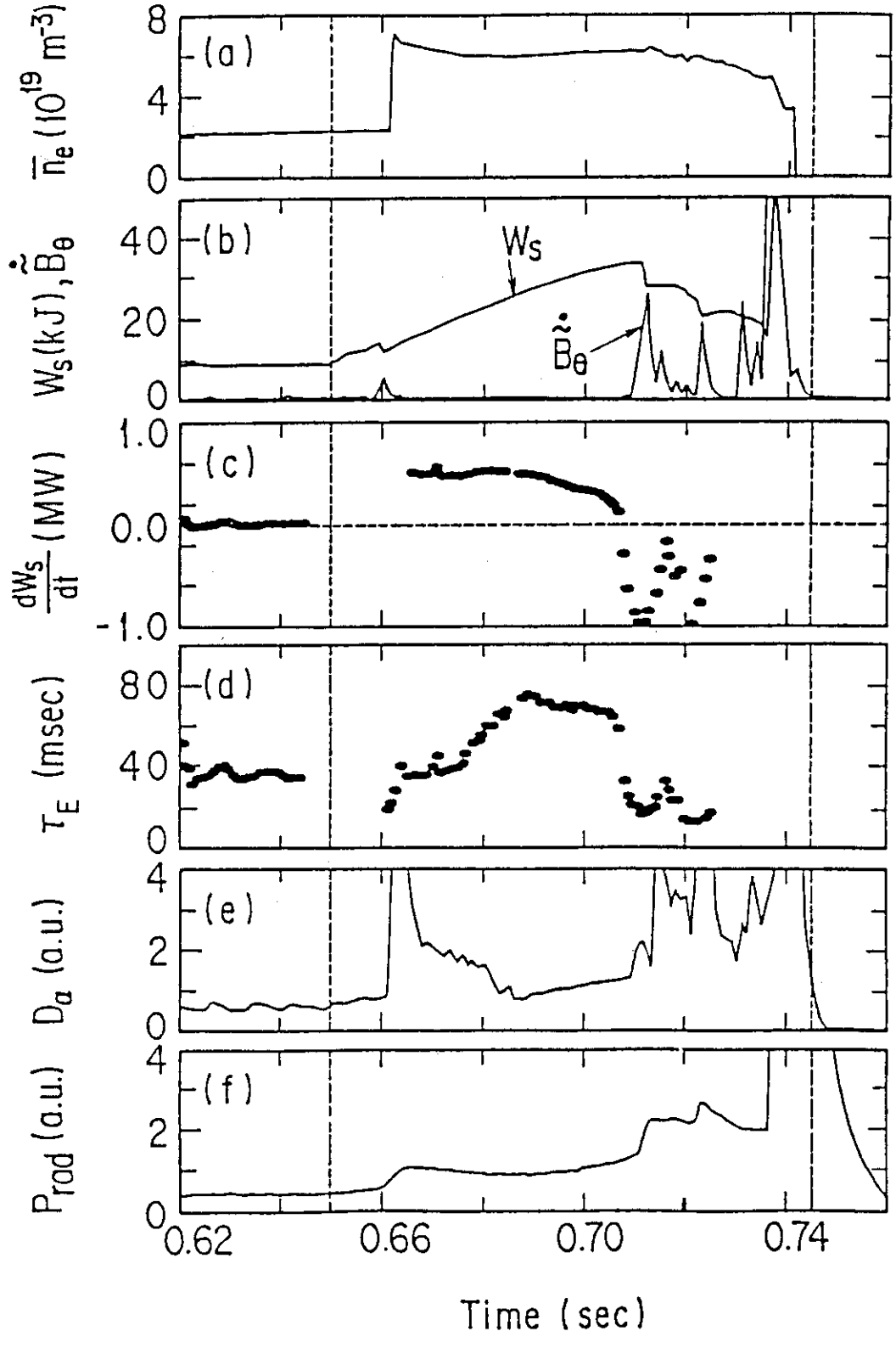

Fig. II.3-2 Time evolution of various plasma parameters: columns from (a) to (f) are the same as Fig. II.3-1.

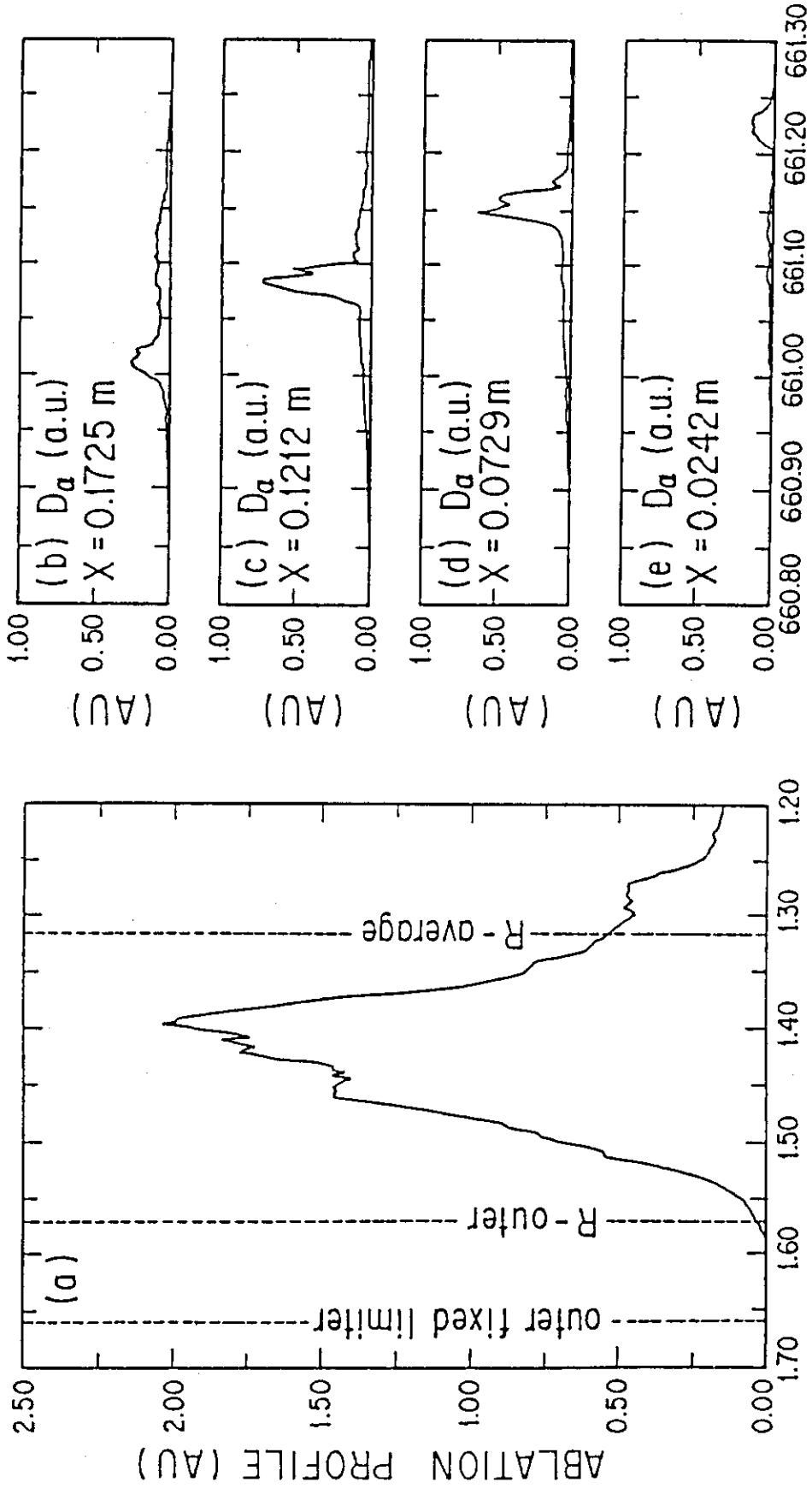

Fig. II.3-3 Ablation profiles of the D_2 pellet: (a) ablation profile measured horizontally by a single H_α/D_α detector, (b), (c), (d) and (e) are measured vertically by H_α/D_α detector array. X in (b), (c), (d) and (e) are the length from the center of the vacuum vessel (R = 1.31 m) on the mid-plane.

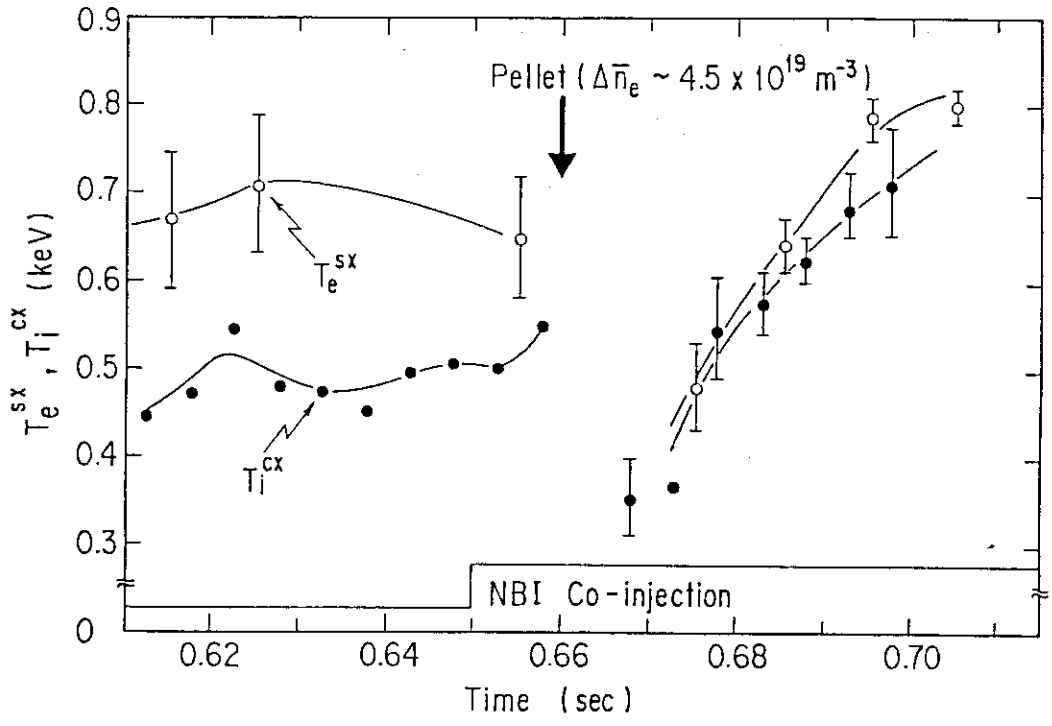

Fig. II.3-4 Time evolution of central electron and ion temperature of large-pellet fueled discharges measured by soft X-ray and mass-separated neutral particle measurement.

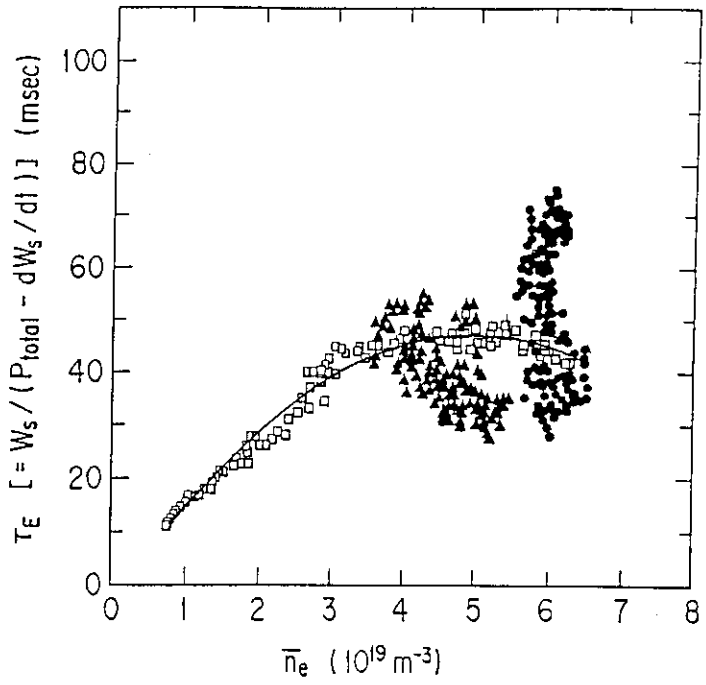

Fig. II.3-5 Line-averaged electron density ($\bar{n}_e$) versus global energy confinement time (τ_E). Squares (□) are τ_E of ohmically heated discharges, closed triangles (▲) are τ_E of small-pellet fueled discharges, closed circles (●) are τ_E of large-pellet fueled discharges.

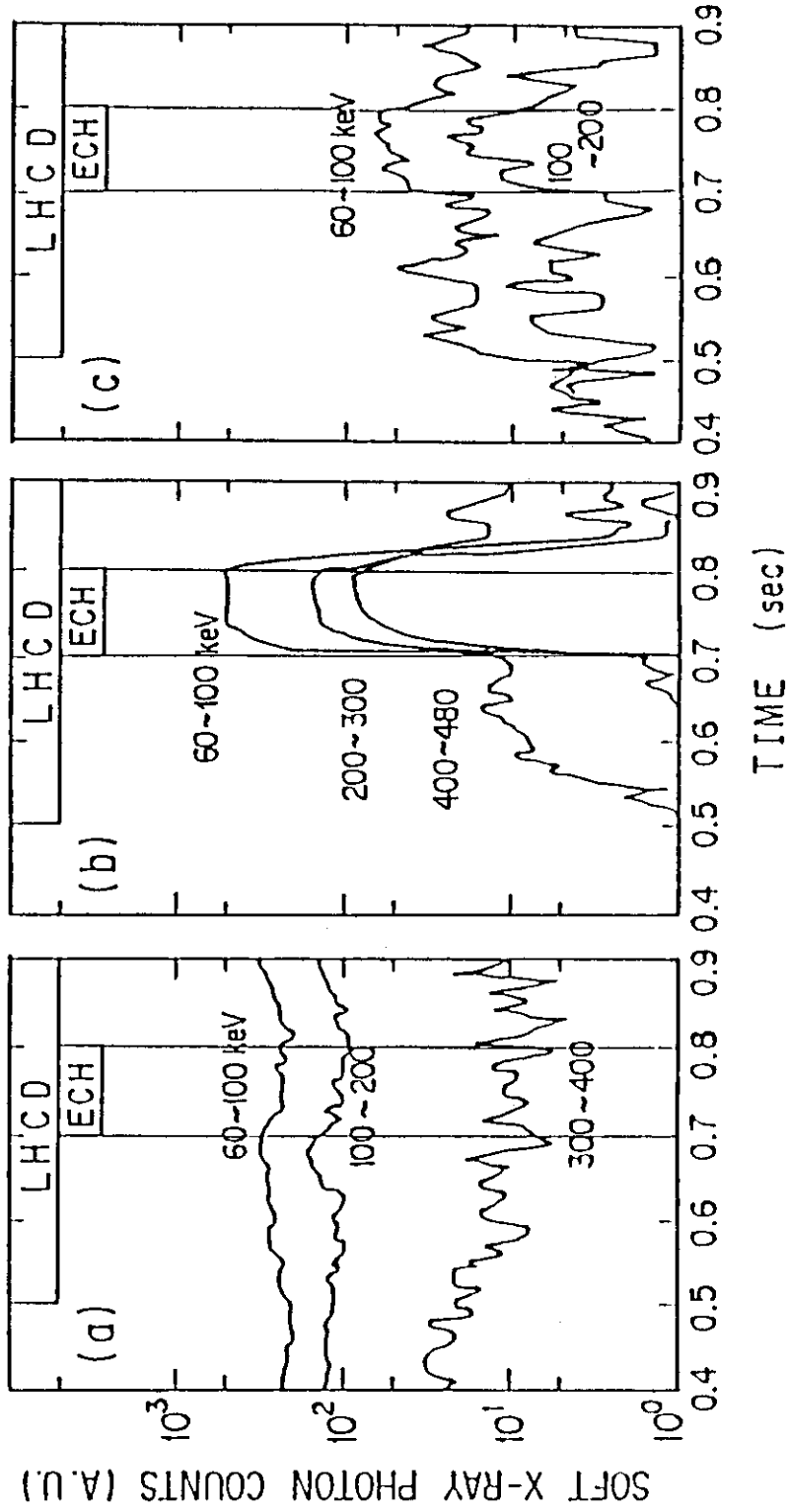

Fig. II.4-1 Time evolution of the soft x-ray photon counts integrated over different energy ranges for three different viewing angles. (a) $\theta_{sx} = 0°$, (b) $\theta_{sx} = 90°$ and (c) $\theta_{sx} = 180°$. $B_t = 1.34$ T, $I_p = 100$ kA, $\bar{n}_e = 2 \times 10^{18}$ m^{-3}, $P_{LH} = 100$ kW and $P_{ECH} = 100$ kW.

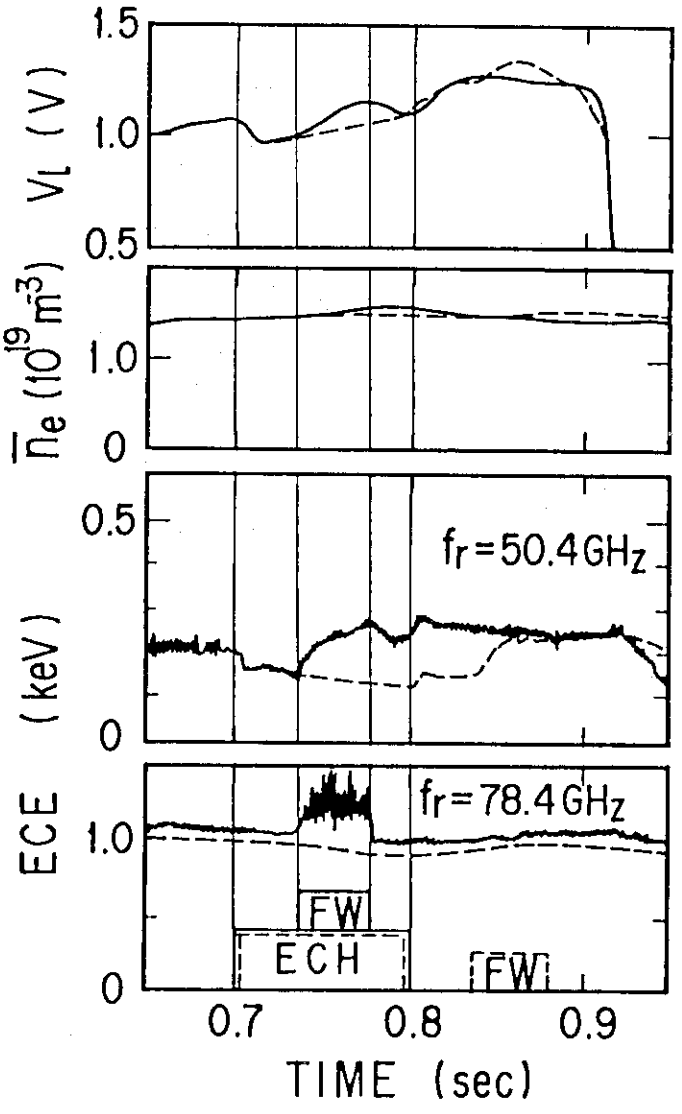

Fig. II.4-2 (a) Time evolution of the relevant plasma parameters with and without (solid and dashed lines) the FW power of 40 kW during the ECH pulse. B_t = 1.32 T, I_p = 200 kA and P_{ECH} = 90 kW.

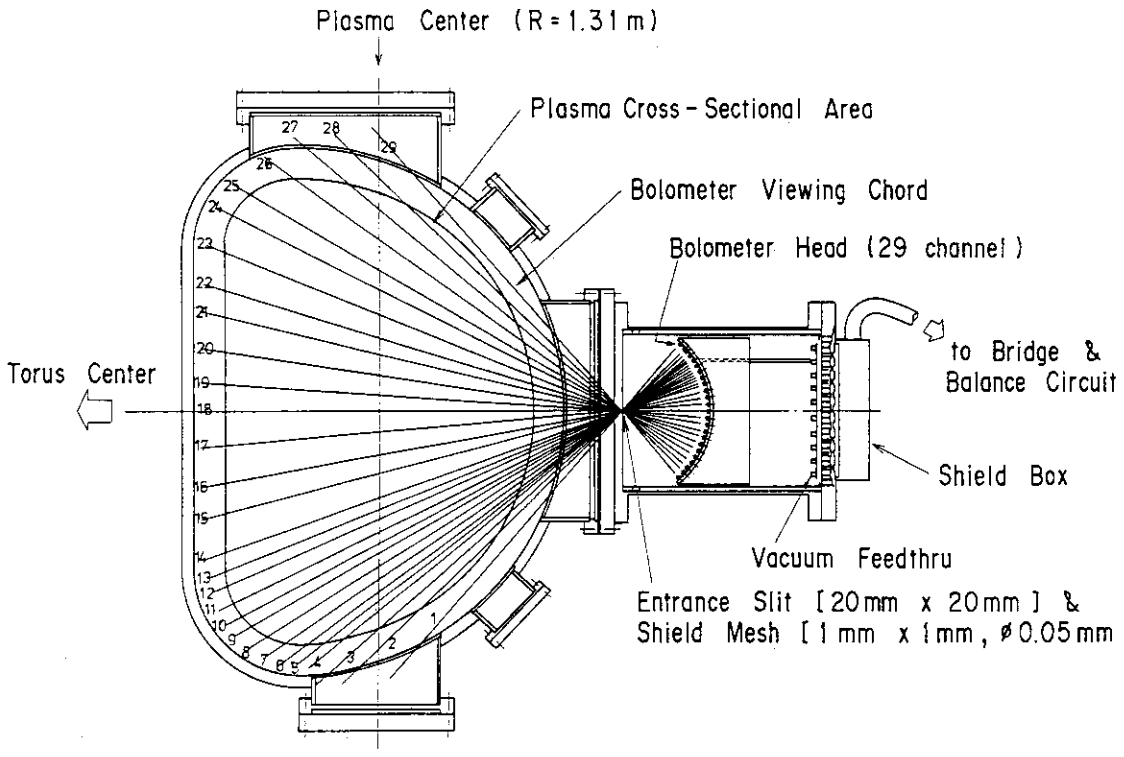

Fig. II.5-1 Installation of the bolometer array on the JFT-2M tokamak.

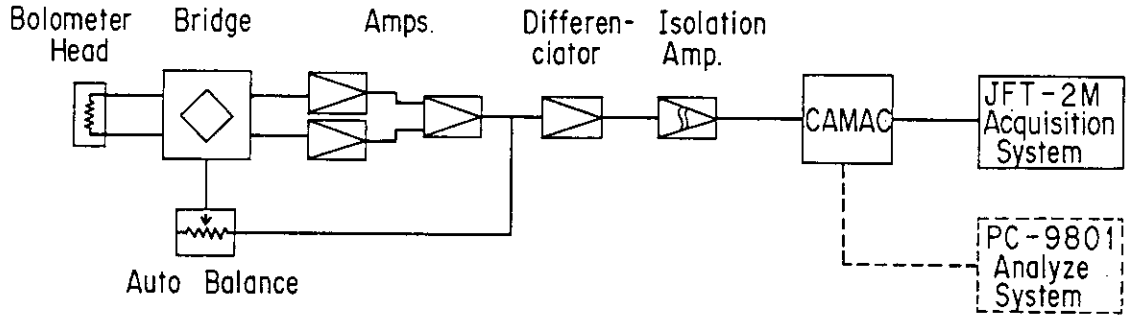

Fig. II.5-2 Block diagram of bolometer measurement system.

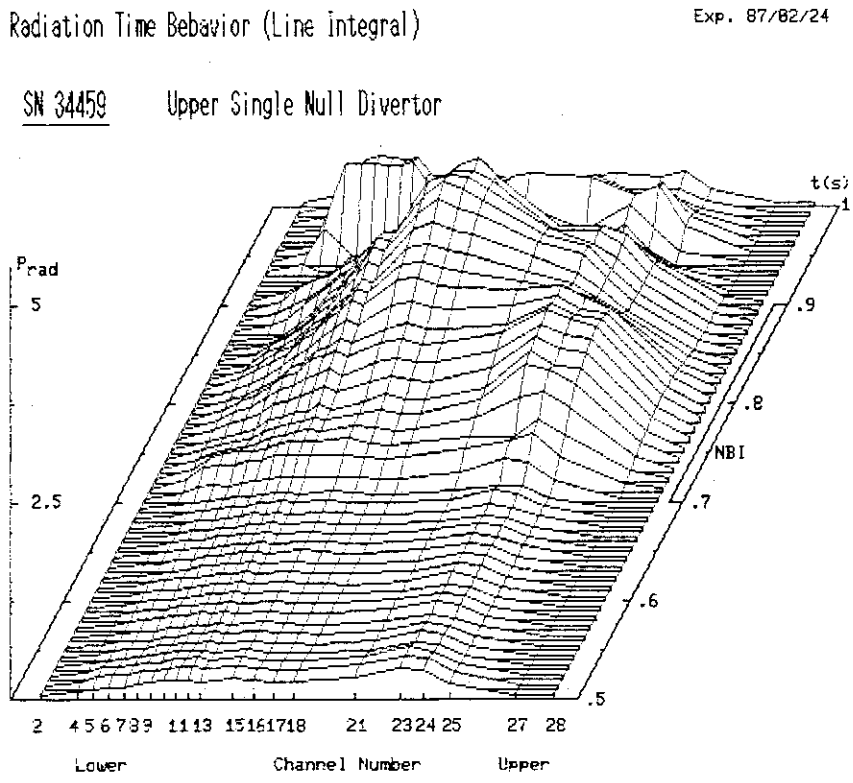

(a)

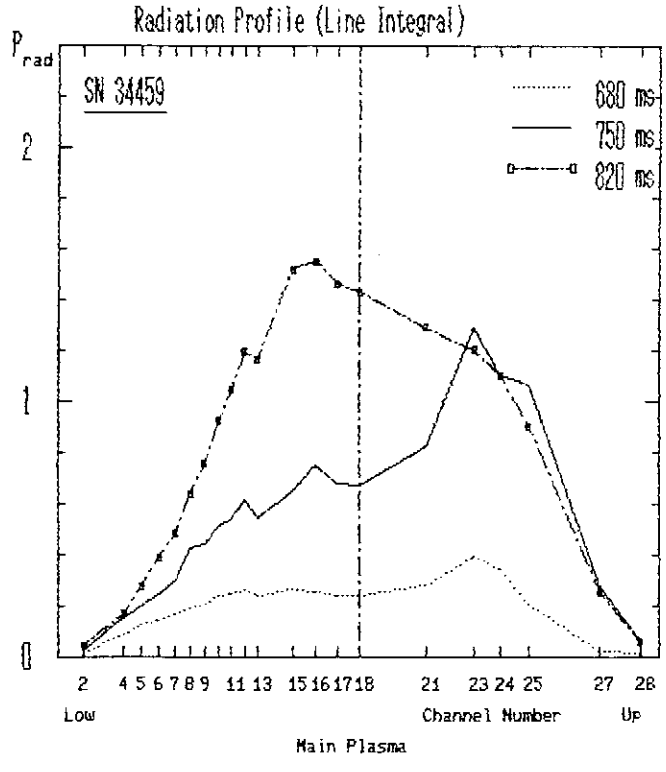

(b)

Fig. II.5-3 (a) Time behavior of the line-integrated radiation profile.
(b) Line integrated radiation profile at a fixed time.

III. OPERATION AND MAINTENANNCE

1. Introduction

Facility Operation and Engineering Division has been engaged in operation and maintenance of JFT-2M, Neutral Beam Injection (NBI) system, RF Heating devices [Lower Hybrid Heating (LHH) and Electron Cyclotron Heating (ECH)] and Flywheel Motor-Generator (MG), and also in development of auxiliary equipments and instruments. In this fiscal year all the devices have been operated smoothly on schedule, and the careful maintenance have been performed daily and periodically.

2. Operation and Maintenance

An overhaul of MG has done because of a drop in insulation, and the insulation resistance of MG has been recovered over 100 MΩ. JFT-2M tokamak was operated on schedule in spite of a few troubles. The main objectives of operation in this fiscal year was the plasma confinement experiments.

NBI system has been operated smoothly on experimental schedule and calibrations of the injection power were done frequently. For the improvement of the ratio of proton, ion sources of B-line have been changed to bucket-type ion sources.

RF heating systems (LHH and ECH) were also operated smoothly on schedule. The results of operation in the MG, JFT-2M, NBI, LHH and ECH are shown in Table III.2-1.

3. Development of Equipments and Instruments

3.1 Pellet injection system

After an enlargement of a pellet which size is 1.65 mmϕ×1.65mm length, a velocity of pellet injected was measured. Figure III.3-1 shows the velocity versus propellant gas pressure. Closed circles are the velocity of H_2-pellet accelerated by He gas, and crosses are the

III. OPERATION AND MAINTENANNCE

1. Introduction

Facility Operation and Engineering Division has been engaged in operation and maintenance of JFT-2M, Neutral Beam Injection (NBI) system, RF Heating devices [Lower Hybrid Heating (LHH) and Electron Cyclotron Heating (ECH)] and Flywheel Motor-Generator (MG), and also in development of auxiliary equipments and instruments. In this fiscal year all the devices have been operated smoothly on schedule, and the careful maintenance have been performed daily and periodically.

2. Operation and Maintenance

An overhaul of MG has done because of a drop in insulation, and the insulation resistance of MG has been recovered over 100 MΩ. JFT-2M tokamak was operated on schedule in spite of a few troubles. The main objectives of operation in this fiscal year was the plasma confinement experiments.

NBI system has been operated smoothly on experimental schedule and calibrations of the injection power were done frequently. For the improvement of the ratio of proton, ion sources of B-line have been changed to bucket-type ion sources.

RF heating systems (LHH and ECH) were also operated smoothly on schedule. The results of operation in the MG, JFT-2M, NBI, LHH and ECH are shown in Table III.2-1.

3. Development of Equipments and Instruments

3.1 Pellet injection system

After an enlargement of a pellet which size is 1.65 mmϕ×1.65mm length, a velocity of pellet injected was measured. Figure III.3-1 shows the velocity versus propellant gas pressure. Closed circles are the velocity of H_2-pellet accelerated by He gas, and crosses are the

III. OPERATION AND MAINTENANNCE

1. Introduction

Facility Operation and Engineering Division has been engaged in operation and maintenance of JFT-2M, Neutral Beam Injection (NBI) system, RF Heating devices [Lower Hybrid Heating (LHH) and Electron Cyclotron Heating (ECH)] and Flywheel Motor-Generator (MG), and also in development of auxiliary equipments and instruments. In this fiscal year all the devices have been operated smoothly on schedule, and the careful maintenance have been performed daily and periodically.

2. Operation and Maintenance

An overhaul of MG has done because of a drop in insulation, and the insulation resistance of MG has been recovered over 100 MΩ. JFT-2M tokamak was operated on schedule in spite of a few troubles. The main objectives of operation in this fiscal year was the plasma confinement experiments.

NBI system has been operated smoothly on experimental schedule and calibrations of the injection power were done frequently. For the improvement of the ratio of proton, ion sources of B-line have been changed to bucket-type ion sources.

RF heating systems (LHH and ECH) were also operated smoothly on schedule. The results of operation in the MG, JFT-2M, NBI, LHH and ECH are shown in Table III.2-1.

3. Development of Equipments and Instruments

3.1 Pellet injection system

After an enlargement of a pellet which size is 1.65 mmϕ×1.65mm length, a velocity of pellet injected was measured. Figure III.3－1 shows the velocity versus propellant gas pressure. Closed circles are the velocity of H_2-pellet accelerated by He gas, and crosses are the

velocity of D_2-pellet propelled by H_2 gas. A solid-line is a velocity of H_2-pellet propelled by He gas calculated from ideal gun-model given by Milora and Foster. These data indicate that the measured velocity reaches 80 to 95% of the calculated velocity, except some data when the gas pressure is 10 kg/cm^2, and the maximum velocity of D_2-pellet propelled by H_2 gas is about 970 m/s at 24 kg/cm^2.

A shadowgraph of pellet gives imformations of a pellet size and shape. The shadowgraph as shown in Fig. III. 3－2 was taken through a Polaroid camera by backlighting the pellet with a spark-lamp (Xenon Corporation: model 437A Nanopulser) as shown in Fig. III. 3－3. The shadowgraph shows that a D_2 pellet with a velocity of 769 m/s flys in its integrity.

A four-pellet injector developed newly for JFT-2M has been operated since March 1987. Four main housing/barrel housing (gun barrel) assemblies are independent each other. However a heat-exchanger is common to four assemblies. This mechanism prevents an ice-pellet from heat which is generated on the gun-fire. Two pellet-size were designed at 1.28mmϕ×1.4mm length (three pellets) and 1.48mmϕ×1.7mm length (one pellet), and a each gun can propell a each pellet with a different velocity. As a careful adjustment the maximum velocity measured is about 1.4 km/s for H_2-pellet propelled by H_2 gas.

3.2 Characteristics of magnetically shielded mass-analyzer

Characteristics of a magnetically shielded quadrupole mass-analyzer (QMA: Balzers QMA-112) was experimented by changing the direction of the QMA to the magnetic field and species and pressures of gases. Figure III.3－4 (a) and (b) show the results in the case that the magnetic field is perpendicular and parallel to the QMA, respectively. In each figure a vertical line indicates the magnitude of the magnetic field when signals of QMA change 5% by the magnetic field, and a horizontal line indicates the mass to electric change (M/e). These figures show that signals of the QMA are hardly affected under approximately 100G and 20G in perpendicularly and parallelly impressed magnetic field, respectively regardless of species and pressures of gases. These experimental results agreed with the magnetic shield effect of mu-metal with 0.5mm thickness and 34mmϕ, which covered a rod system and an ion source of the QMA.

3.3 Development of ion sources in NBI system

On ion sources of NBI, a duo-Pigatron-type ion source has been changed to a bucket-type ion source for the improvement of the heating-efficiency. For comparison with effects of two types the beam-power and the ratio of proton were measured by a multi-element calorimeter and a spectroscopy, respectively. The performance of the bucker-type was as follows. The injection power increased about 200 kW, a divergence of the beam was improved approximately 10% and the ratio of proton improved from 55% to 80% compared with the duo-Pigatron-type.

Table Ⅲ.2-1 Operation of MG, JFT-2M, NBI, LHH and ECH

(Month)	4 5 6 7 8 9 10 11 12 1987 1 2 3
M-G	operation and maintenance
JFT-2M	operation and maintenance
NBI	operation and maintenance
LHH	operation and maintenance
ECH	operation and maintenance

Detail of the operation (M-G, JFT-2M, NBI, LHH and ECH)

	(Fiscal year)	1985	1986 APR-JUN	1986 JUL-SEP	1986 OCT-DEC	1987 JAN-MAR	Total
M-G	M-G (#1) (hours)	1124	238	393	181	268	1080
	M-G (#2) (hours)	1131	240	392	180	270	1082
JFT-2M	Total days of operation (days)	131	33	45	27	31	136
	Times of discharge (shots)	9746	2013	3220	1648	2112	8993
	Baking (times)	5	1	0	1	0	2
	Discharge cleaning (hours)	172	29	54	24	51	158
	Pellet injection (days)	62	13	11	5	2	31
NBI	Total days of operation (days)	77	28	18	12	25	83
	Flashing and injection (shots)	A: 12357 B: 7796	3133 653	1028 5040	2061 2990	4553 1225	A: 10775 B: 9908
	Conditioning (shots)	A: 8524 B: 7395	1134 4610	1334 2706	359 963	1384 8551	A: 4211 B: 16830
LHH	Total days of operation (days)	24	0	11	1	4	16
	Times of power injection (times)	2543	0	1014	119	308	1441
ECH	Total days of operation (days)	29	0	13	8	6	27
	Times of power injection (times)	19922	0	22628	4589	2506	29726

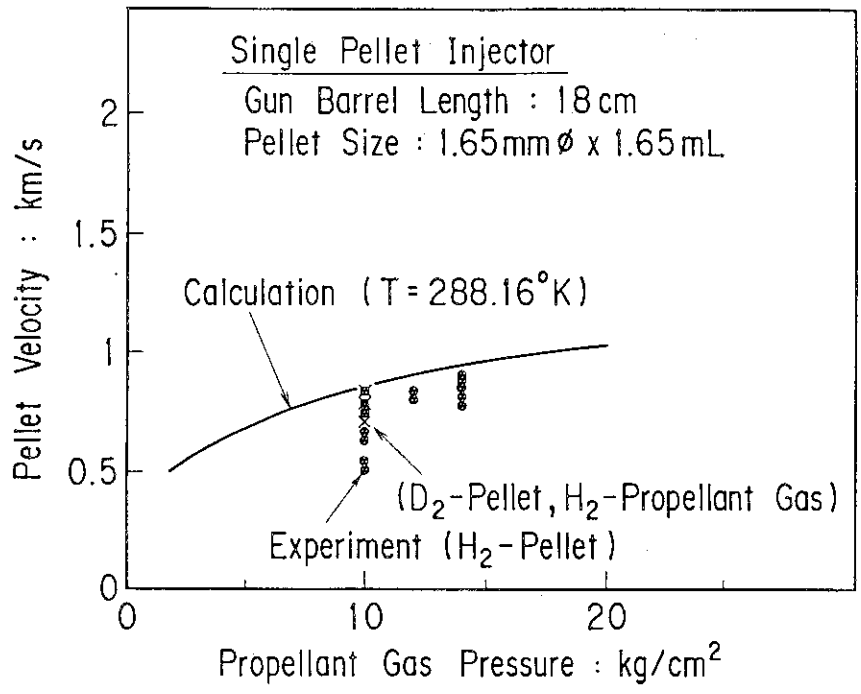

Fig. Ⅲ.3-1 The velocity versus propellant gas pressure. Closed circles are the velocity of H_2-pellet accelerated by He gas, and crosses are the velocity of D_2-pellet propelled by H_2 gas. A solid-line is a velocity of H_2-pellet propelled by He gas calculated from ideal gun-model.

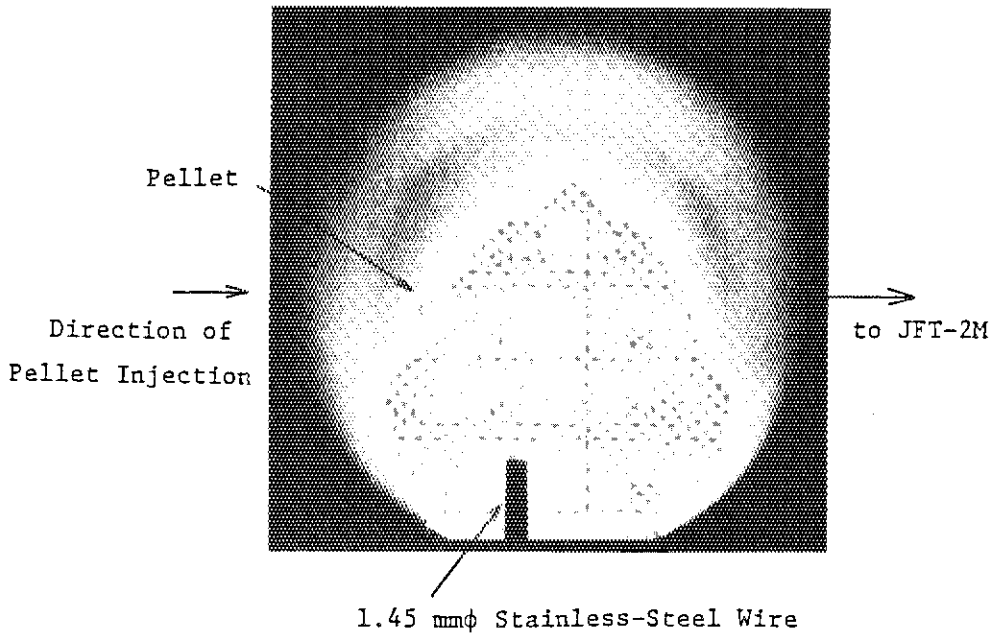

Fig. Ⅲ.3-2 Shadowgraph of D_2-pellet: velocity = 769 m/s.

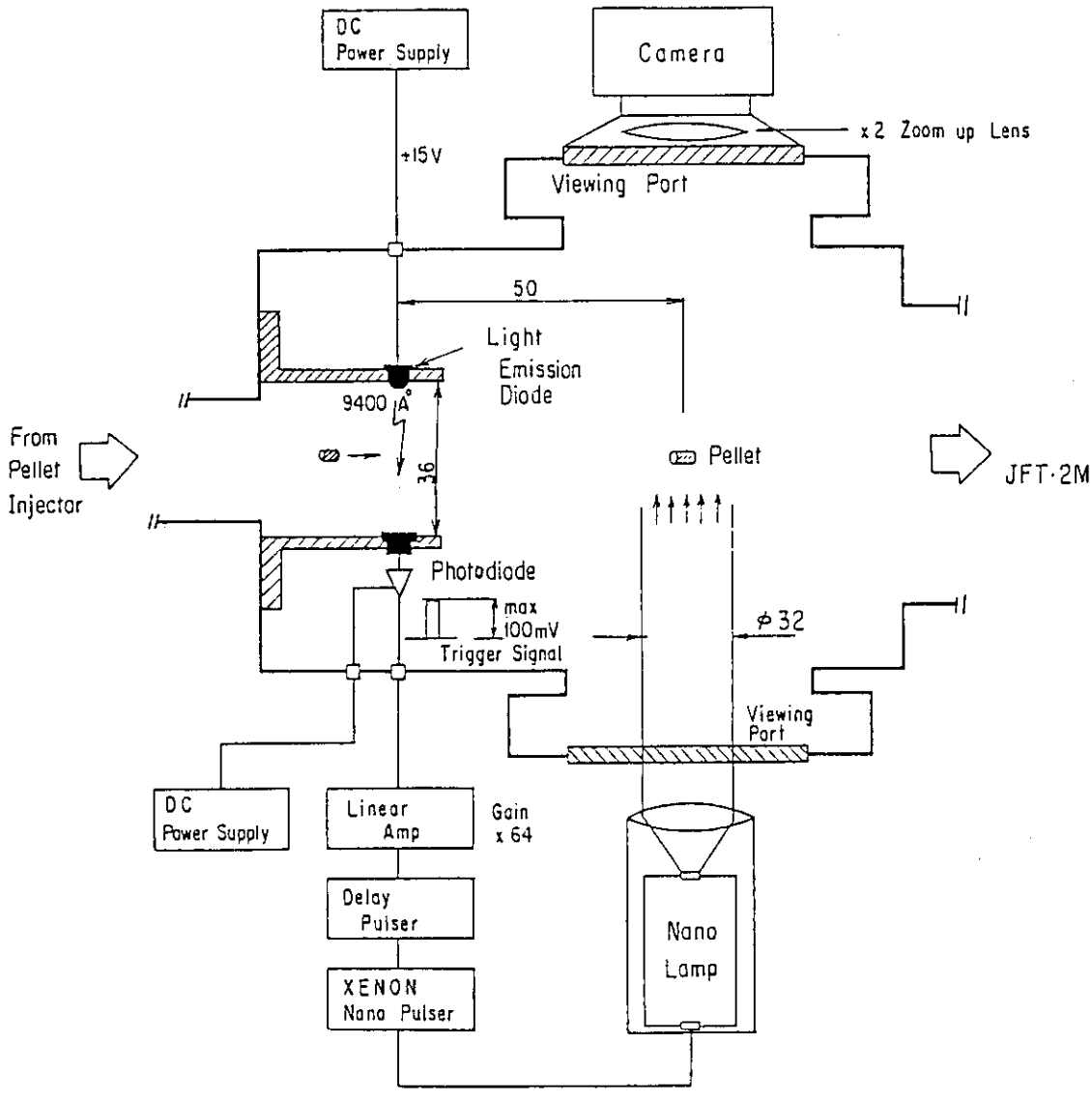

Fig. Ⅲ.3-3 Schematic diagram of pellet shadowgraph measurement.

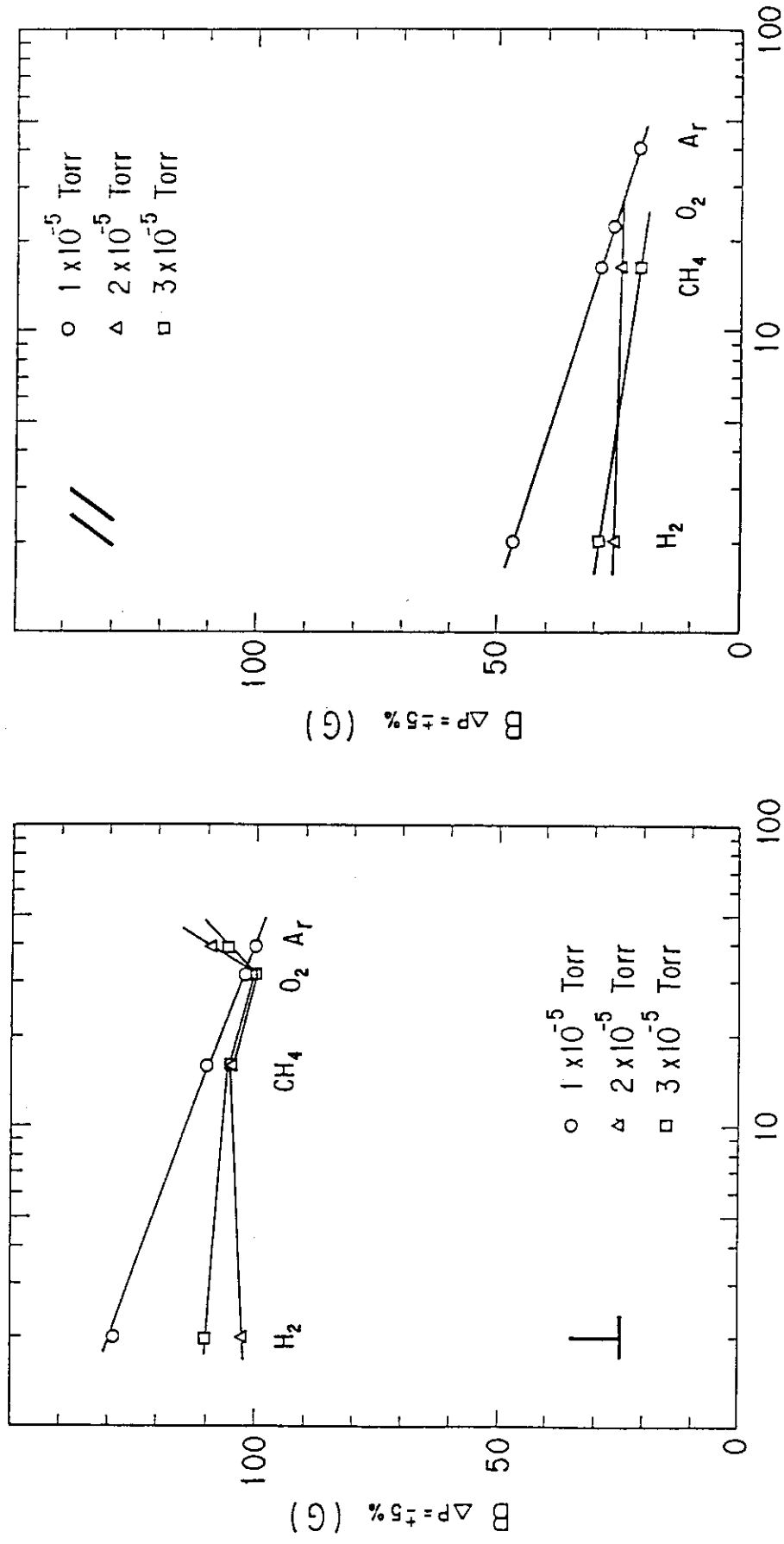

Fig. Ⅲ.3-4 Dependence of the magnitude of magnetic field which causes the 5% change of signals for M/e at different gas pressures in the case that magnetic field is perpendicular(a) and parallel(b) to the QMA rods.

IV. DEVELOPMENT OF PLASMA HEATING SYSTEM

1. Neutral Beam Injection System

1.1 Introduction

The research and development activities in the neutral beam injection systems are composed of two works. One is concerned with positive ion beam systems including the JT-60 NBI and another is a negative ion beam system for furture fusion devices. The JT-60 NBI system was completed in July, 1986 and the neutral beam power of 20 MW at the beam energy of 75 keV were injected successfully into the JT-60 plasma in October 1986. From the view point of plasma heating experiments in JT-60, it is quite important to estimate the exact injection power to the torus plasma in every condition. Therefore, the ion species in hydrogen ion beams, the geometrical transmission efficiency and the reionization loss have been measured in the wide operation regions using a prototype injector unit. Additionally, in order to change deposition profiles of the neutral beams without decreasing the injection power, we tried to lower the proton ratio by controlling the depth of ion source chamber.

In parallel with the developments of the JT-60 NBI, a conceptual design work on a negative-ion-based injector has been performed on 500keV/20MW neutral beam injector for Fusion Experimental Reactor. The development of negative ion sources, which is the most important component in realizing the system, are in progress. A cryosorption pump using the sorbent SF_6 gas layer has been tested for helium evacuation in fusion devices.

1.2 Modified ion source with variable proton ratio

In order to perform the JT-60 plasma heating experiments in the wide operation regions of plasma density with keeping the injection power more than 20MW, we tried to vary the proton ratio in hydrogen ion beams. The proton ratio depends on the volume of the source plasma divided by the ion loss area and also the electron temperature. In order to vary the plasma volume, the chamber of the ion source for JT-60 NBI was modified so that the distance between the plasma grid and the back plate of the arc chamber, namely the thickness of the

source plasma, can be changed. Further, to increase the ion loss area, the magnetic field strength of the line cusp magnet in the back plate was decreased by replacing the original SmCo magnets with AlNiCo magnets. The experimental results showed that the proton ratio can be varied from 92% to 62% by reducing the volume of source chamber and optimizing the position of the filament cathodes. Figure IV.1-1 shows the typical data of the variable region of ion species ratio. This source delivered the neutral injection power of 840kW in the JT-60 prototype injector unit will be expected if the all ion sources are modified.

1.3 Research and development related to the next neutral beam injection system

1.3.1 Conceptual design of 500keV, 20MW negative-ion-based injector

A 500keV, 20MW neutral beam injection system for the Fusion experimental Reactor was designed so as to be used not only for the plasma heating but also for the current drive and current profile control. The most characteristic feature is that the system has a very long gas neutralizer of 24 m long and utilizes poloidal magnetic fields to separate residual ion beams. This makes the beamline compact and simple, and makes it possible to isolate the ion source from the reactor room, so that the maintenance becomes easy. The top view of FER-NBI system is shown in Fig. IV.1-2 and Table IV.1-1 summarizes the major performance characteristics of this NBI system. This NBI system consists of a beamline, a 500keV power supply system, an evacuating system including a tritium handling system, a cooling water circulating system and auxiliary sub-systems. The beamline consists of an intense negative ion source, a beam profile controller, a long gas neutralizer, an ion beam dump, a neutron shutter and an injection port of the torus. The neutralizer and ion source room are shielded magnetically, and the beamline is covered with neutron shields.

The ion source consists of pre-acceleration and main acceleration grid systems. Figure IV.1-3 shows one of the optimized pre-acceleration and main acceleration grid systems, respectively. In the pre-accelerator, a large amount of electrons accompanied by D^- ions must be prevented from entering the main accelerator. In the main

accelerator, in order to obtain a high geometrical transmission efficiency, it is required to produce a very convergent beam with an e-folding half-width divergence angle of less than 5 mrad. The beam energy and beam power can be controlled individually during an injection pulse by varying the gap length of the accelerator and potentials of each grid.

The beam profile controller is used to control the plasma current profile. The beam can be deflected by applying a transverse magnetic field between the exit of the accelerator and entrance of neutralizer. The upper half and lower half beams are deflected in the opposite directions by applying inverse magnetic fields to each beam. Hence, it is possible to produce various kinds of beam profiles from a Gaussian-like profile to a hollow profile at the plasma.

The structure of the ion dump is designed so as to receive all residual ions (D^+, D^-) at all phases in the FER operation. The peak heat flux on the surface of the ion dump is estimated to be 4 kW/cm^2, though the average heat flux on the ion dump is 76W/cm^2. The swirl tube is one of the most promising candidates for the beam dump element. In the present design, it is proposed to use a modified swirl tube with external fin which reduces the thermal stress and prolongs the lifetime.

In designing the 500keV, 100A acceleration power supply, it is important to protect not only the ion source but also the power supply itself against the breakdowns in the ion source. In the present design, it is proposed that an AC switch coupled with an inverter system which can be obtained the cut-off speed of less than 100μs and the ripple of about 3% by increasing the frequency in the AC power line of up to 5kHz is used.

The applicability of this injector to FER tokamak is now being investigated in detail.

1.3.2 Development of a 1A negative ion source [1]

High current and high energy negative deuterium (hydrogen) beams will be required for plasma heating and current drive in future reactors. Out of several approaches to produce D^- or H^- ion beams, volume production seems to be the most favorable method to produce such a high current negative beams, because the structure is simple

enough to scale up and the produced ion beams have good beam qualities. In order to clarify the difficulties in scaling up the volume H^- ion source and demonstrate >1A H^- ion beam production, the large magnetically filterd multicusp plasma generator and the multi-aperture extractor have been fabricated. Figure IV1-4 shows the volume H^- ion source now under study. The entire wall of the chamber including the plasma grid serves as an anode. The magnetic filter is provided to make the transverse magnetic field in the plasma which modifies the electron energy distribution and enhances the H^- yield and is an array of five water cooled copper tubes in which small SmCo magnets are inserted.

The H^- ions produced in the plasma are extracted by an extraction and acceleration grid systems, which consist of plasma, extraction, suppression and acceleration grids. In order to separate the plasma electrons from the H^- ions, small permanent magnets are inserted into the extraction grid. The electrons extracted with the ions are deflected completely by this magnetic field, while the H^- ions are scarecely disturbed and go straight to the acceleration region. The suppression grid is slightly negative with respect to the extraction grid in order to prevent the secondary electrons from the extraction grids and electrons created by beam-gas interactions from leaking out to the acceleration gap.

Up to now, a H^- ion beam of 1.26A/21keV/0.2s has been extracted at a current density of 9.5mA/cm^2 from 12cm×26cm grid system and there is no big problem in scaling up the volume H^- ion source. The extracted beam has good beam qualities; impurity contents in the beam is no more than a few percent and no metal impurities have been observed. The beamlet divergence is as low as 0.8-0.9 deg (e-folding half-width) in spite of low beam energy.

1.3.3 Development of cryosorption pump for helium evacuation

In fusion reactors, a reliable large-scaled vacuum pump system will be required to evacuate helium gas during burns. As a first step, we initiated to study the cryosorption behavior for helium on the sorbent SF_6 gas layer at 4.2K.

The cryopump is a cylinder type, whose surface area for pumping is approximately 1300cm^2. Figure IV.1-5 shows the influence of

pumping speed on the adsorbed quantity of helium gas. The pumping characteristics consists of three stages according to the amount of helium gas introduced. The pumping ability for helium is quite low in the first stage just after helium gas is introduced in the vacuum chamber. In the second stage, however, the pumping abilities for helium increase quickly and the stable pumping speed of 6000-7500 l/sec is obtained. In the third stage, the pumping capacities decrease gradually and the regeneration of cryopumps occurs finally. The flow rate of SF_6 gas in order to form the sorbent layer on the cryopanel hardly influences on the pumping characteristics for helium. The total adsorption capacity for helium is in proportion to the amount of initially condensed SF_6. One mole SF_6 adsorbed approximately 0.5 mole helium gas.

References

[1] Y. Okumura, "A high current volume H^- ion source with multi-aperture extractor", Proc. 4th Int. Symp. on the Production and Neutralization of Negative Ions and Beams, Brookhaven National Lab., Oct. 27-31, (1986).

2. Development of RF Heating System

The launcher which radiates the huge RF power into the tokamak is a most important component for RF heating system for effective plasma heating and/or current drive. In JT-60, the two types of RF heating, i.e., LHRF (Lower Hybrid Range of Frequencies) heating and ICRF (Ion Cycrotron Range of Frequencies) heating, are adopted. Also there are plans of adoption of these for additional heating and current drive on FER.

The R&D works of the launchers have been carried out since 1980 and the essential results of this R&D were devoted to the design, construction and conditioning of the launchers of JT-60. In 1986, our efforts were devoted to examine the developed launchers and obtain the data about RF conditioning and couping, which will be feedbacked to the experiment on the RF test stand for further improvement. In

pumping speed on the adsorbed quantity of helium gas. The pumping characteristics consists of three stages according to the amount of helium gas introduced. The pumping ability for helium is quite low in the first stage just after helium gas is introduced in the vacuum chamber. In the second stage, however, the pumping abilities for helium increase quickly and the stable pumping speed of 6000-7500 l/sec is obtained. In the third stage, the pumping capacities decrease gradually and the regeneration of cryopumps occurs finally. The flow rate of SF_6 gas in order to form the sorbent layer on the cryopanel hardly influences on the pumping characteristics for helium. The total adsorption capacity for helium is in proportion to the amount of initially condensed SF_6. One mole SF_6 adsorbed approximately 0.5 mole helium gas.

References

[1] Y. Okumura, "A high current volume H^- ion source with multi-aperture extractor", Proc. 4th Int. Symp. on the Production and Neutralization of Negative Ions and Beams, Brookhaven National Lab., Oct. 27-31, (1986).

2. Development of RF Heating System

The launcher which radiates the huge RF power into the tokamak is a most important component for RF heating system for effective plasma heating and/or current drive. In JT-60, the two types of RF heating, i.e., LHRF (Lower Hybrid Range of Frequencies) heating and ICRF (Ion Cycrotron Range of Frequencies) heating, are adopted. Also there are plans of adoption of these for additional heating and current drive on FER.

The R&D works of the launchers have been carried out since 1980 and the essential results of this R&D were devoted to the design, construction and conditioning of the launchers of JT-60. In 1986, our efforts were devoted to examine the developed launchers and obtain the data about RF conditioning and couping, which will be feedbacked to the experiment on the RF test stand for further improvement. In

addition to this, the development of high power gyrotron for ECRH (Electron Cycrotron Range of Frequencies) heating was started. The specification of the first stage development is the output power of more than 150kW at 120GHz with the pulse duration of more than 10msec. This development is continued in 1987.

Also, the shield room for high power test of RF components or improvement of the launcher were constructed, and the experiment of RF injection to the plasma produced by ECH at 6 GHz has started.

In the following subsection, the main results of RF conditioning and coupling test on the JT-60 is described.

2.1 LHRF Heating Launcher [1]

The launchers of LHRF heating system of JT-60 are a phased array of 4 columns and 8 rows waveguides. These are installed in JT-60 in December 1985 and the launcher conditioning was started in November 1986 for current drive launcher and in January 1987 for heating launchers. The conditioning was carried out with vacuum loading or plasma loading including the TDC plasma using the conditioning technique developed in the study of Plasma Heating Laboratory II. In addition to normal injection, amplitude modulation of RF power or pulsed injection with the time duration of a few ten μsec were carried out for effective conditioning. In the case of conditioning at TDC plasma, RF was injected with pulse duration of 30~50msec in every 5sec. Figure IV.2-1 shows the time history of attained total output power at klystrons. Up to now, a total power of 6.3MW, 0.5sec has been injected successfully into plasma by three launchers. The maximum power has reached up to 2.4MW (4.1 kW/cm^2), 0.65sec for current drive launcher and 2.1MW (2.1 kW/cm^2), 1.0sec for heating launchers. A long pulse operation of 8 sec at P_{in}=0.5~0.8 MW has been also carried out successfully for each launcher. However, the attained injection power seems to be at P_{in}=2.0 MW ~ 2.5 MW per one launcher in the present stage. One cause of this power limit is breakdown at the front mouth of the launcher. This problem has to be clarified in the experiment on the RF test stand and the counter-measure has to be found.

Figure IV.2-2 shows the reflection coefficient of each row against the distance between the separatrix and the limiter Δ1 for the

current drive launcher and heating launchers operated at $\Delta\phi$=90° and 120°, respectively, in divertor operation of I_p=1.5 MA, $\bar{n}_e = 1.0\times10^{13}$ cm^{-3}. The position of the launcher was 0.5 cm behind the limiter. The solid and dashed curves in the figure indicate the reflection coefficient for each launcher calculated by the Brambilla's theory on the assumption of the density gradient at the launcher mouth $\nabla n=\nabla L^{-1} n_s \exp(-\Delta 1/\lambda)$, where n_s, ΔL and λ are density at the separatrix, distance between launcher and limiter, and density decay length, respectively. In the calculation, $n_s=10^{12}$ cm^{-3}, ΔL=0.5 cm and λ=0.5 cm are assumed. The figure indicates that good agreement between theoretical values and experimental results. These resuls also indicate that the optimization of $\Delta 1$ is important to obtain good coupling coefficient for all waveguides due to the sharp density decay length in the divertor operation of JT-60 [1].

2.2 ICRF Heating System [2]

The launcher is composed of a 2×2 phased loop antenna array, which can be changed the toroidal and poloidal phase differences between each loops in order to control parallel and perpendicular wave number spectra of radiation power. The length and width of each antenna element are 23 cm and 7.5 cm, respectively. Four loop antennas are enclosed in a metal casing with open-type Faraday shield. The coupling properties were investigated with respect to the four phasing modes, which are (0,0), (π,0), (0,*), (π,*) as shown in Fig. IV.2-3. The two symbols in the parenthesises are the toroidal and poloidal phase differences, respectively, and "*" means only upper 2 loop (II, III lines) operation. Figure IV.2-4 shows experimental and theoretical loading resistances in the four phasing modes versus line averaged density. Assuming a parabolic density profile of the main plasma and an e-fold length of 3 cm in the scrape off region, the cold plasma theory including the effect of the antenna feeder current can explain the experimental results. The coupling efficiency; $\eta[=(R_c-R_v)/R_c$, R_v; vacuum loading] in (0,0), (π,0), (0,*) and (π,*) phasings are 94%, 92%, 85% and 70%, respectively. The maximum launched power is 2.1 MW and 1.5 MW in (0,0) and (π,0) phasing, respectively.

In (0,0) and (π,0) phasing modes, the plasma loading resistances of the upper 2 loops; (II, III) are higher than those of the lower 2 loops; (I, IV). The same tendency is also observed in the vacuum condition. One reason for the difference is the asymmetry of the resonance mode in a mdetal casing due to a difference between antenna feeder lengths and the gaps to the casing wall of the upper and lower loops.

On the test stand, the model antenna of 2×2 loops is constructed and the stub tuning test in various phasing is carried out and the feedback to the high power operation of JT-60 antenna will be done.

References

[1] Y. Ikeda, T. Imai, K. Sakamoto, M. Honda, T. Kato, S. Maebara, M. Sawahata, K. Suganuma, N. Suzuki, M. Tsuneoka, K. Uehara, K. Yokokura, and JT-60 Team: 7th Topical Conf. on Plasma Heating, Florida, U.S.A. (1987).

[2] M. Saigusa, N. Kobayashi*2, H. Kimura, T. Fujii, K. Hamamatsu, K. Anno, K. Kiyono, M. Seki, M. Terakado, T. Nagashima, and JT-60 Team: ibid. of Ref. [6].

Table IV.1-1 Performance of a 500keV/20MW Injector

Overall	
Neutral Beam Power	22.2 MW
Power Density	16.4 MW/m^2 (average)
Beam Energy	200 - 500 keV
Pulse Length	10 sec - DC
Ion Species	D
Power Efficiency	46 % (at 500 keV)
Acceleration	96 %
Neutralization	59 %
Geometrical	85 %
Re-ionization	96 %
Ion Source	
Number	1
Type of D^- Source	Volume Production
Size	0.2 m X 2.4 m (grid)
Extracted Current	120 A
Accelerated Current	96 A
Current Density	50 mA/cm^2
Divergence(e-folding half width)	5 mrad
Transparency	50 %
Neutralizer	
Size	(0.26-0.4)m X (2.4-1.4)m X 24 m
Line Density	7.5×10^{15} $molecules/cm^2$
Pressure	1.6×10^{-2} Pa (at entrance)
Injection Port	
Size	(0.44-0.5)m X (1.8-2.8)m X 11 m
Pressure	4×10^{-3} Pa (at entrance)
Gas Flow into Torus	0.13 Pa m^3/s
Cryo-Pump	
Source Chamber	700 m^3/s
Beam Dump Chamber	150 m^3/s

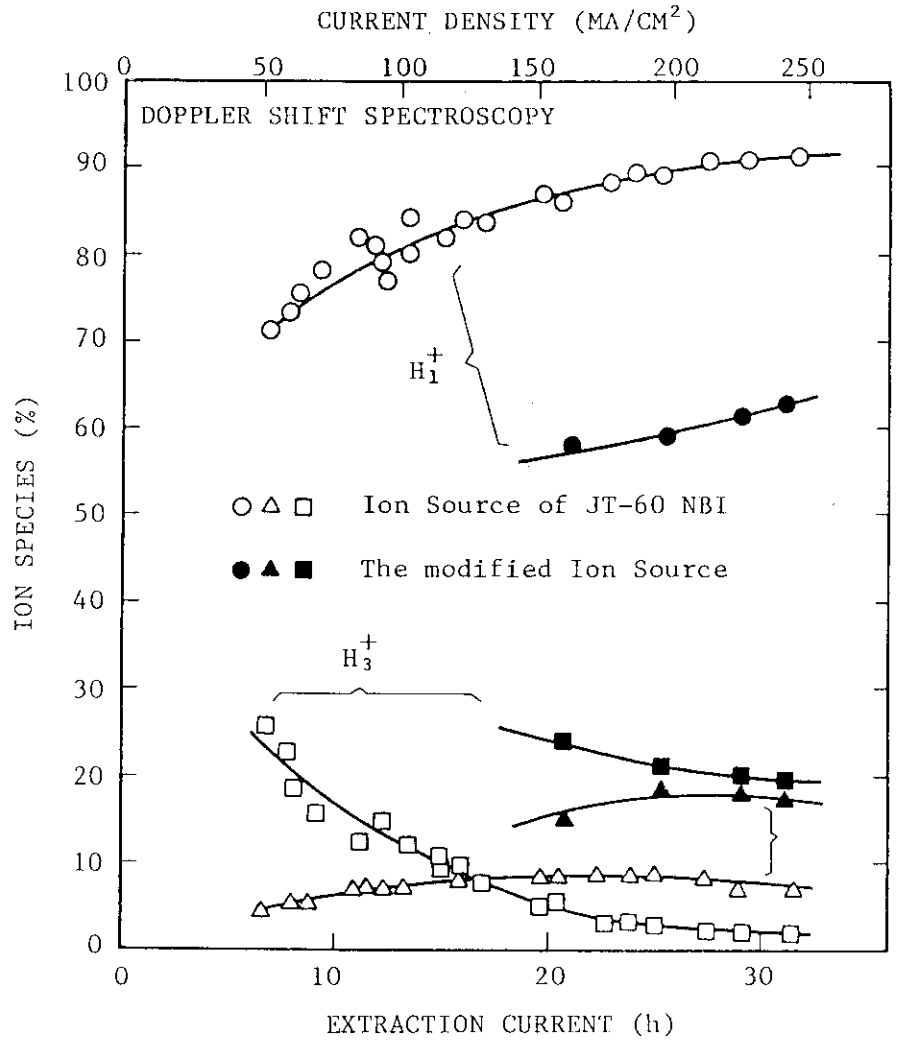

Fig. IV.1-1 Variable region of ion species ratio.

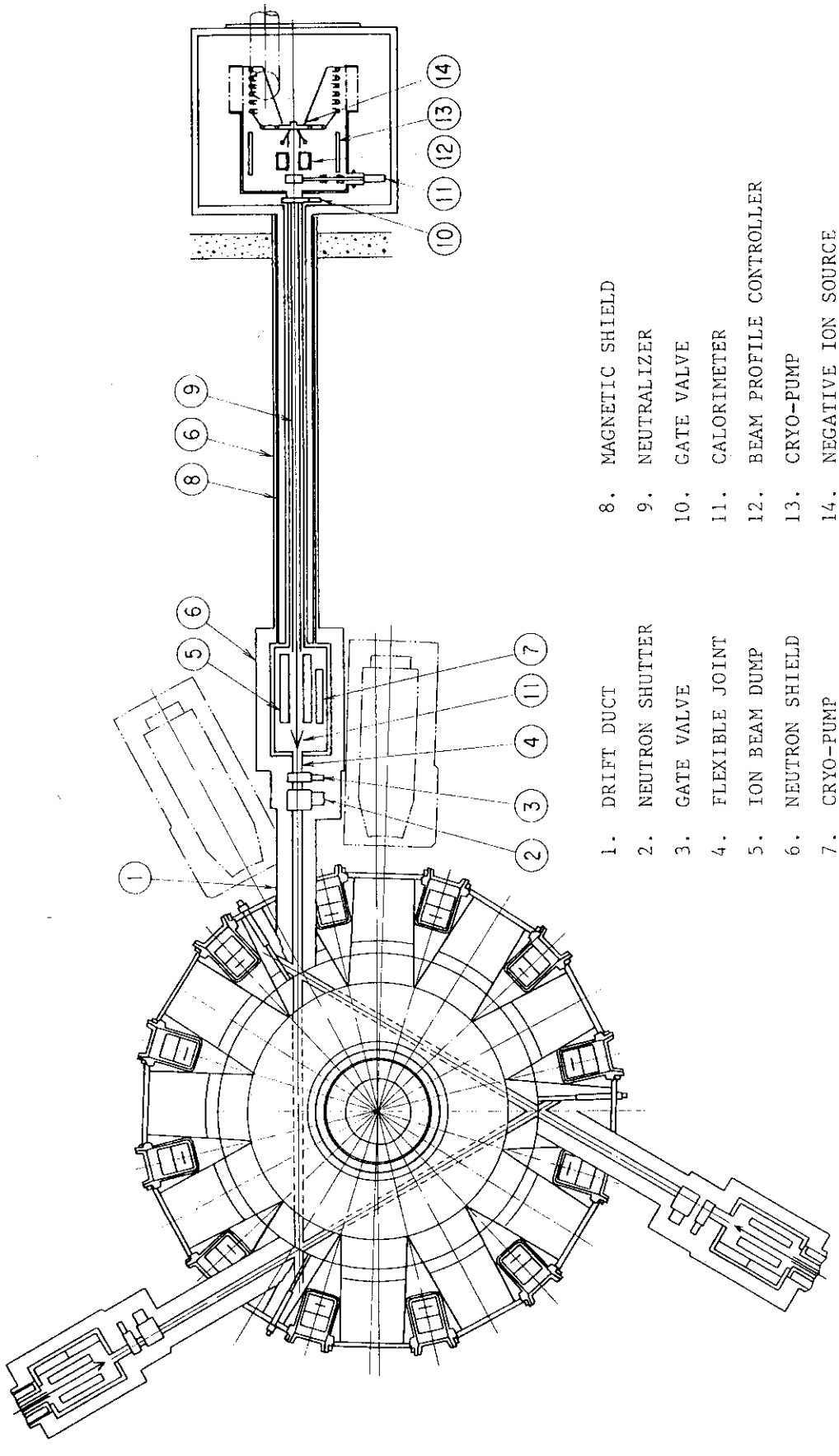

Fig. IV.1-2 Conceptual design of 500 keV, 20 MW negative-ion-based injector for FER.

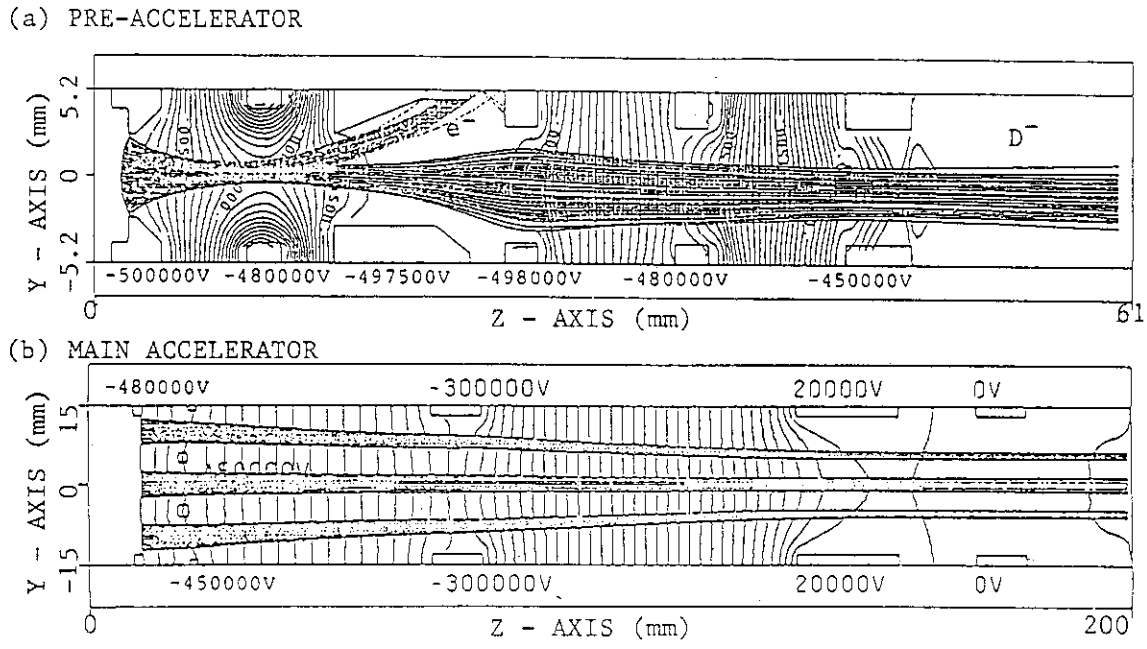

Fig. IV.1-3 An optimized D^- extraction and acceleration system which produces a convergent 2D sheet beam.

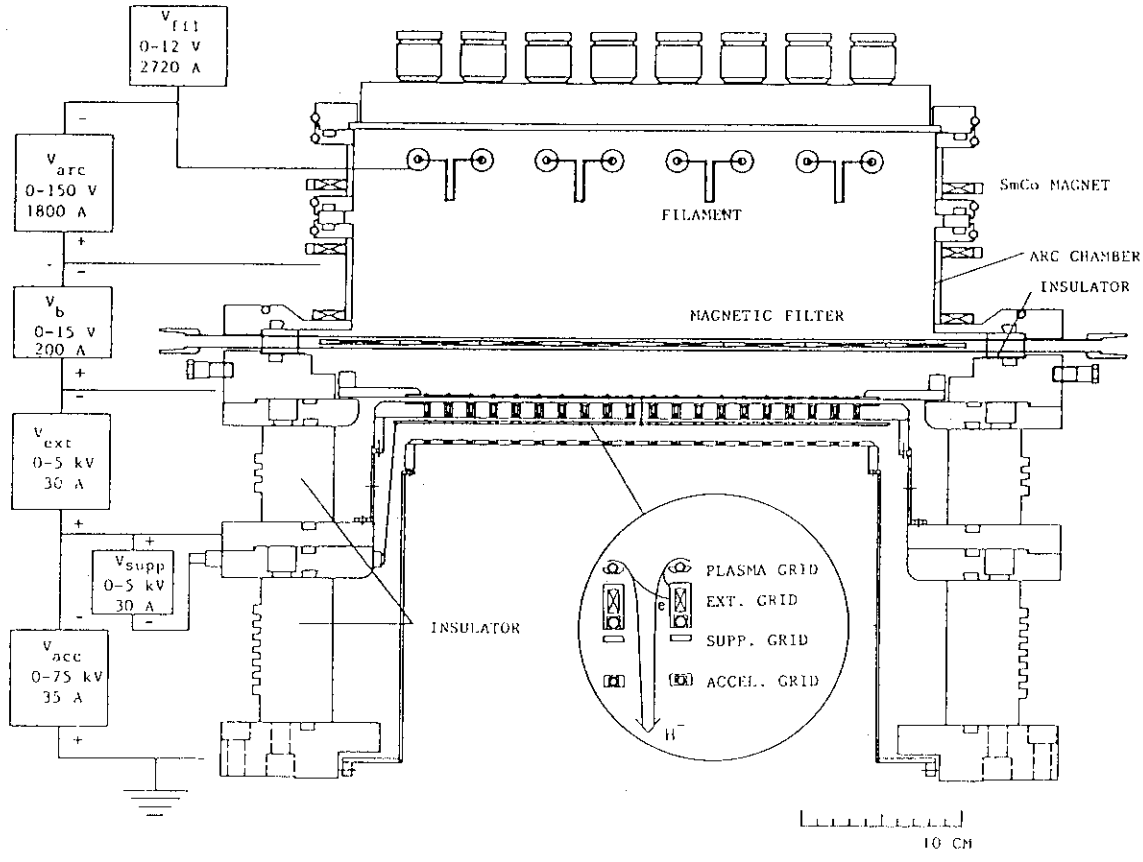

Fig. IV.1-4 Cross section view of one ampere volume H^- ion source and electrical connection of power supplies.

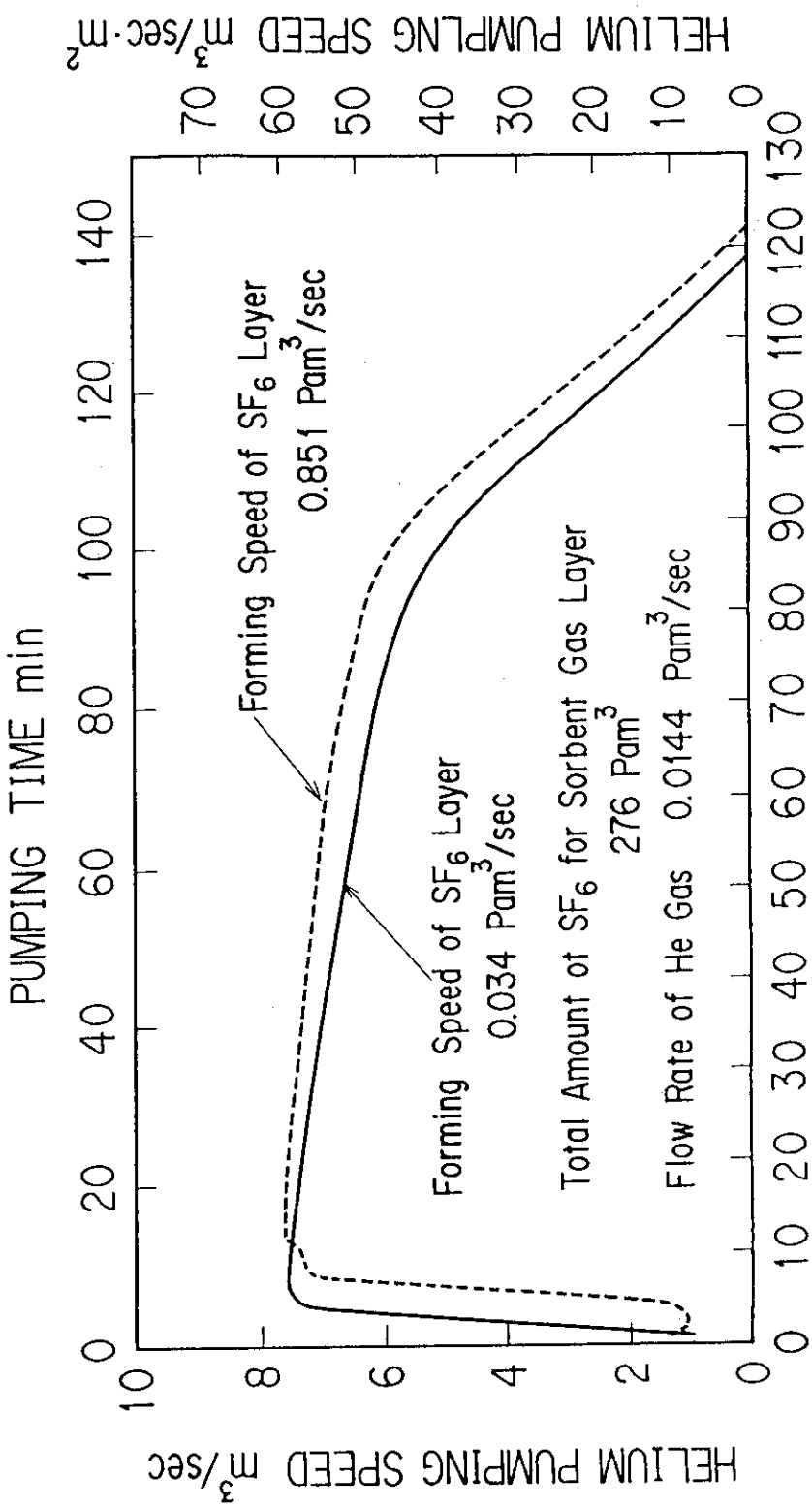

Fig. IV.1-5 Pumping speed of helium by SF_6 condensed layer with continuous helium flow.

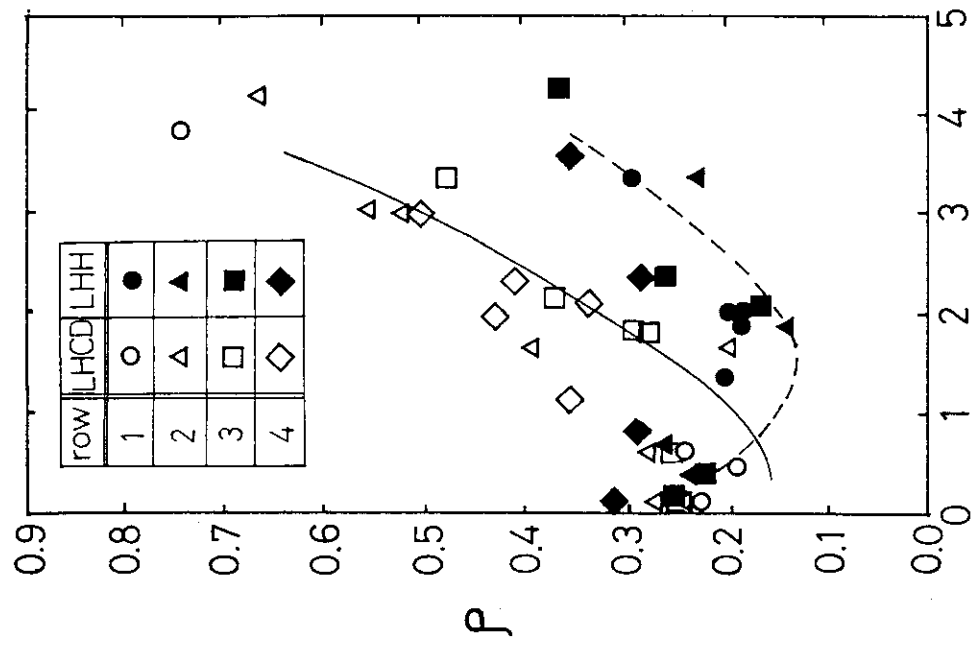

Fig. IV.2-2 Reflection coefficiencies at each rows depending on the separatrix-limiter distance Δl.

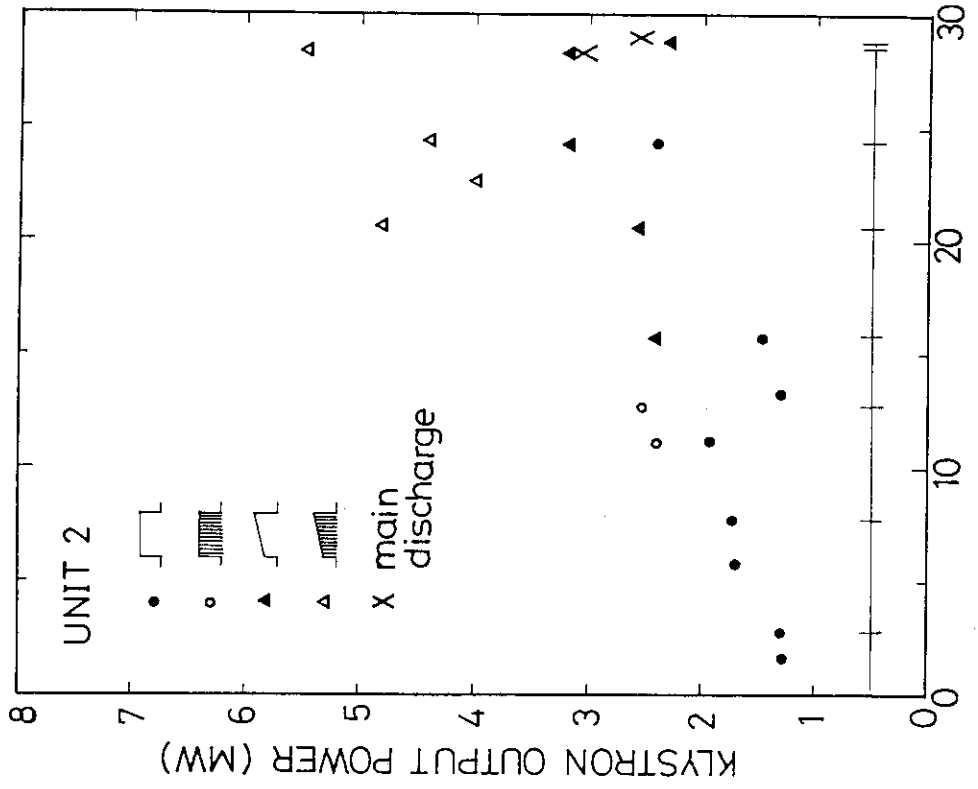

Fig. IV.2-1 History of LHRF launcher conditioning with TDC plasma.

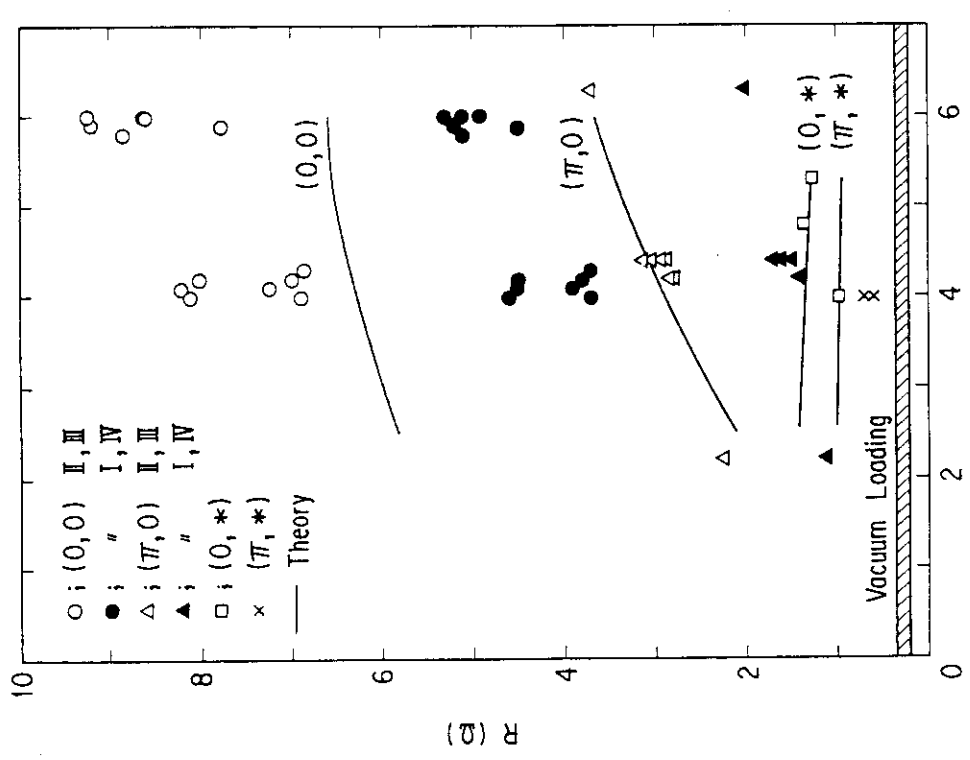

Fig. IV.2-4 Loading resistance of four phasing modes.

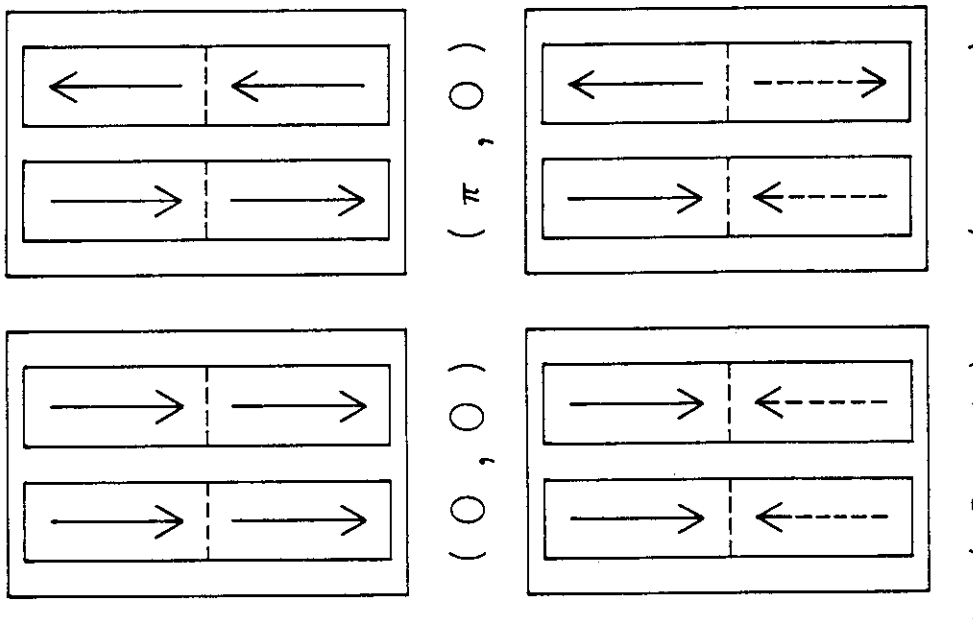

Fig. IV.2-3 Four types of phasing modes. Broken lines are induced currents.

V. SURFACE PHYSICS AND VACUUM TECHNOLOGY

1. Surface Physics

1.1 Introduction

Surface physics studies which are related to plasma surface interactions have been continued in close connection with the JT-60 project, the design study of the next step tokamaks and the tokamak experiments in JFT-2M. The primary objective of these studies is to investigate the interaction of the plasma with wall and limiter materials using ion accelerators and tokamak machines to find conditions which minimize impurity production and control hydrogen recycling rate.

In this fisical year, progress was made with the chemical sputtering measurement of carbon materials with different crystal structures, the measurement of oxygen atmospheric effect on molybdenum surface during sputtering, permeation measurement of implanted deuterium in nickel and the measurement of the scrape-off plasma in JFT-2M.

1.2 Crystal structure dependence of chemical sputtering yields of carbon materials

In order to investigate the crystal structure dependence of chemical sputtering, the chemical sputtering of sintered diamond compacts and diamond film have been measured as a function of target temperature and incident energy of protons. In Fig. V.1-1 are shown the energy dependencies of the yields as well as those of graphite for comparison[1]. The yields of C_2 and C_3 hydrocarbon were estimated by a newly developed method[2], using the hydrocarbon signal intensities measured by a quadrupole mass spectrometer. The C_2 hydrocarbon production yields were 25-55% smaller for the diamond compacts and the diamond film as well as the CH_4 production yields 12-14% smaller for the diamond compacts than for graphite, depending on incident energy, whereas the diamond film had the similar CH_4 yields of graphite. The results of Raman spectroscopy in Fig. V.1-2 show that the bombarded surfaces of diamond compacts and film still had sp^3 configuration of diamond structure even though they were irradiated up to a high

fluence of more than 10^{20} H/cm^2, whereas the bombarded graphite surfaces changed into microstructure domains. These results are considered to be the reasons why the yields are lower for the diamond compacts and film than for graphite and also why the steady yields of graphites differently fabricated have the similar values after the prolong irradiation.

1.3 Oxygen atmospheric effect on molybdenum surface during sputtering[3,4)]

It has been shown that the oxygen exposure during sputtering influences strongly the composition of the sputtered flux and the sputtering yield itself[5)]. The cause of these effects is considered to be due to the incorporated oxygen in the near surface from the oxygen atmosphere during sputtering. The present study aimed to investigate the oxygen uptake during sputtering and to clarify the chemical states of oxygen-incorporated surfaces.

The methods used were secondary ion mass spectrometry (SIMS) and Auger electron spectroscopy (AES), respectively and ion bombardments were made by using 4 keV and 5 keV Ar^+ ions. In Fig. V.1-3 are shown the depth profiles of incorporated oxygen for various oxygen exposure conditions measured by AES. It is clearly seen that the incorporation of oxygen is greatly promoted by simultaneous particle impact during the exposure. From detailed analysis of depth profiles and of Auger electron spectra the followings were obtained.

(1) The amount of incorporated oxygen depends on the fluence of concurrent ion impact and on the oxygen partial pressure.

(2) The distribution of incorporated oxygen extends deeper into the sample with increasing fluence.

(3) The promoted oxygen incorporation causes a chemical compositional change as well as a chemical state change in the surface layer showing the formation of oxides with various valence.

(4) The maximum equilibrium concentration of oxygen at the top surface is limited by the highest-valence oxide (MoO_3) formed on the surface.

From these results it is likely to consider that this promoted oxygen uptake is caused by defect-enhanced diffusion of oxygen atoms from the

surface into the sample; recoil implantation of adsorbed oxygen by the primary beam is only of minor importance.

1.4 Simultaneous ion and gas driven permeation of deuterium through nickel[6)]

The permeation rate of deuterium through nickel exposed to deuterium ion beam has been measured as a function of temperature (100-1000°C), incident ion flux (0.2-1.1×10^{15} D-atoms/cm²/s), incident ion energy (1-2.5 keV/D-atom), and deuterium partial pressure. In Fig. V.1-4 are shown the temperature dependence of the permeation flux of implanted deuterium (a) and that of n value (b), where the value of n are obtained from the ion current (i_p) dependence of the permeation flux (J_p) (i.e. $J_p \propto i_p^n$). It is clearly seen that the transition temperature of n corresponds to that of the permeation flux showing the two temperature regions in which the deuterium transport process is controlled in a different way. In addition both dependencies of the permeation flux on the ion energy and on the deuterium partial pressure are also characterized by a certain temperature corresponding to the transition temperature mentioned above. These results are analyzed with a model which is developed to describe ion driven permeation when gas driven permeation also exists simultaneously and the rate-limiting process of recycling during ion implantation is identified as surface recombination above 400°C and as bulk diffusion below 300°C.

1.5 Plasma wall interaction studies on JFT-2M

Measurements of the scrape-off plasma have been continued being put an emphasis on the improved confinement region. During the limiter H-mode, for example, we have observed a clear drop of the scrape-off density (1/3 or less), as if it were in the "detatched" state.

Improved confinement has also been observed in a lower hybrid (LH) current drive experiment. By using top/bottom movable limiters as potential sensors (Langmuir probe), we found that a grad-B-drift originated charge separation affects the particle confinement. An application of the LH wave, when it couples well with the parallel electron motions, reduces such potentials (namely, E×B convections),

then improves confinement. Fig. V.1-5 shows the result; we can find that in the Joule phase the polarity of the limiter potential agrees with the grad-B-drift direction; with the LH wave application these potentials are reduced and at the same time the confinement is improved (average density increases whereas the boundary density decreases). An importance of this result is that it shows a possibility of reduction of an intrinsic plasma loss in the tokamak device.

References

1) R. Yamada: J. Vac. Sci. Technol. A5 (1987) 2222.
2) R. Yamada: J. Vac. Sci. Technol. A5 (1987) 305.
3) M. Saidoh, H. Gnaser and W. O. Hofer: Nucl. Instrum. Methods B28 (1987) 540.
4) M. Saidoh and R. Yamada: J. Vac. Sci. Technol. (1988) (in press).
5) Annual Report of the Naka Fusion Research Establishment for the Period of April 1, 1985 to March 31, 1986, JAERI-M 87-018 (1987) p.70.
6) T. Nagasaki, R. Yamada, M. Saidoh and H. Katsuta: J. Nucl. Mater. 151 (1988) (189).

2. Vacuum Technology

2.1 Introduction

The operation and experiment of JT-60 and the design study of the next generation devices create a necessity for solving new technical issues in the areas of vacuum and surface technology. They include wall preparation techniques, surface diagnostics, in-vessel manipulation, leak hunting and repairing techniques, and special vacuum components such as pumps and valves.

In this fiscal year 1986, significant progress has been made in the following topics:

- Development of multi-joint manipulator for the next generation devices.
- Development of a new vacuum gauge in fusion environment,

then improves confinement. Fig. V.1-5 shows the result; we can find that in the Joule phase the polarity of the limiter potential agrees with the grad-B-drift direction; with the LH wave application these potentials are reduced and at the same time the confinement is improved (average density increases whereas the boundary density decreases). An importance of this result is that it shows a possibility of reduction of an intrinsic plasma loss in the tokamak device.

References

1) R. Yamada: J. Vac. Sci. Technol. A5 (1987) 2222.
2) R. Yamada: J. Vac. Sci. Technol. A5 (1987) 305.
3) M. Saidoh, H. Gnaser and W. O. Hofer: Nucl. Instrum. Methods B28 (1987) 540.
4) M. Saidoh and R. Yamada: J. Vac. Sci. Technol. (1988) (in press).
5) Annual Report of the Naka Fusion Research Establishment for the Period of April 1, 1985 to March 31, 1986, JAERI-M 87-018 (1987) p.70.
6) T. Nagasaki, R. Yamada, M. Saidoh and H. Katsuta: J. Nucl. Mater. 151 (1988) (189).

2. Vacuum Technology

2.1 Introduction

The operation and experiment of JT-60 and the design study of the next generation devices create a necessity for solving new technical issues in the areas of vacuum and surface technology. They include wall preparation techniques, surface diagnostics, in-vessel manipulation, leak hunting and repairing techniques, and special vacuum components such as pumps and valves.

In this fiscal year 1986, significant progress has been made in the following topics:

- Development of multi-joint manipulator for the next generation devices.
- Development of a new vacuum gauge in fusion environment,

- Calculational analysis of high energetic gases,
- Development of carbonization techniques for JT-60 application, and
- Development of prototype turbomolecular pump with ceramic rotor for fusion application.

2.2 Development of multi-joint typed vacuum manipulator

A multi-joint typed vacuum manipulator which has many degrees of freedom benefits in-vessel work of the thermonuclear devices.

However, we have to solve many problems in fabrication of the manipulator. Above all, the lubrication on heavy loaded mechanical elements and the release mechanism of troubled joints are important development times.

We have fabricated a simulated multi-joint typed vacuum manipulator having two degrees of freedom in FY.1986, and investigated about these problems.

A. Specification of simulated multi-joint typed vacuum manipulator

Maximum load capacity	40 kgf
Degrees of freedom	2
Movable angle of a joint	45 deg
Power	DC Servo. motor
Dimensions	170 mm in diameter
	900 mm in length
Exposed surface area in vacuum	2 m^2
Lubricant	Grease (Pentaphenyl Ether)
Power for release mechanism	SMA (Ti-Ni) wire

Figure V.2-1 shows the simulated manipulator which is installed in the JVX-II.

B. Experimental items

1) Life time test
2) Temperature measuring test
3) Measuring of outgassing rate
4) Functional test of release mechanism of troubled joint

C. Results

Figure V.2-2 shows a change in the motor current at the angle of joint of 43 deg and applied load capacity of 40 kgf. The current is

about 25% of the maximum rate current. This value shows that the motor is operated without troubles.

The maximum surface temperature of the motor was 35°C. This temperature is sufficently low compared with the allowable operating temperature of 65°C.

Figure V.2-3 shows a change in the outgassing rate from the manipulator. The rate is estimated to be 10^{-10} Torr.1.s^{-1}.cm^{-2}. It is conclused that there is contamination from the decomposition of the grease in vacuum environment.

Figure V.2-4 shows the SMA wire temperature as a function of the joint angle of the release mechanism. The temperature rises as the number of the movement increases. These phenomena are caused by the strain in the SMA wire.

2.3 Development of a new diaphragm gauge for vacuum measurement in fusion environments

In fusion machines, vacuum gauges are inevitable tools to monitor the gas density near the fusion plasmas and the gas flow rate into and out of the plasma vessel. The gauges commonly used for these machines are ionization gauge and diaphragm gauge for total pressure measurement and mass spectrometer for partial pressure measurement[(1)]. However, there have been some limitations in using these gauges since high magnetic fields produced by magnet coils and plasmas deform the trajectory of charged particles and stray electromagnetic waves affect the solid state electronics. They change the gauge sensitivity and induce heavy electronic noises.

In order to overcome these problems, we have been developing a new diaphragm vacuum gauge which uses optical fibers to read distortion of the diaphragm optically and does not use any electricity. The gauge is composed of a pressure-sensitive diaphragm made of Inconel 600, which separates a system with an unknown pressure from a reference pressure, long bundle optical fibers fixed to the gauge housing, an air-tight sapphire window to read the diaphragm position, and a set of light source (tungsten lamp) and light receiver (photo diode), as shown in Figure V.2-5. The reference pressure room was sealed-off after evacuation and then a chemcal getter was used to maintain a low pressure of $<10^{-4}$ Pa.

In this gauge, the diaphragm is irradiated with a constant amount of light and the intensity of the reflected light is detected by the photo diode, both through the bundle optical fibers. We have confirmed that the intensity of the reflected light changes with good reproducibility with the diaphragm position which reflects the pressure difference between the diaphragm. In Figure V.2-6, the output voltages are shown as a function of the pressure difference for three different gaps between the fibers and the window, in which the voltage is proportional to the reflected light.

2.4 Fundamental study of molecular flow by Monte-Carlo method

Usually, for the calculation of the conductance by Monte-Carlo method, the cosine law is used as the basic reflection law on the wall. And the use of the cosine law is right for the molecules having the thermal energy. Because the adsorption time of the molecules having a thermal energy is enough long for lossing the incident momentum. But, in the vacuum system of the fusion reactor, we have to deal with a large amount of the energetic molecular gases. In such cases, as the energy of the incident molecules on the wall is very high, the adsorption time is shorter than in the case of low energy. In result, it is expected that the molecules having the high energy are reflected without lossing the most part of the incident momentum and the distribution of the reflected molecules gradually comes to be similar to specular reflection. We call this reflection "quasi-specular reflection". The concept of quasi-specular reflection is explained in Figure V.2-7. The molecules which are incident from the left on the wall is reflected to the right, and the distribution of the reflected molecules obey the n-th power of cosine around the axis of specular reflection. The results to calculate the clausing factor of rectangular duct by two dimensional model is shown in Figure V.2-8. It is apparent that the geometory of the corner of the duct have large influence on the clausing factor in case of quasi-specular reflection than in case of cosine reflection. Therefore careful attention need to be paid to the results for the evaluation of the conductance with the high energy molecules.

2.5 Fundamental study of carbonization (II)

We made experiments on decarbonization of carbonized film, deposited from C_2H_2 or CH_4 source gas, by d.c. glow discharge of H_2, N_2, CO, CO_2 and O_2 gases. Removal rates of each gases are shown in Figure V.2-9. Removal rates were estimated from ratios of total removing atoms and total incident ions in unit time (e.g. 1 sec.). The numbers of removing atoms in unit time were calculated from weight change of quartz oscillator monitor and numbers of incident ions were calculated from cathode current flux on quartz oscillator monitor. Removal rate of O_2 gas was 10 times and more larger than that of H_2 or N_2 gases. Removal rate of O_2 gas was as same as that of CO_2 gas. Removal rate of CO_2 gas was same as deposition rate of C_2H_2 gas. But no weight change was detected by d.c. glow discharge of CO gas.

On deposition of carbon film, numbers of deposited atoms are more than that of incident ions, so neutral atoms or molecules may be included in carbonized film. Sputtering rates of gold film by N_2 or CO_2 gas (0.4-0.7) are smaller than 1, for incident energy of ions may spread for lower energy region. But sputtering rates of gold film by H_2 gas, -1-, is larger than 10^{-2}-10^{-3} [2], for gold film may be sputtered by impurity gas or ions, e.g. CH_x^+ or CH_x^*.

Sputtering rate of carbon film by CO_2 gas, 3.2 atom/ion, is 4-5 times larger than that of gold film by CO_2 gas, for carbon film may be removed by neutral atoms, ions or radicals(O*).

2.6 Development of new turbomolecular pump with ceramic rotor(II)

In order to develope a turbo molecular pumps resistant to magnetic fields, we manufactured a test machine consisting of a sintered silicon nitride ceramic rotor with high electrical resistivity, oil-free gas bearings and a gas turbine, and carried out various performance tests using this machine.

Figure V.2-10 schematically shows the construction of the test machine.

The rotational performance test of this machine in magnetic fields was made using circular magnet. Figure V.2-11 shows the schematic of the testing apparatus and the magnetic field at and around the test machine.

The machine was installed in such a way that the rotor blades were on the center line of the magnetic field and the rotor was at right angles to the direction of the magnetic field since it had been noticed that this position produces the maximum eddy current loss in metallic rotors. The stationary magnetic flux density produced by the arrangement was about 0.046 Tesla at the test machine. A rapid flux change of 0.02Tesla $msec^{-1}$ was also produced by pulsed currents applied to the pulse coil. A special thermosensitive paint was coated on the rotor blade surface to examine the temperature rise during operation.

Figure V.2-12 shows a typical result of the experiment, where the test machine was rotated at speeds up to 30,000 rpm, and then the stationary magnetic field was applied for 1 hour. The experiment result shows that the rotation speed of the rotor was not affected by the magnetic field. The special thermosensitive paint coated on the rotor blades showed no change in color.

In the pulsed magnetic field test, the test machine was again rotated at speeds up to 30,000 rpm. In this case, 60 pulses were applied in 10 minutes (Fig. V.2-13). We did not detect any change in rotation speed, vibrational amplitude and temperature due to the magnetic fields.

These experimental results have demonstrated the integrity and the appropriateness of the rotor assembly of the test machine. They have also verified the merits of the turbomolecular pump having a ceramic rotor and a gas turbine instead of a metallic rotor and an electric motor for fusion applications.

References

(1) H.F. Dylla: J. Vac. Sci. Technol., 20 (1982) 119.
(2) J. Bohdansky et al.: J. Appl. Phys. 48 (1977) 4722.

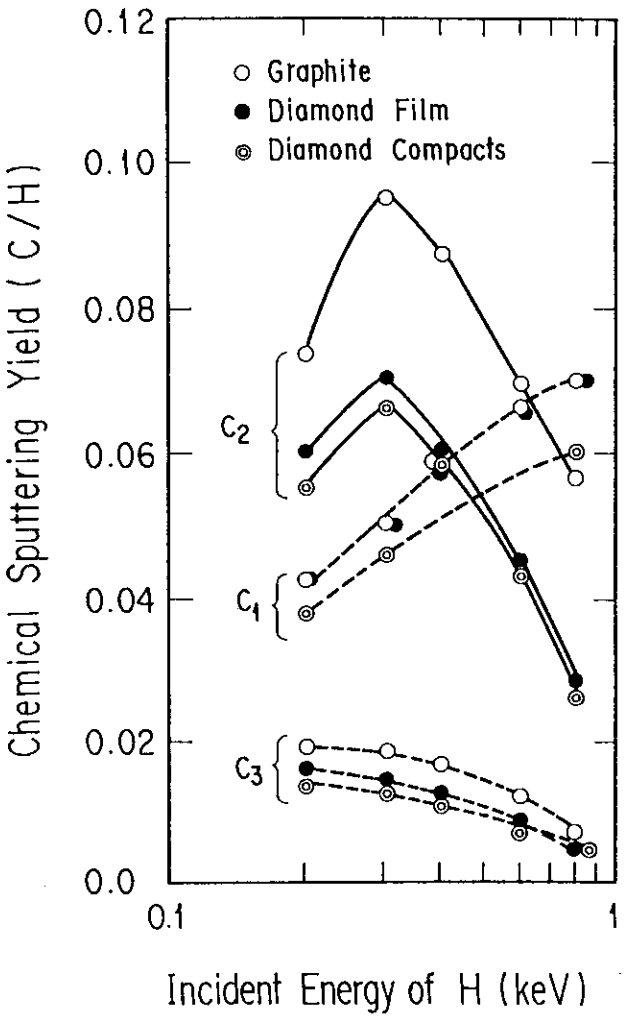

Fig. V.1-1 Energy dependences of the evaluated chemical sputtering yields (C/H) of C_1, C_2 and C_3 hydrocarbons at the peak temperature, T_m.

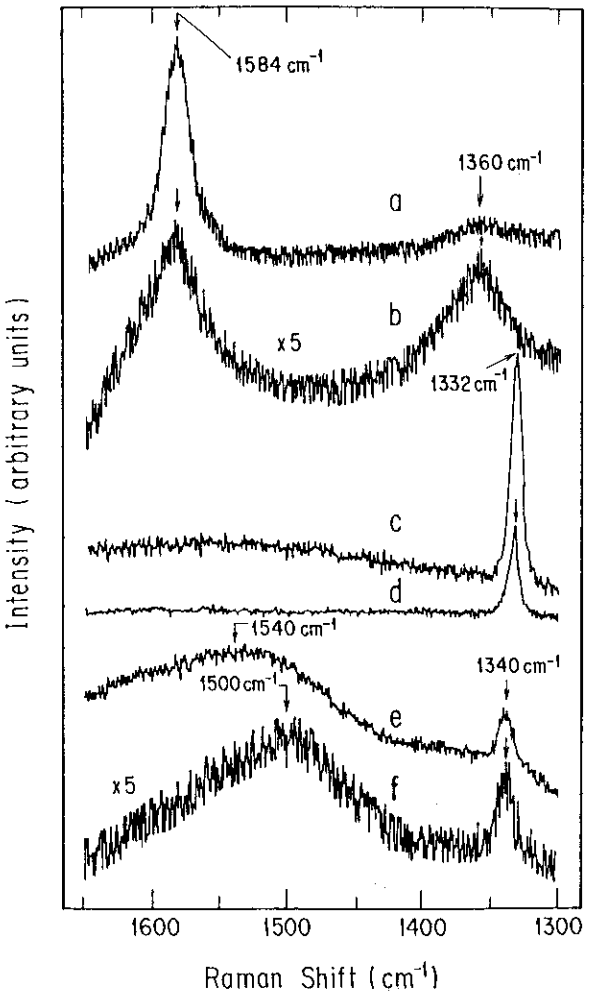

Fig. V.1-2 Raman spectra of graphite (a,b), sintered diamond compacts (c,d) and diamond film (e,f): (a), (c), (e); non-irradiated, (b), (d), (f); irradiated with H_2^+ ions up to 2×10^{20} H/cm^2 at target temperatures of 350 - 600°C, whose energy ranges between 0.4 and 1.6 keV.

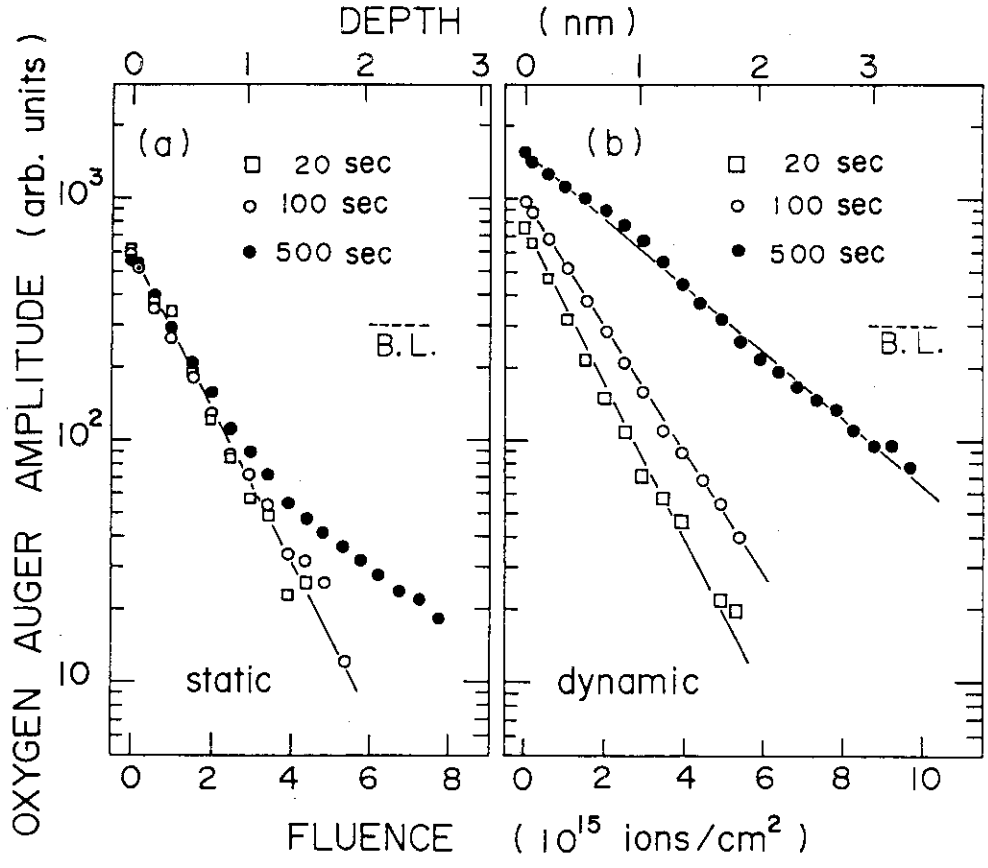

Fig. V.1-3 Variation of the oxygen Auger amplitude during sputtering of a molybdenum surface previously exposed to oxygen (a) without (static) and (b) with (dynamic) concurrent 4 keV Ar^+ ion bombardment at room temperature for various exposure conditions. The mean current density is 2.5 μA/cm^2 both for the irradiation during exposures and for the analysis. The steady-state signals ("B.L.") obtained after the complete oxygen removal have been subtracted from the data. The given depth scale is taken from the sputtering yield of molybdenum with clean surface.

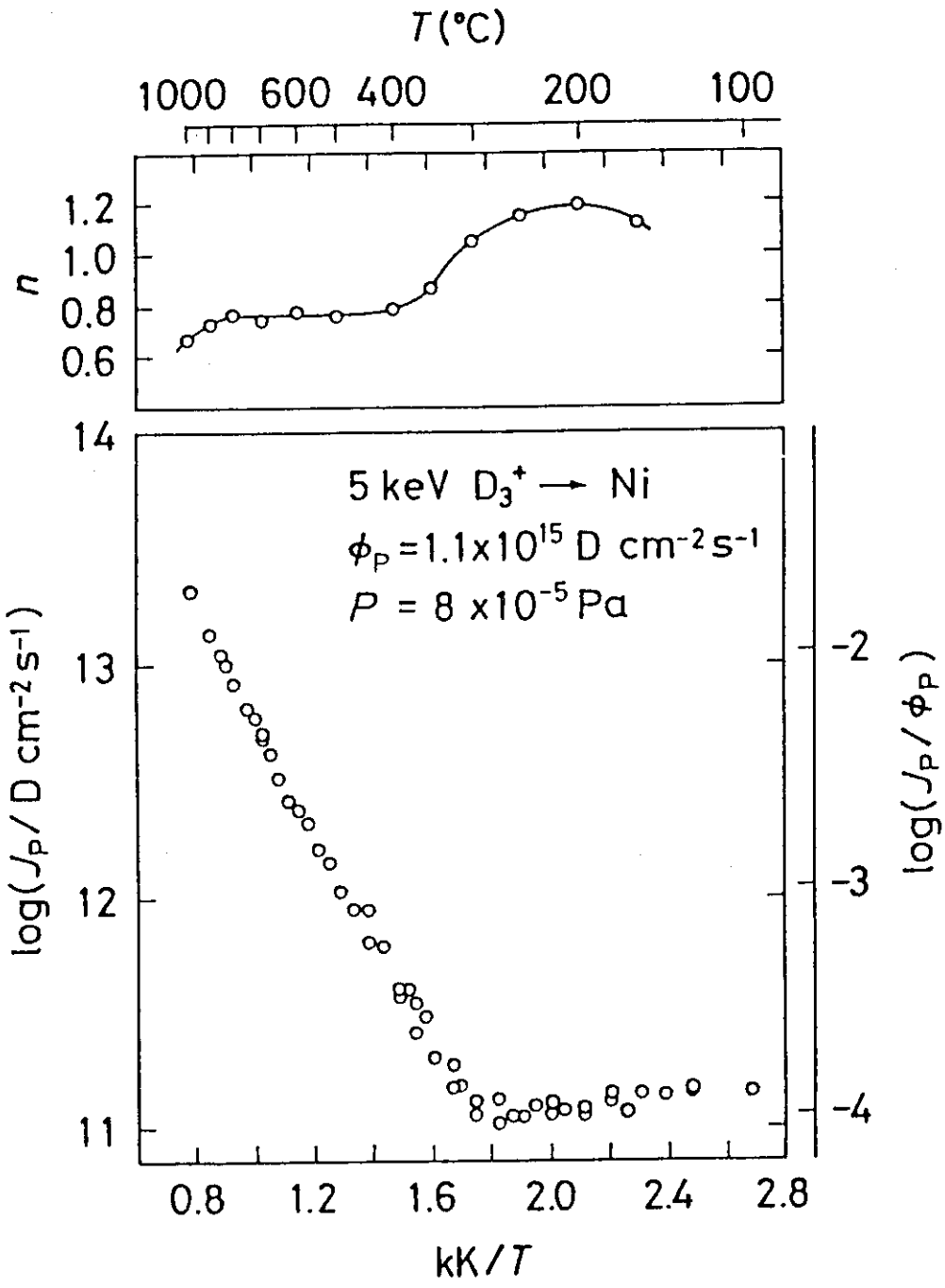

Fig. V.1-4 Temperature dependence of the permeation flux, J_p, (a) and n (b). The value of n are obtained from the ion current (i_p) dependence of the permeation flux (i.e. $J_p \propto i_p^n$).

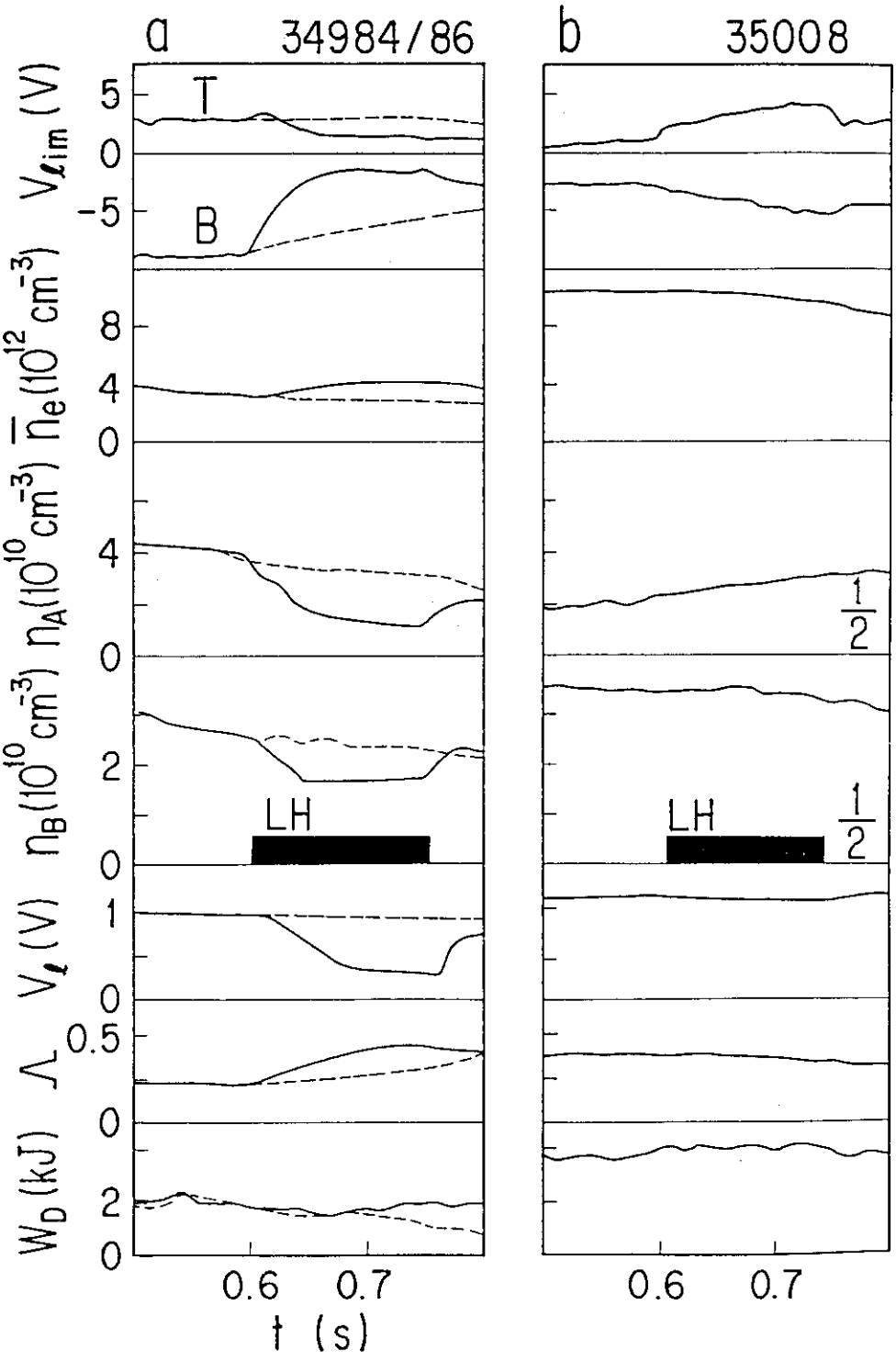

Fig. V.1-5 Effect of LH wave on Joule plasma. (a) Solid/dashed lines show with/without LH wave. The black time interval refers to the LH phase. V_{lim} is limiter potential (T/B means the top/bottom limiter), n_A and n_B are scrape-off densities and W_D is diamagnetic plasma energy. Others are by the standard notation (Λ is ordinary lambda). (b) Average density is increased up to 10×10^{12} cm^{-3}. In this case no clear effect of LH wave can be observed.

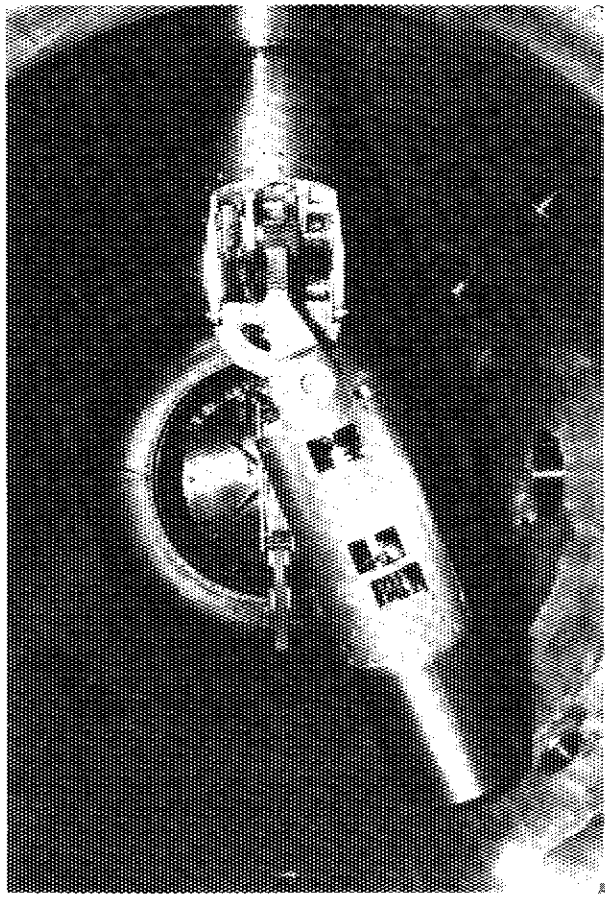

Fig. V.2-1 The manipulator which was installed in the JVX-II vacuum chamber. A dummy load (Weight of 40 kgf) is attached the tip of the manipulator.

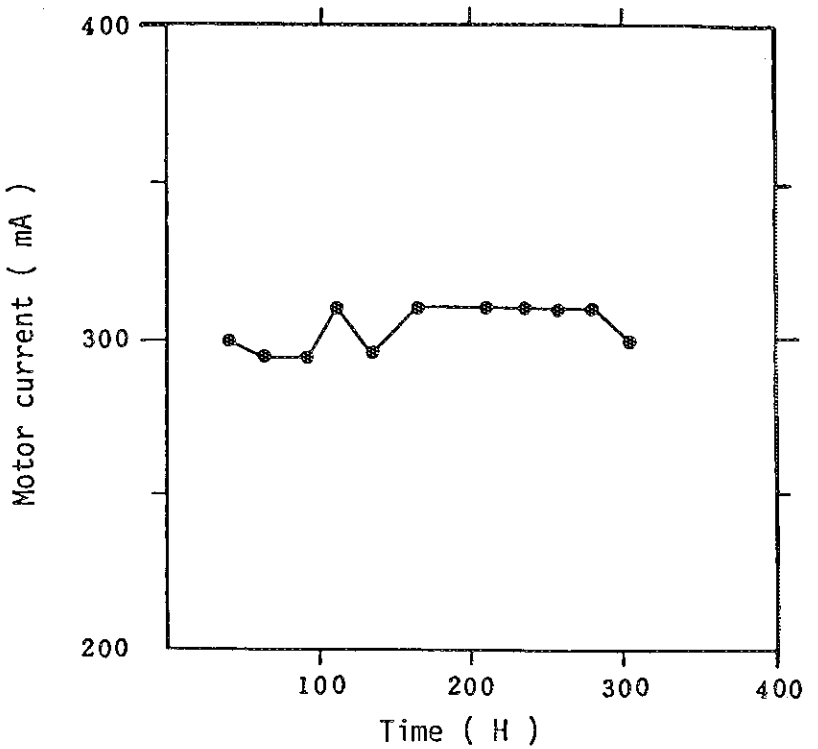

Fig. V.2-2 A change of the motor current. Position of the manipulator : Horizontal, Maximum moment : 2000 kg-cm, Set up range of the joint : 43 deg.

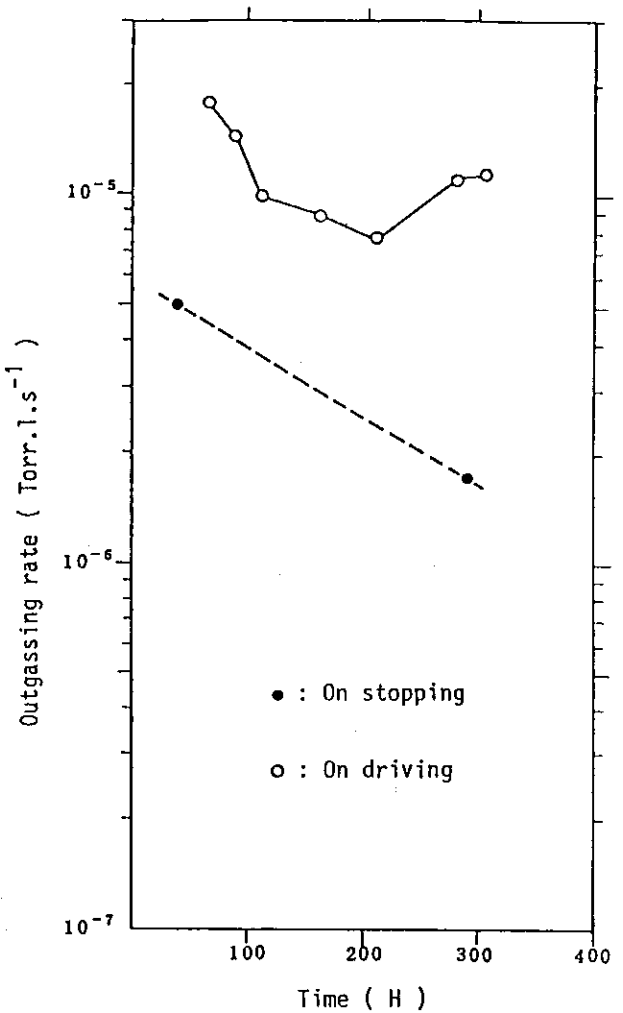

Fig. V.2-3 Time dependence of outgassing rate from the simulated multi-joint type vacuum manipulator. Position of the manipulator : Horizontal, Maximum moment : 2000 kg-cm.

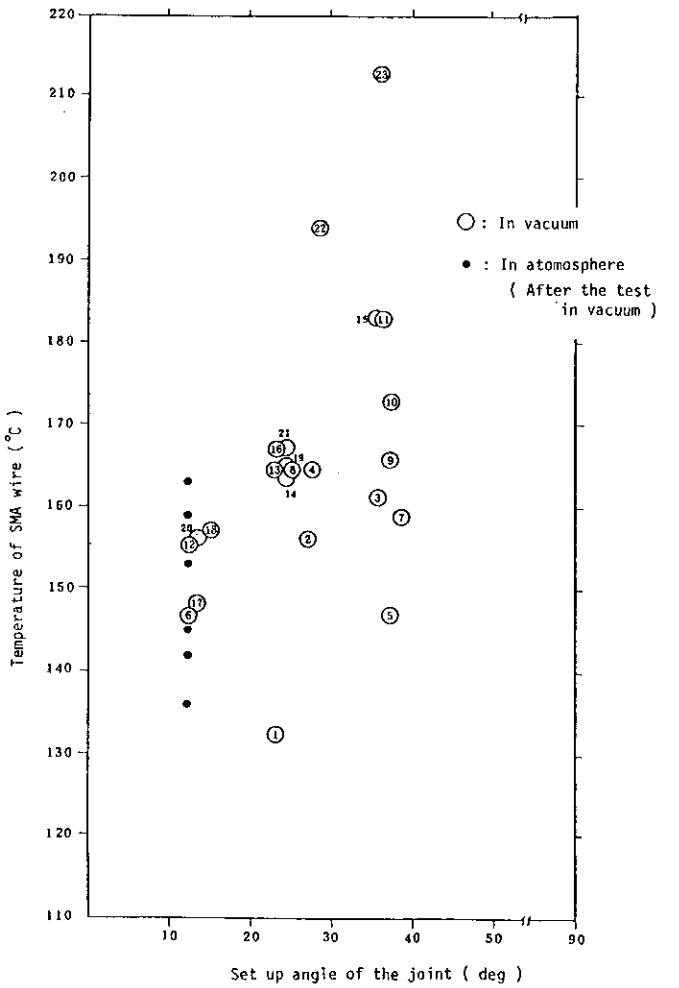

Fig. V.2-4 Temperature of SMA wire as a function of the set up angle of joint for the release mechanism. The number in a circle shows the number of the movement.

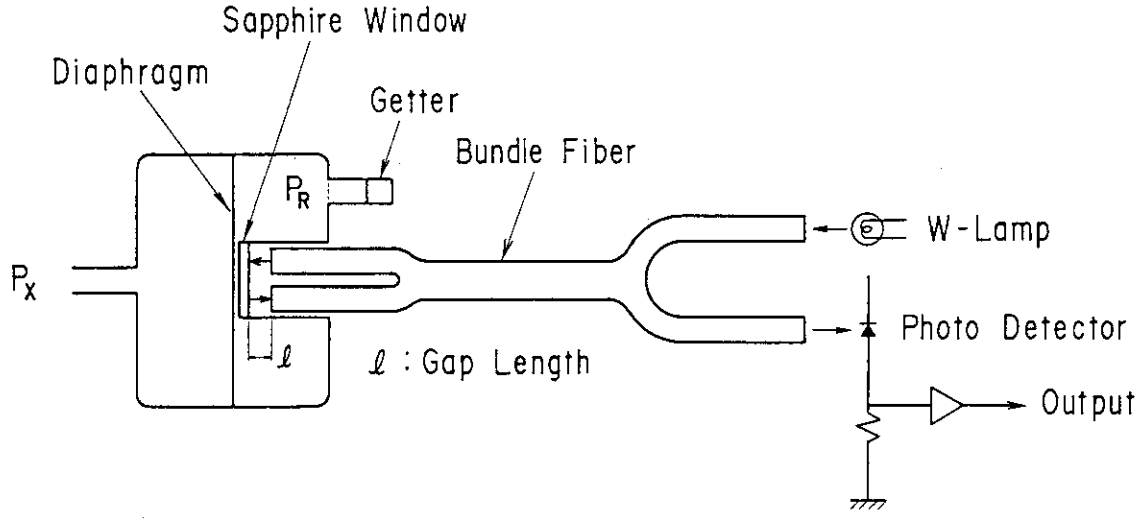

Fig. V.2-5 Schematic of a new diaphragm vacuum gauge.

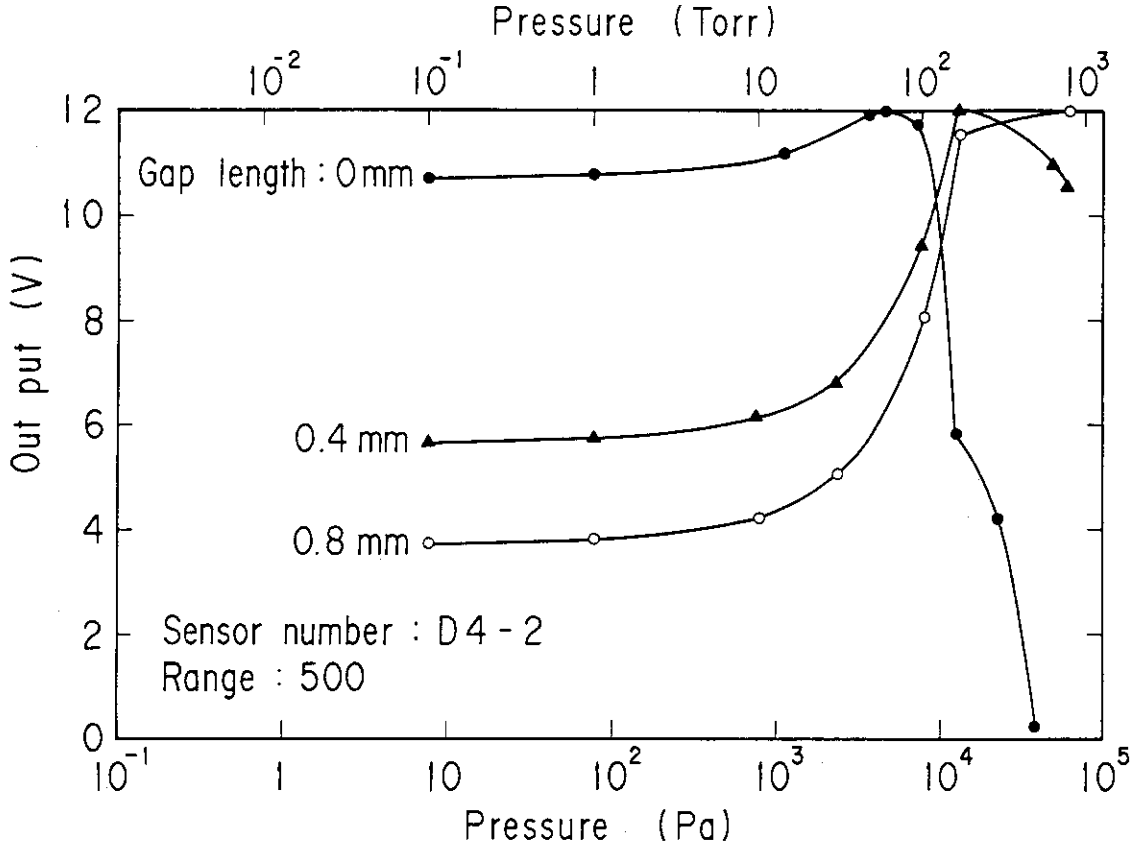

Fig. V.2-6 Relation between pressure change and output voltage. The voltage corresponds to the intensity of the refrected light

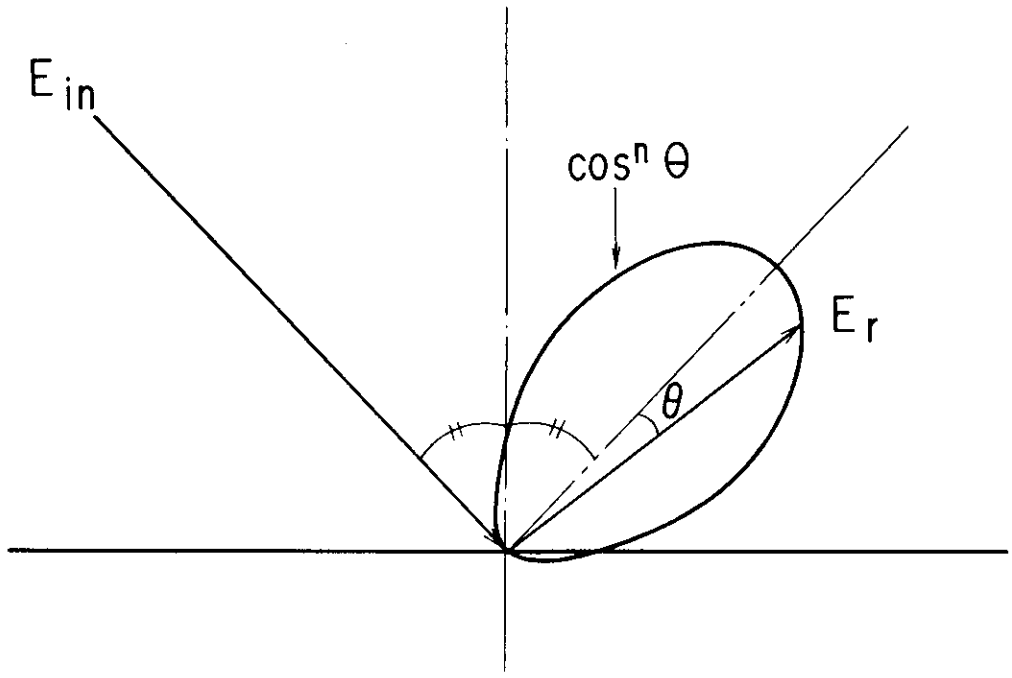

Fig. V.2-7 The concept of quasi-specular reflection.

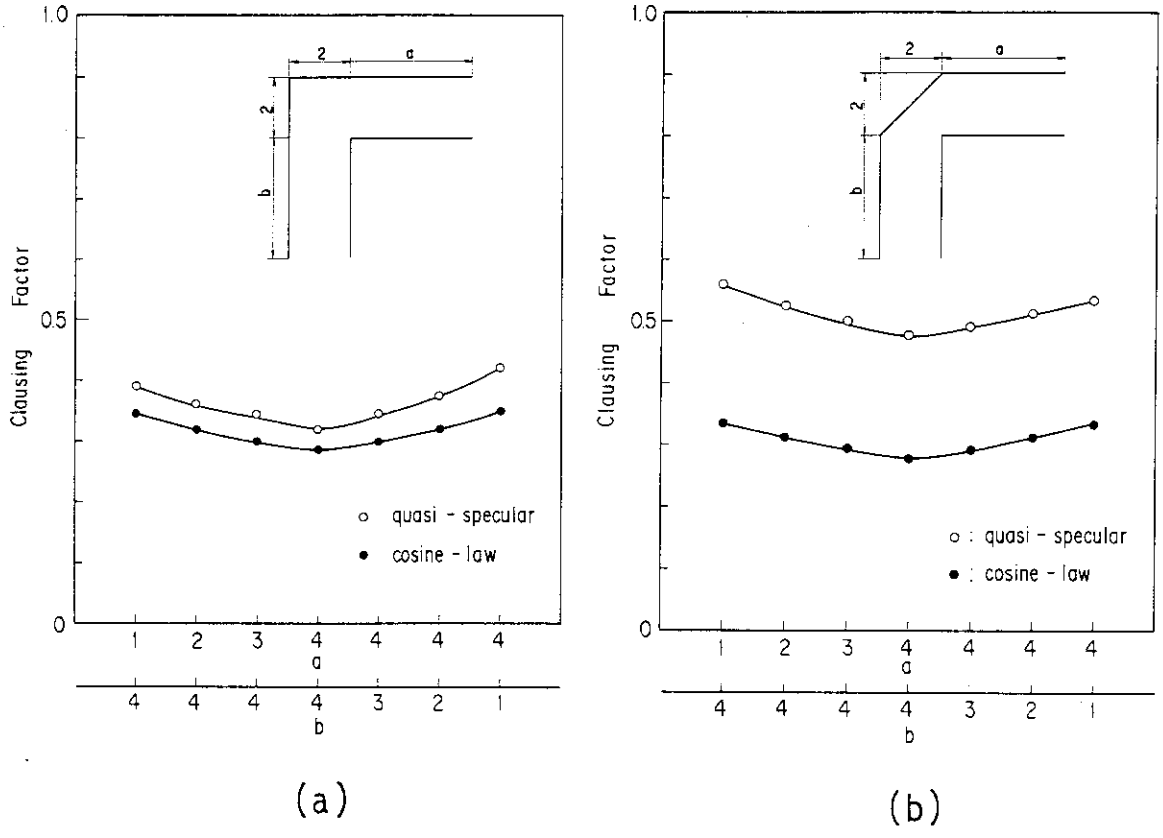

Fig. V.2-8 The clausing factor of rectangular duct.
(a) in case of the corner without a inclined plane
(b) in case of the corner with a inclined plane

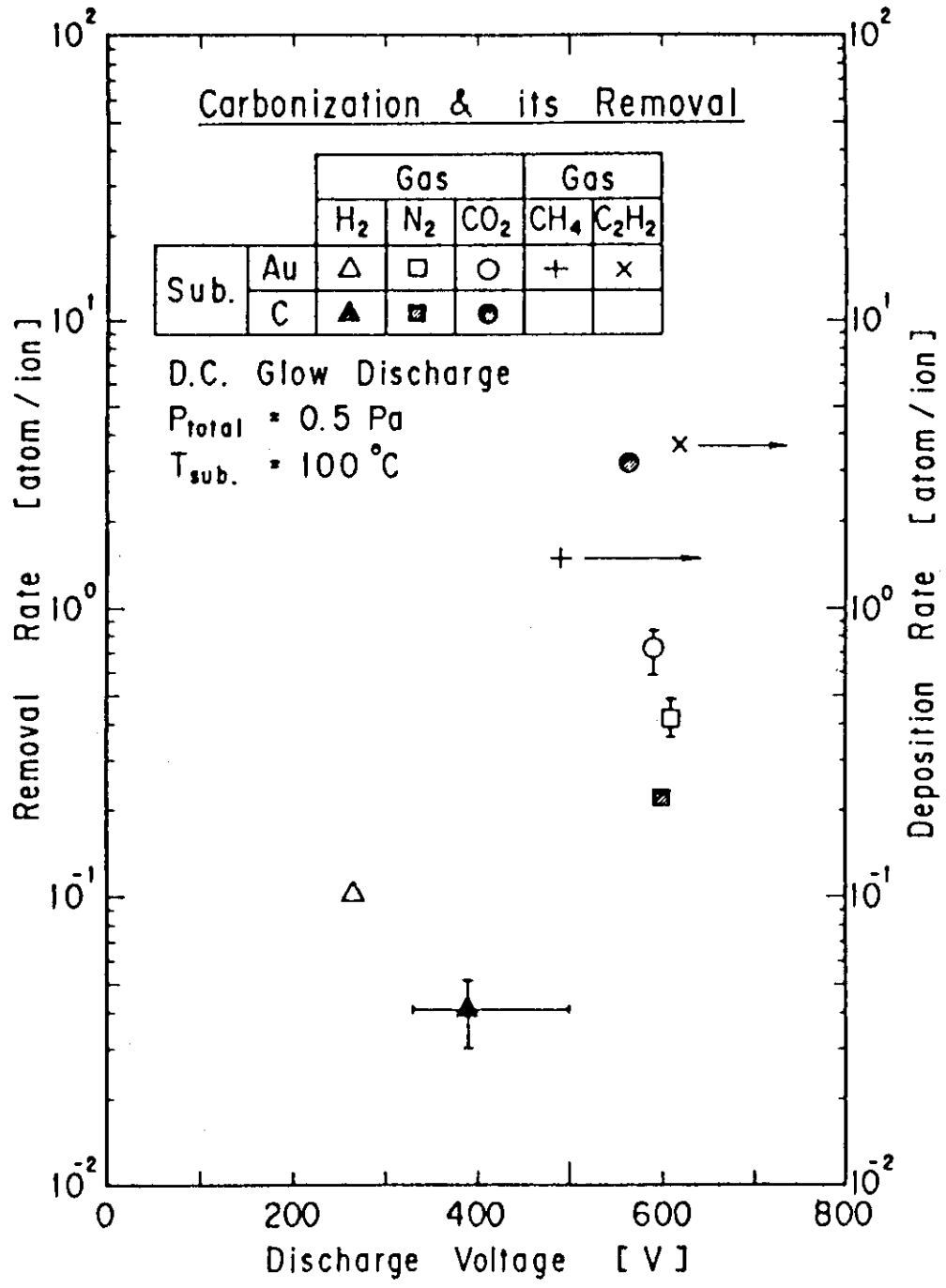

Fig. V.2-9 Removal and deposition rate of carbon as a function of discharge voltage and gas.

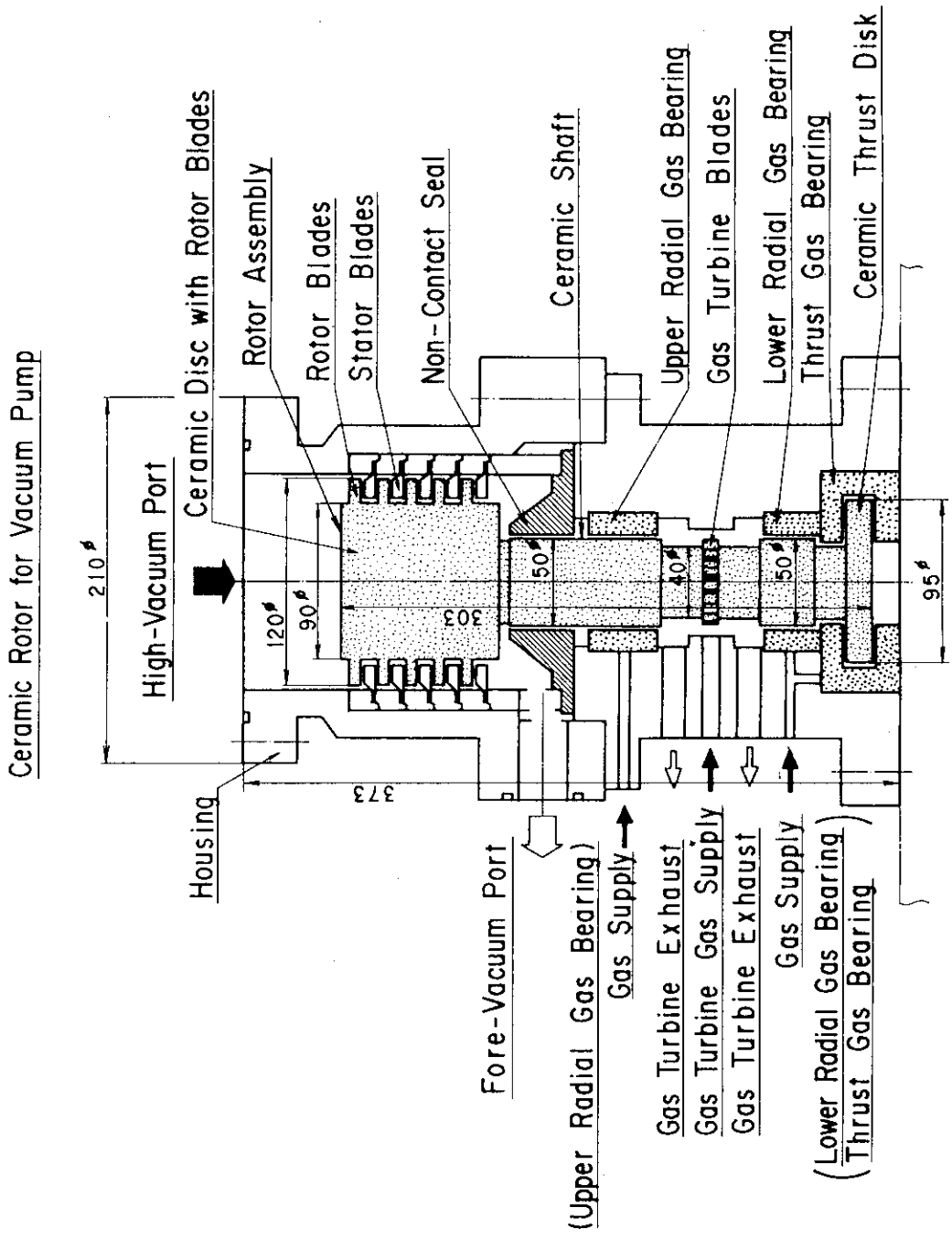

Fig. V.2-10 Cross-sectional view of the test machine.

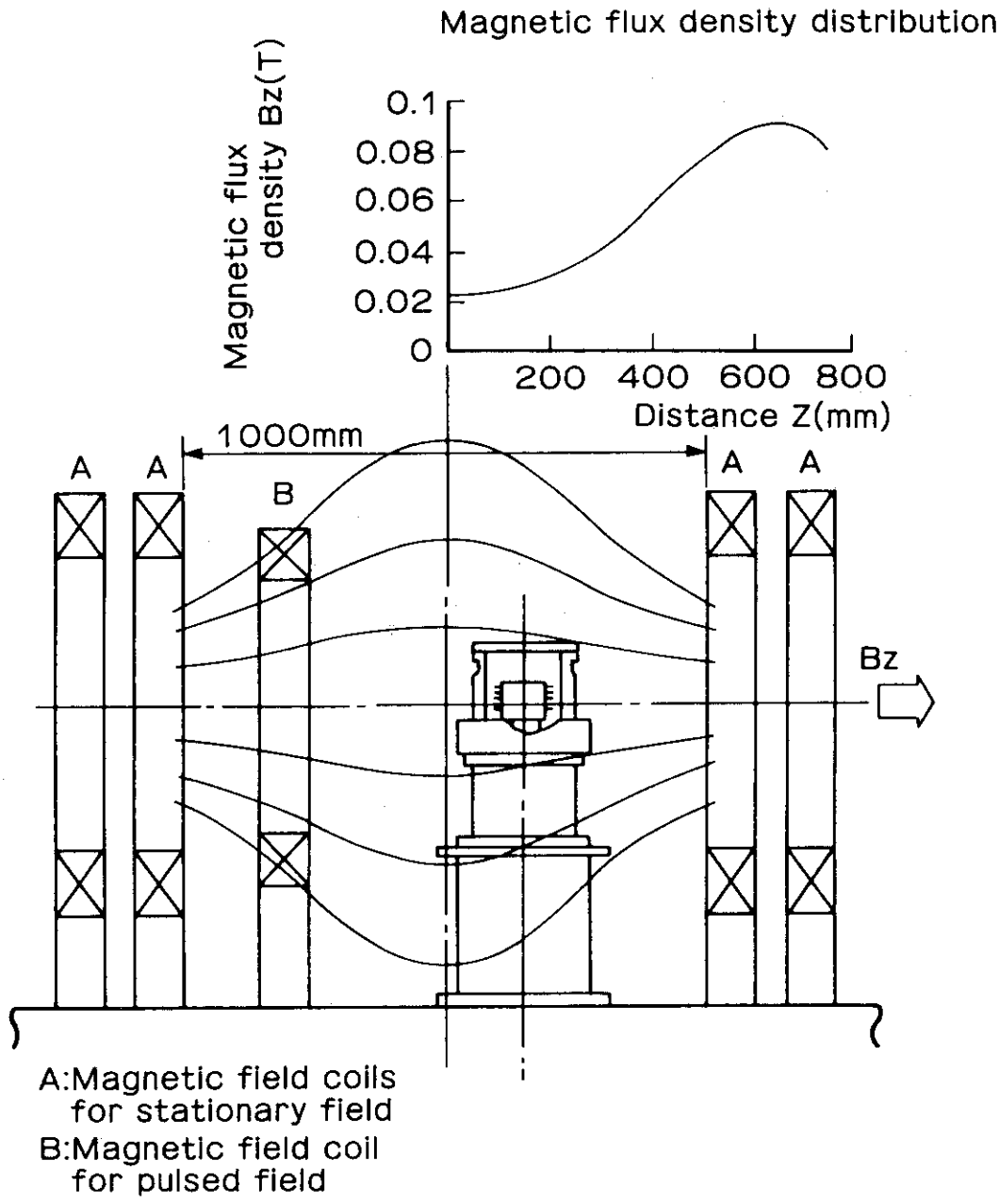

Fig. V.2-11 Schematic of testing apparatus and magnetic field at around the test machine.

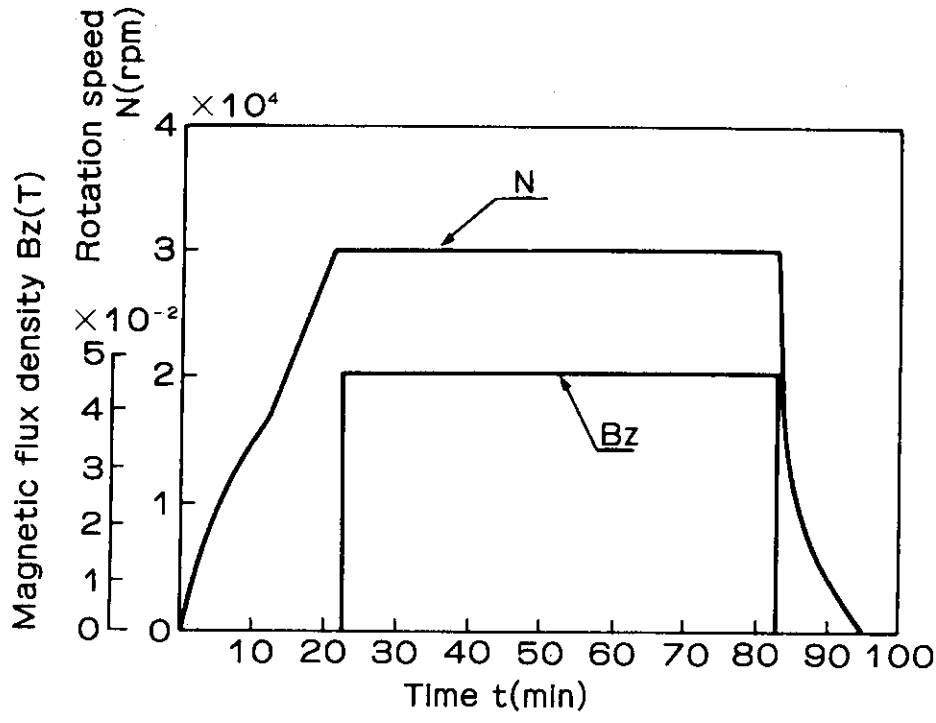

Fig. V.2-12 A typical result of rotational test in stationary magnetic field.

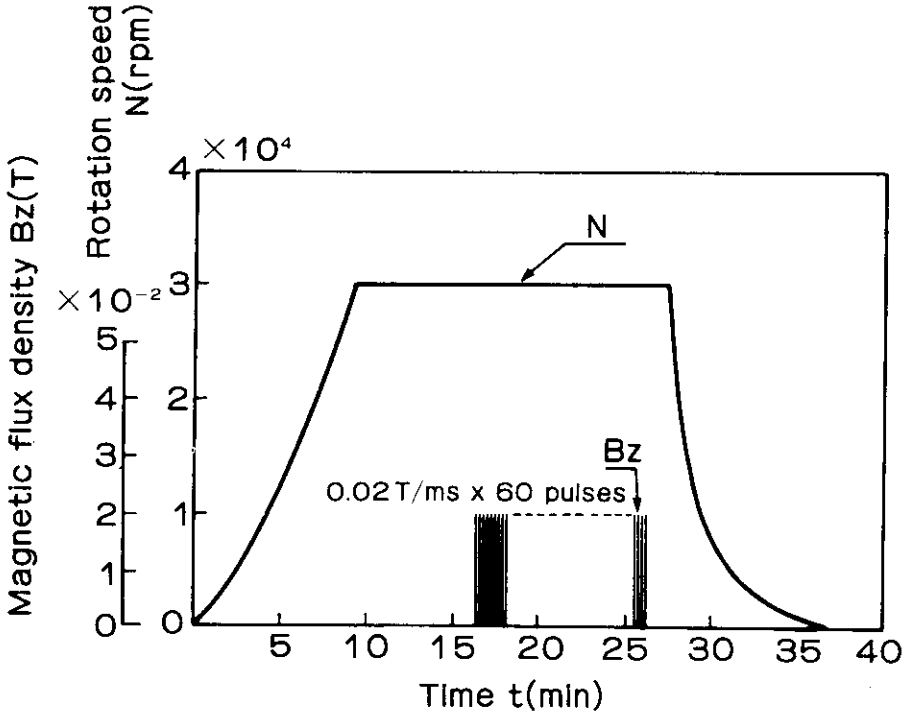

Fig. V.2-13 A typical result of rotational test in pulsed magnetic field.

VI. SUPERCONDUCTING MAGNET DEVELOPMENT

1. Introduction

The superconducting magnet development work at JAERI is being carried out for the purpose of engineering establishment on Fusion Experimental Reactor.

There are three major developments; toroidal coil, poloidal coil and helium refrigerator. The toroidal coil development has progressed through Cluster Test Program and Large Coil Task. The poloidal coil development was practically started in 1985 with Demo Poloidal Coil Program. The helium refrigerator technique has advanced in parallel with these developments. The main achievements in FY 1986 are as follows.

1) Successful testing of the Japanese LCT Coil with 8T in ORNL
2) Advances in Demo Poloidal Coil Program
   - Conductor fabrication
   - Cryogenic system
   - Power supply system
   - Data acquisition system
3) Further evaluation of cryogenic structural material
4) Preliminary study on Proto Toroidal Coil Program

2. Demo Poloidal Coil Program

2.1 General

Demo Poloidal Coil (DPC) Program, aiming to develop large pulsed coil technology required for the construction of superconducting poloidal coils of the Fusion Experimental Reactor (FER), has been carried out at JAERI. As shown in Fig. VI.2-1, the DPC program has the role to make an approaching step to the inner OH coils of FER, based on the achievements obtained through JAERI pulsed coils (Pulser-C, -D, -E, -F, -G).

The DPC program is organized by the tasks to develop the following components and to establish a system technology for the superconducting pulsed coils;

VI. SUPERCONDUCTING MAGNET DEVELOPMENT

1. Introduction

The superconducting magnet development work at JAERI is being carried out for the purpose of engineering establishment on Fusion Experimental Reactor.

There are three major developments; toroidal coil, poloidal coil and helium refrigerator. The toroidal coil development has progressed through Cluster Test Program and Large Coil Task. The poloidal coil development was practically started in 1985 with Demo Poloidal Coil Program. The helium refrigerator technique has advanced in parallel with these developments. The main achievements in FY 1986 are as follows.

1) Successful testing of the Japanese LCT Coil with 8T in ORNL
2) Advances in Demo Poloidal Coil Program
   - Conductor fabrication
   - Cryogenic system
   - Power supply system
   - Data acquisition system
3) Further evaluation of cryogenic structural material
4) Preliminary study on Proto Toroidal Coil Program

2. Demo Poloidal Coil Program

2.1 General

Demo Poloidal Coil (DPC) Program, aiming to develop large pulsed coil technology required for the construction of superconducting poloidal coils of the Fusion Experimental Reactor (FER), has been carried out at JAERI. As shown in Fig. VI.2-1, the DPC program has the role to make an approaching step to the inner OH coils of FER, based on the achievements obtained through JAERI pulsed coils (Pulser-C, -D, -E, -F, -G).

The DPC program is organized by the tasks to develop the following components and to establish a system technology for the superconducting pulsed coils;

1) reliable, low-pulsed loss Nb-Ti coils (DPC-U1 and DPC-U2),
2) highly advanced, stable Nb_3Sn pulsed coil (DPC-EX),
3) cryogenic helium pump to supply supercritical helium flow up to 500 g/s at 4 K, and
4) electric connecting system with the power supply of the JT-60 to get high charging power up to 260 MW.

In 1986, detailed design and verification tests on DPC-U1, DPC-U2, and DPC-EX have been carried out and the construction work for the cryogenic system and power supply connection was started.

2.2 Coil system[1,2)]

Table VI.2-1 summarize the major characteristic parameters to be achieved by DPC-U1, DPC-U2, and DPC-EX. These three coils have the same inner diameter and are to be placed coaxially as shown in Fig. VI.2-2. So as to assure the high-voltage performance and high mechanical reliability, JAERI selected forced-flow cooling for all the coils. Detailed fabrication designs of both Nb-Ti and Nb_3Sn conductors have been carried out in parallel with test fabrication and verification tests on the samples.

Figure VI.2-2 shows also the resulting design of the conductor for the three pulsed coils. The conductor of DPC-U1 and DPC-U2 has obtained the both characteristics of low pulsed loss and high stability by a unique arrangement of CuNi resistive barriers. Verification tests for the conductor of the DPC-EX have also been conducted extensively and reliable technology to get low pulsed loss Nb_3Sn pulsed conductor using Ta barrier was established.

2.3 Power Supply System and Data Acquisiting System

The coil system is designed to generate a pulse field of 7 T/s at a maximum magnetic field of 7 T. In order to investigate mechanical interactions for both normal-mode charging and cusp-mode charging, the coil system is separated into three coils: DPC-U1, U2, and EX. DPC-U1 and DPC-U2 are Nb-Ti pulse coils with operating currents of 30 kA and DPC-EX is a Nb_3Sn pulse coil with an operating current of 10 kA. Consequently, the power supply system, which is composed of several power supply components as listed in Table VI.2-2, is designed to satisfy the various operation modes for each coil. In addition, power

supplies for a resistive heater with a capacity of 20 A and 400 V, and for an inductive heater with 1 kA, 600 V, and 5 kHz are prepared for stability measurements of these coils.

The JT-60 F and V power supplies have been constructed to use for the poloidal field coils of bi-polar transformer and precise control of vertical magnetic field of JT-60 being operated at JAERI. These power supplies, which are composed of thyristor converters and a 500-MVA generator, are connected to the coil system of the DPC for pulse operation. In addition, 30-kA and 12-kA DC power supplies are also connected for DC operation. These power supply components are schematically connected to each other as shown in Fig. VI.2-3 and various operation modes of each coil can be available by using the mode switch. For coil protection, a DC circuit breaker and a dump resistor are installed in the DC power supplies and a by-pass switch is used for protection of the power supply itself. In case of pulse power supplies JT-60 F and V, coil protection can be obtained by an inverted operation but a dump resistor is installed for the coil protection if power supplies fail.

The data acquisition system is composed mainly of two mini-computers and micro-computers which gather more than 400 signals from the coil system, the cryogenic system, and the power supply system as shown in Fig. Vi.2-4. The computer system is especially designed to have sufficient capability both for high speed acquisition during pulse operation of the coil system and for slow acquisition for the facility. All signals are led to patching panels at which principal signals in each operation mode can be selected. After that, the selected signals are acquired in the computer system through signal conditioners and AD converters for high speed and slow speed acquisition. In addition, signals to be stored into transient recorders with digital memory, which includes available channels about 128, can be selected at the patching panel.

3. Large Coil Task of IEA

3.1 General

The Japan Atomic Energy Research Institute (JAERI) is one of the four participants in an international collaboration program, the Large Coil Task (LCT). The major objective of this program, is to explore the engineering problems of design and construction of large toroidal coil for tokamak machine. For this purpose, each participant, the United State of America, EURATOM, Switzerland, and Japan, designed and fabricated an unique test coil and brought it to the International Fusion Superconducting Magnet Test Facility (IFSMTF) in Oak Ridge National Laboratory (ORNL) operated by the United State. Six test coils (US: 3, Japan, EURATOM, Switzerland: 1) are being tested in compact torus array. All coils have a 2.5 m × 3.5 m D-shaped bore and are designed for stable operation at 8 T. However, the detailed structure such as the cooling concept, conductor design, coil structure, and thermal design are decided by each participant.

In FY 1986, the test in full six-coil array was started after the preliminary single coil tests. All test coils were tested according to the test sequence, US-DG, JA, EURATOM (EU), Swiss (CH), US-GE and US-WH coil, and successfully achieved the design field of 8 T at full operating current. As the second step of the six-coil test, 8 T operation with pulsed field of 0.14 T/s was begun in December 1987 and being continued. The test items on each test coil, which were completed in FY 1986, are summarized in Table VI.3-1. The six-coil test in ORNL including the extended test conditions to explore the limit of coil performance will be continued until the middle of 1987.

3.2 Six Coil Test

3.2.1 NORMAL-I Test (8 T Operation without pulsed field)

The test of full six-coil toroidal array was started in the middle of August 1986. As the second test coil in full coil array, the JA coil was tested from August 25 to September 19, 1986. In the first trial, the JA coil achieved the design field of 8 T at the nominal current (10,220 A), with a total stored energy of 645 MJ. The charge was successfully carried out without any appearance of normal zone. Fig. VI.3-1 shows how the magnetic field increased to 8 T in

the first charge. The measured maximum peak field of the JA coil was 8.07 T in the corner of D shape.

During the 8 T operation, mechanical behavior of test coil was carefully observed by a number of strain gauges which were attached to the conductor and the coil case. The measured conductor strains along the conductor length are shown in Fig. VI.3-2, both for 8 T field generation and for the single coil operation. As shown in the figure, the differences among each test coils are observed both in strain values and in its distributions because of the difference of winding methods and coil structure. The detailed comparison of experimental results with the design calculation are in progress by each participant.

The half-turn recovery test of the JA coil, at 8 T, was performed by means of a heater in the conductor of the middle pancake where the peak field exists. In the test, 4,800 W was applied for 250 ms; the corresponding energy density in the conductor was 0.9 J/cc at the heated zone. As shown in Fig. VI.3-3, spontaneous recovery to the superconducting state was observed. The recovery from the normal zone was initiated not from both cold end, but from the center of heated zone. This indicates the JA coil is fully cryostable at 8 T in the sense of unconditional recovery.

In the simulated nuclear heating test, thermal disturbance was produced in widely distributed 8 heaters over a 60 sec interval that resembles a tokamak burning pulse. The total power of 548 W, which corresponds to the local power density of 52 mW/cc, was applied to the JA coil during 8 T operation. The test was successful and the coil showed no evidence of a normal zone.

3.2.2 NORMAL-II Test (8 T Operation with pulsed Field of 0.14 T/s)

The second step of six-coil test was to demonstrate the stable coil performance at 8 T under the pulsed field of 0.14 T/s. A pair of copper pulsed coil are installed in the inner bore of test coil. The JA coil showed the stable performance in this test condition. The measured eddy current (AC) loss in the JA coil induced by the pulsed field was 15.0 W at 8 T, and is in good agreement with the design calculation of 14.3 W. The recovery test and simulated nuclear heating test were also performed in this condition as shown in Fig.

VI.3-4. The JA coil showed the stable coil performance at 8 T with pulsed field of 0.14 T/s, even in the condition that the thermal disturbance of heater pulse (4,800 W - 250 ms, 0.9 J/cc) and the simulated nuclear heating (555 W - 60 sec, 53 mW/cc in the heated zone) were applied to the test coil at the same time.

4. High Field Coil Development

The magnetic field of 12 T was achieved by the coil named FC15OM, which was manufactured to demonstrate tha the coil wound with Nb_3Sn cable-in-conduit forced-flow-type superconductor can generate 12 T, the target field of the toroidal coil of the next generation tokamak[3]. 12 T is the world record as the magnetic field obtained by the coil wound with this type of superconductor. Table VI.4-1 shows the major parameters and the achieved results of FC15OM.

The $(NbTi)_3Sn$ small coil named BC15S was manufactured, and the magnetic field of 15.7 T was got with the average current density of 178 A/mm^2 which is much higher current density value than those of other existing high field coils. Table VI.4-2 shows the major parameters and the achieved results of BC15S.

The study of Nb_3Al, which is expected to be the high-field-use superconductor after $(NbTi)_3Sn$, was started. Nb_3Al wires were manufactured and their test is in progress.

In order to compact the toroidal coil, the possibilities of 16-T toroidal coil[4] and 12-T high-current-density coil were discussed. The prospects of these coils were bright.

5. Cryogenic System Development

The construction of Fusion Engineering Reactor (FER) inevitably requires a large, reliable and efficient helium cryogenic system with a refrigeration capacity of more than 30 kW as one unit. Since extremely larger cryogenic system than the present one is indispensable, JAERI has been developing cryogenic technology and cryogenic devices by using the Superconducting Engineering Test

VI.3-4. The JA coil showed the stable coil performance at 8 T with pulsed field of 0.14 T/s, even in the condition that the thermal disturbance of heater pulse (4,800 W - 250 ms, 0.9 J/cc) and the simulated nuclear heating (555 W - 60 sec, 53 mW/cc in the heated zone) were applied to the test coil at the same time.

4. High Field Coil Development

The magnetic field of 12 T was achieved by the coil named FC15OM, which was manufactured to demonstrate tha the coil wound with Nb_3Sn cable-in-conduit forced-flow-type superconductor can generate 12 T, the target field of the toroidal coil of the next generation tokamak[3]. 12 T is the world record as the magnetic field obtained by the coil wound with this type of superconductor. Table VI.4-1 shows the major parameters and the achieved results of FC15OM.

The $(NbTi)_3Sn$ small coil named BC15S was manufactured, and the magnetic field of 15.7 T was got with the average current density of 178 A/mm^2 which is much higher current density value than those of other existing high field coils. Table VI.4-2 shows the major parameters and the achieved results of BC15S.

The study of Nb_3Al, which is expected to be the high-field-use superconductor after $(NbTi)_3Sn$, was started. Nb_3Al wires were manufactured and their test is in progress.

In order to compact the toroidal coil, the possibilities of 16-T toroidal coil[4] and 12-T high-current-density coil were discussed. The prospects of these coils were bright.

5. Cryogenic System Development

The construction of Fusion Engineering Reactor (FER) inevitably requires a large, reliable and efficient helium cryogenic system with a refrigeration capacity of more than 30 kW as one unit. Since extremely larger cryogenic system than the present one is indispensable, JAERI has been developing cryogenic technology and cryogenic devices by using the Superconducting Engineering Test

VI.3-4. The JA coil showed the stable coil performance at 8 T with pulsed field of 0.14 T/s, even in the condition that the thermal disturbance of heater pulse (4,800 W - 250 ms, 0.9 J/cc) and the simulated nuclear heating (555 W - 60 sec, 53 mW/cc in the heated zone) were applied to the test coil at the same time.

4. High Field Coil Development

The magnetic field of 12 T was achieved by the coil named FC15OM, which was manufactured to demonstrate tha the coil wound with Nb_3Sn cable-in-conduit forced-flow-type superconductor can generate 12 T, the target field of the toroidal coil of the next generation tokamak[3]. 12 T is the world record as the magnetic field obtained by the coil wound with this type of superconductor. Table VI.4-1 shows the major parameters and the achieved results of FC15OM.

The $(NbTi)_3Sn$ small coil named BC15S was manufactured, and the magnetic field of 15.7 T was got with the average current density of 178 A/mm^2 which is much higher current density value than those of other existing high field coils. Table VI.4-2 shows the major parameters and the achieved results of BC15S.

The study of Nb_3Al, which is expected to be the high-field-use superconductor after $(NbTi)_3Sn$, was started. Nb_3Al wires were manufactured and their test is in progress.

In order to compact the toroidal coil, the possibilities of 16-T toroidal coil[4] and 12-T high-current-density coil were discussed. The prospects of these coils were bright.

5. Cryogenic System Development

The construction of Fusion Engineering Reactor (FER) inevitably requires a large, reliable and efficient helium cryogenic system with a refrigeration capacity of more than 30 kW as one unit. Since extremely larger cryogenic system than the present one is indispensable, JAERI has been developing cryogenic technology and cryogenic devices by using the Superconducting Engineering Test

Facility. In this period, a cold circulation pump, a cold compressor, a pair of 30-kA current lead have been developed and tested as a development step. In addition, the detail design of the cryogenic system for the Demonstration Poloidal Coil (DPC) have been established.

5.1 Cryogenic component development

A cold circulation pump[5] with double acting bellows type, which is to generate and supply supercritical helium with a mass flow rate of 500 g/sec to forced-flow superconducting coils, has been developed. Figure VI.5-1 shows the cross-sectional view of the cold circulation pump. We have tested the cold circulation pump at cryogenic temperature and demonstrated that the cold circulation pump can produce supercritical helium of around 500 g/sec and the thermal efficiency is more than 55%.

In order to effectively introduce lower operating temperature of forced-flow superconducting coils than 4 K, a cold compressor[1], which is a centrifugal compressor with a maximum capacity of 100 g/sec, has been developed. The cold compressor is driven by a inductive motor and is designed to have the dynamic gas bearing as shown in Fig. VI.5-2. The performance test results at cryogenic temperature shows that a minimum temperature of 3.5 K can be achieved at a frequency of 1.4 kHz and a maximum thermal efficiency is around 63%. These cryogenic pump and compressor are the biggest one in a world and their performances are sufficiently high.

A pair of 30-kA current lead[6] has been tested as the final development step after the development of 3-kA, 6-kA, and 15-kA current leads. The performance test result shows that the current lead has both a ideal self-cooling condition which is the optimum thermal condition corresponding to around 1.0 W/kA and a high insulation voltage of more than AC 45 kV.

5.2 DPC cryogenic system

In order to demonstrate superconducting pulse coil technology required for FER, the Demonstration Poloidal Coil program (DPC) has been conducted since 1986. There are three forced-flow superconducting pulse coils (DPC-U1, U2, and EX) cooled by

supercritical helium with a mass flow rate of 350 g/sec. For this purpose, a newly developed cryogenic pump system described in 5.1 is installed to the existing 1.2-kW helium cryogenic system. Furthermore, three pairs of 30-kA current leads developed in the cryogenic component development mentioned in 5.1 are also installed. Figure VI.5-3 shows the schematic flow diagram of the cryogenic system. The system design[7] of the cryogenic system has been established and the construction work will be started from April, 1987. The total performance test of the cryogenic system will be carried out during the early of 1981.

6. Development of the Cryogenic Structural Materials

The development of base metals of the Japanese Cryogenic Steels (JCS) has almost completed. The Demo Poloidal Coil (DPC) project required the application of the JCS to real superconducting coils. The JCS was applied to the conduit materials of the DPC. It is required that conduit material has to withstand cold work and/or heat treatment. It was verified that the JCS satisfied the requirements by tensile test with thin plates at 4 K.

On the other hand, thick plate will be applied to toroidal coil cases and supporting structures of the Fusion Experimental Reactor (FER). Figure VI.6-1 shows the new cryogenic tensile test machine which capacity is 100 tons. It was installed to evaluate the mechanical properties of the JCS with a large size specimen at 4 K. The relation between a fracture toughness and a specimen thickness is shown in Fig. VI.6-2. It was demonstrated that the JCS plates of 75, 100 mm thickness have enough fracture toughness.

7. Design Study of PROTO Toroidal Coil

In FY 1986, the design studies of prototype (PROTO) toroidal coil and its backup coil system were started. The major objective of this program is to develop a 12-T large toroidal coil, which satisfies the

supercritical helium with a mass flow rate of 350 g/sec. For this purpose, a newly developed cryogenic pump system described in 5.1 is installed to the existing 1.2-kW helium cryogenic system. Furthermore, three pairs of 30-kA current leads developed in the cryogenic component development mentioned in 5.1 are also installed. Figure VI.5-3 shows the schematic flow diagram of the cryogenic system. The system design[7] of the cryogenic system has been established and the construction work will be started from April, 1987. The total performance test of the cryogenic system will be carried out during the early of 1981.

6. Development of the Cryogenic Structural Materials

The development of base metals of the Japanese Cryogenic Steels (JCS) has almost completed. The Demo Poloidal Coil (DPC) project required the application of the JCS to real superconducting coils. The JCS was applied to the conduit materials of the DPC. It is required that conduit material has to withstand cold work and/or heat treatment. It was verified that the JCS satisfied the requirements by tensile test with thin plates at 4 K.

On the other hand, thick plate will be applied to toroidal coil cases and supporting structures of the Fusion Experimental Reactor (FER). Figure VI.6-1 shows the new cryogenic tensile test machine which capacity is 100 tons. It was installed to evaluate the mechanical properties of the JCS with a large size specimen at 4 K. The relation between a fracture toughness and a specimen thickness is shown in Fig. VI.6-2. It was demonstrated that the JCS plates of 75, 100 mm thickness have enough fracture toughness.

7. Design Study of PROTO Toroidal Coil

In FY 1986, the design studies of prototype (PROTO) toroidal coil and its backup coil system were started. The major objective of this program is to develop a 12-T large toroidal coil, which satisfies the

supercritical helium with a mass flow rate of 350 g/sec. For this purpose, a newly developed cryogenic pump system described in 5.1 is installed to the existing 1.2-kW helium cryogenic system. Furthermore, three pairs of 30-kA current leads developed in the cryogenic component development mentioned in 5.1 are also installed. Figure VI.5-3 shows the schematic flow diagram of the cryogenic system. The system design[7] of the cryogenic system has been established and the construction work will be started from April, 1987. The total performance test of the cryogenic system will be carried out during the early of 1981.

6. Development of the Cryogenic Structural Materials

The development of base metals of the Japanese Cryogenic Steels (JCS) has almost completed. The Demo Poloidal Coil (DPC) project required the application of the JCS to real superconducting coils. The JCS was applied to the conduit materials of the DPC. It is required that conduit material has to withstand cold work and/or heat treatment. It was verified that the JCS satisfied the requirements by tensile test with thin plates at 4 K.

On the other hand, thick plate will be applied to toroidal coil cases and supporting structures of the Fusion Experimental Reactor (FER). Figure VI.6-1 shows the new cryogenic tensile test machine which capacity is 100 tons. It was installed to evaluate the mechanical properties of the JCS with a large size specimen at 4 K. The relation between a fracture toughness and a specimen thickness is shown in Fig. VI.6-2. It was demonstrated that the JCS plates of 75, 100 mm thickness have enough fracture toughness.

7. Design Study of PROTO Toroidal Coil

In FY 1986, the design studies of prototype (PROTO) toroidal coil and its backup coil system were started. The major objective of this program is to develop a 12-T large toroidal coil, which satisfies the

technical specifications of the toroidal coil for the Fusion Experimental Reactor (FER). Based on the 12-T high-field technologies established by the Test Module Coil (TMC) in the Cluster Test Program at JAERI, and on the 8-T, large-scale magnet technologies demonstrated by the Large Coil Task (LCT), the major design parameters listed in Table VI.7-1 are selected for the PROTO toroidal coil. JAERI selected froced-flow cooling with the cable-in-conduit type conductor for PROTO toroidal coil from the following view points in addition to the fact that JAERI has enough experience in pool-boiling cooling through the development of LCT coil and TMC coil;

1) high voltage characteristics can be obtained by forced-flow cooling because the conductor can be fully insulated,
2) high mechanical toughness of the winding against the large magnetic forces can be obtained because the conductor can be wound compactly without cooling spacers.

The test configuration of PROTO toroidal coil is shown in Fig. VI.7-1. Since it is difficult to test the PROTO toroidal coil at 12-T only with the backup field of LCT coils, whose maximum field is limited to 8-9 T, an employment of additional backup coils, named LCT Backup Coil (LBC), which has the maximum field of 12-16 T, is being investigated for the backup coil system. The PROTO toroidal coil is placed in the cluster configuration with LCT coils and LBC coils.

References

1) H. Tsuji, et al., "Design selections for the fabrication of the Demonstration Poloidal Coil", Proc. of the 7th Topical Meeting on the Technology of Fusion Energy (1986).
2) S. Shimamoto, et al., "Evolutions in the Development of Superconducting Materials and Magnet Technology for the Coming Fusion Machines in Japan", Proc. of the 11th International Conf. on Plasma Physics and Controlled Nuclear Fusion Research, Paper IAEA-VN-47/H-III-6 (1986).
3) M. Nishi, et al., "A 12-T Forced Flow Type Superconducting Magnet", Proc. of 1986 Applied Superconductivity Conf., Baltimore (1986), to be published.

4) M. Nishi, et al., "A 16-T Superconducting Toroidal Coil Development for A Tokamak Fusion Machine", Porc. of ANS 7th Topical Meeting on Technology of Fusion Energy, Reno (1986), to be published.

5) T. Kato, et al., "Cryogenic system component development for Fusion Experimental Reactor at JAERI", ANS 7th Topical meeting on Technology of Fusion Energy, Reno, June 15-19, 1986.

6) E. Tada, et al., "Development of 30-kA vapor-cooled current lead for fusion devices", ICEC-11, Berlin, April 22-25, 1986.

7) E. Tada, et al., "System design of the Demonstration Poloidal Coils and the test facility", Applied Superconductivity Conference, Baltimore, September 28-October 3, 1986.

Table VI.2-1 Major parameters of the Demo Poloidal Coils

	DPC-U1,DPC-U2	DPC-EX
Superconductor	Nb-Ti	Nb_3Sn
Design Field	7 T	10 T
Testing Field	7 T	7 T
Design Pulsed Field	7 T/s	7 T/s
Winding Inner Diameter	1.0 m	1.0 m
Winding Outer Diameter	2.0 m	1.6 m
Winding Height	0.32*2 m	0.15 m
Nominal Current	30 kA	10 kA
Magnetomotive Force	4.1*2 MAT	1.2 MAT
Current Density	25 A/mm*mm	25 A/mm*mm
Stored Energy	30 MJ	Total 40 MJ

Table VI.2-2 Major parameters of the power supply system of the DPC

COMPONENTS	MAX. CURRENT	MAX. VOLTAGE
JT-60 F power supply	+ 92 kA	+ 2.5 kV
JT-60 V power supply	+ 58 kA - 8.6 kA	+ 5.0 kV
DC-30 kA power supply	30 kA	12 V
DC-12 kA power supply	12 kA	10 V

Table VI.3-1 The test items of each LCT coil completed in the six-coil test in FY 1986.

	US-GD Coil	JA Coil	EU-Coil	CH Coil	US-GE Coil	US-WH Coil
I. NORMAL-I (8T Operation, without Pulsed Field)	8/14-8/21 1986	8/25-8/29 & 9/19 1986	10/14-10/18 1986	10/21-10/28 1986	10/30-11/4 1986	11/5-11/21 1986
(1) 8T Operation	8/15	8/25	10/16	10/22	10/30	11/6
(2) Stability or Recovery Test	Heater Pulse of 0.5kJ-300ms Cold End Recovery at 8 T	Heater Pulse of 1.2kJ-250ms Unconditional Recovery at 8 T	Stable Operation at 8 T by flowrate of 1.3g/sec /channel in Winding	Heater Pulse of 0.8J-20ms Stable at 8 T	Heater Pulse of 2.2kW-200ms Cold End Recovery at 8 T	Tcs Measurement Tcs = 4.8 K at 6.1 T
(3) Nuclear Heating Simulation Test		548W-60sec (52mW/cc) Stable at 8 T		Continuous Heating of 130W Stable at 8 T	1.5 kW-60sec (60mW/cc) Stable at 8 T	
(4) Nuclear Heating + Recovery Test					190W-60sec and 2.2kW-200ms Cold End Recovery	
II. NORMAL-II (8T Operation with Pulsed Field(0.14T/s)		3/2 - 3/20 1987	12/9-12/16 1986	2/2-2/20 1987		
(1) AC Loss Measurement		Total 15W	Wind. :15 W Case :10 W	Wind. :3.2W Case :10.6W		
(2) Nuclear Heating with Pulsed Field (0.14T/s), (+ Heater Pulse)		555W-60sec (53mW/cc) + 1.2kJ-250msec, Stable at 8 T		Continuous Heating of 140 W, Stable at 8 T		

Table VI.4-1 Major parameters and obtained results of FC15OM coil

Coil	
Winding Inner Diameter	100 mm
Winding Outer Diameter	226 mm
Winding Height	230 mm
Conductor	
Type	Cable-in-Conduit
Size	7.6 mm x 7.6 mm
Superconductor	Nb_3Sn
Test Results	
Achieved Magnetic Field	12.0 T
Background Magnetic Field	8.0 T
Transport Current	4.0 kA
Average Current Density	60.5 A/mm^2

Table VI.4-2 Major parameters and obtained results of BC15S coil

Parameters	
Superconductor	$(NbTi)_3Sn$
Winding Inner Diameter	36.6 mm
Winding Outer Diameter	62.3 mm
Winding Height	151.7 mm
Test Results	
Achieved Magnetic Field	15.7 T
Background Magnetic Field	13.0 T
Transport Current	531 A
Average Current Density	178 A/mm^2

Table VI.7-1 Designed Major Parameters of 12 T PROTO Toroidal Coil

Design Magnetic Field	12.0 T
Superconductor	$(Nb\text{-}Ti)_3Sn$
Operating Current (Ib)	30.0 kA
Critical Current (Ic)	60.0kA
Average Current Density in the Winding	40 A/mm^2
Coil Configuration	D-shaped
Coil Size (I.D.)	3.97 m (Horizontal) 5.95 m (Vertical)
Cooling Concept	Forced Flow*1 (4.5 K, 10 atm)
Winding Concept	11 Double Pancake,*2 330 Turns
Conductor Type	Cable-in-Conduit
Assembly	Epoxy-Impregnation and Coil Case
Self-Inductance	1.015 H
Stored Energy*3	467 MJ
Total Coil Weight	45.2 Tons

Note : *1 Cooling Channel : 250 m/channel x 22 pathes
*2 Total Conductor Length : 5.52 km
*3 Self Stored Energy : 467 MJ
Total Stored Energy: 850 MJ

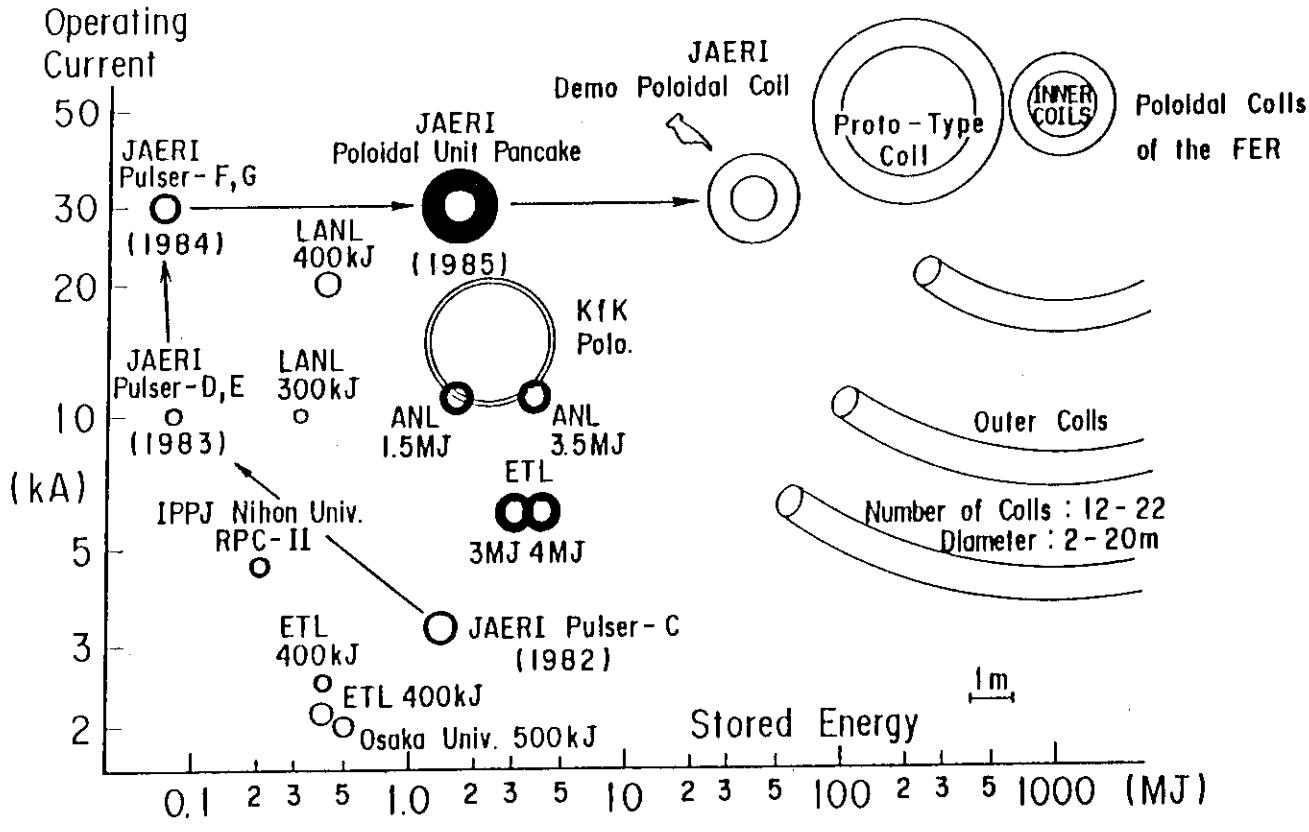

Fig. VI.2-1 Status of superconducting magnet development for poloidal coils of the next tokamak machine.

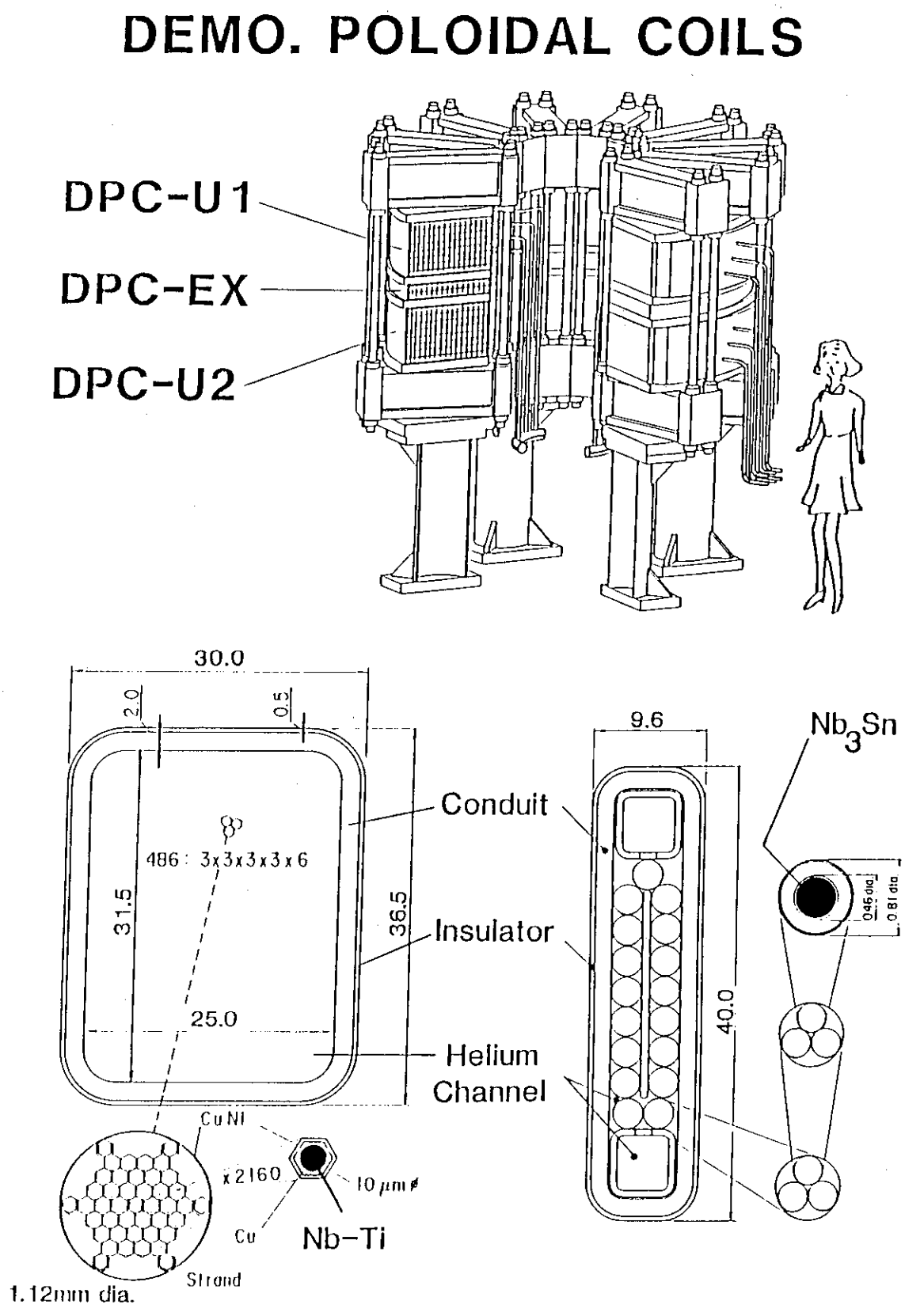

Fig. VI.2-2 Conductor and coil configurations of the Demo Poloidal Coil.

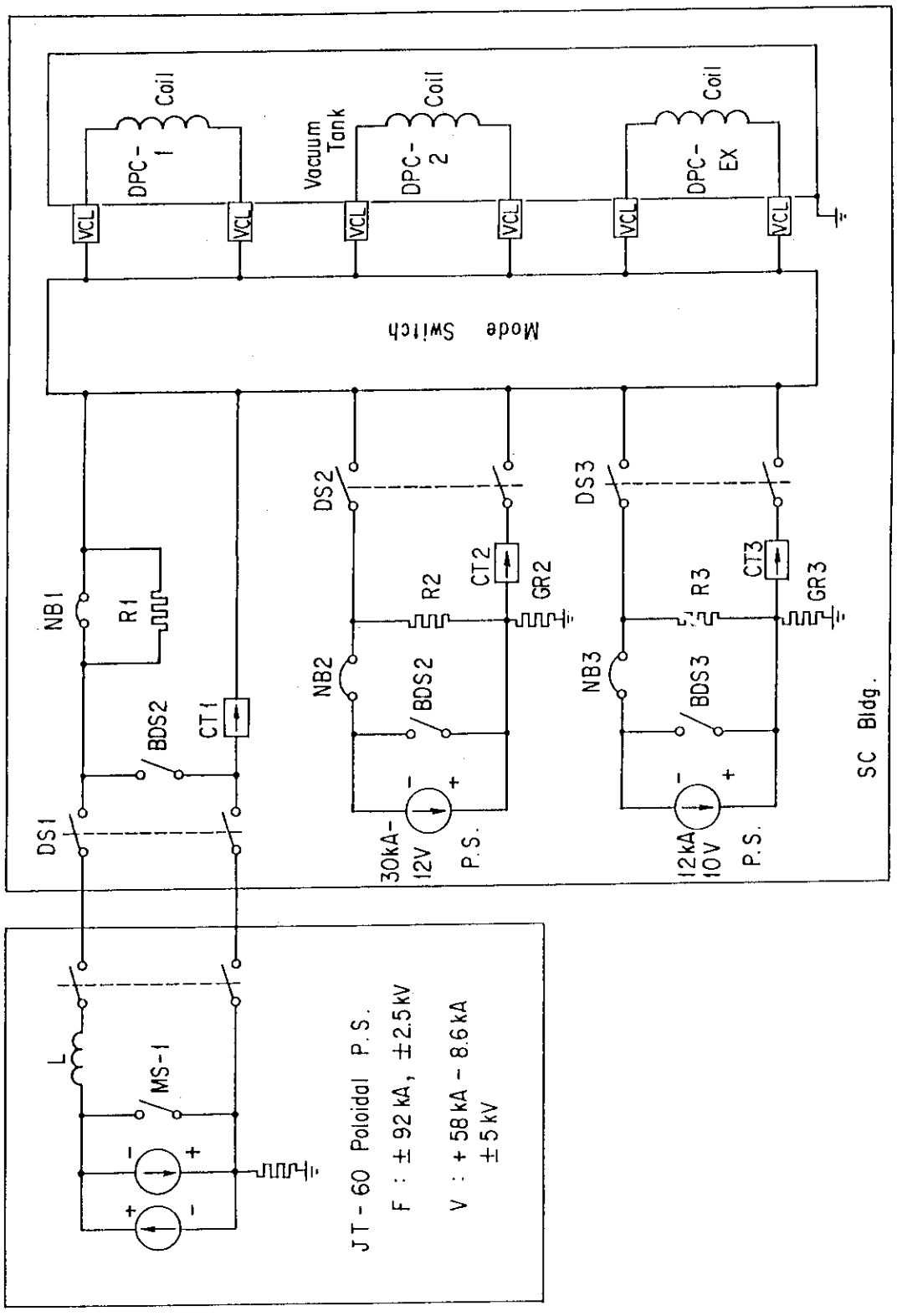

Fig. VI.2-3 Block diagram of the power supply system of the DPC.

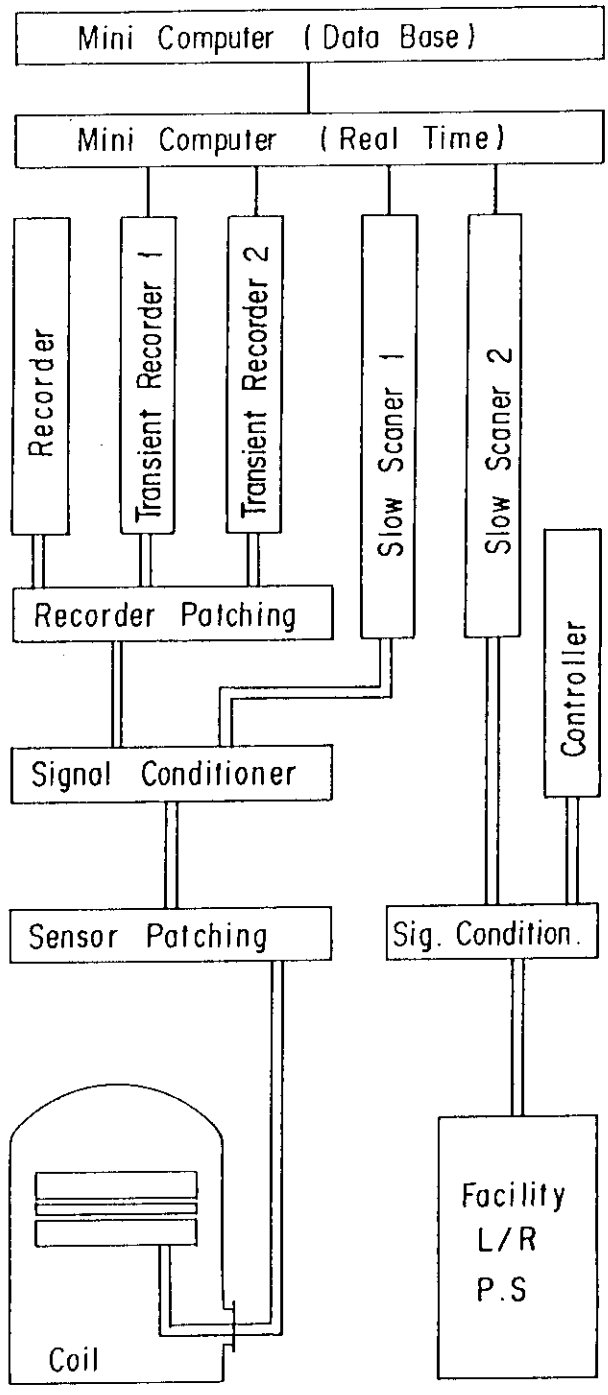

Fig. VI.2-4 Block diagram of the data acquisition system of the DPC.

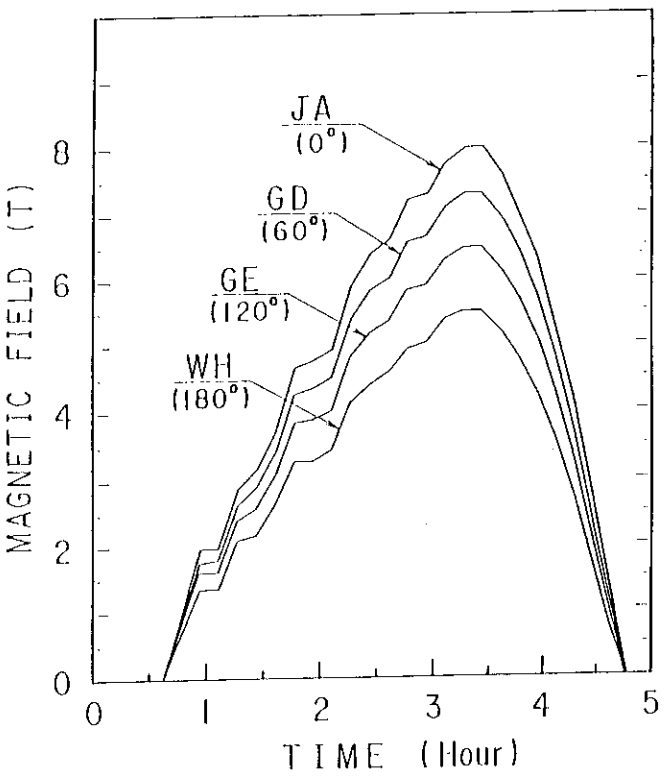

		JA	GD	GE	WH	EU	CN
Iop.	(A)	10,234	8,356	8,780	15,223	9,424	10,335
I^*	(%)	100.1	81.9	83.7	85.7	82.7	79.5
$B_{ref.}$	(T)	8.0	7.4	7.3	7.0	7.2	7.4

Fig. VI.3-1 Magnetic field increase on the innermost turn of the straight part of the D coil shape, obtained in the virgin charge of the JA coil to 8 T.

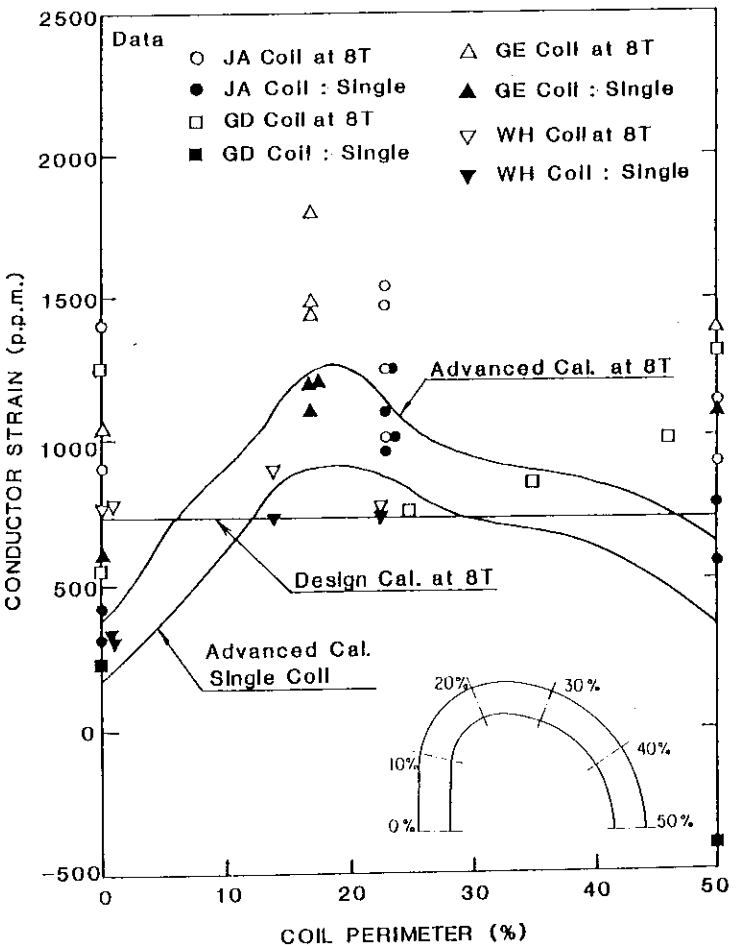

Fig. VI.3-2 The comparison of experimental conductor strains along the conductor length, measured in the 8 T and in the single coil charge at ORNL.

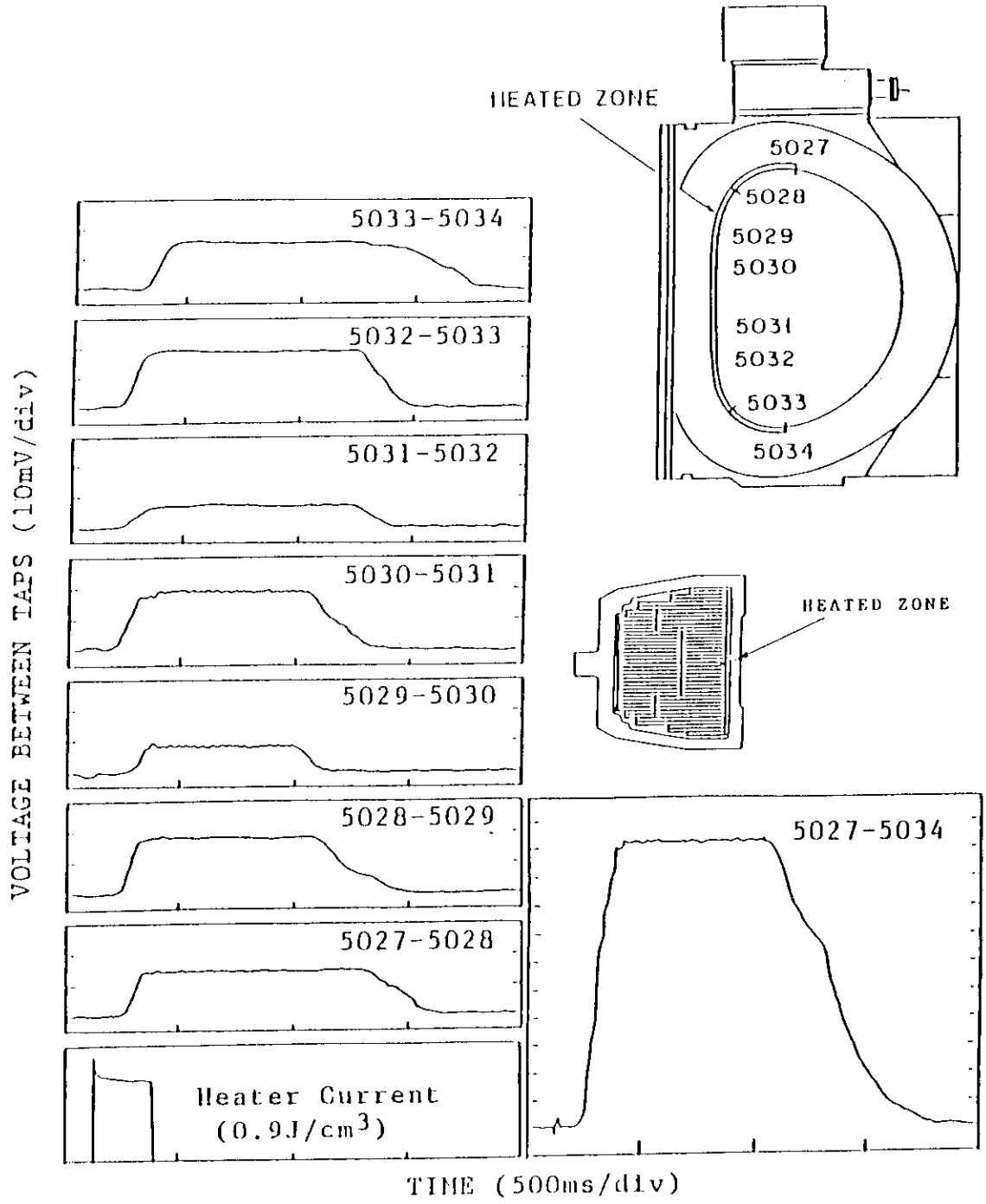

Fig. VI.3-3 Measured voltage profiles of the conductor at heated zone in the recovery test of the JA coil at 8 T. (innermost turn in the middle pancake)

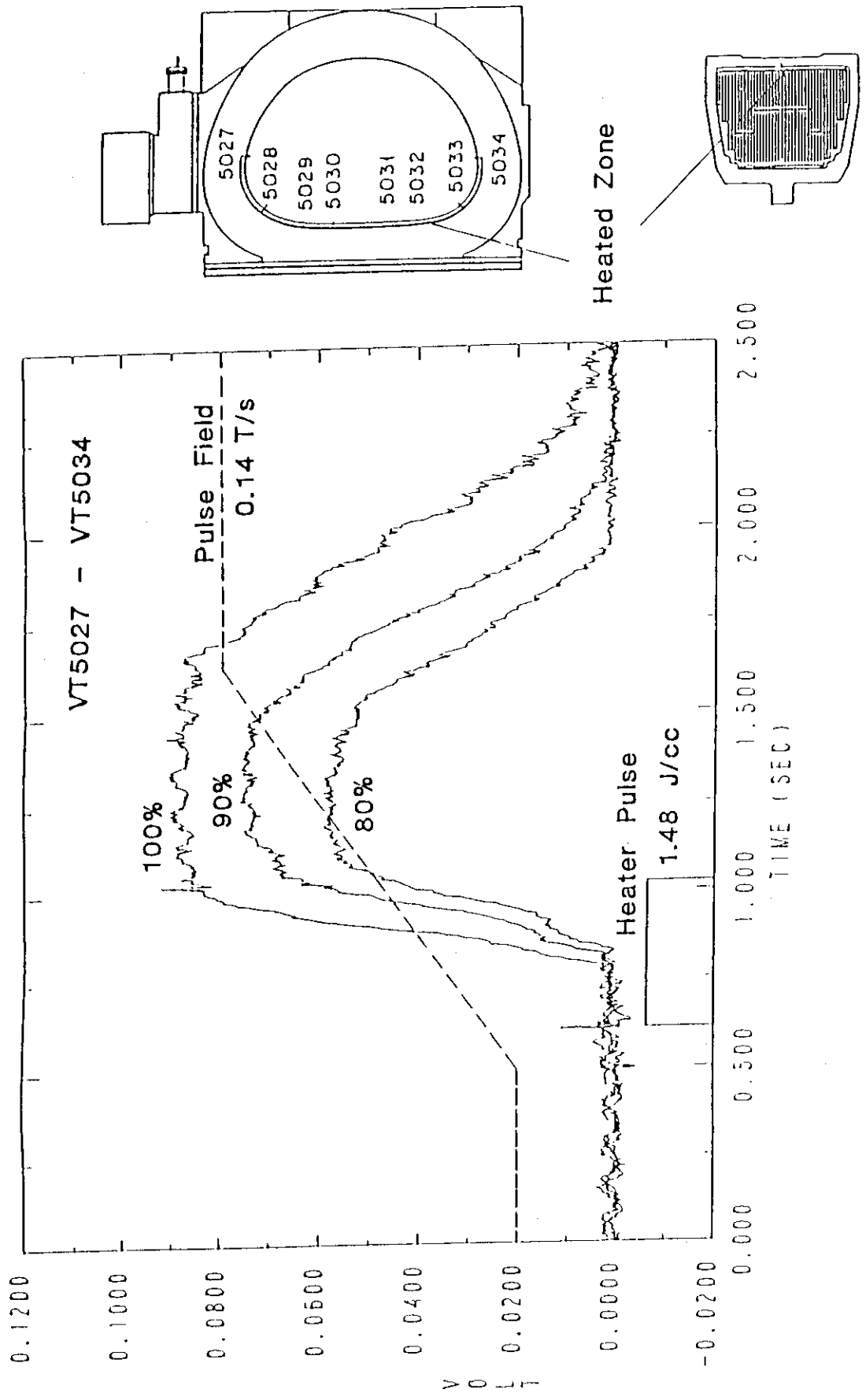

Fig. VI.3-4 Measured voltage profiles of the conductor at heated zone obtained in the recovery test of the JA coil at 8 T with pulsed field of 0.14 T/s.

Type	: Reciprocating double acting bellows pump
Driving	: Oil pressure
Frequency	: 0.5 - 1.0 Hz
Stroke	: 10 - 20 mm

Mass flow rate	: 350 g/s	(500 g/s)
Operating pressure	: 10 bar	(20 bar)
Pump head	: 1.0 bar	(1.5 bar)
Operating temp.	: 4 K	
Adiabatic efficiency	: 60 %	

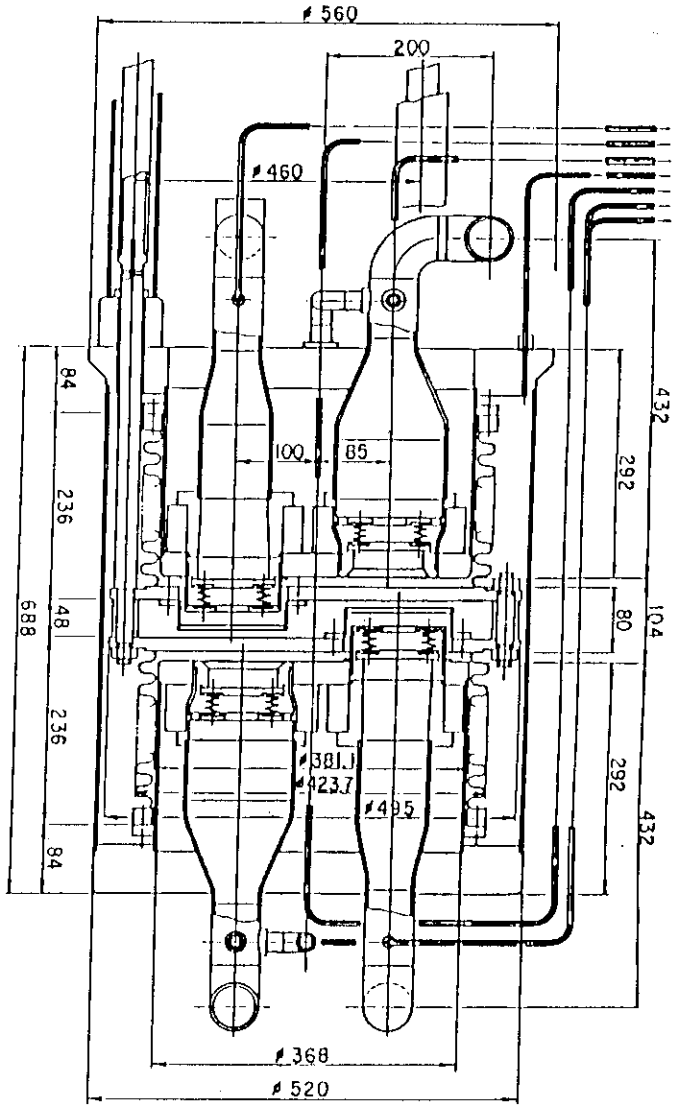

Fig. VI.5-1 Supercritical helium circulation pump.

Type	:	Centrifugal compressor
Driving	:	Induction Motor
Journal bearing	:	Dynamic gas bearing
Thrust bearing	:	Dynamic gas bearing
Max. frequency	:	80,000 rpm
Inlet pressure	:	0.7 bar (0.5 bar)
Inlet temperature	:	3.9 K (3.5 K)
Outlet pressure	:	1.2 bar
design flow rate	:	60 g/s
Adiabatic efficiency	:	60 %

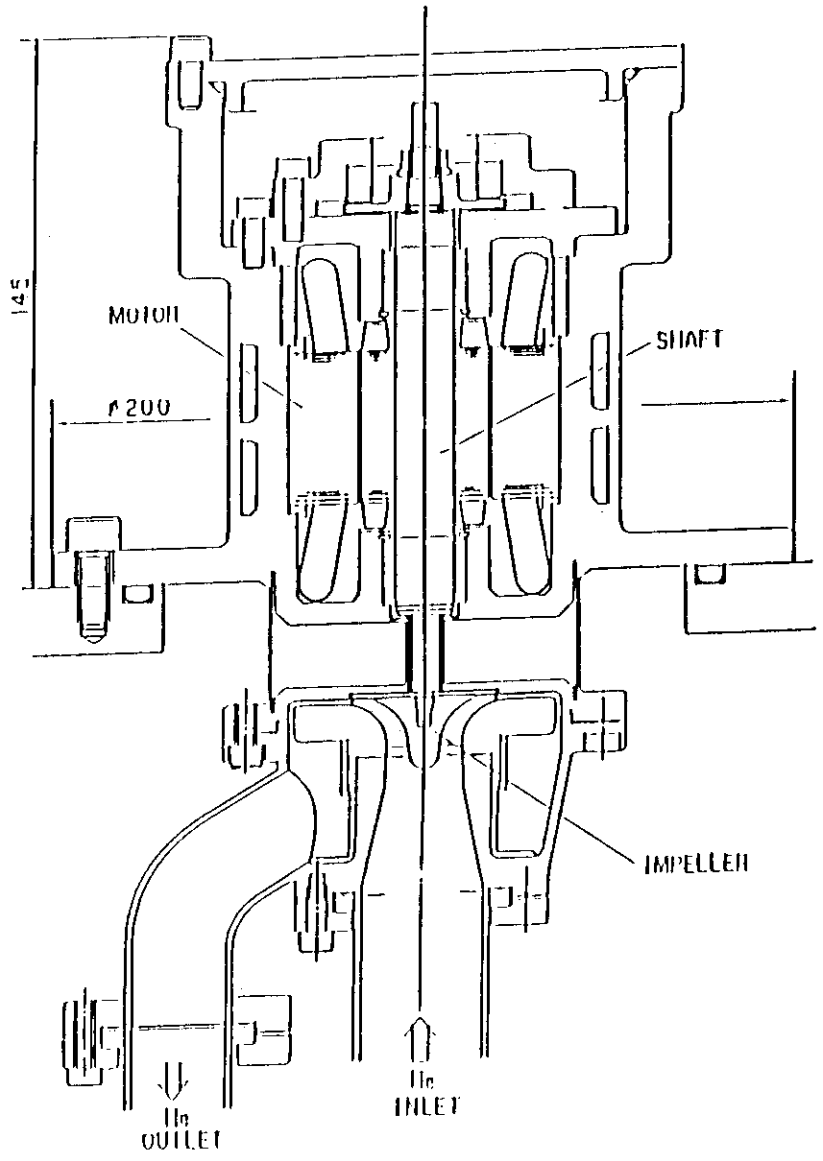

Fig. VI.5-2 Cold compressor.

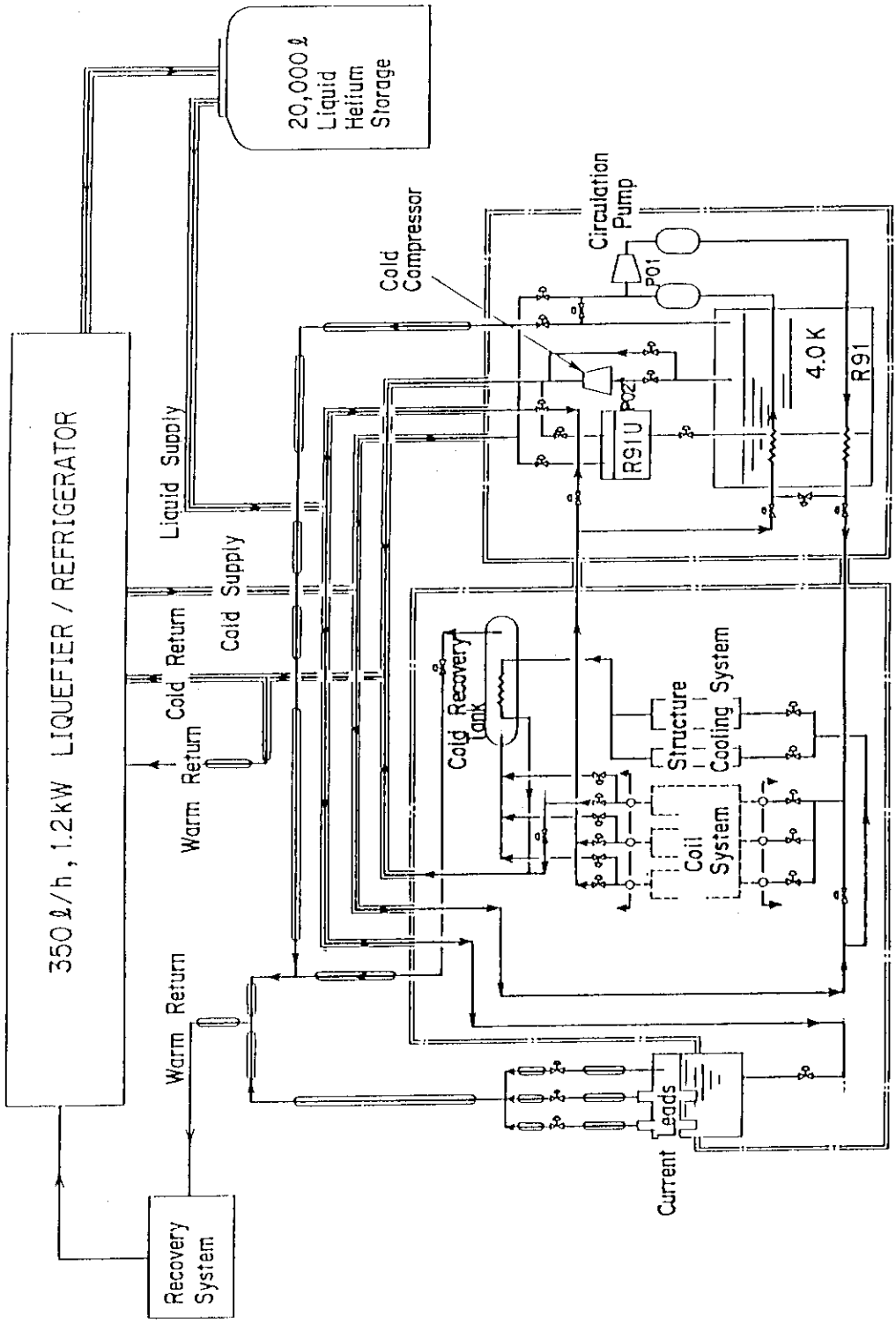

Fig. VI.5-3 Schematic flow diagram of the cryogenic system.

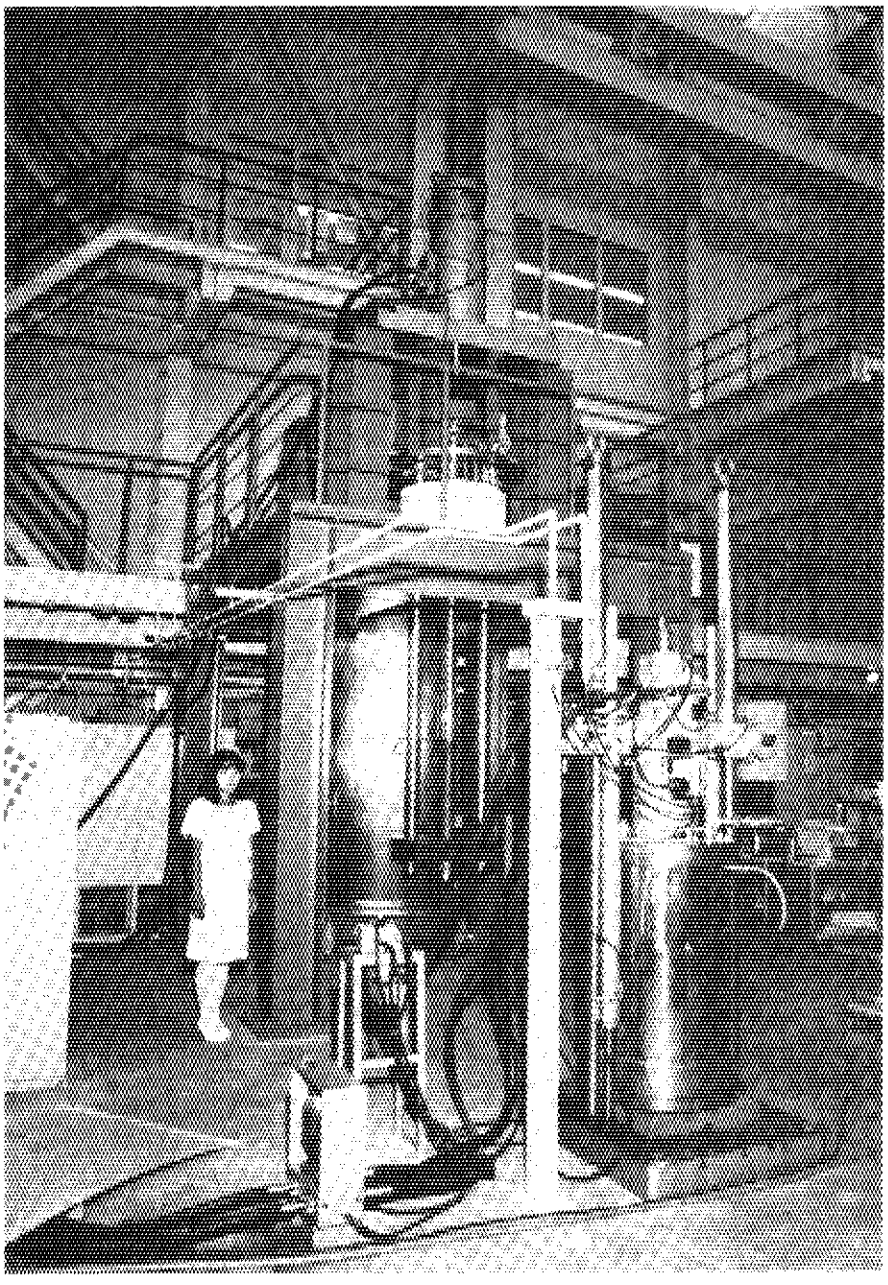

Fig. VI.6-1 100 ton cryogenic tensile test machine.

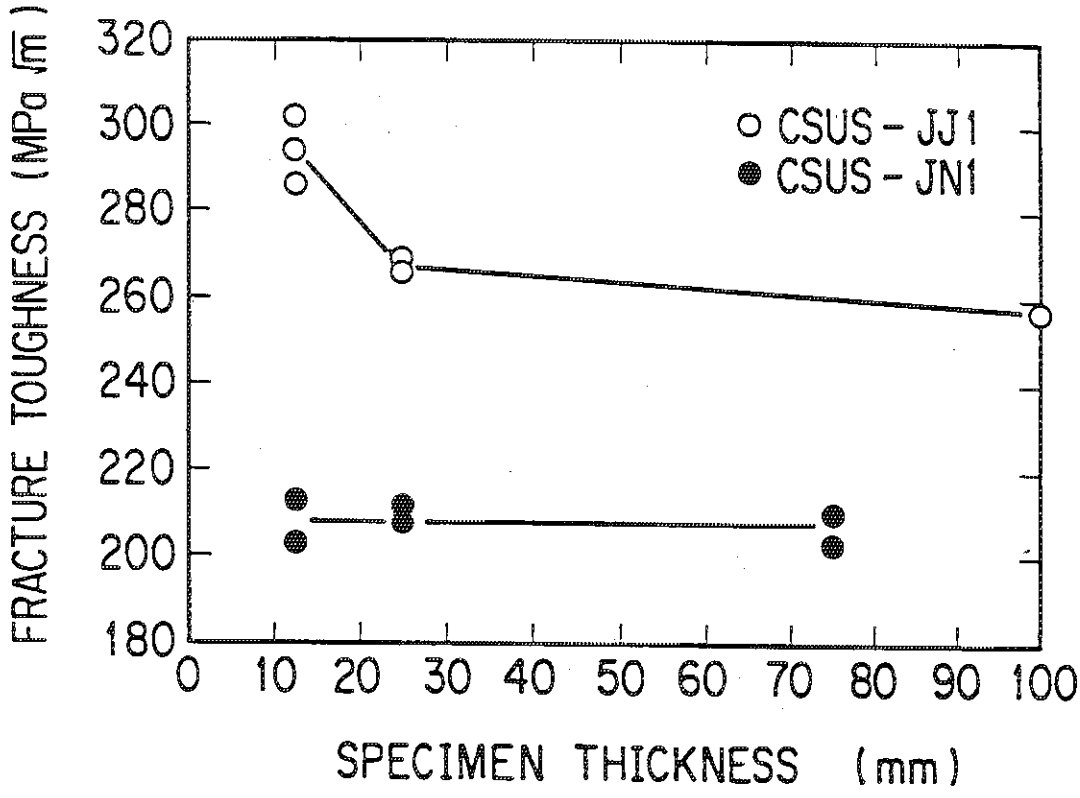

Fig. VI.6-2 The relation between a fracture toughness and a specimen thickness.

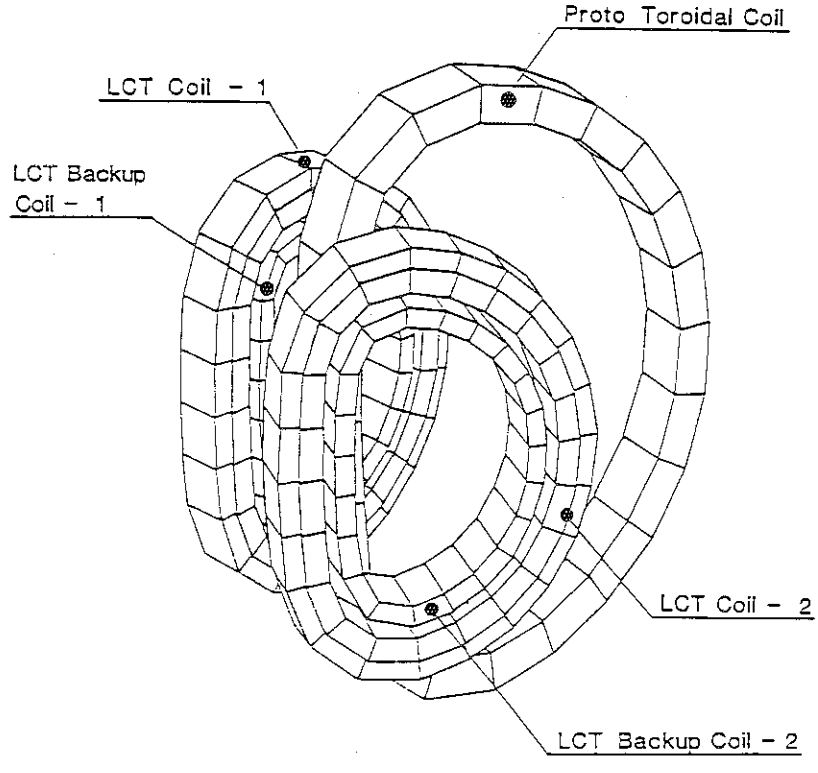

Fig. VI.7-1 Test configuration of PROTO Toroidal Coil placed in the cluster array with LCT coils and LCT backup coils(LBC).

VII. DEVELOPMENT OF TRITIUM TECHNOLOGY

1. Introduction

The development of tritium technology has been continued to establish tritium processing, tritium safety handling and related technologies in fusion reactors. As for tritium processing and related technologies, research and development have been made for (1) Fuel cleanup, (2) Hydrogen isotope separation, (3) Tritium-material interaction and (4) Blanket technology. For the research and development of Fuel cleanup, Hydrogen isotope separation and Tritium-material interaction, experimental apparatuses, in which maximum amount of 1 g-T_2 can be used, have been designed and are being fabricated.

In JAERI-LANL (DOE) collaboration on fuel cleanup, a new program, ANNEX III, was initiated in November 1986. The objective of this program is to test the process-ready palladium diffuser and ceramic electric electrolysis cell in Tritium Systems Test Assembly (TSTA).

System analysis for hydrogen isotope separation system was also carried out.

In parallel with the research and development of tritium processing and related technologies, operation and cold tests of the major subsystems for tritium safety handling system in Tritium Process Laboratory (TPL) have been continued since June 1985.

2. Development of Tritium Processing Technology

2.1 Fuel cleanup

2.1.1 JAERI-LANL (DOE) fusion technology collaboration

The program, "Testing of Small Scale Tritium Handling Components with Tritium", has successfully been finished in this fiscal year. The tests demonstrated that the components, a palladium diffuser and a ceramic electrolysis cell can be effective parts of a Fuel Cleanup System (FCU) that purifies tritium in the exhaust gas from a fusion reactor. Based on this result, next program of the collaboration, "ANNEX III to the implementing arrangement between the Japan Atomic Energy Research Institute and the United States Department of Energy

VII. DEVELOPMENT OF TRITIUM TECHNOLOGY

1. Introduction

The development of tritium technology has been continued to establish tritium processing, tritium safety handling and related technologies in fusion reactors. As for tritium processing and related technologies, research and development have been made for (1) Fuel cleanup, (2) Hydrogen isotope separation, (3) Tritium-material interaction and (4) Blanket technology. For the research and development of Fuel cleanup, Hydrogen isotope separation and Tritium-material interaction, experimental apparatuses, in which maximum amount of 1 g-T_2 can be used, have been designed and are being fabricated.

In JAERI-LANL (DOE) collaboration on fuel cleanup, a new program, ANNEX III, was initiated in November 1986. The objective of this program is to test the process-ready palladium diffuser and ceramic electric electrolysis cell in Tritium Systems Test Assembly (TSTA).

System analysis for hydrogen isotope separation system was also carried out.

In parallel with the research and development of tritium processing and related technologies, operation and cold tests of the major subsystems for tritium safety handling system in Tritium Process Laboratory (TPL) have been continued since June 1985.

2. Development of Tritium Processing Technology

2.1 Fuel cleanup

2.1.1 JAERI-LANL (DOE) fusion technology collaboration

The program, "Testing of Small Scale Tritium Handling Components with Tritium", has successfully been finished in this fiscal year. The tests demonstrated that the components, a palladium diffuser and a ceramic electrolysis cell can be effective parts of a Fuel Cleanup System (FCU) that purifies tritium in the exhaust gas from a fusion reactor. Based on this result, next program of the collaboration, "ANNEX III to the implementing arrangement between the Japan Atomic Energy Research Institute and the United States Department of Energy

on cooperation in fusion research and development for the DOE-JAERI collaborative program in development of Improved Components for the Fuel Cleanup System of the Tritium Systems Test Assembly" was signed in November 1986. The objective of this collaborative program is to test two "Process-Ready components", the palladium diffuser and the ceramic electrilysis cell, that are larger versions of the components tested in the previous program. Both components were designed and manufactured to be compatible in the fusion fuel system such as TSTA. These components were shipped to the LANL in March 1987 and installation to the TSTA was initiated by personnel from both parties.

2.1.2 Development of components

Development of some components for processing of gaseous tritium and its compounds in fusion fuel system has been continued. In this fiscal year, multi-tube ceramic electrolysis cells and some types of ZrCo beds were designed, fabricated and tested.

Multi-tube ceramic electrolysis cells were designed to obtained larger capacity of decomposing tritiated vapor in the tests that will be conducted in LANL under ANNEX III and future experiments in the TPL. Figure VII.2-1 shows the structure of the cell containing 10 stabilized zirconia tubes with platinum electrodes. Internal heater wires and vacuum jacket are equipped for heat insulation and confinement of tritium.

The intermetallic compound zirconium-cobalt had been developed and proved to be a promising substitute of uranium for the purpose of recovering, storing and supplying gaseous tritium last year. Some types of the ZrCo beds were fabricated and tested to meet requirements for the actual tritium services in the TPL. Figure VII.2-2 is a shematic of a bed designed to recover larger amount of pure hydrogen mixtures up to 200 l in a short period of time. Activated ZrCo powder is contained in sintered stainless steel tubres to prevent dispersion. Copper grains are mixted with ZrCo powder to absorb heat of hydriding reaction.

Some tests of ZrCo beds were conducted with hydrogen gas. Figure VII.2-3 shows a typical result of the hydrogen absorption by the bed. Hydrogen in the tank (10 l N volume) was absorbed by the bed quickly so that 99.9% of the gas was recovered in 3 minutes.

2.1.3 Design and fabrication of the experimental apparatus for Fuel Cleanup Process

An experimental apparatus for the development of Fuel Cleanup System has been designed and fabricated. The function of the system is continuous processing of a simulated plasma exhaust and separation of hydrogen isotopes and impurity element in it. Major components are palladium diffusers, catalytic reactors, freezers, an electrolysis cell and zirconium-cobalt beds.

Figure VII.2-4 is a schematic flow diagram of the apparatus. The loop consists of four subsystems; (1) Gas feed subsystem, (2) Purification subsystem, (3) Recovery subsystem, and (4) Water decomposition subsystem. In the gas feed subsystem, D_2, T_2 and impurity gases such as methane, ammonia and He are supplied from ZrCo bed or gas bottle. Tritiated water is synthesized at the catalytic reactor. The purification subsystem is composed of a palladium diffuser and vacuum pumps. Gas mixture from the gas feed subsystem is separated to pure hydrogen stream and bleed where impermeable impurities are concentrated. Bleed stream is then processed in the recovery subsystem where hydrgoen isotopes are converted to water at the catalytic reactor and then separated from the tritium-free species by freezers. Exhaust from the freezers are He, CO_2, N_2 and O_2 and expected to contain minimum amount of tritium. Tritiated water trapped at the freezers is periodically regenerated and converted to tritium gas in the water decomposition subsystem. Gaseous tritium is purified by the second palladium diffuser and bleed is sent to the recovery sybsystem again. An example of material balance in the system is shown in the Table VII.2-1. Gas analysis in this experiment is carried by gas chromatographs, hygrometers and an ion chamber. The system is operated from a local panel and data acquisition will be done by a desk top computer with CAMAC interface. The apparatus will be installed in the glovebox in the TPL from summer 1987 and tests with tritium will be initiated early in next fiscal year.

2.2 Hydrogen isotope separation

2.2.1 Cryogenic distillation experiments

An experimental study of hydrogen isotope separation was performed with a distillation column for H-D system under total reflux operation. As the results of the experiment, indispensable

information has been obtained, which concerns pressure drop through packed column and vapor velocity dependence of HETP as shown in Fig. VII.2-5. Furthermore, it was also certified that the value of HETP can be reduced with the foregoing operation of flooding. The obtained values in the experiments were about 3-4 cm, which were smaller value than those obtained by Sherman et al.

Further study should be accomplished as for the effect of the operational pressure on the value of HETP, in addition to the experimental observation of operational characteristics under total recycle operation.

2.2.2 Design and fabrication of cryogenic distillation apparatus for T-D-H system

A design has been performed for an experimental apparatus for hydrogen isotope separation by cryogenic distillation. The experimental apparatus handles hydrogen isotopes mixture of all six molecular species (H_2, HD, HT, D_2, DT and T_2). The maximum amount of 1 g-T_2 can be used for an experiment in the grovebox of the TPL. Figure VII.2-6 shows a brief system diagram of the apparatus. The apparatus consists of the following systems; (1) cryogenic distillation system, (2) gas circulation system, (3) gas supply and recovery system, (4) refrigeration system, (5) sampling system and (6) vacuum system.

The experimental apparatus is being fabricated and will be installed in the glovebox of the TPL from summer 1987. Experiments with tritium will be initiated early in 1988.

2.3 Tritium-material interaction

2.3.1 Design and fabrication of an apparatus for tritium implanation/permeation experiments

A design has been performed for an apparatus for tritium implantation/permeation experiments. The major objectives of the apparatus are (1) assessment of the extrapolability of H/D data to tritium in implantation driven permeation, (2) assessment of the permeation barrier effects of coating materials, and (3) investigation of the correlation between material surface/bulk conditions and permeation/retention behavior. The apparatus consists of an ultra-high vacuum chamber, a tritium ion source, a downsteam vacuum chamber

with a target membrane, surface analyzers (SIMS and AES), etc. The important features of the apparatus are as follows; (1) tritium ion bombardment (1 g-T_2/batch), (2) low energy high flux ion beam (energy: 20-1000 eV, ion flux: 1.3×10^{15} T^+cm^{-2} at 200 eV and 2.3×10^{16} T^+cm^{-2}at 1000 eV) and (3) simultaneous measurement of sputtered ions (cations are anions) from front surface with SIMS under permeation experiments.

The experimental apparatus has been fabricated and will be installed in the glovebox of the TPL from summer 1987. Experiments with tritium will be initiated early in 1988.

2.4 Blanket technology

2.4.1 Tritium recovery from lithium-bearing materials

To elucidate the fundamental mechanism of tritium release from Li_2O crystals, the valence state and the diffusivity of tritium dissolved in Li_2O crystals under thermal equilibrium with HT gas have been investigated. In HT doped Li_2O crystals, nearly 100% of tritium was found in the T^+ state, while the T^- state of tritium was found in Li_2O crystals irradiated with thermal and 14 MeV neutrons. The thermal release behavior of tritium dissolved in Li_2O crystals resembled the behavior in neutron-irradiated ones, as a whole, but a discrepancy was observed in the diffusivity of tritium between the irradiated and unirradiated crystals, as shown in Fig. VII.2-7.

Tritium release behavior from neutron-irradiated γ-$LiAlO_2$ and Li_8ZrO_6 has been investigated in aspects of tritium recovery from fusion reactor blankets. Tritium produced in both materials was released mainly in the form of HTO when heated in a vacuum after the neutron-irradiation. The HTO(g) release rate of γ-$LiAlO_2$ and Li_8ZrO_6 crystals were found to be controlled by diffusion of tritium in the crystals. The diffusivities determined for γ-$LiAlO_2$ and Li_8ZrO_6 are shown in Fig. VII.2-8, together with that for Li_2O crystals. The diffusivity of tritium in Li_8ZrO_6 was the largest of the three oxides. The diffusion coefficient for tritium in γ-$LiAlO_2$ was nearly two orders of magnitude smaller than that in Li_2O and Li_8ZrO_6. It is interesting to note that the order of tritium diffusivity in these oxides, $D(Li_8ZrO_6)>D(Li_2O)>D(\gamma\text{-}LiAlO_2)$, is parallel to that of the ion conductivity, $\sigma(Li_8ZrO_6)>\sigma(Li_2O)>\sigma(\gamma\text{-}LiAlO_2)$.

2.4.2 Tritium recovery system for fusion reactor blankets

Enhancement of tritium release by hydrogen spiking had been demonstrated in various in-pile experiments in ceramic oxide breeders. This phenomenon can be caused by the following isotopic exchange reactions: $T_2O+H_2 \rightleftarrows HOT+HT$ and $HTO+H_2 \rightleftarrows H_2O+HT$, they should be caused by the catalytic effect of metal surface of sweep gas transter piping. In the in-pile experiment (VOM-21H), hydrogen spiking effects on tritium release were examine by using $He-D_2$ mixtures containing 10, 100 and 1000 ppm D_2 as the sweep gas. Figure VII.2-9 shows a typical result of isotopic measurement of tritium swept out from the irradiation capsule. In the case of 10 ppm D_2, T_2 is the species unreacted with D_2 and HT is assumed to be originated from the reaction H_2O (ads.)$+T_2 \rightleftarrows HT+HTO$ (ads.), where (ads.) means the adsorbed state of moisture. In the case of 100 ppm D_2, major species of tritium is DT. Summary data of composition of each species and equilibrium time of them are shown in Table VII.2-2. From these experimental facts, it can be concluded that hydrogen spiking can reduce the moisture effects and is markedly effective to solve the critical issues (large adsorption inventory as the form of T_2O and LiOT) of the Li_2O blanket.

3. System Analysis

3.1 Hydrogen isotope separation

Development of cascade configuration and startup analysis of cascades has been performed for hydrogen isotope separation system with cryogenic distillation column in the tritium breeding blanket system.

The effects of the dilution of tritium with H_2 or D_2 on characteristics of the hydrogen isotope separation were analyzed in such cases are summarized in Table VII.3-1. On the basis of the analysis, column cascades shown in Fig. VII.3-1 and 3-2 were determined to be available for case 1 and 2 in Table VII.3-1, respectively. After parametric study for major parameters, three important parameters, that is, tritium inventory, refrigeration capacity required and tritium recovery fraction, were estimated under the full normal separating condition as shown in Table VII.3-2.

2.4.2 Tritium recovery system for fusion reactor blankets

Enhancement of tritium release by hydrogen spiking had been demonstrated in various in-pile experiments in ceramic oxide breeders. This phenomenon can be caused by the following isotopic exchange reactions: $T_2O+H_2 \rightleftarrows HOT+HT$ and $HTO+H_2 \rightleftarrows H_2O+HT$, they should be caused by the catalytic effect of metal surface of sweep gas transter piping. In the in-pile experiment (VOM-21H), hydrogen spiking effects on tritium release were examine by using He-D_2 mixtures containing 10, 100 and 1000 ppm D_2 as the sweep gas. Figure VII.2-9 shows a typical result of isotopic measurement of tritium swept out from the irradiation capsule. In the case of 10 ppm D_2, T_2 is the species unreacted with D_2 and HT is assumed to be originated from the reaction H_2O (ads.)$+T_2 \rightleftarrows HT+HTO$ (ads.), where (ads.) means the adsorbed state of moisture. In the case of 100 ppm D_2, major species of tritium is DT. Summary data of composition of each species and equilibrium time of them are shown in Table VII.2-2. From these experimental facts, it can be concluded that hydrogen spiking can reduce the moisture effects and is markedly effective to solve the critical issues (large adsorption inventory as the form of T_2O and LiOT) of the Li_2O blanket.

3. System Analysis

3.1 Hydrogen isotope separation

Development of cascade configuration and startup analysis of cascades has been performed for hydrogen isotope separation system with cryogenic distillation column in the tritium breeding blanket system.

The effects of the dilution of tritium with H_2 or D_2 on characteristics of the hydrogen isotope separation were analyzed in such cases are summarized in Table VII.3-1. On the basis of the analysis, column cascades shown in Fig. VII.3-1 and 3-2 were determined to be available for case 1 and 2 in Table VII.3-1, respectively. After parametric study for major parameters, three important parameters, that is, tritium inventory, refrigeration capacity required and tritium recovery fraction, were estimated under the full normal separating condition as shown in Table VII.3-2.

Results of the analysis show that the dilution with D_2 brings unfavorable effects on the operation of the column cascade.

Startup analysis has been performed under two scenarios for column cascades shown in Fig. VII.3-1 and 3-2, respectively. And it is certified that the composition of the gas mixtures charged into the columns must be carefully prepared because they have large effects on the startup characteristics. One of scenarios discussed is composed of two operational modes and presents the full-normal condition in about 4 hours, but has the shortcomings of the preparation of two different composition gas mixtures. The other avoids such complexity, but comprises four operational modes nd requires about 7 hours the startup.

4. Tritium Process Laboratory

4.1 Construction, operation and maintenance

TPL is designed to handle up to 10 g of tritium as a total inventory. Figure VII.4-1 shows the concept of the multiple barrier tritium containment system in the TPL facility. The experimental apparatus, the gloveboxes and the airtight rooms are respectively designed as the primary, the secondary and the tertialy container and each of them has its main detritiation system based on the catalytic oxidation-molecular sieve adsorption process.

The Effluent tritium Removal System (ERS) processes various effluent gases originated from experimental apparatus, exhaust of the Vacuum System (VPS), and other safety systems at the flow rate of 20 Nm^3 and then releases of the to the stack. Two catalyst beds operated at 500°C and two pairs of mol-sieve beds are used in series in order to obtain decontamination factor (DF) of above 10^4.

The Glovebox gas Purification System (GPS) treats nitrogen atmosphere for the gloveboxes at up to 150 Nm^3/hr in circulation mode. Negative pressures in each glovebox are controlled independently.

The Air Cleanup System (ACS) will remove tritium in the room air in circulation mode at flow rate of 300 Nm^3/hr in the case of incident of tritium spills. This system also has some other functions such as processing of air from air atmosphere glovebox, back-up of other cleanup system.

Results of the analysis show that the dilution with D_2 brings unfavorable effects on the operation of the column cascade.

Startup analysis has been performed under two scenarios for column cascades shown in Fig. VII.3-1 and 3-2, respectively. And it is certified that the composition of the gas mixtures charged into the columns must be carefully prepared because they have large effects on the startup characteristics. One of scenarios discussed is composed of two operational modes and presents the full-normal condition in about 4 hours, but has the shortcomings of the preparation of two different composition gas mixtures. The other avoids such complexity, but comprises four operational modes nd requires about 7 hours the startup.

4. Tritium Process Laboratory

4.1 Construction, operation and maintenance

TPL is designed to handle up to 10 g of tritium as a total inventory. Figure VII.4-1 shows the concept of the multiple barrier tritium containment system in the TPL facility. The experimental apparatus, the gloveboxes and the airtight rooms are respectively designed as the primary, the secondary and the tertialy container and each of them has its main detritiation system based on the catalytic oxidation-molecular sieve adsorption process.

The Effluent tritium Removal System (ERS) processes various effluent gases originated from experimental apparatus, exhaust of the Vacuum System (VPS), and other safety systems at the flow rate of 20 Nm^3 and then releases of the to the stack. Two catalyst beds operated at 500°C and two pairs of mol-sieve beds are used in series in order to obtain decontamination factor (DF) of above 10^4.

The Glovebox gas Purification System (GPS) treats nitrogen atmosphere for the gloveboxes at up to 150 Nm^3/hr in circulation mode. Negative pressures in each glovebox are controlled independently.

The Air Cleanup System (ACS) will remove tritium in the room air in circulation mode at flow rate of 300 Nm^3/hr in the case of incident of tritium spills. This system also has some other functions such as processing of air from air atmosphere glovebox, back-up of other cleanup system.

Several efforts are devoted to be ready for tritium operation of the TPL which will be initiated in FY 1987. A line computer is added to the Central Control System (CCS) for logging and processing of the data from the facility. Several uranium beds are installed in the Tritium Storage System (TSS). These beds will be used to receive and store 10 g of tritium that will be imported in FY 1987. Mechanical improvements and maintenance works are carried out on the ERS, Drier Regeneration System (DRS), GPS, VPS and utilities.

All of the facility have been active or ready for operation in this period except for the TSS that had final check-out after the installation of U-beds. Molecular sieve beds in the ACS were regenerated twice using DRS.

Installation of all of the experimental apparatuses in the gloveboxes is planned in FY 1987. Specification for the each apparatus was prepared, checked and approved. Preparation and modification of the Operation Room-I and the gloveboxes for these apparatus and installation works were designed.

4.2 Operation and cold tests

All of the subsystem in the facility have been operated without tritium in the period FY 1986. The ERS and CCS were active most of the time. GPS had a modification on the control of oxygen concentration and was tested. Background measurements were performed on the Tritium Monitoring System (TMS). Waste Solidification System (WSS) and Sampling System (SPS) were tried with normal water. DRS was operated twice with regenerating ACS molecular sieve bed. Negative pressure control and leak rate of the gloveboxes, and suking velocity on the hoods were measured and both equipments have satisfactory performances of tritium containment.

The Vacuum Pumping System (VPS) consists of some kinds of oil-free vacuum pumps for pumping tritium. Test of the VPS has been made with several combination of the pumps and gases. Figure VII.4-2 shows an example of the results of pumping of air by the combination of two wobble pumps and a reciprocal pump. The pumping speed of the pumps agreed well with the designed values and vacuum of 10^{-2} torr was obtained. Figure VII.4-3 is a comparison of the pumping of nitrogen, hydrogen and their mixtures. Both pumping speed and ultimate pressure with hydrogen were proved to be worse than that for nitrogen. Pumping

characteristics of gas mixture were similar to that of nitrogen. This result suggests that pumping of hydrogen isotopes including tritium could be more difficult than other gases, and purging or mixing of heavier gas would be a help.

4.3 Licenses and safety analysis

All the procedures for application of permission to initiate the tritium operation of the TPL have been completed and the licenses for using tritium, nuclear fuel materials and tritium transport container were obtained. In order to qualify the facility for tritium operation, followings were checked; pressure control and leak rate of the glovebox, capacity of the ventilation system, waste water plumbing and tanks, uranium beds, air tightness of the room, capacity of the tritium cleanup systems, hood system, function of interlocks such as isolation valve, and tritium monitor. Indpection of the facility was performed in February 1987 and the permit was issued on March 19.

Ten grams of tritium is planned to be transported from the Oak Ridge National Laboratory in the USA. Safety analysis of the container was completed in this period. An identical model package was fabricated and drop tests followed by leak were performed. The structure of the package is shown in Fig. VII.4-4. By the 9 m drop tests, there was no significant change of gas cylinder dimensions and helium leak rate after the drop.

Thermal analysis and leak/permeation analysis were conducted numerically. In thermal analysis, pressure and temperature of the gas cylinder, thermal expansion, the effect of thermal stress, and strength in cold exposure were calculated using TRUMP code under specified condition. No thermal effect is expected at the maximum temperature calcualted. Leak rate of the tritium from the package was calculated under the most conservative assumption and the calculated leak rate proved to be negligible.

Table VII.2-1 An example of mass balance in the system

	1	2	3	4	5	6	7	8	9	10	11	12	13	14	15	16	17
X_2		2.955 85.0	2.898 100	0.057 9.9		0.082 0.7	§	§	§	§		0.159 5.1		0.134 100	0.025 1.0	0.0315 100	0.102 100
H_e	0.45 95.0	0.45 13.0		0.45 78.3		11.80 97.2	11.80 97.6	11.80 98.9	2.95 98.9	8.85 98.9	2.50 94.0	2.50 94.9			2.50 99.0		
CX_4	0.009 2.0	0.009 0.3		0.009 1.6		0.009 0.1	§	§	§	§							
NH_3	0.009 2.0	0.009 0.3		0.009 1.6		0.009 0.1	§	§	§	§							
X_2O		0.045 1.3		0.045 7.8		0.045 0.4	0.159 1.3	§	§	§	0.159 6.0	0.0001 0					
N_2	0.0045 1.0	0.0045 0.1		0.0045 0.8		0.0315 0.3	0.036 0.3	0.036 0.3	0.009 0.3	0.027 0.3							
O_2					0.079 100	0.121 1.0	0.055 0.5	0.055 0.5	0.013 0.5	0.042 0.5			0.079 100				
CO_2						0.027 0.2	0.036 0.3	0.036 0.3	0.009 0.3	0.027 0.3							
TOTAL	0.473 100	3.473 100	2.898 100	0.575 100	0.079 100	12.125 100	12.086 100	11.927 100	2.982 100	8.946 100	2.659 100	2.659 100	0.079 100	0.134 100	2.525 100	0.0315 100	0.102 100

MOL/H
%

§ : TRACE, DETECTED WITH ION CHAMBER

Table VII.2-2 Summary data of isotopic measurements

Sweep Gas	Composition of Tritium		Equilibrium Time
Pure He	HTO(T_2O)	80-95%	3-11 days
	HT(T_2)	20- 5%	>0.5 h
10ppmD_2-He	DTO	∿50%	-
	DT(T_2)	∿50%	>0.5 h
100ppmD_2-He	DTO	<3%	-
	DT	>97%	>0.5 h
1000ppmD_2-He	DTO	<3%	-
	DT	>97%	>0.5 h

Table VII.3-1 Three example cases based on FER[a]

	Flow rate of mixture	Percentages[b] of elements
Case 1 : Dilution with H_2 by two orders of magnitude	100 mol/h	H : 99.485 % D : 0.015 % T : 0.5 %
Case 2 : Dilution with H_2 by three orders of magnitude	1000 mol/h	H : 99.93493 % D : 0.01507 % T : 0.05 %
Case 3 : Dilution with D_2 by two orders of magnitude	100 mol/h	H : 0.5 % D : 99.0 % T : 0.5 %

[a] If the H_2 addition were not made, the isotope mixture to be processed would comprise an equimolar mixture of impurity H and bred T, and its flow rate would be 1 mol/h. These are based on the presently-conceived design of the Japanese Fusion Engineering Reactor (FER).

[b] Deuterium contained in natural hydrogen and hydrogen contained in commercially available deuterium are taken into account.

Table VII.3-2 Key parameters estimated for column cascades

	Case 1	Case 2	Case 3	
Total tritium inventory	8.2 g	12 g	43 g	70 g*
Refrigeration capacity	64 W	625 W	510 W	110 W*
Tritium recovery fraction	0.998	0.998	0.990	

*The values for the two column cascade developed by Kinoshita[4] in the main stream fuel circulation system.

Note : Superficial vapor velocity = 7.5 cm/sec, HETP = 5 cm, liquid holdup = 10 % of superficial volume.

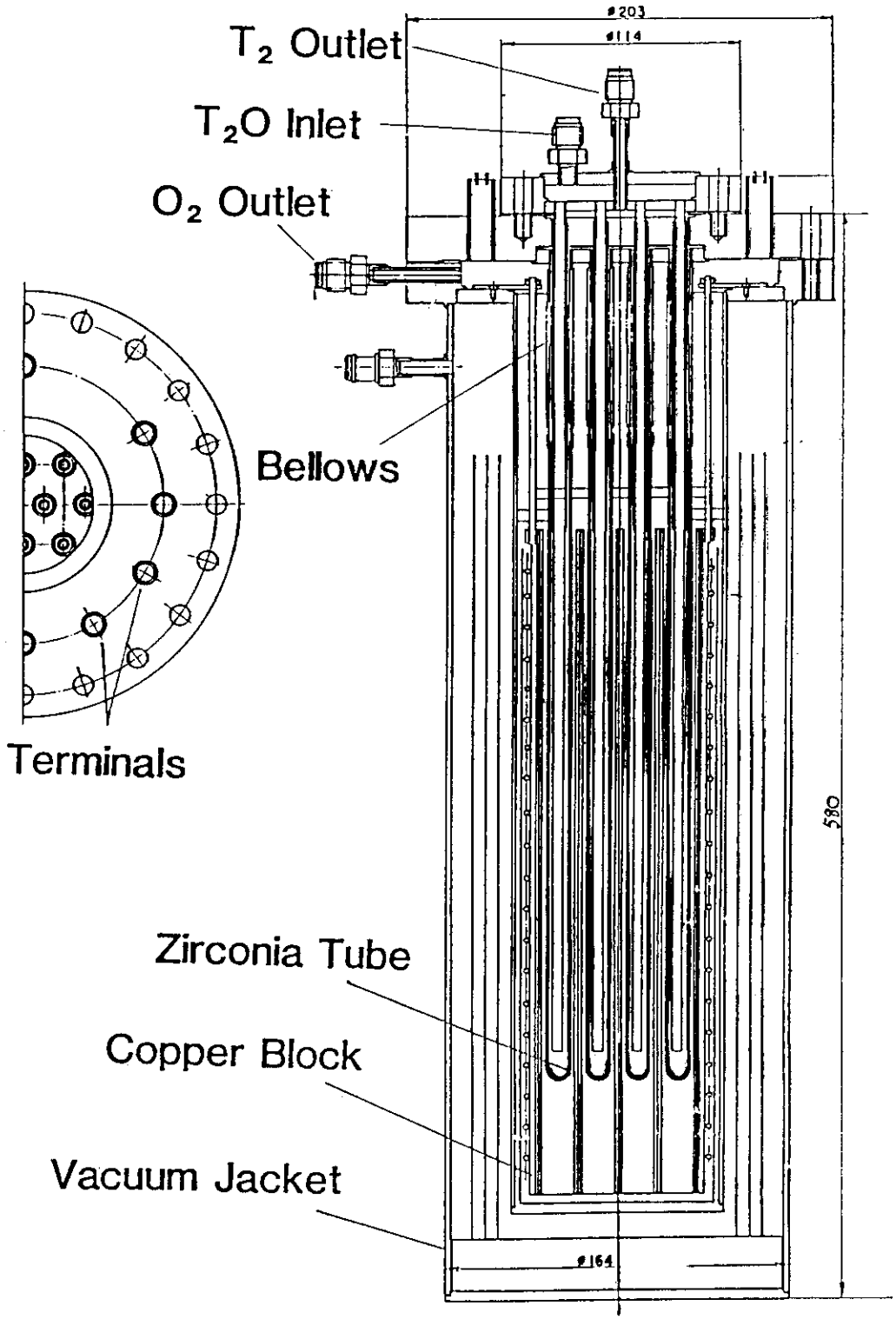

Fig. VII.2-1 Structure of an electrolysis cell.

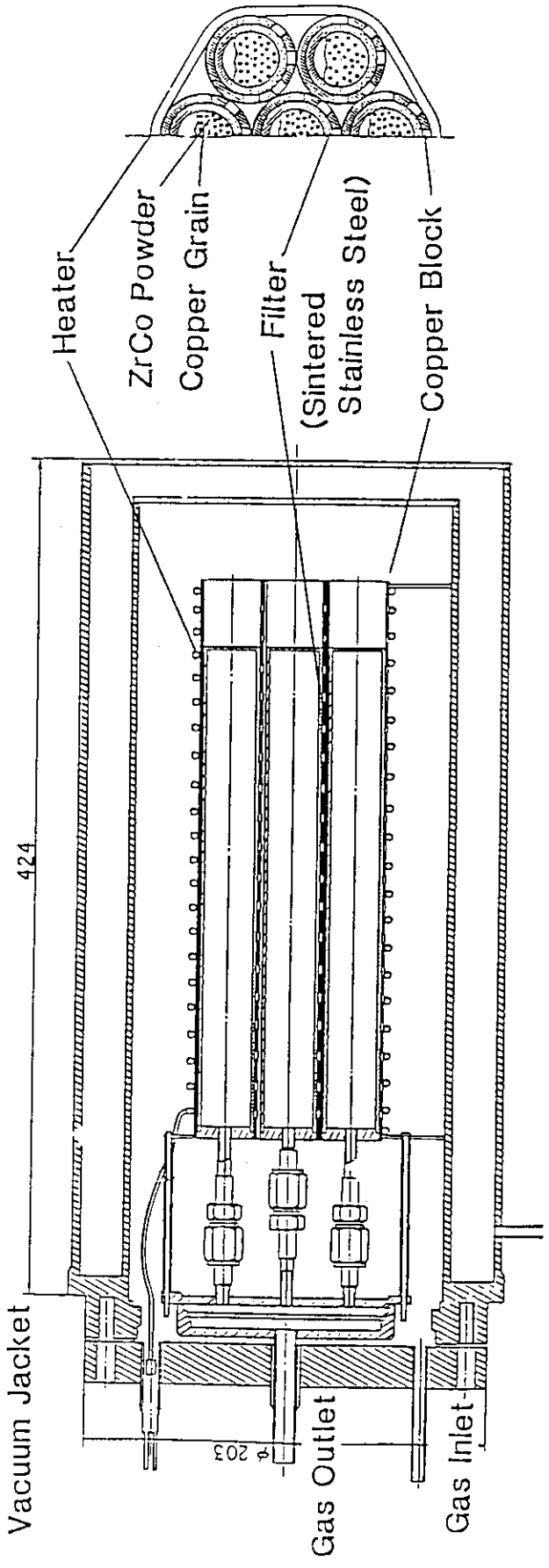

Fig. VII.2-2 Structure of a zirconium-cobalt bed.

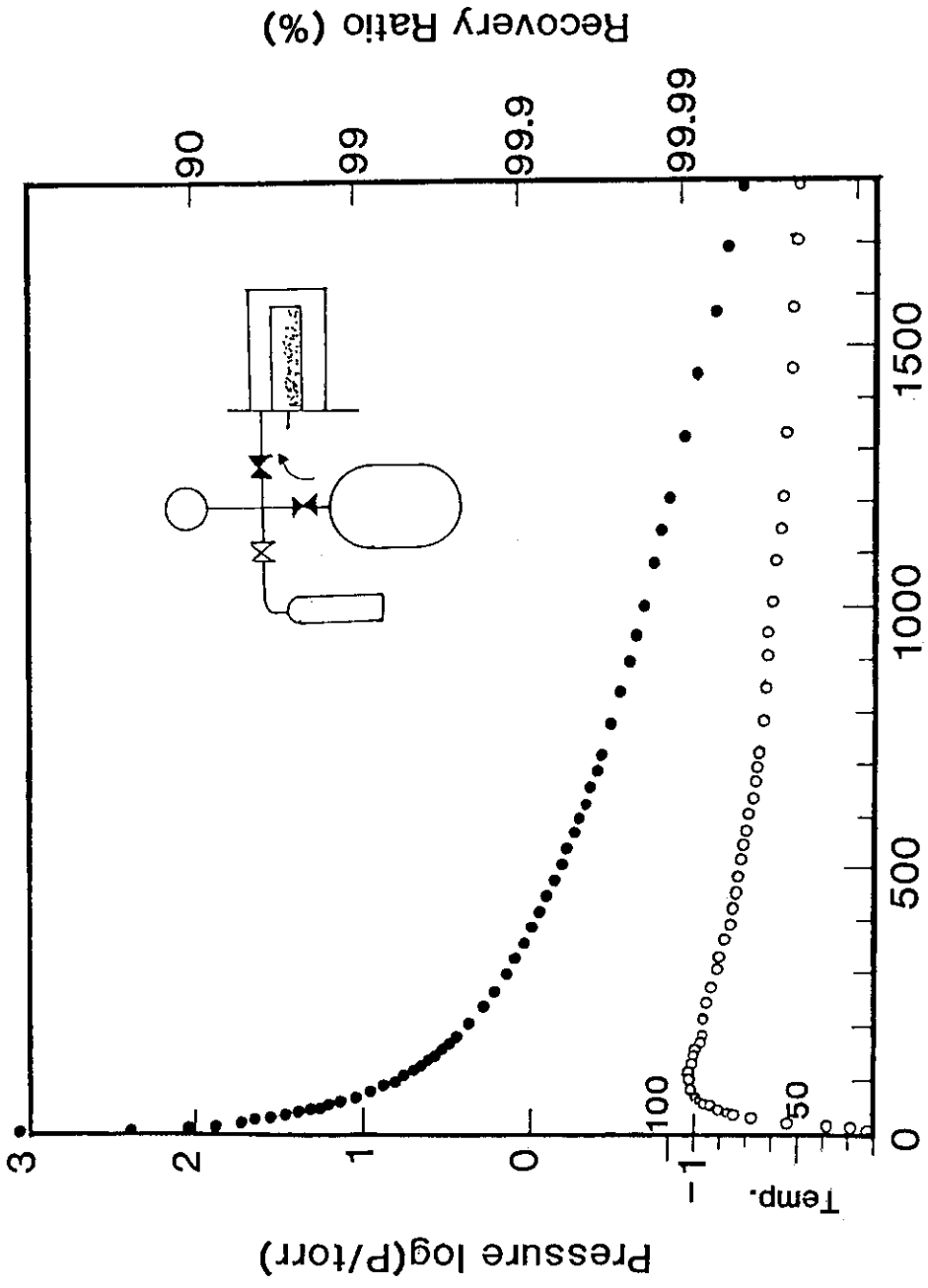

Fig. VII.2-3 Recovery of hydrogen gas with a ZrCo bed.

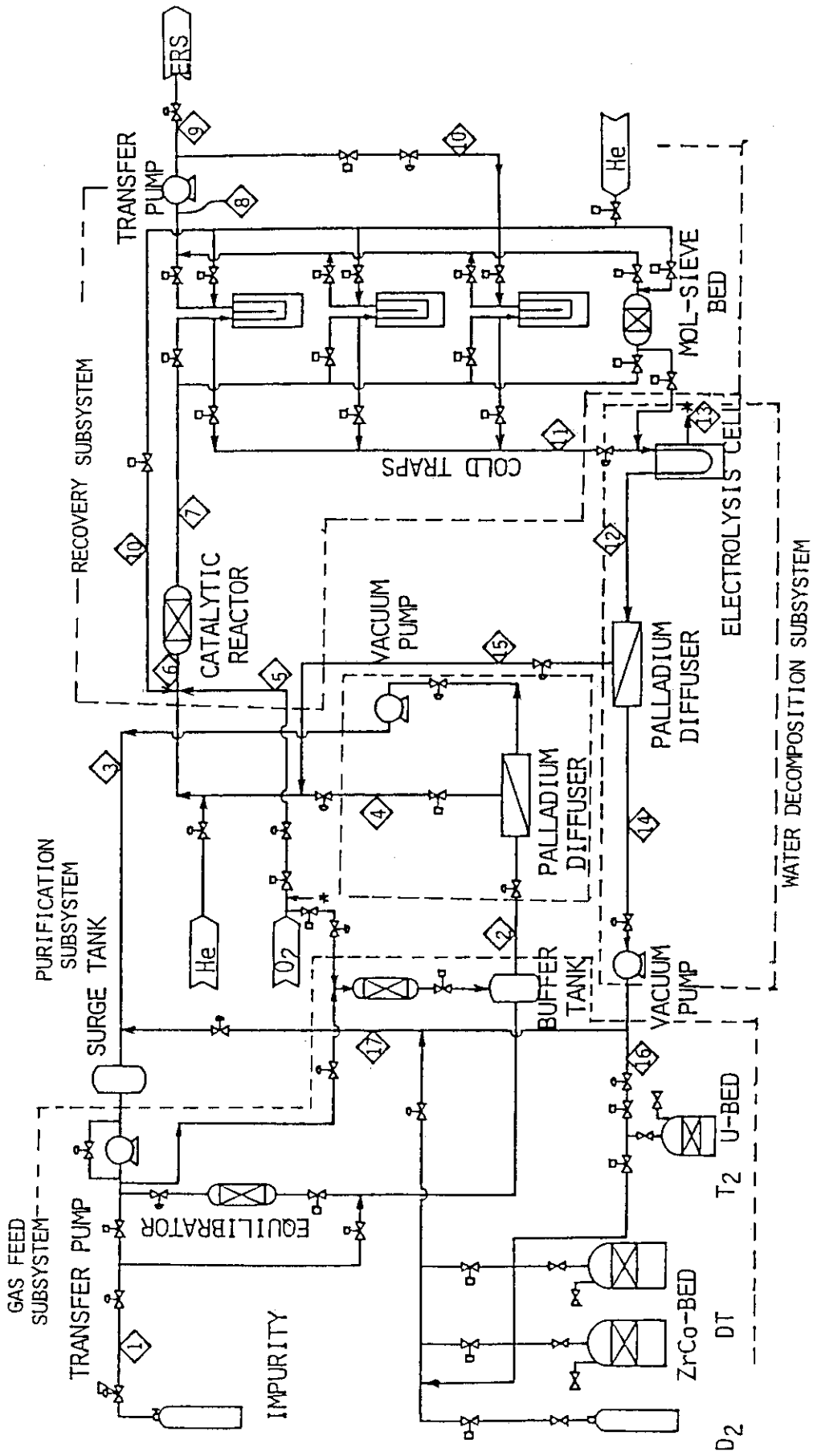

Fig. VII.2-4 Schematic flow diagram of the experimental apparatus for the Fuel cleanup. It consists of four subsystems.

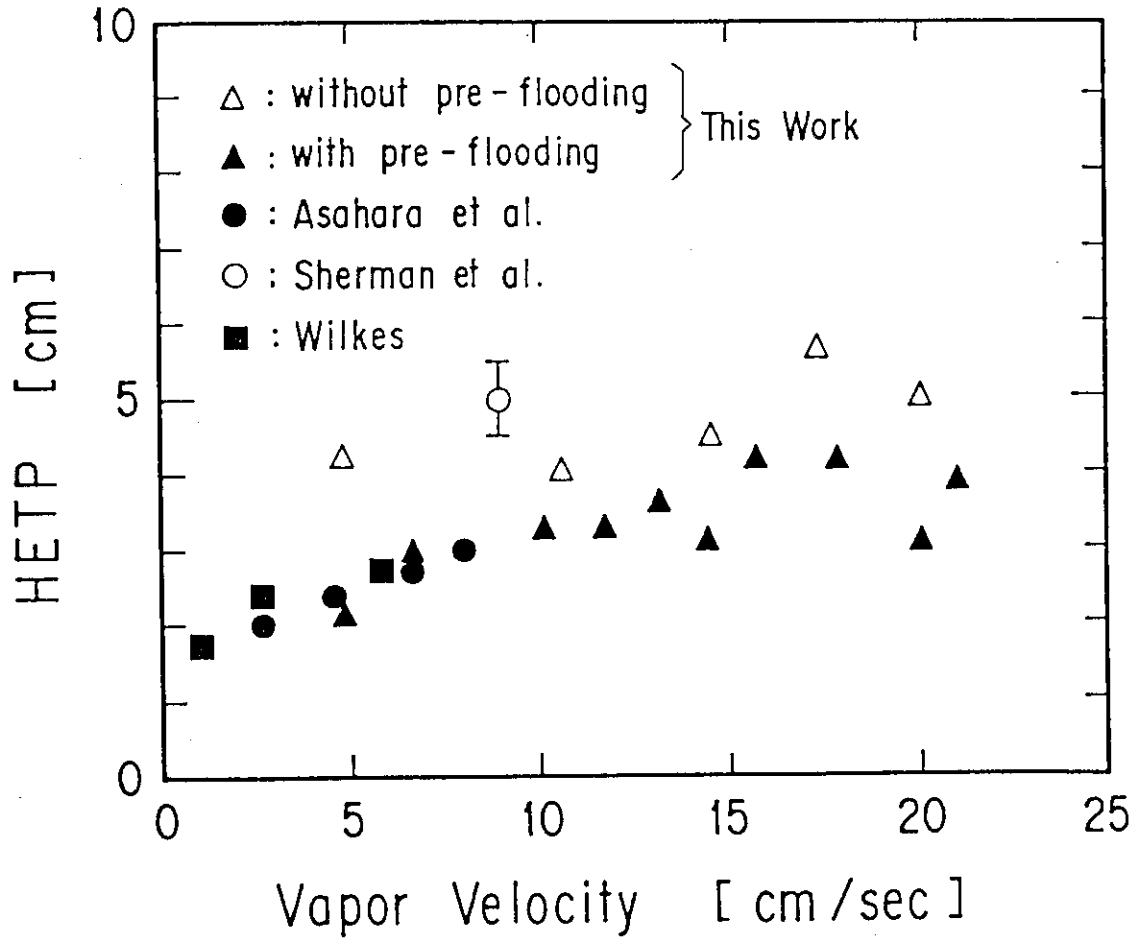

Fig. VII.2-5 Effect of vapor velocity HETP.

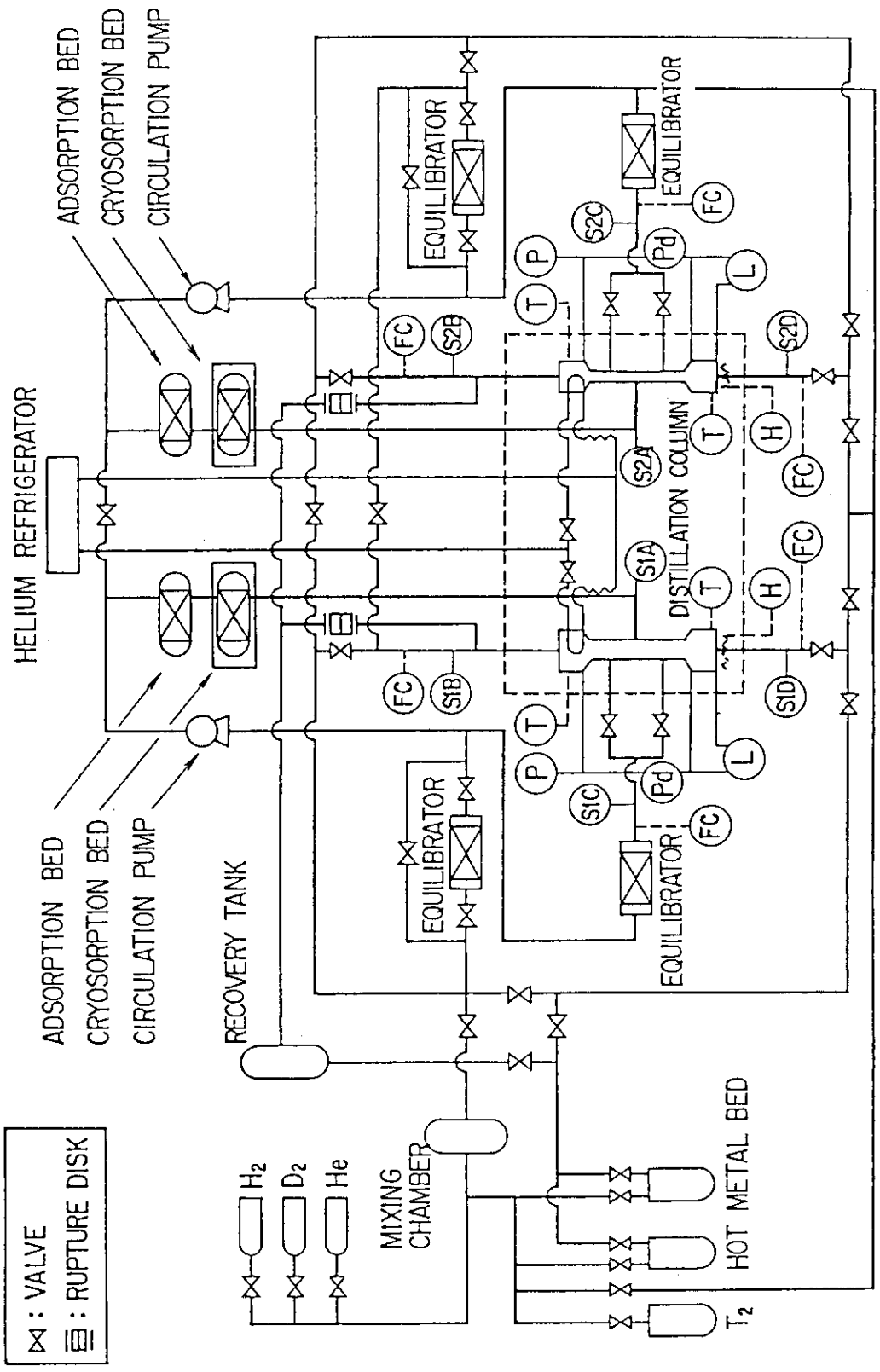

Fig. VII.2-6 Brief system diagram of experimental apparatus.

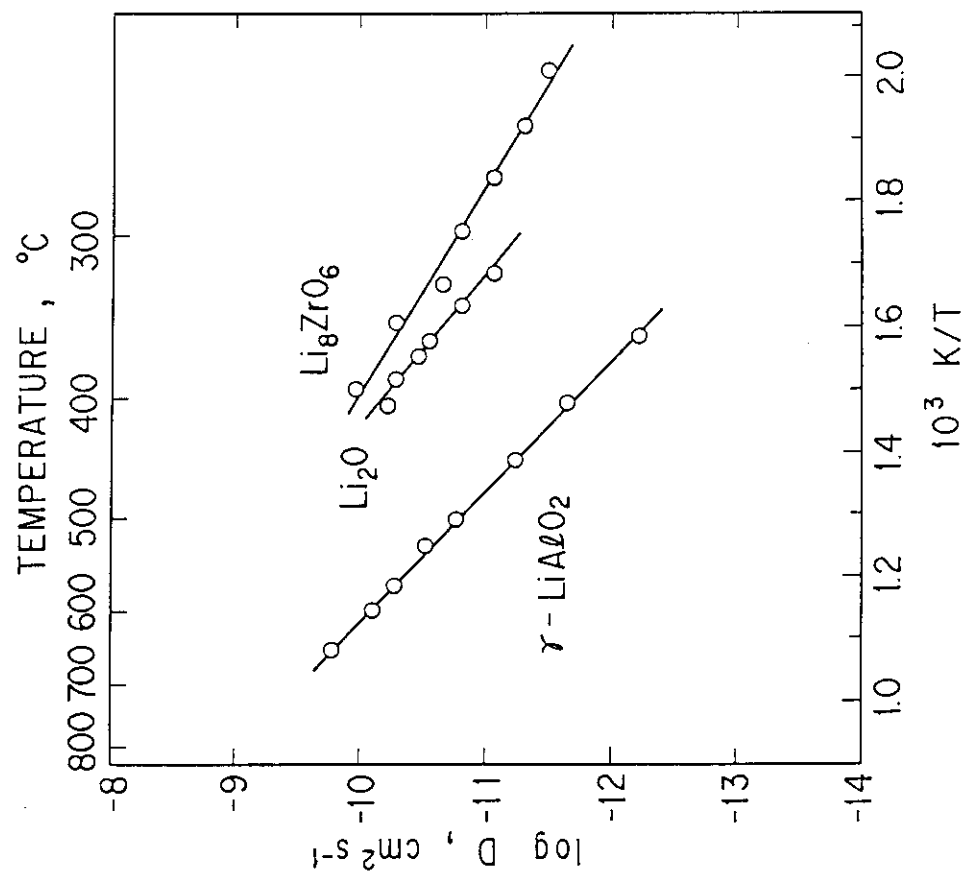

Fig. VII.2-8 Arrhenius plots of diffusion coefficients for tritium in Li_8ZrO_6, Li_2O and γ-$LiAlO_2$ crystals.

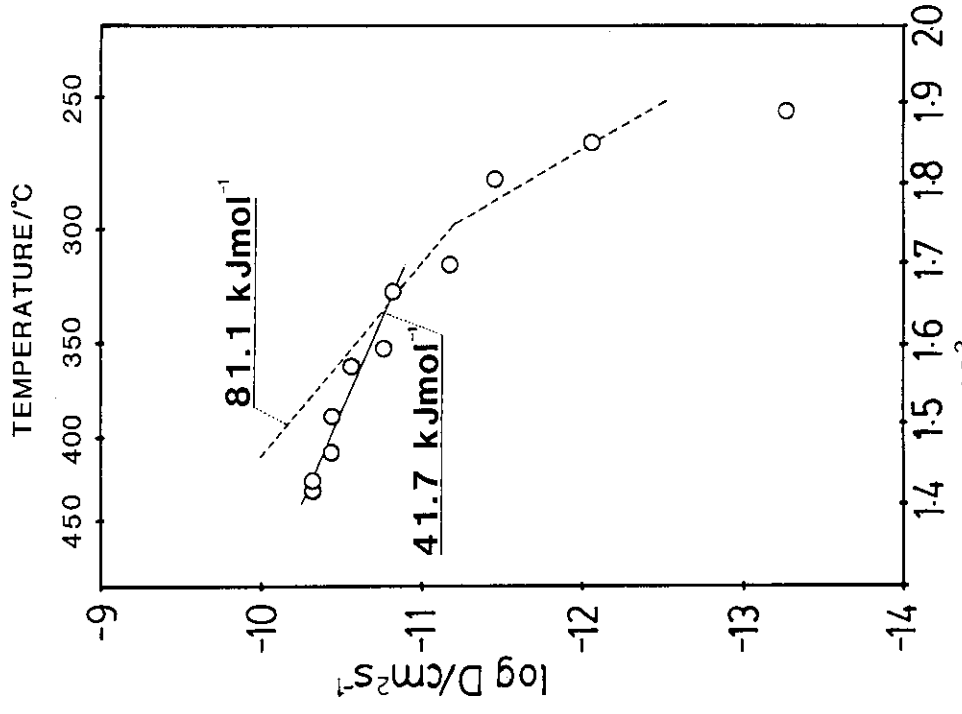

Fig. VII.2-7 Diffusivity of tritium in the unirradiated (—) and irradiated (--) Li_2O crystals.

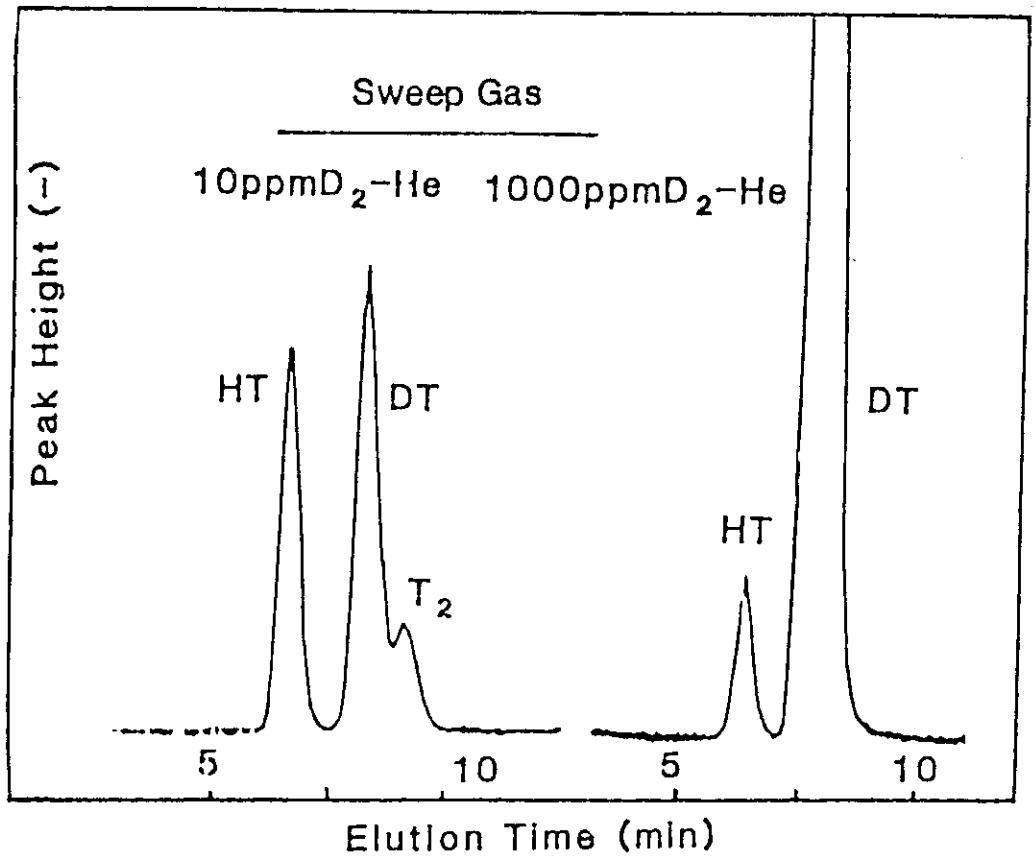

Fig. VII.2-9 Gas chromatography of in-situ release tritium under neutron irradiation.

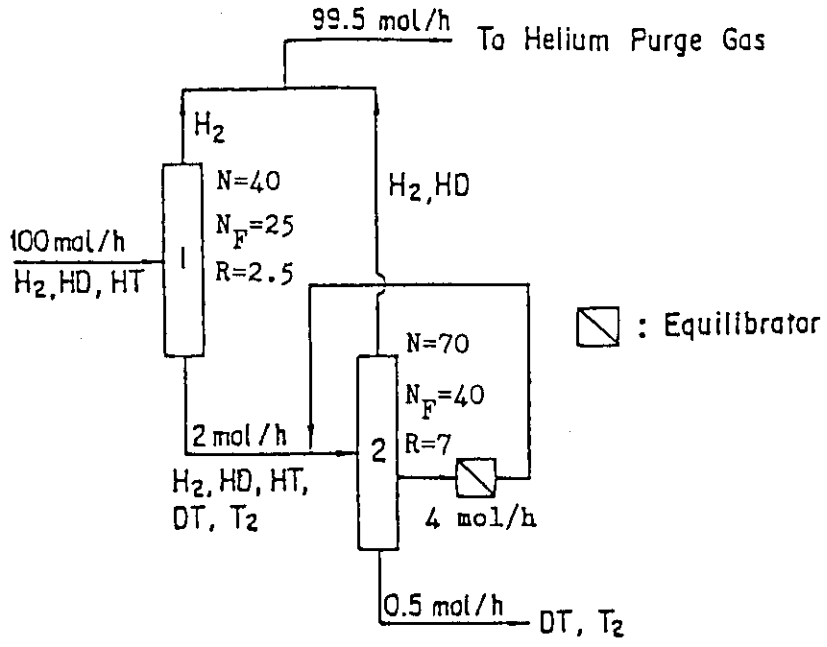

Fig. VII.3-1 Two column cascade developed for case 1. The parameters, N, N_F and R denote the number of total theoreticalstages, feed stage number and reflux ratio, respectively.

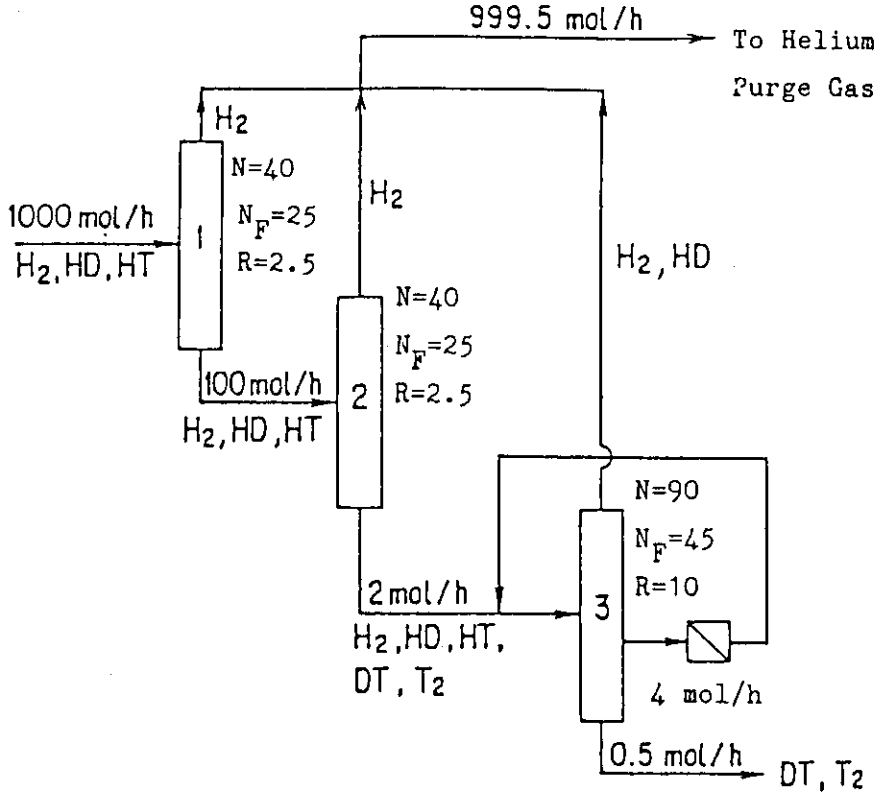

Fig. VII.3-2 Three column cascade developed for case 2.

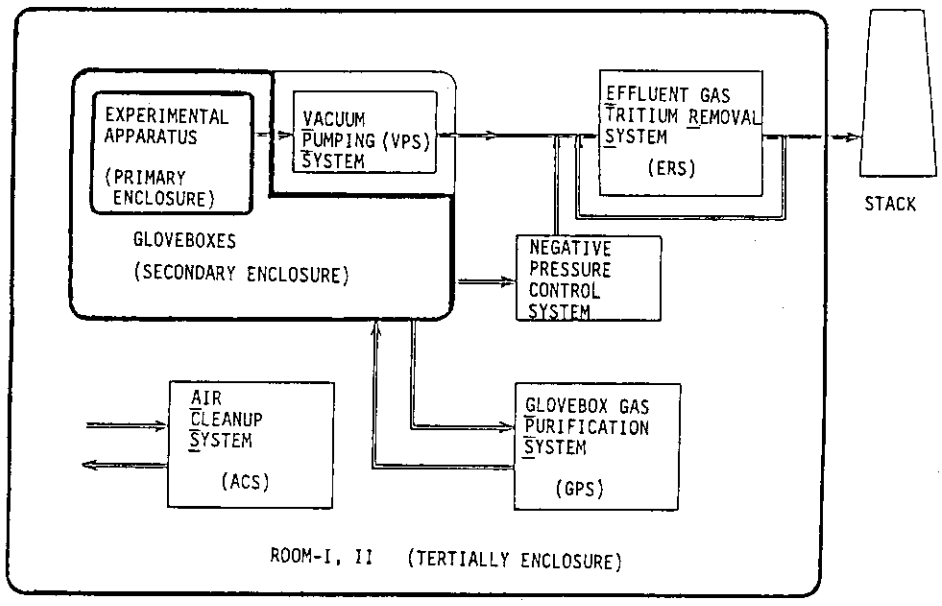

Fig. VII.4-1 Concept of the tritium containment system in the Tritium Process Laboratory.

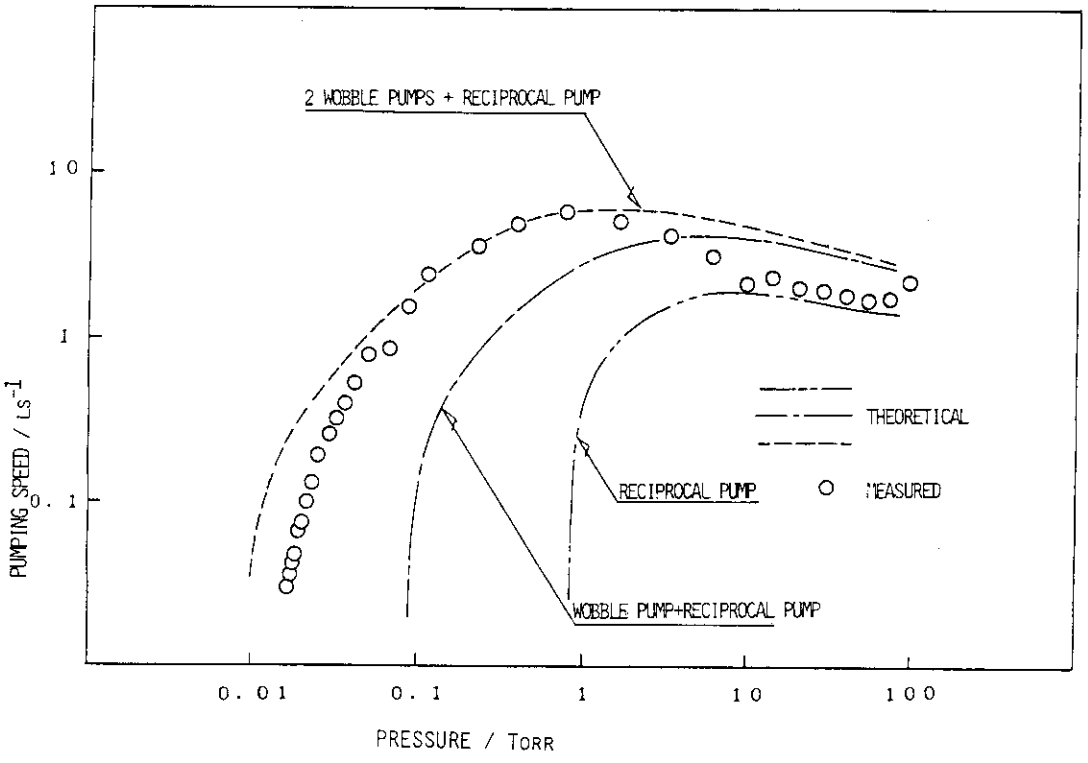

Fig. VII.4-2 Pumping characteristics of the combination of the two wobble pumps and an oil-free reciprocal pump with air.

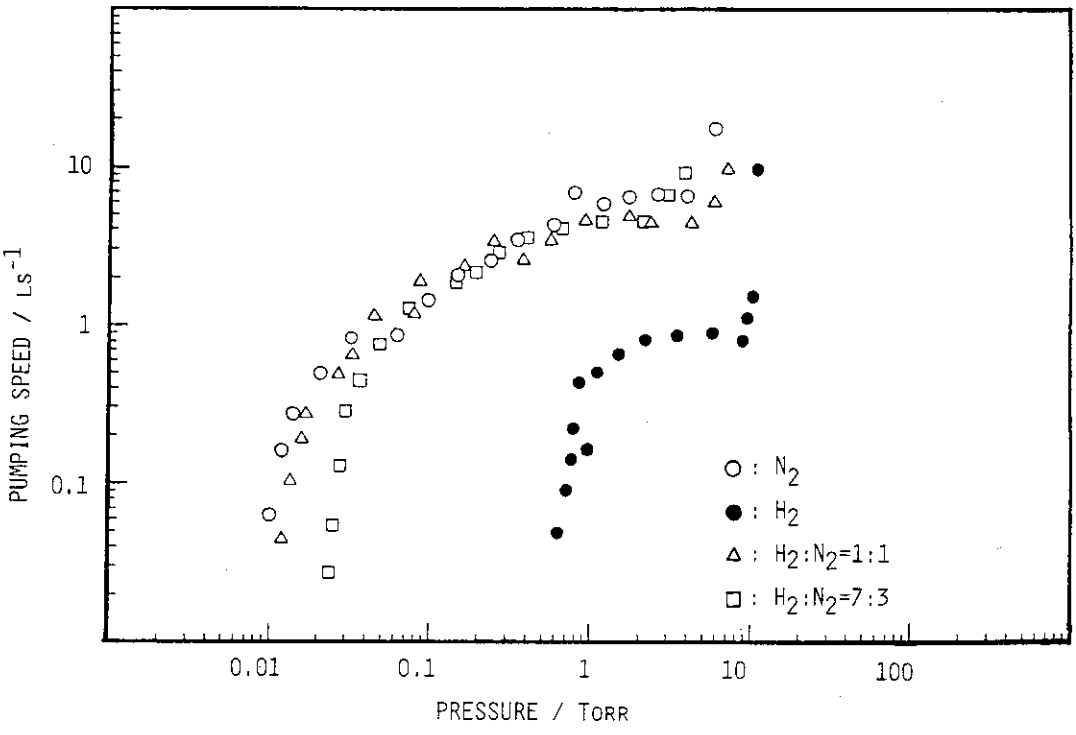

Fig. VII.4-3 Pumping characteristics of the Vacuum Pumping System with nitrogen, hydrogen and their mixtures.

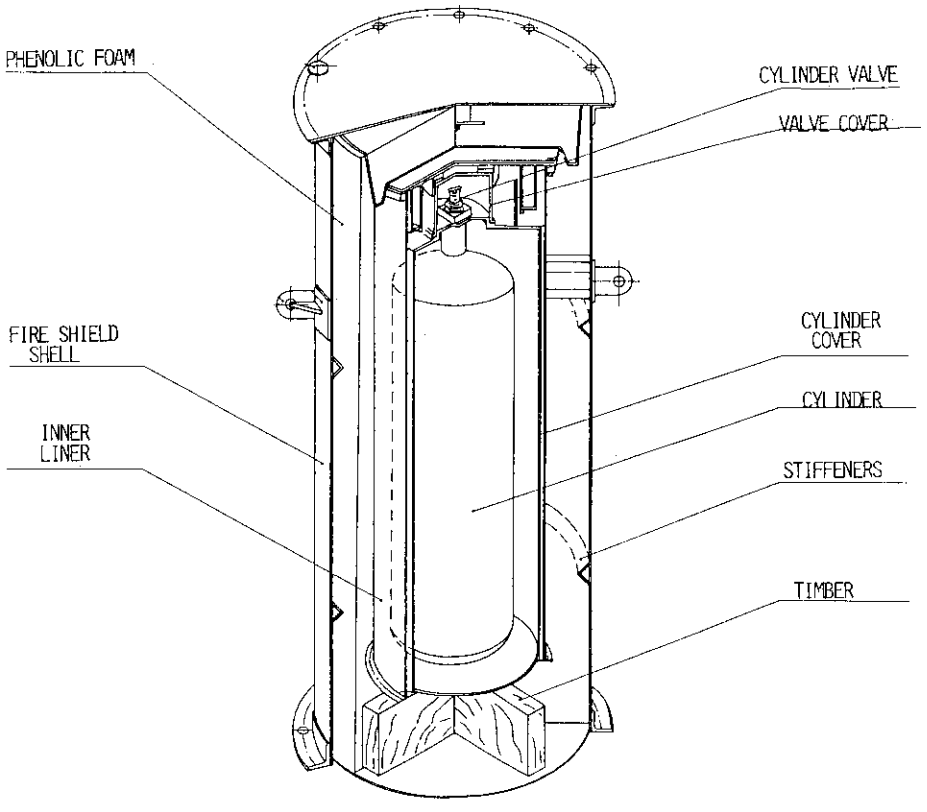

Fig. VII.4-4 Structure of the tritium transport package.

VIII. JAPAN-US RESEARCH COOPERATION IN DOUBLET III

The major achievements of the DIII-D program over the last year are summarized as follows:

- o A plasma current of 1 MA had been attained by May of 1986, and a 2 MA plasma current had been attained by July. In the operating time between March and the end of July the DIII-D device (Fig. VIII-1) realized plasma operation with elongation K=2, q≃3 and Z_{eff}≃2. Rapid clean-up of the vacuum vessel was demonstrated. Both limiter and divertor operation had been achieved.

- o The ability to shape a wide range of both limiter and divetor plasma configurations has been demonstrated. These configurations form an excellent basis for future high beta and confinement experiments.

- o Two new high power pump limiter modules were installed in July. In October, 6 MW of neutral beam injection was successfully accomplished and several weeks of intensive auxiliary heated plasma experiments were conducted in the DIII-D device. These experiments were performed predominantly in the divertor configuration. The H-mode regime of plasma performance was successfully attained for discharges with 1 MA of plasma current, simplified divertor configuration with elongation on the order of 1.8 and 6 MW of auxiliary heating. When operating in the H-mode, there was no apparent deterioration of energy confinement time with up to 6 MW of neutral beam heating power. The scaling of energy confinement time with plasma current is yet to be established and will be addressed with experiments planned for the future. The typical time history of the parameters for an H-mode discharge is shown in Fig. VIII-2, and the MHD equilibrium is shown in Fig. VIII-1 [1]. As shown in the figure, the onset of the H-mode is characterized by a rapid, to date uncontrolled, rise in the line average plasma density. The gas puff to the plasma was held constant. The D_α radiation in both the divetor X-point region and the central plasma also drop

to a fraction of the ohmic value. The central electron temperature and the total energy rises as the global energy confinement time returns to values comparable to the ohmic confinement. And the value corresponds to about three times the L-mode confinement ($\tau_E^H \sim \tau_E^{OH} \sim 3\tau_E^L \simeq 175$ms). The estimated peak kinetic total energy including calculated fast ion contributions is 700±140 kJ and is indicated in Fig. VIII-2. This results in $\beta = 1.4\%$ and $\beta_\rho = 1.1$.

- o ECH heating in the extraordinary mode outside launch at second harmonic was initiated at power levels of 400 kW in November and are continuing. Based on the initial experiments, there is some indication of plasma heating with second harmonic ECH. However, the analysis and the power levels to date are insufficient to determine where the heating is and how the energy confinement time is effected. In addition, future experiments will be conducted in conjunction with high power neutral beams to determine whether or not edge ECH heating can boost the discharge into improved energy confinement. Some indications of plasma heating have been observed with the extraordinary mode fundamental ECH with outside launch. This will also be investigated in greater detail in future experimentation in CY 1987.

- o A plamsa current of 3 MA was successfully obtained during limiter operation in the month of January 1987. It remains to apply high power neutral beam heating to discharges at this level of plasma current.

In August GA proceeded with the installation of the new, long pulse ion sources in lieu of installing the previous short pulse ion sources on the existing beam lines.

Scientists from JAERI and industries have supported the DIII-D program efforts in the areas of impurity study and analysis, edge physics, langmuir probe analysis and preparation work, limiter bias experiments and, finally, in the area of plasma equilibrium, shaping control and divetor operation.

The present cooperation program will be extended by four years to August 1992 for the purpose of investigating the principles of steady

state operation of a tokamak plasma at high beta. This would include experimental evaluation of non-inductive current drive methods such as neutral beams and electron cyclotron waves, and other related high beta and divertor experiments.

Reference

1) Luxon J. et al., "Initial Results from the DII-D Tokamak", The 11th International Conference on Plasma Physics and Controlled Nuclear Fusion Research, Kyoto, 1986 (IAEA-CN-47/A-III-3).

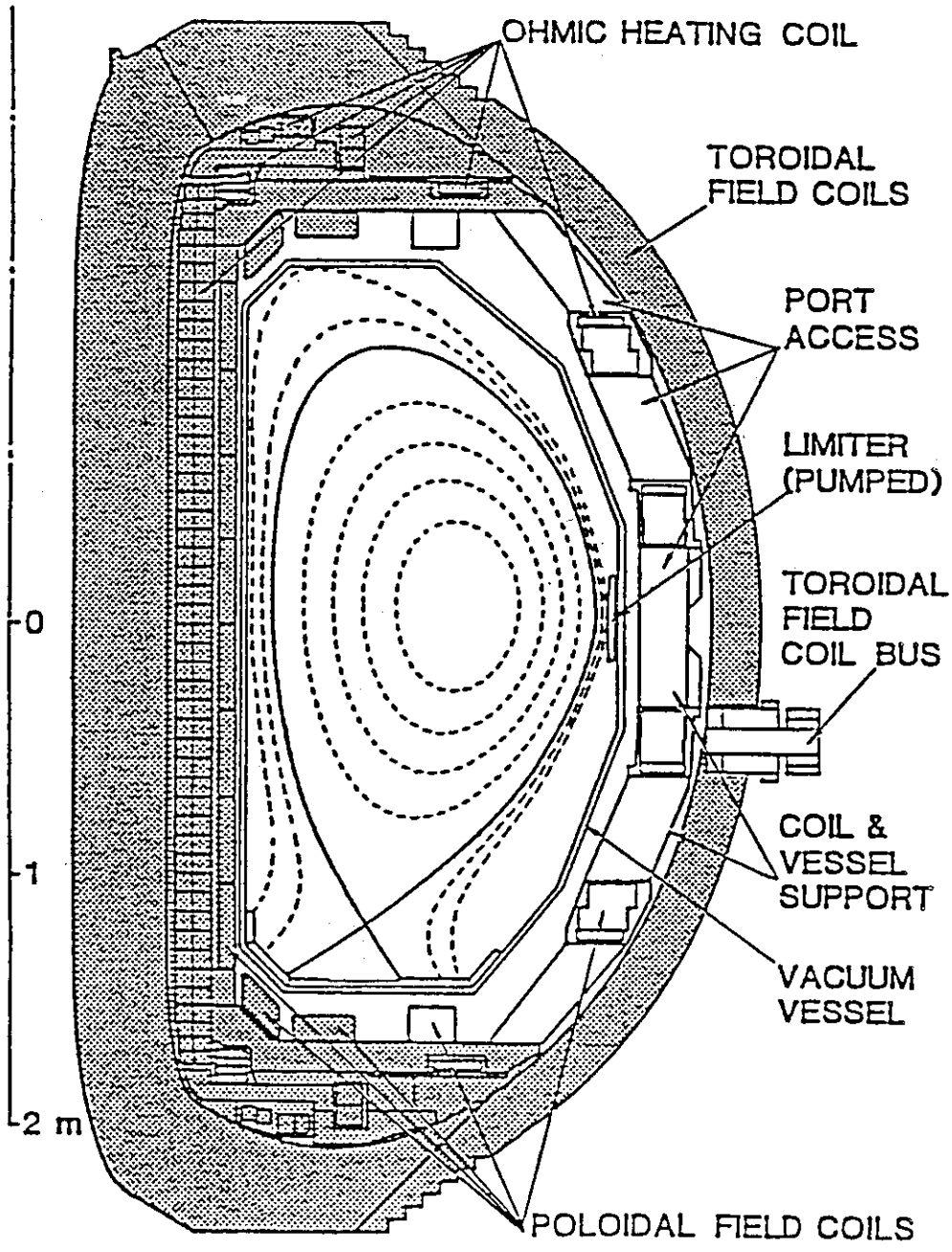

Fig. VIII-1 Cross section of the DIII-D device. Areas not shown in gray are new. Superimposed is the MHD equilibrium of a high beta divertor discharge (Fig. VIII-2 at 2280 ms).

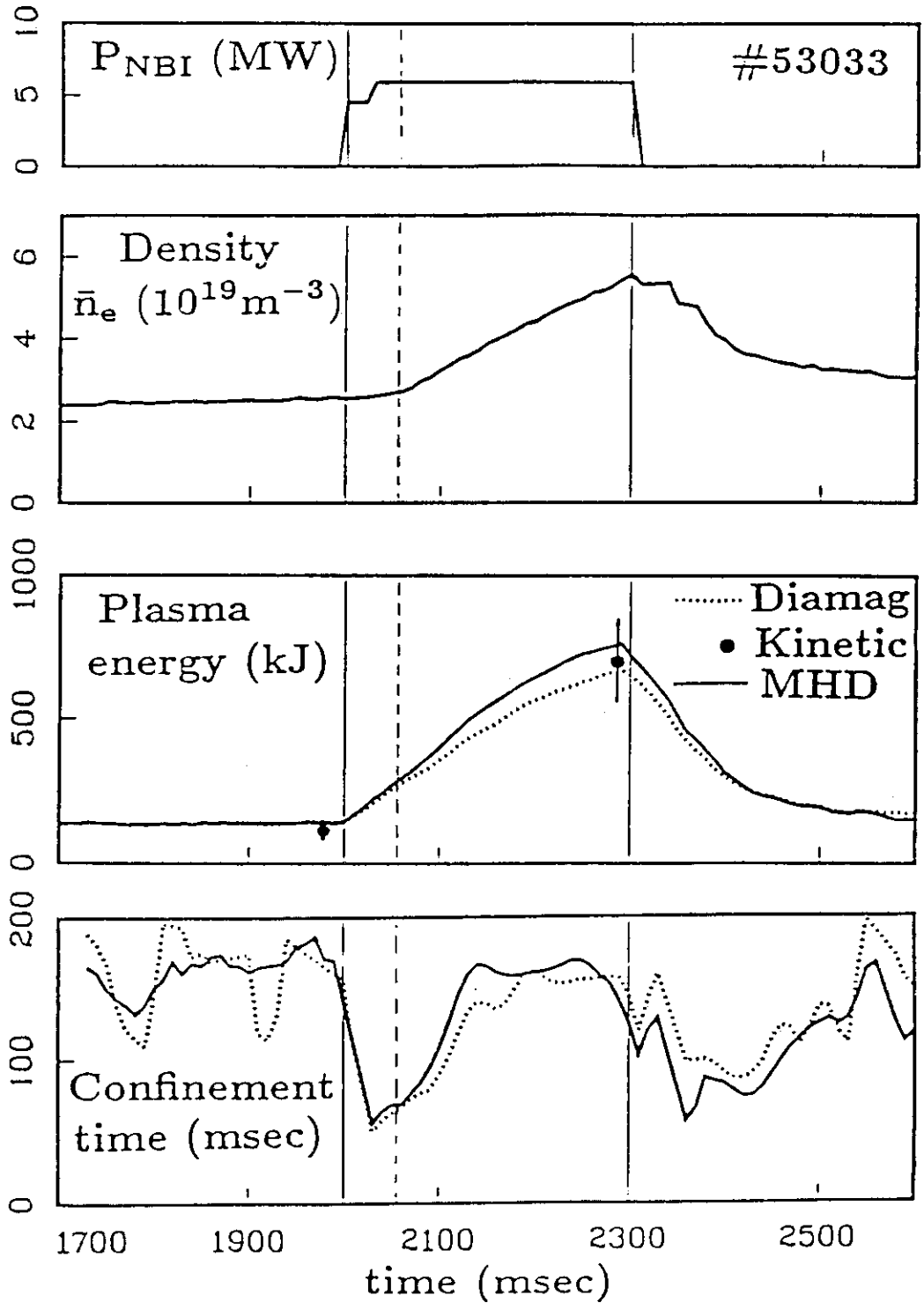

Fig. VIII-2 Time history of a beam heated discharge exhibiting H-mode behavior. Transition from L-mode occurs at ∿60 ms after the beginning of NBI pulse (dashed line). I_p=1 MA, B_T=2.1 T, H° beams into Deuterium plasma.

IX. JT-60 EXPERIMENT

1. Experimental Program and Schedule

The main objective of JT-60 is to attain the quivalent break-even plasma condition with hydrogen or helium plasmas. the exeriments in heating optimization phase were started in FY 1986 succeeding to the ohmic heating experiments (Fig.IX.1-1). Conditioning of the heating devices(NBI & RF) and increase of heating power are baiscally important in this phase.

The target plasmas for additional heating were performed in the second phase of ohmic heating experiment with parameters; plasma current up to 2MA, pulse length of 5-10sec and plasma density of $4\times10^{19}/m^3$ and over.

The first phase of heating optimization experiments with NBI and RF devices were started in August 1986 succeeding to the joule-heating experiments which amount to a total of about five months. Some operational time has been used for the current drive experiments to utilize time without NBI heating because NBI system needs intermittent shut down time for activation of the cryopanels and check of the system. The injected NB power was raised to the full rating of 20MW, ICRF power to 1.4MW and LHCD power to 1MW within two to three months. In these experiments the characteristics of plasma confinement with beem heated discharges were investigated and the first resuls of LHCD were presented, in which the maximum RF driven currents of 1.7MA were successfully obtained. The preliminary results of the initial heating experiments were presented at IAEA Kyoto conference on November.

The second phase of heating optimization was conducted from January to March 1987. In this phase significant extentions in the JT-60 plasma operation regimes have been achieved with the additional heating systems. A typical set of plasma parameters obtained in the NB heated plasma was Ti(0) of 11keV, Te(0) of 7keV. In LHCD experiments enhancement in RF driven currents resulted in maximum value of 2.0MA.

The experimental program and schedule for next fiscal year were reviewd after the first heating optimization phase as shown in Fig. IX.1-1. The basic plan is to get a H-mode discharge in the full power

heating experiments with the proposals for improvement of JT-60 as follows.

1) Graphite limiters and divertor plates

Graphite limiters and graphite divertor plates are being prepared to reduce the migration of metalic impurities. Carbonization of the first wall could avoid titanium impurity contamination during the high power heating discharge. This improvement would be implemented in the beginning of next fiscal year.

2) Increase the plasma current up to 2.7MA(divertor) and 3.5MA(limiter)

JT-60 has a plan increasing the plasma current up to 2.7MA in order to enhance the operational region of the divertor configurations. The currents of the divertor coil and the quadru-pole field coil could be raised beyond the design value. The toroidal field strength could be also increased form 4.5T to 4.8T.

The ohmic heating circuit would be enhanced to increase the plasma current up to 3.5MA in the limiter configurations. This new power supply would raise 20% of the total flux swing.

3) Improvement of divertor configuration

A new divertor coil will be prepared for a lower sigle null open divertor configuration. The lower single null configuration can be another candidate to improve the confinement capability in JT-60. The first plasma operations with new x-point configuration will be operational in the second phase of heating experiments.

4) Pellet injection

Cofinement improvement can be expected by injecting ice pellets into the plasma column. A pellet injector is to start construction in next fiscal year with the pellet speed of 1.3km/s and pellet size of 3.5mmϕ×3.5mm.

2. Auxiliary Heating Results

2.1 NBI heating and confinement[1),2),3)],

NBI experiments were started in August 1986. We could inject up to the maximum NB power, 20 MW, in a month. Figure IX.2－1 shows time evolutions of typical NB heated divertor and limiter discharges in JT-60. In the divertor configuration, the discharge suffers a density clamp during the NB pulse unless excessive gas is fed.

The parameter ranges explored for the NB heating experiments are summarized in Table IX.2－1. About one half of the shots are devoted to the He plasmas partly because shine-through of NB can be reduced in low electron density shots and partly because the threshold heating power for the H-mode is lower in plasmas with high mass number. The fraction of hydrogen in nominally He plasma was estimated to be up to one half from the H_α emission intensity, beam shine-through loss and neutral hydrogen flux measurements.

Central ion and electron temperatures and boundary electron temperatures (3-5 cm inner from the edge) of NB heated plasmas are plotted in Fig. IX.2－2. The ion and electron temperatures are measured by Doppler broadening of titanium XXI line and Thomson scattering, respectively. Hot ion temperatures up to 11 keV in the limiter configuration are discribed in 2.1.4 separately.

2.1.1 Energy confinement

Plasma stored energy is evaluated by two methods; W^* from magnetics (measurement of $\beta_p+\ell_i 2$ assuming ℓ_i doesn't vary during the NB pulse) and W^{tot} from kinetics (transport analysis using measured $T_e(r), n_e(r), T_i(0)$. The results are compared in Fig. IX.2－3, indicates that $W^*=0.92W^{tot}\pm0.13W^{tot}$. W^* is not corrected with the beam component $W_i^b/4$. The term can not be neglected at low electron densities. A Monte Carlo calculation predicts that W^* should be understimated by 10% at $n_e=2\times10^{19}$ m^{-3}. There is not appreciable difference between H and He plasmas.

Figure IX.2－4 shows the heating power dependence of energy confinement time in the restricted electron density range. The divertor plasma has better energy confinement than the limiter plasma. The solid lines show the Goldston scaling for $R_p=3.11$ m and a=0.87 m divided $\sqrt{2}$ taking into account isotope effects. the agreement is

fairly good for the 2-MA shots. I_p dependence of τ_E^*, however, is weeker than the Goldston scaling. JT-60 scalings of τ_E^*, in divertor plasmas are obtained from regression analysis as shown in Fig. IX.2－5. The heating power dependence as $\propto(a+b/P_{abs})$ is fitted slightly better than $\propto P_{abs}^{\alpha}$.

Attempts have been made to produce and environment which is considered to be conducive to the H-mode based on the experience from the medium-sized devices: increasing P_{inj} to 20 MW, lowering B_t to 1.9T and q_{eff} to 2.2, maintaining a large separatrix-limiter distance up to 5 cm, maximizing the volume averaged power density by reducing the plasma volume, the used of helium in stead of hydrogen, fueling through the divertor chamber, etc. These efforts, however, produced no clear reproducible H-mode discharges.

2.1.2 Particle confinement[4),5)]

Global particle confinement time is evaluated based on H_α measurements assuming toroidal symmetry, which is believed to be a good approximation in divertor discharges. Figure IX.2－6 shows the particle confinement time as a function of line averaged electron density and peakedness of the electron density profile. The particle confinement time decreases with density and it has strong correlation with the electron density peakedness.

Beam heated plasmas have shorter particle confinement time than ohmically heated plasmas by a factor of about three when compared with the same electron density peakedness. Data points with $n_e(0)/\langle n_e\rangle \sim 1.25$ are collected in Fig. IX.2－7 to examine the dependence of τ_p on heating power. The result indicates that the particle confinement time decreases with nearly inverse equare root of heating power similarly to the energy confinement time. considering that beam fueling is deep inside the plasma compared with gas fueling, the deterioration in particle confinement should be severer than it appears to be.

2.1.3 Divertor characteristics[6)]

Figure IX.2－1 demonstrates a dramatic effects of the divertor in reducing the radiation loss in the NB heated plasma. The radiation loss is typically 5 ~ 10% of P_{abs} in divertor discharges and 50 ~ 90% in limiter discharges.

The hydrogen neutral pressures measured in the main and divertor chambers are plotted against n_e in Fig. IX.2 - 8 for ohmic and NB heated discharges. The pressure ratio, P_{div}/P_{main}, which is sometimes regarded as an indicator of efficient divertor function was about 45 and 50 in H and He plasma, respectively, regardless of NB heating. Owing to the high compression ratio, Zr-Al getter pumps connected to the divertor chamber can pump out injected particles (~3Pam^3/s) by 20-MW, 75-kV NBI at $n_e=6\times10^{19}$ m^{-3}.

With respects to the heat transport through the throat to the divertor chamber, the temperature rise ΔT of the divertor plates is measured during the NB heating by a set of thermo-couples embedded in the plates. The half-width of the ΔT distribution across the separatrix is less than 2 cm, which corresponds to a half-width of less than 1 cm at the divertor throat, small enough to assure unobstructed transport of heat to the divertor plates. The power losses from the plasma are accounted fairly well as shown in Fig. IX.2 - 9. The heat load on the divertor plate is reduced with electron density, which demonstrates remote radiative cooling in effect. The missing power may be partly explained by radiation loss out of the bolometer's view in the divertor chamber.

2.1.4 High ion temperature mode[7),8),9)]

Central ion temperatures of 11±2 keV were achieved by NB injections into hydrogen plasmas in the limiter configuration. Figure IX.2 - 10 shows time evolutions of a typical 1-MA shot, in which the density increases from 0.8×10^{19}/m^3 to 2.8×10^{19}/m^3 fueled only by NB injection. The ion temperature measured by spectral analysis of forward scattering of 190-keV helium beam is 11±2 keV while that measured by Doppler broadening of titanium XXII line is 8.3±1.5 keV. This difference is caused by the difference of measurement volumes. T_i^{AB} is the central ion temperature, while T_i^{XXII} is an averaged ion temperature of a more extended volume. The central electron temperature is 3.0 keV just before NB heating and increases to 5.2 keV. The radiation loss is about 50% of the absorbed power. Z_{eff} is in the range 4 ~ 7, which is evaluated by visible bremsstrahlung and soft X-ray measurements. The main impurities are oxygen and titanium based on the spectroscopic measurements.

The Chang-Hinton neoclassical multiplier is deduced using our transport analysis code with the measured Z_{eff}, $T_e(r)$ and $n_e(r)$ as inputs. Figure IX.2 - 11 shows the central ion temperatures of T_i^{AB}, T_i^{XXII}, T_i^{XXI}, and a calculated T_i^{CAL} assuming $\chi_i = 5\chi_i^{CH}$. There seems to be a reasonable agreement between T_i^{AB} and T_i^{CAL}. The confinement time is ~70 msec and is almost equal to that of divertor discharges with the same plasma current and absorbed power. The comparison of the limiter and divertor plasmas suggests that higher electron temperature and higher Z_{eff} may be essential in obtaining high ion temperatures.

References

1) Yoshikawa, M., and et al., IAEA Kyoto Conference, 1986, IAEA-CN-47/A-I-1.
2) JT-60 Team presented by Nagami, M., ibid., IAEA-CN-47/A-II-2.
3) JT-60 Team, JAERI-M 87-009 (1987)(in Japanese).
4) Yamada, K., et al., to be published in Nucl. Fusion.
5) Tsuji, S. and JT-60 Team, 14th EPS (Madrid), 1987.
6) Nakamura, H. and et al., submitted to Nucl. Fusion.
7) JT-60 Team presented by Yoshino, R., 14th EPS (Madrid), 1987, invited paper.
8) JT-60 Team, to be printed as JAERI-M (in Japanese).
9) Hosogane, N., and et al., to be submitted.

2.2 LHRF Heating and Current Drive

2.2.1 Current Drive

The high power current drive experiment was carried out using the LHCD launcher and LHH launchers. The phase differences of adjacent waveguides were adjusted to $\Delta\phi = 90^\circ$ for LHCD launcher and $\Delta\phi = 120^\circ$ for LHH launcher to obtain the travelling waves. With a combined injection of LHCD and LHH units, a driven current of more than 2MA was attained in a helium plasma of $\bar{n}_e = 0.32 \times 10^{19} m^{-3}$, $I_p = 2MA$ and $B_T = 4.5T$ as shown in Fig. IX.2 - 12. Total injected power is 3.1MW(2GHz), in which 0.8MW was injected from LHCD launcher. In this shot, the one turn voltage stays at zero level or slightly negative during RF injection (time duration is about 2.5sec), which indicates the current was driven completely by RF power.

Figure IX.2 － 13 shows the current drive efficiencies which were obtained in the experiment using CD-launcher. Here, the current drive efficiency is defined as

$$\eta_{CD}=\bar{n}_e(10^{19}m^{-3})I_{RF}(MA)R_p(m)/P_{LH}(MW).$$

The phase difference between adjacent waveguides was set at $\Delta\phi=90^{\circ}$. Noninductive current estimated from the loop voltage ($I_{RF}=I_p|\Delta V_1|/V_1$) is presented against the LHRF power normalized by line averaged density. Open symbols indicate the case of current drive by LHRF only. The surface loop voltage is zero or negative for all points. η_{CD} for this case is between 0.8 and 1.7, which is relatively high comparing with the results of middle sized tokamaks. Furthermore, when NB heating is combined, the current drive efficiency was remarkably improved as shown in the figure with closed symbols. Here, points marked by (*) mean the cases of positive surface voltage. The obtained efficiency was η_{CD}=1.7-3.0. On the other hand, $\eta_{CD}$is 0.5~0.8 when the heating launcher(H-launcher) is used. Maximum efficiency is obtained at $\Delta\phi$~120°. This degradation of current drive efficiency comes from $N_{//}$ spectrum of H-launcher, which is not optimized for current drive. The peak of $N_{//}$ of H-launcher is about 1.2 for $\Delta\phi=120^{\circ}$, however, the accessibility condition requires larger value of $N_{//}$. For instance, $N_{//}$ has to be larger than 1.24 at $\bar{n}_e=1.0\times10^{19}$ m^{-3}, B_T=4.5T. Large part of injected power cannot access to the center part of the plasma.

Also, the current drive of 8 sec is demonstrated as shown in Fig. IX. 2 － 14. Plasma is initiated ohmically and the OH-coil current is controlled to be constant after 100 msec from the break down and the plasma current decreases with time constant of L/R. LHRF power is injected from 1 sec to 9 sec with the RF power P_{LH}=2.1MW. Plasma current is ramped up from 440kA to 580kA at $\bar{n}_e=5.5\times10^{18}$ m^{-3}. In addition to these, current modification using LHCD, which is an important theme for improvement of plasma confinement or research of β-limit, was examined. Fig. XI.2 － 15 shows the time evolutions of the internal inductance ℓ_i obtained from the Faraday rotation measurement along one vertical code at r~0.5a, Shafranov lambda Λ ($\beta_p+\ell_i/2$) measured by magnetics, LHRF power and loop voltage. The figure shows that the Shafranov lambda Λ decreases by LHRF injection

after ramp up at the onset of LHRF, which is considered to be caused mainly by increase in β_ρ due to suprathermal electrons and/or change of peripheral current. On the other hand, $\Delta\ell_i$ also decreases with LHRF injection, which coincides with the behaviour of Shafranov lambda, except onset of LHRF injection. This indicates that the decrease in Shafranov lambda means the decrease in $\Delta\ell_i$, i.e., the broadening of current profile. Fig. IX.2 - 16 presents the dependence of normalized the Shafranov lambda $\Delta\Lambda_{LH}/P_{LH}(MW)/\bar{n}_e(10^{19}$ $m^{-3})$ on the phase difference $\Delta\phi$ for CD and H-launcher. This shows that the current profile clearly depends on $\Delta\phi(N_{//}$ spectrum), which suggests the current profile can be controlled by phase control of LHRF.

2.2.2 Electron Heating

The electron heating was carried out in a helium plasma for the density range of $\bar{n}_e = 1.0\text{-}4.0\times10^{19}$ m^{-3}. The two heating launchers were used at $\Delta\phi=180^o$ ($N_{//\ peak}=1.8$ and $\Delta N_{//} = 0.5$), which were usually accompanied by the LHCD unit at $\Delta\phi=90^o$. In Fig. IX.2 - 17, the obtained central temperature T_{e0} are plotted against $P_{abs}/\bar{n}_e$ for OH, NBI and LHEH in He plasmas of $I_p = 1.5$ MA (P_{abs} means OH input power plus total additional power). The central electron heating efficiency defined by $n_e=\bar{n}_e\Delta T_{eo}/P_{LH}(eV.10^{19}$ $m^{-3}/kW)$ is found to be 2-3 and is very good compared with other additional heating methods on JT-60. The maximum T_{e0} of 6 keV was attained in LHEH with $P_{LH} = 2.4$ MW at $\bar{n}_e=1.7\times10^{19}$ m^{-3}. The profile of electron temperature of this shot is shown in Fig. IX.2 - 18, with that of ohmic shot.

The figure IX.2 - 19 shows the density dependences of T_{e0}, hard X-ray signal (E>260keV) and incremental ECE signal at $3f_{ce}$ during LHRF injection with the power of about 3MW. Though T_{e0} decreases as $\bar{n}_e$ increases, the signal of hard X-ray and ECE extend to $\bar{n}_e=4.0\times10^{19}$ m^{-3}. The increase in ion temperature up to 1 keV was observed in the electron heating region. As no fast ion tails were observed, the ions were heated via collision with electrons. The ion heating region and density limit to couple electrons will be found at a higher density.

The LHEH seems to show a very good heating performance at least in the central region. As for the global confinement characteristics, however, it shows usual L-mode dependence. The power dependence of

global confinement time is shown in Fig. IX.2 －20 and is approximately on Kaye-Goldston scaling.

2.2.3 NB heating combined with LHCD

LHCD can change the current profile independently of the temperature profile and may stabilize the MHD activities and improve the energy confinement. As an application of the lower hybrid wave the NB heating in the entirely current driven plasma were examined. Figure IX. 2 －21 shows the comparison of the energy confinement between the NB alone (a) and LHCD+NB (b,c). In the case of NB alone (a), the increase of the stored energy ΔW of 0.21MJ is observed with the absorption power of NB P_{abs}=3.4MW.

The corresponding incremental energy confinement time τ_E^{INC} of 61msec and the global energy confinement time τ_E of about 69msec are estimated. In almost the same condition LHCD is applied before the NB pulse. The loop voltage becomes slightly negative value before the NB as shown in Fig. (b). In this case ΔW=0.4MJ with P_{abs}=4.6MW then τ_E^{INC}=88msec and τ_E=100msec are estimated. The energy confinement time is improved by the combination of NB and LHCD. In the case of high power NB heating as shown in Fig. (c) ΔW=0.96MJ with P_{abs}=10.7MW, τ_E^{INC}=90msec and τ_E=107msec. So that the energy confinement is improved also in the high power case and the global confinement time is not degraded with NB power up to 11MW.

The increase of the stored energy are plotted in the Fig. IX.2 －22 as a function of the effective absorption power $P_{abs}-\dot{W}$. Open and closed symbols are NB alone and LHCD+NB, respectively. The maximum incremental energy confinement time $\tau_E^{INC}\equiv\Delta W/(P_{abs}-\dot{W})$ for NB alone is around 70msec while τ_E^{INC}=90msec for the combination of LHCD and NB heating. The energy confinement time is not always improved by LHCD and sometimes stays in the usual NB heating level. It is important to know what condition is required for the improvement. We found that the change of the current profile by LHCD is one of the key parameters to the improvement. This fact is shown in Fig. IX.2 －23 where the vertical axis is $\tau_E^{INC}\equiv\Delta W/(P_{abs}-\dot{W})$ and the horizontal is the change of the Shafranov lambda $\Lambda=\beta_\rho+\ell_i/2-1$ during LHCD alone. The increase of β_ρ by the LH power is estimated to $\Delta\beta_\rho<0.05$ and so we can regard roughly $\Delta\Lambda_{LH}\tilde{}\Delta\ell_i/2$. This figure shows that the reduction of ℓ_i by LHCD may correlate to the improvement of energy confinement.

The measurement of Faraday rotation angle viewing the half radius of the plasma have shown that the internal inductance of ℓ_i changes during LHCD consistently with the Shafranov lambda, and ℓ_i slightly decreases during LHCD+NB.

According to the reduction of ℓ_i by LHCD, the change of MHD activities are observed in the beam heated plasma as shown in Fig. IX.2 - 24 , where Fig. (a,b) are NB alone and (c,d) are LHCD+NB. The left hand side of this figure indicates time evolution of the soft x-ray signals S_x from the center plasma and the right is radial profiles of the fluctuation level of soft x-ray $\Delta S_x/S_x$. In the case of NB alone as shown in Fig. (a,b), strong MHD fluctuations localized sharply near the plasma center have been observed and fluctuation level reaches about 40%. This oscillation is thought to be mainly the m=1 oscillation. These MHD fluctuations near the plasma center are suppressed in the case of LHCD+NB as shown in Fig. (c,d). The different MHD fluctuation having $\Delta S_x/S_x$=0.1 have been found near the half radius and this is supposed to be the m=2 oscillation. These results imply that the current profile is rearranged by LHCD and is consistent to the change of the Shafranov lambda during LHCD alone.

The combined NB heating with LHCD in I_p=1.5MA were also tried, however, the flatter current profile than OH plasma is not realized by LHCD and so the clear improvement of confinement is not observed yet. More systematic investigations are necessary to understand what mechanism improves the confinement in the flat current profile realized by LHCD and to obtain a plasma with better confinement.

2.3 ICRF Heating

2.3.1 Introduction

In JT-60, the second harmonic ICRF heating experiment (120MHz) is now being carried out with hydrogen plasma in order to demonstrate equivalent Q=1, where Q is the fusion power multiplication factor, in combination with neutral beam injection (NBI) heating and lower hybrid range of frequency (LHRF) heating. The 2×2 loop antenna array has been developed for the optimization of the second harmonic heating [1].

The results of the antenna-plasma coupling and antenna conditioning are presented in IV.2.2.

In this sub-section, heating properties and beam acceleration associated with the two phasing modes, $(\pi,0)$ and $(0,0)$, are described.

2.3.2 Heating results with $k_{//}$-shaping

The peak positions of the $k_{//}$-spectra of $(0,0)$ and $(\pi,0)$ modes are calculated to be 0 m^{-1} and 10 m^{-1}, respectively. Figure IX.2 - 25 (a) and (b) compare time evolution of the line-averaged electron density $\bar{n}_e$, Shafranov Λ $(=\beta_p+\ell_i/2-1)$ and the loop voltage V_L associated with (a) $(\pi,0)$ mode and (b) $(0,0)$ mode, respectively. Clear difference was found between the two phasing modes. In $(0,0)$, V_L increased significantly and $\bar{n}_e$ also slightly increased in spite of the $\bar{n}_e$-feedback control. The gas feed became zero during the rf pulse. Λ grew gradually with the rf pulse, indicating that the absorbed power in the plasma core was very small. On the other hand, in $(\pi,0)$, clear response was found in Λ, $\bar{n}_e$ and the gas feed did not change and V_L slightly decreased.

The incremental stored energy from the magnetics ΔW_S^* is evaluated as a function of the additional power P_{add} $(= P_{IC}+I_p.\Delta V_L)$. The incremental energy confinement time τ_E^{inc} $(= \Delta W_S^*/P_{add})$ is about 70 ms for $(\pi,0)$, which is comparable with NBI heating [3]. In $(0,0)$, τ_E^{inc} is only 40 ms.

Such large differnce in heating effects between $(\pi,0)$ and $(0,0)$ may be explained with the shape of the power deposition profile, which is now being evaluated with the two-dimensional kinetic code [5]

Actually, we observed cavity resonance in (0,0) [2], which indicates a weak wave damping. In this case, the power deposition profile broadens significantly. On the contrary, we observed no cavity resonance in (π,0), which suggests stronger wave absorption. Then, the power deposition profile becomes more centrally-peaked. Hence, the heating efficiency is much better in (π,0) than in (0,0).

The radiation loss during ICRF heating is also dependent on the $K_{//}$ -shaping. In OH plasma with $n_e \sim 6\times10^{19}$ m^{-3}, $\Delta P_{rad}/P_{IC}$ was about unity in (0,0) but it decreased to 0.65 in (π,0), where ΔP_{rad} is the increment of the total radiation loss with rf.

2.3.3 Beam acceleration

In combination heating with NBI, we observed significant beam acceleration above injection energy. Figure IX.2 - 26 shows the charge exchange (cx) spectra in the perpendicular direction. Fast ions, which are injected at 60 keV, are accelerated up to more than 150 keV. The result of the Fokker-Planck calculation, whose detail will be described elsewhere [5], is also indicated in Fig. IX.2 - 26.

We can estimate the rf power density ~0.3 W/cm^3 from the analysis.

The region where the beam acceleration takes place efficiently was identified by chopping the neutral beams whose lines coincide with the line of sight of the cx analizer in the plasma core. The cx fluxes were enhanced by an order of magnitude when the fast neutrals were injected from the beam lines mentioned above and it was only at that time when the acceleration of the beam component was observed, indicating that the beam acceleration occurs in the plasma core.

We measure the efficiency of the beam acceleration in $\Delta T_i^{tail}/P_{IC}$, where $\Delta T_i^{tail} = T_i^{tail}(NB+IC) - T_i^{tail}(NB)$ and T_i^{tail} is the slope of the energy sepctra above the injection energy. $\Delta T_i^{tail}/P_{IC}$ is 3.8 keV/MW in (π,0) at $n_e \sim 4.2 \times 10^{19}$ m^{-3} and 1.8 keV/MW in (0,0) at $n_e = (2.9\sim3.5)\times10^{19}$ m^{-3}. The efficiency of the beam acceleration is about two times higher in (π,0) than in (0,0).

We investigated $\bar{n}_e$-dependence of ΔT_i^{tail} at P_{NB}=4.9~6 MW with fixed P_{IC}. In Fig. IX.2 - 27 (a), ΔT_i^{tail} is summarized as a function of a slowing-down time τ_s ($\propto T_e^{3/2}/n_e$) which is evaluated from measured $T_e(0)$ and $n_e(0)$.

A linear relation

$$\Delta T_i^{tail} \propto \tau_s$$

is confirmed from the experiment. From theoretical consideration, one can write

$$\Delta T_i^{tail} \propto P_{rf} \cdot \tau_s / n_b \quad ,$$

where n_b and P_{rf} are the density of the beam component and the rf power density coupled to the beam component, respectively.

Then, we obtain an important result,

$$P_{rf} \propto n_b \quad .$$

The rf power density absorbed by the beam component in the plasma core is proportional with the number of the beam component.

If we increase the neutral beam power much higher, what happens? P_{NB}-dependence with fixed rf power and electron density was also investigated. ΔT_i^{tail} is almost constant up to $P_{NB} \sim 16$ MW. Thereby,

$$P_{rf} \propto n_b / \tau_s \propto P_b \quad ,$$

where P_b is the beam power density in the core. This relation is confirmed by the plot of $n_b \cdot \Delta T_i^{tail} / \tau_s (\propto P_{rf})$ against P_{NB} as shown in Fig. IX.2 - 27 (b), where we use the cx date at 60 keV as n_b in arbitrary unit. The result suggests that P_{rf} deviates from the line of $P_{rf} \propto n_b$ but scales as $P_{rf} \propto P_b$ with high power beam injection.

2.3.4 Summary

(1) $k_{//}$-shaping is of paramount importance in optimization of the second harmonic ICRF heating.

(2) In combination heating with NBI, remarkable beam acceleration in the plasma core was observed. Favourable scaling $P_{rf} \propto P_b$ is found up to $P_{NB} \sim 16$ MW. Significant Q enhancement can be

expected in the combination heating of high power NBI and the second harmonic ICRF.

References

[1] T. Nagashima, et al., Fusion Engineering and Design 5 (1987) 101.
[2] M. Saigusa, et al., in Proceedings of the 7th Topical Conf. on Application of Radio-Frequency Power to Plasmas, Kissimmee, Florida (1987).
[3] JT-60 Team (presented by M. Nagami), in Proceedings of the 11th Conf. on Plasma Physics and Controlled Nuclear Fusion Research, Kyoto (1986), IAEA-CN-47/A-II-2.
[4] A. Fukuyama, et al., Computer Phys. Rep.4 (1986) 137.
[5] M. Yamagiwa, et al., JAERI-M 87-127 (1987); to be published in Plasma Phys. Controlled Fusion.

3. Theoretical Studies and code Development

3.1 Transport Analysis

3.1.1 Transport Properties of OH and NBI Heated Discharges [1]

Transport properties of ohmically and neutral beam heated plasmas in JT-60 have been analysed by using the one dimensional tokamak transport code (LIBRARY). The very flat density profiles observed in ohmically heated discharges are explained by no inward flow velocity of hydrogen. The saturation of energy confinement time at high density discharges are due to the increase of the ion energy loss channel. The combination of the neoclassical ion heat diffusivity χ_i^{CH} with multiplication factor of around 6 and the electron heat diffusivity $\chi_e=5.0\times10^{19}/n_e q\ m^2sec^{-1}$ well reproduce experimental data in the density range of $(2\sim8)\times10^{19}m^{-3}$. Density dependence of effective charge number, Z_{eff}, is shown in Fig. IX.3－1, on the assumption of Spitzer resistivity (a) and neoclassical resistivity with trapped electron correction (b). The value of Z_{eff} by Spitzer resistivity agrees well with that of experiment obtained by visible bremsstrahlung or X ray pulse-height analysis, wheres Z_{eff} by

expected in the combination heating of high power NBI and the second harmonic ICRF.

References

[1] T. Nagashima, et al., Fusion Engineering and Design 5 (1987) 101.
[2] M. Saigusa, et al., in Proceedings of the 7th Topical Conf. on Application of Radio-Frequency Power to Plasmas, Kissimmee, Florida (1987).
[3] JT-60 Team (presented by M. Nagami), in Proceedings of the 11th Conf. on Plasma Physics and Controlled Nuclear Fusion Research, Kyoto (1986), IAEA-CN-47/A-II-2.
[4] A. Fukuyama, et al., Computer Phys. Rep.4 (1986) 137.
[5] M. Yamagiwa, et al., JAERI-M 87-127 (1987); to be published in Plasma Phys. Controlled Fusion.

3. Theoretical Studies and code Development

3.1 Transport Analysis

3.1.1 Transport Properties of OH and NBI Heated Discharges [1]

Transport properties of ohmically and neutral beam heated plasmas in JT-60 have been analysed by using the one dimensional tokamak transport code (LIBRARY). The very flat density profiles observed in ohmically heated discharges are explained by no inward flow velocity of hydrogen. The saturation of energy confinement time at high density discharges are due to the increase of the ion energy loss channel. The combination of the neoclassical ion heat diffusivity χ_i^{CH} with multiplication factor of around 6 and the electron heat diffusivity $\chi_e=5.0\times10^{19}/n_e q\ m^2sec^{-1}$ well reproduce experimental data in the density range of $(2\text{-}8)\times10^{19}m^{-3}$. Density dependence of effective charge number, Z_{eff}, is shown in Fig. IX.3 - 1, on the assumption of Spitzer resistivity (a) and neoclassical resistivity with trapped electron correction (b). The value of Z_{eff} by Spitzer resistivity agrees well with that of experiment obtained by visible bremsstrahlung or X ray pulse-height analysis, wheres Z_{eff} by

neoclassical resistivity is less than one at $n_e > 3.0\times10^{19}m^{-3}$. This result shows that the electrical conductivity has the Spitzer-type dependence and the trapped electron correction is small.

In the neutral beam heated discharges, the power deposition profile is calculated by using the Orbit Following Monte Carlo code (OFMC code). The degradation of energy confinement under the high power neutral beam heating is due to the enhancement of electron heat diffusivity. Figure IX.3 - 2 shows the numerical simulation results of neutral beam hated helium discharge (shot no. E2154) with $\chi_e = 2.0\times\chi_e^{INTOR}$ and the assumption of $n_{He}/n_H = 2.0$. They agrees well. For discharges with 20 MW NBI heating, electron heat diffusivity increases to $\chi_e = 5.0\ m^2sec^{-1}$ at $n_e = 5\times10^{19}\ m^{-3}$. In the high density plasmas ($n_e > 6.0\times10^{19}m^{-3}$), electron thermal conductivity shows weak dependence on the density. By taking account the beam pressure, it was also shown that stored energies evaluated by the shift of the magnetic axis are consistent with the value evaluated from the transport analysis.

3.1.2 Two Dimensional Neutral Particle Transport Analysis [2]

Neutral particle transport in JT-60 plasmas has been studied by using newly developed 2-D neutral transport code with divertor configuration. Magnetic surfaces, on which plasma parameters are assumed to be constant, are calculated by magnetic fitting code. Neutral particle distribution are calculated by path-length estimation method. Intensity of Hα is calculated by collisional-radiative model. In the OH experiment of divertor discharges in phase I, neutral particles, which are neutralized at the divertor plate, mainly move behind sub-magnetic limiter coils and are released from near 30 degree limiter. In the OH experiment of divertor discharges in phase II, when the neutral particle shield are set up behind sub-magnetic limiter coils, neutral particles are mainly released through divertor throat. In both cases, calculated Hα intensities obtained by neutral particle distribution and particle confinement time have shown good agreement with experimental data. In the neutral beam heated plasmas, halo neutrals becomes important to evaluate the atomic process near the plasma center. Comparison of neutral particle distributions in

ohmic and neutral beam heating phase are shown in Fig. IX.3 - 3 Results of calculation show that disbribution of halo neutrals is spatially constant and it affects little on the charge exchange loss in the neutral beam heating. Neutral particle distribution in the high beta plasma in the high power additional heating phase (P_{NBI} =20 MW, P_{RF} = 10 MW) has been also calculated. It is shown that neutral particles reach plasma center easier than the low beta case, because of outward shift of magnetic axis.

3.1.3 Impurity Transport in Ohmically Heated Plasmas [3]

In the ohmically heated plasma of JT-60, the transport of impurities has been studied by VUV and soft X-ray crystal spectroscopies, and from bolometer and soft X-ray diode signals, along with one dimensional tokamak transport code. Changing over a discharge from the limiter mode to the divertor mode, the decay of the bolometer signals was measured and the time constant was about 0.3 sec in the central chord. Temporal evalution of Ti XIII (23.365 A), Ti XX different discharges with I_p = 2 MA which a piece of titanium was accidentally injected into. The comparison of the respective lines with the simulation results by a diffusive/convective transport model is shown in Fig. IX.3 - 4. The anomalous transport coeffcient, D_A, is about 1.0 m^2sec^{-1} and convective inward flow is not seen.

3.1.4 Transport analysis by Drift Wave Turbulence Model [4]

Numerical analysis of JT-60 plasmas in both ohmic and neutral beam heating phase has been carried out by using one dimensional tokamak transport code with thermal conductivities based on the drift turbulence. Dissipative trapped electron mode, collisionless trapped electron mode, collisional circulating electron mode, collisionless circulating electron mode and toroidal ion temperature gradient mode (η_i mode) candidate to the thermal conductivities. The numerical results show good agreement with experimental data in the medium electron density range $n_e \sim 4\times10^{19}m^{-3}$ both for ohmic and neutral beam heating phase. On the contrary, this model overstimates thermal conductivities in the low electron density range and high temperature plasmas can not be reproduced because of the strong dependence of

thermal conductivities on electron temperature, for example χ_e has $T_e^{7/2}$ dependence in the dissipative trapped electron mode and has $T_e^{3/2}$ dependence in other modes. Figure IX.3 - 5 shows comparison of central electron and ion temperature by calculation and experiment in the neutral beam heated plasmas with I_p = 1.5MA, and P_{abs} ~ 9 MW. At the density of 2.5×10^{19} m^{-3}, experimental data show the central temperature $T_e(0)$ ~ 4 KeV and $T_i(0)$ > 5 KeV, whereas results of calculation show $T_e(0)$ =2.6 KeV and $T_i(0)$ = 2.4 KeV. This discrepancy cannot be compensated by changing the stability condition of n_i mode.

References

[1] Hirayama T., Shimizu K., Kikuchi M., Shirai H., "Transport Analysis of OH and NBI Heated Discharges in JT-60" JAERI-M 87-029 (1987)

[2] Simizu K., Azumi M., "Two Dimensional Neutral Transport Analysis in Tokamak Plasma", JAERI-M 87-028 (1987)

[3] Hirayama T., Sugie T., Sasaki A., Kubo H., Koide Y., Akaoka N., Takeuch H., Nagami M., "Impurity Transport in Ohmically Heated JT-60 Plasma", JAERI-M 86-161 (1986)

[4] Shirai H., Hirayama T., Shimizu K., Takizuka T., Azumi M., "Transport Analysis of JT-60 Plasma by Drift Wave Turbulence Model", to be published in JAERI-M report

3.2 Additional heating and current drive

3.2.1 Neutral beam injection (NBI)

NBI current drive in tokamaks has been studied on two stages of theoretical model. Firstly, using an orbit-following Monte-Carlo (OFMC) code, we have calculated the neutral beam driven current in order to investigate effects of fast ions: (1) the effect of finite banana size, (2) the effect of loss of fast ions during slowing down, (3) the effect of energy diffusion and (4) the effect of particle trapping. It was found that the energy diffusion as well as the effect of particle trapping are important to make a precise prediction of beam driven current. the finite banana size effect on the driven current profile is not important, if the neutral beam is diffused.

The effect of fast ion loss during slowing down is not important for beam driven current. A new analytical model in which first two effects are taken into consideration has been developed. Calculated results by the analytical model show a very good agreement with those by OFMC code.

Secondly, we have extended analysis of beam driven current. Purposes of this extension are to analyze the beam driven current with bootstrap effects in steady state tokamak reactors and to develop and algorism to solve the beam driven current consistent with MHD equilibrium. Using the new code, we confirmed that the current drive efficiency is substantially improved by bootstrap effect in a high β_p plasma [Fig.IX.3 - 6]. Bootstrap current is very important for the design of tokamak reactors.

The new OFMC code has been developed, to analyze spectra of charge-exchange neutral observed at an actual diagnostic port and estimate the effect of charge-exchange loss particle on neutral specta. The problem in use of the old OFMC code is a large statistical error because of very few number of test particles getting into an actual diagnostic port. The newly developed code can describe exactly the behavior of fast ions during slowing down and calculate charge-exchange neutral spectra with very low level of statistical error. Figure IX.3 - 7 shows the obtained spectra of fast neutral.

3.2.2 Second harmonic ion cyclotron resonance heating

Theoretical model of ICRF (ion cyclotron range of frequency) wave heating combined with NBI has been developed, taking account of the slowing down velocity distribution by NBI and the high-energy ion tail formation by second harmonic ICRF wave. This model is constituted by two model equations: wave equation in real space and the Fokker-Plank equation in velocity space. Propagation and absorption of ICRF wave is obtained by the one dimensional kinetic wave code (1D-ICRF code). This code solves the full electromagnetic wave equation in an inhomogeneous and dispersive plasma as a boundary value problem. To describe the ICRF waves in the slowing down distribution, the dielectric tensor of a non-Maxwell plasma was formulated and newly entried into the 1D-ICRF code. The velocity distribution function,

which is assumed as isotropic is obtained on each magnetic surface by solving the Fokker-Planck equation in steady state. We have developed the computer code to solve the wave equation and the Fokker-Planck equation simultaneously.

This model has been applied to the second harmonic ICRF heating combined with NBI in JT-60. For given wave launching conditions and NBI deposition profile, we obtained th rf-wave field structure, power deposition profile [Fig. IX.3 - 8], power partition rate and ion velocity distribution function on each magnetic surface [Fig. IX.3 - 9] Cavity resonance mode, which is easily excited in low density plasma, is suppressed by the high-energy ion tail for the $(\pi,0)$-phasing. In low density plasma, the most part of the launched wave power is directly absorbed by ions. The ion absorbed power is almost transfered to electrons by the Coulomb collision. ICRF power partition between ions and electrons is hardly affected by NBI (beam power and energy). Furthermore, to compare the present calculation with the results of recent ICRF excperiments in JT-60, charge-exchange neutral spectrum is calculated using the obtained velocity distribution function. Parameter dependence of experimental results was explained qualitatively by this numerical analysis.

3.3 MHD Stability Analysis

3.3.1 Kink Instability of the Divertor Configuration in JT-60 [1]

JT-60 has a poloidal divertor with a stagnation point in the outer side of torus. The divertor configuration has a large shear near the plasma surface by the effect of the X-point, as shown in Fig. IX.3.3.1. therefore kink modes are expected to be stabilized by this shear. Characteristics of N=1 free boundary kink instability in a divertor configuration plasma are numerically analyzed by using the ideal MHD stability code ERATO-J [2]. And following results were obtained: 1) The kink instability displacement in a divertor configuration is localized near the plasma surface as shown in Fig. IX.3 - 10 and the growth rate is reduced by the shear. 2) The stability window in a divertor configuration with low β ($\beta_p \geq 0.5$) is

wider than that in a limiter configuration, but the difference becomes small as the beta increase ($\beta_p \geq 1.0$). 3) In high β, the growth rate in a divertor configuration is smaller than that in a limiter one, but the improvement of critical beta in a divertor configuration is small.

3.3.2 Beta Enhancement of Tokamak Plasma with Nearly Circular Cross Section [3]

The access to the second stability region of the ballooning modes is studied by optimizing the profiles of a plasma pressure and a safety factor for the conventional shape of a tokamak plasma. Figure IX.3－11 shows that the nearly circular plasma locally enter the second stability region when the local negative shear region extend to the good curvature region. This local negative shear is produced more easily in a low shear than in a high shear region. The transitional beta value is lower for small elongation and the second stability region is easily accessed in a tokamak with nearly circular cross-section, as shown in Fig. IX.3－12. The result indicates the possibility of improving the beta limit of a tokamak without increasing the total plasma current or the elongation.

3.3.3 Numerical analysis of Sawtooth Oscillations in Joule Heating Plasma in JT-60

Characteristics of sawtooth oscillations in soft X-ray intensity emitted from JT-60 plasma in Joule heating phase have been numerically studied by using 1-D Tokamak transport code with the model of helical magnetic flux exchange by m=1/n=1 multi-tearing mode. From the recent experimental results, the inversion radius of soft X-ray intensity and the period of sawtooth oscillations increase with increasing the plasma current, and double sawtooth oscillations occur among single sawtooth oscillations. Occurrences of double sawtooth oscillations are closely related to resistive skin time τ_R.($= \mu_0 r_I^2/\eta$, where r_I is inversion radius of soft X ray intensity and η is plasma resitivity), and double sawtooth oscillations occur beyond the critical value τ_R^c.

The double sawtooth oscillations are numerically reproduced by 1-D Tokamak transport code, and the transition form a single sawtooth

oscillation to a double one is obtained as shown in Fig. IX.3.3.3-1. These results show the τ_R^c is about 3.0 second, which is in good agreement with the value obtained in experiments (3.4-4.5 sec). And the mechanism of a occurrence of double sawtooth oscillation is made clear.

Reference

[1] Ozeki, T., Seki, S., Ninomiya, H., Azumi, M., JAERI-M 87-004 (1987).

[2] Tokuda, S., Tsunematsu, T., Azumi, M., et al., JAERI-M 9899 (1982).

[3] Seki, S., Tsunematsu, T., Azumi, M., Nemoto, T., Nucl. Fusion 27 (1987) 330.

[4] Shirai, H., Nagashima, K., Nishitani, T., JT-60 Team, JAERI-M 87-014 (1987).

3.4 Code Development

3.4.1 New Program organization system (NEWORG)

NEWORG is the system to control and manage large scale FORTRAN programs. This system selectively edits subroutines which are necesarry for a calculation model through following procedures. First, an objective program source is analyzed to obtain its tree structure. Second, user specifies the calculation model by a conversational processing. Third, after discarding unexecution source lines from the program by a pre-processor, all the selected modules are linked. This system is of great used to produce a compact code from a subroutine library. Since the information on the calculation model is preserved, NEWORG is also useful for the management of load modules.

3.4.2 Graphic utilities GPREP and LIBGR

Plotting utilities, which are widely apprecable to problems of computational physics, have been developed as a part of library system for a one dimensional tokamak transport code. Utility routines are composed of two procedures, i.e., the pre-processor "GPREP"

registrates graphic data to a data file with a set format, and "LIBGR" processes the data to match with the required format of "ARGUS" and plotts the graph. The regular form of data by "GPREP" enables us to read out data without any information on data recording so that these utilities are very useful for dealing with a lot of disorder data with different type.

3.4.3 JT-60 experimental data base retrieval system (DARTS)

In JT-60, about 30 shots of experiments are made per day. Expermental data, 5MB of plant data and 3MB of plasma diagnostic data, are written on disk shot by shot. Users can easily access to those data base if they know the objective shot number. However, as the total number of shots increases, it becomes very difficult for them to look for the shot number they want without index informations. DARTS (Data base ReTrieval System) provides those index data files. DARTS consists of three kinds of data file, bit, summary and bulk data file (about 500 data points in total per shot), respectively. We sample those index data from the exerimental data base of JT-60. The bit data is a set of data with bit form, which will be referred first to retrieve shot numbers. The summary data is of ingeger type, which will be referred secondly. About 15 data are employed as summary data which may mainly characterize a tokamak discharge. The bulk data will be referred at the final retrieval step. It consists of representative plant data, some important plasma diagnoistic data, some magnetic analysis data and some results of one dimensional transport analysis. The schema of the system is shown in Fig. IX.3－14.

4. Diagnostics

4.1 Introduction

The introduction of the initially planned diagnostic system onto JT-60 has been completed in 1985 and the additional introduction and the some modification of the several diagnostics has proceeded in 1986. The present activity of JT-60 diagnostics are summarized in Table IX.4-1, which shows the diagnostics in operation.

The improvement of the JT-60 diagnostics in 1986 is briefly described as follows.

The real time feedback control of the electron density has been carried out with the sampling time of 10 msec. The peripheral chord of the 2 mm microwave interferometer has been installed. The Faraday rotation angle has been measured and the current profile control has been confirmed by this measurement at the LHRF experiment.

The electron cyclotron emission (ECE) is used for the electron temperature measurement. One observing port is newly prepared for ECE measurement in 1986 in order to improve the spatial resolution to 5.7 cm.

The ion temperature is successfully obtained by the active beam scattering method using with the neutral ^{3}He beam. The impurity contents in the plasma are estimated by this scattering data. the charge-exchange recombination method is also attempted for the ion temperature measurement using with the ^{3}He neutral beam. The high ion temperature plasma is produced at the low density regime in JT-60, and their temperature is consistently obtained by two different diagnostics of the active beam scattering device and the crystal spectrometer, which observes the Doppler broadening of Ti XXI and Ti XXII line radiations.

The radiation profile is estimated from the data obtained by a 15-channel bolometer array associated with 4 verically viewing bolometers, which are additionally installed in 1986. The peaked radiation is observed in the null point region of the divertor plasma located at the outer side of the main plasma.

In the following sections, the interesting results and the significant progresses are presented in each diagnostic system.

4.2 Electron Density Measurement

4.2.1 Apparatus

The electron density was inferred from the measurement of the phase shift experienced by far-infrared (FIR) laser beams and microwaves. All the data were degitized with 5 μs sampling time over a whole duration of the discarge.

The FIR laser (CH_3OH, 118 μm) interferometer provided time resolved measurement of the line-integrated electron density. The laser system consisted of two FIR lasers, a pumping CO_2 laser, a reference CO_2 laser, and their frequency stabilization system. As the radiation of this wavelength is absorbed by atmospheric moisture, the whole system was enclosed hermetically and pressurized with dry air. The laser beams were situated along three vertical chords at R=2.53 m (U_{23} port), 3.04 M (U_4 port) and 3.55 m (U_6 port) in a poloidal cross-section of the torus, and pass through the divertor room of the lower side.

The microwave (2 mm) interferometer measures the line-integrated electron density along a single vertical chord at R=3.25 m (U_5 port). In this year, a new microwave interferometer was installed with the oversized waveguides inside the vacuum vessel to supplement the diagnostic by measuring the line density near the plasma periphery along a vertical chord at R=2.19 m.

In respect to the density measurement, Thomson scattering diagnostics were in good agreement with the data from these interferometers. For the study of fluctuations like sawteeth, m=1 osicllations and other MHD instabilities, the interferometers complement the soft X-ray and magnetic diagnostics.

4.2.2 Activities

Electron density profiles were routinely obtained by inversion of the line densities measured with the four chords assuming the shape of the flux surfaces calculated from the magnetic measurements.

Real time feedback control of the density had been demonstrated, using one vertical channel (U_4) of three FIR interferometer channels measuring the main plasma density as a feedback signal to the gas inlet system. Figure IX.4-1 illustrates the temporal evolution of the line densities from the three channels showing the modulated waveforms by feedback control for the duration of 4-7 sec.

Another vertical channel (U_6) of the FIR interferometer channels was available to measure the Faraday rotation angle which is proportional to $\int n_e B_p dl$. The values of ℓ_i, q_0 and β_p were calculated with the quilibrium code combined with magnetic flux measurements at the surface exploiting the additional constraints on β_p in the interior of the plasma.

Particularly in LHRF experiments, this Faraday rotation measurement had demonstrated its ability associated with significant changes of the current profiles observed. For a typical discharge of LHCD experiments, the measured $\bar{B}_z$ and the inferred ℓ_i values as a function of time are shown in Fig. IX.4-2 where $\bar{B}_z$ is defined as $\int n_e B_p dl / \int n_e dl$. It was clearly found that the current profile comes to be flattened during the application of LHRF waves for non-inductive current drive.

The density measurement of the divertor plasma was obtained, although the system suffered occasional fringe count errors due to the large displacement of the mirror mounted on the divertor plate inside the vacuum vessel. From the data obtained, we found a certain positive correlation between the line densities of the divertor plasma and the main plasma for ion and electron drift sides, respectively, as shown in Fig. IX.4-3.

The measurement of the peripheral density in the inner side of the plasma was attempted to study the edge fluctuations and obtain a more accurate shape of the density profile. However, this measurement was frequently plagued by the movements of the vacuum vessel and the refractive effects due to the density gradients leading to the errors of the fringe counts. Most recently, we have succeeded to obtain the reliable data after a careful adjustment of the optical alignment, so that the density in the scrape-off layer was found to be somewhat higher than could be expected.

The MHD fluctuations within the plasma were studied primarily by using the soft X-ray and the line density measurements. For instance, m=1 oscillations observed on the soft X-ray signals, which are believed to be induced when q value is below unity, were well correlated with the line density signals with the same frequency. By noticing the different locations of these diagnostics in the toroidal direction, we found from the phase shifts of the signals that the toroidal mode number of the m=1 oscillation is unity.

4.3 Electron Temperature Measurement

4.3.1 ECE System

Electron cyclotron emission (ECE) is measured by Fourier transform spectroscopy. It is easy for the Fourier transform spectroscopy to measure the ECE spectrum. We have developed the measuring system of Fourier transform spectrometer (FTS) in order to measure the ECE and the electron temperature profile from the JT-60 plasma. Fig. IX.4-4 shows the schematic diagram of the layout of FTS in JT-60. We can use the two ports by changing the angle of the mirror (M1) for the ECE measurement. The one port is nearly vertical. The angle between the port axis used and a horizontal line is 75 degree. The port is called IN4 port (incline 4 port). The angle between another port axis and a horizontal line is 46.7 degree. The port is called IN2S port (incline 2 small port). The diameters of IN4 port and the light pipe are 70[mm] and 110[mm], respectively. For the measurement of IN2S port, we use the wave-guide of X band due to the interference of the other apparatus. The ratio of the S/N in the observation of IN2S port to the S/N in the observation of IN4 port is about 1/20. These reasons are following. In the observation of IN2S port, the effective solid angle is small and the cross-section of the wave-guide of X band is small. The frequency resolution of FTS is 3.66GHz. In the case of B_t=4.5 T, this value of 3.66 GHz corresponds to the spatial resolutions of 5.7 cm and 16.6 cm for IN2S port and IN4 port, respectively. The frequency of the scanning mirror is normally about 20Hz. The ECE spectrum is obtained at rate of about 20Hz. ECE of X mode from JT-60 plasma is defined by a polarizer and a Brewster window for the measurements of two ports. ECE of O mode can be observed when the polarizer is rotated.

It is necessary for the measurement of the electron temperature to calibrate the FTS system. The FTS system is calibrated by the combination of two methods. The source of first method is the plasma. The electron temperature in the plasma is measured by other diagnostic methods, for instance. Thomson scattering of a laser, the pulse height analysis of soft x-rays etc. The temperature in radial position at a time measured by the FTS is normalized by one in the same radial position at same time measured by the other diagnostic method. The calibration source of second method is a continuous black body radiation using a microwave absorber. It is best that the

calibration source is located in the plasma. But it is difficult for the sources of the second method to be located into the vacuum chamber. The calibration of the sensitivity of the system was performed by the combination of two methods. The calibration from the mirror (M1) to FTS is performed by applying the black body radiation using the microwave absorber (ECCOSORB). The calibration from the plasma to mirror (M1) is performed using the value measured by Thomson scattering. In other words, the frequency dependence of the sensitivity was obtained by applying the black body radiation using the microwave absorber. The absolute value of the sensitivity was normalized to the value which is infered from the Thomson scattering method.

In the observation of IN4 port, the radial profiles of the electron temperature can not be obtained due to the broadened viewing sight by the reflection of inside of port. the length of the IN2S port is smaller than one of the IN4 port. In the observation of IN2S port (theta=46.7 degree), we insert the apertures in the sight in order to avoid the broad of the viewing sight. The radial profiles of the electron temperature is derived from the X mode of second harmonic ECE.

Fig. IX.4-5 shows the comparison of the central electron temperature determined by the Fourier transform spectroscopy and those determined by homson scattering method. The typical electron temperature profile derived from ECE is shown in Fig. IX.4-6. The electron temperature measured by the Thomson scattering is also shown in the figure. The standard deviation of these measured values is 0.11. The ratios of the electron temperatures measured by the Thomson scattering to those measured by Fourier transform spectroscopy in the radial positions are shown in the Table IX.4-2. The ratios are almost constant and the standard deviation of the ratio is less than 0.2 except for the radial position of 0.83[m]. The second harmonic ECE of X mode in this position is not optically thick. Therefore the electron temperature can not derived from the second harmonic ECE in the position. The disagreement of the electron temperature in this position is reasonable. The agreement between the electron temperature profiles measured by Fourier transform spectroscopy and those measured by the Thomson scattering method is satisfactory except

the pheripheral region. We can easily obtain the time evolutions of the electron temperature profile by Fourier transform spectroscopy.

In the case of discharges of the low electron density and the lower hybrid current drive (LHCD) etc., the ECE spectrum is not the emission from the thermal electron. We can not derived the electron temperature from the ECE spectrum. The ECE spectra from the supra-thermal electron in the case of the application of LH power are shown in Fig. IX.4-7. The spectra in the low frequency region are not shown due to the large error of the calibration of the sensitivity. Before application of LH power, the spectra of ECE are the typical spectra due to the thermal electrons. The peak positions in the spectrum correspond to the second and third harmonic electron cyclotron frequencies corresponding to the plasma center. We can obtain the electron temperature in this phase. After the application of LH power, the radiance of ECE is increased suddenly and the spectra are continuous from the fundamental electron cyclotron frequency to fifth harmonic electron cyclotron frequency corresponding to the plasma center. There are dips in second and third harmonic electron cyclotron frequencies corresponding to the plasma center. This spectra are the typical ECE from the supra-thermal electrons. The electron temperature can not be obtained because of the emission of supra-thermal electron. We found from the observcation of ECE spectrum that the signal of ECE can be interpreted as the electron temperature or the emission from the supra-thermal electron.

4.3.2 Thomson Scattering System

The electron temperature and density at six positions inside the JT-60 plasma are simultaneously measured by a multi-pulse Thomson scattering diagnostic system with spatical resolution of ~10 cm. The light source is a ruby laser which is operated by 10 J output at 0.25 Hz or 5 J output at 0.5 Hz. The laser beam goes vertically into the plasma from the bottom to the top and the scattered lights are observed through the inclined port of 30 degree relative to the horizontal plane.

Figure IX.4-8 shows the electron temperature profiles measured by the JT-60 Thomson scattering system in ohmically and NB heated hydrogen divertor dischages with q_{eff}=3.4 ~ 4.0 and $\bar{n}_e$=3×10^{19} m^{-3}. In this case the electron temperatures rose up with the increase in the

absorption power, their profile shapes remaining unchanged : $T_{e0}/\langle T_e \rangle$ =2.1 ~ 2.3.

Figure IX.4-9 shows the electron density profiles also measured by Thomson scattering system in ohmically, NB heated and ICRF heated hydrogen divertor dischages in the wide range of $\bar{n}_e$. The extremely flat profiles were observed, suggesting no inward flow in the peripheral region.

Figure IX.4-10 shows the gross electron energy confinement time $\tau^G_{E,e}(\equiv \frac{3}{2}\int n_e T_e dV/P_{abs})$ plotted against $P_{abs}/\bar{n}_e$. The $\tau^G_{E,e}$ was roughly in inverse proportion to $\sqrt{P_{abs}/\bar{n}_e}$, and this tendency was not changed for ohmically, NB heated, RF heated and combined heated (NB+RF) hydrogen divertor discharges.

4.4 Charge Exchange Neutral Particle and Ion Temperature Measurement

Neutral particle measurement system consists of an electrostatic energy analyser, E//B type mass-separated energy analyser and an active beam scattering apparatus. The energy spectrum of charge exchange neutrals is measured by two passive neutral particle analysers, and ion temperature in the central region is measured by the active beam scattering method. The active beam is injected perpendiculary to the plasma and the energy spectrum of particles scattered by plasma ions is measured with an E//B type mass-separated energy analyser. The maximum injection energy of the active beam is 200 keV with the maximum neutral beam equivalent current of 0.6 A, the divergence angle is 0.18° and the total pulse length is 0.1 s.

4.4.1 Energy spectra of charge-exchange neutrals in additionally heated plasma

JT-60 plasmas are additionally heated by NBI, ICRF and LHRF. The tail formation by ICRF and LHRF is expected to enhance the Q vale by the TCT effect. Typical energy spectra in ohmic and additional heating are shown in Fig. 1(a), (b). A high energy tail was produced by NBI and peaks with energy of a half and one third of injection energy were also observed. These peaks were not observed in some plasma conditions. When ICRF was applied to an NB-heated plasma, a tail with the energy higher than the neutral beam injection energy was formed. As shown in Fig. IX.4-11(a), in which averaged electron density was 2.2×10^{19} m^{-3} and NB power was 5.6 MW, ions injected with

60 keV were accelerated up to more than 120 keV by the application of 1.28 MW ICRF.

Figure IX.4-11(b) shows the energy spectrum in the combined heating with NB and LHRF. Averaged electron density was 2.2×10^{19} m^{-3}, plasma current was 1.5 MA, central troidal field was 4.5T. In this case, hydrogen beam and LHRF were applied to an Helium plasma. The powers of NB and LHRF were 21 MW and 3.6 MW, respectively. The injection energy of NB for full energy component was 70 keV and tail was observed up to 400 keV.

4.4.2 Central ion temperature

In recent experiments, a high ion-temperature mode was obtained by the high power, up to 22 MW neutral beam injection in a limiter configuration, in which plasma current was 1 - 1.5 MA and the central toroidal field was 4-4.5 T. The initial plasma of low density (n_e~0.7×10^{19} m^{-3}) was produced by only the prefilling of H_2 gas. The ion and electron temperatures of the initial plasma were 3 and 4 - 5 keV, respectively. The typical energy spectrum of scattered particles and converted one are shown in Fig. IX.4-12(a) and (b). In this case, the active beam was injected with energy of 190 keV. The ion temperature was obtained to be 11 keV with the fitting error of 2 keV. During the active beam injection, the averaged density was 2.7×10^{19} m^{-3} and the neutral beam power was 20 MW. The dependence of central ion temperatures on additional heating power normalized by averaged electron density is shown in Fig. IX.4-13. Central ion temperature increases with the additional heating power and central ion temperatures in the high ion temperature mode were 1 - 1.5 times higher than those in a limiter configuration.

4.5 Impurity measurement

In order to diagnose impurity behaviors in the plasma and to determine plasma parameters, such as ion temperature, various kinds of spectrometers are installed in the JT-60 device.

4.5.1 Impurity behavior

Many impurity lines were simultaneously measured by a flat field grazing incidence spectrometer composed of a holographic grating and multi-channel detector. The flat field grazing incidence spectrometer

(we call it a unit type spectrometer) and an array system of these spectrometers are shown in Fig.IX.4-14. As an example, spectra measured by the unit type spectrometer which wavelength range is 5 Å to 500 Å are shown in Fig. IX.4-15(a) and (b). Fig. (a) is the spectrum in the divertor configuration at 0.5 sec after the discharge started. It should be remarked that the configuration of the discharge was switched from limiter to divertor at 0.3 sec before the time. Molybdenum, titanium, oxygen and carbon lines were strongly observed. Fig. (b) is the spectrum at 5.5 sec. Oxygen and carbon lines are mainly observed. From these figures, it is expected that the impurity concentrations are reduced in the divertor configuration and the main impurities are oxygen, carbon and titanium.

Z_{eff} value is measured from the intensity of the visible bremsstrahlung (5232 Å) with the 0.5-m visible spectrometer. The concentrations of titanium ions were calculated from the intensity of the TiXX(259.3Å) line with the 3-m grazing incidence spectrometer. And the density ratio of oxygen to carbon ions was roughly estimated from the intensity ratio of the OVIII(18.97Å) to the CVI (33.74Å) line. In the JT-60 divertor plasmas, those results were as follows,

$$Z_{eff} \sim 1.5 \quad (\bar{n}_e \sim 3 \times 10^{19}\ m^{-3})$$

$$n_{Ti}/n_e \sim 10^{-5} \quad (\bar{n}_e \sim 3 \times 10^{19}\ m^{-3})$$

$$n_{oxygen}/n_{carbon} \geqq 0 - 20$$

Next, a diffusion coefficient D_A and a shape parameter C_v for titanium ions, which are related to a convective velocity $V_A = -C_V D_A (2r/a^2)$, were estimated from comparing the time evolutions of TiXXI, TiXX and TiXIII lines with the results of the 1-D impurity transport simulation. For the OH plasma, these values were obtained when the accidental titanium injection was occurred. For the NB heated plasma, these values were obtained by impurity injection with switching the configuration as divertor - limiter - divertor. The duration of the limiter configuration was 50 msec.

*OH plasma ($\bar{n}_e \sim 3 \times 10^{19}\ m^{-3}$)

$D_A \sim 1\ m^2/sec$, $C_V = 0$~1

*NB heated plasma ($\bar{n}_e \sim 4 \times 10^{19} m^{-3}$)

$D_A \sim 1\ m^2/sec\quad C_v=0 \sim 2$ (for co- and counter-injection)

4.5.2 Ion temperature measured by a crystal spectrometer

The ion temperatures were obtained from Doppler broadenings of TiXXI, XXII Kα line with a 2.5-m Johann type crystal spectrometer. The wavelength ranges are 2.5 Å ~ 2.75 Å for Ti Kα lines with Si(220) and 1.54A ~ 1.66A for Ni Kα lines with SiO_2 $(22\bar{4}\bar{3})$. The line profiles are detected with the multi-channel detector which is composed of a micro-channel plate, a PCD linear image sensor and an electric circuit.

X-ray spectra measured by the crystal spectrometer are shown in Fig. IX.4-16(a) and (b). The resonance line of TiXXI and satellite lines were observed in the figure (a) and TiXXII resonance lines in the figure (b). The time evolution of the ion temperature calcurated from the Doppler broadening of the TiXXII reasonance line is shown in Fig. IX.4-17. This is the high-Ti mode of the JT-60 with NB injection. In this figure, the value of ion temperature is about 9 keV on the NB heated plasma.

4.6 Radiation flux measurement

A pulse height analyzer using a high purity germanium is provided for the measurement of the spectrum of the soft X-ray radiation. The high purity germanium is mounted behind 0.025 mm thick beryllium window which isolates from vacuum environment of the JT-60. The germanium has an active area of about 80 mm^2 were is most sensitive to the X-ray with the energy between 2 and 100 keV. The titanium concentration measured by this system is showed in the Fig. IX.4-18. The titanium concentration is decreasing exponentially with the electron density and typically n_{Ti}/n_e is 1.0×10^{-5} at $n_e=3\times10^{19}\ m^{-3}$ in the divertor OH discharge.

The PIN diode array system measures the soft X-ray intensity emitted from the plasma in order to investigate the MHD oscillation the inversion radius, the electron thermal conductivity from the sawtooth oscillation and the electron temperature profile by the filter obsorption method.

The diode array consists of 30 PIN diodes and one pin-hole collimater. Each diode detects the soft X-ray from the pin-hole throught the beryllium foil. All signals of the diodes are recorded

by the mass data recorder at every 20 μsec time interval for a whole discharge.

The radiation profile are measured by the bolometer array, which consists of 15 bolometers mounted in the same toroidal location as the PIN diode array system, 4 bolometers viewing the main plasma vertically and 4 bolometers viewing the divertor plates. Change of the resistivity of the bolometer is measured by a bridge circuit in the preamplifier. The data of this system are recorded in the CAMAC transient recorders at 10 msec time interval for a whole discharge.

Figure IX.4-19 represents the radiation profile reconstructed by these bolometer arrays. The radiation is peaking toward the plasma outer region near the null point.

A hard X-ray pin-hole camera has been developed in order to measure the spatial distribution of the hard X-ray emission using a 2-dimensional array of $CdWO_4$ scintillators. The photons of the scintillation transfered via optical fiber are measured by a high sensitive TV camera used with an image intensifier. The signal of the camera is memorized in the VTR.

The particle recycling measurement system is constructed by the divertor H-alpha detecters and the four channel main plasma H-alpha detectors. The H-alpha detectors are the pin-type photo-diodes with the optical band-pass filter. The data of these detectors are recorded in the CAMAC transient recorders at 400 micro-sec time interval.

4.7 Peripheral Plasma Measurement

The surface temperature of divertor plates is monitored by the infrared TV system. The optical fiber is replaced by the light guide which consists of lenses and mirores so as to measure lower temperature. We are now able to measure about temperature higher than $100^{\circ}C$ by modified infrared TV system, ohterwise $400^{\circ}C$ by fiber. And we get more spatial resorution too.

The ON-line TV system observes plasma tangentially and inner struncture of vaccuum vessel. It has TV camera and hight speed 16 mm film camera (max. 4000 frames/sec). To observe plasma tangentially, we must use periscope because there is not good tangential port in JT-60. The head of periscope is made by Macore, one of ceramics, to avoid the force of eddy-current, and the rest is by SUS. In the TV

picture of the periscope, we can clearly recognize tiles of liners, limiters, NBI ports, diagnotic ports and the launcher of LHCD (lower hybrid current drive) wave. We can observe the grid of launcher of LHCD wave, so we can know which section of the launcher is arcing. When the launcher is arcing, we often recognize the increase of impurity by spectroscopic data. We can know whether divertor operation is successful or not by observing limiters. Sometimes limiters and liners shine even when we aimed divertor discharge. The limiter nearest from divertor (30° limiter) and the covers of bellows (bellows liner) shine most frequently. At disruption, we sometimes observe pieces of limiter or liner fly in the vacuum vessel. Expecially bellows liner melt and scatter piecies to plasma.

The Magnetic probe system measures plasma current, one-trun voltage, magnetic field and magnetic fluctuation. Zenkei system also measures equibrium field, so we concentrate to study MHD fluctuation. At normal OH plasma, fluctuation is too small to measure against electrical noise. When safety factor on the plasma surface is neary integer, or NBI or RF heating are applied, we can observe strong fluctuation.

Thermo couples measure temperature of limiter, liner and divertor plate. But thermo couples in those have too long time constant to measure time resoluted surface heat flux from plasma in discharge. We can know the increase of temperature between before discharge and after discharge.

The Peripheral spectrometer measures visible Bremsstrahlung and near ultra violet lines of impurities. It has rotating mirror, we can get space resolutional data. Its space resolutions is about 4.5 cm and 16 point. Sampling-time is 10 ms. If we can get spatial profile of Bremsstrahlung, we can calucurate Z_{eff}(squre mean ion charge). But we cannot get it because of three reason. One is that it has no view-line through the center of plasma. The nearest view-line to the center is about 25 cm below, so we cannot know whole profile of Z_{eff}. Other is that the refrection from wall is strong. The ratio of reflection is about one third in center view-line, and about hundred times in peripheral view-line. The ohter is the window is coated, so the absolute value of intensity of line is uncertain. Since reflection of UV light at the wall is small, we can get spacial profile of intensity of some line, for example line of titanium XVII,

by Abel inversion. But others do not have axial symmetry, so it cannot get spacial pofile, for example may oxigen lines. Asymmetry occures near divertor and limiter. Fig. IX.4-20 profile of forbiden line (383.44nm) of titanium XVII observed in the OH plasma. Fig. IX.4-21 is same line when ICRF wave was injected. We can know the profile was changed. We can observe virious behaviors of profile. In some cases, we observe the change of profile is lager and more sudden.

4.8 Data Processing system

Data processing system controls the diagnostics. It collects data from the diagnostics, processes and stores the data. The 50 million words of data (2 Bytes/word) are obtained by the diagnostics at one discharge, and some data are processed immediately and presented in the control room for the operators preparing next discharge. The major part of data is stored in the mass data recorder which has the recording capability of 30 input channels, 4 mega bits per second for each channel simultaneously. An intershot processor (ISP) has one set of large computers to store and process data so that the sophisticated analysis is rapidly performed using a large amount of the stored data. The CAMAC standard is used for the interface between the data processing system and the diagnostics. The CAMAC crates near the JT-60 machine are installed in a shield box (EMI locker) which is able to reduce the electromagnetic noise by 60 dB. The components which are especially weak against the magnetic field are protected by placing in an iron box to avoid any malfunction.

These crates are connected by optical serial highways to prevent electromagnetic noise interference, and to realize the high speed data transmission of 5 MBytes/sec.

The real-time processor (RTP) has a role to supply the ZENKEI control computer with realtime feedback data got from diagnostic systems via PU-A and FFTP modules.

The main activities of this period are the follows.

i) Establishment of graphic data display for overall diagnostic system within a shot interval.

A typical processing steam subordinated to ZENKEI sequence is shown in Fig. IX.4-22. After a normal end of plasma discharge,

CAMAC data aquisition, reconstruction, transfer to diagnostic DB, and graphic display processes are automatically activated to be completed, and wait for the next discharge. Fig.IX.4-23 shows the display example of obtained diagnostic data.

ii) Establishment of the diagnostic data management system by the Front End Processor (FEP) of the JAERI computer center, for general and quick use of the obtained data. These data are transftered from ISP to FEP shot by shot. Table IX.4-3 shows typical items of the diagnostic data. Item names represent the reconstructed data files, which are convenient for the usage in FEP, and correspond to the diognostic system A1 ~ A6. Data lengths are the reconstructed data amounts represented by Byte unit. The schematic diagram of the data management system is shown in Fig. IX.4-24. ISP is interfaced to FEP through disk stranges (DASD) which is used commonly by the both systems. In this figure, the cartridge tape library system (CTL) is introduced in order to preserve MDR data permanently, and to manage the obtained MDR data over about passed 1000 shots.

iii) Establishment of a realtime feedback control about the electron line density. The density detection is made by A-1-a FIR interferometer system, and the signal is processed to control the JT-60 Gas Injection system by ZENKEI, via A-7 RTP diagnostic data acquisition system. The Fig.IX.4-1 is an example of density evolution feedback by this function. It is seen that density was controled from 4 to 7 sec.
The schematic diagram of the RTP system is shown in Fig. IX.4-25.

Table IX. 2-1 Parameter ranges of NB heating

Parameters	Range
Configuration	Divertor/Limiter
I_p	1.0 - 2.0 MA
$\bar{n}_e$	$0.65\text{-}7.4\times10^{19}$ m^{-3}
B_T	1.9 - 4.5 T
q_{eff}	2.2 - 6.2
R_p	3.09 - 3.28 m
a_p	0.72 - 0.91 m
δ_{30}	0.2 - 5.1 cm
Plasma gas	H_2/He
P_{inj}	1 - 20 MW
E_{beam}	50 - 75 keV
$P_{co}/(P_{co}+P_{ctr})$	0 - 1

Table IX.4-1 Summary of the JT-60 diagnostic systems.

Plasma parameter	Sub-systems	
Electron Density	FIR Interferometer	3ch, CH_3OH Laser (118.8 μm)
	2-mm Interferometer	1ch
Electron Temperature	Fourier Transform Spectrometer	ECE
	Thomson Scattering System	Multi-pulse Ruby Laser (6ch)
Ion Temperature	CX Particle Analyser	E = 0.1 ∿ 110 keV, E//B
	Active Beam Scattering System	200 keV - 3.5 A, He, θ = 7°
	CX Recombination Spectrometer	(on Active Beam)
	Neutron Counter	E = 1.5 ∿ 4 MeV
Impurity	VUV Spectrometer (2)	0.2 ∿ 500 Å, Holographic Grating
	Doppler Spectrometer	5 ∿ 9000 Å
	Crystal Spectrometer	0.6 ∿ 2.7 Å
	Visible Spectrometer I	2000 ∿ 7000 Å, Spectrograph, Photo-Multiplier
	Visible Spectrometer II	The same as above, Rotating Mirror
	Grazing Incidence Spectrometer	10 ∿ 1300 Å
Radiation Flux	SX High Speed PHA	1ch
	PIN Diode Array	17ch
	Bolometer Array	16ch
	HX Detector	
Peripheral Plasma	Visible TV	3ch
	Magnetic Probes, Thermocouples	61ch
	Hα Diode Array	4ch, 3ch, 1ch
Divertor Plasma	FIR Interferometer	2ch, CH_3OH Laser
	Visible Spectrometer	2ch
	VUV Spectrometer	2 ∿ 1200 Å, Holographic Grating
	Hα Diode Array	4ch
	Bolometer Array	4ch
	Thermocouple Array	(on Divertor Plate)
	IR & Visible TV	2ch

Table IX.4-2 Comparison of the electron temperature measured by ECE system and Thomson scattering system.

r/[m]	T^{TS}/T^{ECE}
-0.22	1.013 ± 0.126
0	1.073 ± 0.109
0.23	1.030 ± 0.134
0.45	1.066 ± 0.156
0.65	1.026 ± 0.191
0.83	0.418 ± 0.190

Table IX.4-3 Item list of the diagnostic data transferred from ISP to FEP.

SHOT-NUMBER = 3992 TYPE = 11

DATE = 87.03.27 TIME = 18:04:04

DATA SEQNO.	ITEM NAME	USE/ NOUSE	SHOT STATE	DATA LENGTH
I001	1A4	USE	NOW	160514
I002	1A5	USE	NOW	120514
I003	1A6	USE	NOW	20514
I004	1B1	NOUSE	NOW	0
I005	2A1	USE	LATE	142002
I006	2A2	USE	LATE	4610
I007	2A3	USE	LATE	1234
I008	2C1	NOUSE	NOW	0
I009	2C2	NOUSE	NOW	0
I010	3A1	USE	NOW	389314
I011	3A2	USE	NOW	8322
I012	3B1	USE	NOW	260462
I013	3B2	USE	NOW	8322
I014	4E1	USE	NOW	5254
I015	4F1	NOUSE	NOW	0
I016	5B1	USE	NOW	524634
I017	5B2	USE	NOW	524634
I018	5B3	USE	NOW	65882
I019	5C1	USE	NOW	524634
I020	5D1	USE	NOW	41306
I021	6D1	USE	NOW	193174
I022	6C1	USE	LATE	246090
I023	6C2	USE	LATE	206254
I024	6C3	USE	LATE	246090
I025	6C4	USE	LATE	5494
I026	6C5	USE	LATE	16554
I027	4D1	USE	NOW	22110
I028	4A1	USE	NOW	22110
I029	5A1	USE	NOW	524634
I030	5A2	USE	NOW	590
I031	4C1	USE	LATE	838
I032	4C2	USE	LATE	2450

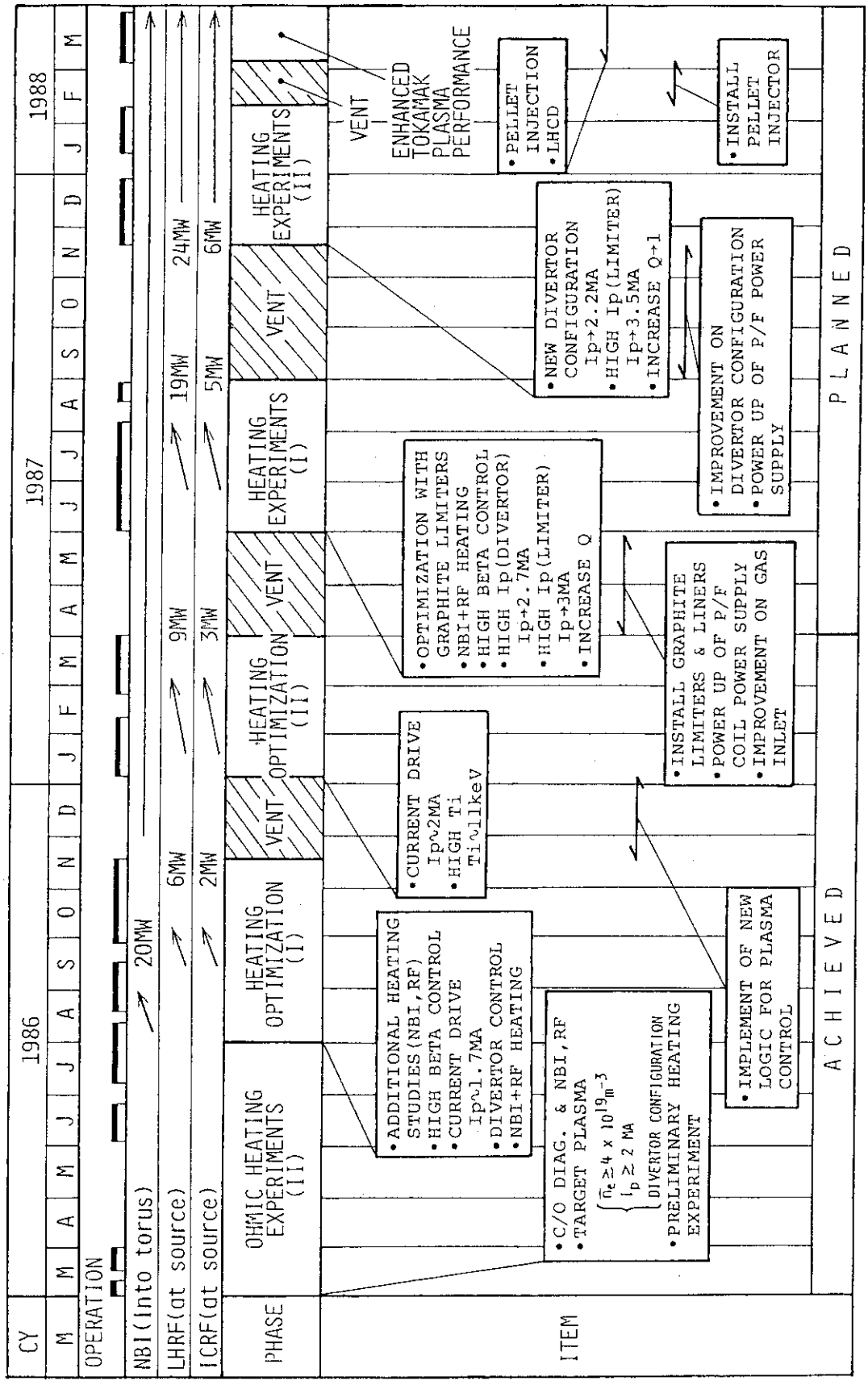

Fig. IX.1-1 Experimental plan of JT-60.

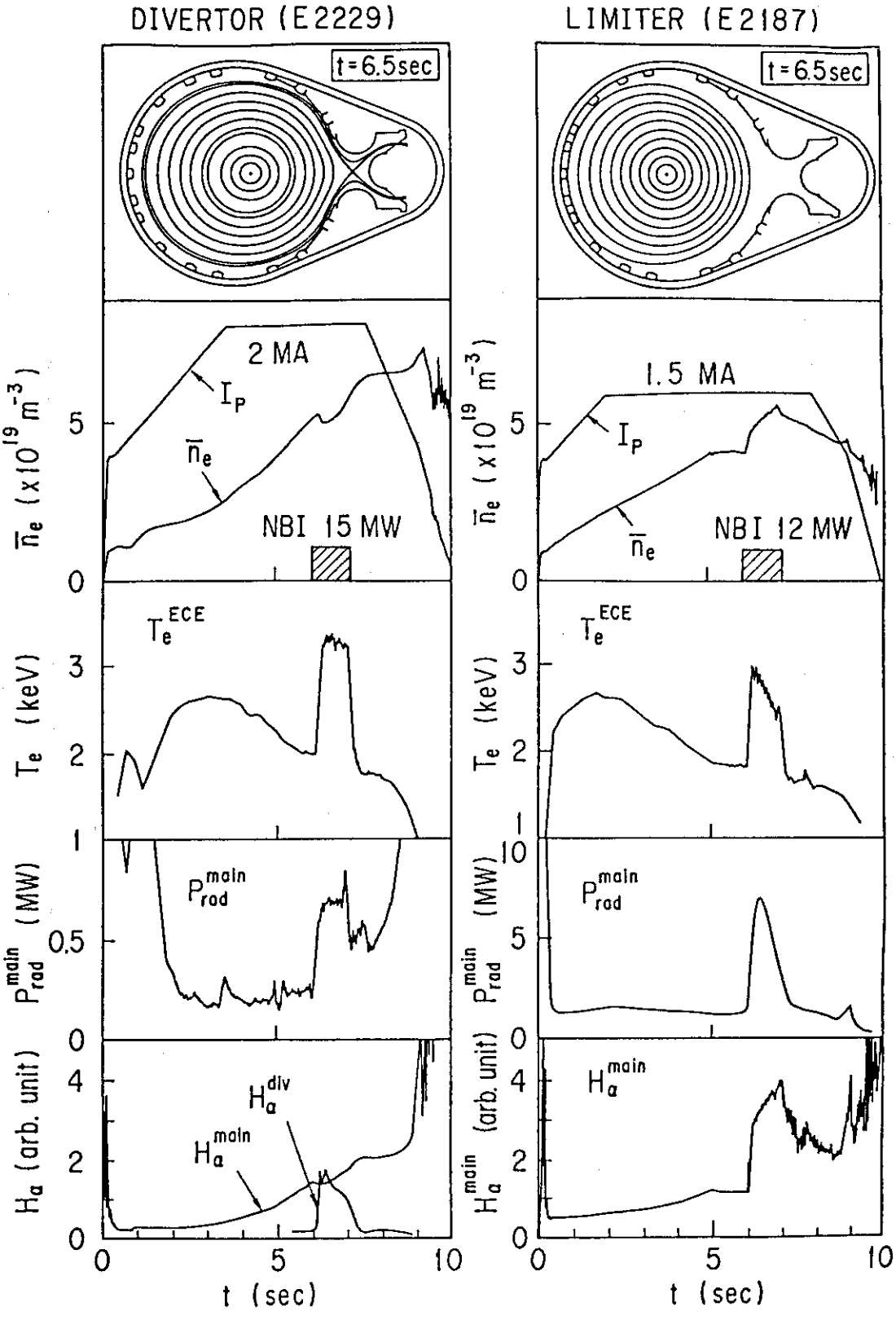

Fig. IX.2-1 Typical discharge waveforms with NB heating in the divertor and limiter configurations.

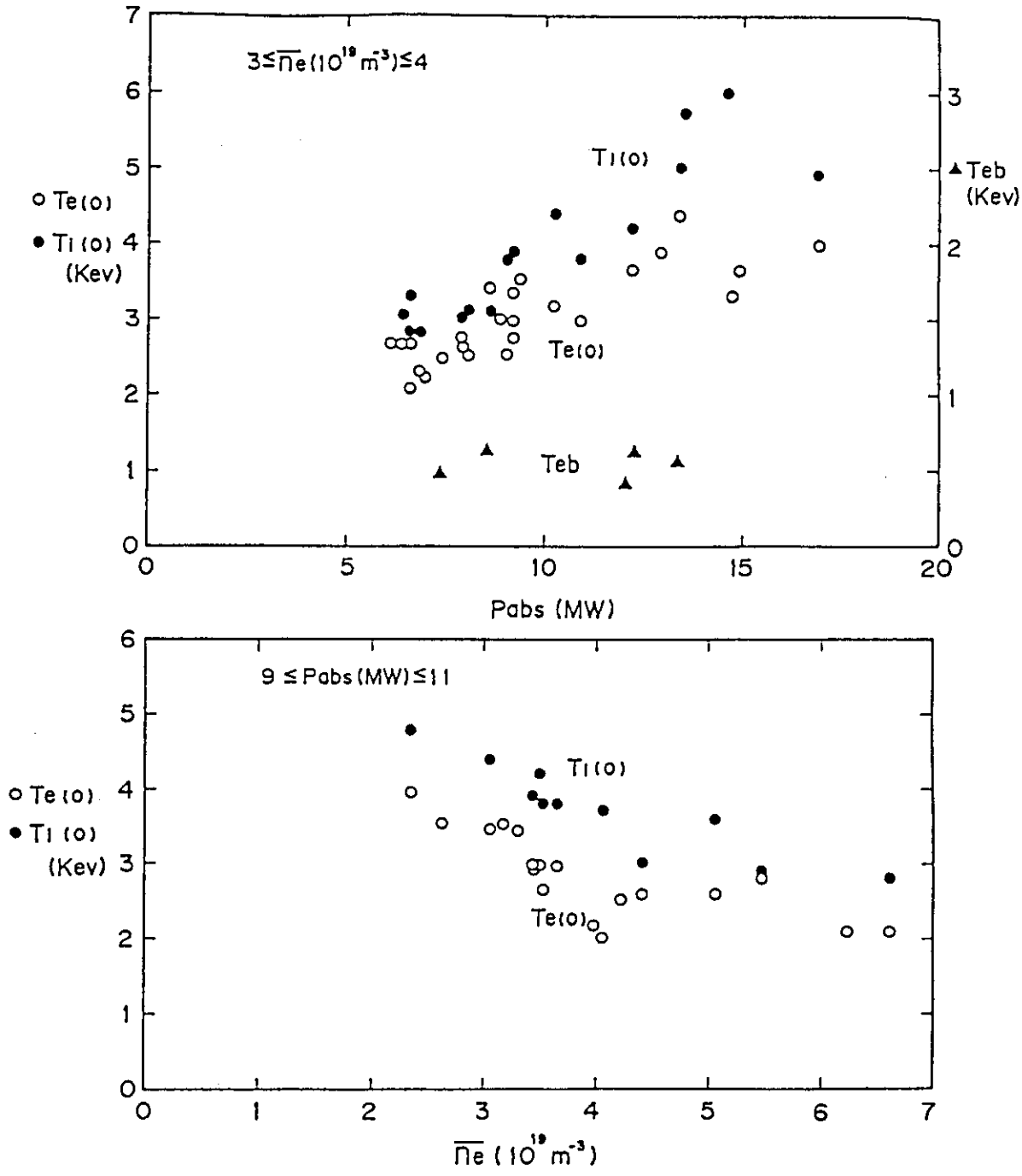

Fig. IX.2-2 Central and boundary temperatures of NB heated plasmas.

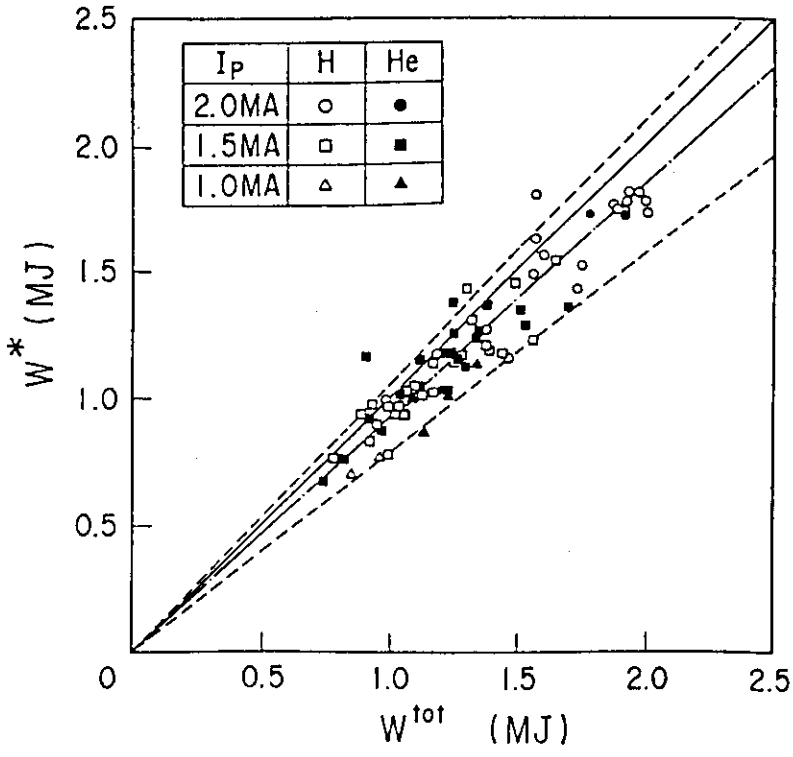

Fig. IX.2-3 Comparison of plasma stored energy evaluated from magnetics (W^*) and kinetics (W^{tot}).

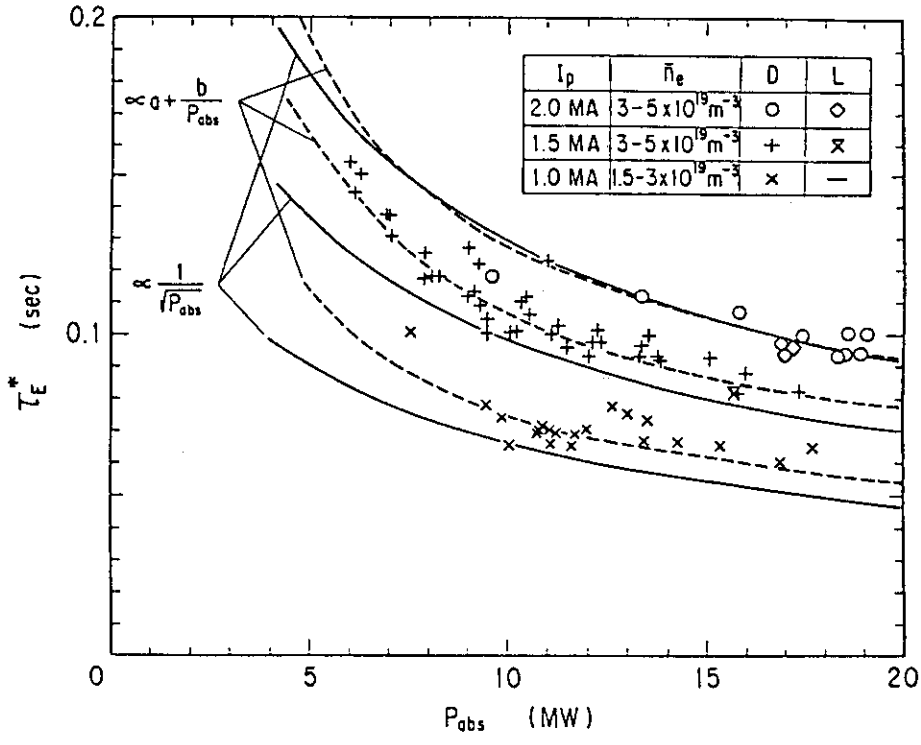

Fig. IX.2-4 Heating power dependence of energy confinement time in beam heated plasmas.

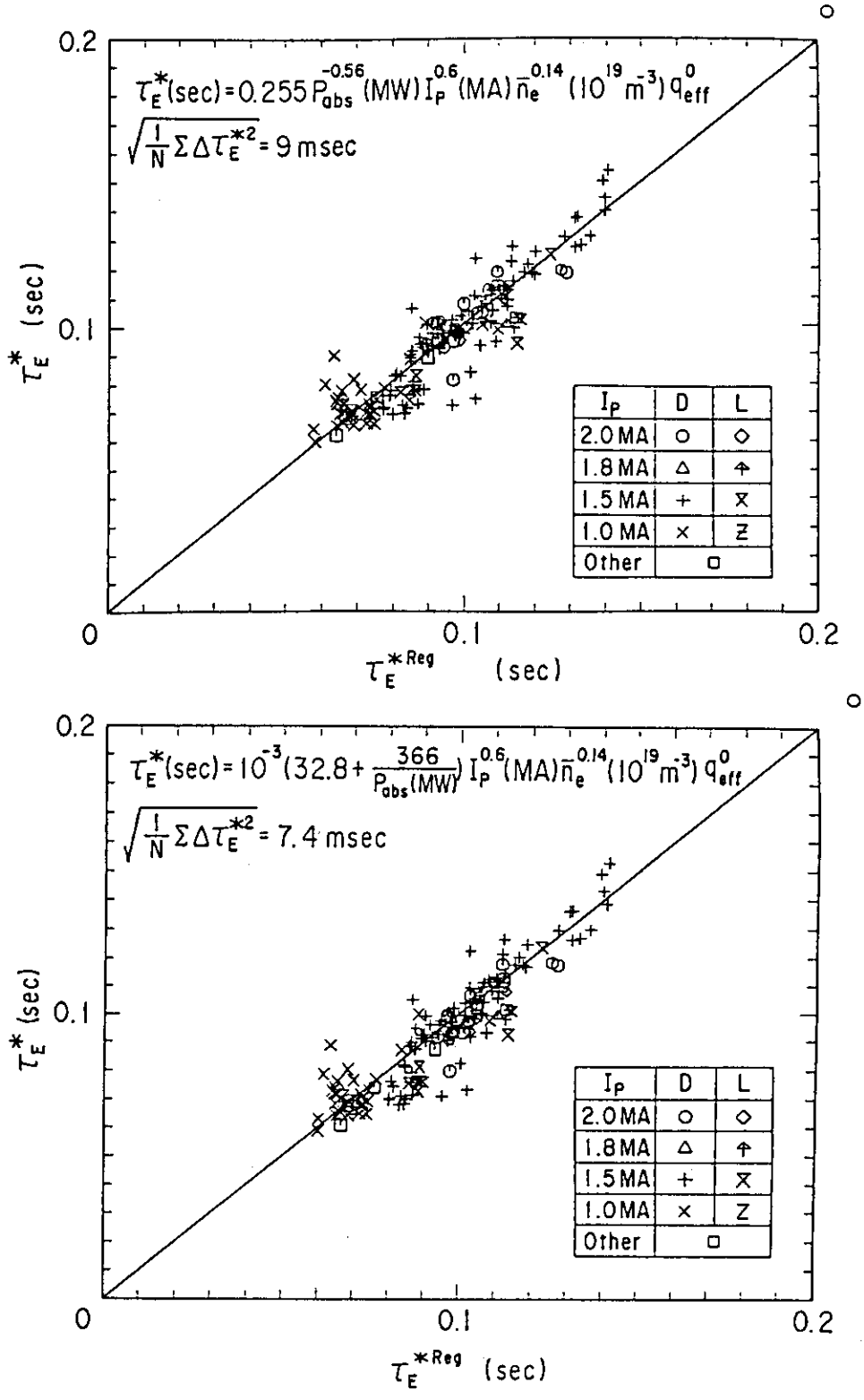

Fig. IX.2-5 Energy confinement time scalings of beam heated divertor plasmas in JT-60.

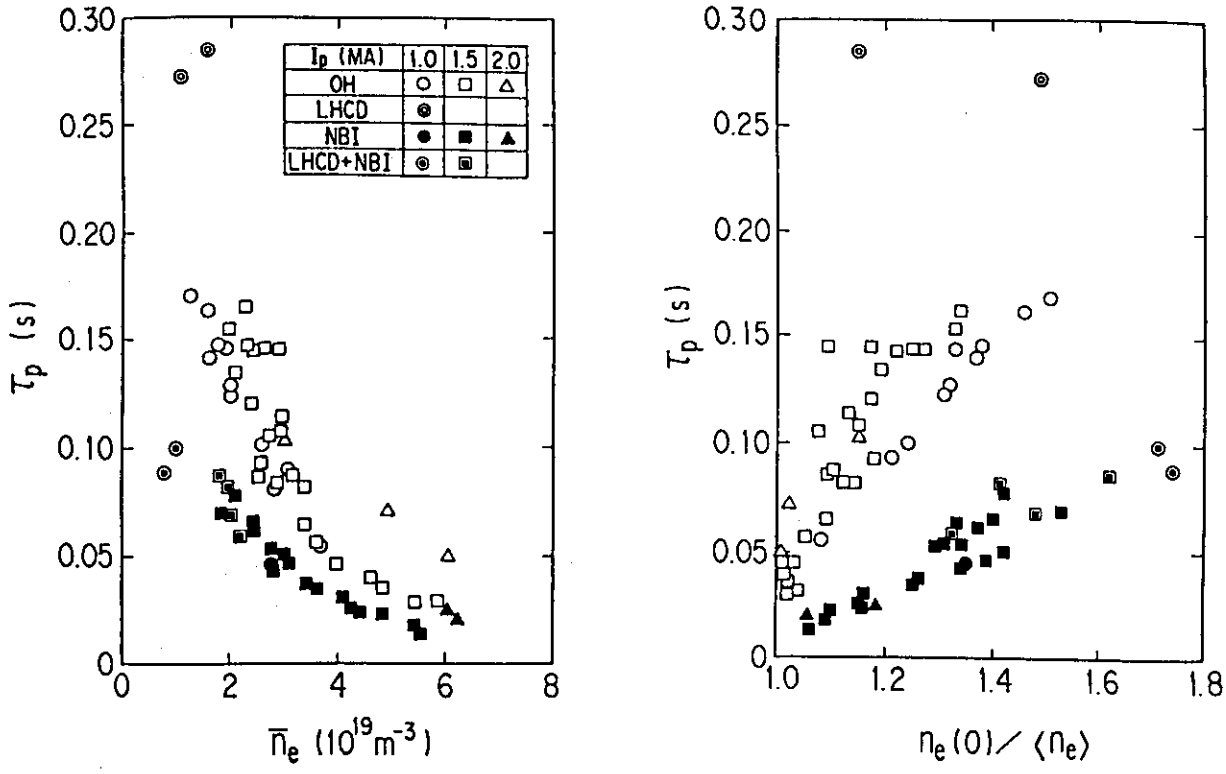

Fig. IX.2-6 Particle confinement time against the line averaged electron density and peakedness of the electron density profile.

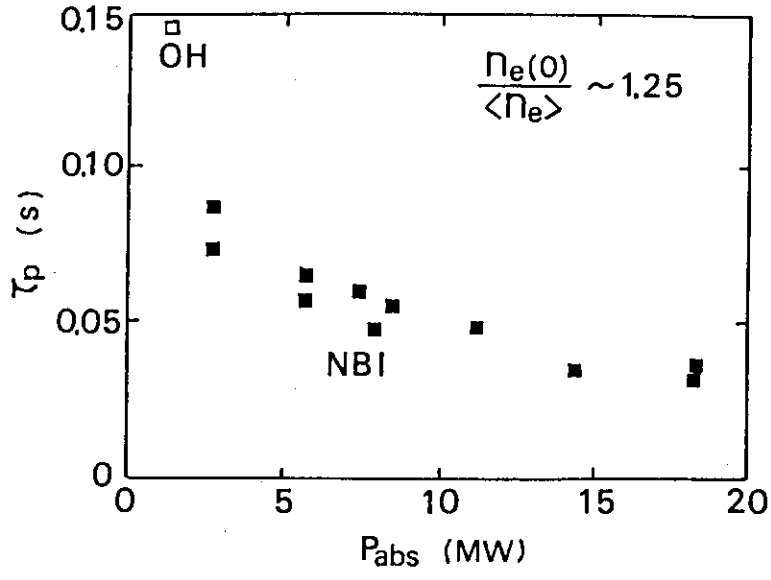

Fig. IX.2-7 Particle confinement time as a function of heating power with nearly the same electron density peakedness.

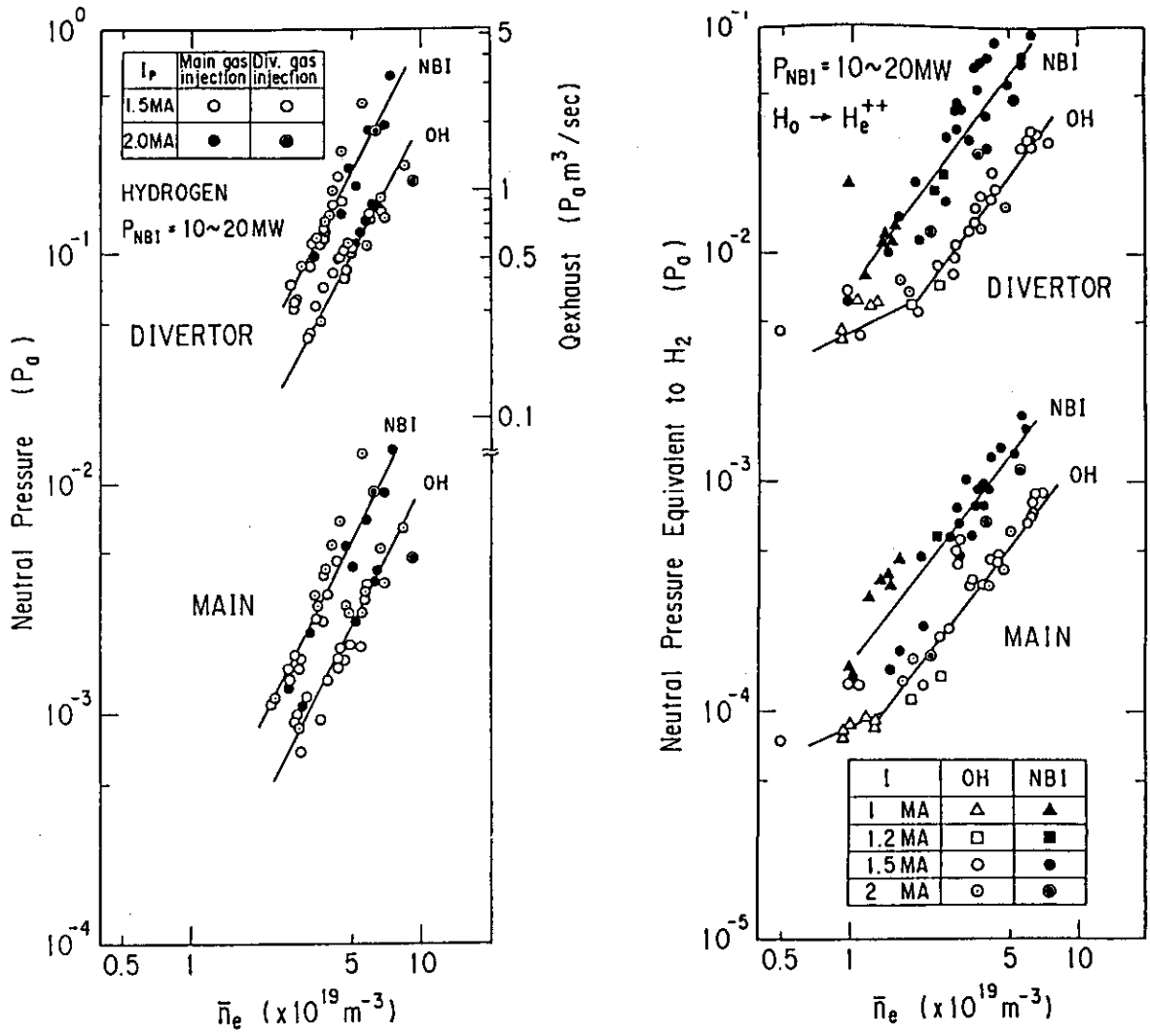

Fig. IX.2-8 H_2 and He neutral pressures measured in the main and divertor chambers against $\bar{n}_e$ for OH and NBI plasmas.

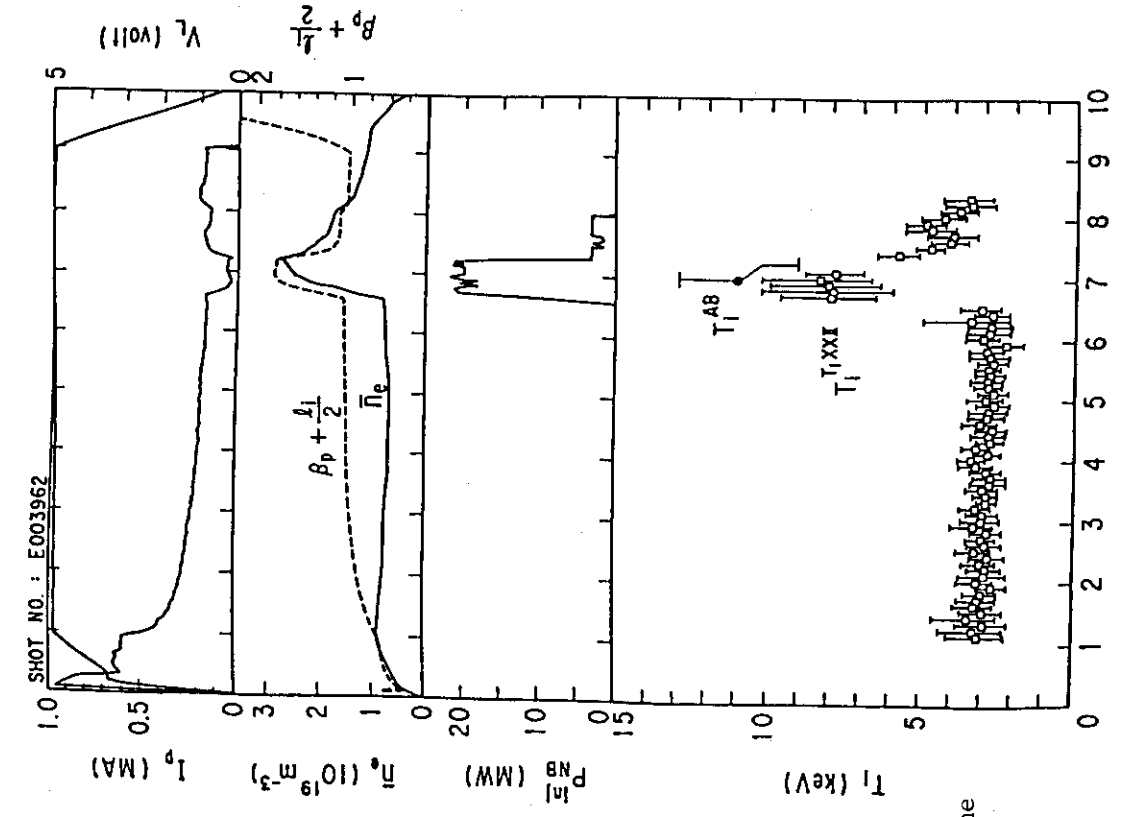

Fig. IX.2-10 Discharge waveforms and time evolutions of T_i^{XXII} and T_i^{AB} (central ion temperature measured by an active beam) in the hot ion temperature mode.

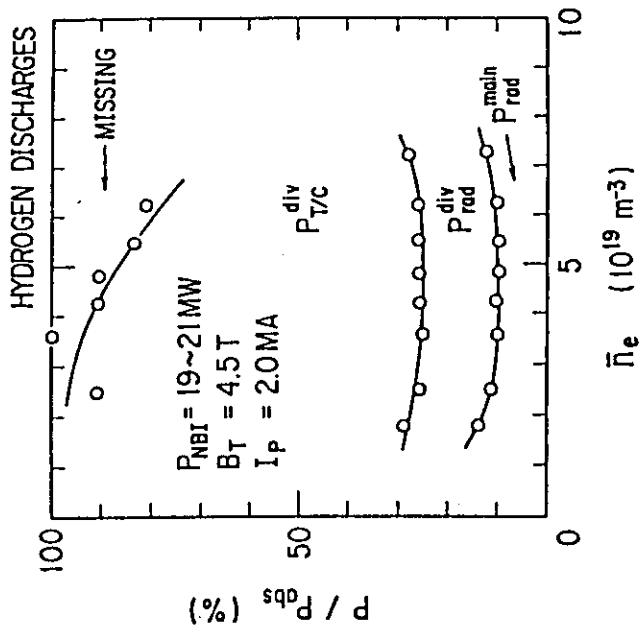

Fig. IX.2-9 Power balance of NB heated plasmas in the divertor configuration.

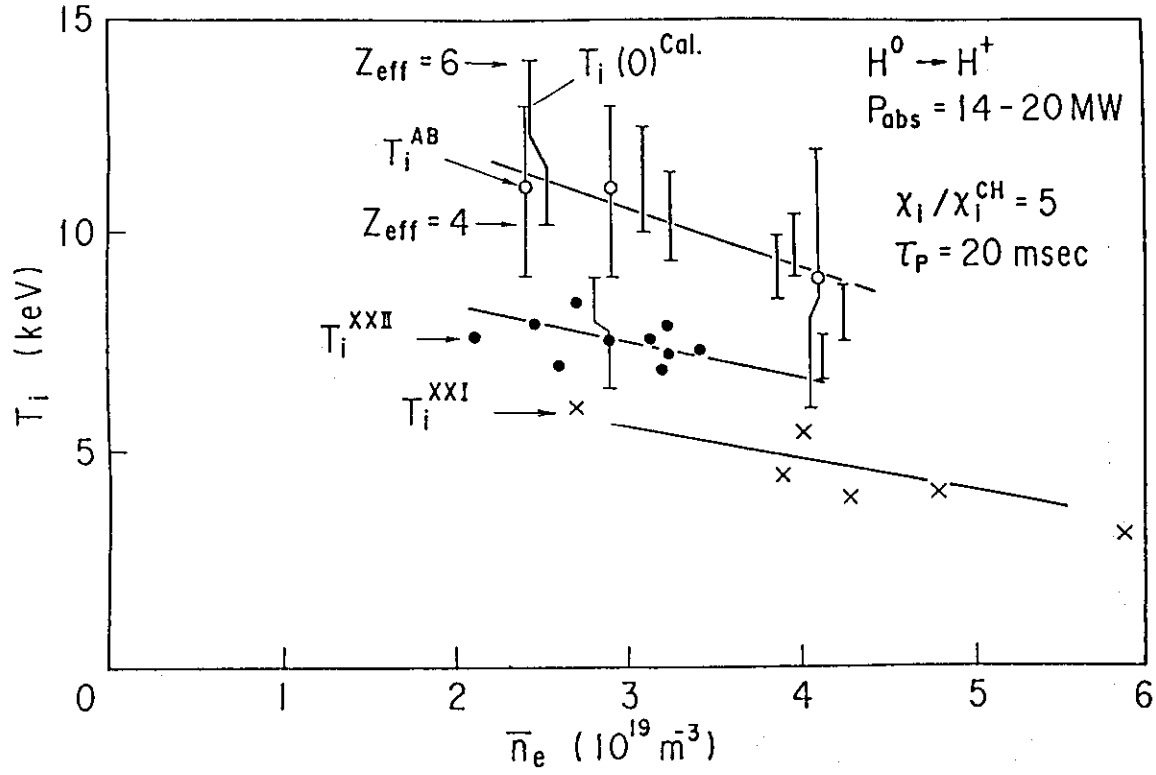

Fig. IX.2-11 Density dependence of the ion temperature. T_i^{CAL} is calculated temperature by a transport code assuming $\chi_i = 5\chi_i^{CH}$ and $Z_{eff} = 4 \sim 6$ with oxygen as the dominant impurity.

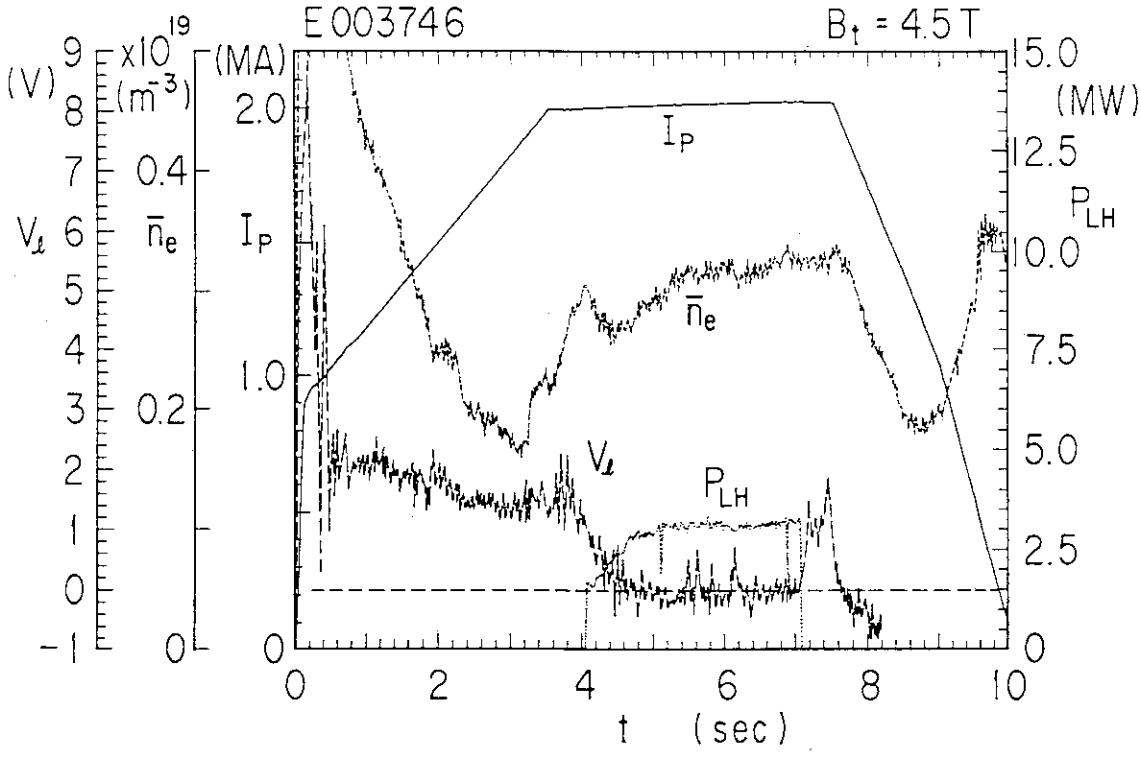

Fig. IX.2-12 Time evolution of I_p, $\bar{n}_e$, one turn voltage and LHRF power of demonstration shot of I_{RF}=2MA using the LHCD($\Delta\phi$=90°) and LHH launchers($\Delta\phi$=120°).

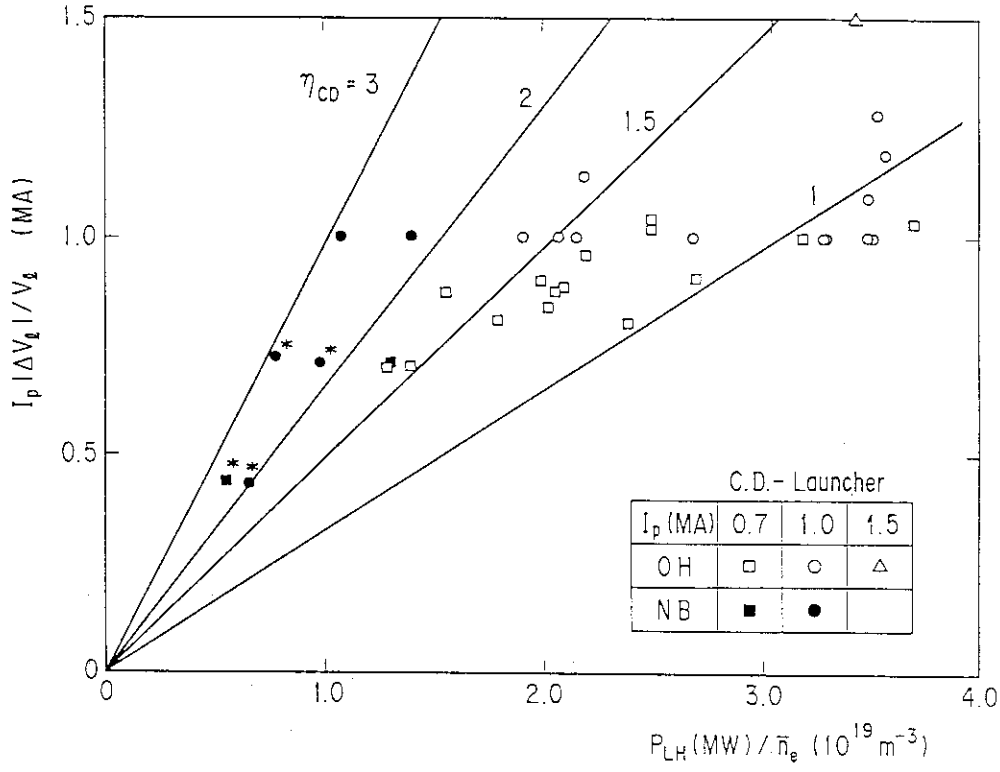

Fig. IX.2-13 Current drive efficiency of CD-launcher. LHCD shot and LHCD+NBI shot are indicated with open notation and closed notation, respectively. The data shown in the figure is $|\Delta V_1/V_1|>1$. except the data shown by (*).

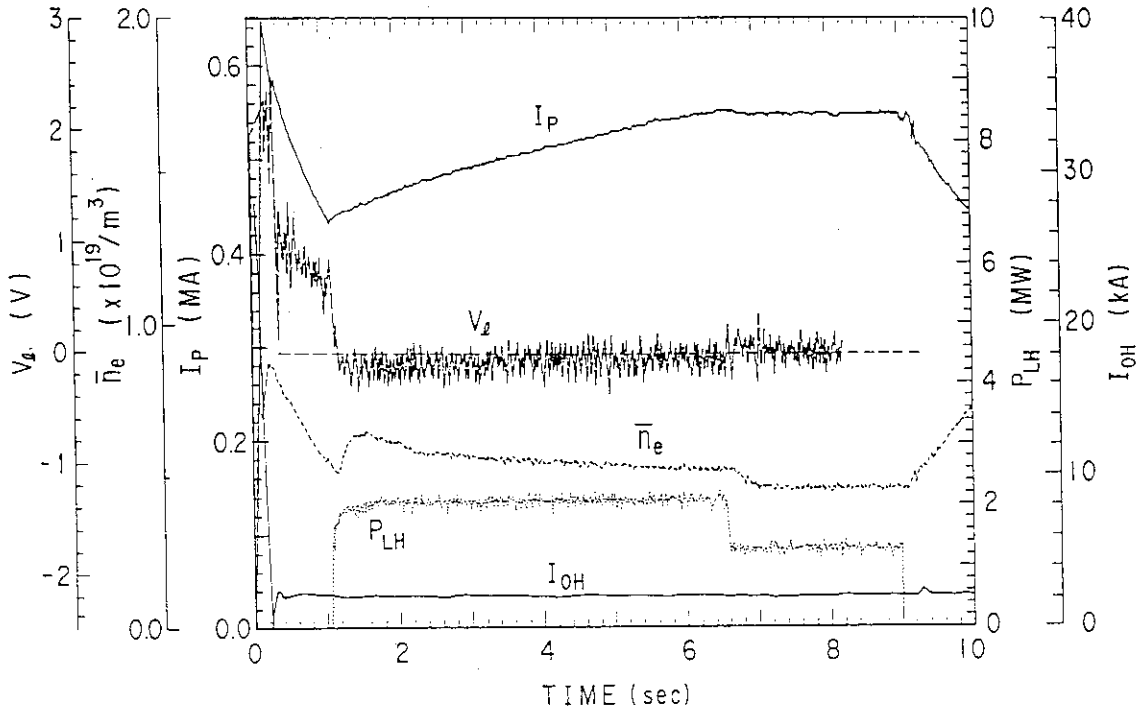

Fig. IX.2-14 Current ramp up without any assistance from the OH-coil. current (I_{OH}) is controlled to be constant during LHCD.

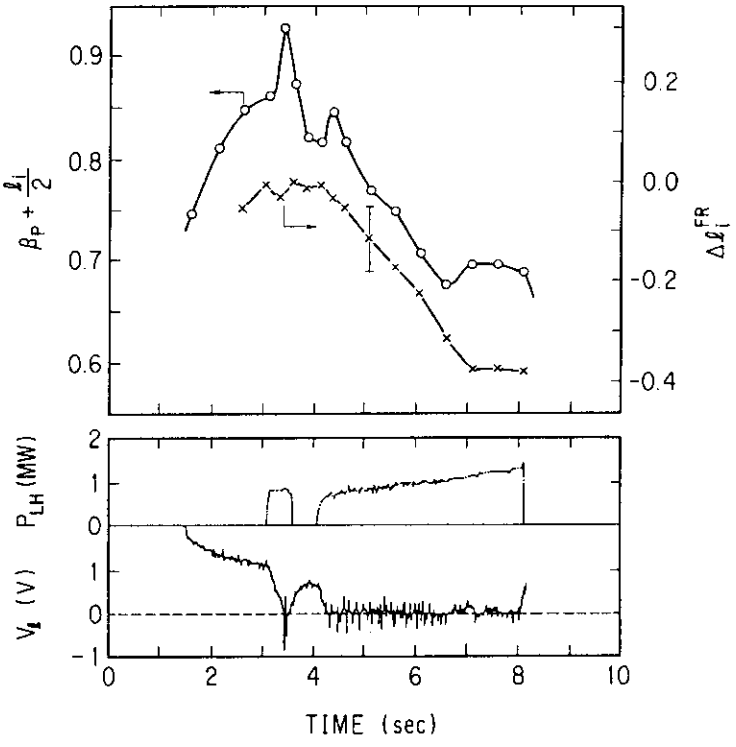

Fig. IX.2-15 Time evolution of $\beta_p+1_i/2$ obtained from magnetics and Δ_i obtained from Faraday rotation. Completely noninductive current of I_p=1 MA is driven by LHRF using CD-launcher.

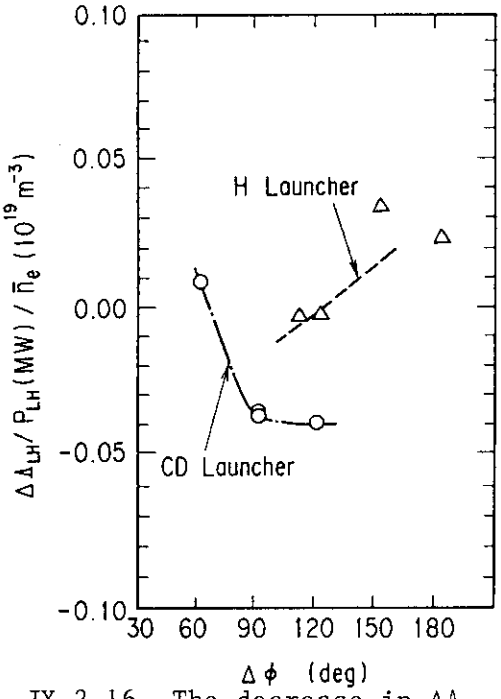

Fig. IX.2-16 The decrease in $\Delta\Lambda_{LH}$ ($\Lambda_{\text{before LH}}-\Lambda_{\text{during LH}}$) normalized by the LHRF power and line averaged density against phase difference of the launcher.

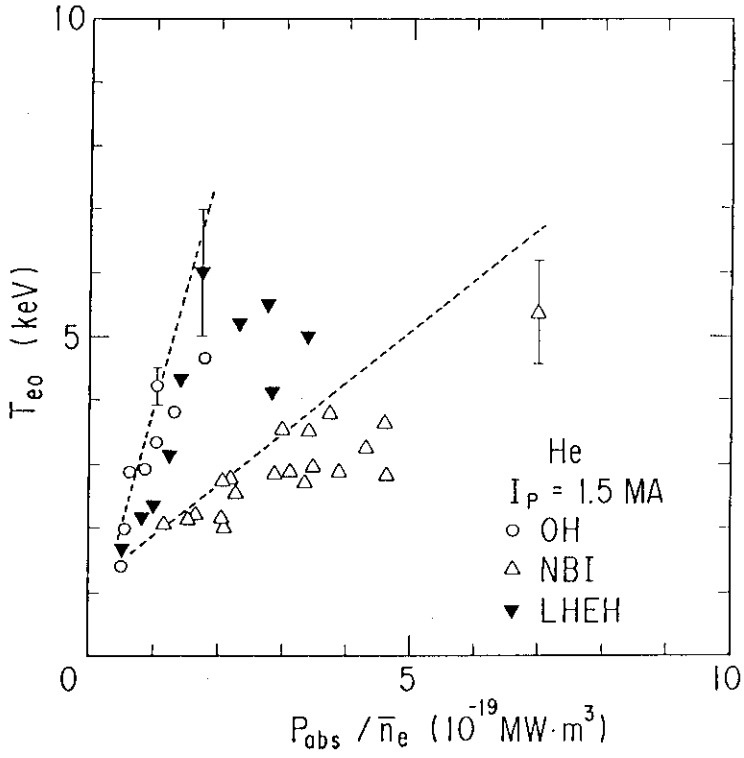

Fig. IX.2-17 Power dependence of Central electron temperature in various heating methods.

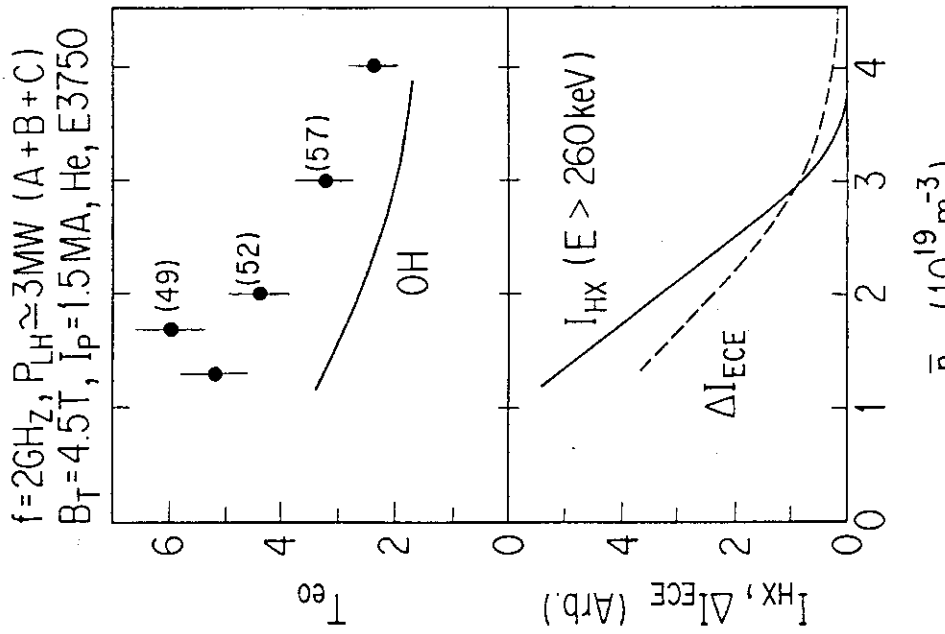

Fig. IX.2-19 Density dependence of T_{eo}, hard X-ray signal and incremental ECE signal at $3f_{ce}$ during LHRF injection. I_p=1.5 MA. He discharge.

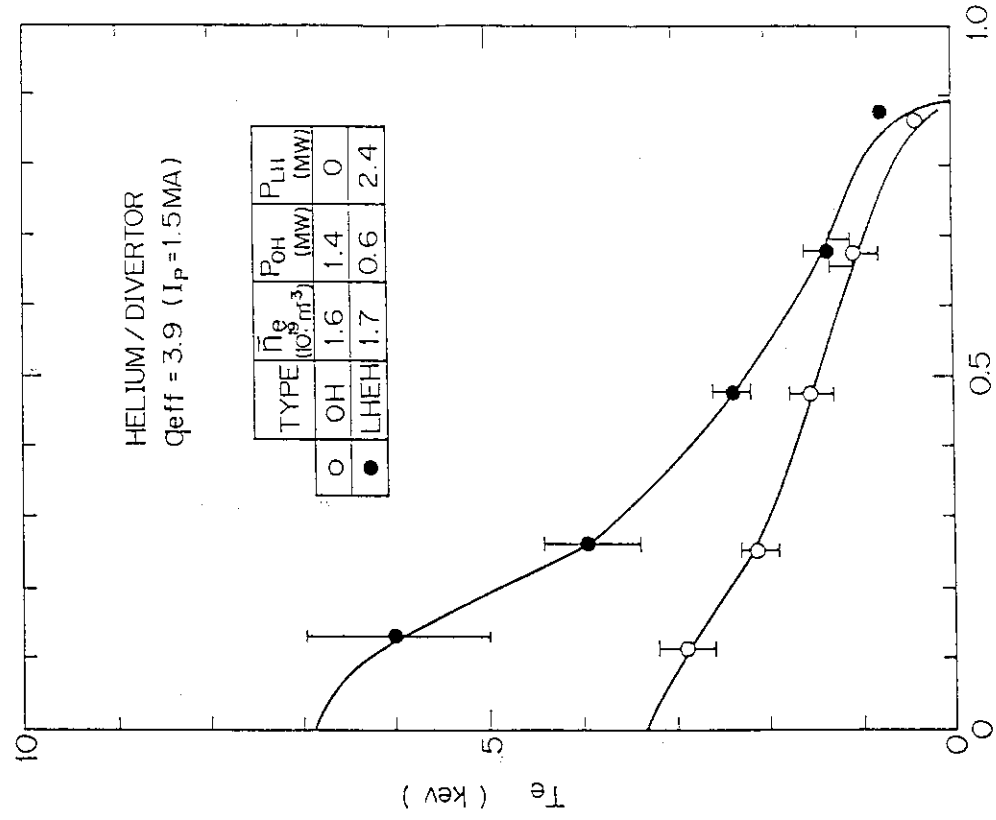

Fig. IX.2-18 Radial profile of electron temperature with $T_{eo} \simeq$ 6keV, and that of ohmic discharge.

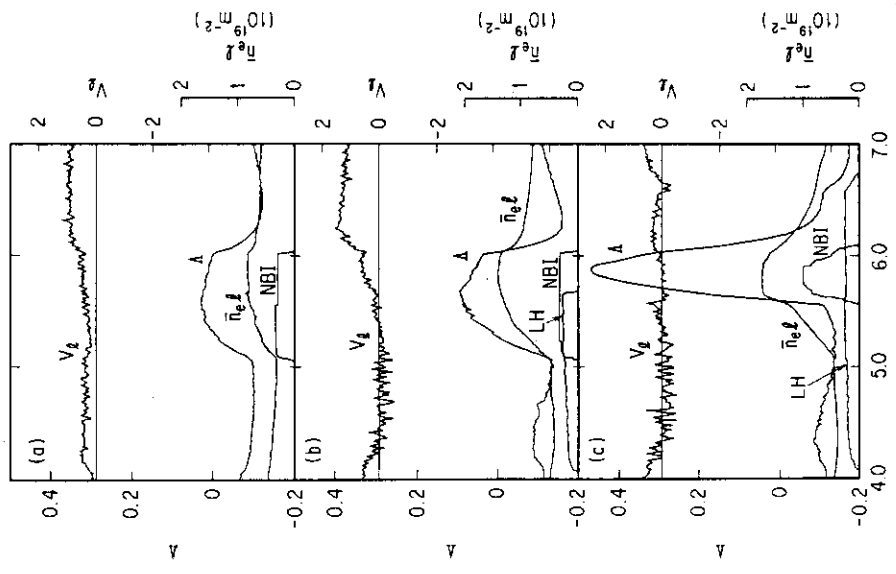

Fig. IX.2-21 Time evolution of the loop voltage V_ℓ, the Shafranov lambda Λ, the line integrated electron density $n_e\ell$, and the LH and NB pulses. (a) is the case of NB alone (b) and (c) are LHCD+NB. B_T= 4T, I_p=1MA, H_e plasma.

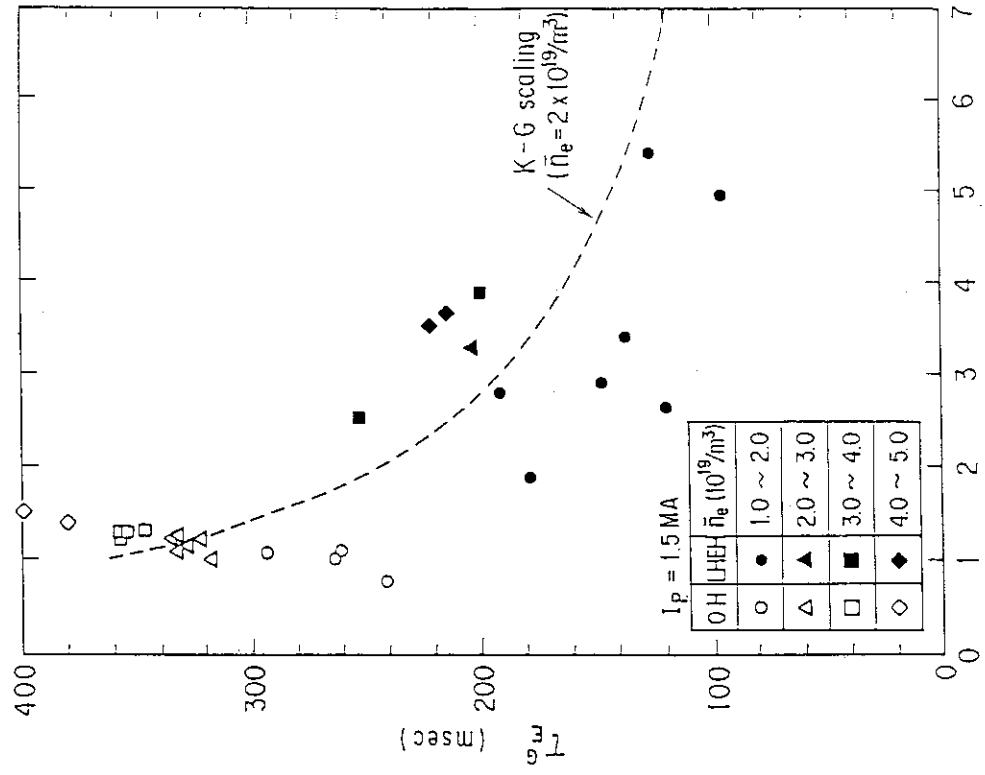

Fig. IX.2-20 Power dependence of global confinement time of LHEH.

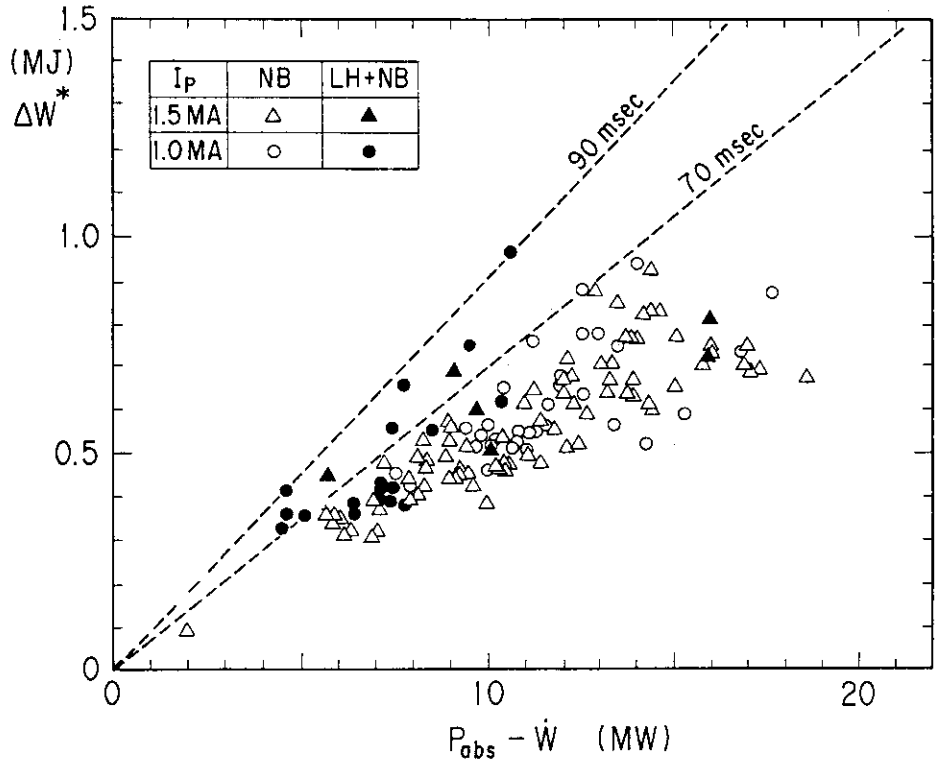

Fig. IX.2-22 The incremental stored energy ΔW against the effective absorption power $P_{abs}-\dot{W}$ for NB alone (open symbols) and for LHCD+NB (closed symbols).

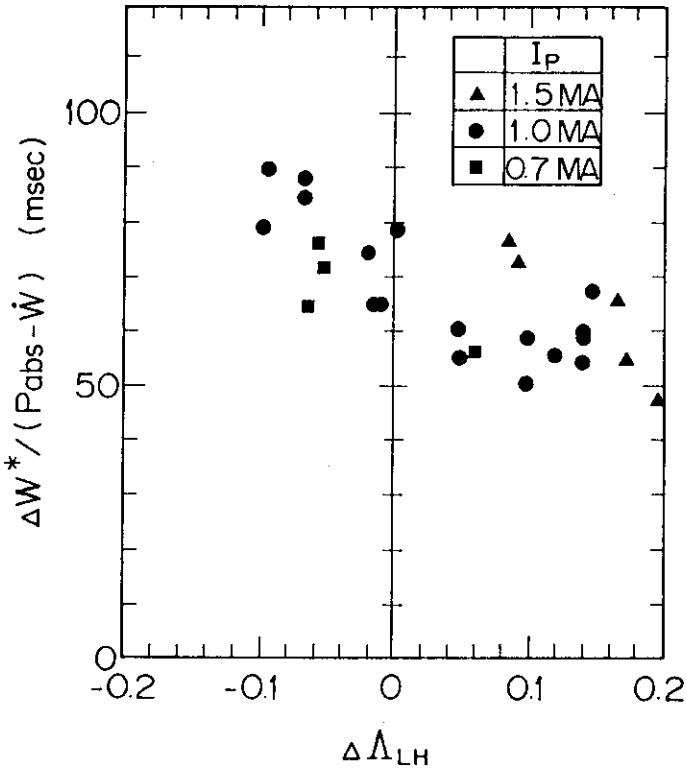

Fig. IX.2-23 $\tau_E^{LNC} \equiv \Delta W/(P_{abs}-\dot{W})$ against the change of the Shafranov lambda during LHCD alone $\Delta\Lambda_{LH}$.

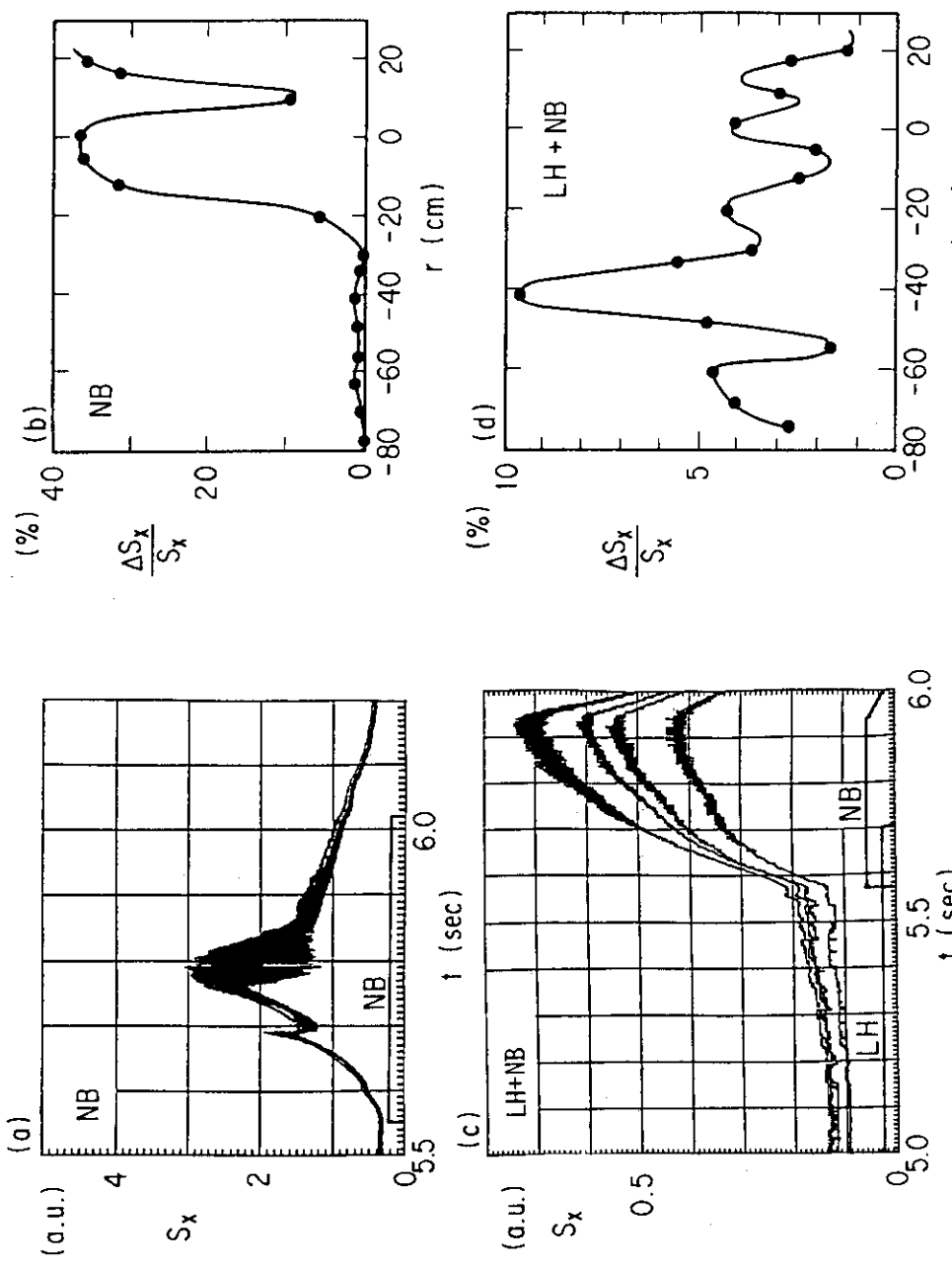

Fig. IX.2-24 Comparison of the fluctuation of soft x-ray signal S_x for NB alone (a, b) and for LHCD+NB (c, d). $\bar{n}_e=0.7\times10^{19}$ m^{-3} and 1.4×10^{19} m^{-3} LHCD+NB and NB, respectively, $B_T=4T$, $I_p=1MA$.

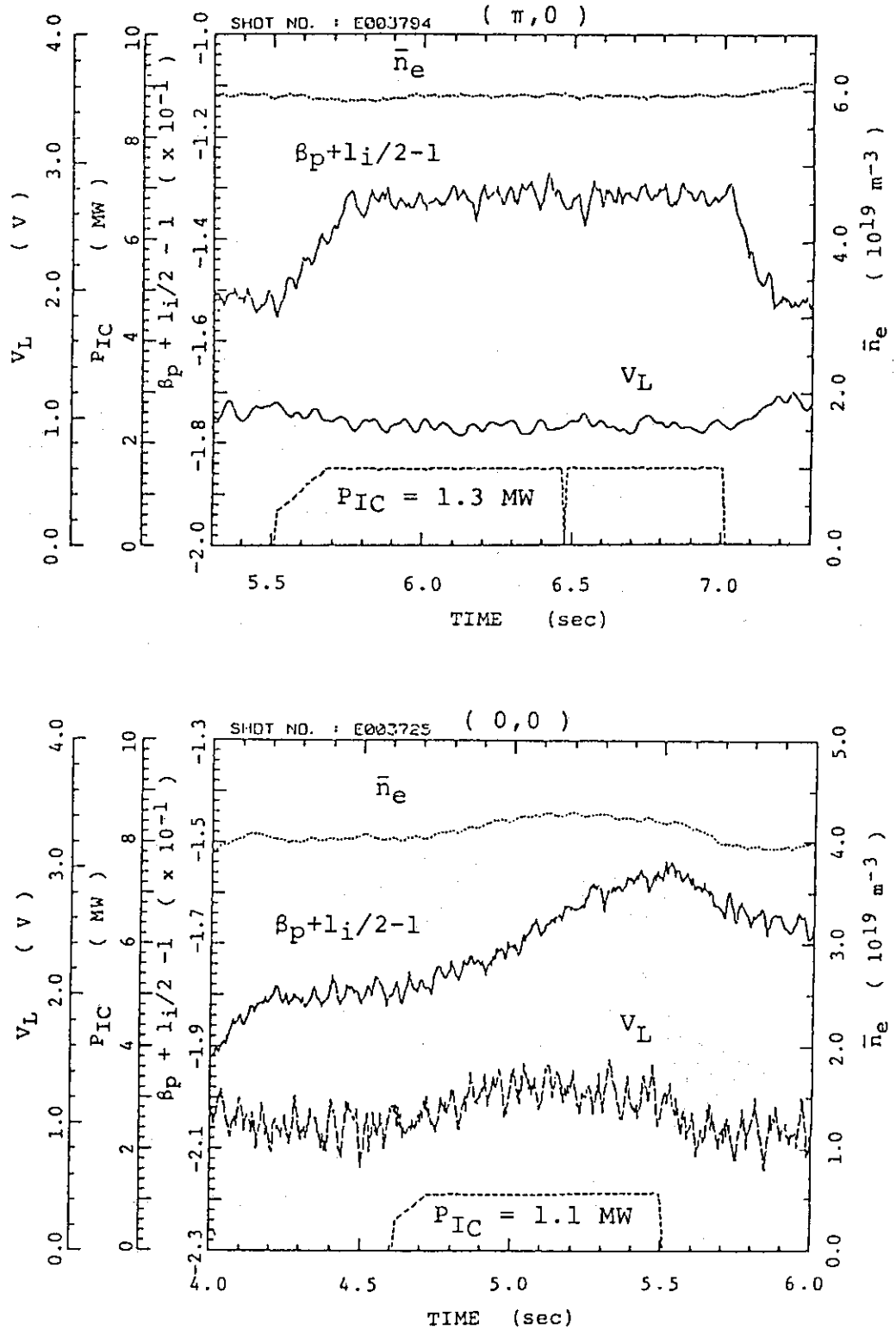

Fig. IX.2-25 Time evolution of $\bar{n}_e$, $\beta_p+l_i/2$ and V_L with (a) $(\pi,0)$ mode and (b) $(0,0)$ mode. (I_p=1.5 MA, B_T=4 T, divertor)

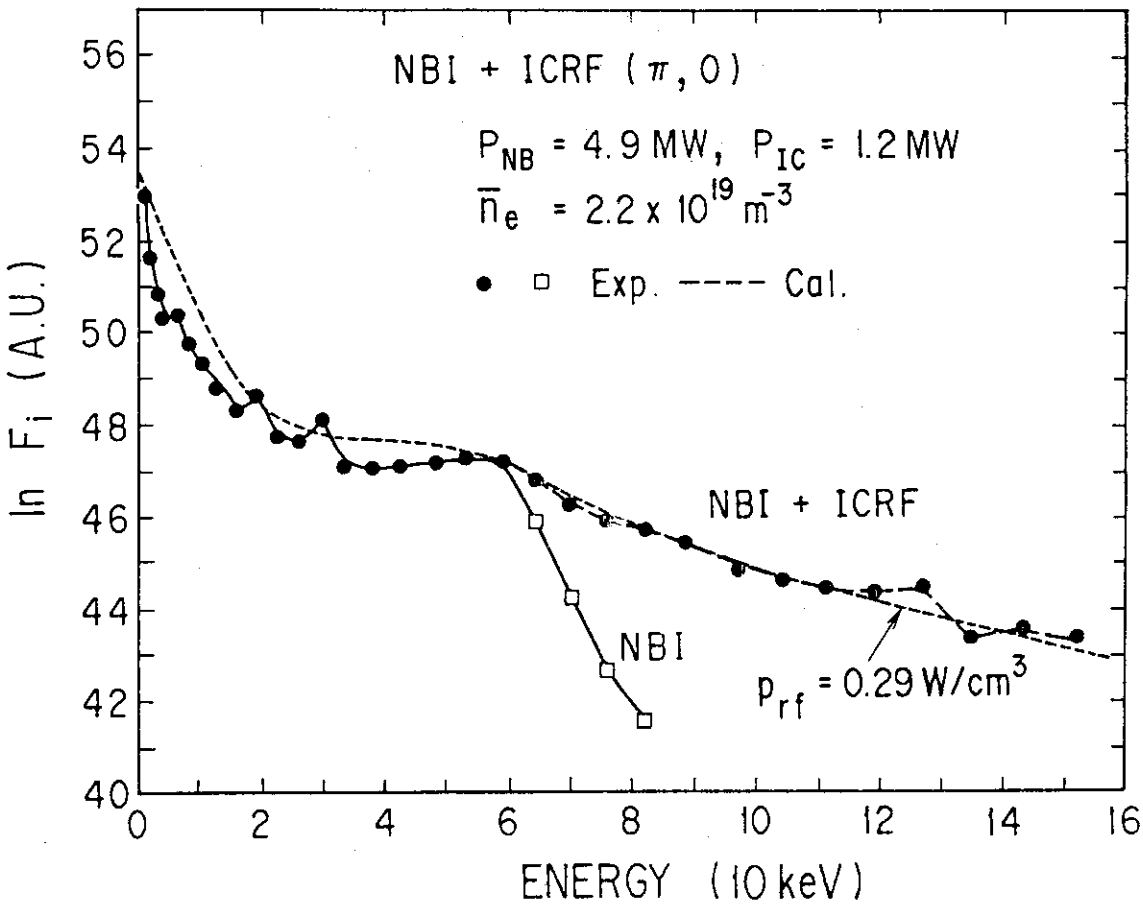

Fig. IX.2-26 Charge exchange neutral energy spectra during NBI+ICRF and NBI alone. The dotted line is simulation by the Fokker-Planck calculation. (I_p=1.5 MA, B_T=4 T, divertor)

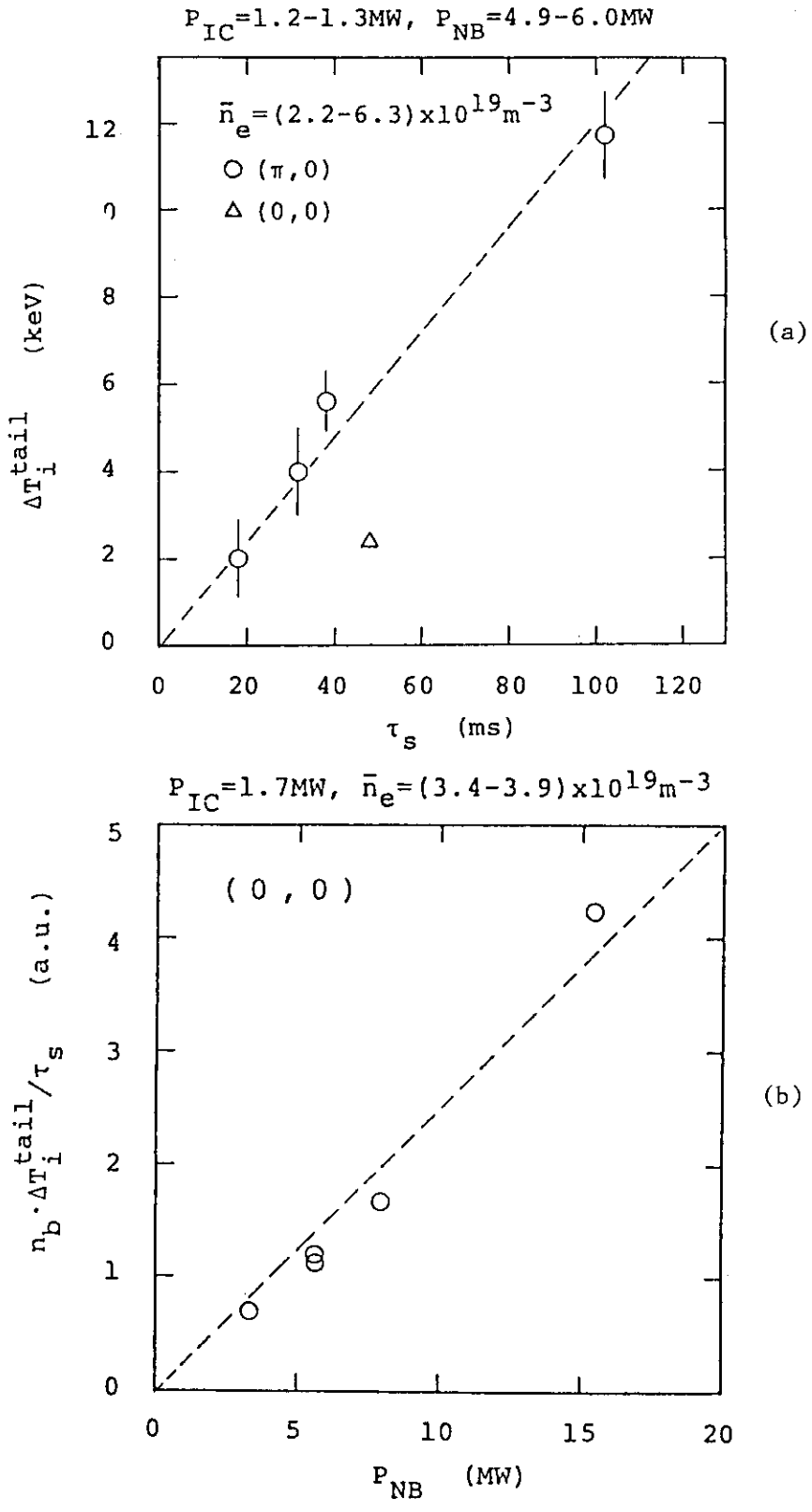

Fig. IX.2-27 (a) ΔT_i^{tail} versus τ_s ($\bar{n}_e$-scan), (b) $n_b \cdot \Delta T_i^{tail}/\tau_s$ ($\propto P_{rf}$) versus P_{NB}. (I_p^i = 1.5 MA, B_T = 4 T, divertor)

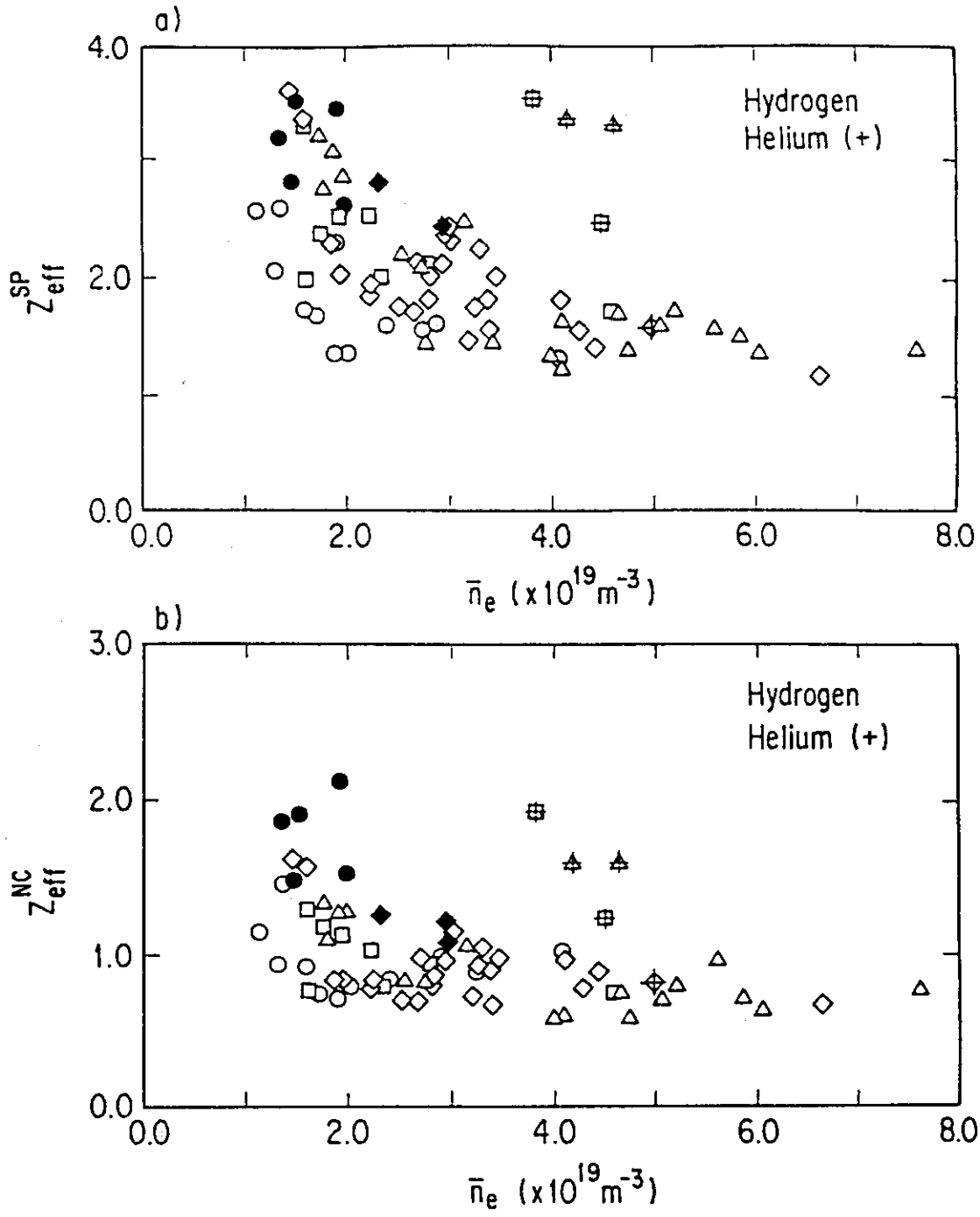

Fig. IX.3-1 The resistive Z_{eff} from Spitzer resistivity (a) and from the neoclassical resistivity with trapping correction (b) versus the line averaged electron density.

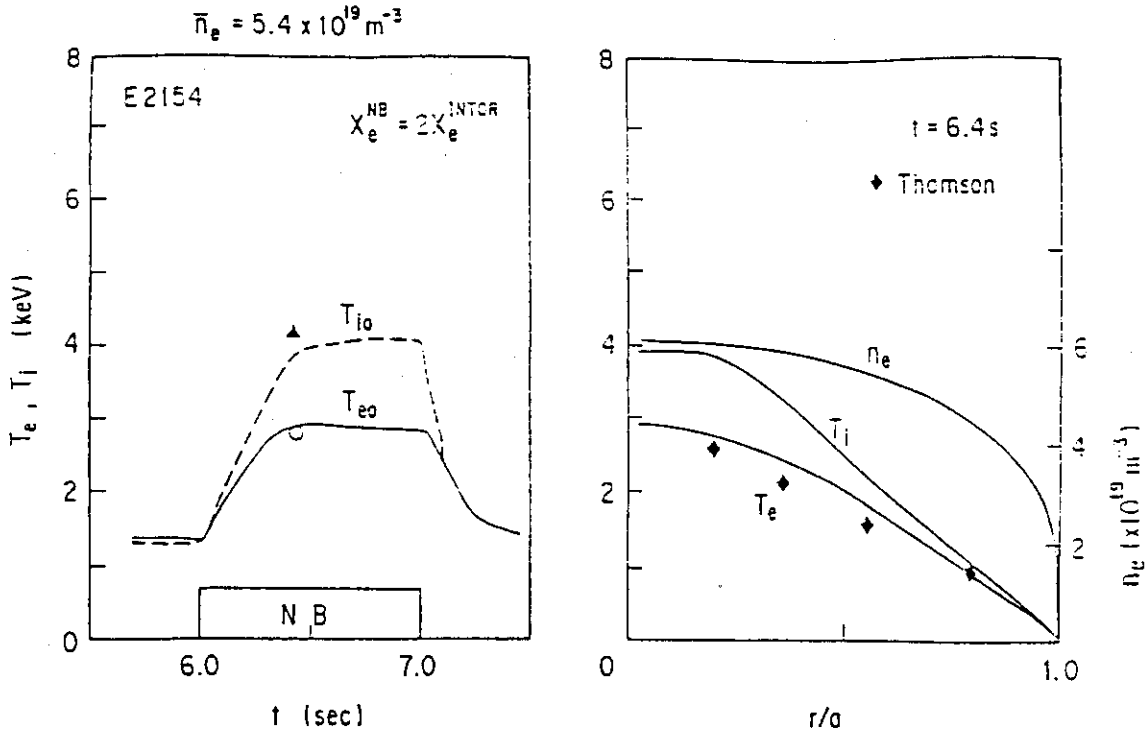

Fig. IX.3-2 The simulation result of E2154 discharge ($\bar{n}_e$= 5.4×10^{19} m^{-3}) using the enhanced electron heat diffusivity $X_e^{NB}=2X_e^{INTOR}$ during NBI heating phase.

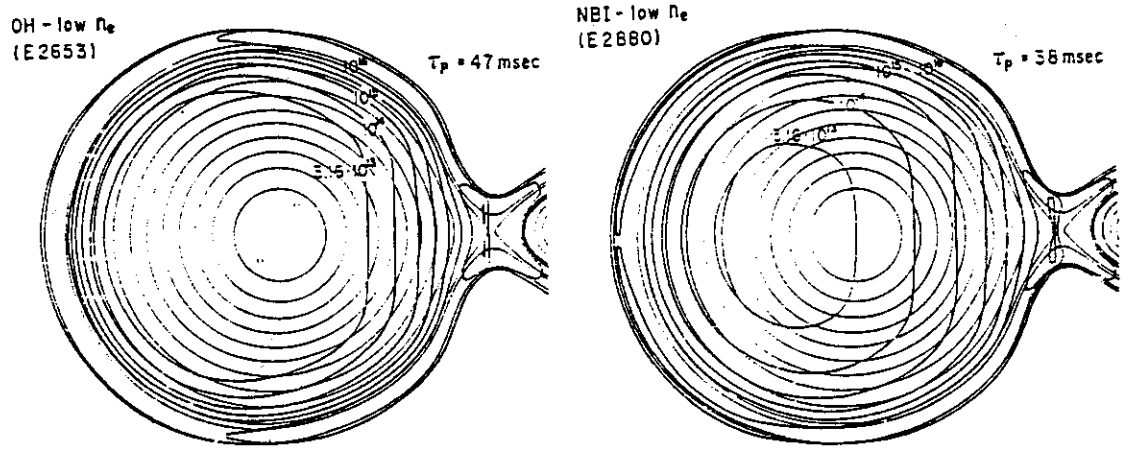

Fig. IX.3-3 The calculated neutral density profile for the ohmically heated plasma (E2653) and neutral beam heated plasma (E2880). During NB heating phase, the plasma density profile becomes more peaked one and the neutral particle can penetrate more easily into the plasma.

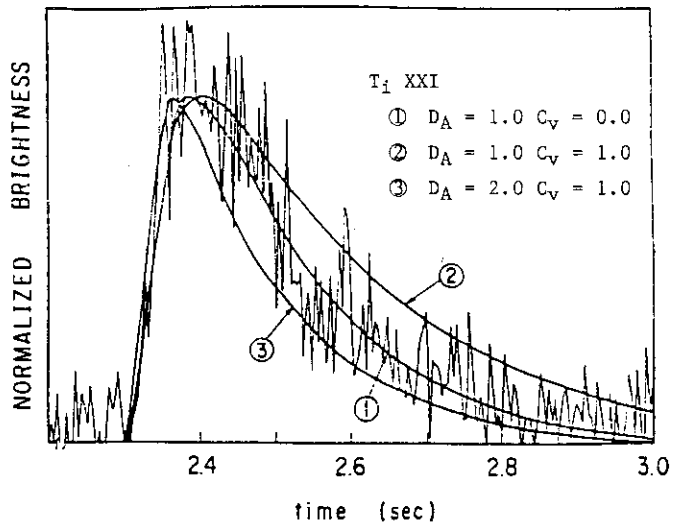

Fig. IX.3-4 The time evolution of the line radiance of center ion (T_i XXI resonance line), which is subtracted the background level, for the shot of E1968. The simulated lines are shown as the case with,
1) D_A = 1.0 m^2/s, C_v = 0.0,
2) D_A = 1.0 m^2/s, C_v = 1.0,
3) D_A = 2.0 m^2/s, C_v = 1.0.

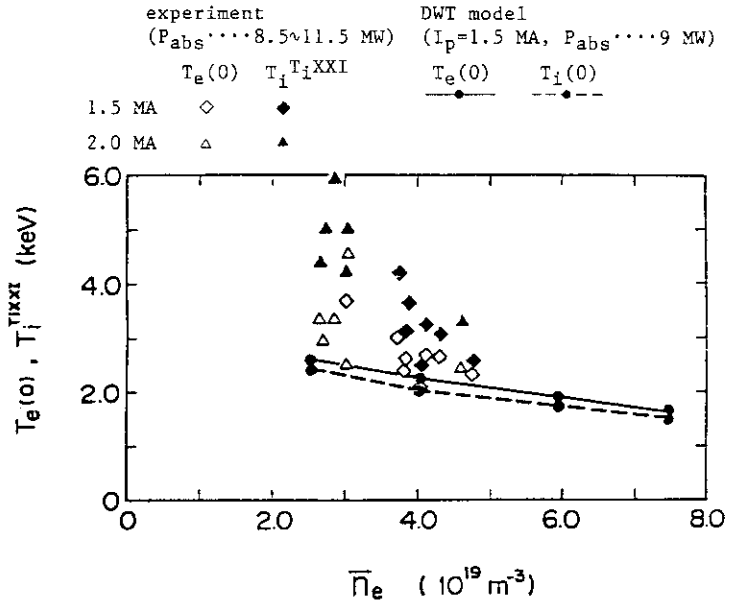

Fig. IX.3-5 Dependense of $T_e(0)$ and $T_i(0)$ on $\bar{n}_e$ in neutral beam heated plasmas. Open symbols indicate $T_e(0)$ measured by laser Thomson scattering and close symbols indicate T_i T_i^{XXI} by Doppler broadening of line radiation of titanium XXI. Diamonds indicate 1.5 MA plasmas and triangles 2.0 MA. The neutral beam heating power is from 8.5 MW to 11.5 MW. Solid line is $T_e(0)$ and broken line is $T_i(0)$ by calculation with I_p=1.5 MA and P_{abs}=9 MW.

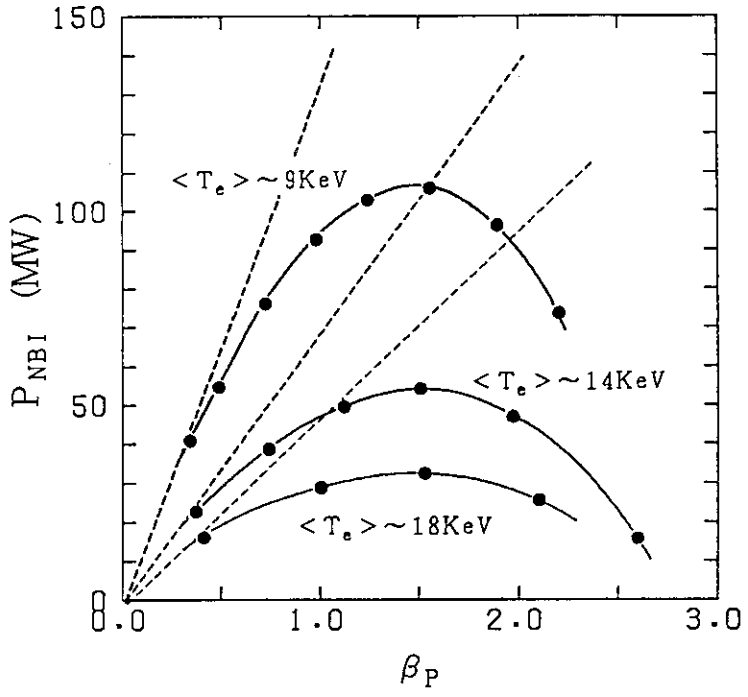

Fig. IX.3-6 Net NBI power to induce I_p=6 MA v.s. β_p. Solid curves are those with bootstrap effect for various plasma temperatures and dotted lines without bootstrap effect.

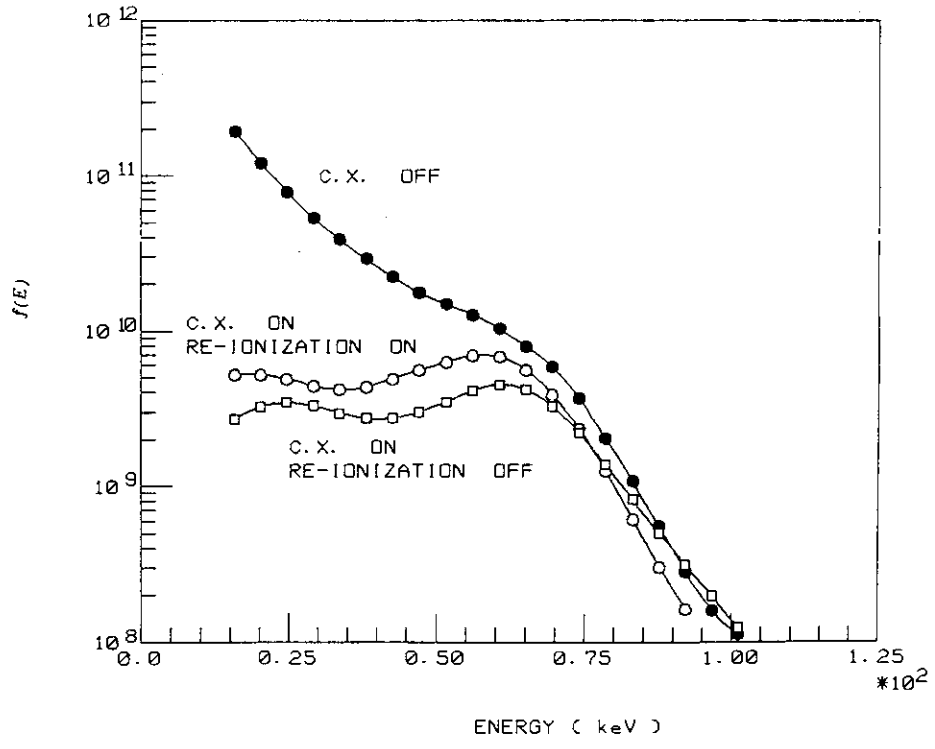

Fig. IX.3-7 Spectra of fast neutral observed at a diagnostic port with and without charge-exchange loss process.

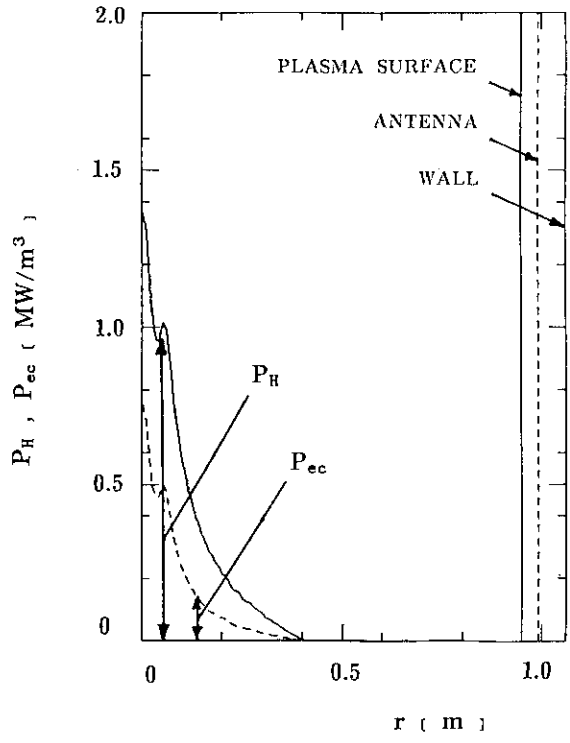

Fig. IX.3-8 Power deposition profiles of each plasma species as a function of minor radius. P_H is a absorbed ICRF power by ions and P_{ec} is a transfered power from ions by the Coulomb collision.

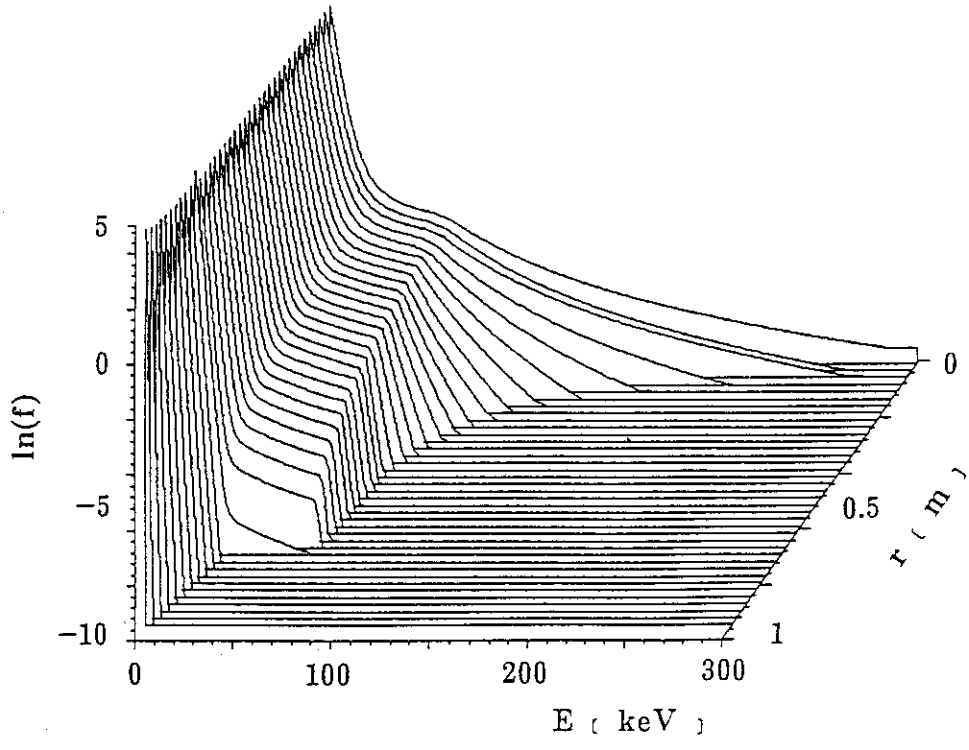

Fig. IX.3-9 Velocity distribution function on each magnetic surface. Magnetic axis is located at r=0. Plasma is heated in central region.

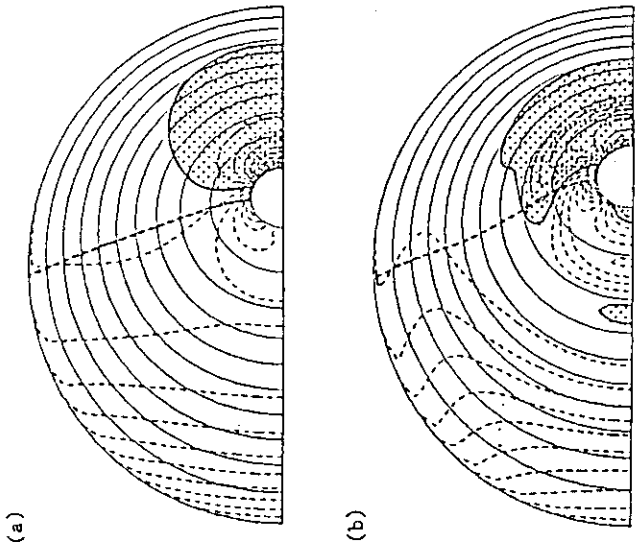

Fig. IX.3-11 Mechanism of accessibility of the second stability region. The local negative shear (the shaded region) is shown (a) for the high shear case (β_t=2.5) and (b) for the low shear case (β_t=4.8). The left hand side of bold broken line is a good curvature region, and solid lines denote contours of the poloidal flux. The negative local shear region extend to the good curvature region for case (b).

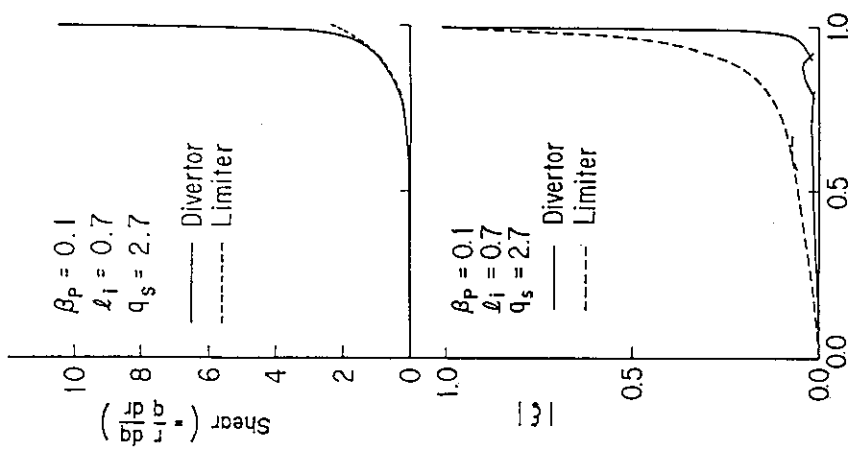

Fig. IX.3-10 Radial dependence of the shear and the displacement $|\xi|$ in the divertor (solid line) and the limiter configuration plasma (dashed line) with low beta of β_p=0.1, flat current profile of ℓ_i=0.7 and safety factor at surface of q_s=2.7.

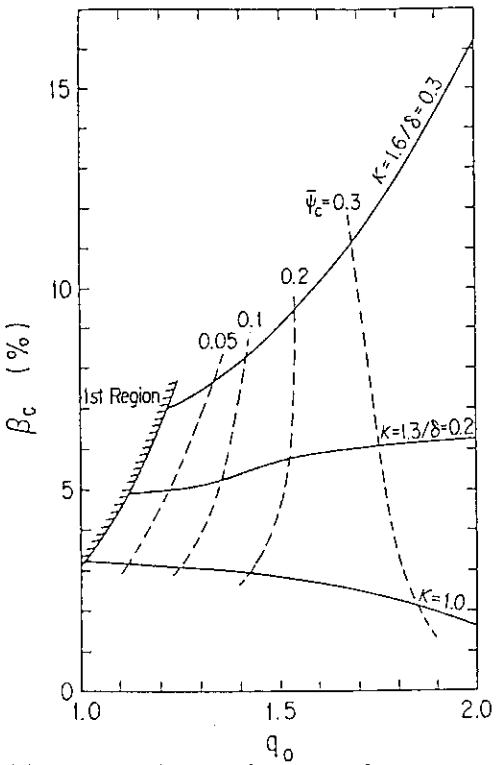

Fig. IX.3-12 Transition beta value versus q_0 for κ/δ=1.0/0.0, 1.3/0.2 and 1.6/0.3, where κ and δ are the ellipticity and triangularity, respectively. Other parameters are A=3, q_s=3.1 and S_w (=$(q(\bar{\psi}=0.5)-q_0)/(q_s-q_0)$)=0.15, where A, q_s and q_0 are the aspect ratio, the safety factors at the surface and center of plasma, respectively. Broken lines show boundary flux of second stability region, $\bar{\psi}_c$, within which a plasma has the capability of maintaining unlimited pressure.

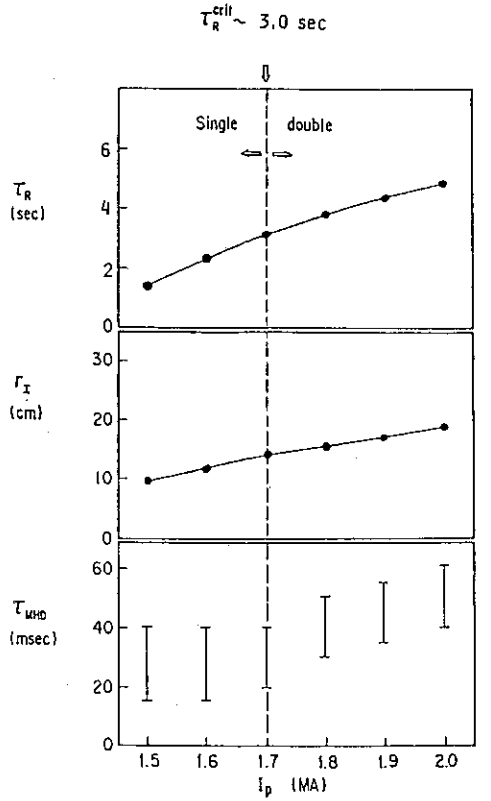

Fig. IX.3-13 Numerically calculated resistive skin time τ_R, inversion radius of soft X ray intensity r_ℓ and period of sawtooth oscillations τ_{MHD} as a function of plasma currents. Transition from single sawtooth oscillations to double sawtooth oscillations occurs at τ_R=3.0 sec.

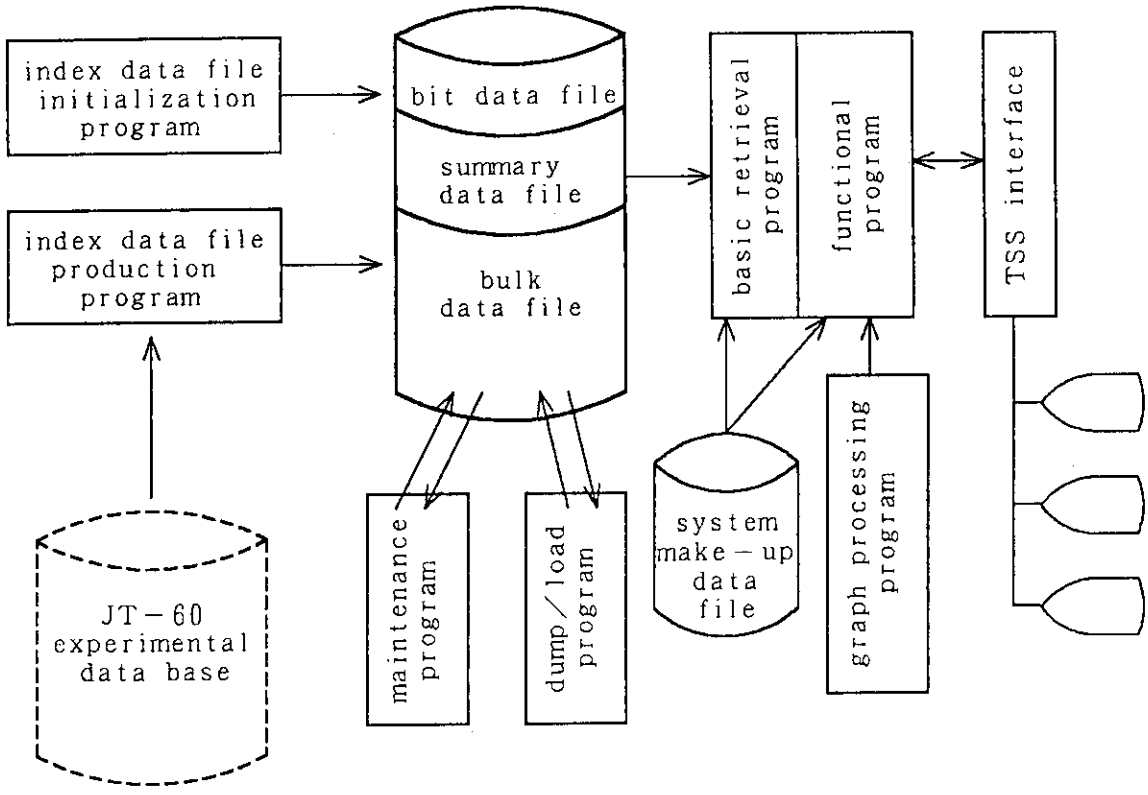

Fig. IX.3-14 Schema of DARTS

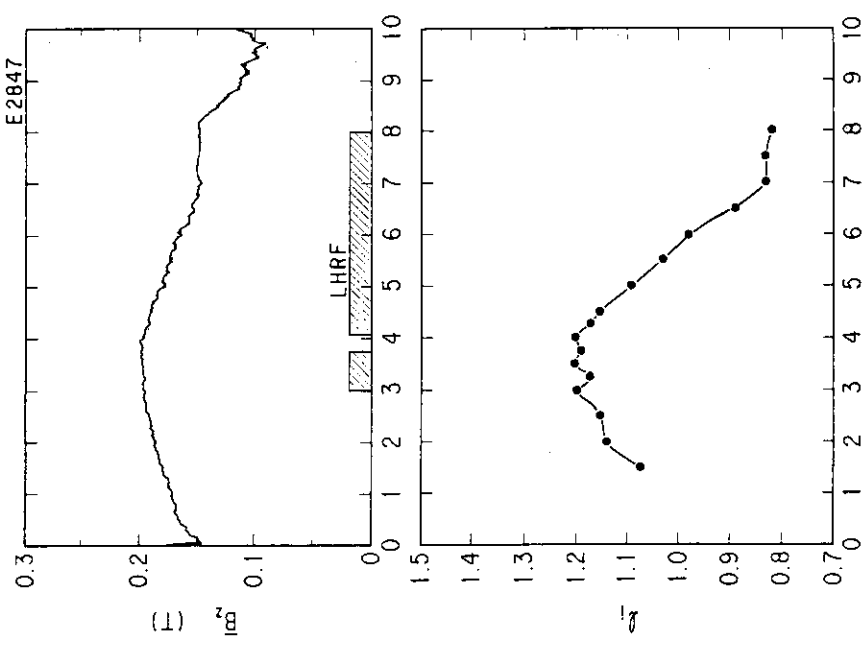

Fig. IX.4-2 The measured $\overline{Bz}$ and inferred li values as a function of time showing the current profile flattened during rthe application of LHRF waves for non-inductive current drive.

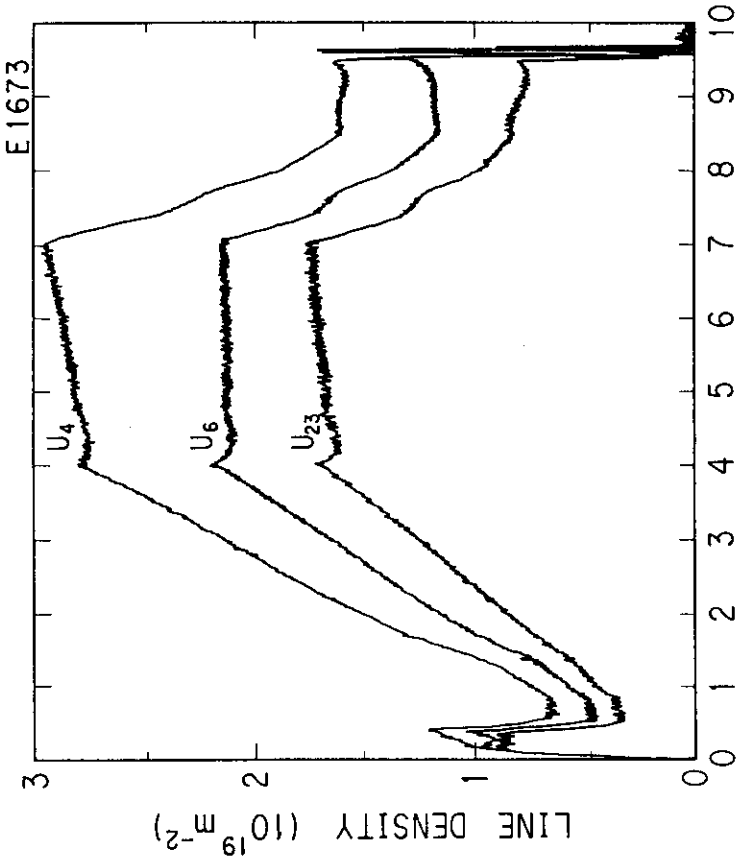

Fig. IX.4-1 Temporal evolution of athe line densities from the FIR interferometer channels showing the modulated waveforms by feedback control for the duration of 4-7 sec.

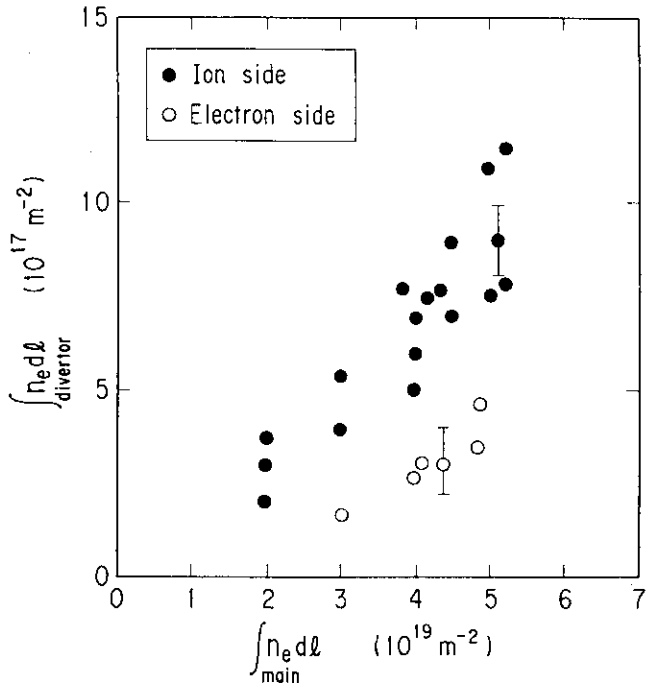

Fig. IX.4-3 Line density of divertor plasma as a function of line density of the main plasma for ion and electron drift sides, respectively.

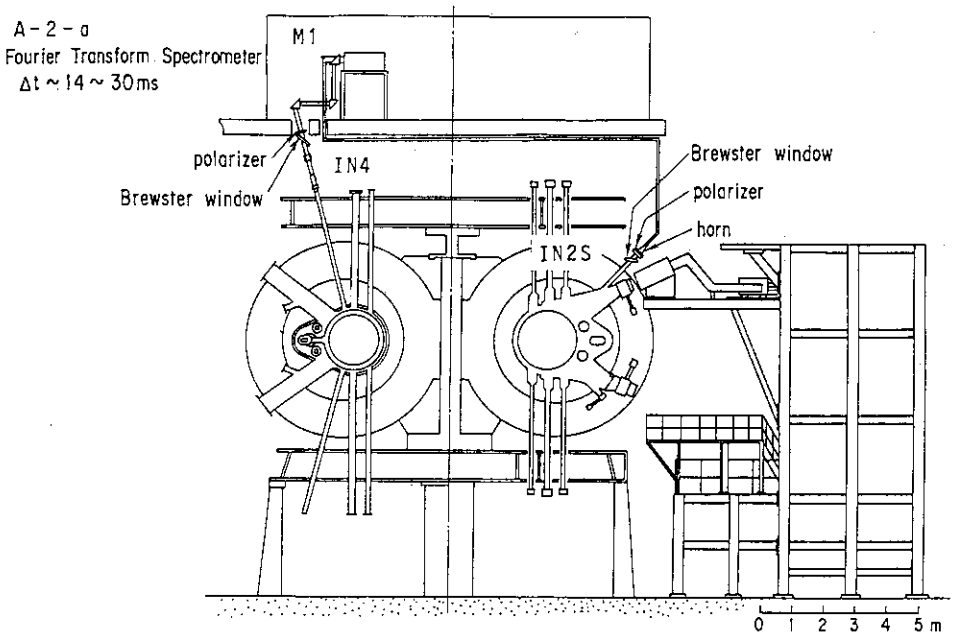

Fig. IX.4-4 The schematic diagram of the layout of FTS in JT-60.

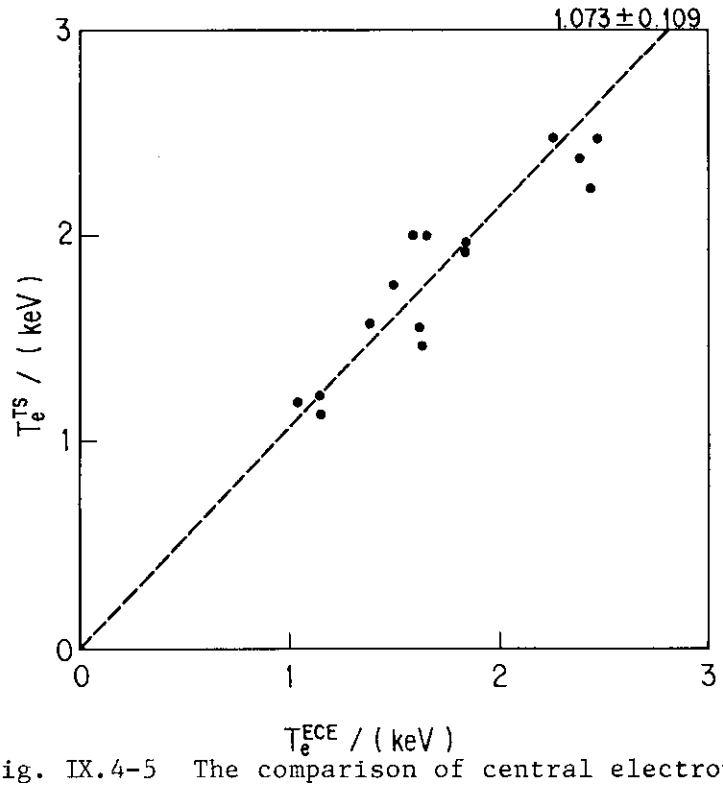

Fig. IX.4-5 The comparison of central electron temperature determined by the FTS method and those determined by Thomson scattering method. The standard deviation of these measured values is 0.11.

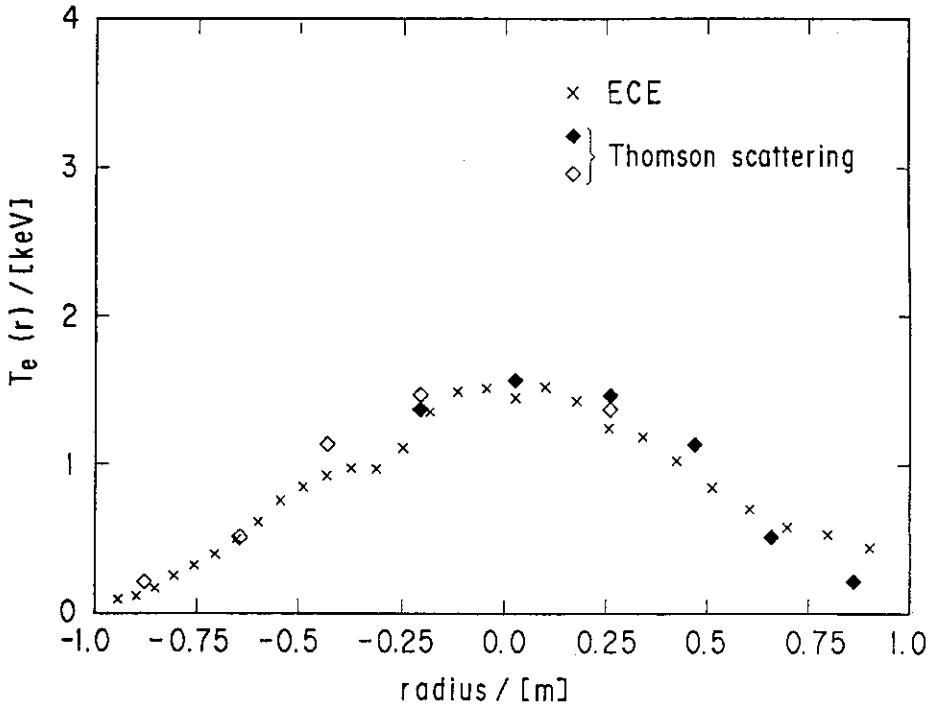

Fig. IX.4-6 The typical electron temperature profile derived from ECE. The electron temperature measured by the Thomson scattering is also shown.

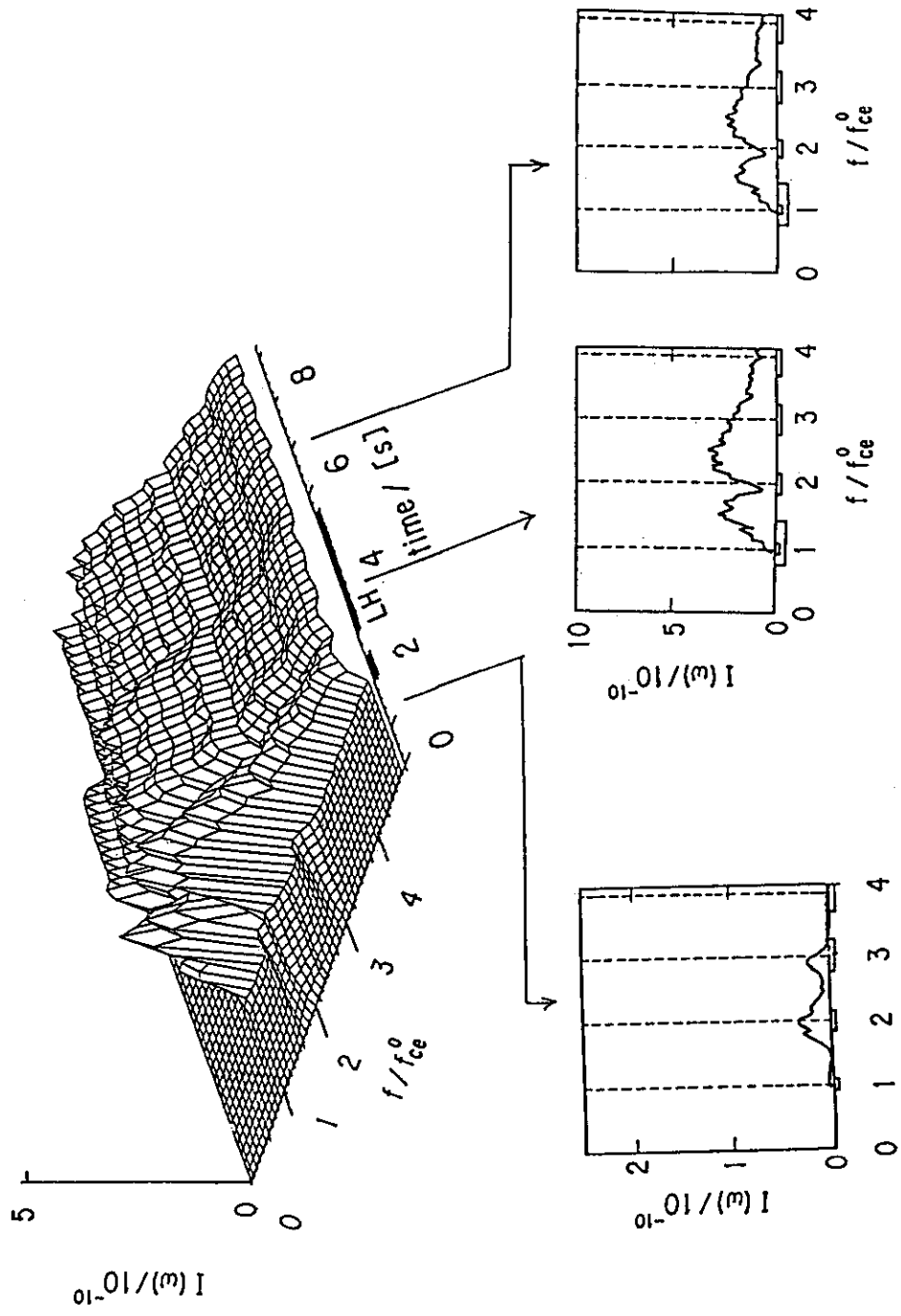

Fig. IX.4-7 The ECE spectrum from the supra-thermal electron in the case of LHCD. The spectrum in the low frequency region is not shown due to the large error of the calibration of the sensitivity.

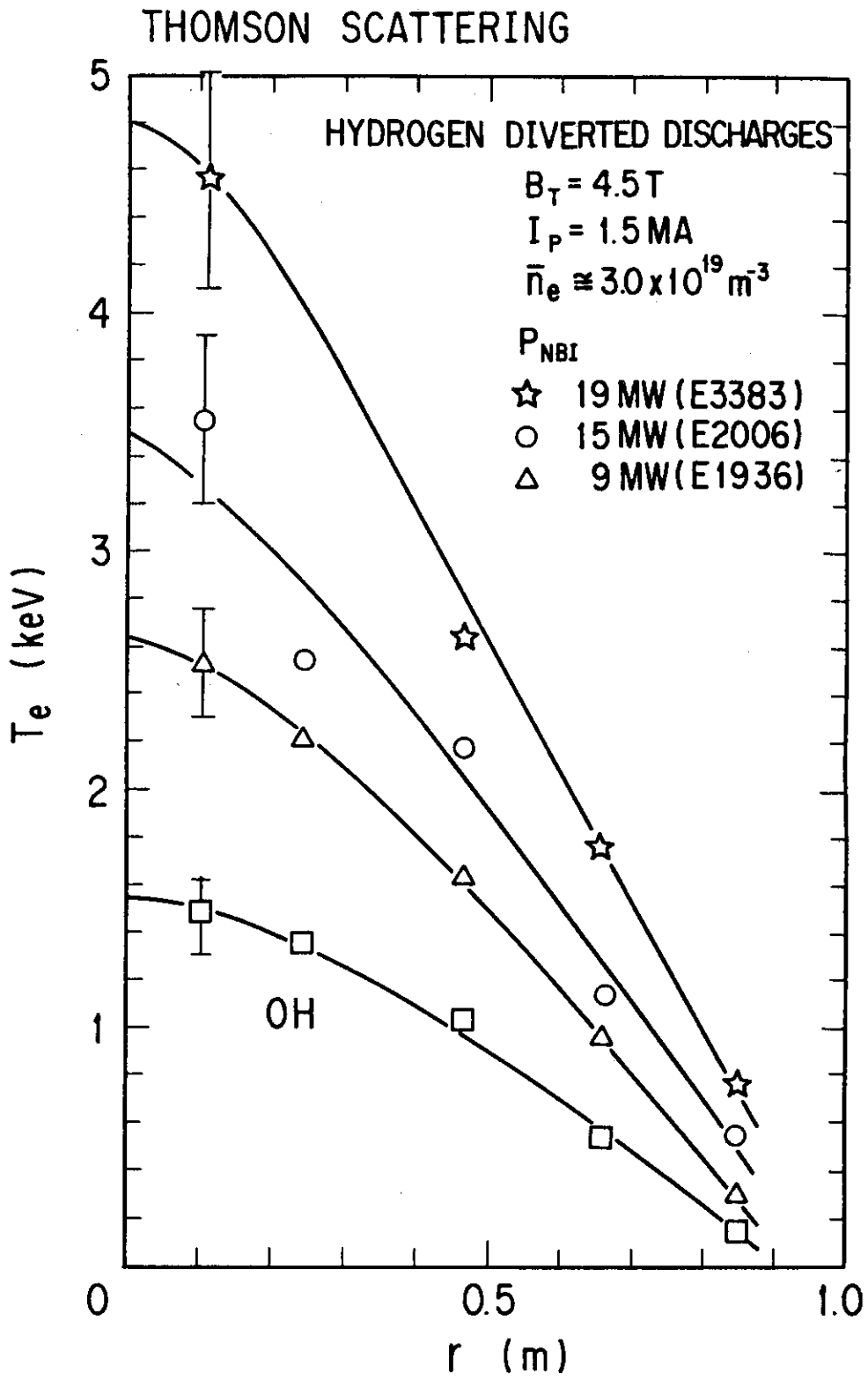

Fig. IX.4-8 The electron temperature profiles of divertor plasmas with the different heating power.

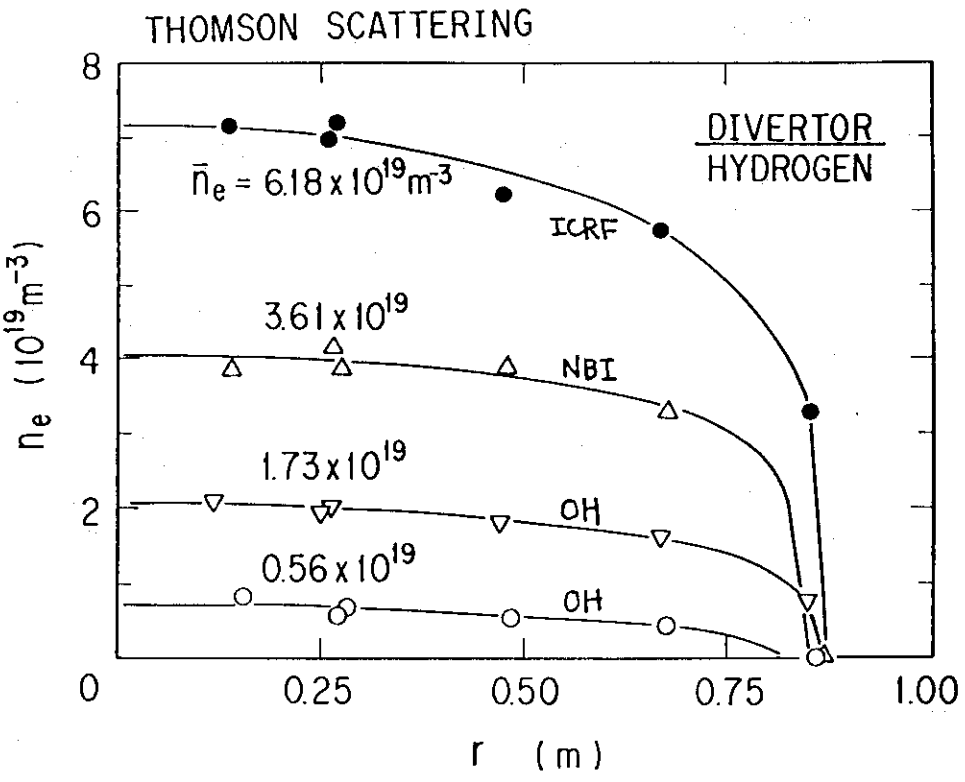

Fig. IX.4-9 The electron density profiles of divertor plasmas measured by Thomson scattering system.

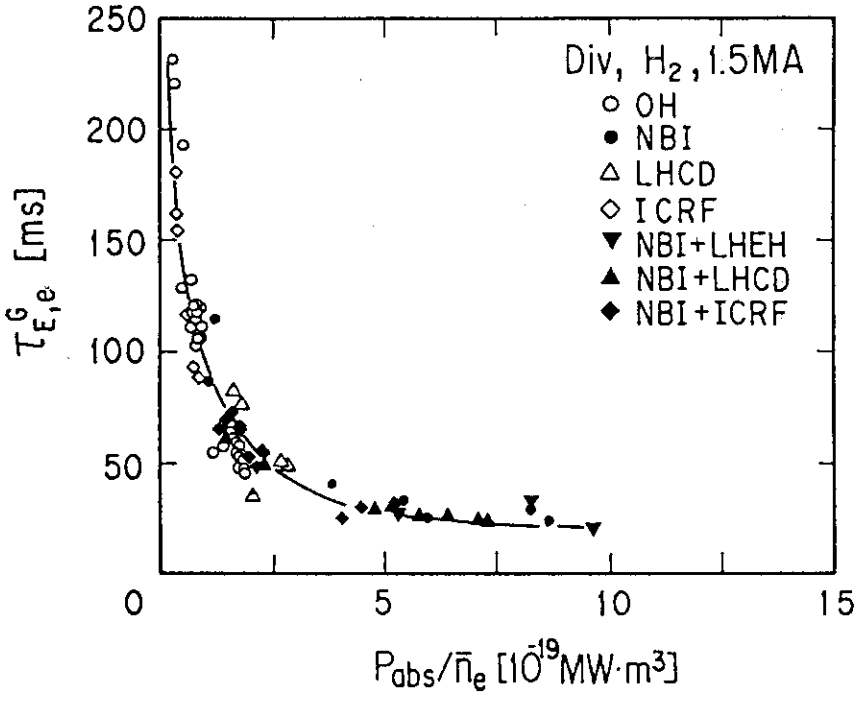

Fig. IX.4-10 The comparison of the gross electron stored energy and the normarized heating power.

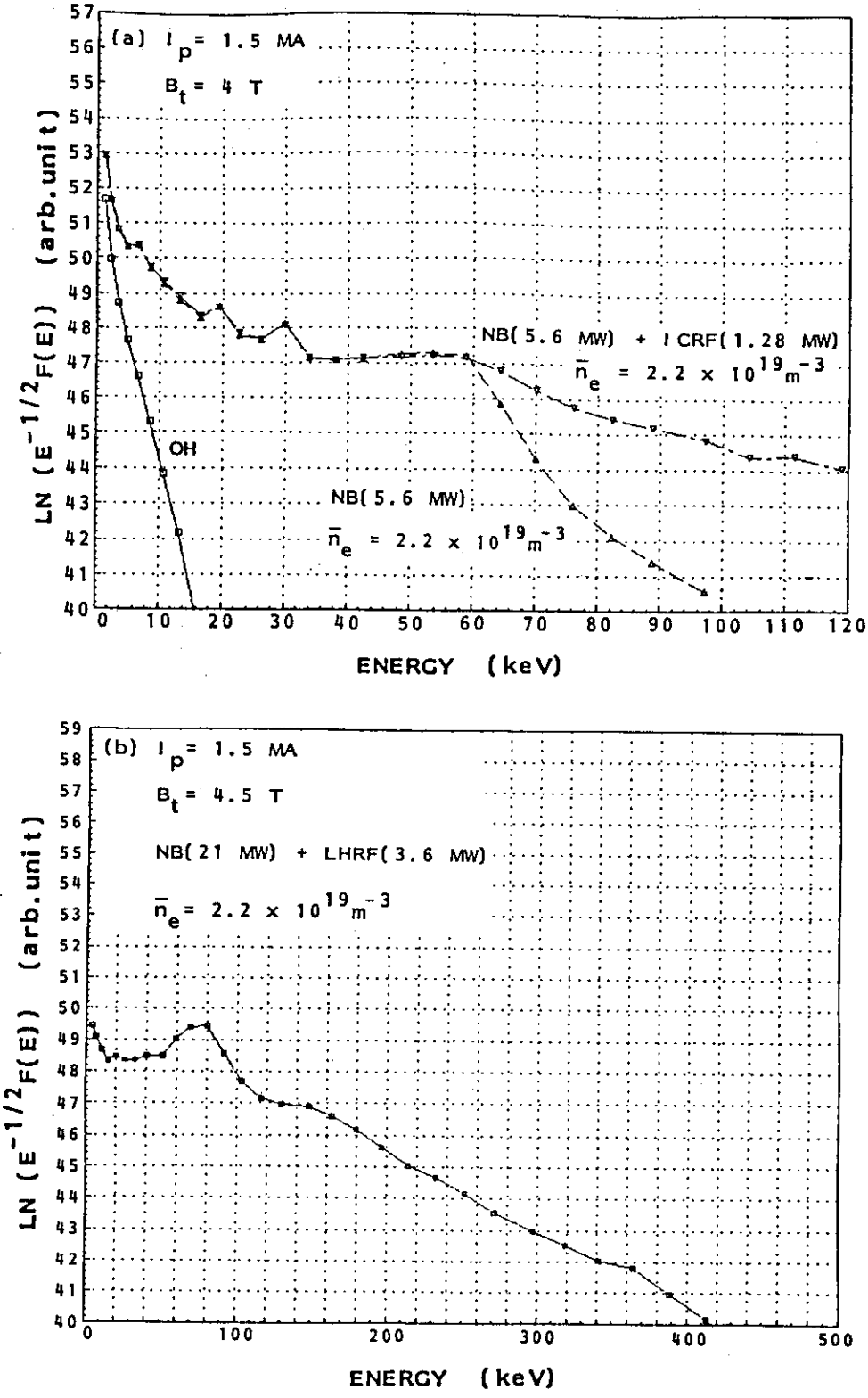

Fig. IX.4-11 Typical energy spectra of charge exchange neutrals in cases of ohmic, NB, NB+ICRF heating(a) and NB+LHRF heating(b).

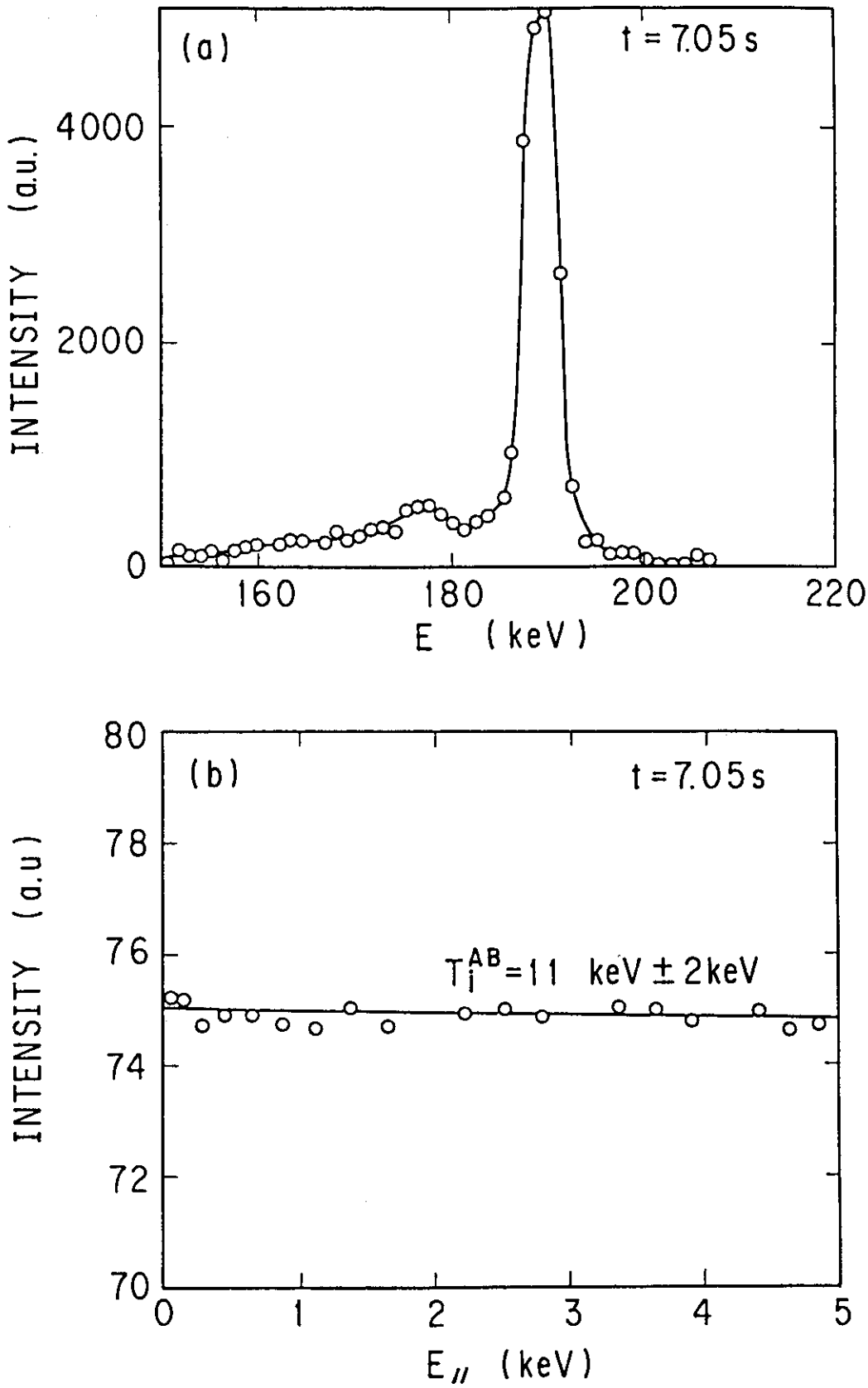

Fig. IX.4-12 The typical energy spectra of the scattered active beam atoms in a high ion temperature mode. (a) and (b) shows the spectrum before and after the conversion.

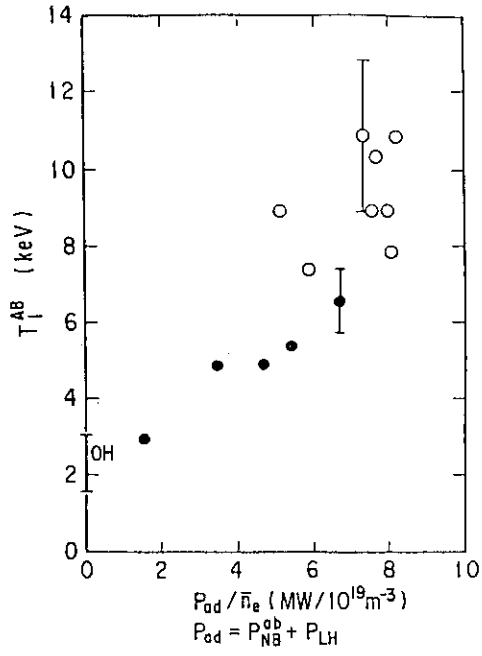

Fig. IX.4-13 The dependence of the central ion temperatures on the absorved neutral beam power normalized by the averaged electron density. Filled and open circles show the central ion temperatures in a divertor configuration and those of a high ion temperature mode in a limiter configuration, respectively.

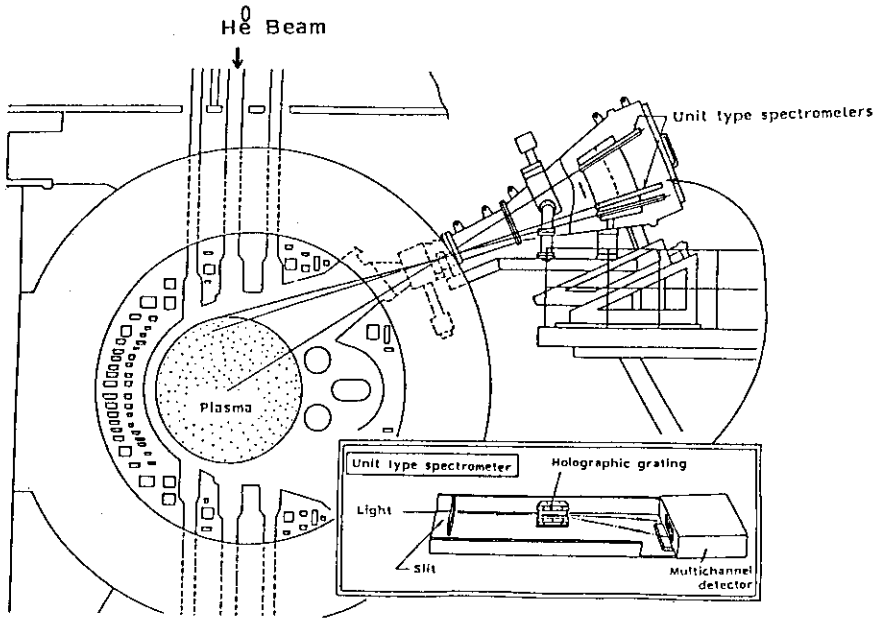

Fig. IX.4-14 Flat field grazing incidence spectrometer (unit type spectrometer) and the array system of these spectrometers for spatial profile measurement of impurity lines.

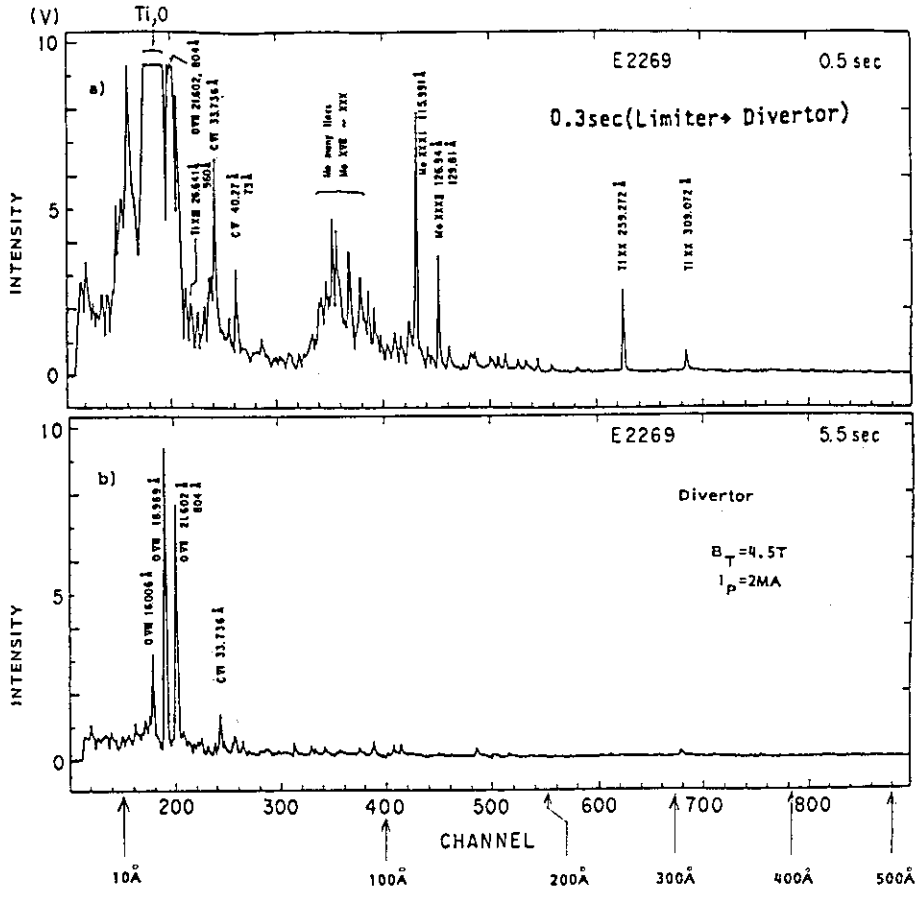

Fig. IX.4-15 (a) Spectrum at 0.5 sec after the discharge started measured by the unit type spectrometer and (b) 5.5 sec. The wavelength range is 5Å to 500Å. TiXIX (169.59Å) line was not observed because of the dead space of the detector.

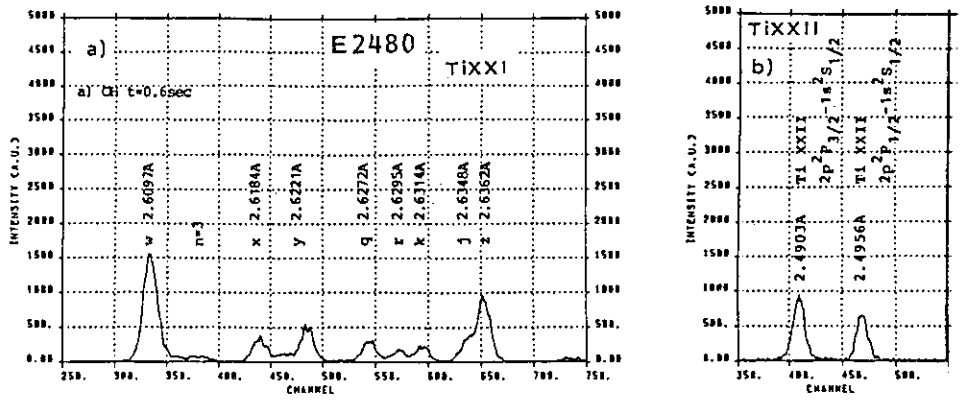

Fig. IX.4-16 (a) Spectrum of TiXXI resonance line and satellite lines measured by the crystal spectrometer (b) TiXXII resonance lines.

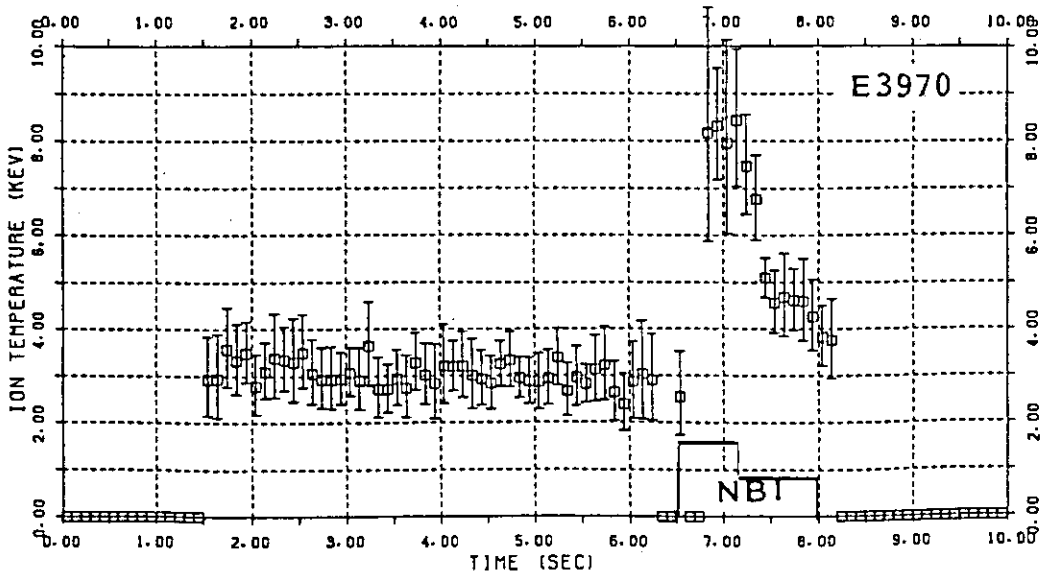

Fig. IX.4-17 Ion temperature obtained from the Doppler broadening of the TiXXII resonance line.

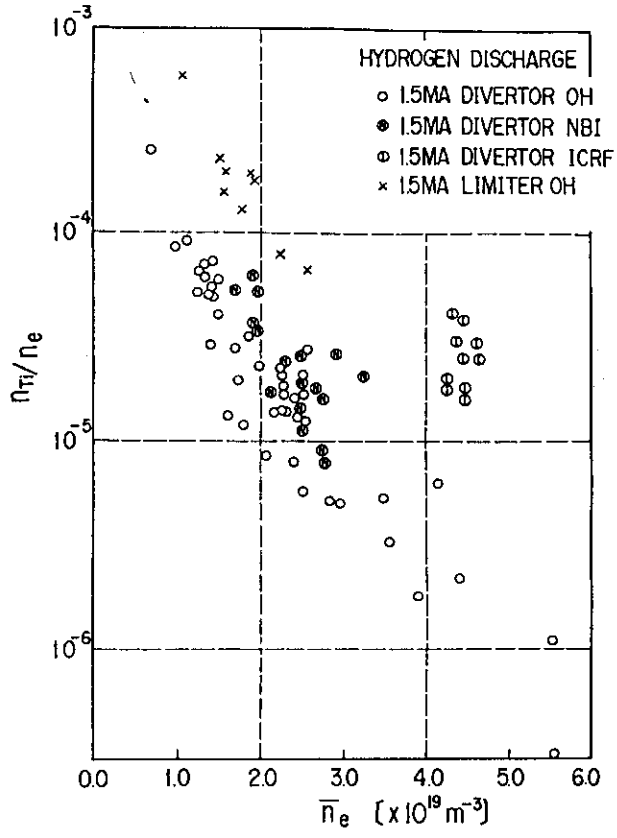

Fig. IX.4-18 The titanium concentration as a function of the averaged electron density.

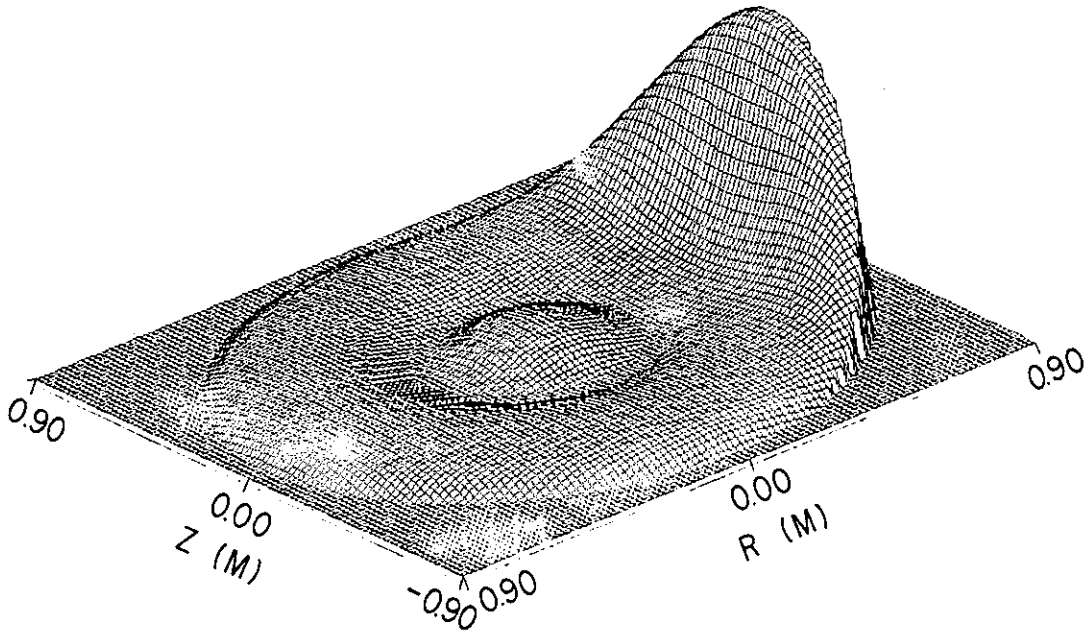

Fig. IX.4-19 The radiation profile reconstructed by the bolometer arrays.

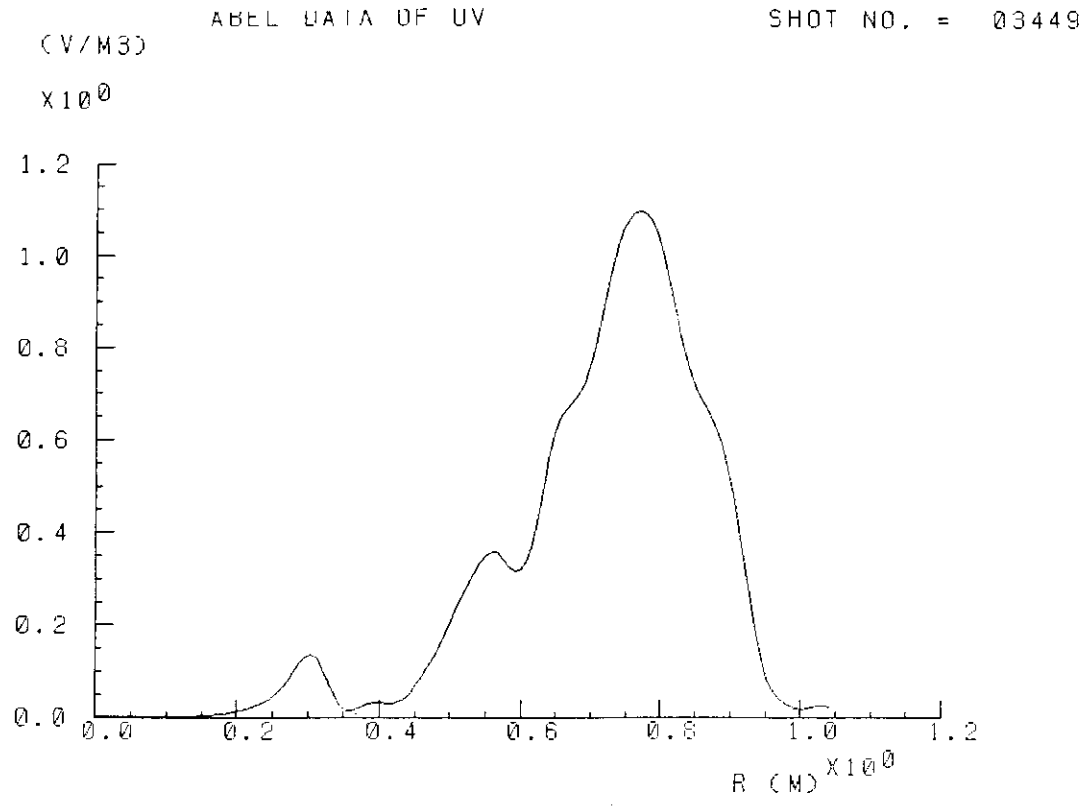

Fig. IX.4-20 A radiation profile of the forbiden line Ti XVII(383.44 nm).

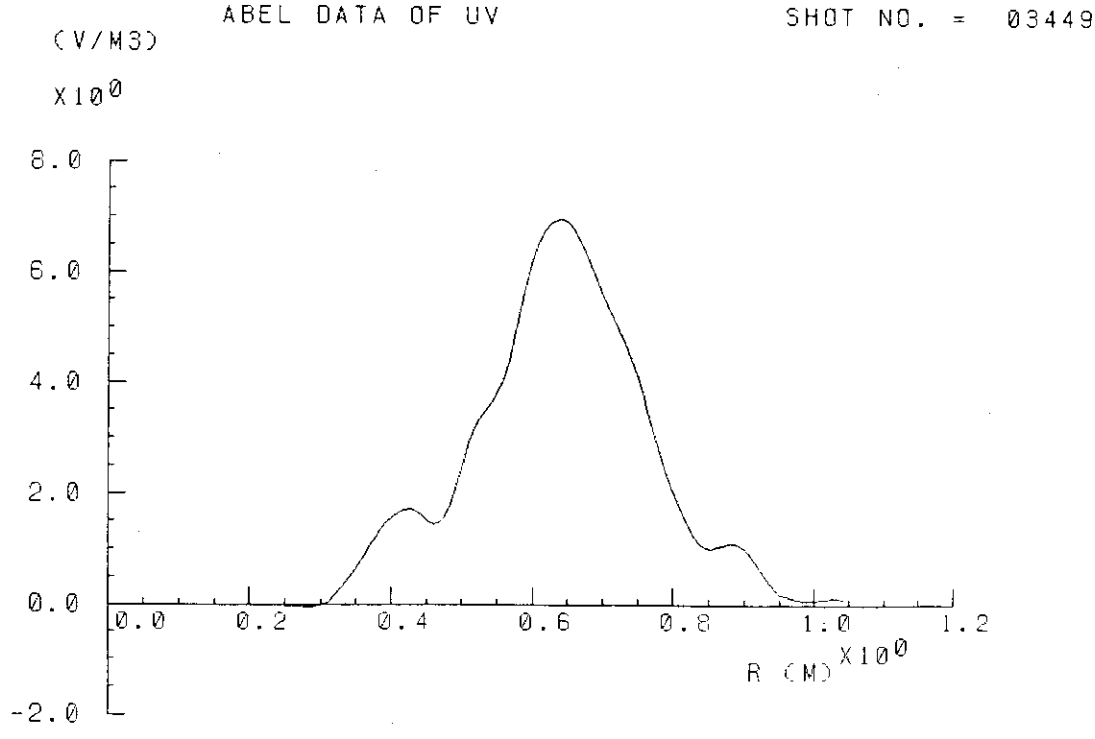

Fig. IX.4-21 The radiation profile of Ti XVII at the ICRF heating.

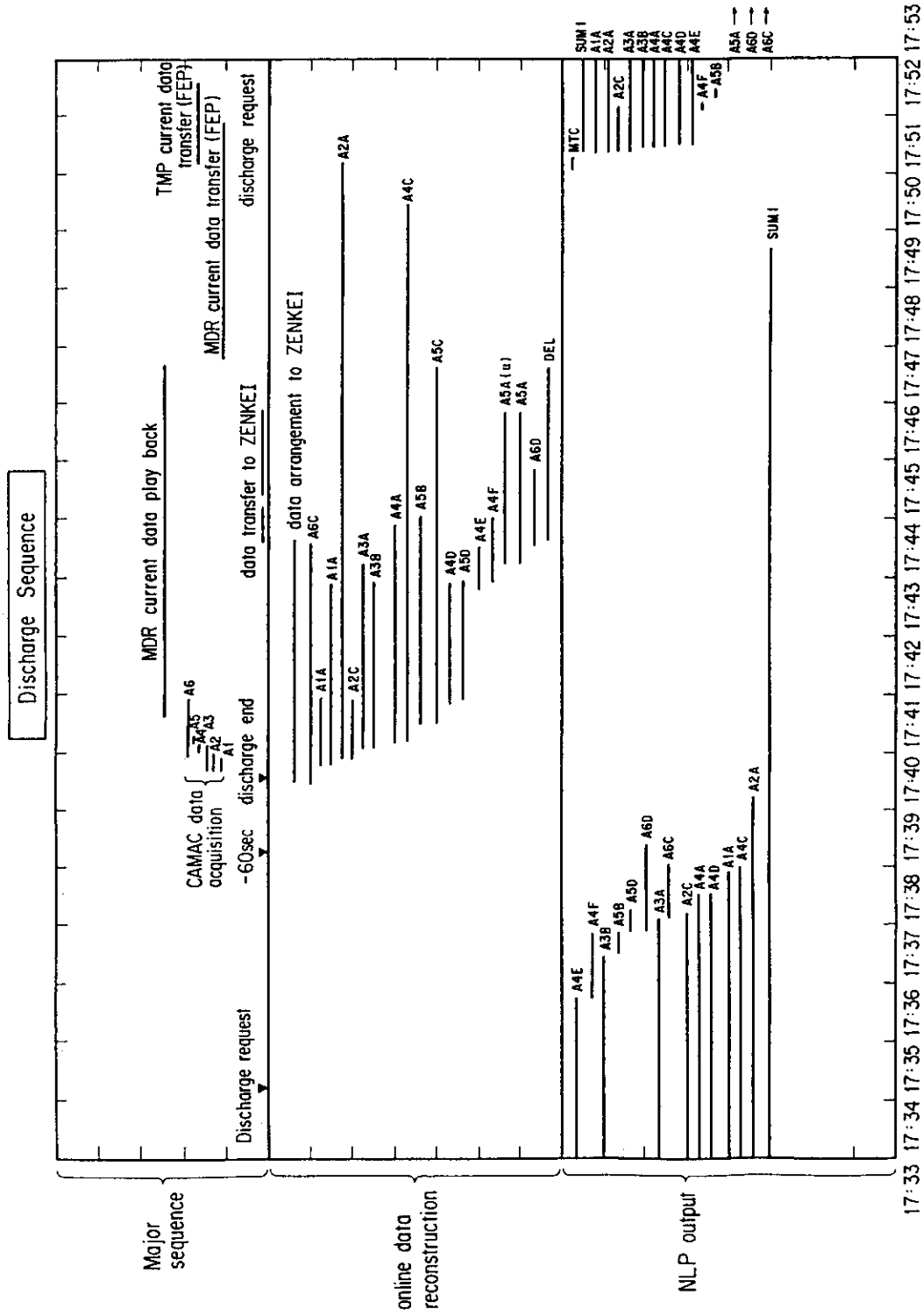

Fig. IX.4-22 A typical processing stream in the ISP.

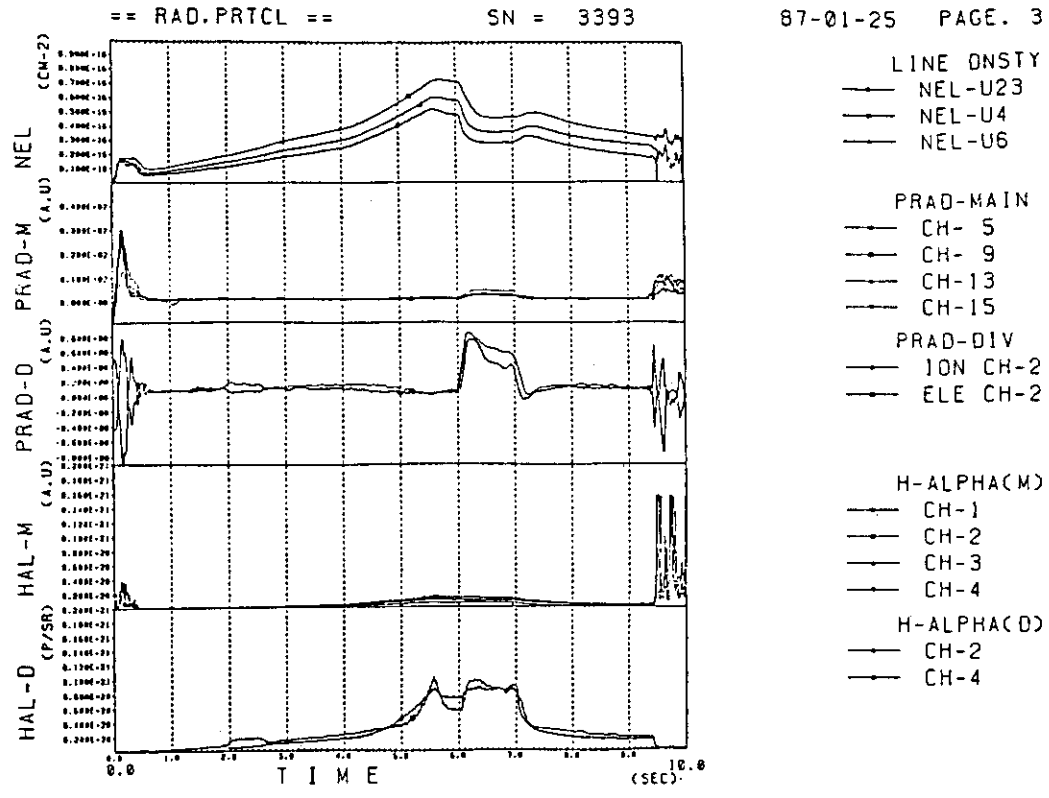

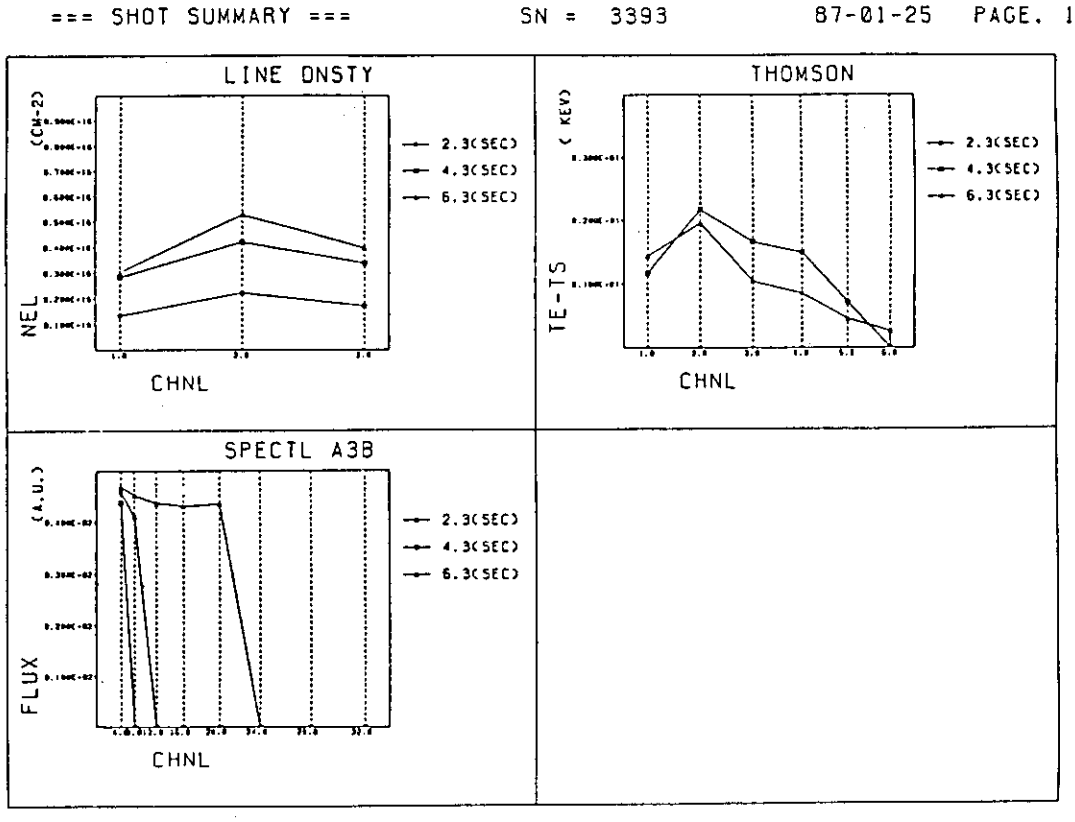

Fig. IX.4-23 A output example of diagnostic data.

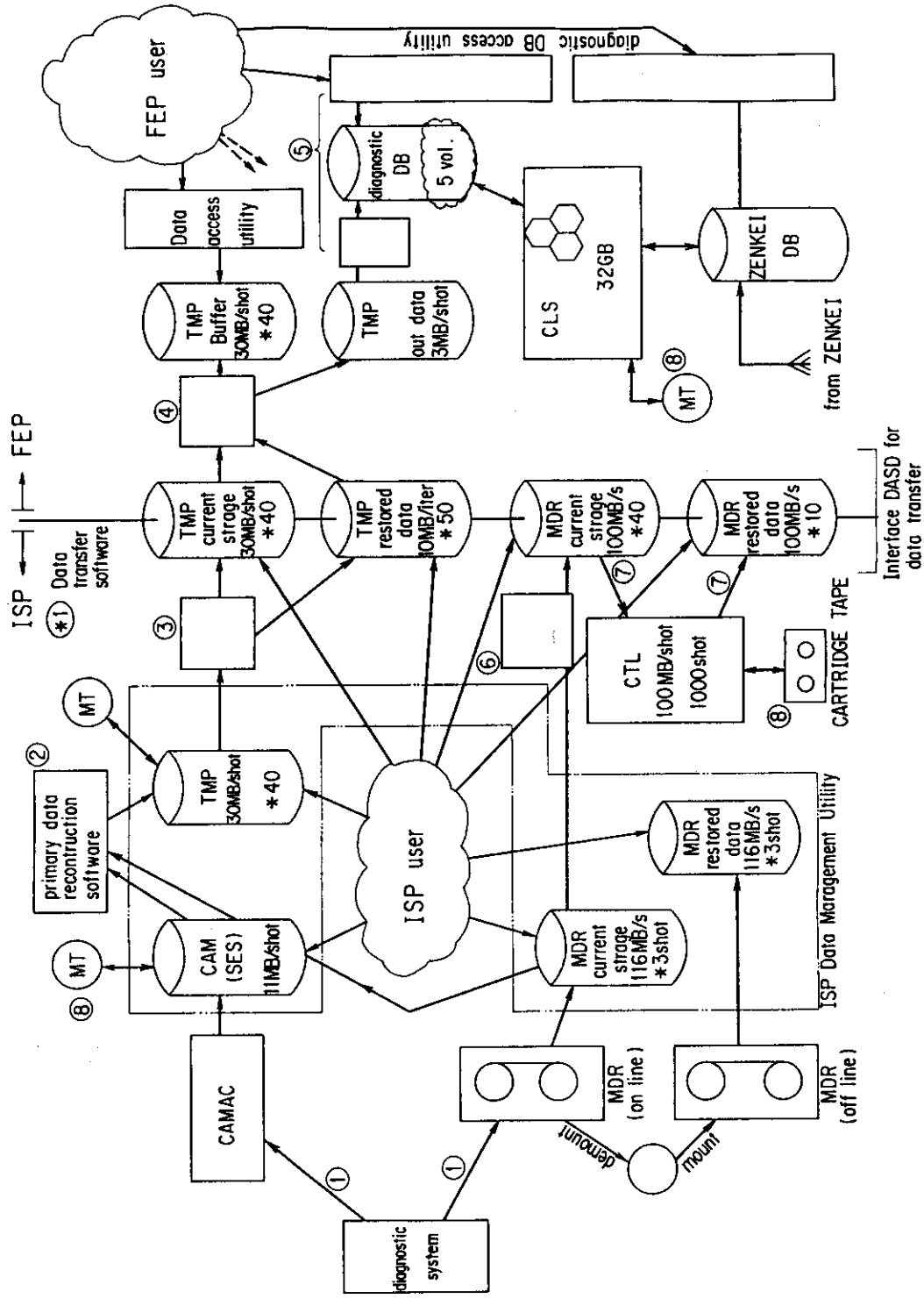

Fig. IX.4-24 A schematic diagram of the data management in ISP.

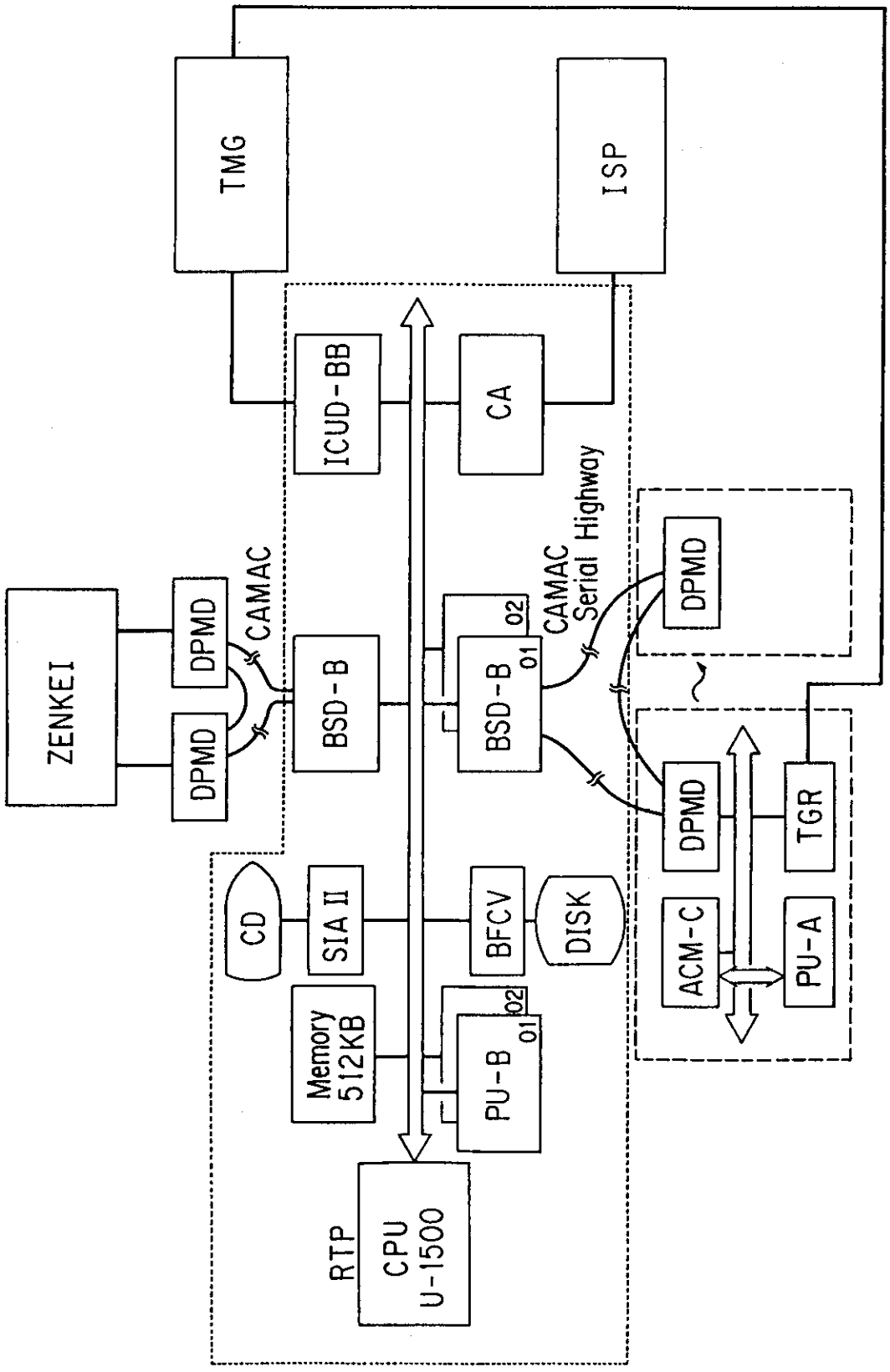

Fig. IX.4-25 The system of the real time feedback control.

X. JT-60 OPERATIONS AND DEVELOPMENT

1. JT-60 Operations

1.1 Operation Schedule and Organization

The operation schedule in FY 1986 presented in Fig. X.1-1. In April and May, the control system of neutral beam injection and radio-frequency system is to be linked with ZENKEI and checked in the performance test. The operation restarts in June and continues to November. After 2 months of maintenance works and remodelling of feedback control system in ZENKEI, JT-60 Operation restarts in January and continues to March. The operation crew is composed of 3 teams with two shifts duty assigned in early shift team (8:00-15:45) and late shift team (15:00-22:45). These two teams keep in charge the operation continuously in a week and early shift team turns to late shift in the next week while late shift team goes to the non-operative work in the ordinary hours. The other team, having worked in the ordinary hours duty in the previous week, comes into the early shift.

Process flow of experiments and operations is shown in Fig. X.1-2. In the first step, a proposal of experimental program of a certain cycle is made by Large Tokamak Experiment division then discussed at the experiment committee and approved by Director of Department of Large Tokamak Research. In the next step, the operation program, based on the approved experimental one, is proposed by JT-60 Facility Division I, then presented to the operation committee and discussed there and finally approved by Director of Department of JT-60 Facility. According to the authorized programs (both of experiment and operation), Floor leader executes the experiment and operation.

The organization for an operation regime is shown in Fig. X.1-3. A floor Leader is on the charge of overall safety and the proceeding of operation and experiment. Under the supervision by a Floor Leader, Operation Leader takes the responsibility of the operation of JT-60 machine and Chief Experimentalist in charge takes the responsibility of proposals of experimental parameters. The summarized results of the operation in the fiscal year 1986 are shown in Table X.1-1.

1.2 The operation in the term of June to November in 1986

In this period, we conducted 11 operation cycles. In the first cycle, after some checks of safety Interlock system, the vacuum vessel was baked up to the temperature 200°C, at which Taylor discharge was conducted for three days. In the second cycle, after the 20 shots of commissioning for the confirmation of tokamak machine, control system, monitor system, and diagnostic system, the experimental shots started and I_p=2 MA in divertor operation was achieved after several operation days. In the third cycle, operation started from baking of vacuum vessel after 2 weeks cease of operation, during which the official duty inspection test of the high pressure vessel was implemented.

After baking, magnetic field correction test of NBI system started at JT-60 OH operation and actual injection of NB was tested to obtain 17 MW at the end of July and achieved to get 20 MW power injection until the beginning of October. In the following cycles, RF power injection test also started, but some defects in the system was revealed after 1 month test operation and the pace of power-up was forced to be made slow and 1.4 MW at each mode of LHRH and ICRH was obtained at the end of this term. Statistical operation results in this term are shown in Fig. X.1-4.

1.3 The operation in the term of January to March in FY 1986

After approximately two months of operation cease, the operation started in January with baking, Taylor discharge cleaning and 25 shots of commissioning. In November and December, ZENKEI remodelled the feedback system in order to control plasma current, position and shape with matrix feedback control in real-time calculation. Therefore, the debugging of software was aimed at the relatively low plasma currents discharges. In this term, combined heating of NB and RF was pursuited in the 6 cycles of operation until the end of March. Statistical operation results in this term are shown in Fig. X.1-5.

1.4 Summary of operation results in FY 1986

The accumulated statistical data in this year is presented in Fig. X.1-6. As you see in Fig. X.1-6a, Average number of shots per day increases gradually from '85.5 to '86.11, but it decreases in '87.1 and recovers the level of '86.11 in March. It shows that since we have started JT-60 operation in '85.5, the operation has been

gradually improved, while the remodelling of ZENKEI in Nov. and Dec. in '86 affected the operation performances in Jan. '87 badly, which was, however, recovered in March. Fig. X.1-6c shows that approximately 50% of operation hours are consumed in Experiment and TDC & Commissioning, while 17% is a repair time for the troubles which is analysed in Fig. X.1-6f. Major troubles are found to be vacuum leak, break down of electric insulation of Tokamak machine and down of vacuum control system in diagnostics. Those are investigated and gradually improved.

2. Torus System

2.1 Operation and maintenance

A torus system consists of vacuum vessel, toroidal and poloidal field coils, support structures, movable and adjustable limiters, a vacuum pumping system and other subsystems[1]. The system is also connected by facilities such as neutral beam injectors, a radio-frequency heating system and diagnostics.

Moreover, it was connected in this fiscal year by new equipments such as a in-vessel inspection system, a in-situ coating system and a glow discharge system. the in-vessel inspection system was developed to observe the interior of the vacuum vessel during intervals of plasma shots without break of the high vacuum. th in-situ coating system was developed to repair of the TiC coated first walls in the vacuum vessel, keeping the vessel at high temperature and high vacuum. The glow discharge system is installed to clean the inside vacuum vessel.

The torus system is affected by high heat flux from the plasma and electromagnetic force induced by transient behaviors of the plasma. Therefore these systems are required to have high reliability.

The torus and other systems were operated on schedule owing to great efforts of members despite of many occurrences of troubles with the vacuum system and grounding. The insulation resistance of main components of the vacuum vessel and the support structure were measured every day. The results between 25th of August and 31st of September is shown in Fig. X.2-1.

gradually improved, while the remodelling of ZENKEI in Nov. and Dec. in '86 affected the operation performances in Jan. '87 badly, which was, however, recovered in March. Fig. X.1-6c shows that approximately 50% of operation hours are consumed in Experiment and TDC & Commissioning, while 17% is a repair time for the troubles which is analysed in Fig. X.1-6f. Major troubles are found to be vacuum leak, break down of electric insulation of Tokamak machine and down of vacuum control system in diagnostics. Those are investigated and gradually improved.

2. Torus System

2.1 Operation and maintenance

A torus system consists of vacuum vessel, toroidal and poloidal field coils, support structures, movable and adjustable limiters, a vacuum pumping system and other subsystems[1]. The system is also connected by facilities such as neutral beam injectors, a radio-frequency heating system and diagnostics.

Moreover, it was connected in this fiscal year by new equipments such as a in-vessel inspection system, a in-situ coating system and a glow discharge system. the in-vessel inspection system was developed to observe the interior of the vacuum vessel during intervals of plasma shots without break of the high vacuum. th in-situ coating system was developed to repair of the TiC coated first walls in the vacuum vessel, keeping the vessel at high temperature and high vacuum. The glow discharge system is installed to clean the inside vacuum vessel.

The torus system is affected by high heat flux from the plasma and electromagnetic force induced by transient behaviors of the plasma. Therefore these systems are required to have high reliability.

The torus and other systems were operated on schedule owing to great efforts of members despite of many occurrences of troubles with the vacuum system and grounding. The insulation resistance of main components of the vacuum vessel and the support structure were measured every day. The results between 25th of August and 31st of September is shown in Fig. X.2-1.

The insulation resistance shouled be higher than 600Ω and 20 kΩ for the support structure and the vacuum vessel respectively. The resistance was sometimes lower than the control values, owing to the reason such as mistake and the break of insulater for the seath of thermocouples.

Cooling channels mounted on the vacuum vessel and the support structure are insulated between the components. However, the resistance changed by the operation of the cooling system as shown in Fig. X.2-1.

The JT-60 divertor pumping system has been operated in Joule heated and neutral beam heated divertor discharges. The objective of this system is an active particles control in long pulse and high power neutral beam heated divertor discharges. The pumps are composed of compact nonevaporable Zr-Al getter pumps with a total pumping speed of 5.6 m^3/s for hydrogen in the divertor chamber. It was found from the pumping experiment that the pressure in the divertor chamber increases approximately in proportion to the square of the line averaged electron density ne of the main plasma. A total particle exhaust rate of 3 Pam^3 is posible for $n_e=6\times10^{19}$ m^{-3}, which is as large as the fueling rate by the neutral beam injection with a heating power of 20 MW. The density decay characteristics of the main plasma in the discharges with getter pumps-on and no pumping show an evident particle control effect by this pumping system.

2.2 Related development

2.2.1 Development of in-vessel inspection system on JT-60

JT-60 in vessel inspection system was developed to observe the interior of the JT-60 vacuum vessel during intervals of plasma discharges without break of the high vacuum. The objective of this system is the detection of the damages of the first walls attached on the inner surface of the vacuum vessel.

A schematic diagram of the in-vessel inspection system is shown in Fig. X.2-2. This system consists of four sets of perimeters including perioscopes, illumination equipments, viewing systems, vacuum systems and control systems. Four perimeters are placed on the diagnostics platform in the torus hall and are connected to the vacuum vessel via four vertical ports; U4P4U. U4P7U. U4P12U and U4P15U.

High resolution pictures are provided by the periscope, which relays images of the vessel interior with a mirror and a set of lenses. Images provided by the perioscope can be observed not only by eyepieces but also by a TV camera and a still camera. The pictures of the TV camera are transmitted to the JT-60 control room and can be observed through a monitor television. This system can be operated by local consoles placed on the diagnostics platform as well as remote consoles placed in the control room. Automatic operation is also possible from the control system.

This system was completed December, 1986 and has been well in operation since January, 1987. Typical pictures taken by this system are shown in Fig. X.2-3 with (a) 1 x magnification and (b) 3 x magnification, which shows a protection plate of the submagnetic limiter coil casing hardly damaged during additional heating experiments from January to March, 1987.

2.2.2 Design and fabrication of graphite first walls

A significant amount of TiC-coated molybdenum and Inconel 625 first walls are to be removed and new graphite first walls are to be installed within the JT-60 vacuum vessel during the venting period at the beginning of the next fiscal year in order to prepare the in-vessel hardware for high-power and long-pulse additional heating experiments. This change of the first wall material was based on the results of the initial additional heating experiments showing the degrading effect of locally melting TiC-coated molybdenum and Inconel 625 on confinement characteristics of the main plasma.

Figure X.2-4 illustrates the cross section of the JT-60 vacuum vessel and the graphite first walls. The graphite first walls cover about 45% of the total inner surface area of the JT-60 vacuum vessel, including about 70% coverage of the innermost area (midplane ± 70°) and 100% coverage of the divertor plates. Two kinds isotropic graphites (Ibiden ETP-10 and Hitachi-Kasei HCB-18S) were selected for the first wall materials for their superior outgassing characteristics, high thermal shock resistance and very low ash content. Laboratory measurements have shown that both of the two kinds of graphites have the outgassing rate less than 4×10^{-8} $Pa.m^3 \times s.m^2$ after 35 h baking under the temperature of $350^{\circ}C$. They have the thermal shock parameters $\sigma_f \lambda / E\alpha$ higher than 130 kW/m and ash

contents less than 20 ppm after purification procedure under the temperature over 2000°C.

The graphite first walls have a flattened structure to increase the contact area with plasma and to minimize the heat flux to the first walls. A set of graphite tiles are mounted on a SS 316 backing plate with a barrel nut and a bolt individually. The size of each graphite tile is designed to be small, typically 60-mm-square and 25-mm-thick, to increase the structural integrity under the thermal shock. All of the tiles were examined by non-desctructive inspection technique (CT-scanning and ultrasonic testing) during fabrication so as to exclude the tiles having the defects larger than 3 mm.

2.2.3 Fabrication of the in-situ coating system

The in-situ coating system was fabricated on FY.1986.
The purposes of this system are the titanium flashing, the inspection and repair of the TiC coated walls in the JT-60 vacuum vessel without enterance of personnel or dismantling, keeping the vessel at high temperature (RT. - 300°C) and vacuum (10^{-7} Pa).

The system is composed of a manipulator arm, a titanium evaporator, an observation device, a computer system, and so forth.

The manipulator arm has four degree of freedom, and it's possible to move on three dimensions in the vacuum vessel. One of the important technical issues is the lubrication of the moving parts since the friction at solid-solid contacts increases markedly in high temperature and high vacuum. Therefore the mechanical components which are exposured in vacuum are used dry lubricants (MoS_2, SL alloy, Ag), and the vacuum seals are used the magnetic fluid and bellows.

We used the reactive evaporation method on the fabrication of TiC. The evaporator of carring four titanium filaments is attached the tip of the mainpulator arm, and the dimensions are 170 mm diameter, 160 mm length and weight of 3kgf. The acetylene gas is introduced from the C_2H_2 injector into the vacuum vessel through the vertical and horizontal ports.

The observation device consists of the guide scope which is bundled the number of 12000 glass fiber cores.

The major components of the computer system consists of a super mini-computer and a three dimensions graphic display. This computer

system very benefits for the remoto operation of the in-situ coating system.

The in-situ coating system was started to design at the beginning of FY. 1985, and the first operation was begun on March 1987.

2.2.4 Glow discharge system

The rf-assisted glow discharge system is installed in the JT-60 machine. The important components of the system are shown in Fig. X.2-5. A glow discharge is made by biasing one or two anodes located in the vessel, roughly 180 apart in the toroidal direction. Figure X.2-6 shows an coil-electrode (5 windings, 100 mm diameter) cooled by air. The electrode is made of a stainless steel pipe coated by a TiC material. It can be inserted to 45 cm from the plasma center.

Rf power supplies of 13.3 MHz, 1000 W Max coupled with matching network through transmitters are used to assist the DC glow discharge. Seperate 600 V, 10 A DC current-controlled power supplies are used for biasing each. An active current regulation circuit and arc-supression circuit in the bias supplies eliminate the need for a large resister in the plasma circuit. The power supplies are interlocked to thermocouple measurement of the anode temperature to shut down the system. Typically, both anodes were operated at a current of 5 A DC each. At a hydrogen pressure of 0.5 Pa, the anode voltage was about 340 V DC.

References

1) Shimizu M., Ohkubo M., Yamamoto M., Takatsu H., Ando T., Nakamura H., Akino N., Kawasaki K., Urakawa H., Ohtsu K., Ohta M., Ohwada K., Sato H. and Kajiura S., Proc. 8th Int. Conf. on SMAIRT (Brussel, August, 1985).

3. Power Supplies : Operations and Related Developments

3.1 Operations

In FY 1986, JT-60 poloidal and toroidal field power supplies (PFPS and TFPS) were under operation for 14.5 cycles totally. The

system very benefits for the remoto operation of the in-situ coating system.

The in-situ coating system was started to design at the beginning of FY. 1985, and the first operation was begun on March 1987.

2.2.4 Glow discharge system

The rf-assisted glow discharge system is installed in the JT-60 machine. The important components of the system are shown in Fig. X.2-5. A glow discharge is made by biasing one or two anodes located in the vessel, roughly 180 apart in the toroidal direction. Figure X.2-6 shows an coil-electrode (5 windings, 100 mm diameter) cooled by air. The electrode is made of a stainless steel pipe coated by a TiC material. It can be inserted to 45 cm from the plasma center.

Rf power supplies of 13.3 MHz, 1000 W Max coupled with matching network through transmitters are used to assist the DC glow discharge. Seperate 600 V, 10 A DC current-controlled power supplies are used for biasing each. An active current regulation circuit and arc-supression circuit in the bias supplies eliminate the need for a large resister in the plasma circuit. The power supplies are interlocked to thermocouple measurement of the anode temperature to shut down the system. Typically, both anodes were operated at a current of 5 A DC each. At a hydrogen pressure of 0.5 Pa, the anode voltage was about 340 V DC.

References

1) Shimizu M., Ohkubo M., Yamamoto M., Takatsu H., Ando T., Nakamura H., Akino N., Kawasaki K., Urakawa H., Ohtsu K., Ohta M., Ohwada K., Sato H. and Kajiura S., Proc. 8th Int. Conf. on SMAIRT (Brussel, August, 1985).

3. Power Supplies : Operations and Related Developments

3.1 Operations

In FY 1986, JT-60 poloidal and toroidal field power supplies (PFPS and TFPS) were under operation for 14.5 cycles totally. The

motor-generator for the additional heating systems (MG for AH) was operated in much more times than PFPS or TFPS to condition NBI and/or RF simultaneously with or independently of JT-60 experiments. In the shutdown period of JT-60, all the equipments of PFPS, TFPS and MG for AH were inspected as the annual inspections done by Toshiba Corp., Mitsubishi Electric Co. and Hitachi Ltd. respectively. Concerning the everyday's operation and maintenance of PFPS, TFPS and MG for AH, JAERI made a contract with Kaihatsu Denki Co. Ltd. on their commissions.

3.1.1 PFPS operation

As the main purpose of the first 3.5 cycles' experiments was to establish joule-heated target plasmas for additional heating, various operational parameters of PFPS were tried. The output currents of PFPS were reached to the following values in operation, including the cases of uncontrolled plasmas, for instance disruptive one.

	Actual values (kA)	Nominal values (kA)
OH coil current	+85.4 ~ -92.0	±92.0
VF coil current	+26.1	+58.0 ~ -8.6
HF coil current	+17.2	±22.0
QF coil current	+25.0	±25.0
ML coil current	84.9	120.0

The typical waveforms of PFPS output currents and voltages in this phase were shown in Fig. X.3-1, which was the well-operated case of 2 MA flattop current - 10 sec pulse length plasma in divertor configuration (Shot No. : E001735).

In last 11 cycles' experiments with NBI and RF, PFPS was operated in the same region as previous operations. But, from the point of OH coil current control, the plasma current drive experiment by LHRF resulted in different OH coil current swing from joule-heating experiment. Figure X.3-2 shows that OH coil current changed its own direction of swing (OH coil was recharged), while the plasma current was sustained constant by LHRF.

PFPS had some faults in operation, for example CAMAC system errors, overvoltage on thyristor convertors, MG system faults, etc. On the overvoltage problem of thyristor convertors in OH circuit, ZnO

arrestors were connected to the primary circuits of transformers for thyristor convertors.

3.1.2 TFPS operation

TFPS was modified to output DC 52.1 kA current with 10 sec flattop as maximum in last fiscal year. With such a expanded parameter, TFPS operated for 14.5 cycles' experiments of FY 1986, though some faults (CAMAC system errors, MG acceleration failure, etc.) occurred in operation.

3.1.3 MG for AH operation

The conditioning of NBI and RF required long time operation with excitation of MG for AH. Total running time of MG for AH in FY 1986 reached to about 2800 hours, which was twice of PFPS or TFPS MG's (PFPS : ~1300 hours, TFPS : ~1400 hours). Figure X.3-3 shows the output voltage and current of MG for AH in the case of 70 kV - 62 A - 13 units NBI only. As faults in operation, CAMAC system errors, the carbon brush abrasion of the MG slipring, etc. occurred.

3.2 Related Developments

Based on the plasma experimental results, the following modifications on PFPS and TFPS were proposed.

i) The maximum output current of the quadrupole field power supply should be increased to +35 kA. New thyristor convertors of 10 kA output current will be added to QFPS.

ii) Much more inductance should be necessary in the main DC circuit of the vertical field power supply by the reason of decreasing mechanical stress on the PF coils in disruption. The dummy coil used for the tests will be converted and connected to the VF circuit.

iii) By the same reason mentioned above, an interlock system proportional to VF coil current and the magnetic limiter coil current should be added. This modification has been completed in 1986.

iv) TF coil maximum current should be increased to 57.3 kA (= 52.1 kA × 1.1). TFPS control and protection systems will be modified to enable themselves to output 57.3 kA within the margin of TFPS hardwares.

The modifications of i), ii) and iv) will be completed in next fiscal year.

From the point of operational reliability, some air filters were installed in the power supplies' local control room, and the demineralizing equipments of cooling water for TFPS diode convertors were modified.

As the new type of DC circuit breaker, GTO (Gate Turn-Off) thyristor circuit breaker was developed for the OH circuit of tokamak device. A prototype of GTO thyristor circuit breaker, the ratings of which are shown below, has been manufactured in Toshiba Corp. by the contract with JAERI.

Voltage and Current : 3 kV - 10 kA
GTO thyristor : SG2500GXH22 (4.5 kV - 2.5 kA)
Duty : 1 sec / 30 sec
Connection : 2 series - 8 parallel
Cooling : air forced
Control : 500 Hz PWM

4. Control System: Operations and Related Development

4.1 Operations

The control linkage performance tests between the JT-60 central control system "ZENKEI" and the NBI/RF heating systems were finally carried out for executing the additional heating experiments which followed the second phase of ohmic heating experiment (OH(II)). At these tests the following items were confirmed: (1) message transfer of various kinds of plant data, (2) transfer of the JT-60 operation mode according to the conditions, (3) message communication and transfer of timing signals according to each discharge sequence and (4) error handling including protective interlock in each discharge sequence.

The following functions installed in the real-time control computer I_b^R in "ZENKEI" were confirmed to be very useful for plasma control in the OH(II) experiment: the feedback control of plasma density, the interlocks relevant to phase shift during discharge and the control of discharge termination. It is shown in Fig. X.4-1 that

The modifications of i), ii) and iv) will be completed in next fiscal year.

From the point of operational reliability, some air filters were installed in the power supplies' local control room, and the demineralizing equipments of cooling water for TFPS diode convertors were modified.

As the new type of DC circuit breaker, GTO (Gate Turn-Off) thyristor circuit breaker was developed for the OH circuit of tokamak device. A prototype of GTO thyristor circuit breaker, the ratings of which are shown below, has been manufactured in Toshiba Corp. by the contract with JAERI.

Voltage and Current : 3 kV - 10 kA
GTO thyristor : SG2500GXH22 (4.5 kV - 2.5 kA)
Duty : 1 sec / 30 sec
Connection : 2 series - 8 parallel
Cooling : air forced
Control : 500 Hz PWM

4. Control System: Operations and Related Development

4.1 Operations

The control linkage performance tests between the JT-60 central control system "ZENKEI" and the NBI/RF heating systems were finally carried out for executing the additional heating experiments which followed the second phase of ohmic heating experiment (OH(II)). At these tests the following items were confirmed: (1) message transfer of various kinds of plant data, (2) transfer of the JT-60 operation mode according to the conditions, (3) message communication and transfer of timing signals according to each discharge sequence and (4) error handling including protective interlock in each discharge sequence.

The following functions installed in the real-time control computer I_b^R in "ZENKEI" were confirmed to be very useful for plasma control in the OH(II) experiment: the feedback control of plasma density, the interlocks relevant to phase shift during discharge and the control of discharge termination. It is shown in Fig. X.4-1 that

the plasma line density was well controlled according to its reference value in a divertor discharge with plasma current of 2 MA. The real-time control functions on NBI and RF heating were also confirmed to be well performed in the period of heating experiment. The neutral beam injection with a power of 20 MW into the torus and the plasma current drive up to 2 MA by LHRF waves were achieved. The waveforms of plasma current, horizontal position, vertical field coil current and NBI power in the discharge with neutral beam injection are shown in Fig. X.4-2.

From the beginning of this year the pipelined feedback control system which is described in the next subsection has been fully used for plasma equilibrium control. It has been realized that the plasma state variables such as position and shape can be computed faster with the array processor according to the formula derived from the reggression analysis. The multi-variable control has also been realized in the feedback control computer II^b in "ZENKEI".

In the experiments from June this year the temperature of vacuum vessel has been elevated up to 300°C because the first walls of TiC coated molybdenum was replaced to those of graphite. It has been verified that the function of temperature control and monitoring and the interlock between the coil excitation and the operation of electric baking heater in the discharge sequence are well performed in this high temperature operation.

4.2 Related Development

4.2.1 Upgrade System for Plasma Equilibrium Control

Faster and more accurate computation is necessary for the JT-60 feedback control of high beta plasmas which are produced in the additional heating experiments. In order to satisfy this requirements, the feedback control system has been improved to be a three-step pipelined system [1] with fast array processors as a preprocessor for the feedback control system which consists of two minicomputers of HIDIC-80E (Hitachi Ltd.). (See Fig. X.4-3)

Two fast array processors of ZIP-3216 (Mercury Co., USA) with an execution speed of 100 nsec for 16-bit multiplication with accumulation have been adopted for parallel processing of the controlled state variables such as plasma position and shape. One of the minicomputers is dedicated for data input of the desired and

calculated state variables from its supervisory computer and the preprocessor respectively. The other executes the multivariable feedback control computation and gives the control commands of coil current to the DDC's in the poloidal field power supply.

Each state variable is expressed as a 24-term polynomial form including multiplication and division. The block floating format is used for minimizing errors in multiplication. The method of table look-up is also adopted for reducing its execution time in division. Fast input and output devices of A/D converter, digital interrupt input, pulse counter and D/A converter which are directly connected to the local bus with a speed of 40 MHz in the array processor have been developed for fast DMA data transfer. The timing system which generates three kinds of clock pulse with a period of 1 msec and a proper delay from a master clock has been prepared for synchronizing data transfer between these processors and minicomputers in this pipeline processing.

4.2.2 JT-60 Database Management System

The JT-60 central control system, "ZENKEI" collects the control and instrumentation data relevant to discharge and device status data for plant monitoring. The former of the engineering data amounts to about 3 Mbytes per shot of discharge. The "ZENKEI" control system which consists of seven minicomputers for on-line real-time control has little performance of handling such a large amount of data for physical and engineering analysis. In order to solve this problem, it was planned to establish the experimental database on the Front-end Processor (FEP) of general purpose large computer in JAERI Computer Center. The database management system (DBMS), therefore, has been developed for creating the database during the shot interval. The engineering data are shipped up from "ZENKEI" to FEP through the dedicated communication line after the shot. The hierarchical data model has been adopted in this database, which consists of the data files with tree structure of three keys of system, discharge type and shot number. The JT-60 DBMS[2] provides the data handling packages of subroutines for interfacing the database with user's application programs. The subroutine packages for supporting graphic processing and the function of access control for security of the database are also prepared in this DBMS. (See Fig. X.4-4) The data of more than

2500 shots of experimental discharge are now stored as the database in the FEP. They are fully used for various applications such as plasma equilibrium analysis by magnetic fitting and control system identification.

References

1) Kimura T., Kurihara K. and Matsukawa M., Proceedings of the 14th Symposium on Fusion Technology, Avignon, September (1986) pp. 1439-1444.
2) Kurihara K., Yonekawa I., Itoh Y. and Kimura T., Proceedings of the 12th Symposium on Fusion Engineering, Monterey, October (1987) (to be published).

5. Status of Auxiliary Systems

The construction of the secondary cooling system and the power distribution system/emergency power supply was finished in October 1983 as scheduled. These auxiliary systems are now in operation for the conbination test with the plasma heating systems (Neutral Beam Injection system and Radio Frequency Heating system) and JT-60 device experiment.

5.1 Secondary cooling system

The outline of this system is as follows.

(i) Total circulation of water; 10,070 m^3/hr
(ii) Outlet temperature of cooling water; 31 ^oC
(iii) Inlet temperature of cooling water; 37 ^oC
(iv) Constitution of cooling system; four separate cooling lines
(tokamak secondary cooling line, power supplies secondary cooling line, heating system secondary cooling line and auxiliary equipment cooling line)
(v) Water treatment; the quality of water is maintained through scale prevention, slime prevention and corrosion prevention treatments.

2500 shots of experimental discharge are now stored as the database in the FEP. They are fully used for various applications such as plasma equilibrium analysis by magnetic fitting and control system identification.

References

1) Kimura T., Kurihara K. and Matsukawa M., Proceedings of the 14th Symposium on Fusion Technology, Avignon, September (1986) pp. 1439-1444.
2) Kurihara K., Yonekawa I., Itoh Y. and Kimura T., Proceedings of the 12th Symposium on Fusion Engineering, Monterey, October (1987) (to be published).

5. Status of Auxiliary Systems

The construction of the secondary cooling system and the power distribution system/emergency power supply was finished in October 1983 as scheduled. These auxiliary systems are now in operation for the conbination test with the plasma heating systems (Neutral Beam Injection system and Radio Frequency Heating system) and JT-60 device experiment.

5.1 Secondary cooling system

The outline of this system is as follows.

(i) Total circulation of water; 10,070 m^3/hr
(ii) Outlet temperature of cooling water; 31 ^{o}C
(iii) Inlet temperature of cooling water; 37 ^{o}C
(iv) Constitution of cooling system; four separate cooling lines
(tokamak secondary cooling line, power supplies secondary cooling line, heating system secondary cooling line and auxiliary equipment cooling line)
(v) Water treatment; the quality of water is maintained through scale prevention, slime prevention and corrosion prevention treatments.

Total time of operation at fiscal year (from April 1986 to March 1987) is as follows.

Tokamak secondary cooling line : 2,621 hour
Power supplies secondary cooling line: 3,065 hour
Heating system secondary cooling line: 2,899 hour
Auxiliary equipment cooling line : 8,312 hour

5.2 Power distribution system/emergency power supply

5.2.1 Power distribution system

The outline of this system is as follows.

(i) the capability of the system: 13 MVA
(ii) 6.6 kV M/C : 19 lines
(iii) 400 V P/C : 3 banks
(iv) 200 V P/C : 3 banks

capacity of electric power at fiscal year (from April 1986 to March 1987) used about 9,532 MWH.

5.2.2 Emergency power supply

The outline of this power supply is as follows.

(i) the capability of the power supply : 8.3 MVA
(ii) 6.6 kV M/C : 11 lines
(iii) 400 V P/C : 3 banks
(iv) 200 V P/C : 2 banks
(v) the AC no break power supply
static type invertor (CVCF) : 500 kVA, 4 sets
(vi) battery (HS-2500) : 2500 AH, 2 sets
(vii) the DC no break power supply
rectifier device : 250 kVA, 2 sets
(viii) battery (HS-500) : 500 AH, 2 sets

capacity of electric power at fiscal year (from April 1986 to March 1987) used about 5,703 MWH.

6. Construction of Heating System

6.1 Construction of neutral beam injector (NBI)

The JT-60 NBI system is rated to inject 20MW neutral hydrogen beams at energy of 75-100 keV for 10s. The bird's eye view of the whole system is shown in Fig. X.6 - 1. After the installations of JT-60 NBI systems such as 14 beam line units, the performance tests including the beam extraction test were started.

The performance tests were finished at the end of July in 1986, and then the beam injection tests into JT-60 plasma were started immediately in August.

6.1.1 Beam injection test into JT-60 plasma

The beam injection test into JT-60 plasma were started in August 1986. The injection power and beam pulse length were increased gradually as investigating the NBI performances and the JT-60 plasma condition. And a rated 20 MW neutral injection at energy of 75 keV was achieved in October 1986 with 20 days operation as in Figure X.6 - 2.

Reionization loss of neutral beams in the drift duct decreased rapidly from more than 40% to 6 ~ 7% of injection power with ~50 injection shots.

The beam injection using the beam energy control which is changed the beam energy and beam current during a pulse, was tested in February 1987. and a validity of this technique was confirmed for NB heating experiment.

Through some minor problems were occurred during a few months since the performance test including beam extraction had been started, there was no serious trouble in the whole system.

6.1.2 Automatic control of cryogenic systems

The operations of the helium refrigerator with the capacity of 3 KW at 3.6 K and 14 cryopumps are controlled in all operation modes automaticaly by a process computer.

Features of the automatic control of the cryogenic systems are as follows;

(1) Parallel control of cooling down and filling of 14 cryopumps,

(2) Control of the imbalance cool down behaviors amoung 14 cryopumps in the cool down mode,

(3) Stable control of refrigerator against the changeable load from cryopumps.

The results of automatic operation of the refrigerator and cryopumps are shown in Fig. X.6 - 3. In this figure, the cool down curves of cryopumps are those of the first unit and the last unit in 14 cryopumps which reached steady state. It took about 8 hours to cool down the refrigerator and to fill the liquid helium as much as 1800 ℓ in the helium dewar from room temperature.

It took 15 hours to cool down all of 14 cryopumps from room temperature to the steady state. The maximum cool down time difference of 14 cryopumps could be decreased form 8 hours at the fist trial to 3 hours by controlling the imbalance cool down behaviors among 14 cryopumps in the cool down mode.

6.2 RF heating system

One of the notable features of JT-60 is the huge RF power for heating and steady current drive. The RF heating system for JT-60 consists of three units of Lower Hybrid Range of Frequencies (LHR, ~2GHz) heating systems and one unit of Ion cycrotron Range of Frequencies (ICRF, ~120MHz) heating system. Each of them has a 6~8MW RF generator. The construction of the RF heating system started in 1983 and a RF performance test was completed in summer of 1986 and the RF coupling test with JT-60 plasmas was started in October 1986. One unit of LHRF and ICRF heating systems were operated at first and successful initial results with 1.7MA current drive and heating were obtained. All four units have been operated from January of 1987 and driven current of 2MA was obtained with 3 units of LHRF launcher. The results of RF performance testing and present operation of the RF heating systems are described in the following sections of LHRF and ICRF heating system.

6.2.1 LHRF heating system

The high power generator (1MW klystrons), which was first developed for plasma heating in JT-60, without any output circulators

was applicable even with high reflection power from the plasma load. The special circuits of Automatic Gain Control (AGC) and Automatic Phase Control (APC), which were equipped in amplifier chains, could stabilize the RF wave transmission to the grill mouth against the unstable plasma load. The output characteristics with and without the AGC circuit is shown in Fig. 6 - 4.

Before launching LHRF power into JT-60 plasmas, LHRF testing was performed to check the phase and power control, the output microwave circuit, the protection system and the monitor system. The phase control is the most important in LHRF heating system since this determines $N_{//}$ spectrum radiated from a launcher, where the $N_{//}$ is a refractive index parallel to the magnetic field. The APC circuit can provide a stable and intentional phase difference setting among waveguide mouths even against the unstable load. The stable waveforms of output power and phase difference are shown in Fig. 6 - 5, where reflection power and phase are intentionally changed using a high speed power phase shifter placed between the klystron and the launcher, which was specially developed for this system. As a tool for protecting the klystrons from the steady high reflection power, the high speed power phase shifter, which optimizes the reflection phase to the klystron. The combination of magic tees and movable phase shifters, which was also developed for this system, are employed.

A knotching circuit in combination with various reflection alarms is also employed in order to condition the launcher efficiently. The arc detector for protecting launcher windows works well and the LHRF heating system is operated safely without worries of window cracking even in heavy duty breakdown during launcher conditioning. After conditioning of the launcher for several days, the input power into a torus of ~2 MW/launcher for several seconds has been achieved and the successful experiment of 2 MA current drive, electron heating, and combination heating with NBI were carried out.

6.2.2 ICRF heating system

The ICRF heating system has similar amplifier chains of 8 lines but, instead of klystrons, Eimac 8973 tetrodes are used as final tubes.

The grounded grid type amplifier with a 3/4 wavelength coaxial cavity is employed. A ferite ring efficiently suppreses parastic oscillations. The power of 750 kW/tube for 10 s in the frequency range of 110~130 MHz, which is the new operation regime of this tube at a high frequency, have been achieved in the real system. Two amplifier chains are combined with a 3 dB hybrid coupler and connected to one of the elements of the 2×2 loop array. One of the notable features of the JT-60 ICRF heating system is programmable stub tunning control, which enables us to find the tunning point of complicated stub control for 2×2 loop antenna in one shot. The impedance matching is further refined with the calculation of the tunning point based on the measurement of the antenna impedance. Phase control of the 2×2 loop antenna works well. Clear response is seen in coupling and heating with phase control. A knotching circuit similar to LHRF heating system is also employed. Furthermore, power regulation circuit is equipped in order to protect the launching system against high voltage of standing wave. The ICRF launching system employs an open Farady Shield, which works quite well and has achieved a power density of 1.1 kW/cm^2. The maximum power so far is 2.1 MW into a torus. Typical waveform of injected ICRF power is shown in Fig. 6－6.

Table X.1-1 The summarized results of the operation in the fiscal year of 1986

Operation days	118 days
Scheduled days for Plasma Pulses	102 days
Average Number of shots per day	18.5
Number of Shots OH NB RF NB+RF Sequence Stop	1886 765 423 370 272 56
Number of Troubles	332
Hours of Taylor Discharge Cleaning	Hr Min. 140 37
Pulses of Taylor Discharge Cleaning	383,055
Commissioning Shots	64

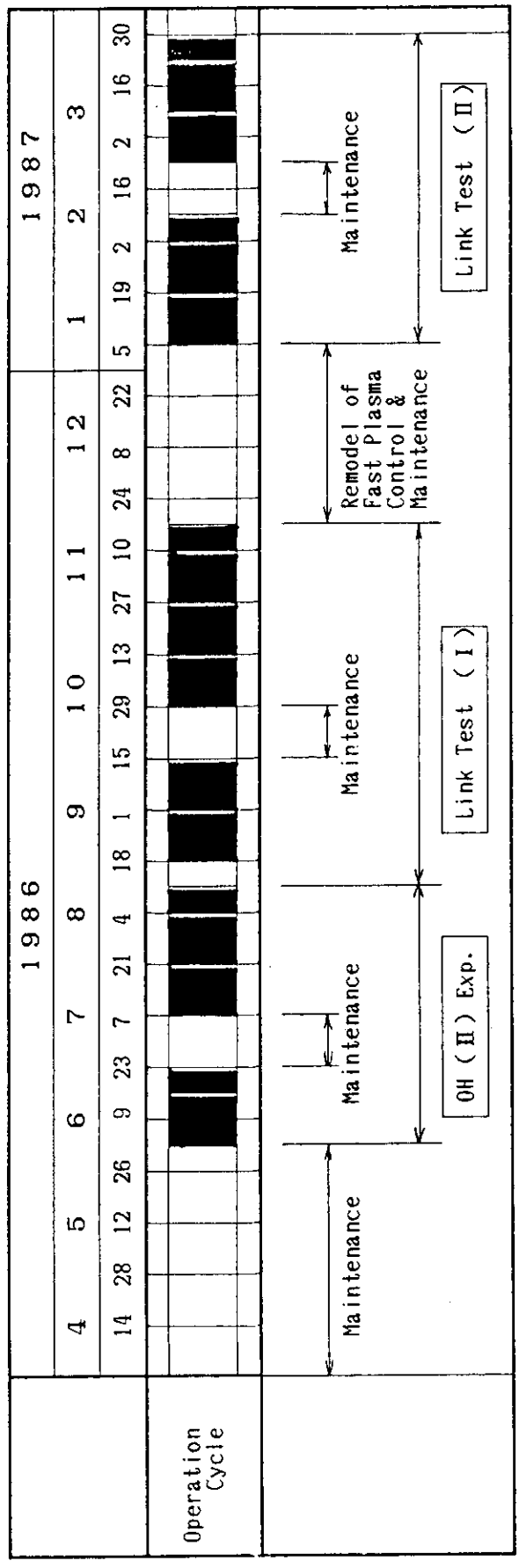

Fig. X.1-1 The operation schedule in FY 1986.

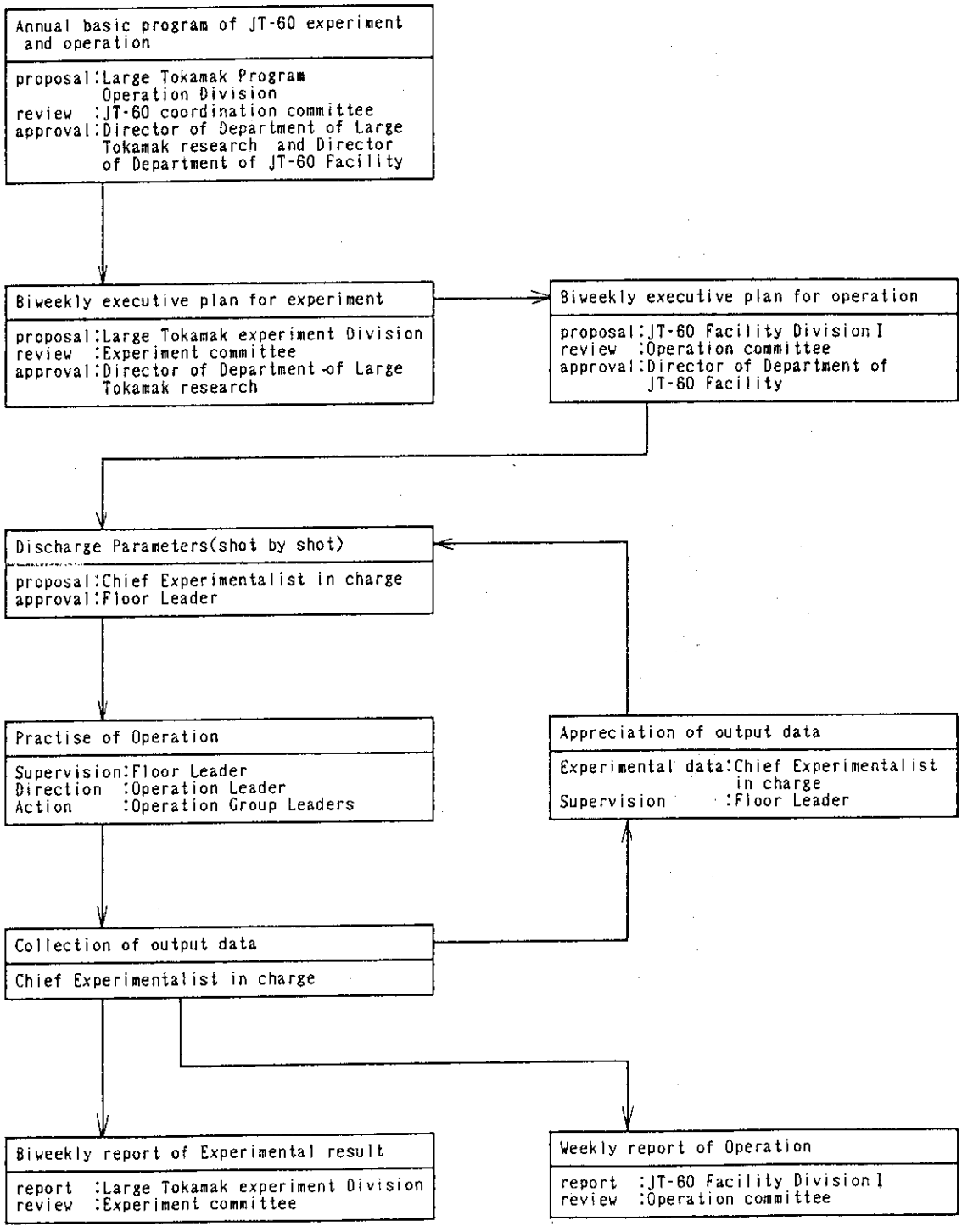

Fig. X.1-2 Process flow of experiments and operations.

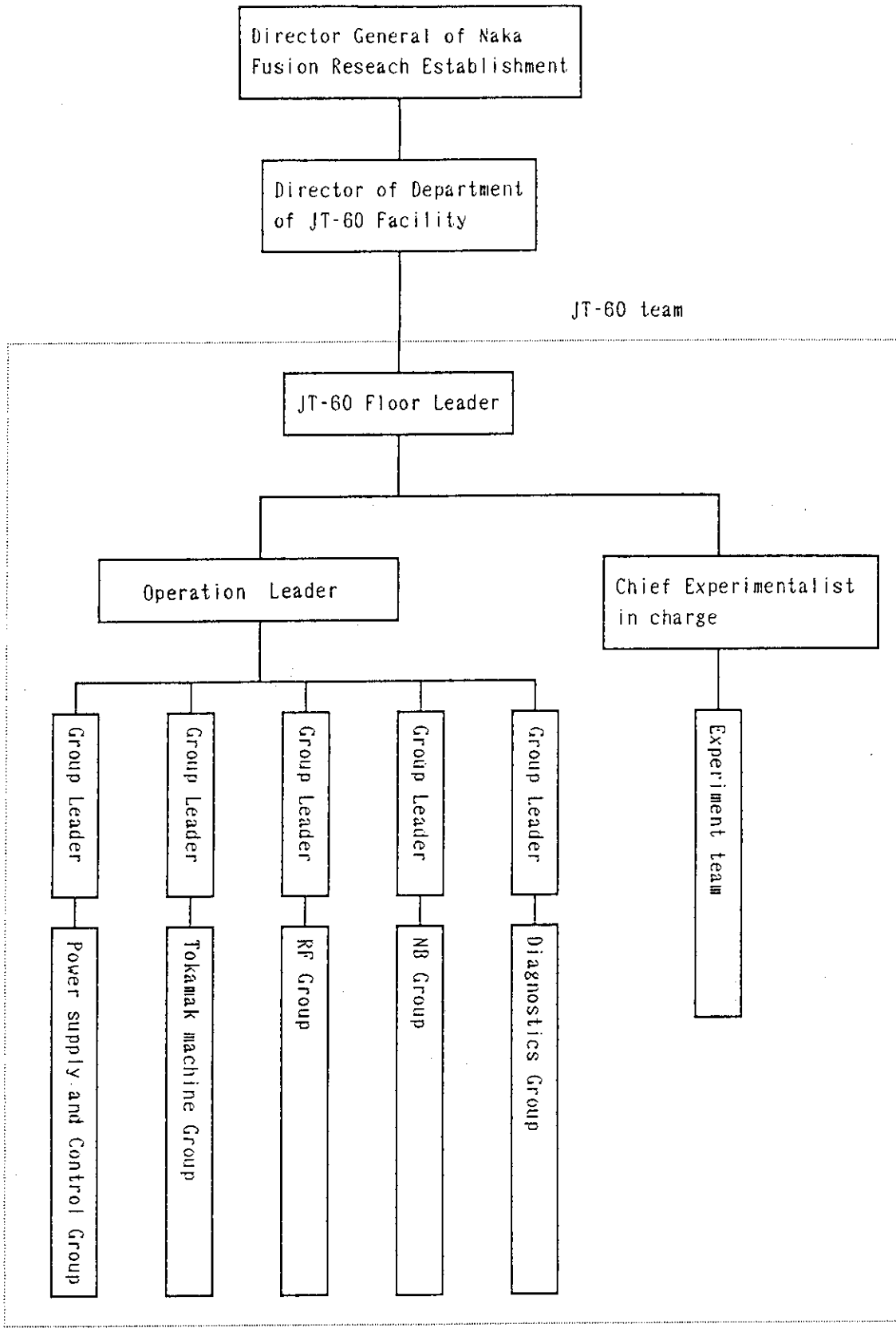

Fig. X.1-3 The organization for an operation regime.

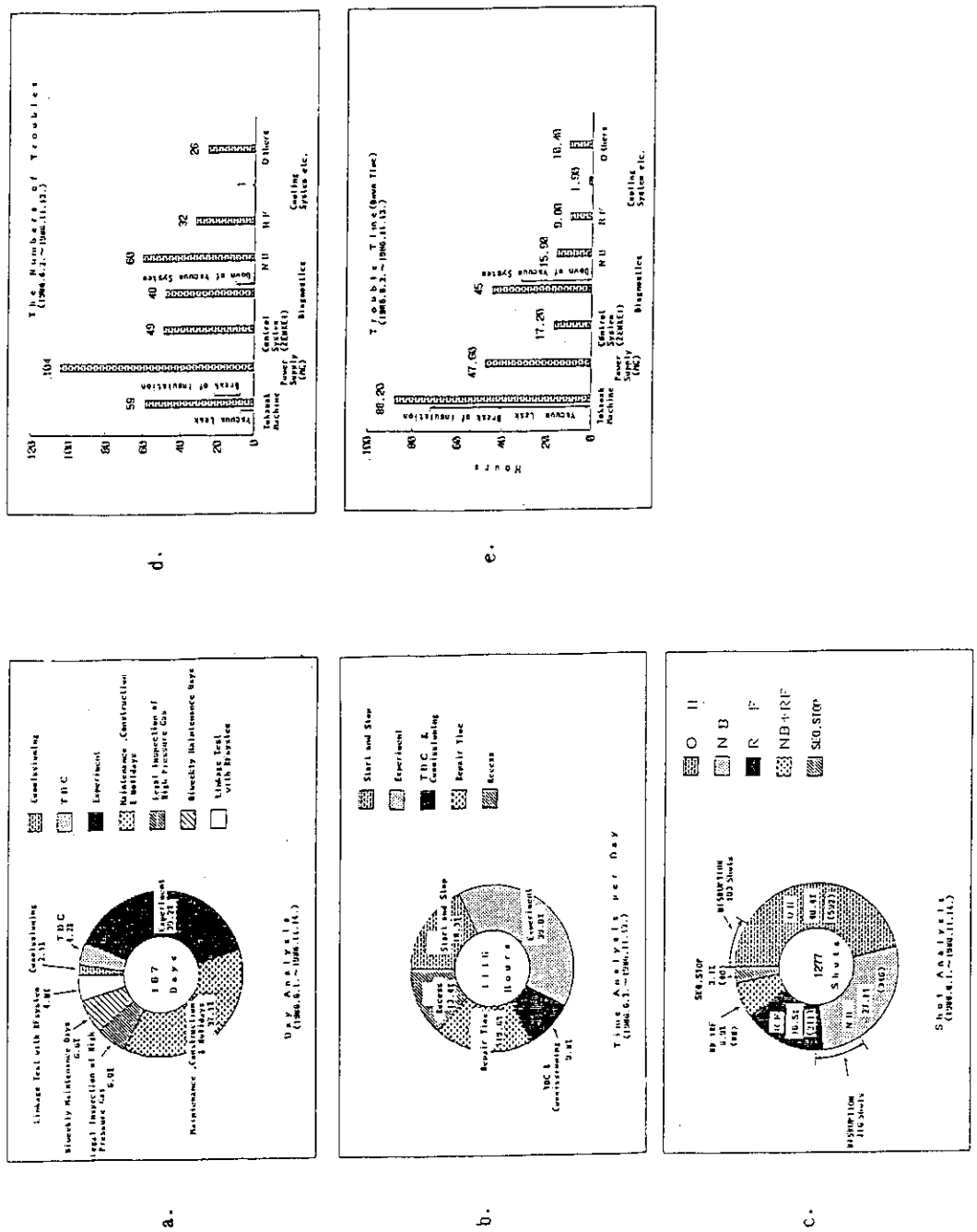

Fig. X.1-4 Statistical operation results in the term of June to November in 1986.

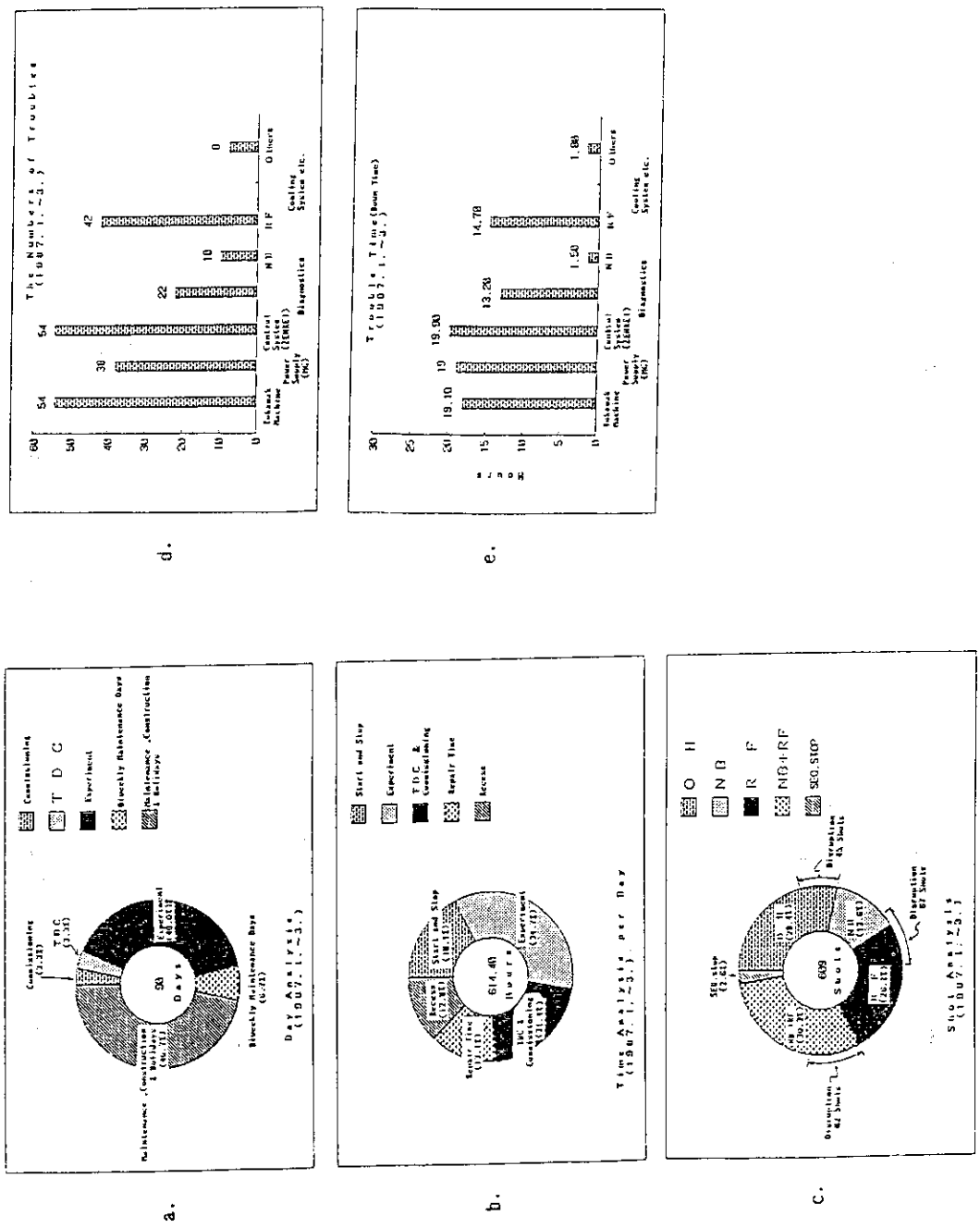

Fig. X.1-5 Statistical operation results in the term of January to March in 1986.

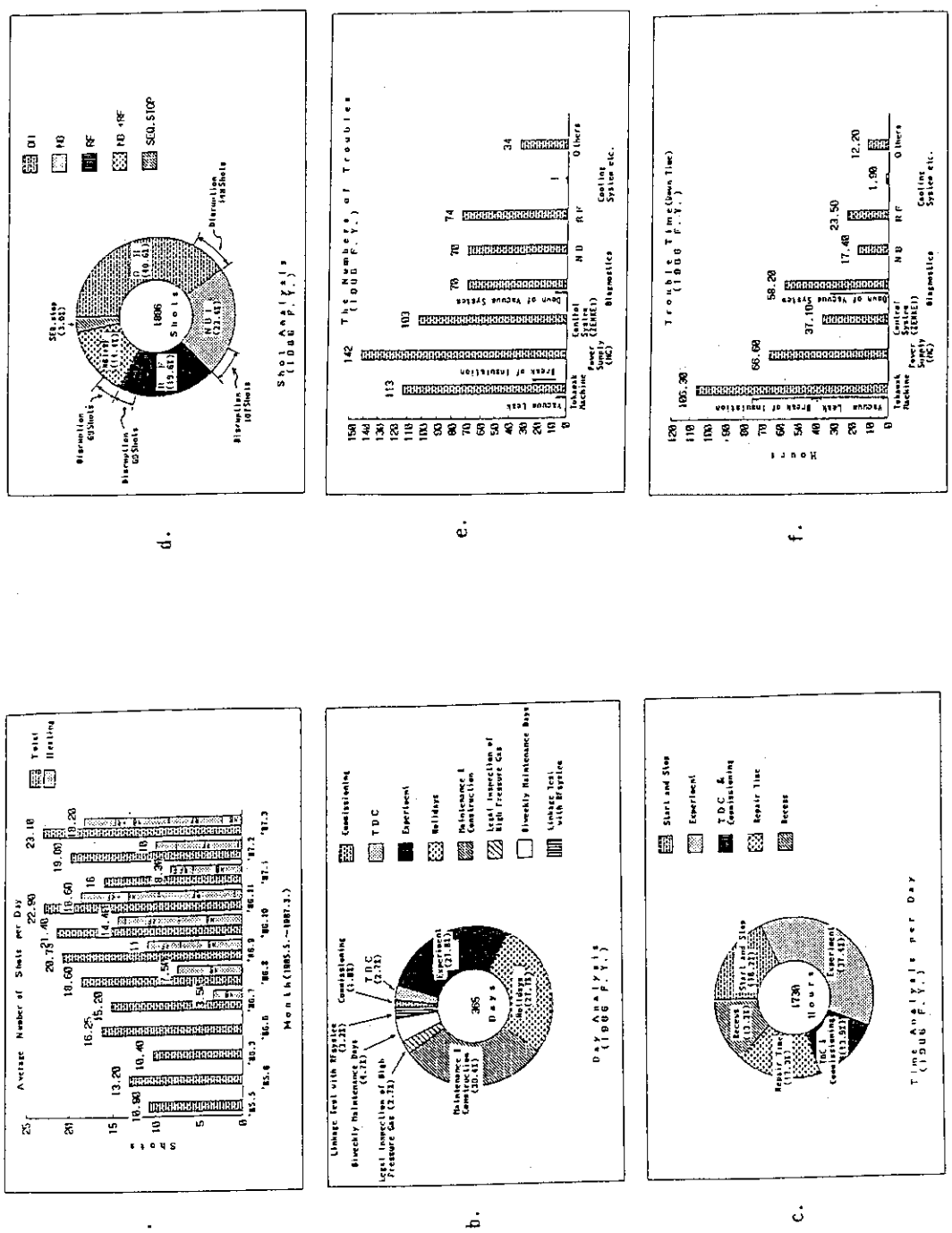

Fig. X.1-6 Accumulated statistical operation results in the fiscal year of 1986.

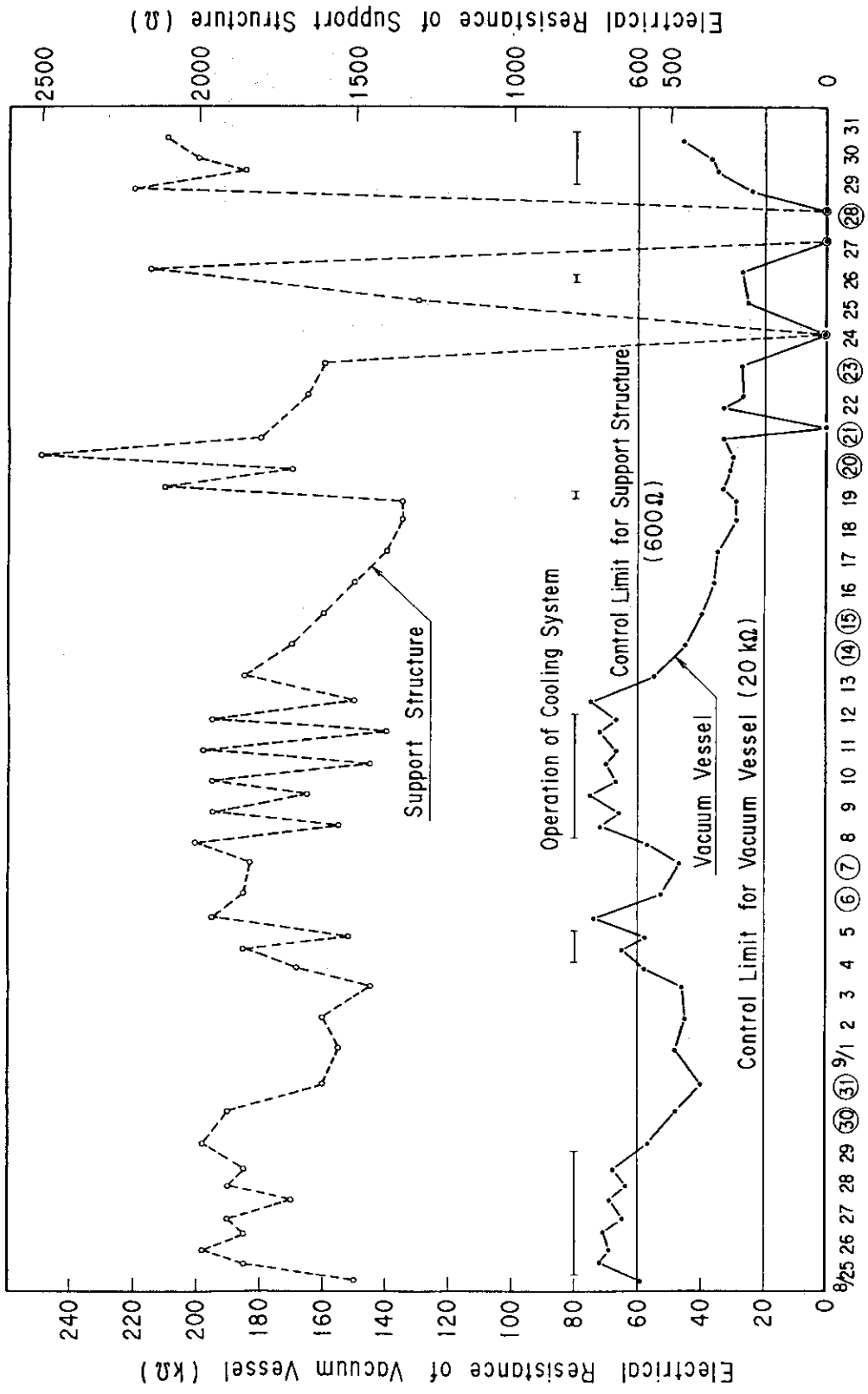

Fig. X.2-1 Time dependence of the electrical resistances.

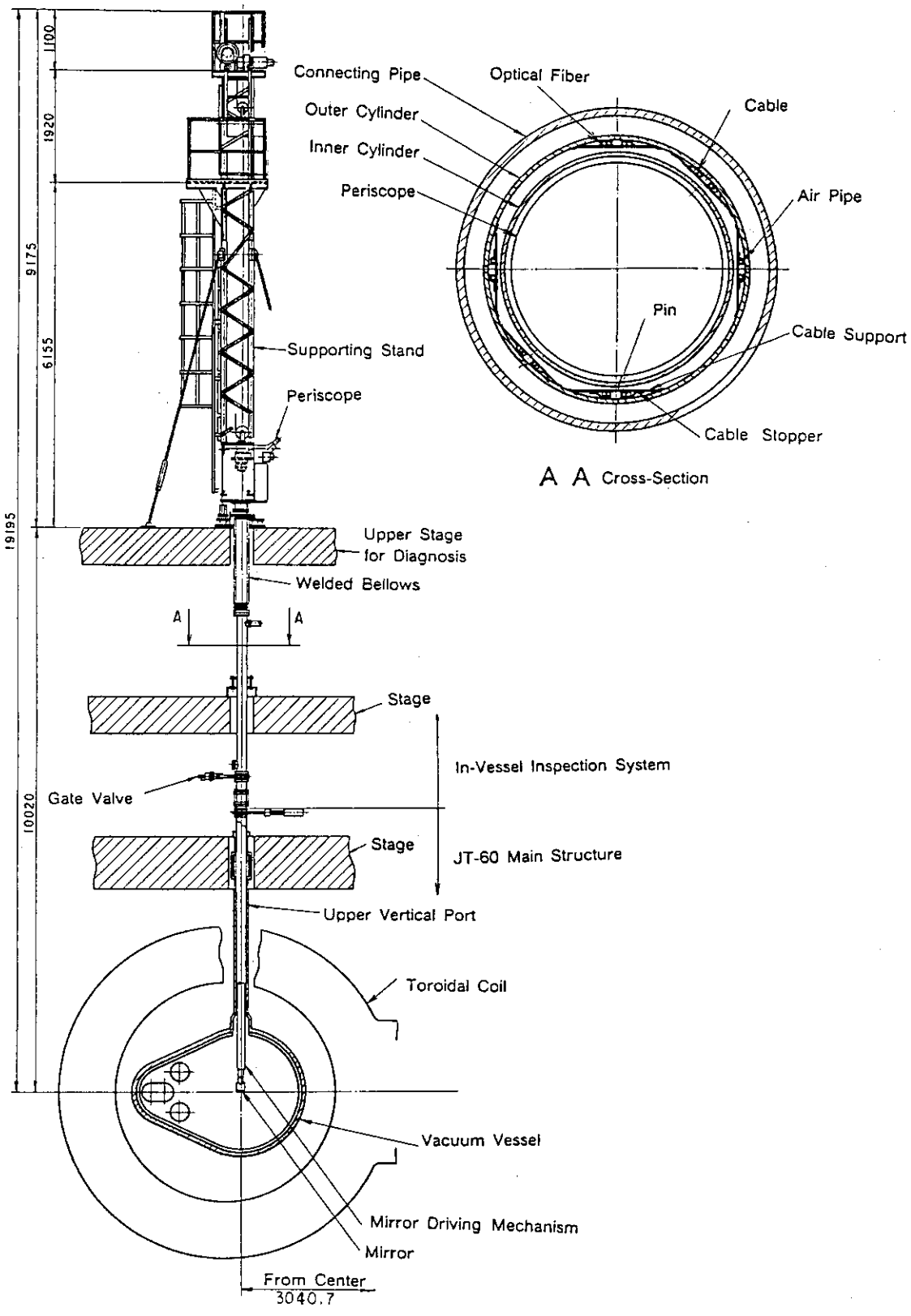

Fig. X.2-2 Schematic diagram of the JT-60 in-vessel inspection system.

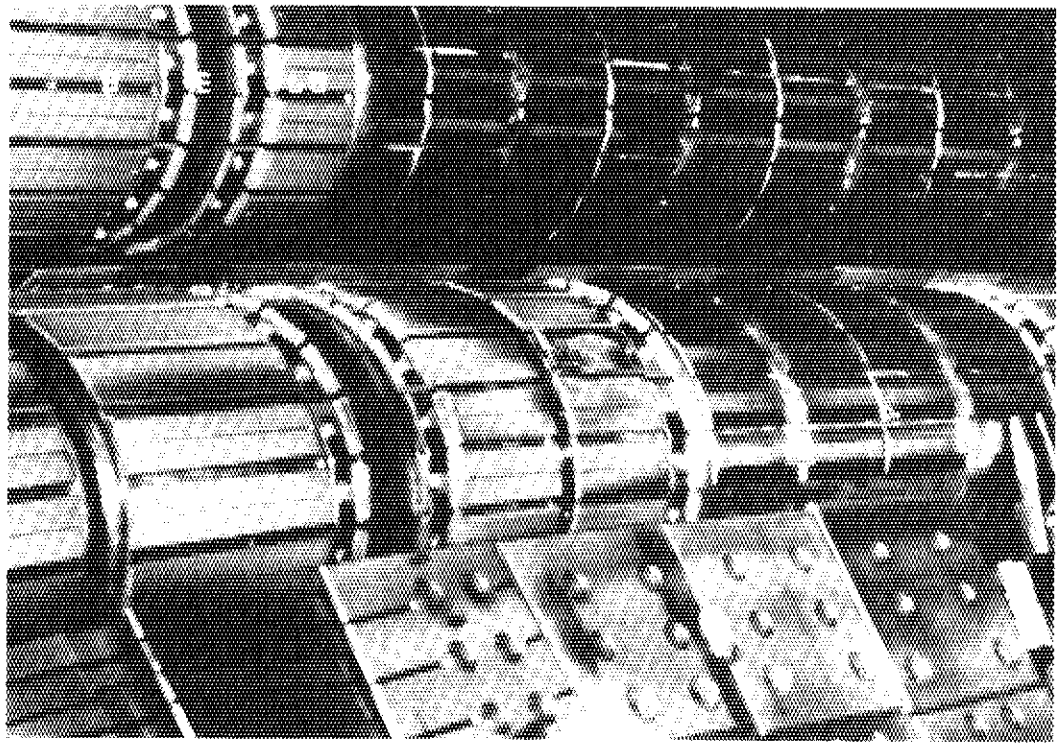

(a)

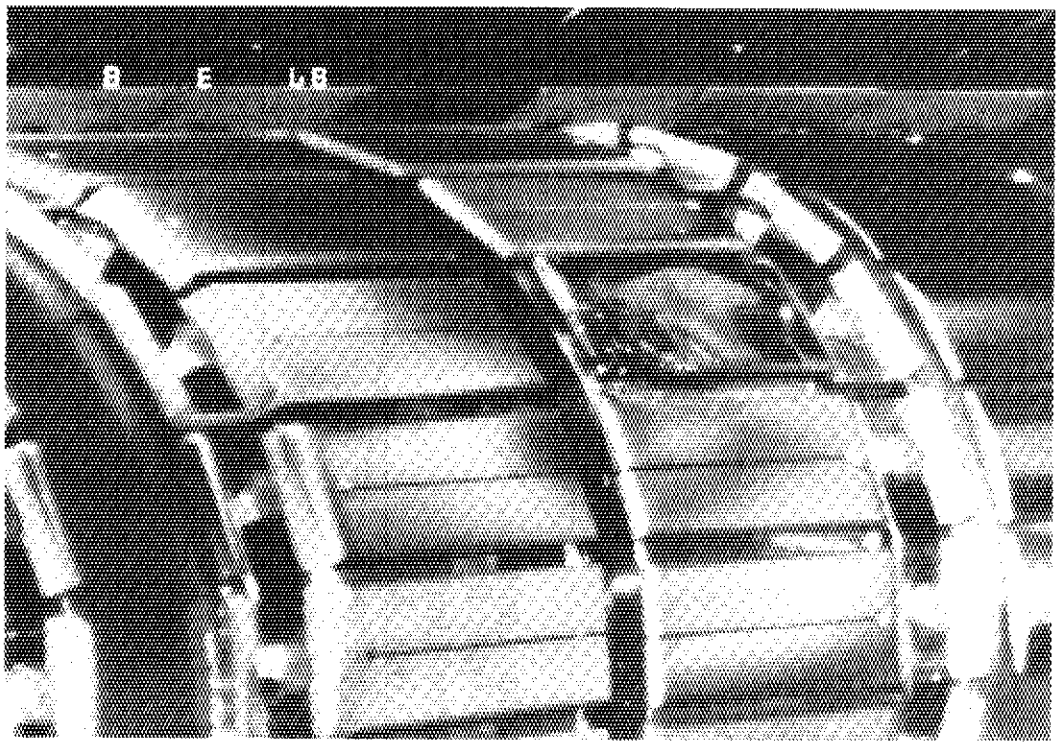

(b)

Fig. X.2-3 Typical pictures taken by the in-vessel inspection system.

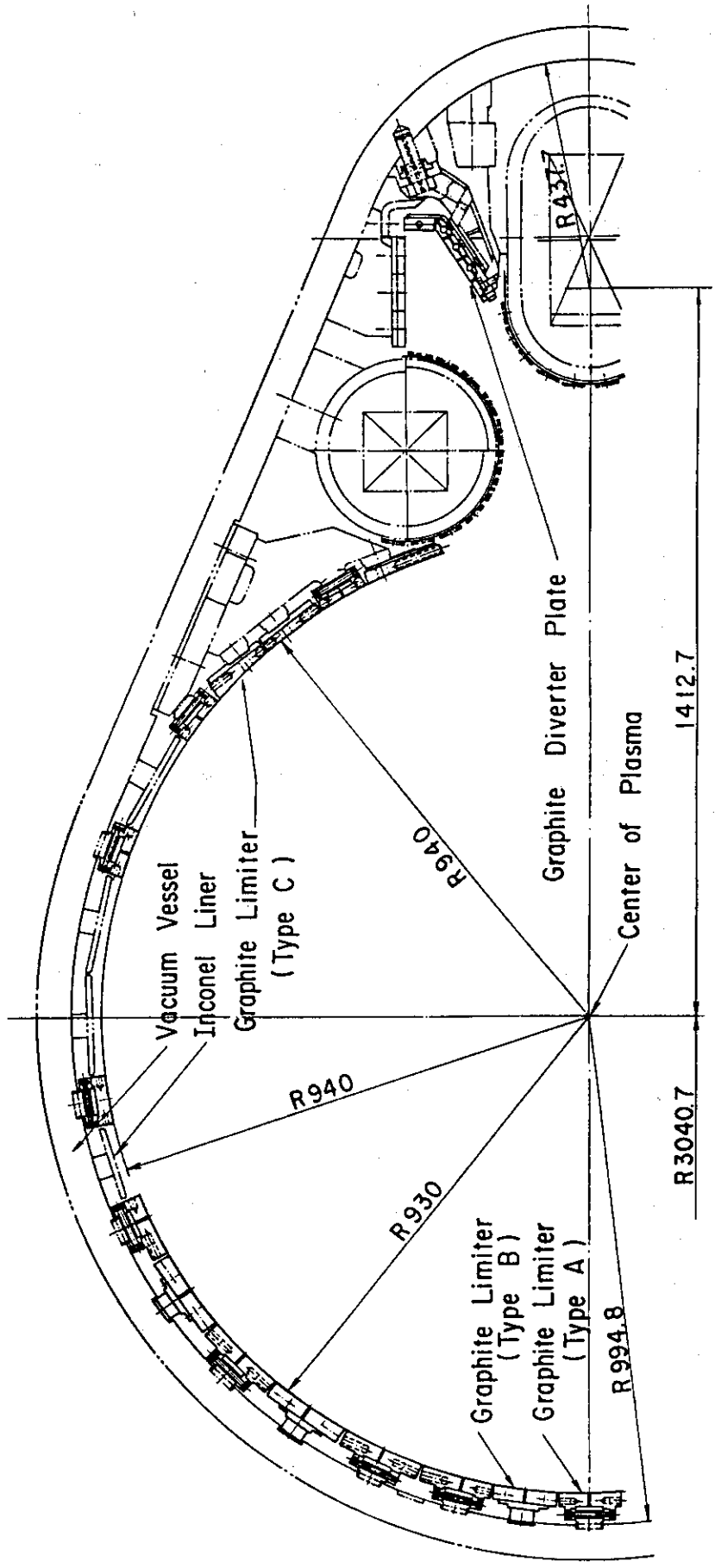

Fig. X.2-4 Cross sectional view of the JT-60 vacuum vessel.

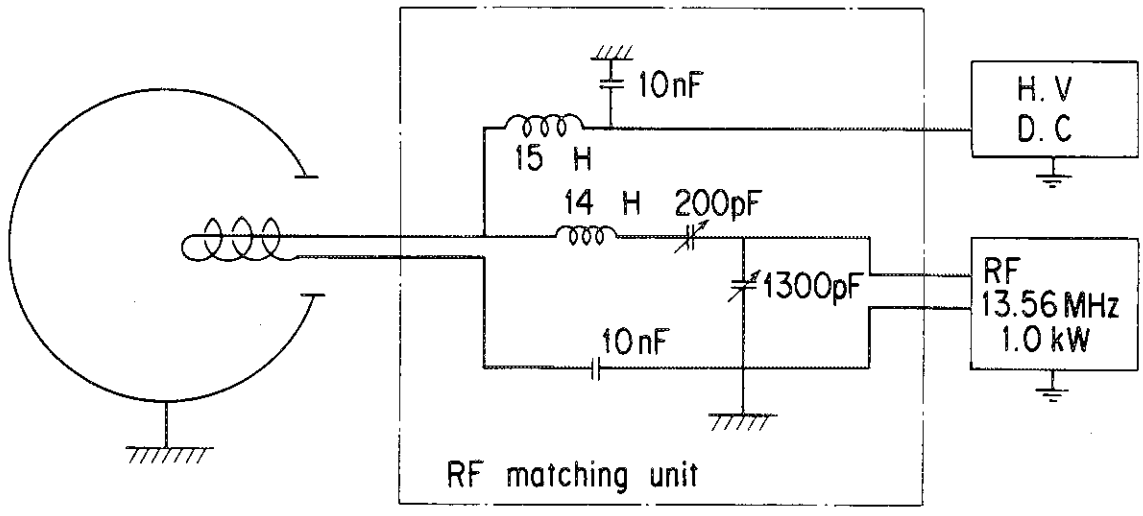

Fig. X.2-5 Schematic diagram of the electrical supply.

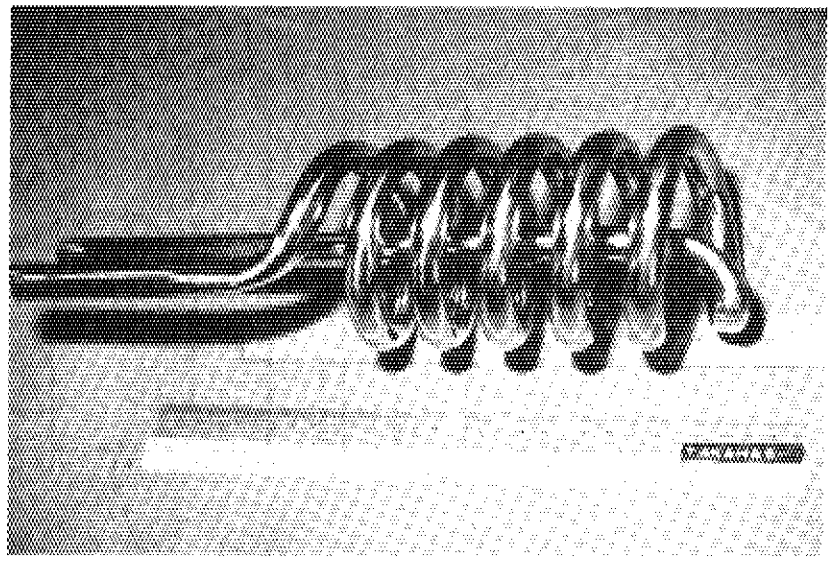

Fig. X.2-6 Photograph of the coil-electrode.

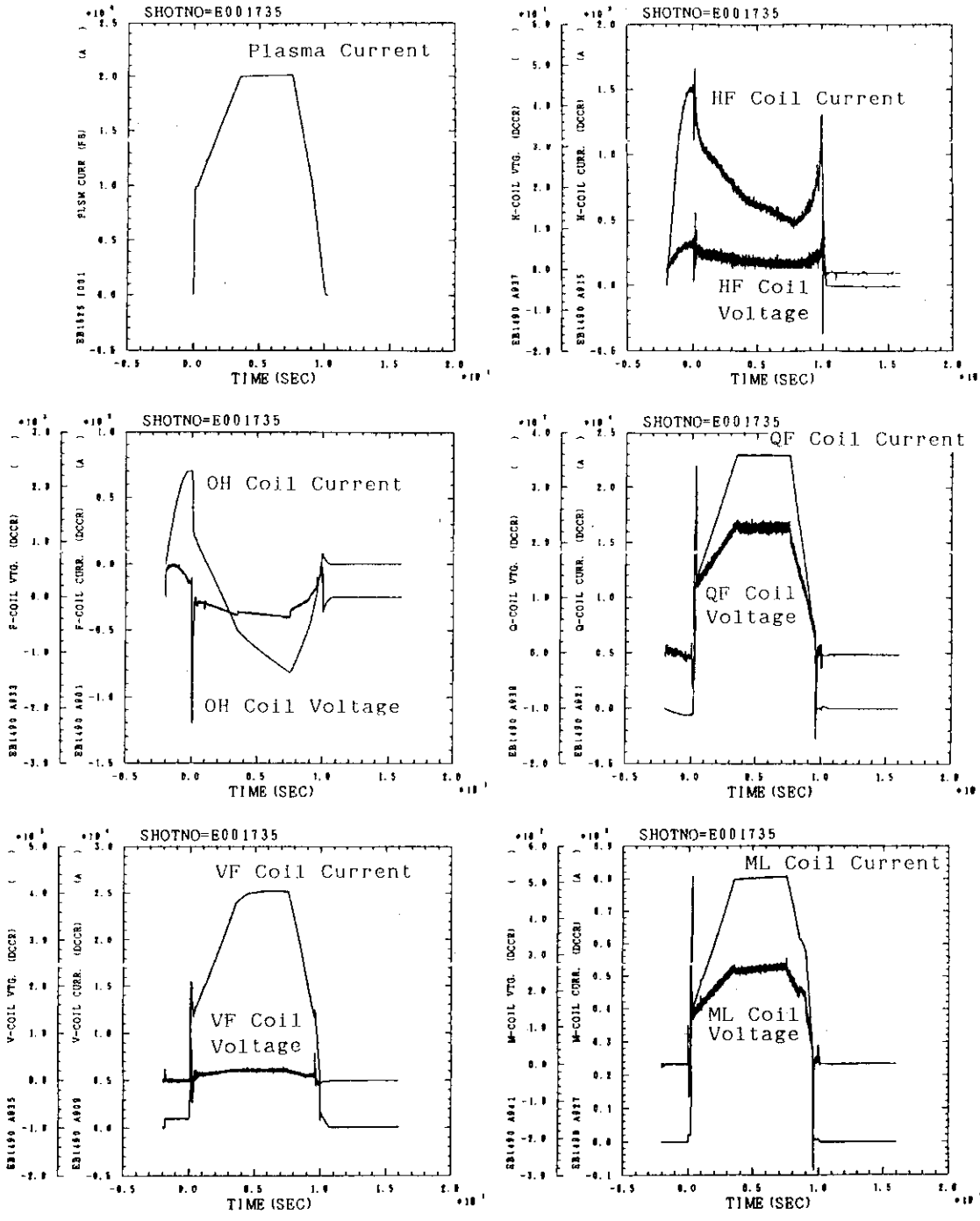

Fig. X.3-1 Typical waveforms of PFPS output currents and voltages (2 MA - 10 sec divertor plasma : Shot No. E001735).

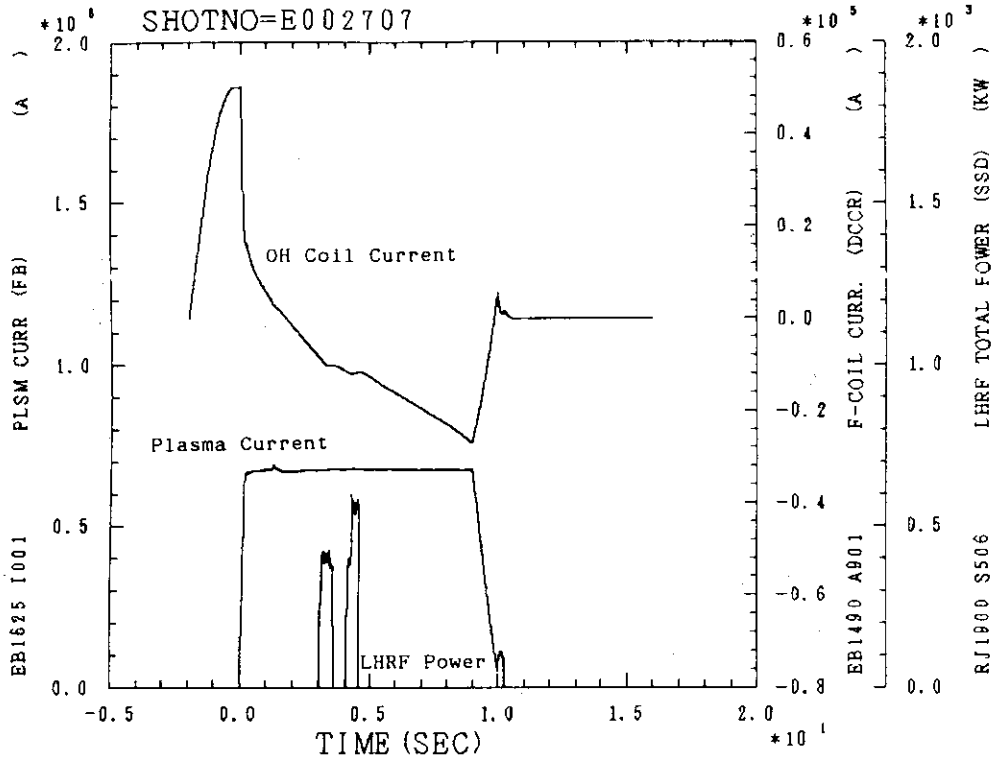

Fig. X.3-2 OH coil current waveform in plasma current drive experiment by LHRF (Shot No. E002707).

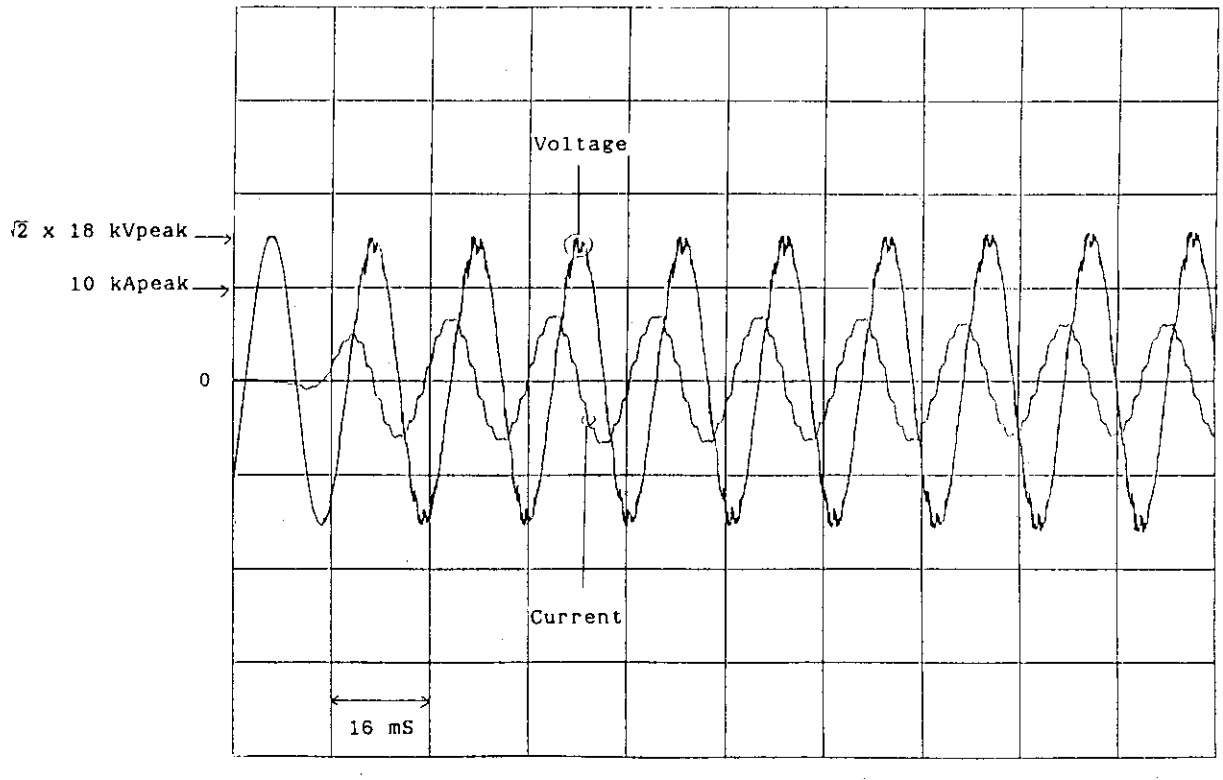

Fig. X.3-3 Output voltage and current of the generator (at 70 kV, 62 A, 0.5 s, 13 units NBI injection).

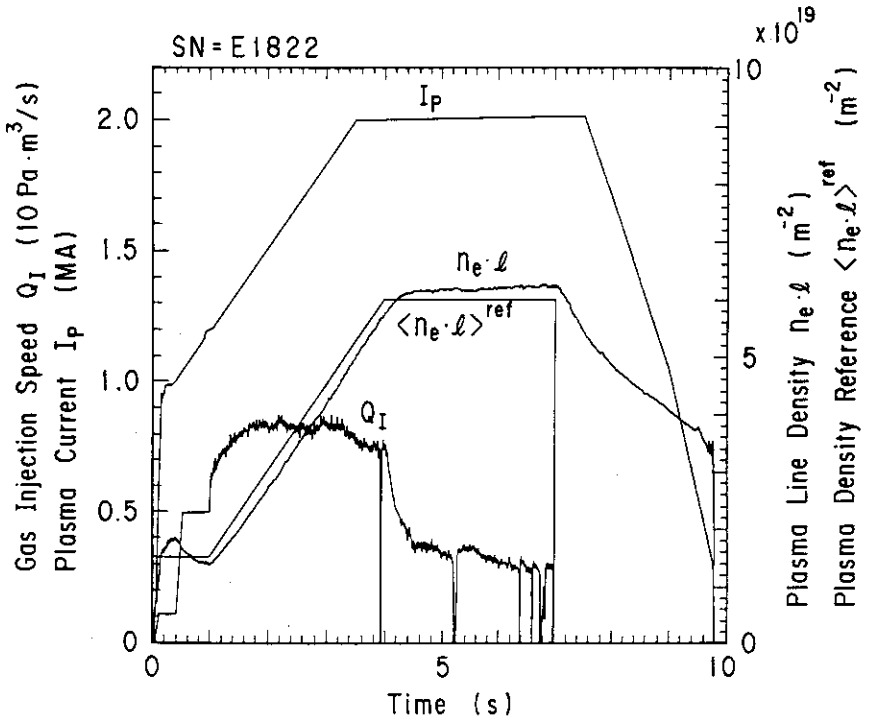

Fig. X.4-1 Divertor discharge with plasma current of 2 MA. The plasma density are well controlled according to its reference value.

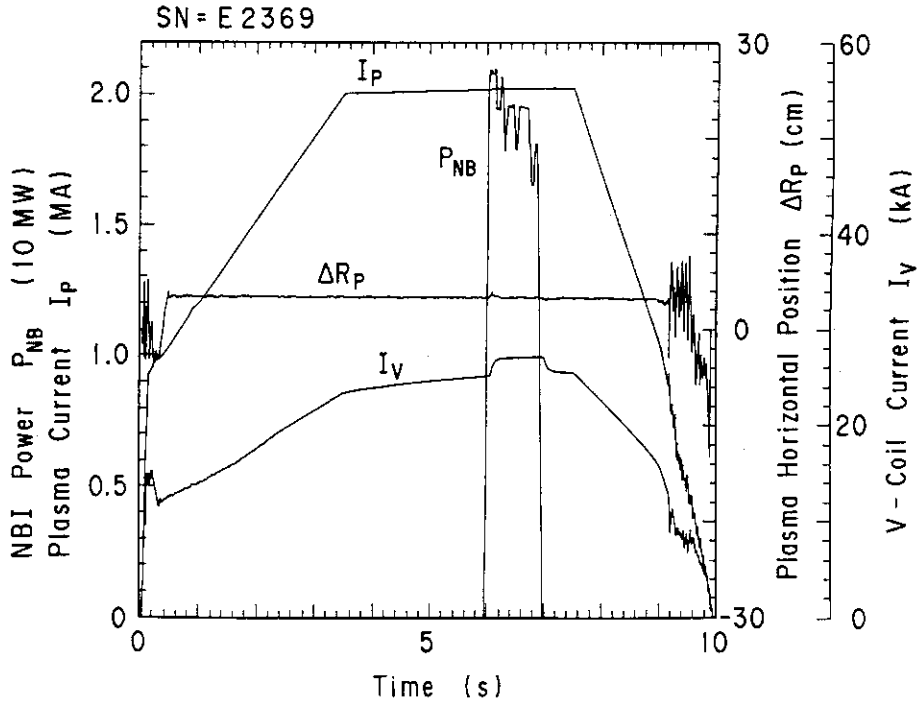

Fig. X.4-2 Stable 2 MA divertor discharge with neutral beam injection.

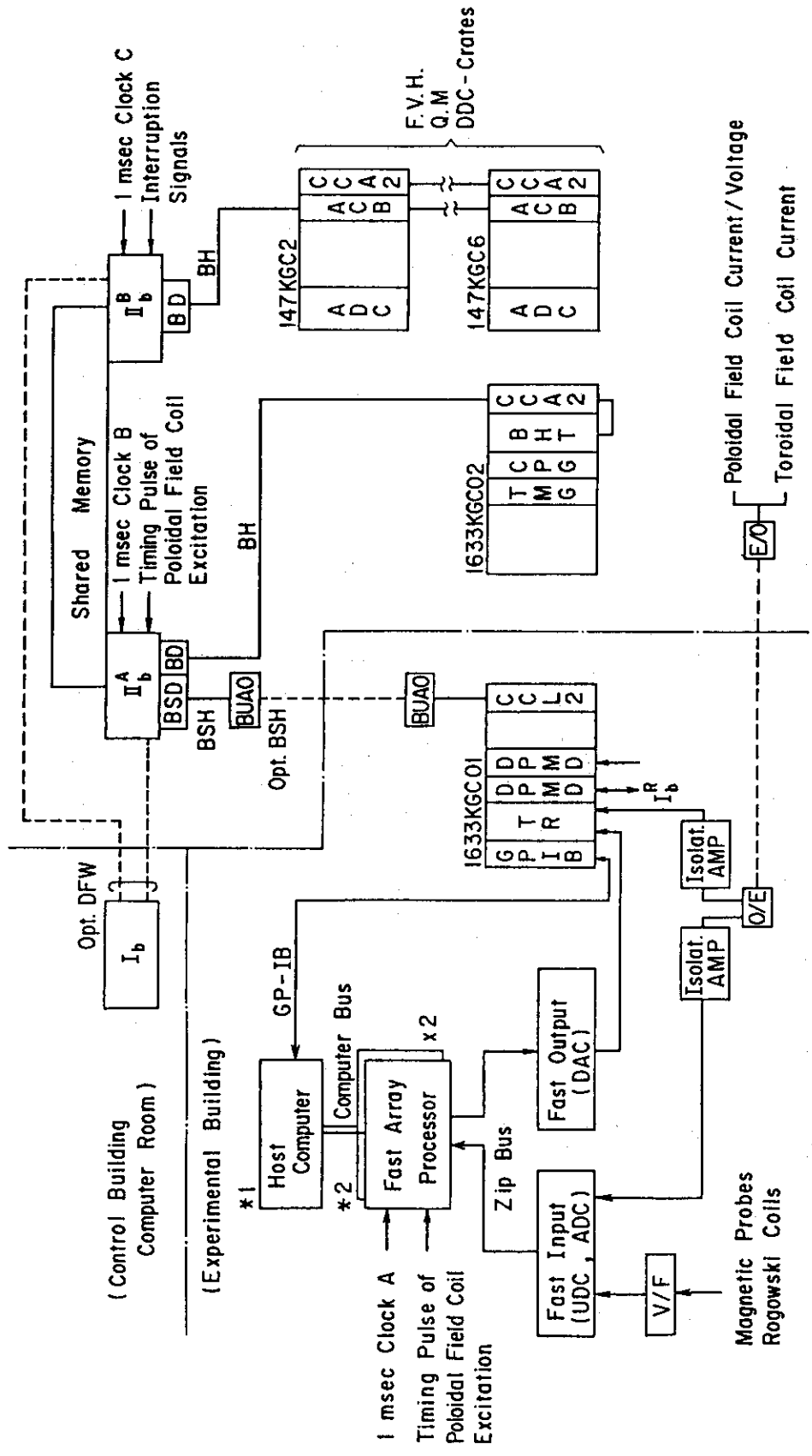

Fig. X.4-3 Configuration of the three-step pipelined system for plasma equilibrium control in JT-60.

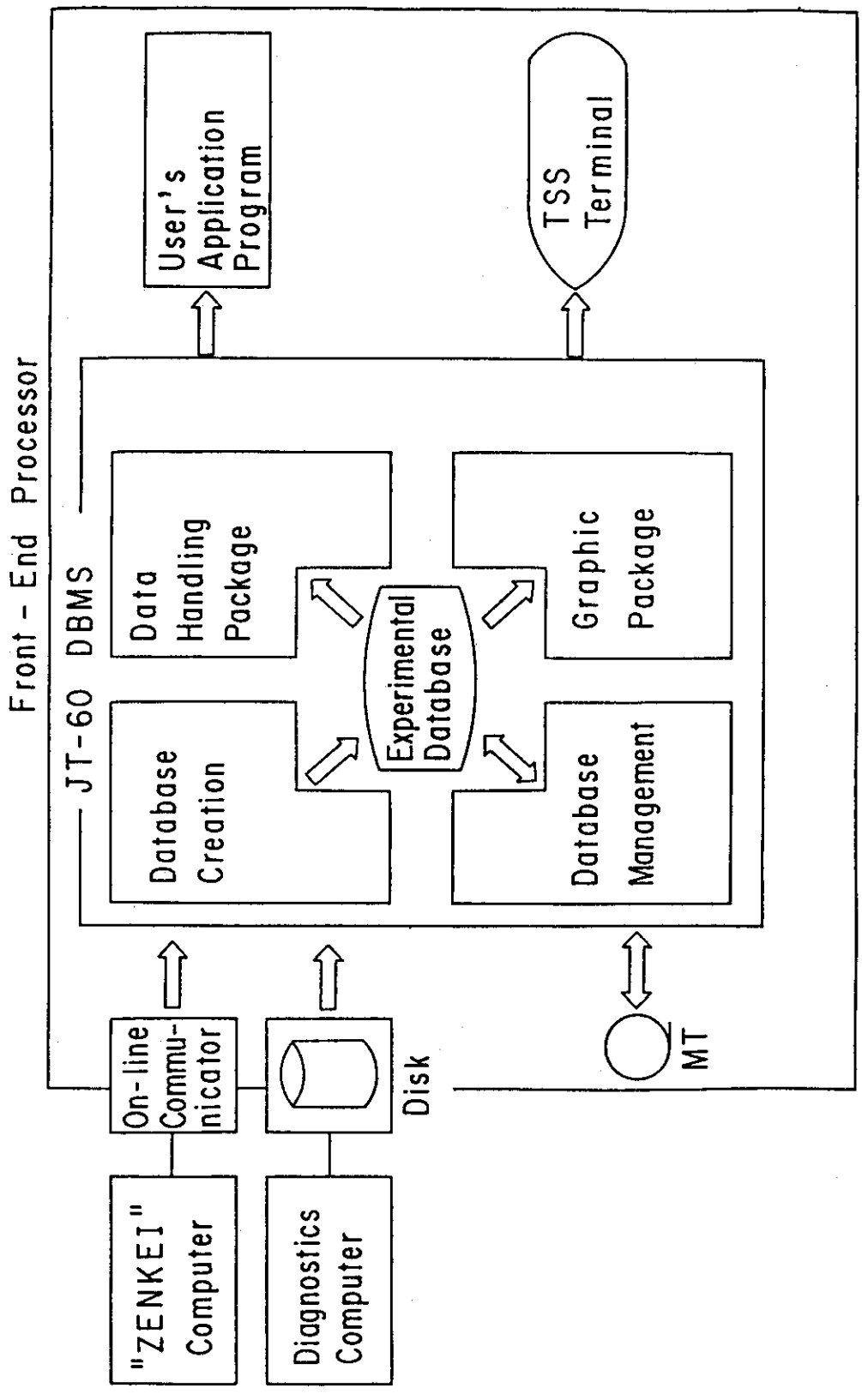

Fig. X.4-4 Structure of the JT-60 experimental database management system.

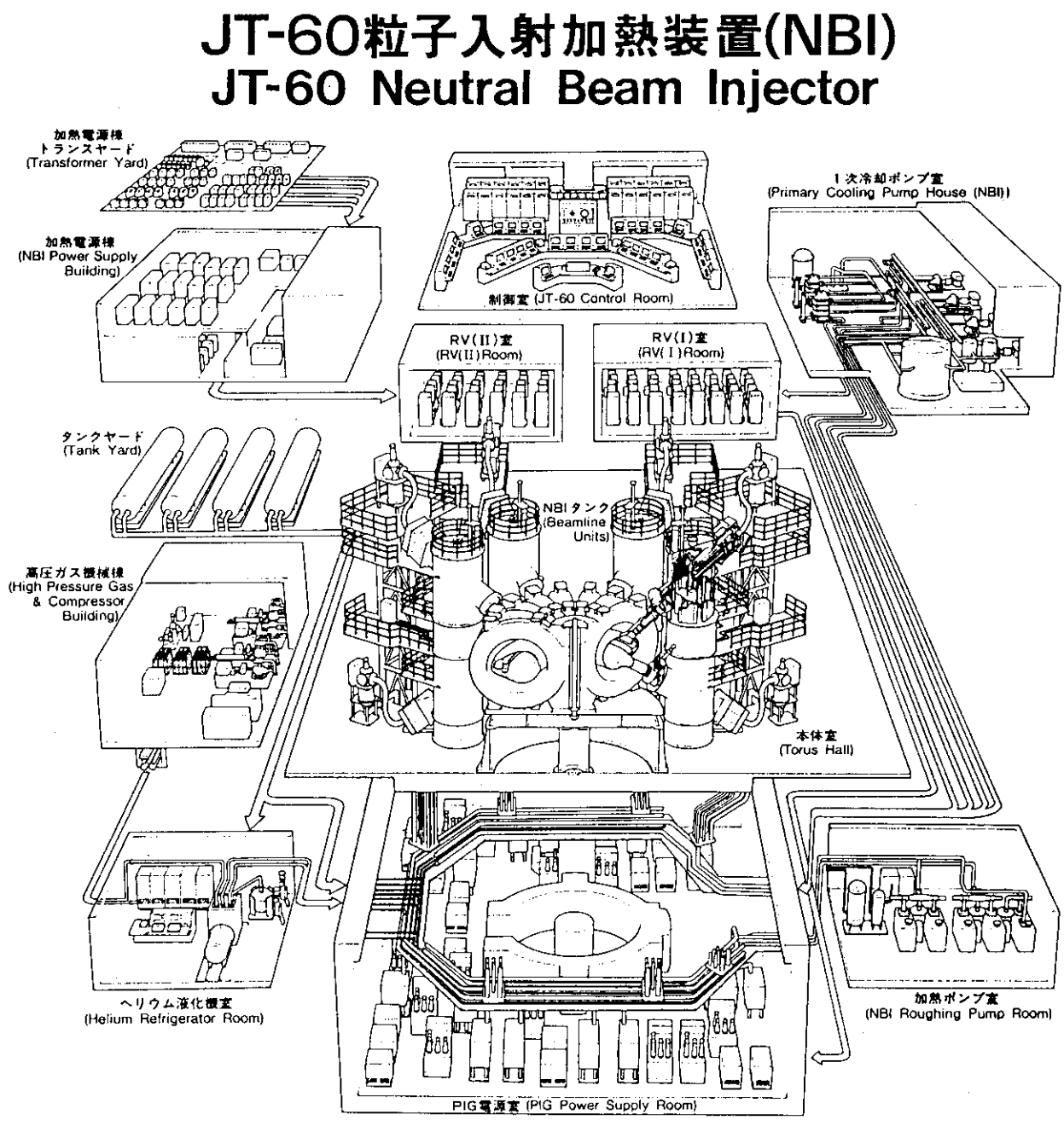

Fig. X.6-1 The bird eye view of the JT-60 neutral beam injector system.

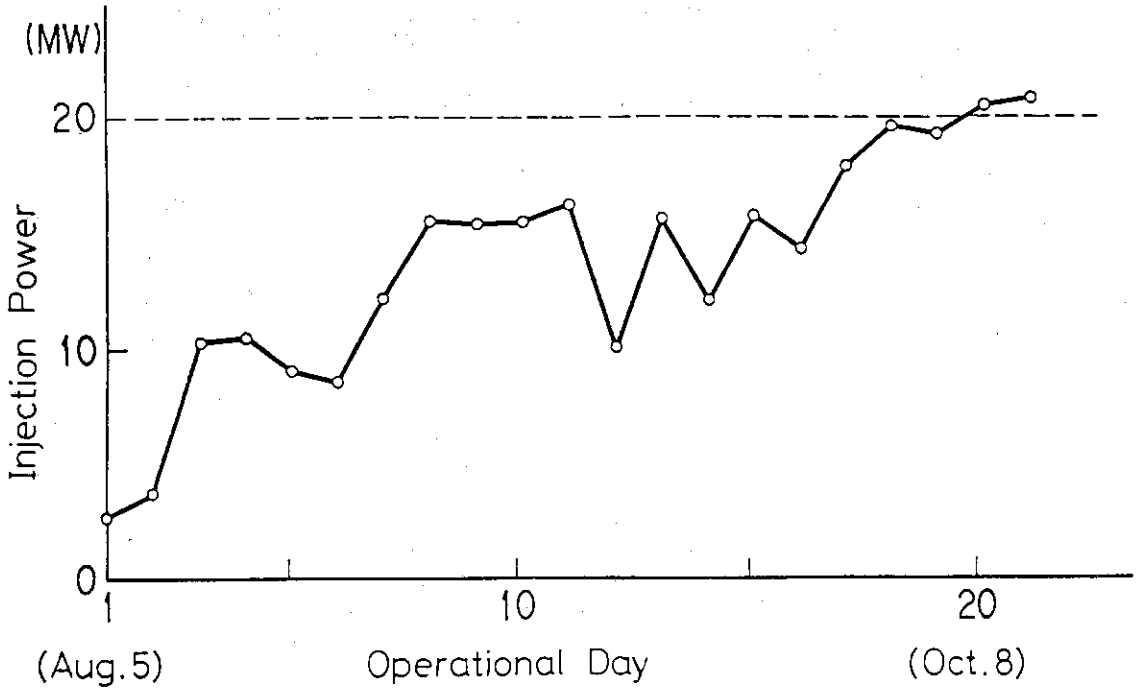

Fig. X.6-2 Daily progress of the achieved injection power.

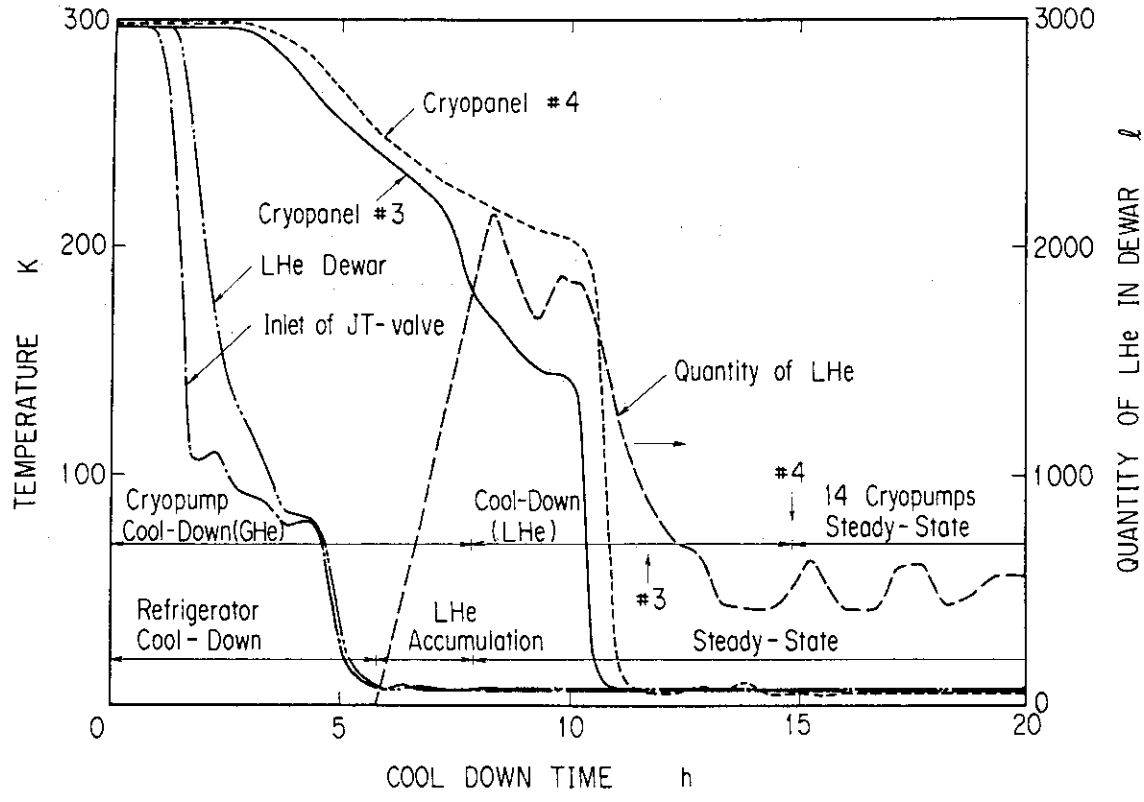

Fig. X.6-3 Automatic operation results of cryogenic systems.

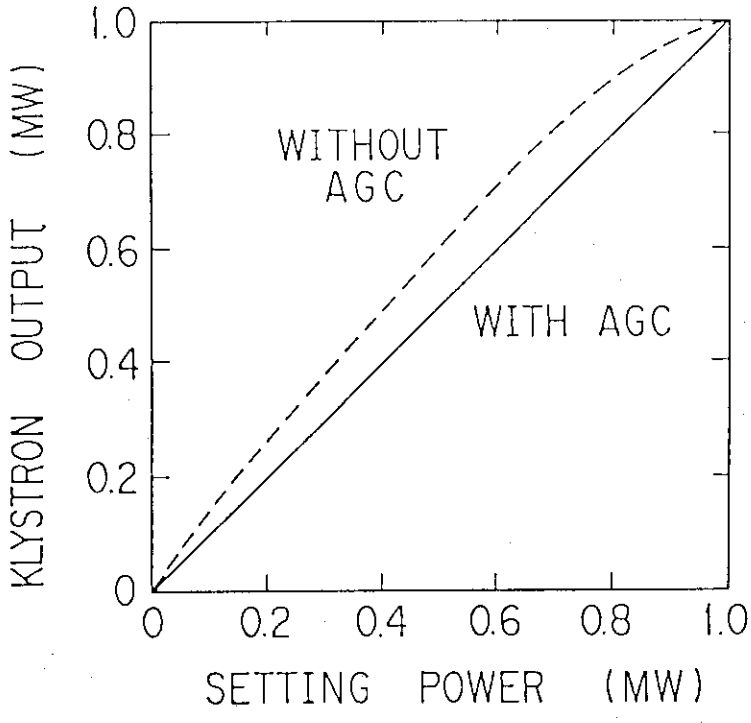

Fig. X.6-4 Output characteristics with and without the AGC circuit.

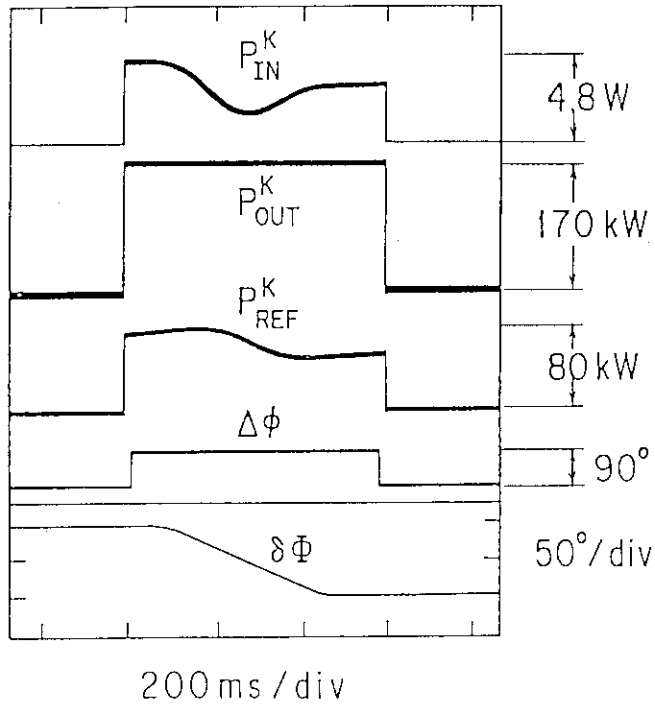

Fig. X.6-5 Waveforms of klystron input, output, reflection power and phase difference between 2nd and 3rd lines with phase to klystron is intentionally shifted with the high speed power phase shifter (Δφ).

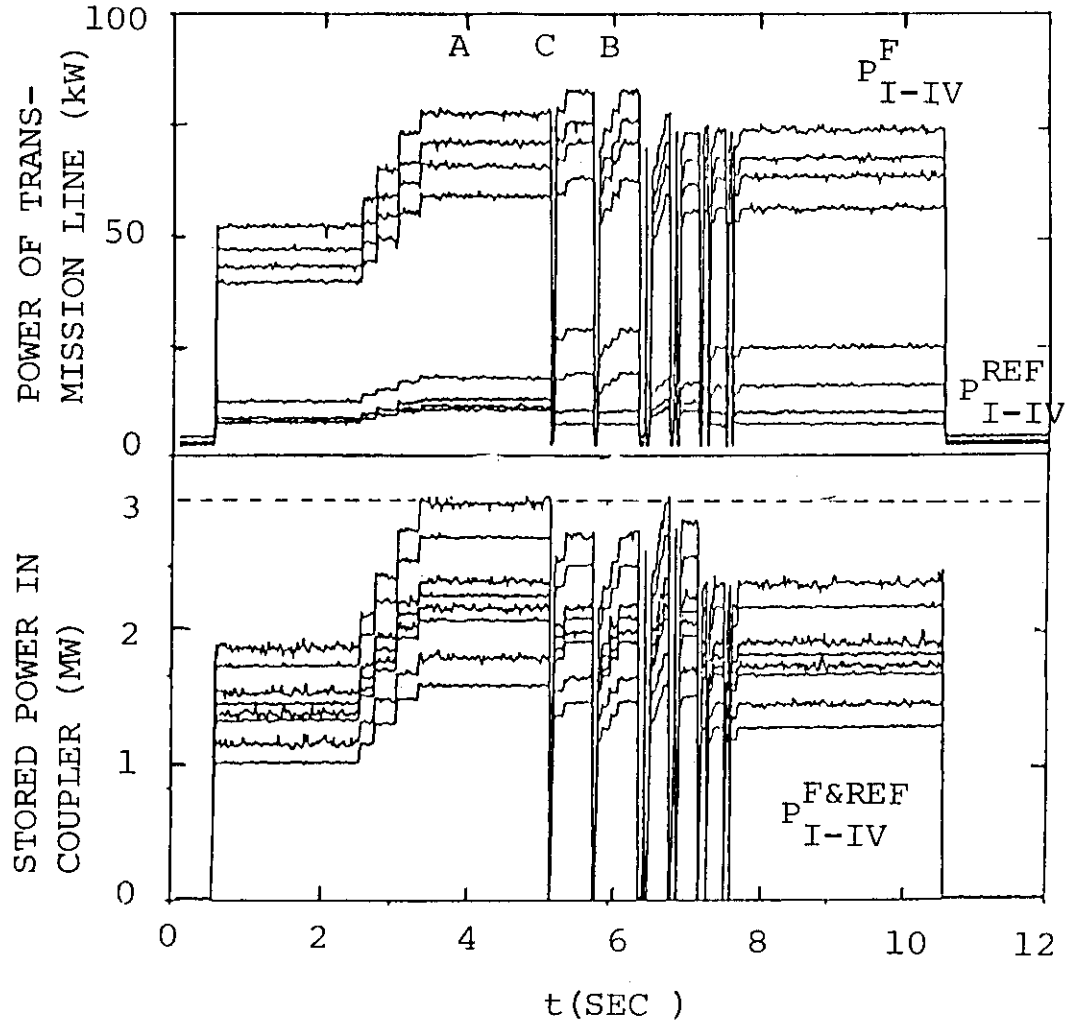

Fig. X.6-6 Typical waveform of ICRF power during injection to JT-60 plasmas with knotching and regulation. Arrows indicate the timings of standing wave voltage limit on (A), off (B) and reflection alarm knotching (C).

XI. DESIGN STUDY OF THE NEXT GENERATION DEVICE AND FUSION REACTOR SYSTEM

1. Fusion Experimental Reactor (FER)

1.1 System Studies of FER

A wide range of parameter studies were done by using the conceptual design study code "TRESCODE" to select the candidate operation modes for detailed design studies.

The following items were studied for evaluation of cost-effectiveness. (1) Inductive flux for central solenoids (150, 100, 50, 15 vs), (2) Elongation (1.5, 1.7, 2.0), (3) Distance between plasma inner separatrix and the inner leg of TF coil (Δ=1.0 m for single null divertor, Δ=0.9 m for double null divertor), (4) Constraints on TF and PF coil design, (5) Partial usage of normal conductor for PF(OH) coils. Several candidate options were chosen by combining the above items to reduce the device size and overall cost. Their major parameters are summarized in the Table XI.1-1. The Option C is the nominal candidate device recommended by the Subcommittee on the Next Step Device set up by the Nuclear Fusion Council of AEC. The Option ACS is a similar device to the Option C with reasonably advanced engineering being employed. The Option ACD is a similar device to the ACS with a double null divertor and higher elongation (κ=2.0). The Option Cost-Mini is a reduced volt·second option with single null divertor and higher elongation (κ=2.0). The option Inter-link is a similar device to the ACS with inter-linking normal OH coils inside the TF coils. The Option NBI-R is the same device as the Option C except for the heating and current drive scheme (NBI). To explain the rationale for the selection of these candidate options, the major system quantities which greatly affect the overall cost are evaluted as follows.

The effect of available volt.seconds or major radius on TF coil systems are studied. The length of the TF coil perimeter 1_t is very insensitive to the available volt·second, since the required plasma minor radius to achieve ignition is very insensitive to volt·second under the present physics assumptions, which results in nearly the same TF coil bore size. However, the stored energy E_s^{TFC} and total ampereturn-meter $NI.1_t$, which represents the TF coil volume are

greatly reduced when volt·second is reduced. The effect of volt·second on PF coil systems is also studied. The maximum ampere-turn and stored energy during the assigned flux swing decreases with the volt.second.

The effect of elongation, coil location and number of nulls (double/single) on the PF coil system quantities was then studied. PF coil location is closely related to the method of access of the maintenance of the reactor core component. Two typical access methods are considered, i.e. vertical access and horizontal access. As shown in Fig. XI.1-1 in the case of vertical access, coils located between 30° and 90° in poloidal direction from the outer-midplane are removed, while, in the case of horizontal access, coils between 0° and 45° in poloidal direction are removed. For comparison, an ideal case (uniformly distributed in poloidal direction) was also studied. The results are shown in Fig. IX.1-2. In the case of single null, the dependence of the stored energy on the elongation is rather weak, and takes a minimum at (average elongation) ~1.7 in the horizontal access case. This value of elongation is also favorable for the vertical position stability, which gives the rationale for option ACS. When we allow higher elongation ($\kappa \sim 2.0$), the stored energy can be reduced further, if vertical or ideal distribution is assumed, which leads to in-situ maintenance without extracting any reactor core components. This gives the rationale for the option Cost-Mini. In the double null case, the stored energy is greatly reduced as the elongation is increased if the vertical access is assumed. If the horizontal access is assumed, the stored energy takes the minimum at $\kappa \sim 2.0$. This gives the rationle for the option ACD.

1.2 Torus Design of FER

The design was intended to meet the physical and engineering mission of the next step device which was decided by the subcommittee on the next step device of the nuclear fusion council. The objectives of the design study in FY1986 are to advance and optimize the design concept of the last year because the recommendation of the subcommittee was basically the same as the design phitosophy of the last year.

Regarding the reactor structure, the following items were investigated intensively: minimization of reactor size, protection of

first wall against plasma disruption (installation of protection limiters), simplification of shield structure (water-tank type shield), reactor configuration which enables optinum arrangement of poloidal field coils.

Regarding the critical issues, accuracy evaluation of shielding calculation and crack growth prediction of first wall and divertor based on the elastic-plastic fracture mechanics were performed. Further, feasibilities of innovative ideas were examined, such as the ripple insert effect and the application of shape memory alloys. To reduce the reactor size, the magnet design was modified. The following possibility of the design modification were investigated.

(1) Increase of the TF coil current density to reduce the coil thicknes..
(2) Reduction of the TF coil structural area in order to reduce the coil thickness.
(3) Increase of the nuclear heating load as a means of reducing the inboard shield thickness.
(4) Increase of the OH coil current density and magnetic field to reduce the OH coil radial build.

For plasma heating/current drive, the application of the neutral beam method and the wave methods are studied. The concepts of the negative ion-based neutral beam injector, the ICRF launcher, the LHRF launcher and the ECRF launcher are constructed. In the study of the power supply system, the capacity estimation of the poloidal coil power supply is carried out in relation to the rump-up scenario.

Fig. XI.1-3 shows the overall configuration of the typical FER design.

2. INTOR

The International Tokamak Reactor (INTOR) Workshop is a collaborate effort among the European Comunity, Japan, the USA and the USSR. It is conducted under the auspices of the International Atomic Energy Agency (IAEA), in terms of reference defined by the International Fusion Research Council (IFRC), an advisory body to the Director General of the IAEA which supervises the INTOR Workshop.

first wall against plasma disruption (installation of protection limiters), simplification of shield structure (water-tank type shield), reactor configuration which enables optinum arrangement of poloidal field coils.

Regarding the critical issues, accuracy evaluation of shielding calculation and crack growth prediction of first wall and divertor based on the elastic-plastic fracture mechanics were performed. Further, feasibilities of innovative ideas were examined, such as the ripple insert effect and the application of shape memory alloys. To reduce the reactor size, the magnet design was modified. The following possibility of the design modification were investigated.

(1) Increase of the TF coil current density to reduce the coil thicknes..
(2) Reduction of the TF coil structural area in order to reduce the coil thickness.
(3) Increase of the nuclear heating load as a means of reducing the inboard shield thickness.
(4) Increase of the OH coil current density and magnetic field to reduce the OH coil radial build.

For plasma heating/current drive, the application of the neutral beam method and the wave methods are studied. The concepts of the negative ion-based neutral beam injector, the ICRF launcher, the LHRF launcher and the ECRF launcher are constructed. In the study of the power supply system, the capacity estimation of the poloidal coil power supply is carried out in relation to the rump-up scenario.

Fig. XI.1-3 shows the overall configuration of the typical FER design.

2. INTOR

The International Tokamak Reactor (INTOR) Workshop is a collaborate effort among the European Comunity, Japan, the USA and the USSR. It is conducted under the auspices of the International Atomic Energy Agency (IAEA), in terms of reference defined by the International Fusion Research Council (IFRC), an advisory body to the Director General of the IAEA which supervises the INTOR Workshop.

The INTOR Workshop of Phase Two A, Part 3, which started September 1985, will be completed at the end of 1987. The principal tasks of the Part 3 were: (1) work upon certain critical technical issues that are essential to the feasibility and improvement of the INTOR concept; (2) reassessment of the scientific and technical data base supporting the INTOR concept; (3) in addition to those continuing activities, evaluate innovative ideas, leading to significant improvement of the INTOR concept; and (4) revision of the INTOR design.

Critical issues studies are being carried out in six areas: impurity control, beta enhancement and confinement, heating and current drive, electromagnetics, configuration and maintenance, and blanket and first-wall. The physics, engineering and nuclear data bases which would support the INTOR design concept are also being re-evaluated.

During the FY 1986, however, ITER project, the acronym for International Thermonuclear Experimental Reactor, has been emerged, which was originated from the Geneva Summit between the USA and the USSR. In view of the proposal for the new design and supporting research initiative, and preliminary positive reactions from EC and Japan, the IFRC recommended a change of the INTOR workshop objectives form those addopted. The new objective changed is to discontinue the task of incorporating innovations into and updating the design concept, and instead, to conduct critical analyses of existing INTOR-like designs with the aim of preparing a useful information base for future design work for the ITER project, which will be conducted for three years from 1988. The INTOR activities, which are continued for nine years from 1979, will be closed at the end of 1987.

As a first step, members of the INTOR, FER(Japan), NET(EC), OTR(USSR), TIBER(USA) design teams met together in the IAEA Specialists' Meeting, which was held 23-27 March 1987, to document in a common format, discuss and compare the programmatic and technical objectives, the engineering and physics design constraints (i.e. physical limitations such as stress limits, beta limits), the main features which drive the design concept (i.e. choices made by the desiners such as to incorporate non-inductive current drive or a horizontal maintenance and assembly scheme), and the design

specifications (e.g. major parameters, choice of materials, choice of heating method) for five designs. On the basis of those informations, activities on the critical analyses of existing INTOR-like deisgn are under way.

The INTOR design parameters were modified somewhat during the course of the Phase Two A, Part 2 Workshop. These parameters are given in Table XI.2-1. A cross-section view of the INTOR design concept is shown in Fig. XI.2-1.

3. Studies on Fusion Reactor System

3.1 Design study of power-producing breeding blankets

A comparison of major candidate blanket concepts is made in terms of the present material data base, economic performance, prospects for future improvements, and engineering feasibility and difficulties based on the results of design studies on each concept. Five options of structure/breeder/coolant/neutron multiplier materials selected for the present study are (1) PCA/Li_2O/H_2O/Be, (2) Mo-alloy/Li_2O/He/Be, (3) Mo-alloy/$LiAlO_2$/He/Be, (4) V-alloy/Li/Li/none, (5) Mo-alloy/Li/He/none. The key functions discussed through the design studies include (1) self-sufficient tritium breeding, (2) in-situ tritium recovery and low tritium inventory, (3) high temperature cooling giving a high efficiency of electricity generation, and (4) thermomechanical reliability and simplified remote maintenance to obtain high plant availability. Table XI.3-1 summarizes the design parameters and performances of selected blanket concepts.

3.2 Safety analysis

A code system called TRIMAP for tritium inventory mapping, is being developed under a three year program starting from 1985. In 1985, as the first step, the tritium inventory in the components of the fuel circulation system was calculated.

In 1986, a computer code TPERM[1] was developed to calculate the permeation characteristics of tritium in the first wall and divertor plate. In order to check the validity of the code, the tritium permeation in the INTOR[2] first wall was calculated and the results are compared with the calculated results by the DIFFUSE code[3] in

specifications (e.g. major parameters, choice of materials, choice of heating method) for five designs. On the basis of those informations, activities on the critical analyses of existing INTOR-like deisgn are under way.

The INTOR design parameters were modified somewhat during the course of the Phase Two A, Part 2 Workshop. These parameters are given in Table XI.2-1. A cross-section view of the INTOR design concept is shown in Fig. XI.2-1.

3. Studies on Fusion Reactor System

3.1 Design study of power-producing breeding blankets

A comparison of major candidate blanket concepts is made in terms of the present material data base, economic performance, prospects for future improvements, and engineering feasibility and difficulties based on the results of design studies on each concept. Five options of structure/breeder/coolant/neutron multiplier materials selected for the present study are (1) PCA/Li_2O/H_2O/Be, (2) Mo-alloy/Li_2O/He/Be, (3) Mo-alloy/$LiAlO_2$/He/Be, (4) V-alloy/Li/Li/none, (5) Mo-alloy/Li/He/none. The key functions discussed through the design studies include (1) self-sufficient tritium breeding, (2) in-situ tritium recovery and low tritium inventory, (3) high temperature cooling giving a high efficiency of electricity generation, and (4) thermomechanical reliability and simplified remote maintenance to obtain high plant availability. Table XI.3-1 summarizes the design parameters and performances of selected blanket concepts.

3.2 Safety analysis

A code system called TRIMAP for tritium inventory mapping, is being developed under a three year program starting from 1985. In 1985, as the first step, the tritium inventory in the components of the fuel circulation system was calculated.

In 1986, a computer code TPERM[1] was developed to calculate the permeation characteristics of tritium in the first wall and divertor plate. In order to check the validity of the code, the tritium permeation in the INTOR[2] first wall was calculated and the results are compared with the calculated results by the DIFFUSE code[3] in

Fig. IX.3-1 and XI.3-2. Although there are some differences in the calculated results, the agreement is considered to be reasonable at the present stage of experimental data on tritium permeation.

References

(1) K. Nakahara and Y. Seki, "Development of a Computer Code TPERM for the Tritium Diffusion in Structural Material of a Fusion Reactor," JAERI-M 87-118 (1987)(in Japanese).

(2) INTOR, International Tokamak Reactor, Phase Two A Part I Report, International Atomic Energy Agency, Vienna (1983) p.337

(3) M.I. Baskes, "A Code to Calculate One-Dimensional Diffusion and Trapping," SAND 80-8201 (1980)

Table XI.1-1 Major plasma and device parameters of five reference options.

Type	Option C Case 1	ACS Case 2	ACD Case 3	Cost-Mini Case 4	Inter-link Case 5	NBI-R Case 6
R (m)	4.92	4.42	4.02	3.84	4.74	
a (m)	1.32	1.25	0.95	1.02	1.67	
A	3.7	3.54	4.24	3.76	2.84	
κ	1.7	1.7	2.0	2.0	1.7	
δ	0.2	0.2	0.35	0.2	0.2	same as
B_T (T)	4.68	4.61	5.07	4.58	3.08	opt. c
I_p (MA)	8.69	8.74	7.96	8.37	10.6	
T (keV)	12.0	12.0	12.0	12.0	12.0	
β_T (%)	4.94	5.31	5.79	6.28	7.22	
β_{DT} (%)	4.02	4.31	4.70	5.10	5.87	
n_e (m^{-3})	1.09×10^{20}	1.14	1.50	1.33	0.69	
n_i (m^{-3})	0.98×10^{20}	1.03	1.35	1.19	0.62	
q_ψ	2.6	2.6	2.6	2.6	2.6	
q_I	1.98	1.92	2.13	1.97	1.76	
P_f (MW)	459	406	435	375	286	
P_w (MW/m^2)	1.03	1.07	1.47	1.23	0.53	
null	Single	Single	Double	Single	Single	
Magnet level	I	I ~ II	I ~ II	I ~ II	I ~ II	

$$q_I = \frac{5aB_T}{A\ I_p}\ \frac{1+\kappa^2(1+2\delta^2)}{2}$$

$$\ell_i = 0.824$$

Table XI.2-1 Major design parameters of INTOR.

Plasma major radius (m)	5.0
Plasma minor radius (m)	1.2
Plasma elongation	1.6
Plasma volume (m^3)	227
Axial toroidal field (T)	5.5
Plasma current (MA)	8.0
Average ion temperature (keV)	10
Average ion density ($10^{20}/m^3$)	1.4
Energy confinement time (s)	1.4
Average beta (%)	4.9
Q value	ignition
Peak fusion power (MW)	585
RF heating power (MW)	
ICRF (85 MHz)	50
ECRF (140 GHz)	10
Burn time (s)	150
Duty cycle (%)/Availability (%)	67/25
Neutron wall load (MW/m^2)	1.3
Toroidal magnetic field coil	superconducting
Poloidal magnetic field coil	superconducting
Divertor	yes
Tritium consumption (kg/year)	6.1
Initial tritium inventory (kg)	3.1-4.6
Tritium breeding ratio	0.65

Table XI.3-1 Design Parameters and Performances of Candidate Blanket Concepts (1/4)

Item	PCA/Li_2O/H_2O/Be	Mo-alloy/Li_2O/He/Be	Mo-alloy/$LiAlO_2$/He/Be	V-alloy/Li/Li/none	Mo-alloy/Li/He/none
Fusion power (MW)	3200	3200	3200	3200	3200
Neutron wall load (MW/m^2)	3.3	3.3	3.3	3.3	3.3
Surface heat flux to first wall (MW/m^2)	0.9	0.9	0.9	0.9	0.9
Volumetric heating rate in first wall structural material (MW/m^2)	43	27	27	23	20
Structural material	Ti-modified stainless steel	Mo-alloy	Mo-alloy	V-alloy	Mo-alloy
Coolant	H_2O	He	He	Li	He
Inlet pressure (MPa)	15.5	9	9	1.5	9
Inlet/outlet temperature (°C)	280/320	400/700	400/700	350/530	400/700
First wall configuration	integral with blanket vessel	integral with blanket vessel	integral with blanket vessel	integral with blanket vessel	integral with blanket vessel
Breeder	Li_2O	Li_2O	$LiAlO_2$	Li	Li
Configuration	outside tube (spherical pebble ≤1 mmϕ)	outside tube (spherical pebble 1 mmϕ)	inside tube (spherical pebble 3 mmϕ)	self-cooling (liquid)	outside tube (liquid)
^6Li enrichment (%)	30	30	95	no (natural)	no (natural)
Maximum temperature control method	cooling tube arrangement	cooling tube arrangement	(pebble diameter)	unnecessary	unnecessary
Minimum temperature control method	thermal resistant layer around cooling tube	unnecessary	unnecessary	unnecessary	unnecessary

Table XI.3-1 Design Parameters and Performances of Candidate Blanket Concepts (2/4)

Item	PCA/Li_2O/H_2O/Be	Mo-alloy/Li_2O/He/Be	Mo-alloy/$LiAlO_2$/He/Be	V-alloy/Li/Li/none	Mo-ally/Li/He/none
Neutron multiplier	Be	Be	Be	none	none
Thickness (mm)	50 (in front of breeder region)	50 (in front of breeder region)	50 (in front of breeder region)	——	——
Hot shield	none	none	none	HT-9	HT-9
Thickness (mm)	——	——	——	160 (behind breeder region)	160 (behind breeder region)
Electrical insulator in blanket	none	none	none	surface of duct region	none
Tritium recovery	continuously by He purge stream	continuously by He purge stream	continuously by He coolant	continuously by Li coolant	continuously by Li extraction
Internal pressure of blanket vessel (MPa)	0.1	0.1	0.1	1.5*1	0.1
Outboard/inboard local tritium breeding ratio	1.20/1.13*2	1.37/1.32*2	1.24*4/1.17*2	1.39/1.28	1.36/1.22
Net tritium breeding ratio	1.03*2,*3	1.19*2	1.06*2	1.15	1.14
Maximum coolant velocities in first wall/breeder region (m/s)	7.9/7.1	63/52	63/8.1	0.3/0.25*5	56/60
Coolant pressure losses in first wall/breeder region (MPa)	0.37/0.34	0.10/0.11	0.10/0.09	1.0/~0	0.09/0.10

Table XI.3-1 Design Parameters and Performances of Candidate Blanket Concpets (3/4)

Item	PCA/Li_2O/H_2O/Be	Mo-alloy/Li_2O/He/Be	Mo-alloy/$LiAlO_2$/He/Be	V-alloy/Li/Li/none	Mo-alloy/Li/He/none
Maximum structure temperature/film temperature drop in first well (°C)	423/21	852/140	852/140	730/110	857/146
Breeder temperature (°C)	450∿950	400∿950	400∿725	350∿530	400∿860
Maximum structure temperature at surfaces facing plasma/coolant during plasma disruption (°C)	1970/(535)*7	2009/1554	2009/1554	1979/1113	2009/1554
Melt layer/evaporation thickness during plasma disruption (mm/μm)	0.15/0.25	0/0	0/0	0.055/0.025*8	0/0
Maximum electromagnetic force during plasma disruption (MPa)	1.3	3.0	3.0	9.2	9.2
Growth time of vertical positional instability(msec)	7	22	22	200	200
Maximum primary/primary + secondary stress intensities (MPa)	102/275	67/120	72/124	250/500	67/127
LiOH mass transfer	<Li burnup	<Li burnup	negligibly small	——	——
Total weight of blanket (ton)	1890	2150	2440	2040	2690

Table XI.3-1 Design Parameters and Performances of Candidate Blanket Concpets (4/4)

Item	PCA/Li_2O/H_2O/Be	Mo-alloy/Li_2O/He/Be	Mo-alloy/$LiAlO_2$/He/Be	V-alloy/Li/Li/none	Mo-alloy/Li/He/none
Relative material cost[*12] of blanket	1.0	1.97	2.18	4.20	2.18
Tritium permeation rate[*13] through first wall (g/day)	17	98	98	850	98
Tritium permeation rate through cooling tubes in blanket (g/day)	0.39	9.7	-	-	0.0067
Tritium release rate to environment (Ci/day)	≤10	≤10	≤10	≤10	≤10
Tritium inventory in blanket (g)	∿2600	∿2600[*14]	>8[*15]	1000	250
Tritium inventory in tritium recovery system (g)	260	260	260	510	510
Tritium recovery	large cost for tritium recovery from H_2O coolant	relatively easy	relatively easy	not established	not established
Thermal/gross electric powers (MW)	3820/1320	3720/1810	3510/1710	3670/1450	3500/1700
Pumping power (MW)	26	109	103	30	102
Steam pressure/temperature (MPa/°C)	6.5/280	24.6/538	24.6/538	12.6/483	24.6/538
Gorss thermal efficiency (%)	34.4	47.2	47.2	39.2	47.2

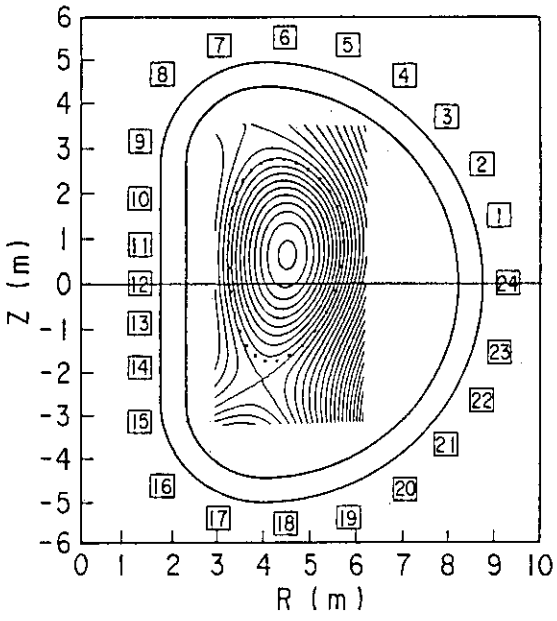

(a) PFC configuration (distribution)

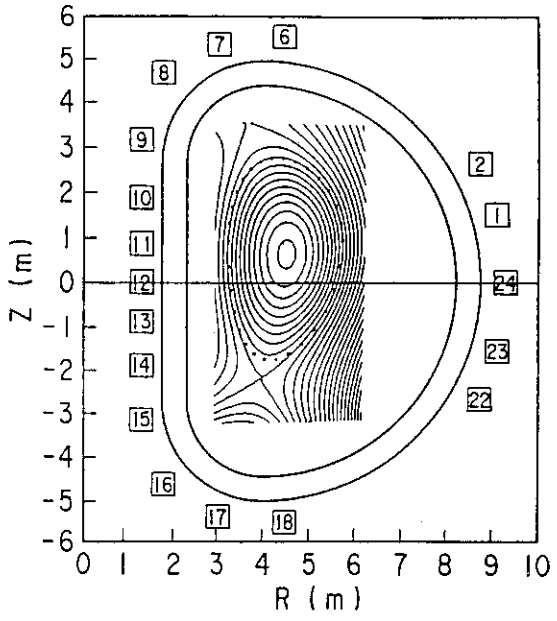

(b) Vertical access
(remove No.3,4,5,19,20,21)

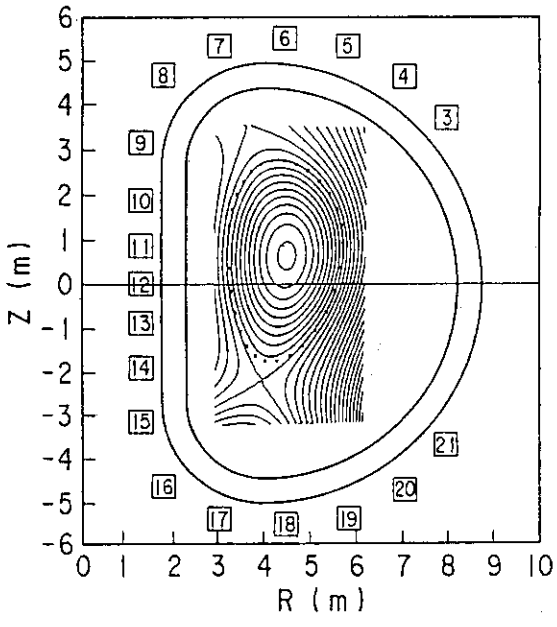

(c) Horizontal access case (A)
(remove No.1,2,22,23,24)

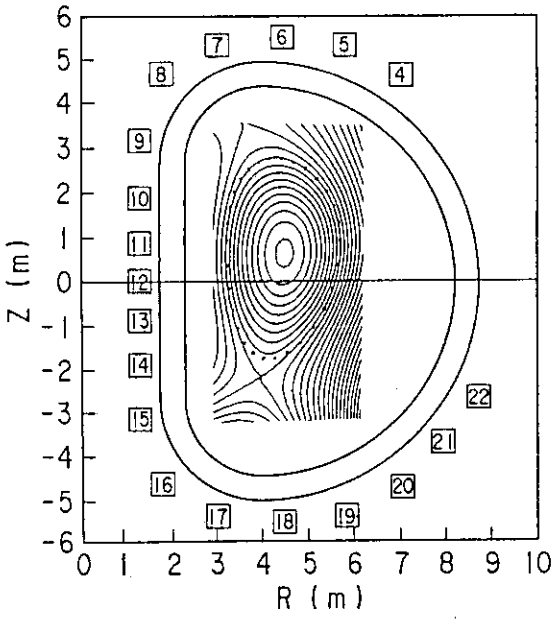

(d) Horizontal access case (B)
(remove No.1,2,3,23,24)

Fig. XI.1-1 Four cases of PFC positions. Case (a) is an idealy distributive configuration, Case (b) corresponds to vertical access and Case (c) and (d) correspond to horizontal access.

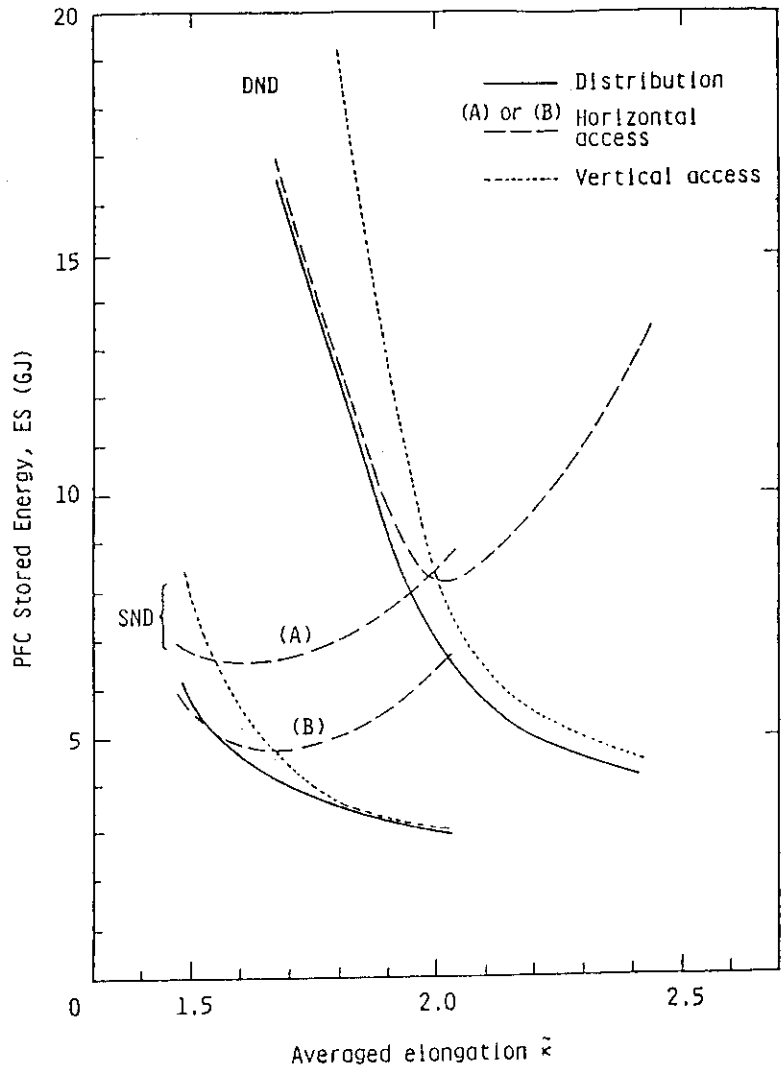

Fig. XI.1-2 Comparison of PFC stored energy between vertical access and horizontal access as a function of plasma elongation at null point κ_{null}.

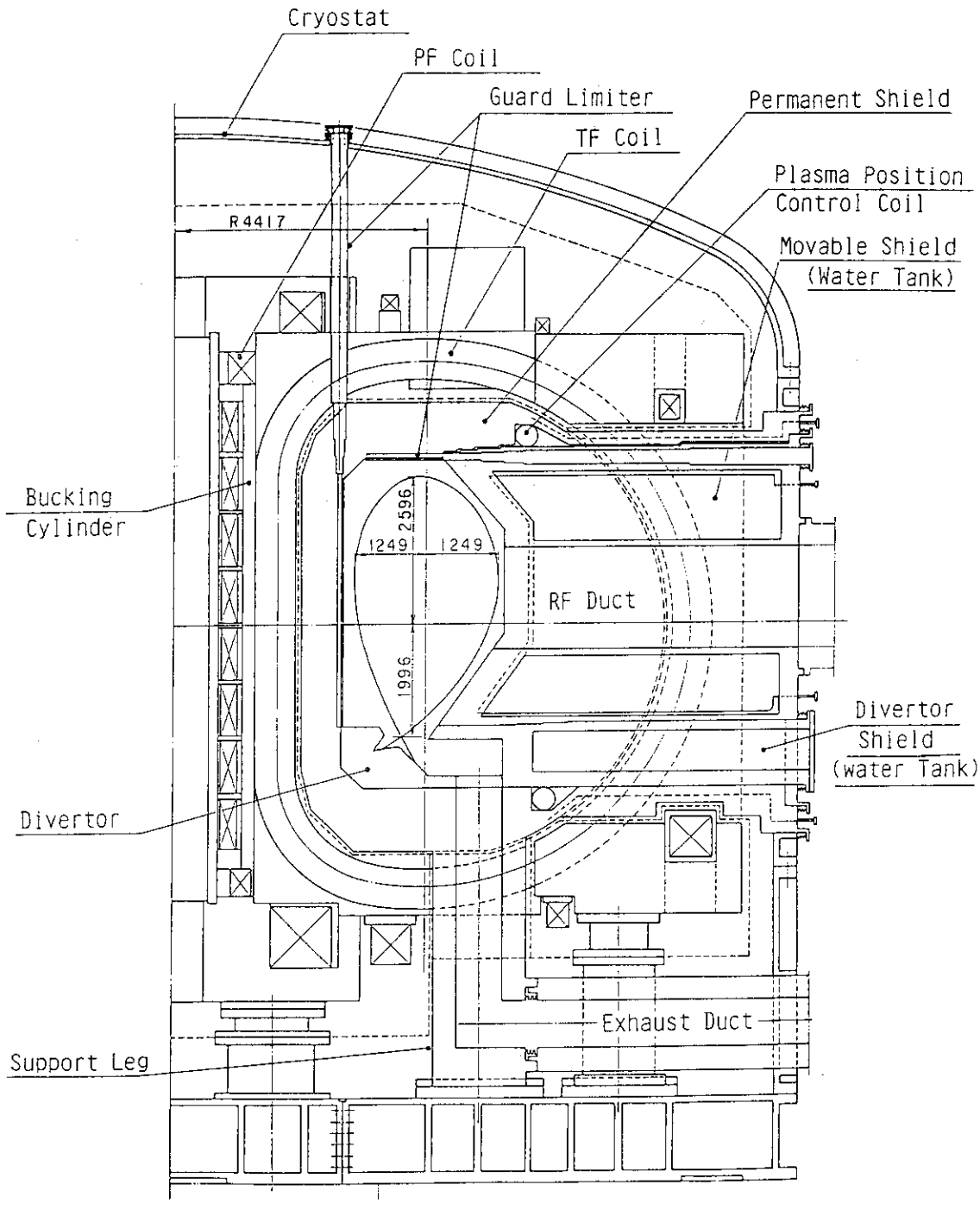

Fig. XI.1-3 Elevation View of FER (Option ACS).

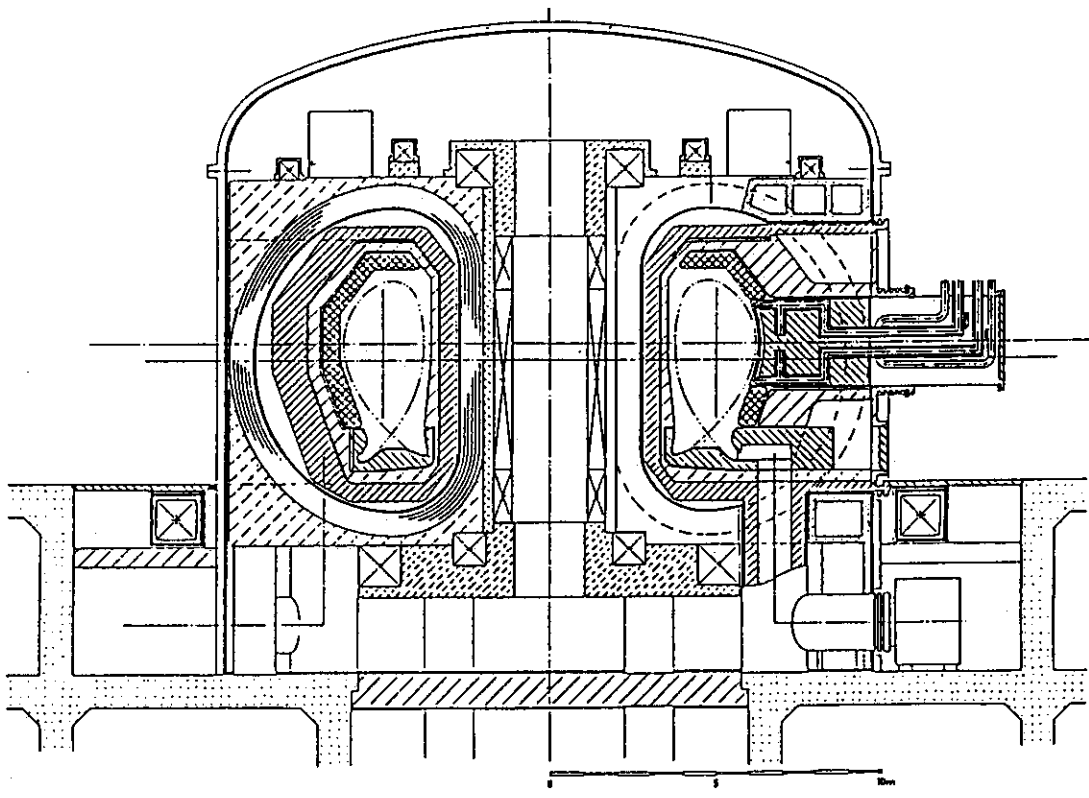

Fig. XI.2-1 INTOR elevation view.

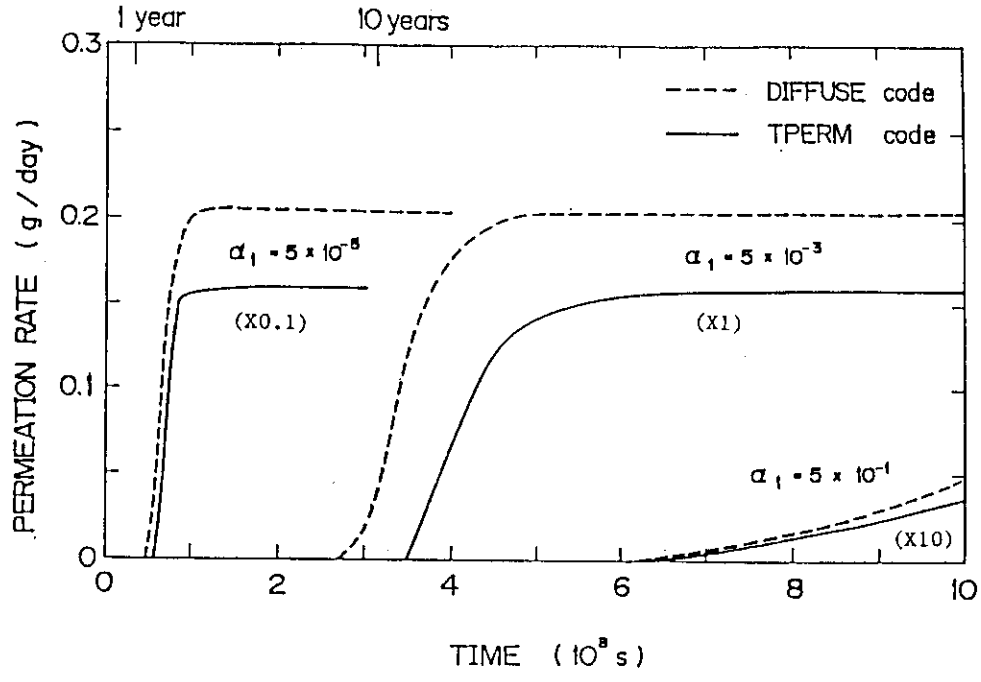

Fig. XI.3-1 Comparison of TPERM and DIFFUSE calculations for the tritium permeation rate through INTOR first wall (α_1 is the molecular sticking coefficient of the plasma-side surface.).

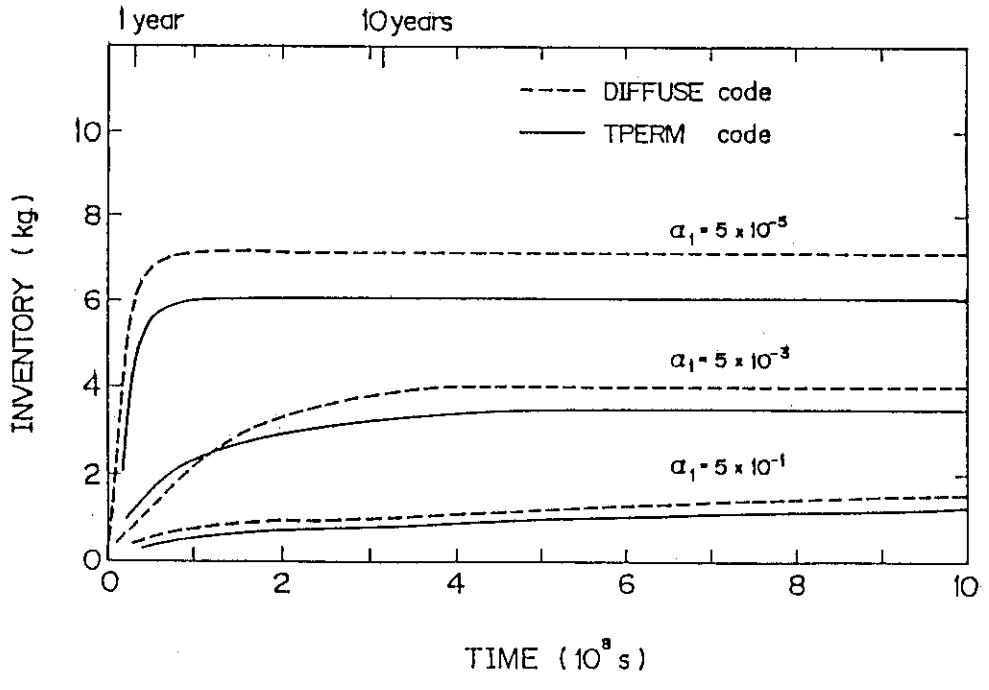

Fig. XI.3-2 Comparison of TPERM and DIFFUSE calculations for the tritium inventory in INTOR first wall (α_1 is the molecular sticking coefficient of the plasma-side surface.).

APPENDICES

A.1 Publication List
(1986.4 ~ 1987.3)

A.1.1 List of JAERI-M report

1) Ozeki T., Azumi M., Seki S., Tsunematsu T., Tokuda S., Takizuka T., "Positional instability analyses in JT-60", JAERI-M 86-022 (March 1986) in Japanese.
2) Kurita G., Takizuka T., Azumi M., Takeda T., "Nonlinear evolution of free-boundary kink mode in a tokamak", JAERI-M 86-156 (October 1986).
3) Tokuda S., Tsunematsu T., Takeda T., "Structured programming supporting tool EOS77", JAERI-M 86-159 (October 1986) in Japanese.
4) Tokuda S., Tsunematsu T., Takeda T., "Numerical computation of FCT equilibria by inverse equilibrium method", JAERI-M 86-171 (November 1986) in Japanese.
5) Tsunematsu T., Tokuda S., Nemoto T.*1, Azumi M., Takeda T., "Data set for benchmark calculation on ideal MHD beta limit of INTOR", JAERI-M 86-172 (November 1986).
6) Hoshino K., Yamamoto T., Kawashima H., Uesugi Y., Kasai S., Kawakami T., Matoba T., Matsuda T., Matsumoto H., Miura Y., Mori M., Odajima K., Ogawa H., Ogawa T., Ohtsuka H., Sengoku S., Shoji T., Suzuki N., Tamai H., Yamauchi T., Hasegawa M.*11, Takada S.*49, Funahashi A.: "Study of the Second Hermonic Electron Cyclotron Heating in JFT-2M Tokamak", JAERI-M 86-076 (May 1986).
7) Uesugi Y., Yamamoto T., Ohtsuka H., Kikuchi K.: "Coupling to Fast Waves via a Phased Loop Antenna Array for Fast Wave Current Drive in the JFT-2M Tokamak", JAERI-M 86-103 (May 1986).
8) Kasai S., Miura Y., Hasegawa K., Sengoku S., Ogawa H., Uesugi Y., Kawashima H., Tamai H., Hasegawa M.*11, Hoshino K., Kawakami T., Matoba T., Matsuda T., Matsumoto H., Mori M., Odajima K., Ogawa T., Ohta K.*11, Ohtsuka H., Shoji T., Suzuki N., Takada S.*49, Yamamoto T., Yamauchi T., Yanagisawa I.*3: "First Results of

Pellet Injection Experiments in JFT-2M Additionally Heated Plasma", JAERI-M 86-109 (July 1986).

9) Shimomura Y., Odajima K.: "Scaling of Incremental Energy Confinement time of L-mode Plasma and Comments on Improved Confinement in Tokamak", JAERI-M 86-128 (Aug. 1986).

10) Yamamoto T., Uesugi Y., Hoshino K., Kawashima H., Ohtsuka H.: "Numberical Study of the Electron Heating and Current Drived by the Fast Waves in the JFT-2M Tokamak Plasma", JAERI-M 86-115 (Aug. 1986).

11) Miura Y., Kasai S., Sengoku S., Hesegawa K., Suzuki N., Hasegawa M.*11, Hoshino K., Kawashima H., Kawakami T., Matoba T., Matsuda T., Matsumoto H., Mori M., Odajima K., Ogawa H., Ogawa T., Ohtsuka H., Shoji T., Takada S.*49, Tamai H., Uesugi Y., Yamamoto T., Yamauchi T.: "Characterislics of Pellet and Neutral-Beam Injected Single Null Divertor Discharges of the JFT-2M Tokamak", JAERI-M 86-148 (Sep. 1986).

12) Tamai H., Ogawa H., Ogawa T., Matsumoto H., Odajima K.: "Suppression of the Metal Impurity Release during ICRF Heating by the Installation of Carbon Block", JAERI-M 86-143 (Oct. 1986) (in Japanese).

13) Matsumoto H., Ogawa T., Tamai H., Odajima K., Hasegawa M.*11, Hoshino K., Kasai S., Kawashima H., Kawakami T., Matoba T., Miura Y., Mori M., Ogawa H., Ohtsuka H., Sengoku S., Shoji T., Suzuki N., Takada S.*4, Uesugi Y., Yamauchi T., Yamamoto T.: "Improved Confinement during ICRF Heating on JFT-2M", JAERI-M 86-147 (Oct. 1986).

14) Hirayama T., Yamada K.*4, Sengoku S., Nagami M., "Ablation of Hydrogen Ice Pellet in JT-60 Plasma", JAERI-M 86-170 (Oct. 1986).

15) Uesugi Y., Matoba T., Mizuno K.**4: "Beat Frequency Stabilization between Two HCN Lasers by Phase Locked Loop", JAERI-M 86-194 (Jan. 1987).

16) Takada S.*49, Matsuda T., Kiura Y., Mori M., Kawakami T., Matoba T.: "Data Storage System for Fusion Experiment", JAERI-M 86-183 (Jan. 1987) (in Japanese).

17) Miura Y., Matsuda T., Yamamoto S., Maeno M., Takeuchi H., Hoshino K., Kasai S., Kawakami T., Kawashima H., Matoba T., Matsumoto H., Mori M., Odajima K., Ogawa H., Ogawa T., Ohta K.*11, Ohtsuka H.,

Sengoku S., Shoji T., Suzuki N., Tamai H., Uesugi Y., Yamamoto T., Yamauchi T.: "Active Ion Temperature Measurement with Heating Neutral Beam", JAERI-M 87-042 (Feb. 1987) (in Japanese).

18) Yamauchi T., Ogawa H., Yamada R., Fukuda T.: "Design Study for Measurement of Neutral Hydrogen Atom Density by Laser Induced Fluorescence Method", JAERI-M 87-045 (March 1987) (in Japanese).

19) Shibata T., Kazawa M., Yokoyama K., Shibuya T., Honda A., Shiina T.: "Development of Bucket Ion Source for JFT-2M Neutral Beam Injector", JAERI-M 87-005 (Feb. 1987).

20) Horiike H., Ohara Y., Okumura Y., Shibata T., Tanaka S.: "Conceptual Design of Negative-Ion-Based 500 keV, 20 MW Neutral Beam Injector", JAERI-M 86-064 (in Japanese), (April 1986).

21) Watanabe K., Itoh T., Kanai T., Matsuoka M., Matsuda S., Shitomi M., Tsukahara Y., Usui K.: "Composition of the power supply system for JT-60 Active Beam Source and Suppression of Surge Current", JAERI-M 86-104, (in Japanese), (July 1986).

22) Itoh T., Horiike H., Matsuoka M., Matsuda S., Ohara Y., Okumura Y., Shitomi M., Takeuchi H., Tanaka S., Tsukahara Y., Usui K., Watanabe K.: "Development of Helium Beam Injection for JT-60 Active Beam Diagnostic System", JAERI-M 86-114, (in Japanese), (August 1986).

23) Kimura H., Fujii T., Ikeda Y., Saigusa M., Sagawa J.*4, Seki M., Uehara M.*40, Kobayashi N.*2, Saito Y.*2: "Power Test of the JT-60 ICRF Launching System", JAERI-M 86-113 AUG. (1986).

24) Ushigusa K., Imai T., Yoshino R., Ikeda Y., Sakamoto K., Ishida, S., Matsuoka M., and JT-60 Team: "Improvement of Energy Confinement of Neutral Beam Heated Plasma by Lower Hybrid Current Drive in JT-60", JAERI-M 87-012 (1987).

25) Pheran P.E.*43: "Investigation of a Nb-Ti cable-in-conduit conductor", JAERI-M 87-013 (February 1987).

26) Kurasawa T., Takeshita H., Yoshida H., Aizawa M., Ohno H., Mimura K., Umei H., Watanabe H.: "In-situ Tritium Release Experiment from Tritium Breeder Materials -- Measurement Apparatus and Safety Assessment of VOM-21H and 22H --", JAERI-M 86-129 (September 1986).

27) Takeshita H., Yoshida H., Kurasawa T., Matsui T., Watanabe H.: "In-situ Tritium Recovery from Li_2O (COM-21H) -- Tritium Chemical

Form as a Function of Sweep Gas Composition ＝Ⅱ", JAERI-M 86-130 (September 1986).

28) Kurasawa T., Takeshita H., Yoshida H., Watanabe H.: "In-pile Test of Tritium Release from Tritium Breeding Materials (VOM-21H Experiment) -- Tritium Release and Behavior form Lithium Oxide --", JAERI-M 86-152 (October 1986).

29) Naruse Y., Yoshida H.: "Proceedings of the JAPAN-US Workshop on Tritium Technology", JAERI-M 86-189 (February 1987).

30) Abe M.*4, Nagami M., Hirayama T., Kameari A.*3, Kitsunezaki A., Konoshima S., Shimada M., Angel T.*5, Blau F.*5, Chase R.*5, Fairbanks E.*5: "Scaling of Thermonuclear Fusion Neutron Yield on Doublet III Tokamak", JAERI-M 87-038 (March 1987).

31) JT-60 Team*), "Review of JT-60 experiment (April-June 1985)", JAERI-M 86-174.

* Abe T., Aikawa H., Akaoka N., Akasaka H., Akino N., Akiyama T., Ando T., Aoyagi T., Arai T., Arakawa K., Azumi M., Fukuda T., Fukuda T., Furukawa H., Hamamatsu K., Haraguchi T., Hayashi K., Hiratsuka H., Hirayama T., Hiroki S., Hiruta K., Hitomi N., Hosoda R., Hosogane N., Ichige H., Iida S., Iijima T., Ikeda Y., Isaji N., Isaka M., Ishihara M., Itoh Y., Kaneko M., Kawamata Y., Kawasaki K., Kikuchi M., Kimura T., Kishimoto H., Kitahara K., Kitsunezaki A., Kodama K., Koide Y., Koike T., Kondo I., Konoshima S., Kubo H., Kunieda S., Kurihara K. Kuroda T., Maeda H., Maeno M., Matsukawa M., Matsukawa T., Matsuo M., Miya N., Miyachi K., Miyo Y., Mizuno M., Murakami Y., Mutoh M., Nagami M., Nagashima A., Nagashima K., Nagaya S., Nakamura H., Nakamura Y., Nemoto M., Neyatani Y., Niikura S., Ninomiya H., Nishitani T., Nishiyama T., Nomata H., Noshiroya S., Ogiwara N., Ohasa K., Ohkubo M., Ohmori K., Ohmori S., Ohmori Y., Ohsato Y., Ohshima T., Ohta M., Otsu K., Oikawa A., Ozeki T., Sakasai A., Sakata S., Sato M., Seimiya M., Seki S., Shiho M., Shitomi M., Shimada R., Shimizu K., Shimizu M., Shimomura Y., Shinozaki S., Shirai H., Sugie T., Sunaoshi H., Suzuki K., Suzuki M., Suzuki S., Suzuki Y., Tahira S., Takahashi M., Takahashi S., Takahashi T., Takatsu H., Takayasu Y., Takeda S., Takeuchi H., Takizuka T., Tamura S., Tanaka E., Tanaka T., Tani K., Terakado T., Tobita K., Tokutake T., Totsuka T., Toyoshima

N., Tsugita T., Tsuji S., Tsukahara Y., Tsuneoka M., Ujiie K., Urakawa H., Uramoto Y., Ushigusa K., Yagyu J., Yamada K., Yamamoto M., Yamashita O., Yamashita Y., Yano K., Yokomizo H., Yonekawa I., Yoshida H., Yoshikawa M., Yoshino R.

32) JT-60 Team*), "Review of JT-60 experiment (March 1986)", JAERI-M 86-175.

* Abe T., Aikawa H., Akaoka N., Akasaka H., Akiba M., Akino N., Akiyama T., Ando T., Anno K., Aoyagi T., Arai T., Arakawa K., Araki M., Azumi M., Dairaku M., Ebisawa N., Fujii T., Fukuda T., Fukuda T., Furukawa H., Hamamatsu K., Haraguchi T., Hayashi K., Hiratsuka H., Hirayama T., Iida K., Hiroki S., Hiruta K., Hitomi N., Honda M., Horiike H., Hosoda R., Hosogane N., Ichige H., Iida S., Iijima T., Ikeda Y., Imai T., Inami H., Isaji N., Isaka M., Ishihara M., Itoh H., Itoh Y., Kanai T., Katoh T., Kawai M., Kawamata Y., Kihara Y., Kawasaki K., Kikuchi M., Kimura H., Kimura T., Kishimoto H., Kitahara K., Kitamura S., Kitsunezaki A., Kiyono K., Kodama K., Koide Y., Koike T., Komata M., Kondo I., Konoshima S., Kubo H., Kunieda S., Kurakada S., Kurihara K. Kuriyama M., Kuroda T., Maeno M., Matsuda S., Matsukawa M., Matsukawa T., Matsuo M., Matsuoka M., Miya N., Miyachi K., MiYo Y., Mizuhashi K., Mizuno M., Murakami Y., Mutoh M., Nagami M., Nagashima A., Nagashima K., Nagashima T., Nagaya S., Nakamura H., Nakamura Y., Nemoto M., Neyatani Y., Niikura S., Ninomiya H., Nishitani T., Nishiyama T., Nomata H., Noshiroya S., Ogiwara N., Ohasa K., Ohga T., Ohhara H., Ohkubo M., Ohmori K., Ohmori S., Ohmori Y., Ohsato Y., Ohshima T., Ohta M., Ohara Y., Ohuchi Y., Okumura Y., Otsu K., Oikawa A., Ozeki T., Saigusa M., Sakamoto K., Sakasai A., Sakata S., Sato M., Sawahata M., Shibanuma K., Shibata T., Seimiya M., Seki M., Seki S., Shitomi M., Shimada R., Shimizu K., Shimizu M., Shimomura Y., Shinozaki S., Shirai H., Shirakata H., Suganuma K., Sugawara T., Sugie T., Sunaoshi H., Suzuki K., Suzuki M., Suzuki N., Suzuki S., Suzuki Y., Tahira S., Takahashi M., Takahashi S., Takahashi T., Takatsu H., Takayasu Y., Takeda S., Takeuchi H., Takizuka T., Tamura S., Tanaka E., Tanaka S., Tanaka T., Tani K., Terakado T., Tobita K., Tokutake T., Totsuka T., Toyoshima N., Tsugita T., Tsuji S., Tsukahara

Y., Tsuneoka M., Uehara K., Uehara M., Ujiie K., Urakawa H., Uramoto Y., Ushigusa K., Usui K., Watanabe K., Yagyu J., Yamada K., Yamamoto M., Yamashita O., Yamashita Y., Yano K., Yokokura K., Yokomizo H., Yonekawa I., Yoshida H., Yoshikawa M., Yoshino R.

33) JT-60 Team*, "Review of preliminary additional heating experiments in JT-60 (Aug.-Nov. 1986)", JAERI-M 87-009.

* Abe T., Aikawa H., Akaoka N., Akasaka H., Akiba M., Akino N., Akiyama T., Ando T., Annoh K., Aoyagi T., Arai T., Arakawa K., Araki M., Arimoto K., Azumi M., Chiba S., Dairaku M., Ebisawa N., Fujii T., Fukuda T., Furukawa H., Hamamatsu K., Hayashi K., Hara M., Haraguchi K., Hiratsuka H., Hirayama T., Hiroki S., Hiruta K., Honda M., Horiike H., Hosoda R., Nosogane N., Iida Y., Iijima T., Ikeda K., Ikeda Y., Imai T., Inoue T., Isaji N., Isaka M., Ishida S., Itige N., Ito T., Ito Y., Kaminaga A., Kawai M., Kawamata Y., Kawasaki K., Kikuchi K., Kikuchi M., Kimura H., Kimura T., Kishimoto H., Kitahara K., Kitamura S., Kitsunezaki A., Kiyono K., Kobayashi N., Kodama K., Koide Y. Koike T., Komata M., Kondo I., Konoshima S., Kubo M., Kunieda S., Kurakata S., Kurihara K., Kuriyama M., Kuroda T., Kusaka M., Kusama Y., Maebara S., Maeno K., Matsuda S., Mase S., Matsukawa M., Matsukawa T., Matsuoka M., Miya N., Miyati K., Miyo Y., Mizuhashi K., Mizuno M., Murai R., Murakami Y., Muto M., Nagami M., Nagashima A., Nagashima K., Nagashima T., Nagaya S., Nakamura H., Nakamura Y., Nemoto M., Neyatani Y., Niikura S., Ninomiya H., Nishitani T., Nomata H., Obara K., Ogiwara N., Ohga T., Ohara Y., Ohasa K., Oohara H., Ohshima T., Ohkubo M., Ohta K., Ohta M. Ohtaka M., Ohuchi Y., Oikawa A., Okumura H., Okumura Y., Omori K., Omori S., Omori Y., Ozeki T., Sakasai A., Sakata S., Satou M., Saigusa M., Sakamoto K., Sawahata M., Seimiya M., Seki M., Seki S., Shibanuma K., Shimada R., Shimizu K., Shimizu M., Shimomura Y., Shinozaki S., Shirai H., Shirakata H., Shitomi M., Suganuma K., Sugie T., Sugiyama T., Sunaoshi H., Suzuki K., Suzuki M., Suzuki M., Suzuki N., Suzuki S., Suzuki Y., Takahashi M., Takahashi S., Takahashi T., Takahashi H.**, Takasaki M., Takatsu M., Takeuchi H., Takeshita A., Tamura S., Tanaka S., Tanaka T., Tani K., Terakado M.,

Terakado T., Tobita K., Tokutake T., Totsuka T., Toyoshima N., Tsuda H., Tsugita T., Tsuji S., Tsukahara Y., Tsuneoka M., Uehara K., Umehara M., Uramoto Y., Usami H., Ushigusa K., Usui K., Yagyu J., Yamada K., Yamamoto M., Yamashita O., Yamashita Y., Yano K., Yasukawa T., Yokokura K., Yokomizo H., Yoshikawa K., Yoshikawa M., Yoshida H., Yoshinari Y., Yoshino R., Yonekawa I., Watanabe K. (** Plasma Physics Laboratory, Princeton University, USA)

34) Niikura S., Nagami M., Hirayama T.: "Evaluation of Fusion Power Multiplication Factor", JAERI-M 86-089 (1986).

35) Ninomiya H., Kikuchi M., Yoshino R., Hosogane N., Hayashi K., Kimura T., Kurihara K., Takahashi M.: "Feedback Control of Plasma Configuration in JT-60", JAERI-M 86-110 (1986) in Japanese.

36) Hirayama T., Sugie T., Sakasai A., Kubo H., Koide Y., Akaoka N., Takeuchi H., Nagami M.: "Impurity Transport in Ohmically Heated JT-60 Plasma", JAERI-M 86-161 (1986).

37) Nakamura H., Ando T., Niikura S., Arai T., Yamamoto M., JT-60 Team: "Plasma Wall Interaction in Ohmically Heated Discharges of JT-60 Tokamak", JAERI-M 86-173 (1986).

38) Ozeki T., Seki S., Ninomiya H., Azumi M.: "Kink Instability of the Divertor Configuration in JT-60", JAERI-M 87-004 (1987) in Japanese.

39) Kikuchi M., Hirayama T., JT-60 Team, et al.: "Energy Confinement and Profile Characteristics during the Initial Neutral Beam Heating in JT-60", JAERI-M 87-008 (1987).

40) Shirai H., Nagashima K., Nishitani T., JT-60 Team: "Numerical Analysis of Sawtooth Oscillations in Joule Heating Plasma in JT-60, JAERI-M 87-014 (1987).

41) Nakamura Y., Ozeki T.: "Finite Element Circuit Theory of the Numerical Code EDDYMULT for Solving Eddy Current Probrems in a Multi-Torus System", JAERI-M 86-096 (1986).

42) Shimizu K., Azumi M.: "Two Dimensional Neutral Transport Analysis in Tokamak Plasma", JAERI-M 87-028 (1987) in Japanese.

43) Hirayama T., Shimizu K., Kikuchi M., Shirai H., JT-60 Team: "Transport Analysis of OH and NBI Heated Discharges in JT-60", JAERI-M 87-029 (1987).

44) Kubo H., Ishii K., Sugie T., Shiho M., Maeda H., Suzuki Y., "Atomic Structure Calculations of Mo XV-XL", JAERI-M 86-081 (May 1986) p224, in Japanese.

45) Nishitani T., Nagashima K., Takeuchi H., "Soft X-ray measurements of the JT-60 tokamak plasma in the initial experiments", JAERI-M 87-011 (Feb. 1987) p24.

46) Hitoki S., Sugihara M., Yamamoto S.: "Effects of Geometry on FER Divertor Plasma", JAERI-M 86-133 (September 1986).

47) Sawada Y., Tone Y., Fujisawa N., Saito R., Seki Y., Kobayashi T., Iida H., Yamamoto S., Sugihara M., Itou Y., Mizoguchi T., Okazaki T., Hitoki S., Kasai M.*3, Ueda N.*3 Saito S.*4, Hatayama A.*2, Shinya K.*2, Kinoshita S.*4, Nishio S., Horie T., Imamura Y.*8, Honda T.,*2, Mori S., Yamanaka T., Kitamura K., Kuroda H., Uchida T.*2, Sato K.*4, Maki K.*4, Adachi J.*18, Yamada M.*3, Miki N.*2, Kuroda T.*18, Niikura T.*8, Matsuoka F.*8, Tachikawa K., Seki M., Minato A., Tachikawa N., Tsujimura S., Fujioka T.*2, Iida F.*4, Ichihara S.*11, Sanada Y.*2, Toyoda K.*11, Kameari A.*3, Ueda Y.*4, Kakiuchi T.*4, Ohta K.*11, Okano K.*2, Tsukamoto T.*11, Saito K.*4, Yamamoto T., Mohri K.*18, Nakahara K., Ohmura H.*2, Suzuki T.*18, Itoh S.*4: "Conceptual Design Study of Fusion Experimental Reactor (FER) (FY 1984, 85 Report)", JAERI-M 86-134 (November 1986) (in Japanese).

48) Iida H., Kuroda H., Yamada M.*3, Suzuki T.*18, Honda T.*2, Ohmura H.*2, Itoh S.*4: "Design Study of Plant System for the Fusion Experimental Reactor (FER)", JAERI-M 86-149 (November 1986) (in Japanese).

49) Okazaki T., Sugihara M., Fujisawa N.: "Two-Dimensional Fokker-Planck Analysis Code for RF Current Drive", JAERI-M 86-160 (November 1986).

50) Tone T., Seki M., Minato A.*18, Horie T., Kawamura H., Ogawa M., Fujimura K., Takeda T., Fukaya K., Iida H., Sugihara M., Hasizume H.**5, Miya K.**5, Tsujimura S.*8, Yamamoto T.*6, Yamazaki S.*18, Tanaka Y.*18, Tachikawa N.*2, Shibutani Y.*2, Nagata A.*2, Miki N.*2, Watanabe T.*25: "Analyses and Experiments on the Integrity and Lifetime Predictions of Plasma-Facing Components in Fusion Reactors", JAERI-M 86-176 (January 1987) (in Japanese).

51) Nishio S., Tone T., Kasai M.*3, Nishikawa M.*3: "Development of Tokamak Reactor Systems Analysis Code "TORSAC"," JAERI-M 87-021 (March 1987) (in Japanese).

52) Tone T., Seki M., Minato A., Horie T., Yamamoto T., Tanaka Y.*18, Abe T.*18, Watanabe T.*18, Kobayashi T., Sato K.*18, Suzuki T.*18, Adachi J., Mori S., Kuroda T.*18, Okazaki S.*18, Yamazaki S.*18, Misumi M., Mohri K.*18, Fujii M.*18, Ise H.*18: "Technical Evaluation of Major Candidate Blanket Systems for Fusion Power Reactor", JAERI-M 87-017 (March 1987)(in Japanese).

53) Yamada K.*25, Minato A.*18, Seki Y., Kawasaki H.*25, Maeda M.*25: "Development of Coupled Nuclear - Thermal Calculation Code System", JAERI-M 86-084 (June 1986)(in Japanese).

54) Haines J.R.**14, Kitamura K., Kobayashi T., Iida H.: "Parametric Study of FER First Wall and Divertor Plate Performance", JAERI-M 86-099 (July 1986)(in Japanese).

55) Miura Y., Matsuda T., Yamamoto S., et al.: "Active Ion Temperature Measurement with Heating Neutral Beam", JAERI-M 87-042 (March 1987).

A.1.2 List of papers published in journals

1) Kurita G., Azumi M., Takizuka T., Tuda T., Tsunematsu T., Tanaka Y.*1, Takeda T., "Bubble formation due to surface tearing mode", Nucl. Fusion 26 (1986) 449.

2) Yamagiwa M., "Tail-anisotropy instability during plasma current rise by lower-hybrid waves in a tokamak", J. Phys. Soc. Japan 55 (1986) 1574.

3) Fujita J.**2, Funahashi A.: "Status of the Researches on Fusion and Plasma Physics in Australia", Kakuyugo-Kenkyu 55 (1986) 431 (in Japanese).

4) Itoh S.-I.**1, Itoh K.**9, Sengoku S.: "Multiple Pellet for Plasma Fueling", Jpn. J. Appl. Phys. 25 (1986) L496. June.

5) Uesugi Y., Matoba T., Ochiai I.*4, Mizuno K.**4, "Hydrogen Cyanide Laser Interferometer of the JFT-2M Tokamak and Feedback Stabilization of the Best Frequency using a Microcomputer", Rev. Sci. Instrum. 57 (1986) 1290.

6) Maeno M., Yamamoto S., Hirayama T., Ogawa H., Ohtsuka H., Matsuda T.: "Mechanism of Light-Impurity Release in a Tokamak", Jpn. J. Appl. Phys. 25 (1986) L604.

7) Odajima K.: "Topics on Recent Plasma Heating (1)/Energy Confinement Characteristics of Additionally Heated Plasma", Kakuyugo-Kenkyu 56 (1986) 81 (in Japanese).

8) Odajima K., Hoshino K., Kasai S., Kawakami T., Kawashima H., Matoba T., Matsuda T., Matsumoto H., Miura Y., Mori M., Ogawa H., Ogawa T., Ohtsuka H., Shoji T., Suzuki N., Tamai H., Uesugi Y., Yamamoto T., Yamauchi T., Hasegawa M.*11, Takada S.*49, Yanagisawa I.*3: "Scaling of Incremental Energy Confinement Time in the JFT-2M Tokamak", Phys. Rev. Letters 57 (1986) 2814.

9) Sengoku S. and the JFT-2M team: "Confinement and Fueling Studies during Additional Heating Phase in the JFT-2M Tokamak", J. Nucl. Mater. 145-147 (1987) 556.

10) Matsuzaki Y., Ogawa H., Miura Y., Ohtsuka H., Suzuki N., Yamauchi T., Tani T., Mori M.: "Experiments of Cleaning Effects by TDC, GDC, ECR-DC", J. Nucl. Mater. 145-147 (1987) 704.

11) Matsuzaki Y., Okano F., Sengoku S., Kikuchi K., Hasegawa K., Kazawa M.: "Calibration of Vacuum Gauges in JFT-2M Tokamak", J. of Vac. Soc. of Japan 29 (1986) 245 (in Japanese).

12) Saidoh M., Bay H.L.*1, Bohdansky J.*2, Roth J.*2: "Oxygen Exposure Effect on Sputtering Yield and Angular Distribution for Light-Ion Irradiation of Polycrystalline Molybdenum", Nucl. Instr. & Methods B13 (1986) 403.

13) Gnaser H.*1, Saidoh M., von Seggern J.*1, Hofer W.O.*1: "Oxygen Coverage Dependent Emission of Sputtered Neutrals and Secondary Ions", Nucl. Instr. & Methods B15 (1986) 169.

14) Saidoh M., Gnaser H.*1, Hofer W.O.*1: "On the Chemical Sputtering of Oxygen-Exposed Molybdenum", Appl. Phys. A40 (1986) 197.

15) Nakamura K., Obara K., Murakami Y.: "Three-dimensional Analysis of Gases Introduced in a Vacuum by Monte Carlo Method", J. Vacuum Soc. Japan 29 (1986) 310.

16) Murakami Y., Shimomura Y., Abe T., Obara T.: "Improvement of Helium Sniffing Method for Locating Fine Leaks", J. Vacuum Soc. Japan 29 (1986) 485.

17) Hiroki S., Ikeda Y., Abe T., Murakami Y.: "Measurement of Secondary Electron Yield of Wall Materials using Auger Electron Spectrometer", J. Vacuum Soc. Japan 30 (1987) 14.

18) Murakami Y.: "Vacuum and Surface Research for Fusion Experimental Devices", Physics Monthly 7 (1986) 528.

19) Murakami Y.: "Vacuum Science and Technology for Fusion Research", Japan Science and Technology 28 No. 243 (1987) 73.

20) Yamada R.: "Chemical Sputtering Yields of Graphite", J. Nucl. Mater. 145-147 (1987) 359.

21) Saidoh M., Bay H.L.*1, Gnaser H.*1, Hofer W.O.*1, Bohdansky J.*2, Roth J.*2: "Projectile Dependent Sputter-Erosion of Oxygen-Exposed Molybdenum at Different Temperatures", J. Nucl. Mater. 145-147 (1987) 387.

22) Ohara Y., Akiba M., Horiike H., Inami H.*19, Okumura Y., Tanaka S.: "3D Computer Simulation of the Primary Electron Orbits in a Magnetic Multipole Plasma Source", J. Appl. Phys. 61 (1987) 1323.

23) Sakamoto K., Imai T., Fujii T., Ikeda Y., Saigusa M., Sagawa J.*4 and Nagashima T.: "Unipole Multipactoring Discharge in LHRF Launcher", IEEE Trans. on Plasma Science Vol. PS-14, P548-553 (1986).

24) Arai H.**8, Goto N.**8, Ikeda Y., Imai T.: "An Analysis of Vacuum Window for Lower Hyrbid Heating": IEEE Trans. on Plasma Science Vol. PS-14, No. 6 P947-954 (1986).

25) Nagashima T., Uehara K., Kimura H., Imai T., Fujii T., Sakamoto K., Ikeda Y., Saigusa, M., Suzuki N., Honda M., Yokakura K., Kimino K., Sawahata M., Suganuma K., Seki M., and Shirakata H.: "JT-60 radio-frequency heating system: Description and R&D Results", Nuclear Engineering and Design Fusion Vol. 5 No. 1 P101-115 (1987).

26) Nakajima H., Yoshida K., Shimamoto S.: "Development of Cryogenic Structural Materials and Structural Design Standards", Cryogenic Engineering Vol. 21, No. 4 (1986) 197 (in Japanese).

27) Kinoshita M., "Progress in Simulation Procedure for Multistage-Type Water/Hydrogen Exchange Column", J. Nucl. Sci. Technol., 23 (1986) 378.

28) Okuno K., Kudo H., "Chemical State of Tritium and Interaction with Radiation Damages in Li_2O crystals", J. Nucl. Mater., 138 (1986) 31.

29) Okuno K., Kudo H., "Diffusion Controlled Tritium Release from Neutron-irradiated γ-$LiAlO_2$", J. Nucl. Mater., 138 (1986) 210.

30) Nagasaki T., Konishi S., Katsuta H., Naruse Y., "A Zirconium-Cobalt Compound as the Material for a Reversible Tritium Getter", Fusion Technol., 9 (1986) 506.

31) Kinoshita M., "Simple Model for Dynamic Simulation for Stage Separation Process with Very Volatile Components", AICHE J., 32 (1986) 872.

32) Kinoshita M., "Drastic Reduction of Computing Time in Dynamic Simulation for Hydrogen Isotope Distillation Column", Fusion Technol., 9 (1986) 492.

33) Okuno K., Nagame Y., Kudo H., "Thermal Release of Tritium from Neutron-irradiated Li_7Pb_2", J. Less-Common Met., 119 (1986) 211.

34) Konoshita M., Yamanishi T., Bartlit J.R., Sherman R.H., Fusion Technol., 10 (1986) 137.

35) Kinoshita M., Yoshida H., Takeshita H., "A Simulation Study for Hydrogen Isotope Distillation Column in the Tritium Breeding Blanket System of a Fusion Reactor", Fusion Technol., 10 (1986) 462.

36) Konishi S., Ohno H., Yoshida H., Katsuta H., Naruse Y., "Solid Oxide Electrolysis Cell for Decomposition of Tritiated Water", Int. J. Hydrogen Energy, 11 (1986) 507.

37) Sesnic S.S.**[19], Bitter M.**[19], Hill K.W.**[19], Hiroe S.**[14], Hulse R.**[19], Shimada M., Stratton B.**[19], von Goeler S.**[19]: "Evaluation of soft x-ray average recombination coefficient and average charge for metallic impurities in beam-heated plasmas", Rev. Sci. Instrum. 57 (8) (1986) 2148.

38) Hill K.W.**[19], Bitter M.**[19], von Goeler S.**[19], Hiroe S.**[14], Hulse R.**[19], Ramsey A.T.**[19], Sesnic S.**[19], Shimada M. and Stratton B.C.**[19]: "Effective Kα x-ray excitation rates for plasma impurity measurements", Rev. Sci. Instrum. 57 (8) (1986) 2151.

39) Yoshikawa M., JT-60 Team*: "Initial Experiments in JT-60", Plasma Physics and Controlled Fusion, 28, 165 (1986).

* Abe T., Aikawa H., Akaoka N., Akasaka H., Akino N., Akiyama, T., Ando T., Anno K., Aoyagi T., Arai T., Arakawa K., Azumi M., Fukuda T., Fukuda T., Furukawa H., Hamamatsu K., Haraguchi T., Hayashi K., Hiratsuka H., Hirayama T., Hiroki S., Hiruta K., Hitomi N., Hosoda R., Hosogane N., Ichige H., Iida S., Iijima T., Ikeda Y., Isaji N., Isaka M., Ishihara M., Itoh Y., Kaneko M., Kawamata Y., Kawasaki K., Kikuchi M., Kimura T., Kishimoto H., Kitahara K., Kitsunezaki A., Kodama K., Koide Y., Koike T., Kondo I., Konoshima S., Kubo H., Kunieda S., Kurihara K., Kuroda K., Maeda H., Maeno M., Matsukawa M., Matsukawa T., Matsuo M., Miya N., Miyachi K., Miyo Y., Mizuno M., Murakami Y., Mutoh M., Nagami M., Nagashima A., Nagashima K., Nagaya S., Nakamura H., Nakamura Y., Nemoto M., Neyatani Y., Niikura S., Ninomiya H., Nishitani T., Nishiyama T., Nomata H., Noshiroya S., Ogiwara N., Ohasa K., Ohkubo M., Ohmori K., Ohmori S., Ohmori Y., Ohsato Y., Ohshima T., Ohta M., Otsu K., Oikawa A., Ozeki T., Sakasai A., Sakata S., Sato M., Seimiya M., Seki S., Shiho M., Shitomi M., Shimada R., Shimizu K., Shimizu M., Shimomura Y., Shinozaki S., Shirai H., Sugie T., Sunaoshi H., Suzuki K., Suzuki M., Suzuki S., Suzuki Y., Tahira S., Takahashi M., Takahashi S., Takahashi T., Takatsu H., Takayasu Y., Takeda S., Takeuchi H., Takizuka T., Tamura S., Tanaka E., Tanaka T., Tani K., Terakado T., Tobita K., Tokutake T., Totsuka T., Toyoshima N., Tsugita T., Tsuji T., Tsukahara Y., Tsuneoka M., Ujiie K., Urakawa H., Uramoto Y., Ushigusa K., Yagyu J., Yamada K., Yamamoto M., Yamashita O., Yamashita Y., Yano K., Yokomizo H., Yonekawa I., Yoshida H., Yoshikawa M., Yoshino R.

40) Tamura S., JT-60 Team*: "Status of JT-60 experiments", ibid., 28, 1377 (1986).

* Abe T., Aikawa H., Akaoka N., Akasaka H., Akiba M., Akino N., Akiyama T., Ando T., Anno K., Aoyagi T., Arai T., Arakawa K., Araki M., Azumi M., Dairaku M., Ebisawa N., Fujii T., Fukuda T., Fukuda T., Furukawa H., Hamamatsu K., Haraguchi T., Hayashi K., Hiratsuka H., Hirayama T., Iida K., Hiroki S., Hiruta K., Hitomi N., Honda M., Horiike H., Hosoda R., Hosogane N., Ichige H., Iida S., Iijima T., Ikeda Y., Imai T., Inami H., Isaji N.,

Isaka M., Ishihara M., Itoh H., Itoh Y., Kanai T., Katoh T., Kawai M., Kawamata Y., Kihara Y., Kawasaki K., Kikuchi M., Kimura H., Kimura T., Kishimoto H., Kitahara K., Kitamura S., Kitsunezaki A., Kiyono K., Kodama K., Koide Y., Koike T., Komata M., Kondo I., Konoshima S., Kubo H., Kunieda S., Kurakada K., Kurihara K. Kuriyama M., Kuroda T., Maeno M., Matsuda S., Matsukawa M., Matsukawa T., Matsuo M., Matsuoka M., Miya N., Miyachi K., Miyo Y., Mizuhashi K., Mizuno M., Murakami Y., Mutoh M., Nagami M., Nagashima A., Nagashima K., Nagashima T., Nagaya S., Nakamura H., Nakamura Y., Nemoto M., Neyatani Y., Niikura S., Ninomiya H., Nishitani T., Nishiyama T., Nomata H., Noshiroya S., Ogiwara N., Ohasa K., Ohga T., Ohhara H., Ohkubo M., Ohmori K., Ohmori S., Ohmori Y., Ohsato Y., Ohshima T., Ohta M., Ohara Y., Ohuchi Y., Okumura Y., Otsu K., Oikawa A., Ozeki T., Saigusa M., Sakamoto K., Sakasai A., Sakata S., Sato M., Sawahata M., Shibanuma K., Shibata T., Seimiya M., Seki M., Seki S., Shitomi M., Shimada R., Shimizu K., Shimizu M., Shimomura Y., Shinozaki S., Shirai H., Shirakata H., Suganuma K., Sugawara T., Sugie T., Sunaoshi H., Suzuki K., Suzuki M., Suzuki N., Suzuki S., Suzuki Y., Tahira S., Takahashi M., Takahashi S., Takahashi T., Takatsu H., Takayasu Y., Takeda S., Takeuchi H., Takizuka T., Tamura S., Tanaka E., Tanaka S., Tanaka T., Tani K., Terakado T., Tobita K., Tokutake T., Totsuka T., Toyoshima N., Tsugita T., Tsuji S., Tsukahara Y., Tsuneoka M., Uehara K., Uehara M., Ujiie K., Urakawa H., Uramoto Y., Ushigusa K., Usui K., Watanabe K., Yagyu J., Yamada K., Yamamoto M., Yamashita O., Yamashita Y., Yano K., Yokokura K., Yokomizo H., Yonekawa I., Yoshida H., Yoshikawa M., Yoshino R.

41) Kishimoto H., JT-60 Team*: "JT-60 Experiments", Jounal of Nuclear Materials, 145-147, 41 (1987).

* Abe T., Aikawa H., Akaoka N., Akasaka H., Akiba M., Akino N., Akiyama T., Ando T., Anno K., Aoyagi T., Arai T., Arakawa K., Araki M., Azumi M., Dairaku M., Ebisawa N., Fujii T., Fukuda T., Fukuda T., Furukawa H., Hamamatsu K., Haraguchi T., Hayashi K., Hiratsuka H., Hirayama T., Iida K., Hiroki S., Hiruta K., Hitomi N., Honda M., Horiike H., Hosoda R., Hosogane N., Ichige

H., Iida S., Iijima T., Ikeda Y., Imai T., Inami H., Isaji N., Isaka M., Ishihara M., Itoh H., Itoh Y., Kanai T., Katoh T., Kawai M., Kawamata Y., Kihara Y., Kawasaki K., Kikuchi M., Kimura H., Kimura T., Kishimoto H., Kitahara K., Kitamura S., Kitsunezaki A., Kiyono K., Kodama K., Koide Y., Koike T., Komata M., Kondo I., Konoshima S., Kubo H., Kunieda S., Kurakada K., Kurihara K. Kuriyama M., Kuroda T., Maeno M., Matsuda S., Matsukawa M., Matsukawa T., Matsuo M., Matsuoka M., Miya N., Miyachi K., Miyo Y., Mizuhashi K., Mizuno M., Murakami Y., Mutoh M., Nagami M., Nagashima A., Nagashima K., Nagashima T., Nagaya S., Nakamura H., Nakamura Y., Nemoto M., Neyatani Y., Niikura S., Ninomiya H., Nishitani T., Nishiyama T., Nomata H., Noshiroya S., Ogiwara N., Ohasa K., Ohga T., Ohhara H., Ohkubo M., Ohmori K., Ohmori S., Ohmori Y., Ohsato Y., Ohshima T., Ohta M., Ohara Y., Ohuchi Y., Okumura Y., Otsu K., Oikawa A., Ozeki T., Saigusa M., Sakamoto K., Sakasai A., Sakata S., Sato M., Sawahata M., Shibanuma K., Shibata T., Seimiya M., Seki M., Seki S., Shitomi M., Shimada R., Shimizu K., Shimizu M., Shimomura Y., Shinozaki S., Shirai H., Shirakata H., Suganuma K., Sugawara T., Sugie T., Sunaoshi H., Suzuki K., Suzuki M., Suzuki N., Suzuki S., Suzuki Y., Tahira S., Takahashi M., Takahashi S., Takahashi T., Takatsu H., Takayasu Y., Takeda S., Takeuchi H., Takizuka T., Tamura S., Tanaka E., Tanaka S., Tanaka T., Tani K., Terakado T., Tobita K., Tokutake T., Totsuka T., Toyoshima N., Tsugita T., Tsuji S., Tsukahara Y., Tsuneoka M., Uehara K., Uehara M., Ujiie K., Urakawa H., Uramoto Y., Ushigusa K., Usui K., Watanabe K., Yagyu J., Yamada K., Yamamoto M., Yamashita O., Yamashita Y., Yano K., Yokokura K., Yokomizo H., Yonekawa I., Yoshida H., Yoshikawa M., Yoshino R.

42) Yoshida H., Ninomiya H., Azumi M., Seki S.: "Numerical Method of Tokamak Equilibrium with Outside Limiter", J. Comp. Phys. 63 (1986) 477.

43) Hosogane N., Ninomiya H., Seki S.: "Method for Measuring Divertor Configuration Parameters for Feedback Control in JT-60", Nucl. Fusion 26 (1986) 657.

44) Edwards A.W., Campbell D.J., Engelhardt W.W., Gill R.D., Tsuji S., et al.: "Rapid Collapse of a Plasma Sawtooth Oscillation in the JET Tokamak", Phys. Rev. Lett. 57 (1986) 210.

45) Edwards A.W., Fahrbach H.U., Gill R.D., Granetz R., Tsuji S., et al.: "JET Soft X-ray Diode Array Diagnostic", Rev. Sci. Instrum. 57 (1986) 2142.

46) Shimomura Y., Odajima K.: "Empirical Scaling of Incremental Energy Confinement Time of L-mode Plasma and Comments on Improved Confinements in Tokamaks", Comments Plasma Phys. Controlled Fusion 10 (1987) 207.

47) Kikuchi M., Ninomiya H., Yoshino R., Seki S.: "A Matrix Transfer Function Analysis Applied to the Active Feedback Control System of a Divertor Tokamak", Nucl. Fusion 27 (1987) 299.

48) Seki S., Tsunematsu T., Azumi M., Nemoto T.: "Beta Enhancement of Tokamak Plasma with Nearly Circular Cross-Section", Nucl. Fusion 27 (1987) p330-334.

49) Hirayama T., Shirai H., Shimizu K., Azumi M., Takizuka T.: "Plasma Performance of Limiter Discharges with Self-Consistent Plasma-Wall Interaction Model", Journal of Nuclear Materials 145-147 (1987) 854.

50) Tobita K. and Takeuchi H.: "One-Electron Loss Cross Section of Helium in Hydrogen Gas", Journal of the Physical Society of Japan 55, 1986, pp.4231-4233.

51) Tobita K., Takeuchi H., Kimura H., Kusama Y. and Nemoto M.: "Absolute Detection Efficiency of a Microchannel-Plate Detector for Ions and Neutrals", Japanese Journal of Applied Physics 26, 1987, pp.509-510.

52) Yokomizo H., Takeuchi H., Sugie T., Ogiwara N., Sato M., Nagashima A., Ohasa K., Nakamura Y., Nishitani T., Neyatani Y., Sakasai A., Fukuda T., Kubo H., Tobita K., Yamashita Y., Nemoto M., Iida S., Nagashima K., Uramoto Y., Yamashita O., Tsugita T., Shitomi M., Tsukahara Y., Ohshima T., Yamagishi K., Tahira S., Konoshima S., Shiho M., Maeda H. and Suzuki Y.: "The JT-60 Diagnostic System", Fusion Engineering and Design 5 (1987) 117-138.

53) Kondo I. and Suzuki Y.: "Technologies and Achievements of Break-Even Plasma Experimental Device JT-60. 4. Control and Diagnostics", Oyo Butsuri, 55 (1986) 465.

54) Okazaki T.*4, Sugihara M., Fujisawa N.: "Lower hybrid current drive in the Presence of a DC electric field", Nuclear Fusion, 26 (1986) 1029.

55) Sugihara M., Singer C.**19: "Energy Confinement in Tokamaks", Nuclear Fusion, 26 (1986) 1547.

56) Mori S.**18, Seki Y.* "Radiation Streaming Analysis through Narrow Gaps in Fusion Experimental Reactor (FER)", J. of Nucl. Sci. Technol., 24 (1986) 1.

57) Seki M., Yamazaki S.*18, Minato A., Horie T., Tanaka Y.*18, Tone T.: "A Simulated Plasma Disruption Experiment Using an Electron Beam as a Heat Source", J. of Fusion Energy 5 (1986) 181.

58) Minato A.*18, Tone T., Miya K.**5: "Three-Dimensional Analysis of Magnetic Field Distortion of Ferromagnetic Beam-Plates by the Boundary Element Method", Int. J. Numerical Methods in Engineering, 23, (1986) 1201.

59) Ogawa M., Seki M., Minato A.*18, Fukaya K., Tone T.: "Durability Tests of Tungsten-Copper Duplex Structures for Use as Divertor Plate against Thermal Fatigue, (1) Results of Brazed Test Pieces", J. of Atomic Energy Society of Japan, 28 (1986) 1038.

60) Yamauchi M.*13, Kawai M.*13, Seki Y.: "Applicability of Neutron-Gamma-Ray-Coupled Albedo Monte Carlo Method to Streaming Analysis in Fusion Reactors", Fusion Technology, 10 (1986) 431.

61) Horie T., Seki M., Minato A.*18, Tone T.: "Analysis and Experiments on Lifetime Predictions for First Wall and Divertor Plate Structures in JAERI", Fusion Technology, 10 (1986) 753.

62) Fujisawa N.: "Status of IAEA International Tokamak Reactor (INTOR)", J. Atomic Energy Society of Japan, 28 (1986) 908.

63) Tamai H., Odajima K., Matsumoto H., Ogawa T., Yamamoto S.: "Impurity Reduction During ICRF Heating in JFT-2M Tokamak", Nuclear Fusion, 20 (1986) 365.

64) Maeno M., Kiuchi K., Ohtsuka H., Yamamoto S., Sengoku S., Ogawa H., Nakamura H.: "Effect of Scrape-off Plasma on the Modification of a TiC-coated Surface", J. Nuclear Material, 138 (1986) 138.

A.1.3 List of papers published in conference proceedings

1) Itoh K.**[9], Fukuyama A.**[3], Morishita T.**[3], Kishimoto Y., "Analysis on ICRF heating and current drive in tokamaks", 13th European Conference on Controlled Fusion and Plasma Physics (Schliersee, 14-18 April 1986) Vol. 10C Part II, p.177.

2) Kishimoto Y., Hamamatsu K., Fukuyama A.**[3], Itoh S-I.**[1], Itoh K.**[9], "ICRF current-drive by use of phase control of antennas", ibid. p.433.

3) Tsunematsu T., Seki S., Tokuda S., Azumi M., "Beta enhancement of tokamak plasma with small elongation", Tokamak concept innovations (IAEA workshop proceedings) TECDOC 373 (IAEA, Vienna 1986) p.137.

4) Yamamoto S., Azumi M., Tanaka Y.*[1], "Control of m=1 MHD activity", ibid., p.149.

5) Tsunematsu T., Nemoto T.*[1], Tokuda S., "Beta enhancement by using low aspect ratio tokamak plasma", ibid., p.575.

6) Hirayama T., Shirai H., Shimizu K., Azumi M., Takizuka T., "Plasma performance of limiter discharges with self-consistent plasma wall interaction", 7th International Conference on Plasma Surface Interactions (Princeton, May 1986).

7) Takeda T., Tsunematsu T., Tokuda S., Kurita G., Takizuka T., "MHD computations in tokamak fusion research", Computational Mechanics (Proceedings of International Conference on Computational Mechanics, May 1986, Tokyo) Vol. 2, IX-3.

8) Tani K., Takizuka T., Azumi M., "Ripple enhanced transport of sprathermal alpha particles", US-Japan workshop on statistical plasma physics (Nagoya, September 1986), Institute of Plasma Physics (Nagoya University) Report, IPPJ-REV-2 (September 1986) p.176.

9) Tuda T., "Nonlinear saturation of ballooning mode", ibid. p.265.

10) Tsunematsu T., Seki S., Azumi M., Tokuda S., Ozeki T., Nemoto T.*[1], Takeda T., "Second stability access in tokamak plasmas; Part B: Second stability access in conventional cross-section", 11th International Conference on Plasma Physics and Controlled Nuclear Fusion Research, Kyoto November 1986, IAEA-CN-47/E-I-2-1.

11) Tuda T., Kishimoto Y., Takeda T., "Second stability access in tokamak plasmas; Part C: Saturation mechanism of ballooning modes", ibid., IAEA-CN-47/E-I-2-1.

12) Fukuyama A.**[3], Morishita T.**[3], Kishimoto Y., Hamamatsu K., Itoh S-I.**[1], "Analysis of ICRF heating and current drive in tokamaks", ibid., IAEA-CN-47/F-IV-1.

13) Engelmann E.**[20], Igitkhanov Y.L.***[1], Knobloch A.**[20], Kukuskin A.***[1], Litunovskij R.N.***[2], Peng Y.-K.M.**[14], Pistunovich V.***[1], Tsunematsu T., "INTOR: Operational limits and confinement", ibid., IAEA-CN-47/G-I-4.

14) Kishimoto Y., "ICRF current drive by use of phase control of antennas", US-Japan workshop on advanced current drive concept (Kyoto, November 1986).

15) Tsunematsu T., Suzuki N., Takizuka T., Seki S., Azumi M., Nemoto T.*[1], "Beta and confinement enhancement", INTOR workshop Phase 2A Part 3, Session 14 Group B.

16) Kishimoto Y., "Fast wave current drive in the ion cyclotron range of frequency (ICRF)", ibid, Group C.

17) Takizuka T., Tani K., Azumi M., "Particle siulation of divertor Plasma", in Proc. of US-Japan workshop on advanced plasma modeling, Nagoya, September 1985, Institute of Plasma Physics (Nagoya Univ.) Report, IPPJ-818 (March 1987).

18) Tuda T., Suzuki N., "Scaling study of JFT-2M plasma", in Proc. of US-Japan workshop an anomalous transport in fusion device, San Diego, February 1987 (April 1987) p.47.

19) Tuda T., "Nonlinear saturation of ballooning mode", ibid. p.67.

20) Kurita G., "Nonlinear evolution of free boundary modes in tokamak", US-Japan workshop on advanced plasma modelling (Nagoya, March 1987).

21) Schweer, B.**[43], Bay, H.L.**[43], Bieger, W.**[43], Bogen, P.**[43], Hartwig, H.**[43], Hintz, E.**[43], Höthker, K.**[43], Lie, Y.T.**[43], Pospieszczyk, A.**[43], Ross, G.**[43], Rüsuldt, D.**[43], Samm, U.**[43], Yamauchi, T., Van Nieuwenhove, R.**[44], Van Oost, G.**[44]: "Effects of ICRF-Heating on the Plasma Edge in TEXTOR", in Controlled Fusion and Plasma Physics (Proc. 13th Europ. Conf., Schliersee, 1986) Vol. 10C, Part I, (1986) 399.

22) Yamamoto T., Hoshino K., Uesugi Y., Kawashima H., Mori M., Miura Y., Suzuki N., Matoba T., Funahashi A., Kasai S., Kawakami T., Matsuda T., Matsumoto H., Odajima K., Ogawa H., Ogawa T., Ohtsuka H., Sengoku S., Shoji T., Tamai H., Yamauchi T., Hasegawa M.*[11], Takada S.*[49]: "RF Heating and Current Drive Experiments on the JFT-2M Tokamak", Conference on Controlled Fusion and Plasma Heating F.R. Germany 14-18 April (1986) Part II, (1986) 437.

23) Wolf, G.H.**[43], Bay, H.L.**[43], Bertschinger, G.**[43], Bieger, W.**[43], Bogen, P.*[43], Brüssan, W.**[43], Campbell, G.A.**[43], Cao, Y.**[43], Conn, R.W.**[43], Dippel, K.H.**[43] Esser, H.G.**[43], Finken, K.H.**[43], Fuchs, G.**[43], Giesen, B.**[43], Goebel, D.M.**[43], Graffmann, E.**[43], Harting, H.**[43], Hintz, E.**[43], Hoenen, F.**[43], Höthker, K.**[43], Kaleck, A.**[43], Kever, H.**[43], Könen, L.**[43], Korten, M.**[43], Li, L.**[43], Lie, Y.T.**[43], Leung, W.K.**[43], Pontau, A.E.**[43], Pospieszczyk, A.**[43], Reiter, D.**[43], Rogister, A.**[43], Ross, G.**[43], Rusbüldt, D.**[43], Samm, U.**[43], Schweer, B.**[43], Schlüter, J.**[43], Soltwisch, H.**[43], Stodiek, W.**[43], Thomas, G.**[43], Waelbroeck, F.**[43], Waidmann, G.**[43], Wienhold, P.**[43], Winter, J.**[43], Yamauchi, T., Delvigne, T.**[44], Descamps, P.**[44], Durodié, F.**[44], Jadoul, M.**[44], Koch, R.**[44], Lebeau, D.**[44], Messiaen, A.M.**[44], Pearson, D.I.C.**[44], Vandenplas, P.E.**[44], Van Nieuwenhove, R.**[44], Van Oost, G.**[44], Van Wassenhove, G.**[44], Weynants, R.R.**[44]: "Properties, Control and ICRF-Heating of the plasma in TEXTOR", Plasma Phys. and Cont. Fusion, 28 (1986) 1413.

24) Odajima K., Funahashi A., Hoshino K., Kasai S., Kawakami T., Kawashima H., Matoba T., Matsuda T., Matsumoto H., Miura Y., Mori M., Ogawa H., Ogawa T., Ohtsuka H., Sengoku S., Shoji T., Suzuki N., Tamai H., Uesugi Y., Yamamoto T., Yamauchi T., Hasegawa M.**[11], Takada S.*[49], Hasegawa K., Honda A., Ishibori I., Kashimura T., Kashiwa Y., Kazawa M., Kikuchi K., Matsuzaki Y., Ohuchi K., Okano H., Shibata T., Shibuya T., Shiina T., Suzuki K., Tani T., Yokoyama K.: "Confinement Studies of Additionally Heated Plasma in JFT-2M Tokamak", 11th Int. Conf. on Plasma Phys. and Cont. Nucl. Fusion Research IAEA-CN-47/paper A-III-2 (Kyoto, Sept. 1986).

25) Yamamoto T., Funahashi A., Hoshino K., Kasai S., Kawakami T., Kawashima H., Matoba T., Matsuda T., Matsumoto H., Miura Y., Mori M., Odajima K., Ogawa H., Ohtsuka H., Sengoku S., Shoji T., Suzuki N., Tamai H., Uesugi Y., Yamauchi T., Hasegawa M.*11, Takada S.*49, Hasegawa K., Honda A., Ishibori I., Kashimura T., Kashiwa Y., Kazawa M., Kikuchi K., Matsuzaki Y., Ohuchi K., Okano H., Shibata T., Shibuya T., Shiina T., Suzuki K., Tani T., Yokoyama, K.: "Electron Cyclotron Heating of Lower-Hybrid current driven Plasma in the JFT-2M Tokamak", ibid. paper F-II-5.

26) Hoshino K.: "Confinement Improvement and Disruption Control by Profile Optimization using Electron Cyclotron Heating", Rep. of a specialists' Meeting on Tokamak Concept Inovations, Vienna, Jan., 1986 (IAEA Vienna, April 1986) p. 167.

27) Sengoku S.: "Confinement Improvement by Particle Fueling Optimization", ibid. p.170.

28) Sengoku S.: "Graphite Wall and Fueling in JFT-2M", Rep. Workshop on Plasma-Surface Interactions, (Sapporo, Jan. 1986) 1986. p.57 (in Japanese).

29) Okumura Y., Horiike H., Inoue T., Kurashima T.*4, Matsuda S., Ohara Y., Tanaka S.: "A high current volume H^- ion source with multi-aperture extractor", 4th Int. Symp. on the Production and Neutralization of Negative Ions and Beams, Brookhaven National Lab., Oct. 27-31, (1986).

30) Ohara Y., Inami H.*19, Horiike H., Okumura Y., Tanaka S.: "3D Simulation of the Primary Electron Orbits in a Magnetic Multipole Plasma Source", 10th Symp. on Ion Source and Ion-Assisted Technology, Kyoto, June, (1986).

31) Tsuji H., Yoshida K., Ando T., Takahashi Y., Nishi N., Tada E., Oshikiri K., Koizumi K., Nakajima H., Kato T., Ohgane Y.*36, Yaguchi E.*36 Shimamoto S.: "Design selections for the fabrication of the demonstration poloidal coil", 7th Topical Meeting on the Technology of Fusion Energy, (Reno, June 1986).

32) Nishi M., Ando T., Takahashi Y., Hiyama T., Kawano K., Oshikiri M., Shimamoto S.: "A 16-T superconducting toroidal coil development for a tokamak fusion machine", ibid.

33) Kato T., Kamiya S.*18, Tada E., Hiyama T., Kawano K., Shimamoto S.: "Cryogenic system component development for fusion experimental reactor at JAERI", ibid.

34) Shimamoto S.: "The present role of superconductivity in fusion", Proc. of the 11th International Cryogenic Engineering Conference, (Berlin-west, April 1986) 127.

35) Tada E., Takahashi Y., Kato T., Hiyama T., Oshikiri M., Kawano K., Shimamoto S., Ishihara A.*6, Ito I.*6, Uede T.*6, Ogushi K.*6: "Development of 30-kA vapor-cooled current leads for fusion devices", ibid. 528.

36) Ando T., Nishi M., Takahashi Y., Yoshida K., Shimamoto S.: "Investigation of stability in cable-in-conduit conductors with heat pulse durations of 0.1 to 1 ms", ibid. 756.

37) Shimamoto S., Ando T., Hiyama T., Tsuji H., Takahashi Y., Nishi M., Tada E., Yoshida K., Koizumi K., Okuno K., Nakajima H., Kato T., Kawano K., Hoshino M.*51, Oshikiri M.: "Evolutions in the development of superconducting materials and magnet technology for the coming fusion machines in Japan", 11 International Conference on Plasma Physics and Controlled Nuclear Fusion Research, (Kyoto, November 1986).

38) Nishi M., Takahashi Y., Ando T., Shimamoto S.: "A 12-T forced flow type superconducting magnet", 1986 Applied Superconducting Conference, (Baltimore, June 1986).

39) Tada E., Shimamoto S., Ando T., Hiyama T., Tsuji H., Takahashi Y., Nishi M., Yoshida K., Okuno K., Koizumi K., Kato T., Nakajima H., Kawano K., Oshikiri M., Hoshino M.*51, Ohgane Y.*36, Yaguchi E.*36, Pheran P.: "System design of the demonstration poloidal coils and the test facility", ibid.

40) Shimamoto S.: "The Japanese LCT coil", ibid.

41) Okuno K., Kato T., Tsuji H., Hiyama T., Shimamoto S., Hattori Y.*11, Kamiya K.*18, Iida F.*4: "Testing of the pool-boil cooled Japanese LCT coil in the international superconducting magnet test facility", ibid.

42) Naruse Y., "Studies on Tritium Processing Technology in JAERI", Proc. Int. Symp. on Fusion Reactor Blanket and Fuel Cycle Technology, Tokai, (1986) p.10.

43) Kudo H., Okuno K., "Tritium Release from Li_2O: The Valence State, Diffusivity and Solubility of Tritium in the Solid", ibid., p.56.

44) Okuno K., Kudo H., "Kinetics of Tritium Release from Neutron-irradiated Breeding Materials for Fusion Reactors", ibid., p.66.

45) Konishi S., Yoshida H., Nagasaki T., Ohno H., Naruse Y., "Improvements of Some Tritium Processing Components", ibid., p.109

46) Yamanishi T., Kinoshita M., Yoshida H., Takeshita H., "A Simulation Study of Hydrogen Isotope Distillation Columns in the Tritium Breeding Blanket System of a Fusion Reactor - Startup Analysis -", ibid., p.121.

47) Yoshida H., Kinoshita M., Takeshita H., Yamanishi T., "Study on Tritium Recovery System for Lithium Oxide Breeder Blanekt", ibid., p.158.

48) Yoshida H. "The Japanese Fusion Safety Program", IAEA Technical Meeting on Fusion Reactor Safety (Culhum, UK, November 1986).

49) Yoshida H., Naruse Y., Matsuda Y., "Tritium Processing Laboratory for the Fusion Research Program at JAERI", ibid.

50) Yoshikawa M., JT-60 Team*: "Recent experiments in JT-60", Plasma physics and controlled nuclear fusion research, IAEA, Vienna, 1986 IAEA-CN-47/A-I-1.

* Abe T., Aikawa H., Akaoka N., Akasaka H., Akiba M., Akino N., Akiyama T., Ando T., Annoh K., Aoyagi T., Arakawa K., Araki M., Arimoto K., Azumi M., Chiba S., Dairaku M., Ebisawa N., Fujii T., Fukuda T., Furukawa H., Hamamatsu K., Hayashi K., Hara M., Haraguchi K., Hiratsuka H., Hirayama T., Hiroki S., Hiruta K., Honda M., Horiike H., Hosoda R., Nosogane N., Iida Y., Iijima T., Ikeda K., Ikeda Y., Imai T., Inoue T., Isaji N., Isaka M., Ishida S., Itige N., Ito T., Ito Y., Kaminaga A., Kawai M., Kawamata Y., Kawasaki K., Kikuchi K., Kikuchi M., Kimura H., Kimura T., Kishimoto H., Kitahara K., Kitamura S., Kitsunezaki A., Kiyono K., Kobayashi N., Kodama K., Koide Y. Koike T., Komata M., Kondo I., Konoshima S., Kubo M., Kunieda S., Kurakata S., Kurihara K., Kuriyama M., Kuroda T., Kusaka M., Kusama Y., Maehara S., Maeno M., Matsuda S., Mase S., Matsukawa M., Matsukawa T., Matsuoka M., Miya N., Miyati K., Miyo Y., Mizuhashi K., Mizuno M., Murai R., Murakami Y., Muto M., Nagami

M., Nagashima A., Nagashima K., Nagashima T., Nagaya S., Nakamura H., Nakamura Y., Nemoto M., Neyatani Y., Niikura S., Ninomiya H., Nishitani T., Nomata H., Obara K., Ogiwara N., Ohga T., Ohara Y., Ohasa K., Ohhara H., Ohshima T., Ohkubo M., Ohta K., Ohta M. Ohtaka M., Ohuchi Y., Oikawa A., Okumura H., Okumura Y., Omori K., Omori S., Omori Y., Ozeki T., Sakasai A., Sakata S., Satou M., Saigusa M., Sakamoto K., Sawahata M., Seimiya M., Seki M., Seki S., Shibanuma K., Shimada R., Shimizu K., Shimizu M., Shimomura Y., Shinozaki S., Shirai H., Shirakata H., Shitomi M., Suganuma K., Sugie T., Sugiyama T., Sunaoshi H., Suzuki K., Suzuki M., Suzuki M., Suzuki N., Suzuki S., Suzuki Y., Takahashi M., Takahashi S., Takahashi T., Takahashi H.*, Takasaki M., Takatsu M., Takeuchi H., Takeshita A., Tamura S., Tanaka S., Tanaka T., Tani K., Terakado M., Terakado T., Tobita K., Tokutake T., Totsuka T., Toyoshima N., Tsuda H., Tsugita T., Tsuji S., Tsukahara Y., Tsuneoka M., Uehara K., Umehara M., Uramoto Y., Usami H., Ushigusa K., Usui K., Yagyu J., Yamada K., Yamamoto M., Yamashita O., Yamashita Y., Yano K., Yasukawa T., Yokokura K., Yokomizo H., Yoshikawa M., Yoshida H., Yoshinari Y., Yoshino R., Yonekawa I., Watanabe K. (* Plasma Physics Laboratory, Princeton University, USA)

51) Nagami M., JT-60 Team*: "Energy and particle confinement of JT-60 plasmas with high power heating", ibid., IAEA-CN-47/A-II-2.
* Abe T., Aikawa H., Akaoka N., Akasaka H., Akiba M., Akino N., Akiyama T., Ando T., Annoh K., Aoyagi T., Arakawa K., Araki M., Arimoto K., Azumi M., Chiba S., Dairaku M., Ebisawa N., Fujii T., Fukuda T., Furukawa H., Hamamatsu K., Hayashi K., Hara M., Haraguchi K., Hiratsuka H., Hirayama T., Hiroki S., Hiruta K., Honda M., Horiike H., Hosoda R., Nosogane N., Iida Y., Iijima T., Ikeda K., Ikeda Y., Imai T., Inoue T., Isaji N., Isaka M., Ishida S., Itige N., Ito T., Ito Y., Kaminaga A., Kawai M., Kawamata Y., Kawasaki K., Kikuchi K., Kikuchi M., Kimura H., Kimura T., Kishimoto H., Kitahara K., Kitamura S., Kitsunezaki A., Kiyono K., Kobayashi N., Kodama K., Koide Y. Koike T., Komata M., Kondo I., Konoshima S., Kubo M., Kunieda S., Kurakata S., Kurihara K., Kuriyama M., Kuroda T., Kusaka M., Kusama Y., Maehara S., Maeno M., Matsuda S., Mase S., Matsukawa

M., Matsukawa T., Matsuoka M., Miya N., Miyati K., Miyo Y., Mizuhashi K., Mizuno M., Murai R., Murakami Y., Muto M., Nagami M., Nagashima A., Nagashima K., Nagashima T., Nagaya S., Nakamura H., Nakamura Y., Nemoto M., Neyatani Y., Niikura S., Ninomiya H., Nishitani T., Nomata H., Obara K., Ogiwara N., Ohga T., Ohara Y., Ohasa K., Ohhara H., Ohshima T., Ohkubo M., Ohta K., Ohta M. Ohtaka M., Ohuchi Y., Oikawa A., Okumura H., Okumura Y., Omori K., Omori S., Omori Y., Ozeki T., Sakasai A., Sakata S., Satou M., Saigusa M., Sakamoto K., Sawahata M., Seimiya M., Seki M., Seki S., Shibanuma K., Shimada R., Shimizu K., Shimizu M., Shimomura Y., Shinozaki S., Shirai H., Shirakata H., Shitomi M., Suganuma K., Sugie T., Sugiyama T., Sunaoshi H., Suzuki K., Suzuki M., Suzuki M., Suzuki N., Suzuki S., Suzuki Y., Takahashi M., Takahashi S., Takahashi T., Takahashi H.*, Takasaki M., Takatsu M., Takeuchi H., Takeshita A., Tamura S., Tanaka S., Tanaka T., Tani K., Terakado M., Terakado T., Tobita K., Tokutake T., Totsuka T., Toyoshima N., Tsuda H., Tsugita T., Tsuji S., Tsukahara Y., Tsuneoka M., Uehara K., Umehara M., Uramoto Y., Usami H., Ushigusa K., Usui K., Yagyu J., Yamada K., Yamamoto M., Yamashita O., Yamashita Y., Yano K., Yasukawa T., Yokokura K., Yokomizo H., Yoshikawa M., Yoshida H., Yoshinari Y., Yoshino R., Yonekawa I., Watanabe K. (* Plasma Physics Laboratory, Princeton University, USA)

52) Takeuchi H., JT-60 Team*: "Impurity and MHD behavior in JT-60 divertor discharges", ibid., IAEA-CN-47/A-IV-3.

* Abe T., Aikawa H., Akaoka N., Akasaka H., Akiba M., Akino N., Akiyama T., Ando T., Annoh K., Aoyagi T., Arakawa K., Araki M., Arimoto K., Azumi M., Chiba S., Dairaku M., Ebisawa N., Fujii T., Fukuda T., Furukawa H., Hamamatsu K., Hayashi K., Hara M., Haraguchi K., Hiratsuka H., Hirayama T., Hiroki S., Hiruta K., Honda M., Horiike H., Hosoda R., Nosogane N., Iida Y., Iijima T., Ikeda K., Ikeda Y., Imai T., Inoue T., Isaji N., Isaka M., Ishida S., Itige N., Ito T., Ito Y., Kaminaga A., Kawai M., Kawamata Y., Kawasaki K., Kikuchi K., Kikuchi M., Kimura H., Kimura T., Kishimoto H., Kitahara K., Kitamura S., Kitsunezaki A., Kiyono K., Kobayashi N., Kodama K., Koide Y. Koike T., Komata M., Kondo I., Konoshima S., Kubo M., Kunieda S.,

Kurakata S., Kurihara K., Kuriyama M., Kuroda T., Kusaka M., Kusama Y., Maehara S., Maeno M., Matsuda S., Mase S., Matsukawa M., Matsukawa T., Matsuoka M., Miya N., Miyati K., Miyo Y., Mizuhashi K., Mizuno M., Murai R., Murakami Y., Muto M., Nagami M., Nagashima A., Nagashima K., Nagashima T., Nagaya S., Nakamura H., Nakamura Y., Nemoto M., Neyatani Y., Niikura S., Ninomiya H., Nishitani T., Nomata H., Obara K., Ogiwara N., Ohga T., Ohara Y., Ohasa K., Ohhara H., Ohshima T., Ohkubo M., Ohta K., Ohta M. Ohtaka M., Ohuchi Y., Oikawa A., Okumura H., Okumura Y., Omori K., Omori S., Omori Y., Ozeki T., Sakasai A., Sakata S., Satou M., Saigusa M., Sakamoto K., Sawahata M., Seimiya M., Seki M., Seki S., Shibanuma K., Shimada R., Shimizu K., Shimizu M., Shimomura Y., Shinozaki S., Shirai H., Shirakata H., Shitomi M., Suganuma K., Sugie T., Sugiyama T., Sunaoshi H., Suzuki K., Suzuki M., Suzuki M., Suzuki N., Suzuki S., Suzuki Y., Takahashi M., Takahashi S., Takahashi T., Takahashi H.*, Takasaki M., Takatsu M., Takeuchi H., Takeshita A., Tamura S., Tanaka S., Tanaka T., Tani K., Terakado M., Terakado T., Tobita K., Tokutake T., Totsuka T., Toyoshima N., Tsuda H., Tsugita T., Tsuji S., Tsukahara Y., Tsuneoka M., Uehara K., Umehara M., Uramoto Y., Usami H., Ushigusa K., Usui K., Yagyu J., Yamada K., Yamamoto M., Yamashita O., Yamashita Y., Yano K., Yasukawa T., Yokokura K., Yokomizo H., Yoshikawa M., Yoshida H., Yoshinari Y., Yoshino R., Yonekawa I., Watanabe K. (* Plasma Physics Laboratory, Princeton University, USA)

53) Imai T., JT-60 Team*: "Improvement of current drive and confinement by combination of LHCD and NBI heating in JT-60", ibid., IAEA-CN-47/K-I-2.

* Abe T., Aikawa H., Akaoka N., Akasaka H., Akiba M., Akino N., Akiyama T., Ando T., Annoh K., Aoyagi T., Arakawa K., Araki M., Arimoto K., Azumi M., Chiba S., Dairaku M., Ebisawa N., Fujii T., Fukuda T., Furukawa H., Hamamatsu K., Hayashi K., Hara M., Haraguchi K., Hiratsuka H., Hirayama T., Hiroki S., Hiruta K., Honda M., Horiike H., Hosoda R., Nosogane N., Iida Y., Iijima T., Ikeda K., Ikeda Y., Imai T., Inoue T., Isaji N., Isaka M., Ishida S., Itige N., Ito T., Ito Y., Kaminaga A., Kawai M., Kawamata Y., Kawasaki K., Kikuchi K., Kikuchi M., Kimura H.,

Kimura T., Kishimoto H., Kitahara K., Kitamura S., Kitsunezaki A., Kiyono K., Kobayashi N., Kodama K., Koide Y. Koike T., Komata M., Kondo I., Konoshima S., Kubo M., Kunieda S., Kurakata S., Kurihara K., Kuriyama M., Kuroda T., Kusaka M., Kusama Y., Maehara S., Maeno M., Matsuda S., Mase S., Matsukawa M., Matsukawa T., Matsuoka M., Miya N., Miyati K., Miyo Y., Mizuhashi K., Mizuno M., Murai R., Murakami Y., Muto M., Nagami M., Nagashima A., Nagashima K., Nagashima T., Nagaya S., Nakamura H., Nakamura Y., Nemoto M., Neyatani Y., Niikura S., Ninomiya H., Nishitani T., Nomata H., Obara K., Ogiwara N., Ohga T., Ohara Y., Ohasa K., Ohhara H., Ohshima T., Ohkubo M., Ohta K., Ohta M. Ohtaka M., Ohuchi Y., Oikawa A., Okumura H., Okumura Y., Omori K., Omori S., Omori Y., Ozeki T., Sakasai A., Sakata S., Satou M., Saigusa M., Sakamoto K., Sawahata M., Seimiya M., Seki M., Seki S., Shibanuma K., Shimada R., Shimizu K., Shimizu M., Shimomura Y., Shinozaki S., Shirai H., Shirakata H., Shitomi M., Suganuma K., Sugie T., Sugiyama T., Sunaoshi H., Suzuki K., Suzuki M., Suzuki M., Suzuki N., Suzuki S., Suzuki Y., Takahashi M., Takahashi S., Takahashi T., Takahashi H.*, Takasaki M., Takatsu M., Takeuchi H., Takeshita A., Tamura S., Tanaka S., Tanaka T., Tani K., Terakado M., Terakado T., Tobita K., Tokutake T., Totsuka T., Toyoshima N., Tsuda H., Tsugita T., Tsuji S., Tsukahara Y., Tsuneoka M., Uehara K., Umehara M., Uramoto Y., Usami H., Ushigusa K., Usui K., Yagyu J., Yamada K., Yamamoto M., Yamashita O., Yamashita Y., Yano K., Yasukawa T., Yokokura K., Yokomizo H., Yoshikawa M., Yoshida H., Yoshinari Y., Yoshino R., Yonekawa I., Watanabe K. (* Plasma Physics Laboratory, Princeton University, USA)

54) Gill R.D., Bartlett D.V., Bracco G., Campbell D.J., Corti S., Tsuji S., et al.: "Sawtooth Activity during Additional Heating in JET", 13th European Conference on Controlled Fusion and Plasma Heating (Schliersee, April 1986).

55) Onozuka M.*, Uchikawa T.*, Nakamura H., Niikura S., et al.: "Surface Analyses of TiC Coated Molybdenum Limiter Material Exposed to High Flux Electron Beam", 14th Symp. on Fusion Technology (Avignon Sept. 1986).

56) Yamazaki K., Naitou H., Arai T., Hamada Y., Matsuoka K., Midzuno Y., Nakayama Y., Sato T., Tsunematsu T., Tuda T., Seki S., Azumi M., Tokuda S., Ozeki T., Nemoto T., Kishimoto Y., Takeda T.: "Second Stability Access in Tokamak Plasmas", 11th Int. Conf. on Plasma Physics and Controlled Nuclear Fusion Research (Kyoto, Nov. 1986) E-I-2-1.

57) Fukuyama A., Morishita T.*, Kishimoto Y., Hamamatsu K., Itoh K., Itoh S.: "Analysis of ICRF Heating and Current Drive in Tokamaks", ibid. F-N-1.

58) Kimura T., Kurihara K. and Matsukawa M.: "Application of the Fast Array Processor for JT-60 Plasma Control", Proceedings of the 14th Symposium on Fusion Technology, Avignon, September (1986) 1439.

59) Tachikawa K., Kobayashi T., Iida H., Sawada Y., Adachi J.*[18], Sato K.*[4], Uchida T.*[2], Yamada M.*[3]: "Maintenance of Torus Components for the Fusion Experimental Reactor (FER)", ANS International Topcial Meeting on Remote Systems and Robotics in Hostile Environments (Pasco, USA, March 1987).

60) Tone T., FER Design Team: "Fusion Experimental Reactor (FER) Design Concept", IAEA-TCM and Workshop on Fusion Reactor Design and Technology, Yalta, USSR (1986).

61) Tone T., Kuroda T.*[18], Tanaka Y.*[18]: "Design Study of Power Reactor Blanket Concepts", IAEA-TCM and Workshop on Fusion Reactor Design and Technology, Yalta, USSR (1986).

62) Seki Y., Iida H., Honda T.*[2], Aizawa K.**[12]: "Safety Scenario for Fusion Experimental Reactor (FER)", IAEA-TCM on Fusion Reactor Saety, Culham (1986).

A.1.4 List of other reports

1) Kishimoto Y., Hamamatsu K., Fukuyama A.**[3], Itoh S-I.**[1], Itoh K.**[9], "ICRF current-drive by use of phase-control of antennas", Institute for Fusion Theory (Hiroshima University) Report, HIFT-120 (April 1986).

2) Hamamatsu K., Kishimoto Y., Fukuyama A.**[3], Itoh K.**[9], Itoh S-I.**[1], Azumi M., "Optimum toroidal phasing for stable loading of

ICRF wave in JT-60", Institute for Fusion Theory (Hiroshima University) Report, HIFT-128 (November 1986).

3) Sengoku S.: "Particle Control in a Tokamak", IPPJ-AM-44 (June, 1986) pp.1-13.

4) Yamada R.: "Formation of C_2 and C_3 Hydrocarbons from Graphite due to Chemical Sputtering", Research Report of IPP, Nagoya University, IPPJ-DT-132 (1986).

5) Hill K.W.**[19], Bitter M.**[19], Von Goeler S.**[19], Hiroe S.**[14], Hulse R.**[19], Ramsey A.T.**[19], Sesnic S.**[19], Shimada M., Stratton B.C.**[19]: "Effective Kα X-ray Excitation Rates for Plasma Impurity Measurements", PPPL-2348 (1986).

6) Yamaguchi S.*[11], Kondoh Y.**[43]: "Current Drive for the Toroidal System", GA-A18516 (1986).

7) Tsunematsu T., Seki S., Tokuda S., Azumi M.: "Beta Enhancement of Tokamak Plasma with Small Elongation", Report of A. Specialist's Meeting on Tokamak Concept Inovations (PP137-40) IAEA Vienna.

8) Singer C.**[19], Ku L.**[19], Bateman G.**[19], Seidl F.**[19], Sugihara M.: "Physics of Compact Ignition Tokamak Designs", PPPL-2317 (1986).

9) INTOR Group: "INTOR Report, Phase Two A Part II", IAEA ST1/PUB/714 (1986).

10) Fujisawa N., FER Plasma Group: "Operation Scenario of Fusion Experimental Reactor with Main Emphasis on Startup", Tokamak Startup (1986) (Plenum Press).

11) "Tokamak Concept Innovations", IAEA-TECDC-373 (1986).

A.2 Personnel of the Establishment

A.2.1 Number of the Staff of the Departments

	FY1984	FY1985	FY1986
Regular staff	275	298	311*1
Staff on loan	34	58	48*2
Guest scientist	2	2	2*3

*1 Including scientists, technicians and secretaries

*2 From industry

*3 From University of Tokyo and Kogakuin University

A.2.2 List of Scientific staff and officers during FY 1986

Naka Fusion Research Establishment

TOMABECHI Ken (Director General)
MIYAMOTO Goro (Scientific Adviser)
YAMAMURA Sakae (Scientific Adviser)
INOUE Kenji (General Manager)

(A) Department of Termonuclear Fusion Research

TANAKA Masatoshi (Director)
KANAI Akihiko (Administrative Manager)

Plasma Theory Laboratory

TAKEDA Tatsuoki (Principal Scientist, Head)
KISHIMOTO Yasuaki
KURITA Gen-Ichi
NEMOTO Toshiyuki*1 (to March 31, 1987)
TAKIZUKA Tomonori (Senior scientist)
TOKUDA Shinji
TSUNEMATSU Toshihide (Senior Scientist)
TUDA Takashi (Senior Scientist)
YAMAGIWA Mitsuru (from April 16, 1986)

Experimental Plasma Physics Laboratory

FUNAHASHI Akimasa (Principal Scientist, Head)
HASEGAWA Mitsuru*11
HOSHINO Katsumichi
KASAI Satoshi (Senior Scientist)
KAWAKAMI Tomohide
KAWASHIMA Hisato
MAEDA Hikosuke (Principal Scientist)
MATOBA Tohru (Principal Scientist)
MATSUDA Toshiaki
MATSUMOTO Hiroshi
MIURA Yukitoshi
MORI Masahiro
ODAJIMA Kazuo (Senior Scientist)
OGAWA Hiroaki
OGAWA Toshihide
SENGOKU Seio (Senior Scientist)
SHOJI Teruaki
SUZUKI Norio (Senior Scientist)
TAMAI Hiroshi
UESUGI Yoshihiko
YAMAMOTO Takumi (Senior Scientist)
YAMAUCHI Toshihiko (Senior Scientist)

Facility Operation and Engineering Division

SUZUKI Kihaciro (General Manager)
HASEGAWA Koichi
HONDA Atushi
ISHIBORI Ikuo
KASHIWA Yoshitoshi
KAZAWA Minoru
KIKUCHI Kazuo
MATSUZAKI Yoshimi
OKANO Fuminori
OHUCHI Katsujyu
SATOH Eiji

SHIBATA Takatoshi
SHIBUYA Toshihiro
TANI Takashi
YOKOYAMA Kenji

Plasma Heating Laboratory I

MATSUDA Shinzaburo (Principal Engineer, Head)
ARAKI Masanori
DAIRAKU Masayuki
HORIIKE Hiroshi
KOMATA Masao
KURASHIMA Tohru*4
MIZUHASHI Kiyoshi
OHARA Yoshihiro (Senior Scientist)
OHTAKA Mitsuo*9
OKUMURA Yoshikazu
TANAKA Shigeru
WATANABE Kazuhiro

Plasma Heating Laboratory II

NAGASHIMA Takashi (Principal Scientist, Head)
SHIHO Makoto (Senior Scientist)
IMAI Tsuyoshi
SAKAMOTO Keishi
SAIGUSA Mikio
KOBAYASHI Noriyuki*2
OSAWA Satoru*16
OTOMO Junich*9
GOTO Masaharu*11

Plasma Engineering Laboratory

MURAKAMI Yoshio (Principal Scientist, Head)
ABE Tetsuya (Senior Scientist)
HIROKI Seiji
KATO Toshinao*19

NAKAMURA Kazuyuki
OBARA Kenjiro
OHTSUKA Hidewo (Senior Scientist)
SAIDOH Masahiro (Principal Scientist)
TAKEDA Ryuji
YAMADA Reiji (Senior Scientist)

Superconducting Magnet Laboratory

SHIMAMOTO Susumu (Principal Engineer, Head)
ANDO Toshinari
IIDA Fumio*4
HIYAMA Tadao
HOSHINO Masahiro*51
KATO Takashi
KAMIYA Shoji*18
KAWANO Katsumi
KOIZUMI Koichi
MUKAI Hiroshi*2
NAKAJIMA Hideo
NISHI Masataka
OHGANE Yasuo*36
OKUNO Kiyoshi
OSHIKIRI Masayuki
PHELAN E. Patrick**43
TADA Eisaku
TAKAHASHI Yoshikazu
TSUJI Hiroshi
YOSHIDA Kiyoshi

Tritium Engineering Laboratory

NARUSE Yuji (Principal Engineer, Head)
FUKUI Hiroshi*8
HONMA Takashi
KINOSHITA Masahiro (- December 31)
KONISHI Satoshi
MATSUDA Yuji (Deputy General Manager)

MISUMI Masahiro[*18]
NAITO Taisei[*3]
OKUNO Kenji (Senior Scientist)
O'HIRA Shigeru
SUZUKI Takumi
YAMADA Masayuki
YAMANISHI Toshihiko
YOKOGAWA Nobuhisa[*10]
YOSHIDA Hiroshi (Senior Scientist)

(B) DEPARTMENT OF LARGE TOKAMAK RESEARCH

YOSHIKAWA Masaji (Director)
TAMURA Sanae (Deputy Director)
SAITO Ryusei
KITSUNEZAKI Akio
KIKUCHI Toshiaki (Administrative Manager)

Large Tokamak Program Division

KISHIMOTO Hiroshi (General Manager)
KITSUNEZAKI Akio (Deputy General Manager)

* Planning and Coordinating Group

OIKAWA Akira
MIYA Naoyuki

* Doublet-III Experiment Group

KONOSHIMA Shigeru (Senior Scientist)
SHIMADA Michiya
SHOJI Teruaki
HOSOGANE Nobuyuki
YAMAGUCHI Satoru[*11]
HANAI Satoshi[*2]
FUKUMOTO Hideshi[*4]

OZAKI Akira*2
YAMAMOTO Masahiro
KAWASAKI Kozo
NAKAMURA Hiroo
KINOSHITA Shigemi*4
UESUGI Yoshihiko

Large Tokamak Experimental Division

SHIMOMURA Yasuo (General Manager)

* Experimental Group

BELL Michel (Visitor from TFTR)
HAYASHI Kazuo*2
HOSOGANE Nobuyuki
KIKUCHI Mitsuru
NAGAMI Masayuki (Senior Scientist)
NAKAMURA Hiroo
NIIKURA Setsuo*3
NINOMIYA Hiromasa (Senior Scientist)
TAKAHASHI Hironori (Visitor from PPPL)
THOMAS Paul (Visitor from JET)
TSUJI Shunji
USHIGUSA Kenkichi
YAMADA Kimio*4
YOSHINO Ryuji

* Analysis Group

AZUMI Masafumi (Principal Scientist)
HAMAMATSU Kiyotaka
HIRAYAMA Toshio (Senior Scientist)
OZEKI Takahisa
SEKI Shogo (Senior Scientist)
SHIRAI Hiroshi
SHIMIZU Katsuhiro
SUZUKI Masanobu*50

TANI Keiji (Senior Scientist)

Diagnostics Development Division

SUZUKI Yasuo (General Manager)
NAKAMURA Yukiharu

* Diagnostics Group I

TAKEUCHI Hiroshi (Senior Scientist)
URAMOTO Yasuyuki
SUGIE Tatsuo
TSUKAHARA Yoshimitsu
NISHITANI Takeo
AKAOKA Nobuo
SUGIYAMA Takashi
SAKASAI Akira
KUSAMA Yoshinori
KOIDE Yoshihiko
KUBO Hirotaka
HARA Makoto
TOBITA Kenji
NEMOTO Masahiro
NAGASHIMA Keisuke
NISHINO Nobuhiro*4

* Diagnostics Group II

YOKOMIZO Hideaki (Senior Scientist)
TAKAHASHI Toranosuke
YOSHIDA Hidetoshi
OGIWARA Norio
SATO Masayasu
NEYATANI Yuzuru
FUKUDA Takeshi
ISHIDA Shinichi
MURAI Ryuichi
YAMASHITA Yukihiko

HARAGUCHI Kazumi
YOSHINARI Youji

* Data Processing Group

NAGASHIMA Akira (Senior Scientist)
TSUGITA Tomonori
IIDA Sachio
NOMATA Hideyuki
OHSHIMA Takayuki
AOYAGI Testuo
YAMAGISHI Koujiro

* Operation and Engineering Group

KONOSHIMA Shigeru (Senior Scientist)
YAMASHITA Osamu
ITOH Takao
SHITOMI Morimasa
KITAHARA Katsumi
CHIBA Shinichi

Heating System Development Division

SHIRAKATA Hirofumi (General Manager)

* NBI Group

AKIBA Makoto
AKINO Noboru
ARIMOTO Kimiko*2
INOUE Takashi
EBISAWA Noboru
KAWAI Mikito
KIKUCHI Kastumi*9
KITAMURA Shigeru
KURIYAMA Masaaki (Senior Scientist)
MATSUOKA Mamoru

MIZUNO Makoto
OHGA Tokumichi
OHUCHI Yutaka
OOHARA Hiroshi
SHIBANUMA Kiyoshi
TSUDA Fumio*4
UMEHARA Masatoshi*9
USAMI Hirotsugu*4
USUI Katsutomi
YOSHIKAWA Kazunobu*9

* RF Group

HONDA Masao
IKEDA Yoshitaka
KIMURA Haruyuki
KIYONO Kimihiko
SEKI Masami
SUGANUMA Kazuaki
SUZUKI Norio
UEHARA Kazuya (Senior Scientist)
YOKOKURA Kenji
ANNO Katsuto
TSUNEOKA Masaki
FUJII Tuneyuki
SAWAHATA Masayuki
MAEHARA Sunao
TERAKADO Masayuki
KATO Tsugio*16
YONEDA Tsuyoshi*16

Fusion Reactor System Laboratory

TAMURA Sanae (General Manager)
ADACHI Junichi*8
FUJISAWA Noboru (Principal Scientist)
HITOKI Shigehisa*11
HORIE Tomoyoshi

IIDA Hiromasa (Senior Scientist)
KOBAYASHI Takeshi
KURODA Hideo*35
MIKI Nobuharu
MIZOGUCHI Tadanori*4
MORI Seiji*18
NAKAHARA Katsuhiko*2
NAKAJIMA Kunihiko
NISHIO Satoshi
OMORI Junji*2
SEKI Yasushi (Principal Scientist)
SUGIHARA Masayoshi (Senior Scientist)
TONE Tatsuzo (Principal Scientist)
TACHIKAWA Katsuzo (Principal Scientist)
YAMADA Masao
YAMAMOTO Shin (Senior Scientist)

(C) Department of JT-60 Facility

IIJIMA Tsutomu (Director)

JT-60 Administration Division

KIKUCHI Toshiaki (General Manager)

JT-60 Facility Division I

KONDO Ikuro (General Manager)

* Operation Planning Group

AIKAWA Hiroshi (Senior Scientist)
SEIMIYA Munetaka
ARAKAWA Kiyotsugu
MASE Shuji*52

* Power Supply Group

AKIYAMA Takashi[*7]
AOYAGI Testuo
ICHIGE Hisashi
IKEDA Yukiharu
MATSUKAWA Tatsuya
MIYACHI Kengo
NAGAYA Susumu
OMORI Kenichirou
OMORI Yoshikazu
OMORI Syunzou
SHIMADA Ryuichi (Senior Scientist)
TAKAHASHI Shunji
TAKESHITA Akira[*11]
TERAKADO Tsunehisa
YAGYUU Junichi

* Control Group

AKASAKA Hiromi
ISAJI Nobuaki[*39]
ITOH Yasuhiro[*39]
KAWAMATA Yoichi
KIMURA Toyoaki (Senior Scientist)
KURIHARA Kenichi
MATSUKAWA Makoto
MUTOH Mitsugu
SAKATA Shinya
TAKAHASHI Minoru
TOTSUKA Toshiyuki
YONEKAWA Izuru

JT-60 Facility Division II

OHTA Mitsuru (General Manager)
TANAKA Takejiro (Deputy General Manager)

* Torus Operation Group

ARAI Takashi
HIRATSUKA Hajime
KAMINAGA Atsushi
KAWASAKI Kozo
KODAMA Kozo
KOIKE Tsuneyuki
KURODA Takeshi
MIYO Yasuhiko
OKUMURA Hiroshi
OHTA Kazuya
SHIMIZU Masatsugu (Senior Scientist)
SUNAOSHI Hidenori
SUZUKI Michio
SUZUKI Sadaaki
TAKASAKI Manabu
TOKUTAKE Toshikuni
YAMAMOTO Masahiro
YASUKAWA Toru

* Torus Development Group

ANDO Toshiro
OHKUBO Minoru (Senior Scientist)
TAKATSU Hideyuki

* Vacuum Technology Group

MAENO Masaki (Senior Scientist)

JT-60 Facility Division III

KUNIEDA Shunsuke (General Manager)
HIRUTA Kazuharu (Deputy General Manager)

* Electrical Facility Group

FURUKAWA Hiroshi[*9]
KUSAKA Makoto[*7]
SHINOZAKI Shinich
TOYOSHIMA Noboru
YAMAGUCHI Takeshi[*4]

* Mechanical Facility Group

HOSODA Ryujiro
ISAKA Masayoshi
YANO Katsuhisa[*7]

**1 Hiroshima University
**2 Nagoya University
**3 Okayama University
**4 Tohoku University
**5 The University of Tokyo
**6 Nihon University
**7 Osaka University
**8 Tokyo Institute of Technology
**9 Kyoto University
**10 National Research Institute for Metals
**11 National Laboratory for High Energy Physics
**12 Power Reactor and Nuclear Fuel Development
**13 Confédération Suisse, Ecole Polytechnique Fédérale de Lausanne
**14 Oak Ridge National Laboratory
**15 Culham Laboratory
**16 FB-National Magnetic Laboratory
**17 Argonne National Laboratory
**18 University of Wisconsion
**19 Princeton Plasma Physics Laboratory
**20 Max-Planck Institute für Plasmaphysik
**21 Centre d'Etude Nucléaires, Fontenay-aux-Rose
**22 Bell Laboratories
**23 JET Joint Undertaking
**24 Institut für Angewandte Physik II, Universitäte Heidelberg
**25 Academia Sinica, Peking, The Peoples Republic of China
**26 The Institute of Fundamental Technological Research, Warsaw/Poland
**27 Institut für Plasmaphysik (Garching)
**28 Lawrence Berkely Laboratory, Univ. of California
**29 Tsukuba University
**30 Toho University
**31 Los Alamos National Laboratory
**32 KFA-IPP, Jülich
**33 University of Maryland
**34 Institute of Isotopes of the Hungarian Academy of Science
**35 Institut Curie, Université de Paris
**36 Idaho National Engineering Laboratory
**37 Hebrew University of Jernsalem

**38 University of California, Los Angeles
**39 Nuclear Research Center Karlsruhe
**40 Kyushu University
**41 Yokohama National University
**42 Imperial College of Science and Technology (U.K.)
**43 Massachusetts Institute of Technology

*1 Fujitsu Ltd.
*2 Toshiba Corp.
*3 Mitsubishi Atomic Power Industry Inc.
*4 Hitachi Ltd.
*5 GA Technologies Inc.
*6 Fuji Electric Co., Ltd.
*7 Kaihatsu Denki Co., Ltd.
*8 Mitsubishi Heavy Ind., Ltd.
*9 Nuclear Engineering Co., Ltd.
*10 Sumitomo Heavy Ind., Ltd.
*11 Mitsubishi Electric Co., Ltd.
*12 Japan Steel Works Ltd.
*13 Nippon Atomic Industry Group
*14 Kobe Steel Ltd.
*15 Saginomiya Johnson Controls Co., Ltd.
*16 Nippon Electric Co., Ltd.
*17 Hitachi Cable Co.
*18 Kawasaki Heavy Ind., Ltd.
*19 Nissin Electric Co., Ltd.
*20 Touyo Information System Co., Ltd.
*21 ULVAC Co.
*22 Nippon Kogaku Co., Ltd.
*23 Osaka Vacuum Ltd.
*24 Nissei Sangyo Co., Ltd.
*25 Century Research Center Co.
*26 Yokokawa Electric Works Ltd.
*27 Irie Koken Co., Ltd.
*28 Ishikawajima-Harima Heavy Ind. Co., Ltd.
*29 Kishikawa Special Valve Co., Ltd.
*30 Mitsui Engineering & Shipbuilding Co.

*31 Japan Information Service Ltd.
*32 Nuclear Data Corporation
*33 Nuclear Energy Data Center
*34 Nippon Steel Co.
*35 Hazama-Gumi, Ltd.
*36 Kanazawa Computer Service
*37 Sumitomo Electric Ind. Ltd.
*38 Nihon Software Kaihatsu Inc.
*39 IBS DATA Center Corporation
*40 Denki Kogyo Ltd.
*41 RCA David Darnoff Research Center
*42 Ryojyu Environment Physical Engineering Co., Ltd.
*43 System Co., Ltd.
*44 Hitachi Setsubi Engineering Co., Ltd.
*45 Fuji Facom Corp.
*46 TRW
*47 McDonnel Douglas Astronautics Co.
*48 Kawasaki Steel Corporation
*49 Mitsubishi Electric Computer Systems Tokyo Co., Ltd.
*50 Computer Services Corporation
*51 Koike Sanso Kogyo Co., Ltd.
*52 Nippon Record Management Co.

A.3 Budget of the Establishment

	FY1984[*1]	FY1985[*1]	FY1986[*1]
JT-60 Construction[*2]	28,346	31,570	31,412
Research & Development[*3]	3,058	3,921	2,746
Japan-US Cooperation	1,672	914	507
Site Construction	1,199	972	390

(Unit: Million ¥)

*1 From April to March

*2 Including cashing of the financial obligation in each FY

*3 Excluding fusion-related R&D in other divisions than the Establishment